

5. SITE 799¹

Shipboard Scientific Party²

HOLE 799A

Date occupied: 14 September 1989
Date departed: 18 September 1989
Time on hole: 5 days, 3 hr, 24 min
Position: 39°22.046'N, 133°86.685'E
Bottom felt (rig floor; m, drill-pipe measurement): 2984.8
Distance between rig floor and sea level (m): 11.8
Water depth (rig floor, m): 2073.0
Total depth (rig floor, m): 2552.7
Penetration (m): 468.7
Number of cores: 52
Total length of cored section (m): 468.7
Total core recovered (m): 440.0
Core recovery (%): 93
Oldest sediment cored:
Depth (mbsf): 468.7
Nature: siliceous claystone
Age: Miocene(?)
Measured velocity (km/s): 3.11

HOLE 799B

Date occupied: ^a19 September 1989 2 October 1989
Date departed: ^a21 September 1989 11 October 1989
Time on hole: 12 days, 9 hr, 54 min
Position: 39°22.048'N, 133°86.645'E
Bottom felt (rig floor, m; drill-pipe measurement): 2083.5
Distance between rig floor and sea level (m): 11.8
Water depth (drill-pipe measurement from sea level, m): 2071.7
Total depth (rig floor, m): 3167.5
Penetration (m): 1084.0
Number of cores: 67
Total length of cored section (m): 633.0
Total core recovered (m): 280.5
Core recovery (%): 44
Oldest sediment cored:
Depth (mbsf): 1084.0
Nature: siliceous claystone
Age: early Miocene
Measured velocity (km/s): 2.44
Comments: ^aDrilling in this hole was conducted during two visits (see text).

HOLE 799C

Date occupied: 12 October 1989
Date departed: 12 October 1989
Time on hole: 14 hr, 10 min
Position: 39°22.0'N, 133°86.666'E
Bottom felt (rig floor, m; drill-pipe measurement): 2083.5
Distance between rig floor and sea level (m): 11.8
Water depth (drill-pipe measurement from sea level, m): 2071.7
Total depth (rig floor, m): 2336.0
Penetration (m): 252.5
Number of cores: 3
Total length of cored section (m): 22.5
Total core recovered (m): 23.9
Core recovery (%): 106
Oldest sediment cored:
Depth (mbsf): 252.5
Nature: diatom clayey mixed sediment
Comments: This was a "dedicated" hole to test the sonic core monitor.

Principal results: Our objectives at Site 799, located in the Kita-Yamato Trough were (1) to determine the depositional and tectonic history of the trough as a sedimented failed-rift environment thought to be ideal or typical for the occurrence of volcanogenic massive sulfide deposits of the Kuroko or perhaps shale-hosted type and (2) to obtain information about the paleoceanographic history of the Yamato Rise area and the Sea of Japan as a whole. Results at Site 799 are summarized below, and a stratigraphic summary is presented in Figure 1.

1. Before drilling, seismic estimates of the thickness of sediment in the Kita-Yamato Trough indicated up to 1300 m of Miocene to Holocene sediments might be present in the axis of this narrow graben structure. Drilling in the trough, we penetrated 1084 m of lower Miocene through Holocene sediments before an increase in hydrocarbon gases and a fluorescent cut forced us to stop drilling. Post-drilling vertical seismic profile (VSP) analysis indicated that acoustic basement was present about 120 m below the base of Hole 799B (1084 mbsf T.D.), indicating a total sediment thickness of about 1200 m.

2. The sedimentary column at Site 799 can be divided into five lithologic units that correspond to variations in composition and depositional style and major post-depositional diagenetic changes. Benthic foraminifers indicate that the entire sediment column at Site 799 was deposited at lower to middle bathyal water depths that were approximately equivalent to the present-day water depth at this site (2084 m). Coarse turbidite sands mark early Miocene deposition in the trough area and indicate close proximity to an insular or continental littoral area and associated terrestrial environments. Middle and upper Miocene intervals are dominated by siliceous claystones, porcellanites, and biosiliceous sediments that include common authigenic carbonate layers and nodules, indicating high surface productivity of both siliceous and calcareous plankton during this period. Significant thicknesses of Miocene laminated sediments rich in

¹ Ingle, J. C., Jr., Suyehiro, K., von Breymann, M. T., et al., 1990. *Proc. ODP, Init. Repts.*, 128: College Station, TX (Ocean Drilling Program).

² Shipboard Scientific Party is as given in list of participants preceding the contents.

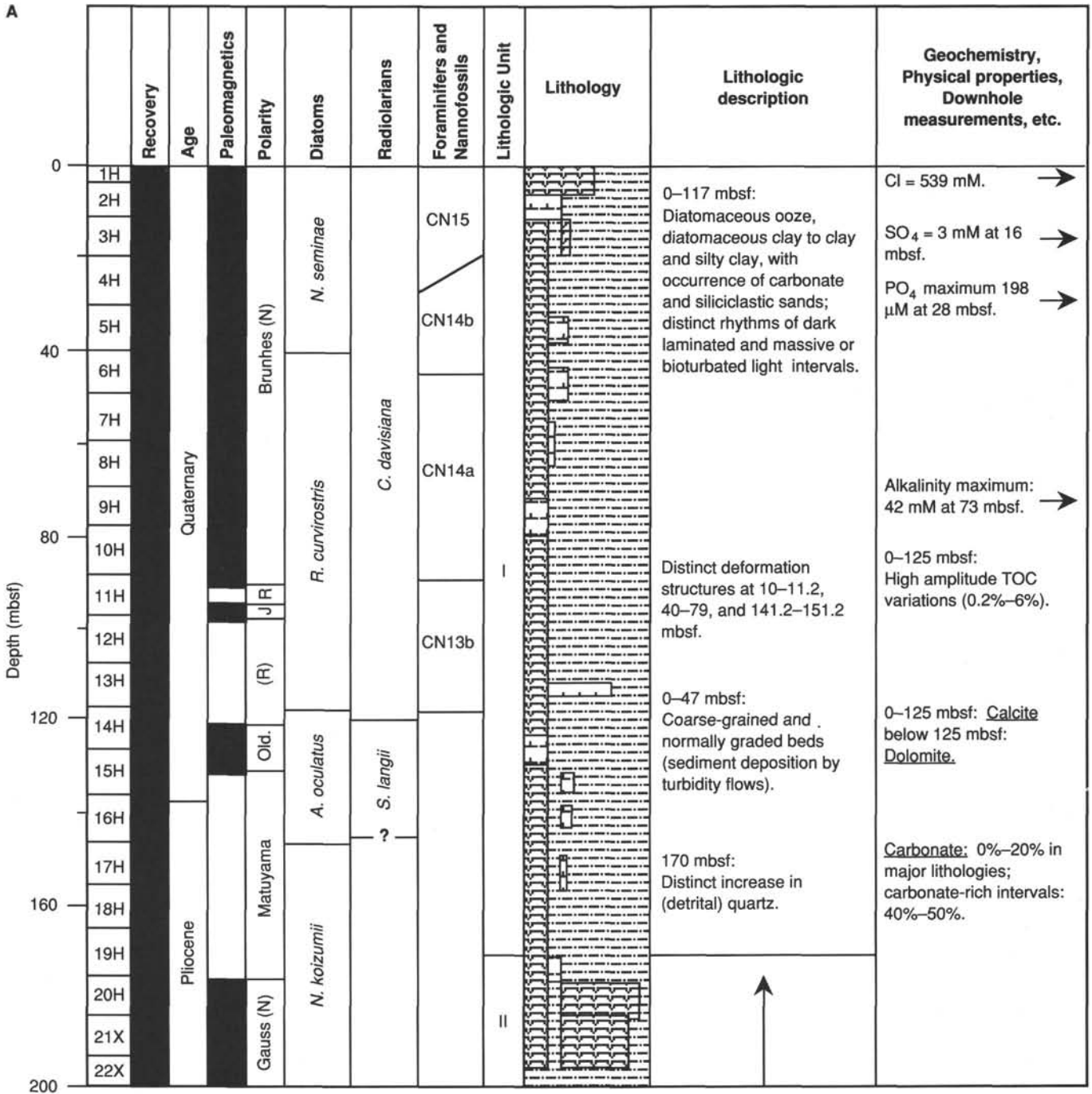


Figure 1. A. Summary of stratigraphy for Hole 799A. B. Stratigraphy for Hole 799B.

organic matter indicate episodic deposition under low-oxygen bottom-water masses. Lower Pliocene sediments are rich in diatoms, with higher amounts of fine-grained terrigenous sediment appearing in late Pliocene through Pleistocene time, accompanied by slump deposits, redeposited foraminiferal sands, and volcanic ashes. There are hints of a causal relationship between the appearance of the slump deposits and the occurrence of volcanic ashes.

3. The opal-A/opal-CT transition occurs at about 435 mbsf and forms a major lithologic and geochemical boundary with the opal-CT/authigenic quartz transition that occurs between 545 and

585 mbsf. These diagenetically altered sediments are manifestations of the common to abundant deposition of biosiliceous sediments in the Site 799 area that began in the early Miocene and continued through the Pleistocene. The biocarbonate fraction also experienced rapid alteration with depth, with abundant dolomite beds and nodules present below 220 mbsf.

4. Most of the sediments within the Site 799 column contain abundant organic carbon (0.25%-5.66%), which reflects both high productivity in the Yamato Rise area and episodic periods of enhanced preservation resulting from oxygen-deficient bottom water. This is emphasized by thick intervals of laminated middle

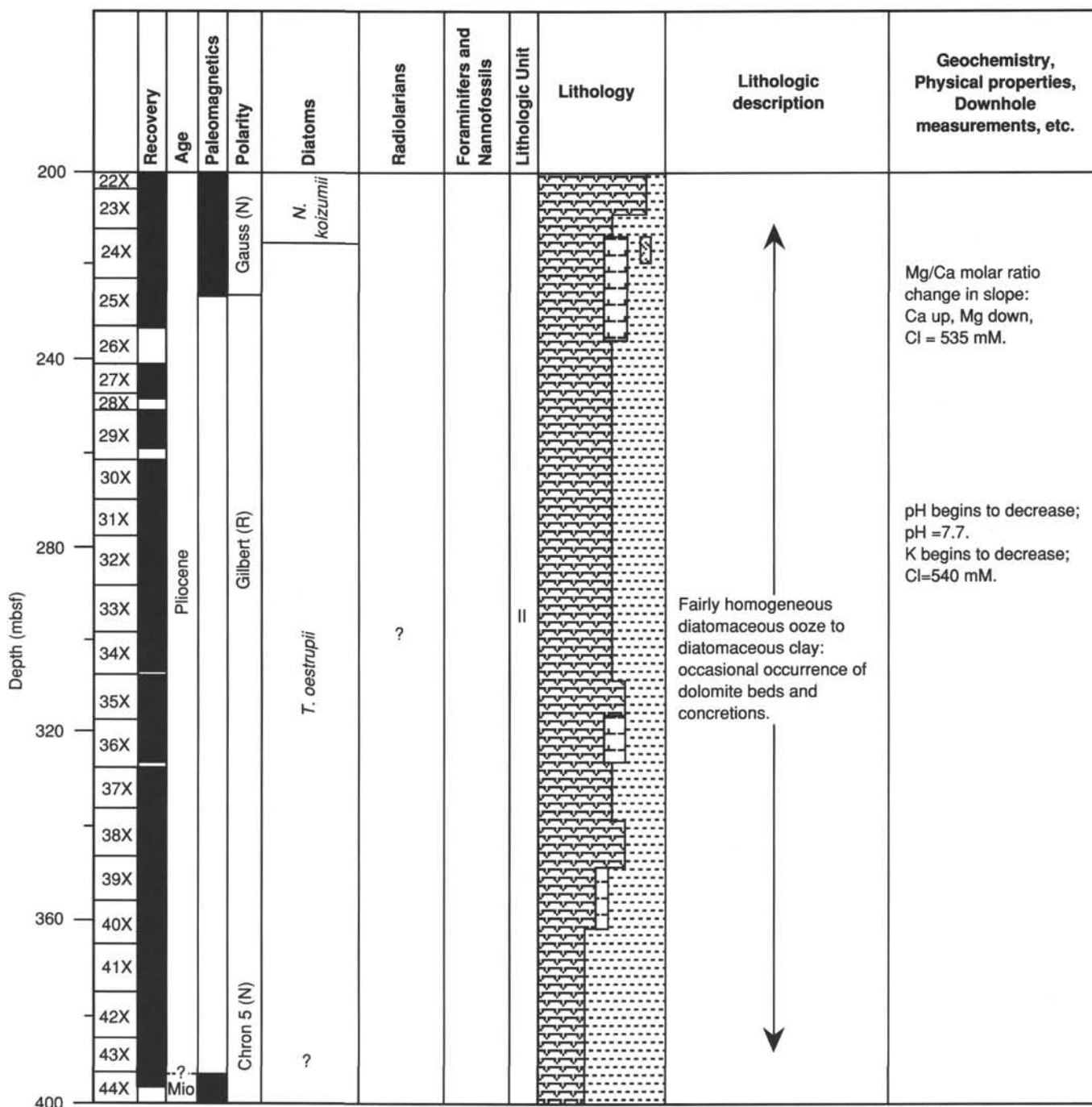


Figure 1 (continued).

and upper Miocene sediments. Significantly, terrigenous organic matter is an important component in the rapidly deposited lower Miocene turbidite units at the base of this sequence.

5. Rough estimates of the subsidence in the Kita-Yamato Trough sequence suggest that differential subsidence may account for the 1200 m of sediment filling the trough. Both sedimentary and structural evidence point to episodic extensional tectonism in this area.

6. Although we did not encounter any direct evidence of massive sulfide deposition or metalliferous hydrothermal deposits at Site 799 (we did not expect to encounter any sulfide

deposits, even if they exist in the trough, because of the statistically low chance of penetrating such a small mass), the middle and lower Miocene portion of the column includes lithologies correlative with those found associated with the Kuroko failed-rift massive sulfide deposits of northern Honshu (Dajima and Nishikurosawa formations). Other lithologies analogous to the Kuroko deposits include a 24-m-thick, altered, rhyolite tuff and tuff breccia in the lower Miocene interval of Hole 799B. After analysis, a post-drilling seismic reflection survey of the Kita-Yamato Trough will permit us to place Site 799 in a detailed structural context, which will enhance the value

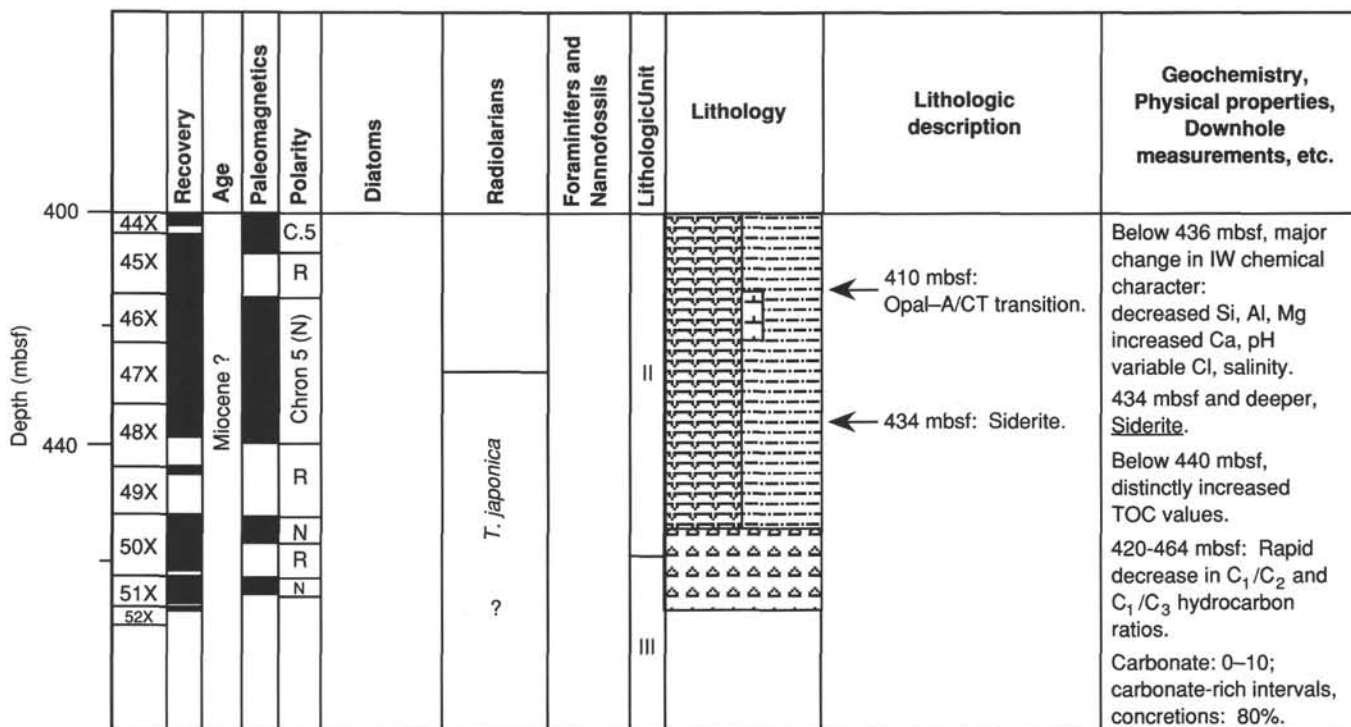


Figure 1 (continued).

of this site for characterizing the failed-rift back-arc environment.

Location and Approach

Site 799 (proposed Site J2a1) is located in the southern Kita-Yamato Trough, a narrow topographic and structural depression that splits the larger Yamato Rise in the south central Sea of Japan. This site was confirmed by two *JOIDES Resolution* seismic lines. One of which, Line 128-3, crossed the site along the track of JNOC multichannel reflection Line 13-4, which was originally used to locate proposed Site J2a-1. A beacon was dropped at a location equivalent to shot point 7120 on JNOC Line 13-4, the exact location originally chosen for proposed J2a-1.

Lithology

Drilling at Site 799 penetrated 1084 m of lower Miocene through Holocene sediments. Dominant lithologies within the 468.7 m of upper Miocene to Holocene sediments cored in Hole 799A include biosiliceous sediments and fine-grained detrital sediments intercalated with carbonate-rich intervals. The Hole 799B sequence consists of 633 m of lower Miocene through upper Miocene, diagenetically altered, biosiliceous sediments; diagenetic carbonates; sandstones; and a prominent, 24-m-thick, altered rhyolitic tuff; and tuff breccia.

Authigenic carbonates are abundant in the Site 799 sequence, with dolomite as the dominant phase. More than 200 intervals of dolomite nodules, layers, and beds were recovered in cores, while many more unsampled horizons were detected by logging (see "Downhole Measurements" section, this chapter). Biogenic calcite is largely restricted to the upper 125 m of the section, with the final smear slide observation of foraminiferal test debris made at 345.9 mbsf.

Biosiliceous sediments form a major component in many intervals within Holes 799A and 799B, with an unusually clear record of silica diagenesis present with depth. The transformation of biogenic opal-A to opal-CT occurs within the interval from 410 to 460 mbsf, with XRD data and visual observations indicating a

major change at 457 mbsf; only traces of original biogenic silica occur below this depth. The opal-A/opal-CT boundary constitutes a major lithologic and geochemical boundary at Site 799 and has a pronounced increase in density and state of lithification below this horizon.

During drilling in Hole 799A, we recovered 198 individual ash layers that were deposited during late Miocene through Holocene time. Alternatively, only 25 ash layers were recovered in Hole 799B between 450 to 1084 mbsf, although a major unit of rhyolitic tuff and tuff breccia is present in lithologic Unit IV. All of the volcanic products are air-fall pyroclastic, including crystal-rich layers. The Pliocene and Quaternary ash record is enhanced by logging data at Site 799, with a major pulse of volcanic activity indicated for the late Pleistocene (1.3–0.6 Ma). By analyzing the ashes at Site 799, we recognized 10 different phases in volcanic activity from early Miocene through Holocene time.

The sedimentary column at Site 799 was divided into five lithologic units on the basis of shipboard analysis of lithologic composition and variability, sedimentary structures, and diagenetic alteration as follows:

Unit I (0–170 mbsf; Quaternary to late Pliocene) is composed of diatomaceous clay and ooze, diatomaceous clayey mixed sediment, clay, clayey silt, silty clay, silt, and vitric ash layers. Diatoms, sponge spicules, silicoflagellates, and radiolarians form the biosiliceous component in this unit. Foraminifer-rich sediments, including oozes are limited to thin beds and laminae in the upper 90 m, with calcareous nannofossils and foraminifers showing progressive alteration and overgrowths below 110 mbsf. Dolomite occurs as shallow as 12.7 mbsf, and authigenic carbonate is commonly observed below 100 mbsf. Siliciclastic sands are a minor but conspicuous lithology in Unit I. These sands are compositionally immature and are restricted to the upper 34 m of the section. Maximum abundances of terrigenous components occur between 0 and 50 mbsf and from 105 to 150 mbsf. Unit I displays both thickly bedded and laminated intervals. Although distinctive light/dark rhythms occur in the upper 117 m, these are not equivalent in origin and cannot be uniformly attributed to

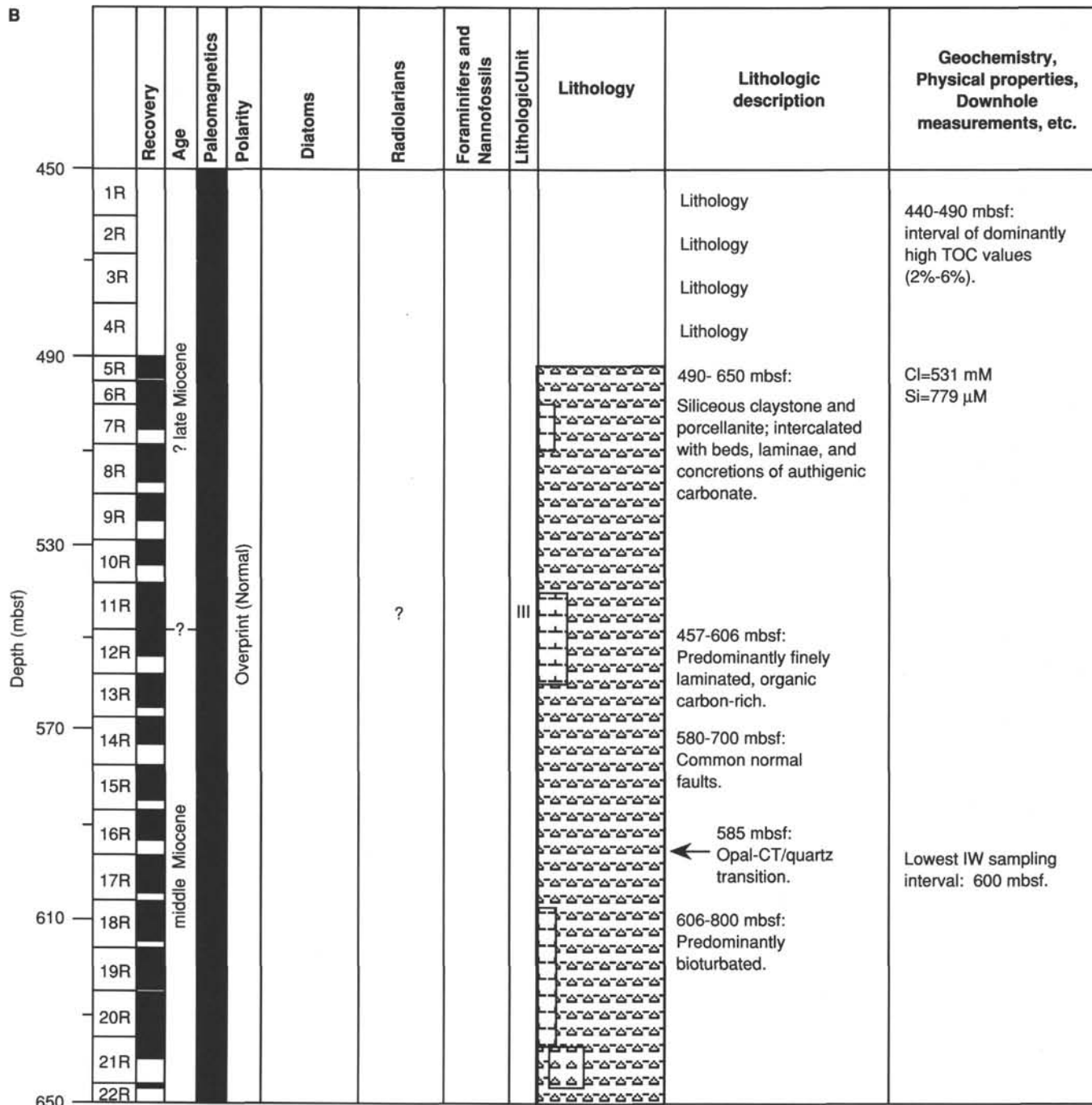


Figure 1 (continued).

paleoceanographic-paleoclimate cycles. Soft sediment deformation is a common feature in Unit I, with harmonic and disharmonic folding and sediment detachment observed. Evidence of debris flows also is present. Coarse-grained and normally graded beds mark turbidite units, which include siliciclastic, foraminiferal, and volcanoclastic-rich sands. Bioturbation also is common in Unit I.

Unit II (170–457 mbsf; late Pliocene to late Miocene) is made up of diatomaceous ooze, clayey diatomaceous ooze, clayey diatomaceous mixed sediment, and diatomaceous mixed clay. Nannofossil- and carbonate-rich sediments and sediments rich in sponge spicules occur as minor lithology throughout Unit II.

Sediments in Unit II contain more abundant biosilica and less abundant terrigenous detritus and vitric ash layers compared with Unit I. Biosiliceous sediments dominated by diatoms are the most abundant component in Unit II. Dolomite beds and concretions are prominent between 247.0 and 394.6 mbsf; these deposits commonly preserve primary sedimentary structures. Carbonate also occurs as chalky layers, probably representing former foraminiferal and/or nannofossil-rich layers. An isolated but important 2-cm-thick glauconite sand occurs at 374.2 mbsf. The top of Unit II (170 mbsf) marks the deepest occurrence of the light/dark rhythmic sedimentation common in Unit I. In contrast, Unit II is

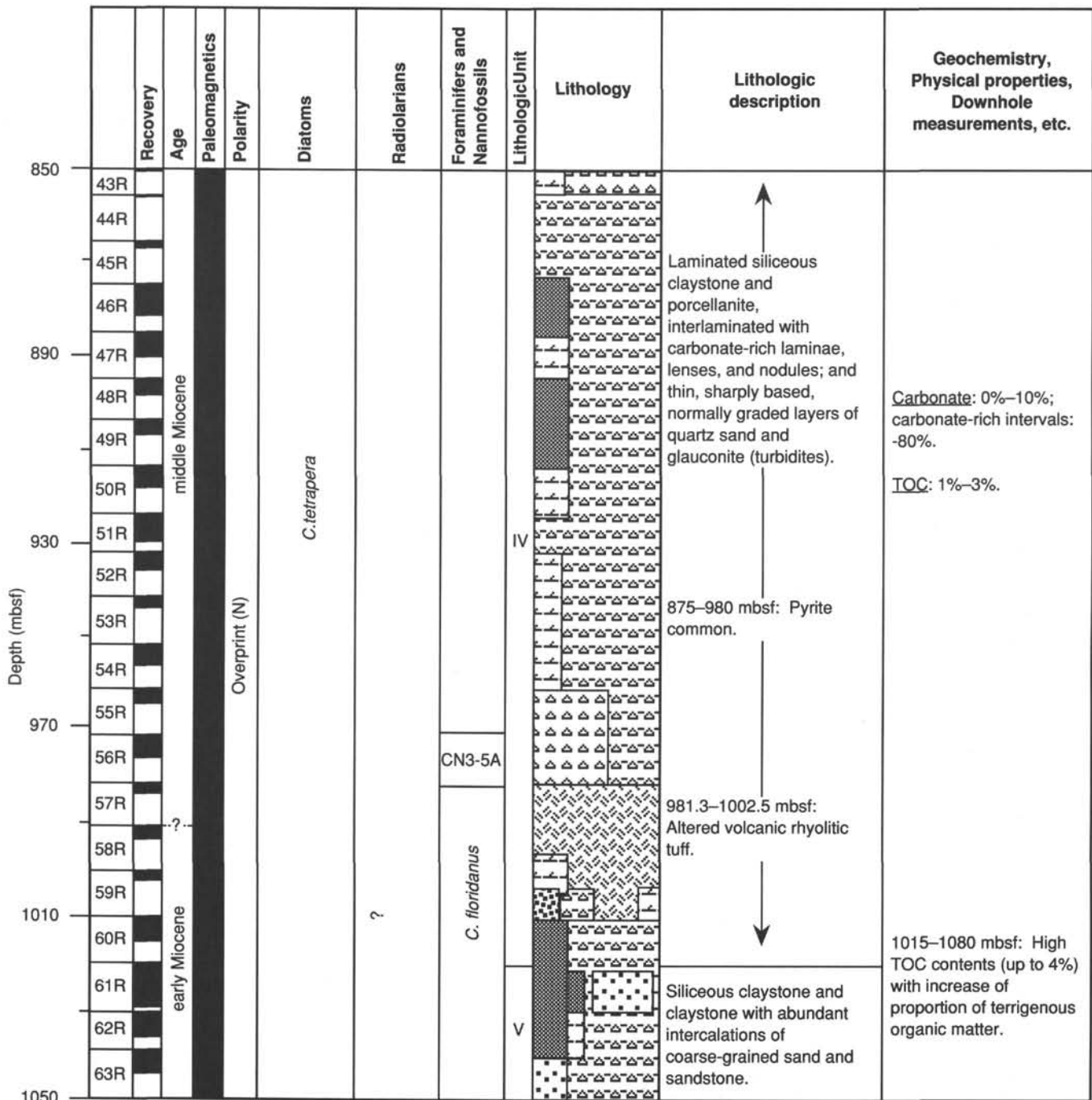


Figure 1 (continued).

of dominantly dolomitic composition, as well as thin normally graded quartz silts, sands, and glauconitic sands. The siliciclastic beds in Unit IV range from 1 mm to 30 cm thick and collectively have been interpreted as distal turbidite deposits. Pyrite is common between 875 and 980 mbsf, occurs within concretions, and is disseminated in the silt-size fraction. An important and prominent altered rhyolitic tuff and tuff breccia is present between 990.8 and 991.3 mbsf. Logging data (see "Downhole Measurements" section, this chapter) indicate that the rhyolitic unit includes at least three discrete depositional units.

Unit V (1020–1084 mbsf; early Miocene) is composed of siliceous claystone and claystone with silt, including abundant intercalated and coarse-grained sand and sandstones. Siliciclastic turbidites are the most conspicuous lithology in Unit V. Immature sands dominate these beds, which have an average thickness of 1 cm, but reach a maximum thickness of 5 m. Individual sand units display normal grading, cross laminations, sharp bases with load casts, and other evidence of gravity-driven flow and redeposition, including displaced shallow water benthic foraminifers, calcareous shell debris, and common terrestrial plant debris. Granule and

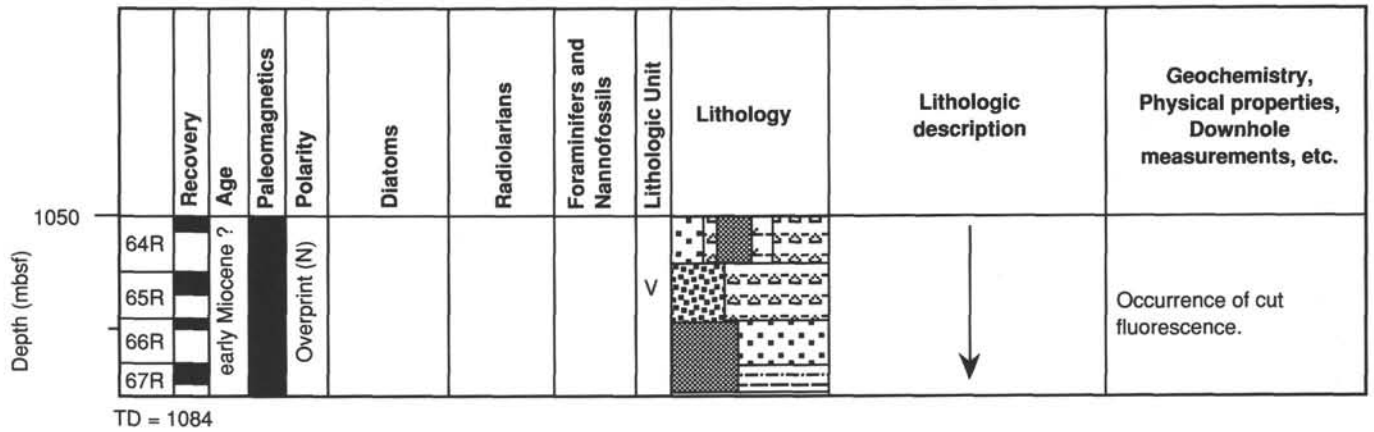


Figure 1 (continued).

pebble-sized rock fragments are present in coarser sand units, along with glauconite, angular quartz, feldspar, biotite, pyrite, and dark lithic fragments. Interbedded siliceous claystones within Unit V contain bathyal *in-situ* benthic foraminifers, indicative of water depths between 1500 and 2000 m or deeper (see "Biostratigraphy" section, this chapter).

Age and Sedimentation Rates

Microfossils are common in the uppermost portion of the sequence at Site 799, but are generally scarce to absent in the majority of the column as a result of diagenesis of both biogenic calcite and silica with depth. In turn, these conditions severely limit biostratigraphic age assignments within lower upper Miocene through lower Miocene sediments. Similarly, polarity transitions are clearly recognized within the Pleistocene and Pliocene and perhaps the uppermost Miocene portions of the column. However, overprinting and other problems prevented recognition of older paleomagnetic events and, in turn, the dating of these sediments.

In general, planktonic foraminifers and calcareous nannofossils are most abundant and best preserved within Quaternary sediments to about 100 mbsf, with only scattered occurrences in Pliocene and Miocene sediments. Consequently, siliceous microfossils, including diatoms, silicoflagellates, and isolated occurrences of identifiable radiolarians and calcareous nannofossils, provide irregular biostratigraphic control in the bulk of the Site 799 sequence. All microfossil groups are generally rare to absent in sediments and rocks below the opal-A/opal-CT diagenetic boundary at 457 mbsf.

Sediment ages are well constrained by diatom zones and calcareous nannofossils in lithologic Unit I, while diatoms and silicoflagellates provide reliable ages in the upper portion of Unit II. Only isolated occurrences of identifiable radiolarians provide age control in the lower part of Unit II and the upper part of Unit IV. Likewise, isolated occurrences of identifiable calcareous nannofossils allow for tentative zonal assignments for limited intervals in Unit III and the base of Unit IV. A calcareous nannofossil flora at 981 mbsf provides the oldest date in the Site 799 column and suggests that these sediments are early Miocene in age (Zone CN4), although the species present also permit the interpretation of an early middle Miocene age. A re-crystallized radiolarian assemblage at 904 mbsf contains *Didymocyrtis mam-mifera* and *Lithopera renza* and also indicates an early Miocene age for the lower part of Unit IV.

Three microfossil datum levels and nine magnetic reversals constrain estimated rates of sedimentation in Quaternary through upper Miocene sediments at Site 799 (0–about 440 mbsf). Sedimentation rates vary within this interval between 15

and 175 m/m.y., with an average rate of about 70 m/m.y. Highest rates occur in upper Pleistocene sediments, whereas below average rates occur in the Pliocene. Calculated accumulation rates vary between 14 and 1.6 g/cm²/k.y.

Inorganic Geochemistry

Based on concentration gradients of interstitial water, the Site 799 column may be divided into four intervals: Interval I (0–44 mbsf), influenced mainly by early diagenesis processes that coincide with intense sulfate reduction; Interval II (44–220 mbsf), marked by compositions that reflect decomposition of organic matter and recrystallization reactions of biogenic carbonate; Interval III (220–435 mbsf), in which the composition of interstitial water is influenced by silica dissolution, dolomitization, and crystallization of clay minerals; and Interval IV (435 mbsf and deeper), marked by interstitial water strongly influenced by a sink for silica, potassium, magnesium, and chlorinity and a source for lithium. The geochemical character of the pore fluids in this interval suggest that at least two different fluid sources may influence this interstitial water mass.

The pronounced lithologic boundary associated with the top of the opal-A/opal-CT transition zone clearly acts as a major barrier to interchange or interstitial waters above and below this zone. Water in sediments above this boundary exhibit normal diagenetic exchange reaction profiles. Below the boundary, waters reflect influence from other sources and sinks, with evidence pointing to advection as a major process that affected the chemical character of these waters. Altered rhyolites in the lower portion of the Site 799 sequence provide evidence that basement alteration is influencing the composition of pore fluids, leading to consumption of magnesium and the addition of calcium to the water. The presence of thick sands in the basal part of Hole 799B might allow for migration of fluids from distant sources, perhaps including relict Neogene fresh or brackish water.

Organic Geochemistry

Sediments at Site 799 contain large amounts of hydrocarbon gases, with methane concentrations ranging from 14 to 155,000 ppm, whereas ethane and propane concentrations range from below detection levels to 2693 and 1476 ppm, respectively. The ratios of methane to higher hydrocarbons decrease gradually with depth to 420 mbsf, where C₁/C₂ decreases rapidly from 900 to 300. These ratios then decrease slowly to 1059 mbsf, where the abundances of propane, *i*-butane, and *n*-butane increase rapidly. Special precautions were taken when analyzing gases from below 450 mbsf in the laboratory. Headspace samples from Cores 128-799B-65X and 128-799B-66X exhibited a slow cut fluorescence and an amber residual cut. These same samples

yielded large amounts of ethane, propane, and butane; prompted by these observations, drilling was halted at 1084 mbsf.

Sediments present at Site 799 contain abundant organic matter, with total organic carbon (TOC) values ranging from 0.24% to 5.66%. Calcium carbonate contents ranged from 0.25% to 79.8% with highest carbonate contents in Units I and II. Unit III contains little carbonate, but has abundant organic carbon, reflecting the common presence of laminated sediments between 457 to 606 mbsf, which indicates an anoxic-suboxic depositional setting. Older bioturbated intervals in Unit II contain less organic carbon, with similarly low values found in Unit IV. Unit V, although characterized by coarse-grained siliciclastic deposits, is richer in organic carbon than Unit IV and exhibits high C/N ratios.

These various patterns indicate that Site 799 sediments are the product of enhanced deposition and/or preservation of organic matter, which in turn may represent a response to high primary productivity, low-oxygen bottom water, rapid burial, or high influxes of terrigenous organic matter. Shipboard data indicate that the majority of organic matter in Site 799 sediments is of marine origin. However, sediments exhibiting the highest TOC values in Unit V are dominated by terrestrial organic matter, probably representing a response to rapid burial via turbidite deposition and close proximity to a source of this material.

Seismic Stratigraphy

Distinct seismic layers are discernible from single-channel records that cross the Kita-Yamato Trough. Four groups of reflection surfaces and groups of reflectors can be recognized from a processed JNOC multichannel seismic reflection profile originally used to locate Site 799. Specifically, the seismic intervals seen in records in the vicinity of Site 799 include (1) an uppermost reflective and well-stratified layer that parallels the shape of the ocean bottom and that represents Quaternary and upper Pliocene terrigenous-rich sediments, (2) a second, relatively transparent, layer representing Pliocene and upper Miocene diatomaceous sediments, (3) a more opaque interval representing highly reflective Miocene sediments below the opal-A/opal-CT transition, (4) a fourth interval marked by a band of strong reflectors thought to correspond to dolomite horizons, and (5) a fifth layer of moderate reflectivity representing lower Miocene sandy units. Signal penetration of the 3.5-kHz record across Site 799 is only 35 mbsf, but this record clearly shows slump structures on the flanks of the Kita-Yamato Trough that can be correlated with the sediment record at this site (see "Lithostratigraphy" section, this chapter).

Of special interest is the velocity log at Site 799, which exhibits a large spike correlative with the density changes associated with the opal-A/opal-CT boundary near 440 mbsf.

Logging

Four tool strings were run successfully in Holes 799A and 799B that included seismic stratigraphy, the formation micro-canner (FMS), and lithoporosity and geochemical tool combinations. In addition, the Lamont-Doherty Geological Observatory's temperature tool (TLT) was added to the base of these tool strings. The Barnes/Uyeda temperature probe was deployed eight times during APC coring in Hole 799A. Finally, a vertical seismic profiling (VSP) experiment was conducted after completing Hole 799B. VSP results indicate that acoustic "basement" rocks are located only 120 m below the base of Hole 799B (T.D. = 1084 mbsf). The quality of logs at Site 799 is generally excellent; however, a minor degree of processing will probably be performed post-cruise.

Results of wireline logging permitted us to divide the lithologic sequence at Site 799 into six units. The most pronounced logging events or responses at this site were associated with resistant dolomite horizons in lithologic Unit IV. Logging detailed these various horizons in a continuous manner, supplementing variable core recovery through the dolomitic sediments. The geochemical tool was able to identify these horizons as calcium-rich confirming resistivity signatures. In addition, the FMS tool also imaged individual dolomite horizons with great clarity. The prominent

rhyolitic tuff and tuff breccia in Unit IV was fully detailed by the natural gamma-ray spectroscopy tool as a result of the high contents of thorium in these sediments and rocks. Finally, the FMS caliper measurements and imaging of dolomite layers yielded data bearing on the stress field in the Yamato Rise area and the dip of beds in the lower portion of the sequence.

BACKGROUND AND SCIENTIFIC OBJECTIVES

Location and Bathymetry

Site 799 is located in the Kita-Yamato Trough, a narrow, sediment-filled graben within the much larger Yamato Rise in the south central Sea of Japan (Fig. 2). The Yamato Rise constitutes the largest and most prominent bathymetric high in the Sea of Japan, excluding the shelves and plateaus that are contiguous with mainland areas. Viewed as a whole, this rise is an oval-shaped feature about 180 km wide and 400 km long, with an east-northeast orientation. The rise exhibits a maximum relief of 2764 m from the floor of the adjacent Japan Basin to its shallowest depths on Yamato Bank (Fig. 2). The Yamato Rise consists of four discrete bathymetric features, including the Kita-Yamato Trough, Kita-Yamato Bank, Yamato Bank, and Takuyo Bank. The crests of both Kita-Yamato and Yamato banks exhibit flat areas thought to represent wave-cut surfaces that were produced during Quaternary lowstands of sea level (Tamaki, 1988). The present-day water depths of the bank tops (<300 m) and the tilted nature of the Yamato Bank terrace suggest that portions of both banks subsided during Quaternary time.

Kita-Yamato Trough neatly divides the Yamato Rise in half and separates the two major banks forming the rise proper. The floor of the trough has an average water depth of about 2000 m, while the flanks of the trough rise 1500 m to the top of adjacent Yamato Bank. In detail, the sides of the trough present a nested configuration, with the bottom of the trough being narrow and steep. Kita-Yamato Trough trends east-northeast, parallel with the long dimension of the Yamato Rise and clearly following the structural grain of the rise (Fig. 2). The sides of the trough demark normal faults that bound the nested structure of this feature, which involves three subgrabens (Fig. 3). Significantly, the 2000-m isobath that outlines the Kita-Yamato Trough is closed, indicating that the depressed central area of the trough is not yet brim full of sediment or, more likely, that the ongoing rate of subsidence is greater than the rate of sediment accumulation in the trough.

Crustal Structure

Sonobuoy records reported by Ludwig et al. (1975) and a two-ship refraction profile of Murauchi (1966) provide the only available deep seismic information across the Yamato Rise, including the Kita-Yamato Trough and Site 799 (Figs. 3 through 5). Sonobuoy data were derived by deploying radio-sonobuoys during seismic-reflection profiling and by extending measurements through simultaneous detonation of explosive charges every 45 s or less. Sonobuoy Station 152 of Ludwig et al. (1975) was located immediately northeast of Site 799 in the Kita-Yamato Trough; it yielded a crustal velocity structure profile of interest for interpretation of the deep structures beneath this site (Fig. 5).

Available crustal velocity measurements directly beneath Yamato Rise do not extend deeper than 10 km (profile 2 of Murauchi, 1966) and hence do not define the crust/mantle boundary (Moho) in this area. However, Yoshii (1972) estimated that depth to the Moho beneath the rise is about 23 km,

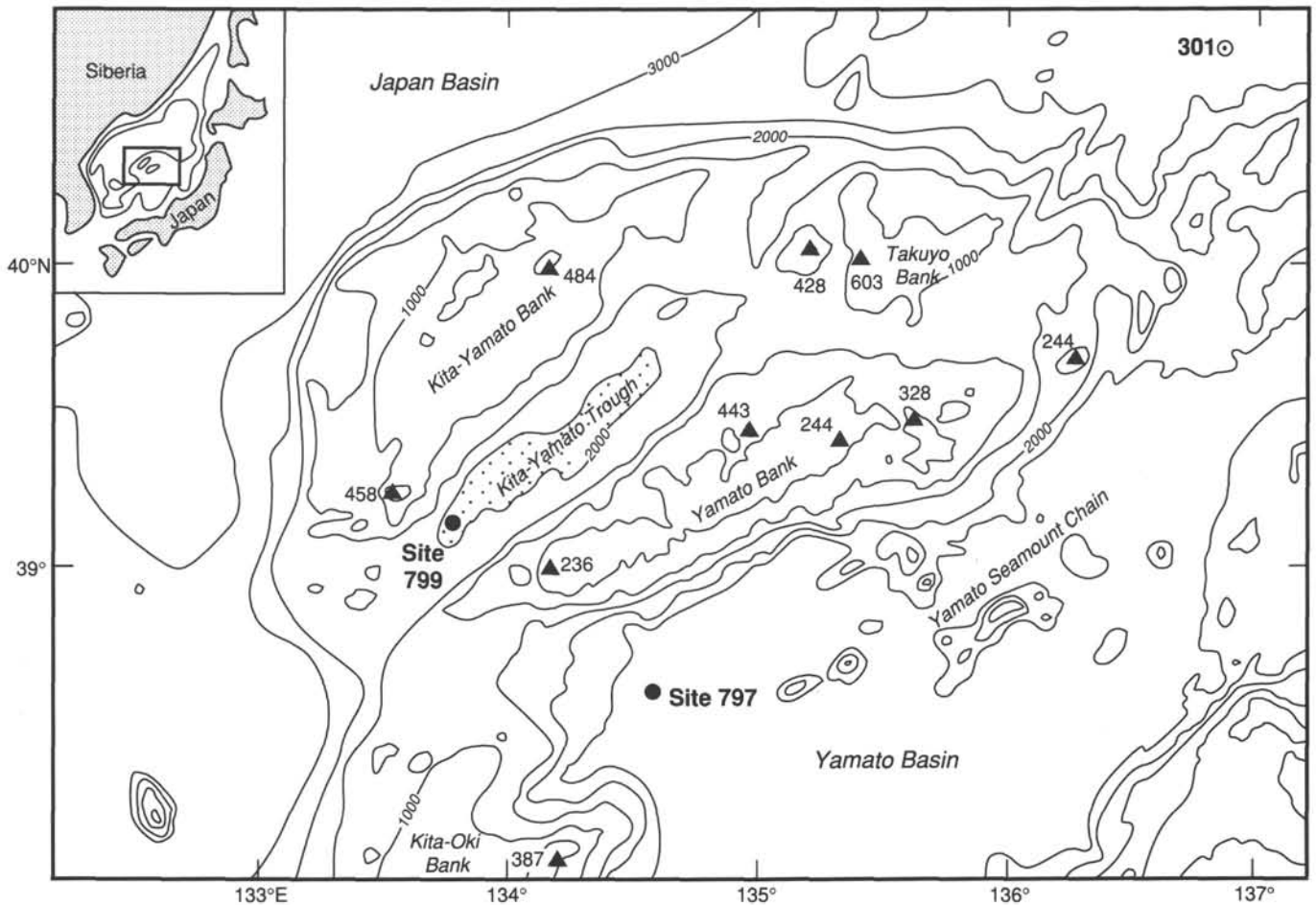


Figure 2. Bathymetric and location map of the Yamato Rise area and Site 799, south central Sea of Japan. Note that the Yamato Rise consists of four discrete features: Yamato Bank, Kita-Yamato Bank, Takuyo Bank, and Kita-Yamato Trough (emphasized by stippling). Shallowest areas on the rise are noted by triangles and associated water depths. Contour intervals in meters.

based on gravity data. More definitive data are available in basins adjacent to the Yamato Rise. Velocity measurements in the Japan Basin (Fig. 4) and the Yamato Basin (Figs. 3 and 4) demonstrate that mantle velocities beneath these areas range from 8.1 to 8.3 km/s, with the crust/mantle boundary at depths of 13 to 14 km below the seafloor in the Yamato Basin (Hirata et al., 1987) and 9 to 10 km in the Japan Basin.

As interpreted by Ludwig et al. (1975), the depth to the Moho beneath the Yamato Rise is much deeper than beneath basins on either side of the rise, although velocity profiles indicate that the thickness of the upper crustal layer ("Layer 2") remains relatively constant in the basin-rise-basin transect presented by these investigators (Fig. 3). In short, both available seismic data and gravity interpretations suggest that crust beneath the Yamato Rise approaches continental thickness (ca. 23 km), in line with the abundant evidence of granitic basement rocks beneath this feature. In contrast, velocity profiles beneath the adjacent basins indicate that crustal thickness beneath these areas apparently is near-oceanic in the Japan Basin (about 9 km) to transitional in the Yamato Basin (about 13–14 km).

Crustal structure above the Moho in the Yamato Rise area is defined by velocities of 6.7 to 6.8 km/s that mark the "lower crust." The top of this "lower crust" ("Layer 3" of Ludwig

et al., 1975) has been estimated to occur at a depth of about 6.5 km beneath the Kita-Yamato Trough (Figs. 3 and 4). A velocity range of 6.5 to 2.7 km/s defines the "upper crust" with this layer, which reaches a maximum thickness of 8 km directly under Yamato Bank (Fig. 4).

Crustal "Layer 1," representing unconsolidated and semi-consolidated sediments, has a velocity of 1.8 km/s at sonobuoy Station 152 in the Kita-Yamato Trough, where it is apparently 0.6 to 0.8 km thick (Fig. 4).

Heat Flow

Heat flow measurements on the Yamato Rise range between 55 and 128 mW/m² (Fig. 6). The average of six heat-flow measurements directly in the Kita-Yamato Trough is 90 mW/m². Heat flow over the rise as a whole is about 77 mW/m², which is significantly lower than the average value of 97 mW/m² for the adjacent Yamato Basin (M. Yamano, pers. comm., 1989), and than the higher values recorded in the Japan Basin to the west (Uyeda and Vacquier, 1968; Ludwig et al., 1975). The lower heat flow over the Yamato Rise is commensurate with the near-continental thickness of the crust beneath the rise. The intermediate heat-flow value in the Kita-Yamato Trough may possibly reflect a wedge of thinner crust beneath this rifted structure.

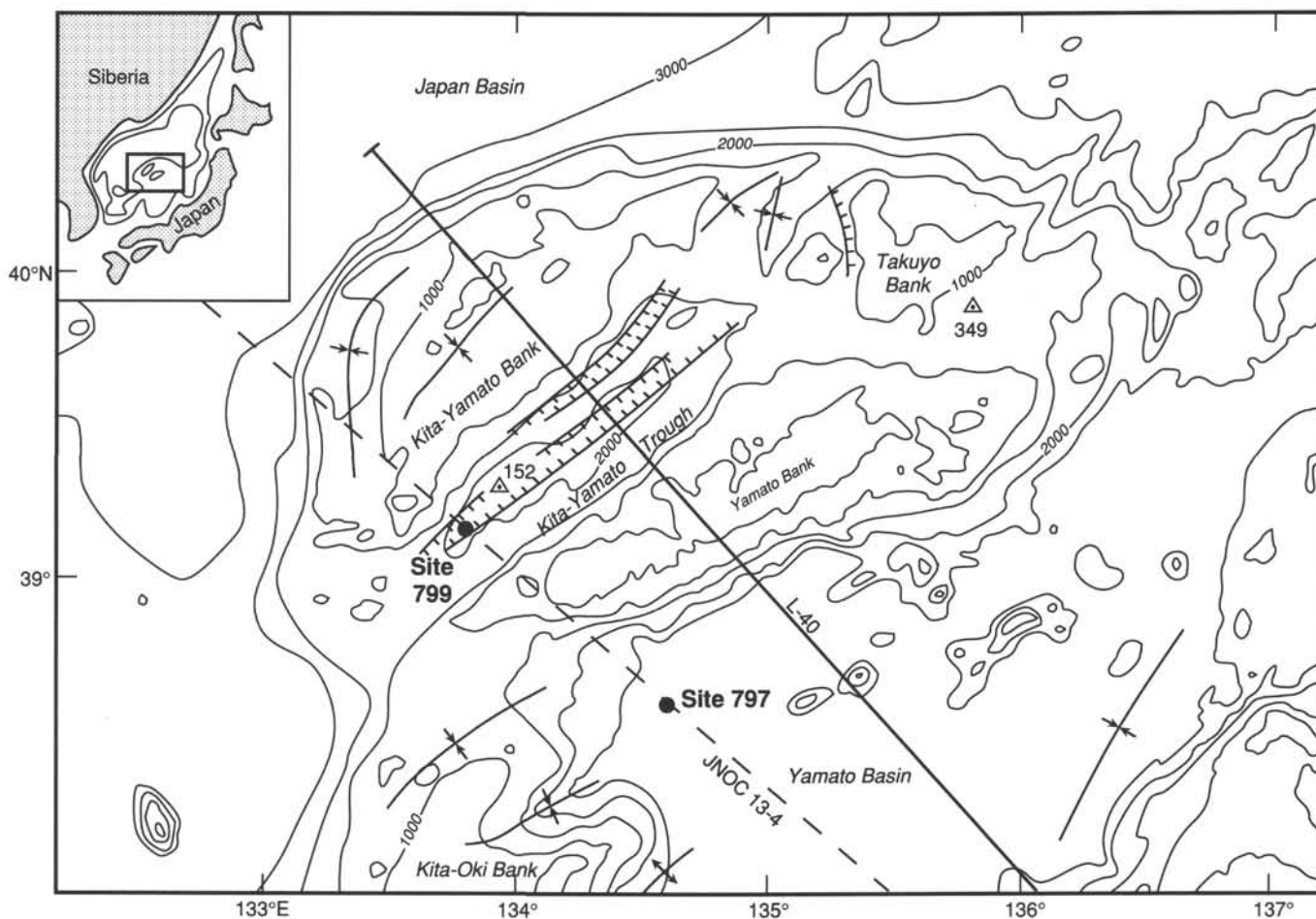


Figure 3. Location map of seismic-refraction sonobuoy Stations 152 and 349 of Ludwig et al. (1975), seismic-reflection profile L-40 of the Geological Survey of Japan (Tamaki, 1988), profile JNOC 13-4 of Japan National Oil Company (unpubl. data), and prominent folds and faults in the Yamato Rise area (mapped by Tamaki et al., 1981).

Magnetics and Gravity

The magnetic anomaly profiles available in the Yamato Rise area (Fig. 7) are typical of the mixed east-west patterns of high amplitude and long wave-length anomalies and low-amplitude, high-frequency anomalies typical of the ridge and bank areas in the eastern Sea of Japan (Miyazaki et al., 1979; Isezaki, 1986). Profile L-38 passing nearest Site 799 exhibits peak-to-peak amplitudes of 200 nT and wave lengths of about 50 km immediately adjacent to the site (Fig. 7). The general patterns of magnetic anomalies on Kita-Yamato and Yamato banks are dominated by short wave lengths and higher-than-average amplitudes, as noted by Miyazaki et al. (1979). The mixed character of anomaly patterns in this general area probably reflects differences in crustal structure and thickness between the Yamato Rise and adjacent basins.

Free-air gravity anomalies on and surrounding Yamato Rise range from 0 to more than 80 mgals (Fig. 8). Contours of gravity anomaly values clearly define topographic highs, with Yamato, Kita-Yamato, and Takuyo banks easily identified by contour patterns. Similarly, a significant gravity low outlines the Kita-Yamato Trough and Site 799, with anomalies reaching -20 mgals in the axis of the trough, reflecting the narrow but thick sediment fill in this structure.

Basement Rocks

The size and location of the Yamato Rise have attracted the attention of geologists and geophysicists for more than half a century, with some of the earliest marine geologic sampling in the Sea of Japan involving rocks collected from Yamato and Kita-Yamato banks (Tsuya, 1932; Niino, 1933, 1935). More intensive submarine sampling of the Yamato Rise began in the 1960s (e.g., Hoshino and Honma, 1966; Iwabuchi, 1968), with accelerated studies beginning simultaneously by the application of seismic reflection profiling and deep sea drilling in this area (e.g., Hotta, 1967; Shimazu, 1968; Milashin et al., 1968; Lelikov and Bersenev, 1973; Iwabuchi and Mogi, 1973; Hilde and Wageman, 1973; Vasiliev et al., 1975; Ludwig et al., 1975; Karig, Ingle, et al., 1975; Honza, 1979; Barash, 1986; Bersenev et al., 1987; and Tamaki, 1988). Dredges and cores on the Yamato Rise have recovered a wide variety of igneous and sedimentary rocks, as described by Honza (1979), Gribidenko (1979), Bersenev et al. (1987), and Tamaki (1988). Locations of key dredges and cores described by Burckle and Akiba (1978), Honza (1979), Yuasa et al. (1979), Barash (1986), and Tamaki (1988) are shown in Figure 9.

Seismic reflection profiles illustrate that rocks representing acoustic basement beneath the Yamato Rise are exposed on

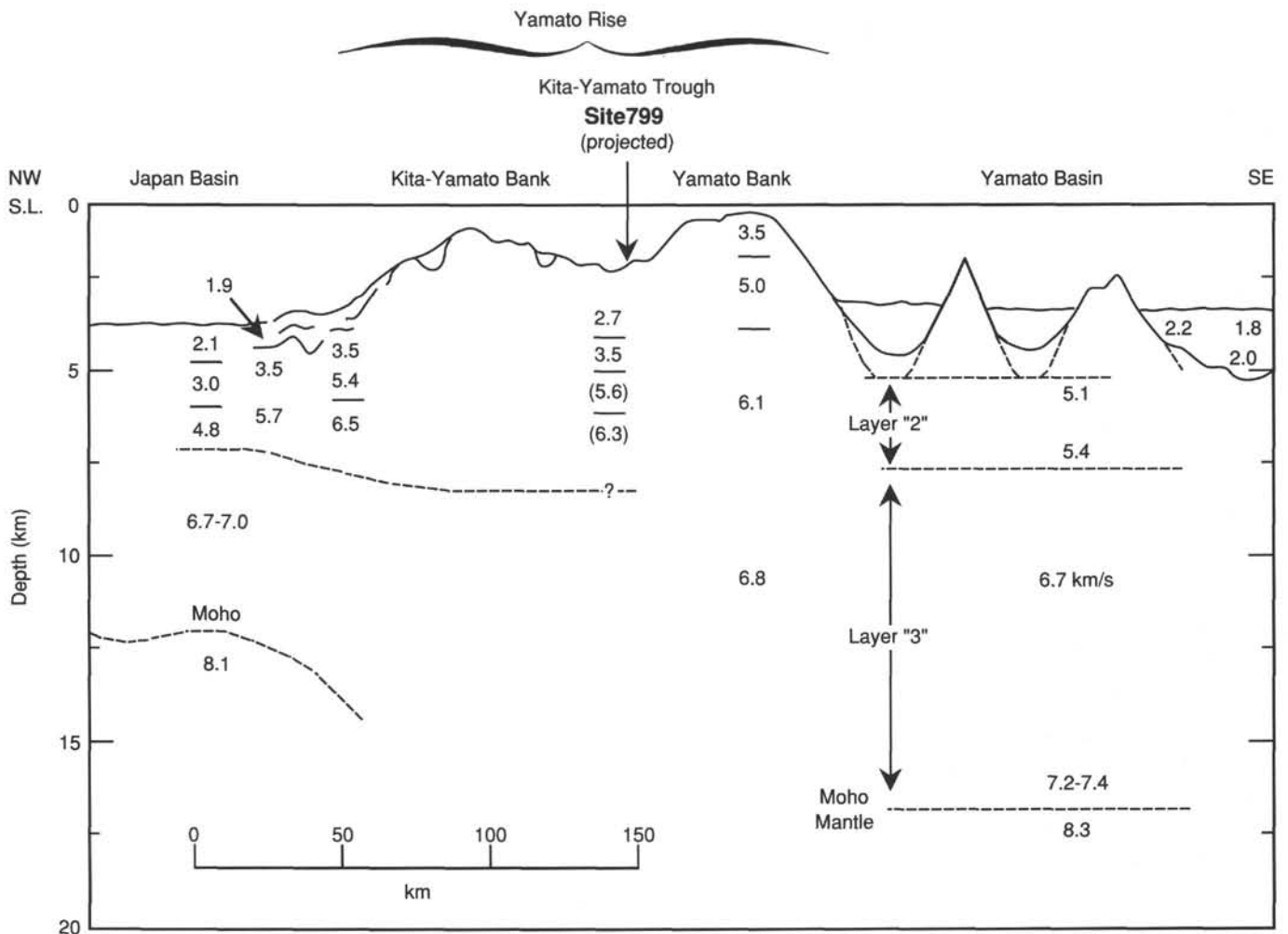


Figure 4. Crustal section beneath the Yamato Rise area, based on seismic-refraction data. This figure represents a portion of NW-SE profile E-F of Ludwig et al. (1975), modified to incorporate the data of Hirata et al. (1987) beneath the Yamato Basin.

the seafloor in many areas of the rise (Fig. 10). Numerous dredges have collected *in-situ* samples of these rocks, demonstrating that acoustic basement in this area consists of Mesozoic granitic rocks and overlying mid-Tertiary volcanic rocks.

Dredge hauls from Yamato and Kita-Yamato banks have repeatedly recovered transported and *in-situ* granitic rocks, while granite also has been reported from the eastern Takuyo Bank (Shimazu, 1968). Potassium-argon analyses of granites from the Yamato Rise have yielded dates that range from 110 to 310 Ma, spanning late Paleozoic through Early Cretaceous time (Tamaki, 1988). However, the majority of these granites have yielded Jurassic and Triassic ages that range from 128 to 220 Ma, including a granite of Triassic age from Takuyo Bank. The composition and dominant Mesozoic age of these rocks indicate that they are correlative with similar granites widely exposed around the rim of the Sea of Japan (Gnibidenko, 1979). The Mesozoic granites commonly intrude a variety of Precambrian and Paleozoic metamorphic rocks also exposed in Japan, Korea, and the U.S.S.R. These older metamorphic basement rocks also occur in the southern Sea of Japan near Ullung Do Island and on the Oki Islands (Lelikov and Bersenev, 1973; Geological Survey of Japan, 1982; Gnibidenko,

1979). Thus, acoustic basement beneath the Yamato Rise may possibly include pre-batholithic metamorphic rocks not currently exposed on the seafloor.

The distribution and character of granite samples collected on the Yamato Rise, together with seismic reflection patterns across this feature, indicate that Mesozoic granite is exposed over a large area of Kita-Yamato Bank and portions of Takuyo Bank (Tamaki et al., 1981; Tamaki, 1988) and forms the dominant basement rock under these two banks. In contrast, most rocks dredged from the Yamato Bank are volcanic or volcanoclastic, with only a small patch of *in-situ* granite mapped on the eastern flank of this feature by Tamaki et al. (1981). Dredge hauls that have sampled these latter rocks also have recovered basalts, rhyolites, and andesites, along with volcanoclastic breccias, tuff breccias, and ash (Honza, 1979). The majority of radiometric dates obtained from these volcanic rocks are Eocene-Oligocene to early Miocene (21–46 Ma), based on analyses by Shimazu (1968), Ueno et al. (1971), Vasiliev et al. (1975), and Gnibidenko (1979), although one basalt yielded a Late Cretaceous age of 76 Ma (Vasiliev et al. (1975).

It seems almost a certainty that most, if not all, of the *in-situ* volcanic rocks exposed over much of Yamato Bank

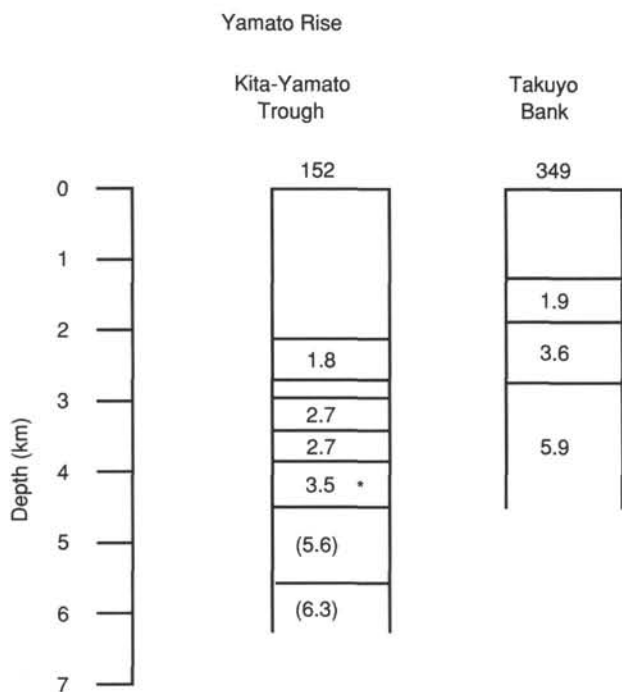


Figure 5. Profiles of crustal velocity structures at sonobuoy Stations 152 and 349 on the Yamato Rise, as presented by Ludwig et al. (1975). Velocities are in km/s. Parentheses indicate unreversed refraction measurements; asterisk denotes assumed velocity. See Figure 3 for location of sonobuoy stations.

and portions of Kita-Yamato and Takuyo banks are correlative with the so-called Oligocene-Miocene "Green Tuff" units of Honshu and that these volcanic units are in turn underlain by the Mesozoic granites forming the acoustic basement complex under the Yamato Rise.

Sedimentary Rocks

A number of dredges and cores from the Yamato Rise have recovered sedimentary rocks, including volcanoclastic rocks of probable Oligocene-Miocene age, marine shales, siltstones, and claystones of middle Miocene through Pliocene age, and semiconsolidated and unconsolidated sediments of Pliocene and Quaternary age (Ichikura and Ujiie, 1976; Burckle and Akiba, 1978; Kato, 1979; Koizumi, 1978, 1979, and 1988; Barash, 1986; Tamaki, 1988). In addition, drilling at DSDP Site 301 on the north flank of the Yamato Rise (Fig. 2) encountered diatomaceous sediments of early Pliocene age (Koizumi, 1978) and terrigenous clays, silts, and sands of Pliocene-Pleistocene age (Karig, Ingle, et al., 1975), with the older diatomaceous unit clearly overlying acoustic basement on the rise.

Two aspects of the Neogene sedimentary rocks dredged and cored from the Yamato Rise have unusual significance for the history of this area and for drilling at Site 799, including (1) Miocene phosphorites and phosphatic sediments (Barash, 1986) and (2) Miocene freshwater diatomaceous sediments and littoral/subaerial sands (Burckle and Akiba, 1978; Tsoy et al., 1985; Barash, 1986; Koizumi, 1988).

Upper Miocene phosphatic sediments were reported in Sample 3111 (Fig. 9), collected by Soviet scientists from the northwest flank of Kita-Yamato Bank. Sediments and microfossils in this sample are thought to represent shelf to slope

deposits of late Miocene age indicative of vigorous upwelling during this period (Barash, 1986). However, phosphatic sediments have not been reported to date from correlative horizons within the Neogene basinal sequences of western Honshu.

Far more enigmatic are reports of Miocene freshwater and/or brackish-water diatomaceous deposits, also collected along the north flank of Kita-Yamato Bank and reported by both Burckle and Akiba (1978) and Barash (1986). Burckle and Akiba (1978) speculated that these freshwater sediments might represent evidence of the eustatic isolation of the Sea of Japan during the late Miocene Messinian event. Alternatively, Tsoy et al. (1985) interpreted correlative deposits as early Miocene in age. More recently, Barash (1986) and colleagues interpreted the freshwater diatomites as sediments deposited in a small lake atop a late Miocene island formed during an emergent stage in the evolution of the Yamato Rise. Barash (1986) also reported late Miocene littoral or nonmarine sands and siltstones in an adjacent sample from the same area (Sample 3122; Fig. 9), adding emphasis to his interpretation. Finally, Koizumi (1988) correlated these sediments with the early Miocene nonmarine Monzen Formation of northern Honshu and viewed them as evidence of a lacustrine stage in the early evolution of the Sea of Japan, in line with the conclusions of Tsoy et al. (1985). Whatever their origin, these freshwater diatomaceous sediments signal a significant event in the Miocene evolution of the Yamato Rise area.

Tectonic Setting

Seismic-reflection profiles across the Yamato Rise (Fig. 10) indicate that the acoustic basement in this area (e.g., Mesozoic granites and mid-Tertiary volcanic rocks) forms a series of horsts and grabens, with evidence of folding and deformation within individual fault blocks. These same profiles indicate that Neogene sediments ubiquitously overlie this irregular basement topography, with the thickest accumulations present in structural and topographic lows. The Kita-Yamato Trough forms the most prominent low on the Yamato Rise, and both seismic-reflection and refraction data (Figs. 5, 10, and 11) indicate that this narrow east-northeast structure is filled with about 1.0 s of sediments of probable Miocene through Quaternary age.

Reflection profiles also reveal a series of north-northeast folds within the Neogene sequence overlying portions of the Yamato Rise and blanketing the adjacent Yamato Basin (Tamaki et al., 1981; Figs. 3 and 10). However, the sedimentary sequence filling the narrow Kita-Yamato Trough is simply faulted, rather than folded, except for structures on the flanks of the trough which may be large-scale slumps (Figs. 10 and 11).

Extensive northeast-trending normal faults cut both the acoustic basement and the overlying Neogene sediments in the Yamato Rise area, as elsewhere in the Sea of Japan (Ludwig et al., 1975; Tamaki et al., 1981). Well-defined normal faults form the sides of the Kita-Yamato Trough (Figs. 10 and 11), with the greatest subsidence and sediment thickness occurring in the central graben within this structure. The geologic ages and character of the basement rocks dredged from the Yamato Rise and other highs in the Sea of Japan, together with the structural patterns apparent in seismic-reflection profiles and the well-established Neogene basin histories described from western Honshu and the southern Korean Peninsula, all indicate that the widespread extensional fault system cutting acoustic basement was initiated during

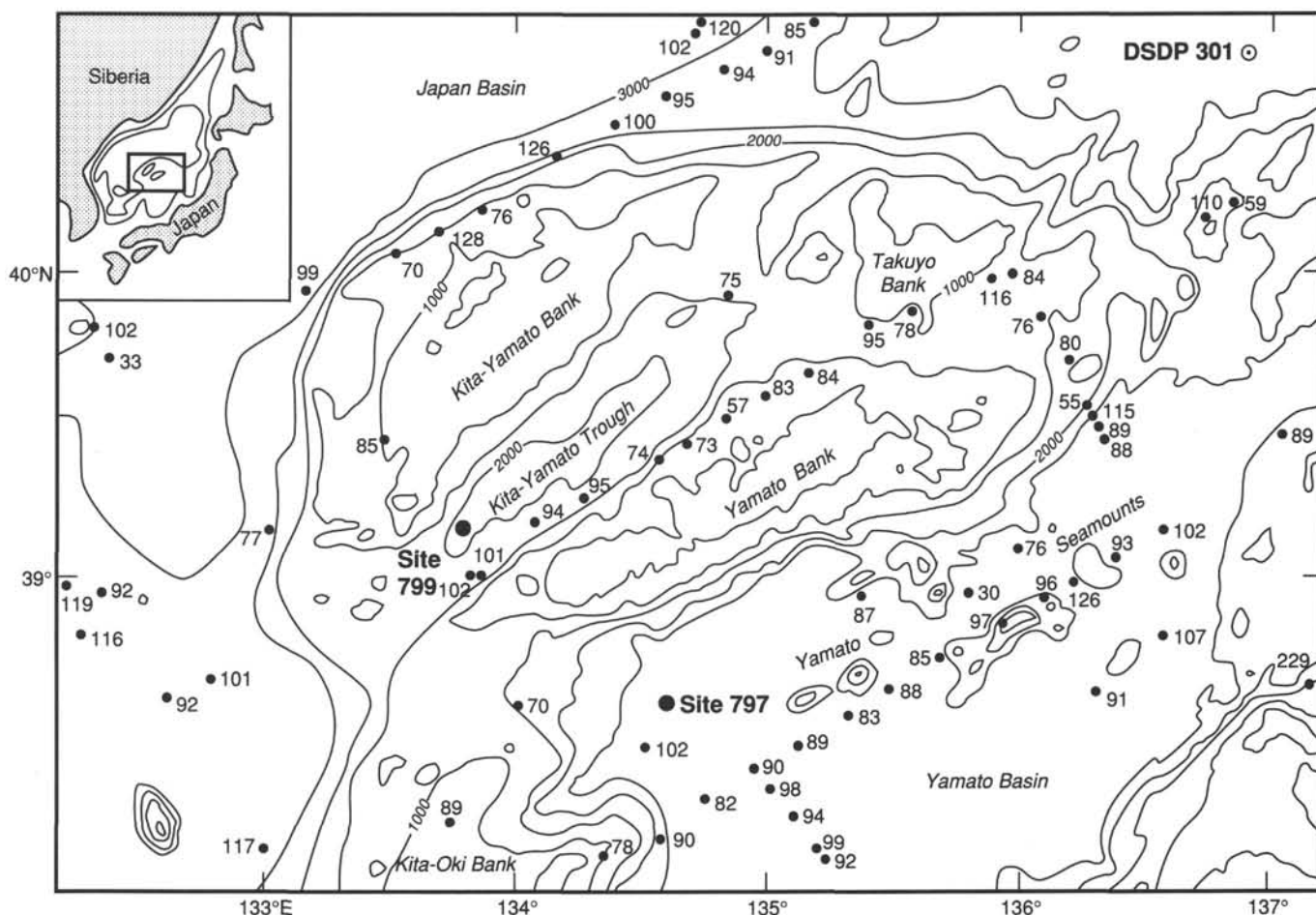


Figure 6. Heat-flow measurements in the Yamato Rise and Yamato Basin areas of the Sea of Japan, as compiled by M. Yamano (pers. comm., 1989). Units are in mW/m^2 .

early Miocene back-arc rifting. Tamaki (1988) and others viewed the Yamato Rise as a continental fragment isolated by the multiple spreading centers that characterize the early Miocene rifting phase in the evolution of the Sea of Japan. In the context of this scenario, the Kita-Yamato Trough represents a failed-rift that subsequently collected Miocene through Holocene sediments. The multiple graben structures within the trough, including faults that displace younger sediments, suggest that renewal of motion may have occurred on the bounding normal faults during Quaternary time, with continuing subsidence in the central graben.

Sedimentation

Prior to ODP drilling, sedimentary deposits filling the Kita-Yamato Trough in the vicinity of Site 799 were thought to be between 1200 and 1400 m thick, depending on the velocities assumed for this sequence (Fig. 11). Four distinctive seismic intervals can be distinguished on the processed JNOC 13-4 reflection profile that crosses Site 799 (Fig. 11), including (1) a lowermost unit having an assumed velocity of 2.62 km/s that displays discontinuous and distorted reflectors thought to represent Miocene sediments, (2) a second unit having an assumed velocity of 1.83 km/s and strong individual reflectors thought to represent upper Miocene sediments, (3) a third, less-reflective unit having an assumed velocity of 1.73 km/s

thought to represent Pliocene sediments, and (4) an upper, highly reflective unit having an assumed velocity of 1.70 km/s interpreted to represent Pliocene-Pleistocene sediments. Acoustic basement beneath the trough is thought to consist of Oligocene-Miocene volcanic rocks similar to those exposed on adjacent Yamato Bank and correlative with the "Green Tuff" formations of Honshu.

Development of a Failed-Rift Setting for Massive Sulfide Mineralization

Our primary objective at Site 799 was to determine the depositional and tectonic history of the Kita-Yamato Trough as an ideal or typical environment for deposition of massive sulfide mineralization in a rifted continental-arc setting. In fact, Site 799 constitutes the first and only DSDP-IPOD-ODP site aimed primarily at testing concepts of deep-sea metallogeny.

The special importance of the Kita-Yamato Trough lies in the idea that it represents a failed-rift created during early Miocene back-arc spreading and extension in the proto-Sea of Japan. Multiple spreading centers associated with this process are thought to have isolated the continental fragment that now forms the Yamato Rise. Subsequent spreading and rifting of this block initiated graben formation, which split the rise. For reasons not clearly understood, this process stopped short of

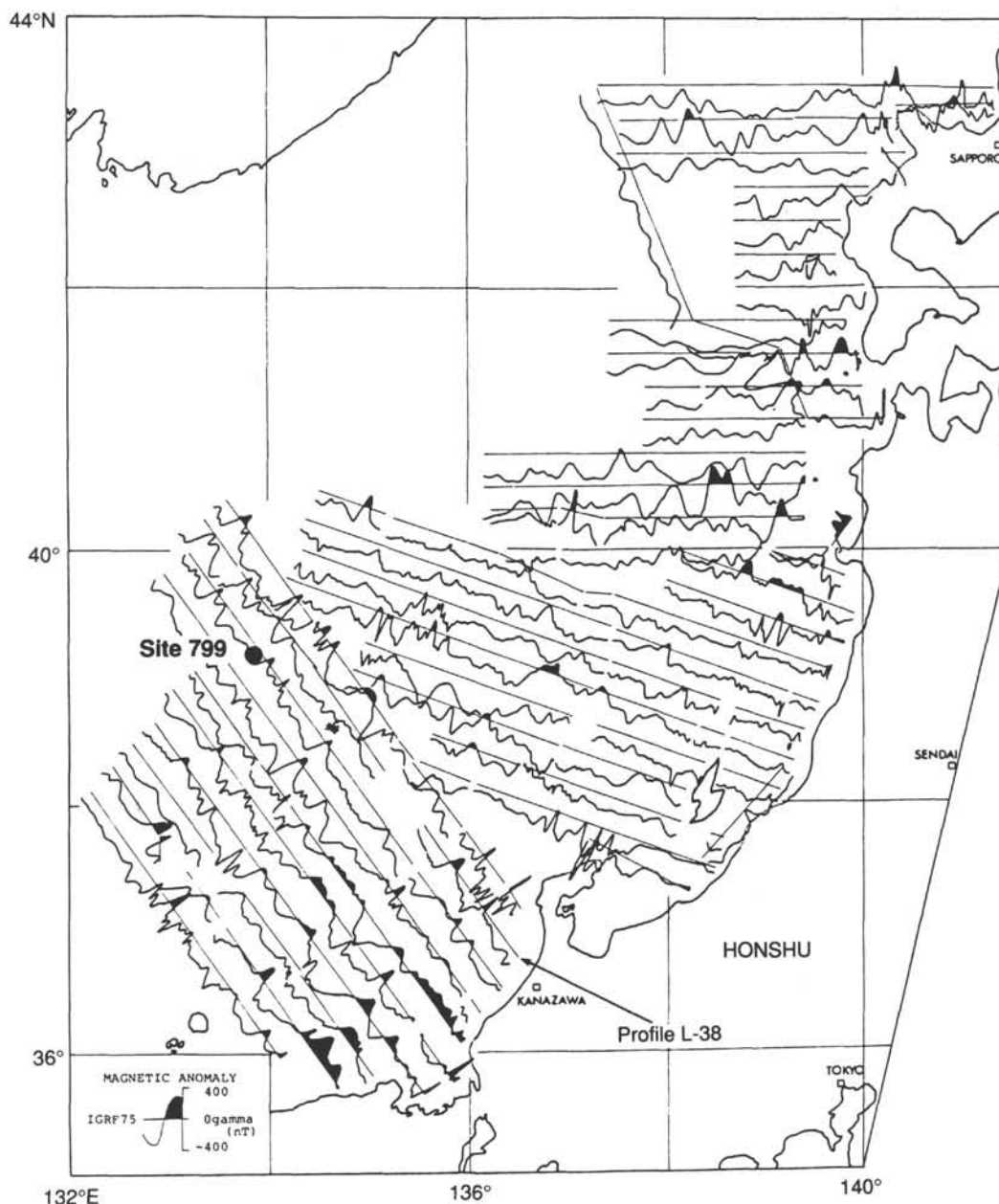


Figure 7. Profiles of magnetic anomalies in the eastern Sea of Japan and location of Site 799. Map from Honza (1979).

complete rifting, leaving the Kita-Yamato Trough as a failed-rift that subsequently accumulated a thick sequence of Miocene through Holocene sediments (Figs. 2 and 10). This unusual geologic setting is broadly analogous to submarine volcanogenic environments that host many of the ancient massive sulfide deposits now being mined for copper, lead, zinc, silver, and gold within continental margin, arc, and back-arc settings in Precambrian through Neogene rocks throughout the world.

Of immediate importance to Site 799 drilling, the Miocene Kuroko deposits of northern Honshu, Japan, constitute one of the prime examples of this type of massive sulfide mineralization. A recent study of these deposits (Ohmoto and Skinner, 1983) presented geochemical and geologic evidence that

points to the formation of the Kuroko ores as precipitates from hot hydrothermal fluids issuing from vent fields within a deep-sea (>2000 m), sedimented, failed-rift setting in the western proto-Sea of Japan during late early Miocene time. The analogy between geologic context of the Kuroko deposits and the geologic setting of the Kita-Yamato Rise and Site 799 could not be more direct, with one exception—we are not aware of any evidence suggesting Miocene caldera formation in the Yamato Rise area, a prominent feature associated with both Kuroko deposition (Ohmoto and Takahashi, 1983) and modern analogues in the Okinawa Trough (Halbach et al., 1989). Even if present, our chances of actually encountering a massive sulfide or shale-hosted deposit at Site 799 were remote; our primary goal was to detail the depositional,

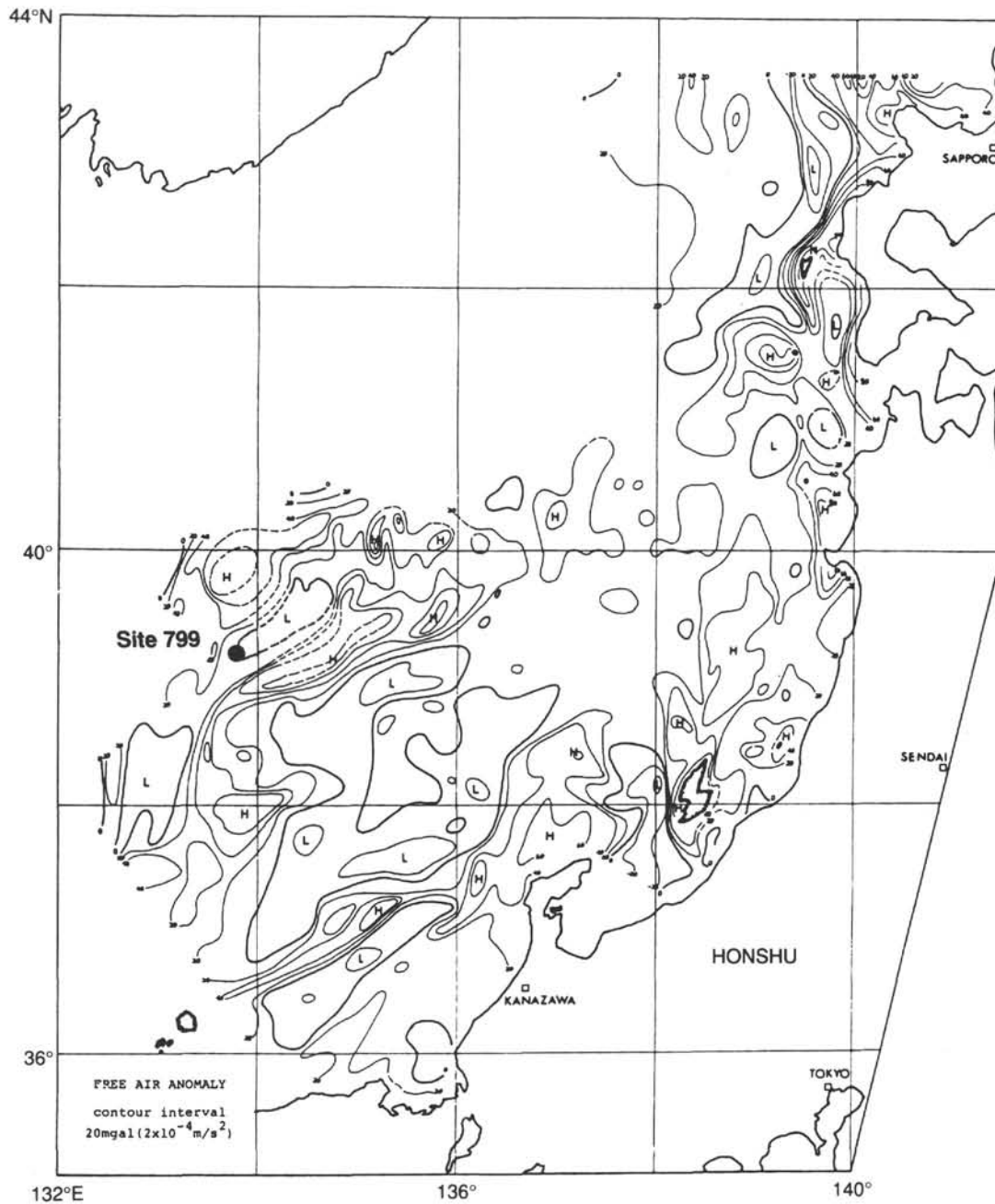


Figure 8. Free-air gravity anomaly map of the eastern Sea of Japan and location of Site 799. Map from Honza (1979).

tectonic, and paleoceanographic evolution of a failed-rift environment essentially identical to that known to contain these deposits.

Depositional and Paleoceanographic History

As with all of the sites drilled during Legs 127 and 128, we anticipated that the stratigraphic sequence at Site 799 would yield a valuable sedimentary, geochemical, and microfaunal record of Neogene paleoceanographic change in the Sea of Japan. In the case of Site 799, we had reason to believe that the unusually thick Miocene to Holocene column in the Kita-Yamato Trough might contain evidence of events not seen elsewhere in this sea. For example, the silled nature of

the modern Kita-Yamato Trough suggests the development of low oxygen phases in the history of bottom water within this feature. In fact, any major changes in the oxic, suboxic, and/or anoxic phases in the bottom water of the trough have import for analysis of the potential sulfide mineralization in this setting, as well as for evolution of the sea as a whole. In addition, the reported presence of Miocene phosphates on the adjacent Kita-Yamato Bank (Barash, 1986) suggested that we might encounter these authigenic sediments at Site 799, either as redeposited material or perhaps *in-situ*. Finally, the confirmed occurrence of Miocene freshwater diatomites on the Yamato Rise (Burckle and Akiba, 1978; Barash, 1986) and the speculative implications of these sediments with regard to the

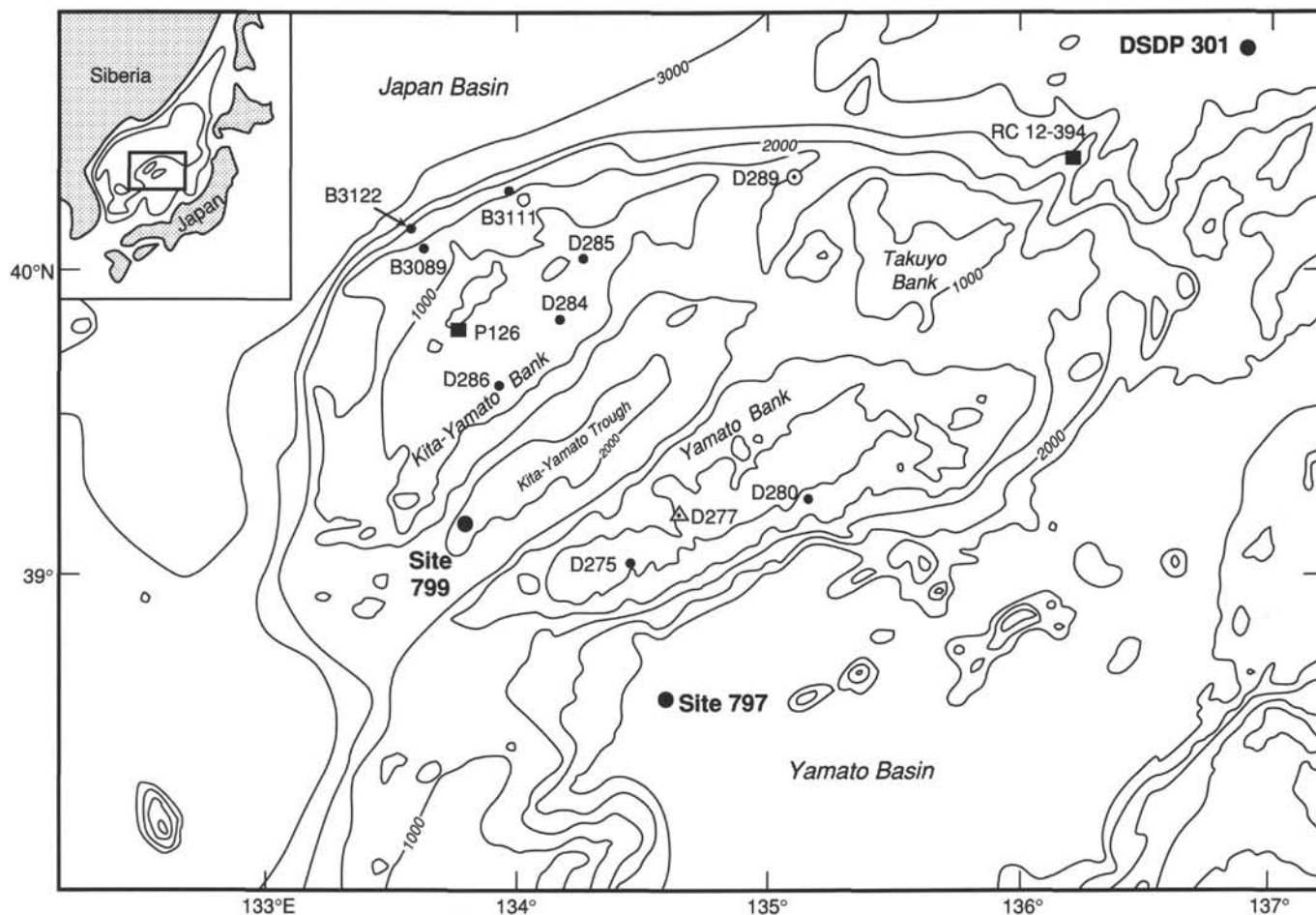


Figure 9. Location of selected dredges, piston cores, and deep-sea drilling sites in the vicinity of the Yamato Rise, Sea of Japan. Sample Stations B3111, B3122, and B3089 were reported by Barash (1986); stations with D and P prefixes represent dredges and piston cores described by Honza (1979); and piston Core RC 12-394 was reported by Burckle and Akiba (1978).

possible impact of Messinian eustatic events in the Sea of Japan vs. their correlation with on shore lower Miocene deposits (Koizumi, 1988) truly set Site 799 apart in terms of a potentially unusual paleoceanographic-paleoenvironmental record.

OPERATIONS

The transit from Site 794 to Site 799 (prospectus Site J2a-1) covered 201 nmi, at an average speed of 10.3 kt. A Datasonics positioning beacon was dropped at 0701 UTC, 14 September 1989, after a 47-nmi site survey, at an average speed of 6.3 kt. A jet-in test was conducted to 101.6 mbsf.

Hole 799A

Hole 799A was spudded at 1635 UTC, 14 September, at a depth of 2073.0 mbsf. Continuous APC Cores 128-799A-1H to 128-799A-20H were taken to 184.1 mbsf (Table 1). Recovery was excellent, with minor gas expansion. All cores were oriented, starting with Core 128-799A-5H. Heat flow was measured every second core, starting with Core 128-799A-6H. XCB Cores 128-799A-21X to 128-799A-52X were taken to 468.7 mbsf. Recovery was good through Core 128-799A-47X, after which there was poor recovery resulting from the presence of hard dolomitic sections that jammed the hard-forma-

tion core catcher. Hard-formation core bits were burned up on Cores 128-799A-51X and 128-799A-52X, as seen by the presence of blackened, crystallized material in the cores and by the severe bit wear. Increasing the pump pressure and pump rate did not prove effective for preventing bit destruction at a low rate of penetration in hard dolomite.

The sonic core monitor (SCM) was run during Leg 128 for only the second time in ODP history. The SCM run at Core 128-799A-31X produced data about core height that correlated well with data for drilling time; however, the run at Core 128-799A-51X was unsuccessful because the power cable between the battery and our electronics apparently was severed when the instrument's sections were installed in the carrier tube. The SCM sections and cables can be altered easily to avoid this problem in the future.

Hole condition was excellent while drilling, tripping, and logging. Capillary suction tests performed on clay samples from 160, 190, 326 and 365 mbsf exhibited a negligible swelling tendency in fresh water, indicating nonreactive clays (see "Downhole Measurements" section, this chapter).

The drill string was pulled up to 104.59 mbsf for logging. This depth is deeper than normal; it was chosen because of the presence of soft sediments near the surface. Logs were run as follows: sonic/seismic stratigraphy, FMS (two runs), litho-

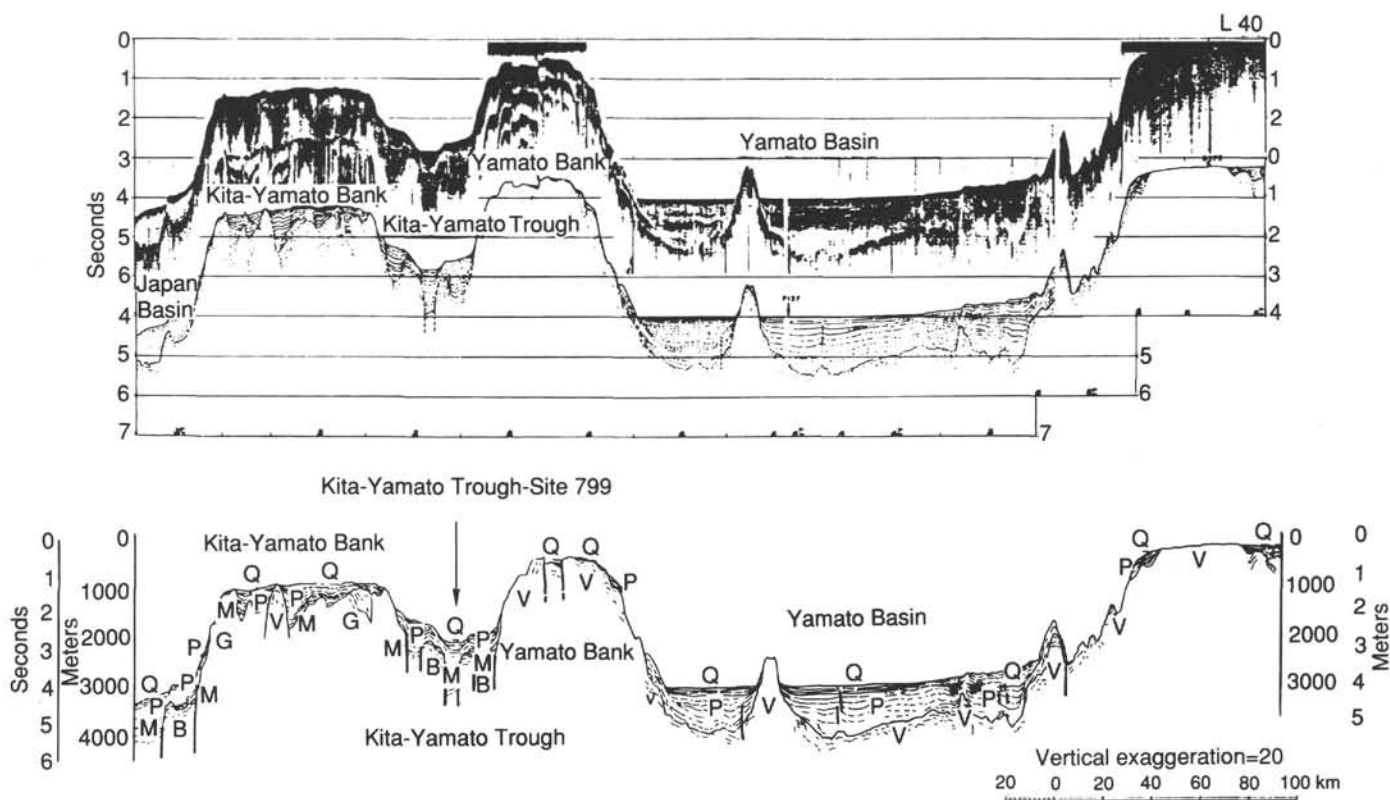


Figure 10. A portion of NW-SE single-channel seismic-reflection profile L-40 across the Yamato Rise and an interpreted line drawing of this profile. Both figures from Tamaki (1988). Location of profile L-40 is shown in Figure 4. Symbols on the interpreted line drawing are M = Miocene sediments, P = Pliocene sediments, Q = Quaternary sediments, and V = volcanic rocks.

porosity combination, and geochemical combination tools. Conditions of the hole and quality of logs were excellent.

While logs were run through the drill pipe, the video-camera frame was run to test an EDO Western 3.5-kHz near-bottom profiler. This profiler worked well and more than 30 m into the seafloor was penetrated; its record had less definition than our current site approach equipment.

The bottom-hole assembly (BHA) was pulled out after logging, which ended drilling of Hole 799A at 1025UTC, 18 September.

Hole 799B

The *JOIDES Resolution* was moved 20 m north. Hole 799B was spudded at 0430UTC, 19 September, with 16-in. casing and a new-style reentry cone having a Datasonics beacon attached. The 16-in. casing was jetted in to 70.3 mbsf, and the hole was drilled to 450 mbsf to allow us to overlap cored material between this hole and Hole 799A. Thirty-four joints of 11-3/4-in. casing were cemented, and operations in Hole 799B were suspended temporarily at 0415UTC, 21 September.

The *JOIDES Resolution* left Site 799 to complete geophysical experiments at Site 794. After the bottom-hole seismometer and electrical resistivity experiments at Site 794 were successfully completed, we returned to finish operations in Hole 799B. The transit to Hole 799B covered 211 nmi in 21.6 hr at an average speed of 9.8 kt and ended at 1336UTC, 2 October. A transit satellite and Decca were used for navigation because the GPS satellite had been nonoperational for 4 days. The beacons at Holes 799A and 799B were located, and

the search for Hole 799B began at 1845UTC, 2 October, using both the video camera and an intermittent Mesotech sonar. No cones were noted above the seafloor, but the sonar identified several mounds. An unidentified hole in the seafloor was reentered at 2150UTC, but it proved to have a total depth of 468.7 mbsf, indicating that we had reentered Hole 799A. The bit cleared the seafloor at 0445UTC, and the search continued. The beacon for Hole 799A was located, and an unidentified hole was reentered at 0945UTC. The bit was run in to 442.1 mbsf, and the hole was identified as Hole 799B. The 11-3/4-in. shoe was drilled, and Core 128-799B-1R was cut from 450.0 to 459.5 mbsf, with no recovery. The drill pipe was advanced 9.5 m, and Core 128-799B-2R was retrieved, with 0.22 m of sediment and a piece of the drill-pipe wiper plug, which had jammed in the shoe. Cores 128-799B-3R to 128-799B-4R had no recovery. After recovering 4.54 m of sediment and another large piece of the drill-pipe wiper plug in Core 128-799B-5R, RCB coring continued to 1084 mbsf, with fair recovery (Table 2). Hydrocarbon gases in the sediments were monitored routinely as part of the ODP pollution prevention and safety procedures. Based on relative and absolute concentrations of hydrocarbons in headspace samples and ultraviolet fluorescence observations of sediments treated with 1,1,1-trichloroethane, drilling was terminated at 1084 mbsf. The chemical data considered for this decision are presented in the "Organic Geochemistry" section (this chapter). The hole was cleaned out and displaced with 2.0% KCl logging mud. Seismic stratigraphy, FMS, lithoporosity combination, and geochemical combination logs, as well as VSP,

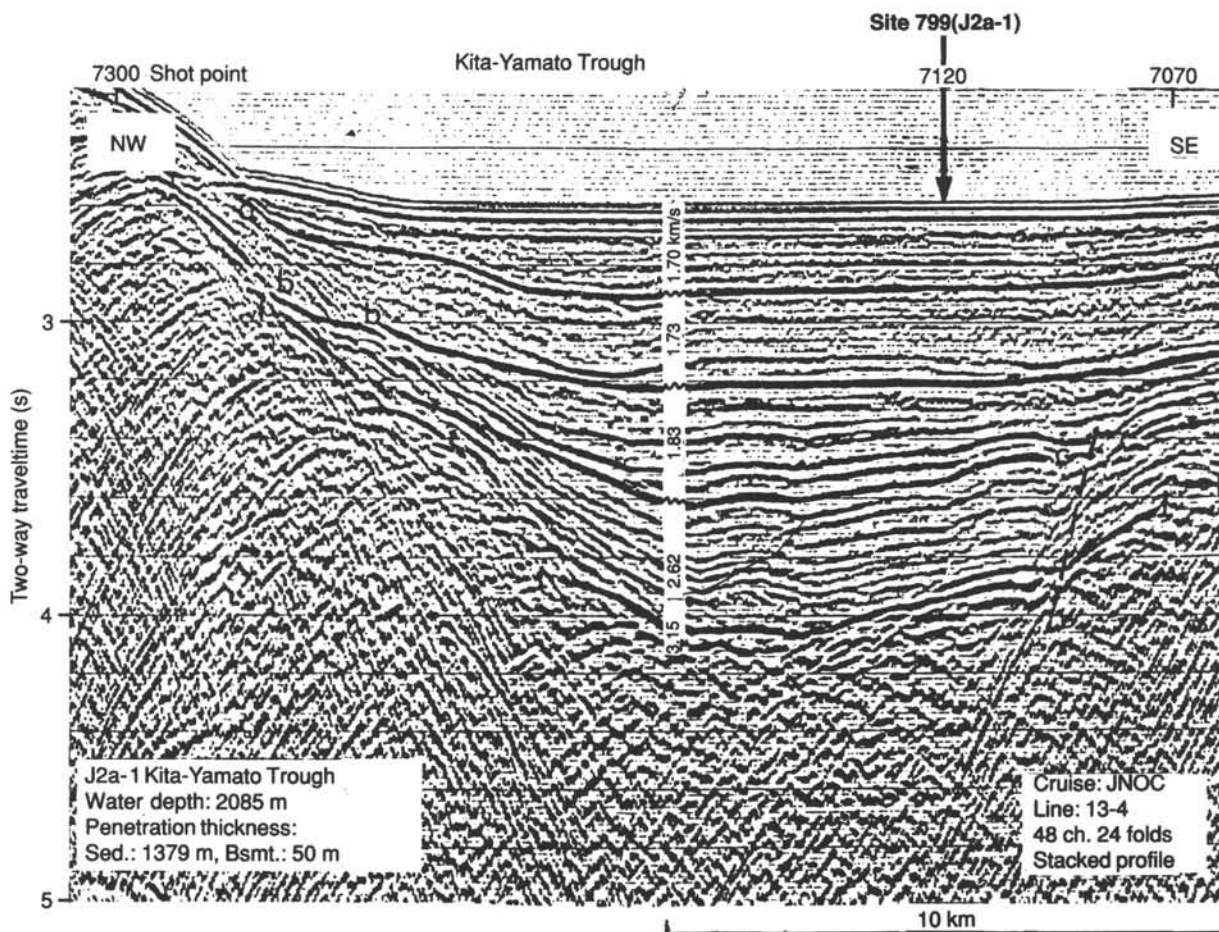


Figure 11. Processed multichannel seismic-reflection profile across the southern Kita-Yamato Trough and the location of Site 799. This profile represents a portion of Japan National Oil Company profile JNOC 13-4 (unpubl. data). See Figure 4 for location of the profile.

were run (see "Downhole Measurements" section, this chapter). Conditions of the hole and quality of logs were excellent.

While logs were being run, the video-camera frame was used to re-test the EDO Western 3.5-kHz near-bottom profiler at various impedance settings. The profiler worked, but as observed before, the record shows less definition than our current hull-bottom transducer.

The BHA was pulled out and cleared the rotary at 1840UTC, 11 October, ending drilling at Hole 799B.

Hole 799C

Hole 799C was spudded at 0015UTC, October 12, with the sole purpose of testing the SCM tool. Three XCB cores were taken between 230.0 and 252.5 mbsf, recovering 23.93 m of a sediment sequence previously cored in Hole 799A. The SCM collected data points during all three runs, but the test was terminated because the tool could not find the target, was functioning erratically, and produced questionable data. Operations at Hole 799C ended at 1730UTC, 12 October.

Post-Site Survey

Thrusters and hydrophones were pulled, and the *JOIDES Resolution* began a survey of the Kita-Yamato Trough and the

Yamato Bank at 1918UTC, 12 October. A distance of 199.8 nmi was covered during the survey, at a speed of 6 kt, which required 31 hr.

LITHOSTRATIGRAPHY

Introduction

The sedimentary sequence recovered at Site 799 is 1084 m thick. The upper 468.7 m was cored in Hole 799A and consists predominantly of biosiliceous and fine-grained detrital sediments intercalated with carbonate-rich intervals. These sediments range from late Miocene to Holocene in age. An interval from 451 to 1084 mbsf was cored in Hole 799B; it is composed mainly of diagenetically altered biosiliceous sediments, diagenetic carbonates, and sandstones. Limited paleontologic data indicate that these sediments record the time span from early to late Miocene. The sediments between 451 and 489.6 mbsf have not been documented because of poor recovery in the uppermost part of Hole 799B.

Sediments from Hole 799A were collected using the APC system to a depth of 184.1 mbsf and using the XCB system, to the base of this hole (468.7 mbsf). Sediments from Hole 799B were recovered with the RCB system.

Table 1. Coring summary for Hole 799A.

Core number	Date (Sept. 1989)	Time (UTC)	Depth (mbsf)	Length cored (m)	Length recovered (m)	Recovery (%)	Age
1H	14	1650	0-1.2	1.2	1.18	98.3	Quaternary
2H	14	1725	1.2-10.7	9.5	9.81	103.0	
3H	14	1750	10.7-20.3	9.6	9.98	104.0	
4H	14	1830	20.3-29.9	9.6	9.46	98.5	
5H	14	1915	29.9-39.5	9.6	9.91	103.0	
6H	14	2120	39.5-49.1	9.6	9.97	104.0	
7H	14	2200	49.1-58.7	9.6	10.05	104.7	
8H	15	0010	58.7-68.3	9.6	10.11	105.3	
9H	15	0050	68.3-77.9	9.6	10.06	104.8	
10H	15	0300	77.9-87.5	9.6	9.99	104.0	
11H	15	0335	87.5-97.2	9.7	10.06	103.7	
12H	15	0520	97.2-106.8	9.6	10.10	105.2	
13H	15	0600	106.8-116.5	9.7	9.95	102.0	
14H	15	0750	116.5-126.1	9.6	9.97	104.0	
15H	15	0830	126.1-135.8	9.7	9.94	102.0	Pliocene
16H	15	1020	135.8-145.5	9.7	9.92	102.0	
17H	15	1105	145.5-155.2	9.7	9.91	102.0	
18H	15	1250	155.2-164.8	9.6	10.15	105.7	
19H	15	1330	164.8-174.5	9.7	10.12	104.3	
20H	15	1520	174.5-184.1	9.6	10.14	105.6	
21X	15	1620	184.1-193.8	9.7	9.95	102.0	
22X	15	1710	193.8-203.5	9.7	9.75	100.0	
23X	15	1745	203.5-213.1	9.6	9.84	102.0	
24X	15	1830	213.1-222.8	9.7	9.70	100.0	
25X	15	1910	222.8-232.5	9.7	9.83	101.0	
26X	15	1950	232.5-241.4	8.9	0.00	0.0	
27X	15	2205	241.4-247.1	5.7	5.41	94.9	
28X	16	0015	247.1-250.9	3.8	0.70	18.4	
29X	16	0100	250.9-260.5	9.6	7.20	75.0	
30X	16	0150	260.5-270.2	9.7	9.72	100.0	
31X	16	0250	270.2-278.2	8.0	8.61	107.0	
32X	16	0330	278.2-287.9	9.7	9.72	100.0	
33X	16	0410	287.9-297.6	9.7	9.64	99.4	
34X	16	0450	297.6-307.3	9.7	9.06	93.4	
35X	16	0530	307.3-316.9	9.6	9.81	102.0	
36X	16	0605	316.9-326.6	9.7	8.91	91.8	
37X	16	0650	326.6-336.2	9.6	9.80	102.0	
38X	16	0730	336.2-345.9	9.7	9.93	102.0	
39X	16	0810	345.9-355.6	9.7	9.81	101.0	
40X	16	0855	355.6-365.3	9.7	9.95	102.0	
41X	16	0940	365.3-375.0	9.7	9.84	101.0	
42X	16	1015	375.0-384.6	9.6	9.91	103.0	
43X	16	1050	384.6-394.3	9.7	9.77	101.0	
44X	16	1135	394.3-403.9	9.6	3.74	38.9	Miocene(?)
45X	16	1220	403.9-413.6	9.7	9.70	100.0	
46X	16	1305	413.6-423.3	9.7	9.84	101.0	
47X	16	1345	423.3-432.9	9.6	9.78	102.0	
48X	16	1430	432.9-442.6	9.7	4.50	46.4	
49X	16	1550	442.6-452.3	9.7	1.42	14.6	
50X	16	1720	452.3-461.9	9.6	8.71	90.7	
51X	16	2000	461.9-466.9	5.0	4.35	87.0	
52X	16	2230	466.9-468.7	1.8	0.36	20.0	Miocene(?)
Coring totals				468.7	440.04	93.9	

Five lithologic units have been defined at Site 799 on the basis of differences in lithologic composition and variability, sedimentary structures, and diagenetic alteration (Fig. 12, backpocket figure).

Unit I

Cores 128-799A-1H through 128-799A-19H; depth, 0-170 mbsf. Age: Quaternary to late Pliocene.

Sediments of Unit I are composed of diatomaceous clay, diatomaceous ooze, diatomaceous clayey mixed sediment, clay, clayey silt, silty clay, and silt. Sediments rich in foraminifers, calcareous nannofossils, siliciclastic sands, and diagenetic carbonate are minor, but commonly conspicuous,

lithologies. Vitric ash layers ranging in thickness from <1 mm to 19 cm are abundant throughout this unit, especially in the uppermost 120 m (see "Volcanic Ash and Tephrochronology" section, this chapter).

Diatoms and monaxon sponge spicules with minor (1%-5%) silicoflagellates and radiolarians comprise the biosiliceous component of Unit I. Maximum abundances of biosilica were observed between 54 and 69 mbsf and from 78 to 99 mbsf; minimum abundances occur in the uppermost 53 m and in the interval from 108 to 138 mbsf (Figs. 12, backpocket, and 13). Note that comparison of the smear-slide data with quantitative geochemical SiO₂ measurements of selected intervals throughout Hole 799A indicate that our visual estimates of biosiliceous debris are generally too high (Table 3).

Table 2. Coring Summary for Hole 799B.

Core number	Date (Oct. 1989)	Time (UTC)	Depth (mbsf)	Length cored (m)	Length recovered (m)	Recovery (%)	Age
1R	3	2155	451.0-460.5	9.5	0.00	0.0	(?)
2R	4	0100	460.5-470.2	9.7	0.22	2.3	
3R	4	0225	470.2-479.9	9.7	0.00	0.0	
4R	4	0525	479.9-489.6	9.7	0.00	0.0	
5R	4	0815	489.6-494.6	5.0	4.54	90.8	late Miocene(?)
6R	4	0940	494.6-499.7	5.1	5.14	101.0	
7R	4	1100	499.7-509.3	9.6	5.67	59.0	
8R	4	1230	509.3-519.0	9.7	8.36	86.2	
9R	4	1340	519.0-528.6	9.6	5.96	62.1	
10R	4	1455	528.6-538.3	9.7	5.94	61.2	
11R	4	1610	538.3-547.9	9.6	9.85	102.0	
12R	4	1720	547.9-557.6	9.7	6.36	65.5	middle Miocene(?)
13R	4	1815	557.6-567.3	9.7	7.69	79.3	
14R	4	1940	567.3-577.0	9.7	6.23	64.2	
15R	4	2100	577.0-586.6	9.6	7.59	79.0	
16R	4	2235	586.6-596.3	9.7	6.10	62.9	
17R	4	2340	596.3-605.9	9.6	8.59	89.5	
18R	5	0040	605.9-615.6	9.7	9.35	96.4	
19R	5	0205	615.6-625.2	9.6	8.76	91.2	
20R	5	0320	625.2-634.9	9.7	9.67	99.7	
21R	5	0505	634.9-644.6	9.7	4.52	46.6	
22R	5	0645	644.6-654.2	9.6	2.06	21.4	
23R	5	0815	654.2-663.8	9.6	3.37	35.1	
24R	5	0955	663.8-673.5	9.7	5.69	58.6	
25R	5	1100	673.5-683.2	9.7	4.41	45.4	
26R	5	1230	683.2-692.5	9.3	3.36	36.1	
27R	5	1400	692.5-702.1	9.6	9.65	100.0	
28R	5	1525	702.1-711.8	9.7	6.69	68.9	
29R	5	1650	711.8-721.4	9.6	9.86	103.0	
30R	5	1850	721.4-730.8	9.4	2.30	24.4	
31R	5	2105	730.8-740.5	9.7	1.81	18.6	
32R	5	2320	740.5-750.2	9.7	0.74	7.6	
33R	6	0120	750.2-759.8	9.6	3.48	36.2	
34R	6	0305	759.8-769.5	9.7	3.61	37.2	
35R	6	0400	769.5-779.2	9.7	2.33	24.0	
36R	6	0620	779.2-788.9	9.7	2.01	20.7	
37R	6	0750	788.9-798.5	9.6	0.71	7.4	
38R	6	0925	798.5-808.1	9.6	2.07	21.5	
39R	6	1055	808.1-817.8	9.7	1.35	13.9	
40R	6	1235	817.8-827.1	9.3	0.59	6.3	
41R	6	1430	827.1-836.8	9.7	0.88	9.1	
42R	6	1630	836.8-846.4	9.6	0.95	9.9	
43R	6	1840	846.4-856.1	9.7	0.55	5.7	
44R	6	2015	856.1-865.8	9.7	0.21	2.2	
45R	6	2220	865.8-875.3	9.5	2.14	22.5	
46R	7	0045	875.3-885.0	9.7	6.53	67.3	
47R	7	0305	885.0-894.6	9.6	5.33	55.5	
48R	7	0505	894.6-904.2	9.6	3.16	32.9	
49R	7	0705	904.2-913.6	9.4	2.79	29.7	
50R	7	0920	913.6-923.3	9.7	5.27	54.3	
51R	7	1115	923.3-932.9	9.6	7.50	78.1	
52R	7	1330	932.9-942.6	9.7	3.13	32.2	
53R	7	1525	942.6-952.2	9.6	2.17	22.6	
54R	7	1725	952.2-961.8	9.6	4.47	46.5	
55R	7	1905	961.8-971.5	9.7	2.36	24.3	
56R	7	2035	971.5-981.1	9.6	4.12	42.9	
57R	7	2155	981.1-990.8	9.7	2.06	21.2	early Miocene(?)
58R	7	2340	990.8-1000.5	9.7	2.94	30.3	
59R	8	0205	1000.5-1010.2	9.7	2.13	21.9	
60R	8	0445	1010.2-1019.8	9.6	5.31	55.3	
61R	8	0615	1019.8-1029.5	9.7	8.77	90.4	
62R	8	0825	1029.5-1039.1	9.6	5.83	60.7	
63R	8	1035	1039.1-1048.8	9.7	3.78	38.9	
64R	8	1235	1048.8-1058.4	9.6	1.94	20.2	
65R	8	1440	1058.4-1068.1	9.7	3.64	37.5	
66R	8	1635	1068.1-1077.7	9.6	1.62	16.9	
67R	8	1900	1077.7-1084.0	6.3	4.27	67.8	early Miocene(?)
Coring totals				633.0	280.48	44.3	

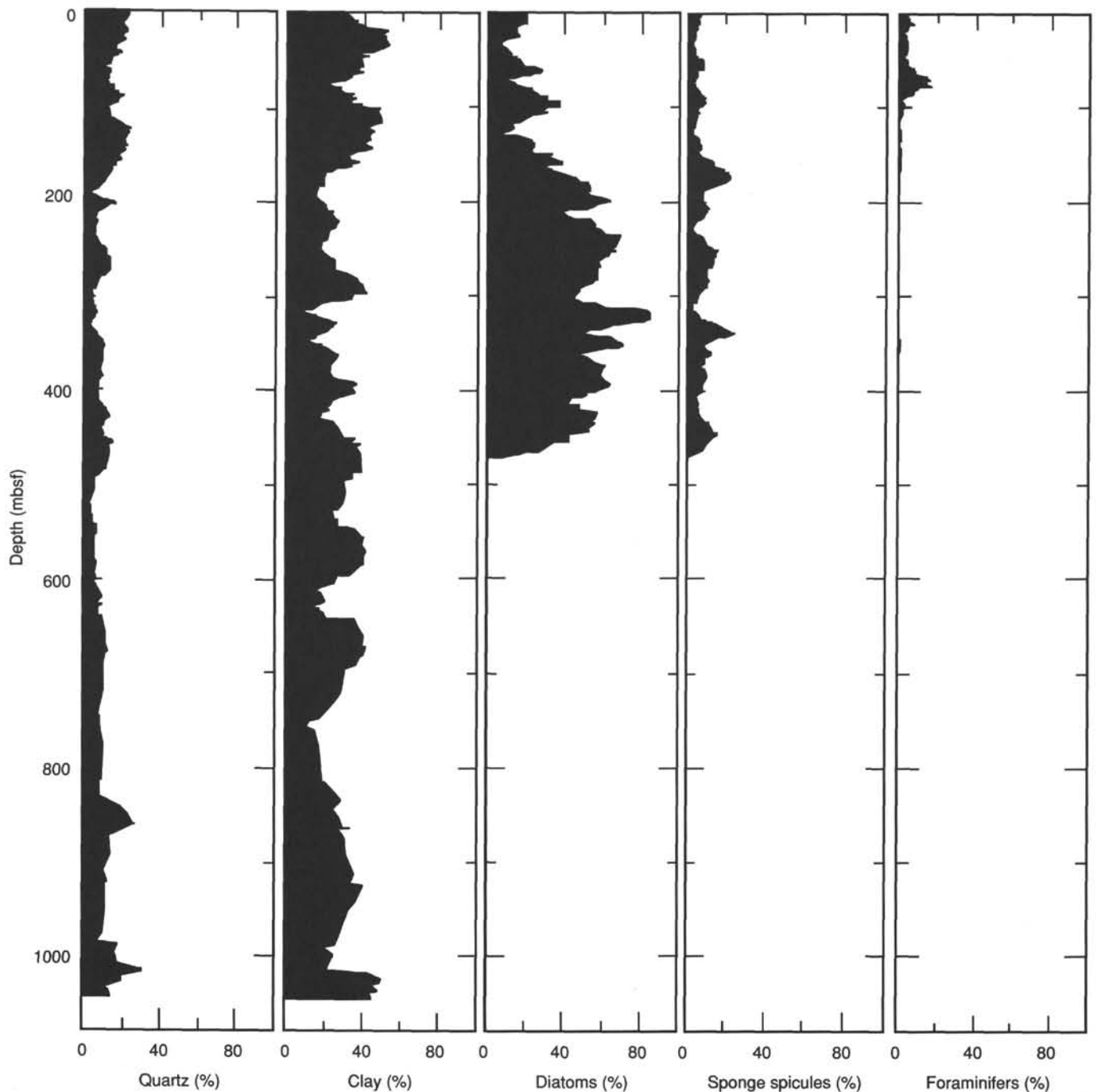


Figure 13. Estimated percentages of detrital quartz, clay, diatoms, spicules, and foraminifers, based on smear-slide observations.

Foraminifer-rich sediments and foraminiferal oozes are limited to thin beds and laminae in the uppermost 90 m. The abundance of foraminifers decreases abruptly below this level, and foraminifers are virtually absent below approximately 170 mbsf (Fig. 13). Pristine, i.e., well-preserved and unaltered, nanofossil-rich sediments and oozes occur as layers up to 90 cm thick at between 39 and 110 mbsf. Below 110 mbsf, calcareous nanofossils and foraminifers exhibit progressive recrystallization and overgrowth with diagenetic

carbonate, rendering their identification in smear slides difficult.

Silt-sized quartz and clay are the predominant detrital components of Unit I. Sediments containing sand-sized siliciclasts and thin, compositionally immature sand layers with rock fragments, quartz, and feldspar grains are restricted to the upper 34 m. Maximum abundance in terrigenous components was observed in the sedimentary intervals between 0 and 50 mbsf and between 105 and 150 mbsf.

Table 3. Comparison of abundances of biosilica with abundances of diagenetic silica estimated visually and values determined from chemical analyses.

Chemically analyzed silica	Rock name	Visually estimated silica*	Sample interval (cm)
Biosilica determined by dissolution (technique of D. Master, 1979):			
53%	Spicular diatom ooze	70%	128-799A-19H-5, 0-5
43%	Spicular diatom ooze with clay	(70%)	128-799A-19H-4, 15-20
27%	Diatom ooze with clay	80%	128-799A-22X-4, 34-38
26%	Diatom ooze with silt	(70%)	128-799A-18H-2, 25-30
13%	Diatom ooze with silty clay	(70%)	128-799A-23X-6, 16-20
5%	Silty clay with diatoms	15%	128-799A-18H-6, 44-45
2%	Silty clay	3%	128-799A-12H-2, 20-25
Biosilica estimated from major oxide analyses:			
63-65%	Diatom ooze	90%	128-799A-35X-4, 55
49-52%	Clayey biosiliceous ooze	55%	128-799A-48X-1, 121
Diagenetic silica estimated from major oxide analyses (Shipboard XRF):			
83%	Chert (opal-CT)	—	128-799A-48X-1, 109
82-83%	Chert (opal-CT)	77%	128-799A-50X-5, 125
71-73%	Porcellanite (quartz)	—	128-799B-39R-3, 59
64-66%	Chert (opal-CT)	—	128-799A-48X-1, 46
61-63%	Porcellanite (opal-CT)	60%	128-799A-51X-1, 50
54-56%	Siliceous claystone (quartz)	—	128-799B-61R-6, 4
44-46%	Siliceous claystone (quartz)	40%	128-799B-51R-3, 59
30-33%	Siliceous claystone (quartz)	35%	128-799B-27R-2, 93
11-15%	Siliceous claystone (quartz)	40%	128-799B-17R-3, 62
11-15%	Siliceous claystone (quartz)	30%	128-799A-51X-1, 66

*Values for visually estimated silica are in most cases not exactly from the same interval as analytical results. Visual estimates taken from the barrel sheets, rather than from a smear-slide estimate near the interval analyzed, are placed in parentheses. In rocks with diagenetic silica, only estimates made near the interval analyzed are included.

Diagenetic carbonates occur at depths as shallow as 12.7 mbsf (Section 128-799A-3H-2 at 50 cm); however, they are rare in the upper 100 m, but become more common in the interval from 100 to 170 mbsf (see "Authigenic Carbonates" section, this chapter).

Unit I consists of thickly bedded to thinly laminated sediments, which commonly are arranged in sequences of light-colored, massive intervals that alternate with dark-colored, laminated intervals. Distinctive dark/light rhythms occur in the upper 117 m below this level. Such rhythms are generally poorly defined. Variegated accumulations of thinly bedded silty clays, clays, diatomaceous clays, and foraminiferal- and nannofossil-rich sediments occur within soft-sediment deformed units (40-77 mbsf); these accumulations probably represent thin, turbiditic deposits that were stacked prior to soft-sediment deformation.

Soft-sediment deformation is a common feature within Unit I. Major intervals of deformed soft sediments are present between 10.0 and 11.2 mbsf, from 40.0 to 79.0 mbsf (shown as an acoustical transparent zone in the 3.5-kHz seismic profile; Fig. 14), and from 141.2 to 151.2 mbsf. Deformation structures include harmonic and disharmonic folding, horizontal and oblique faulting, and sediment detachment (Figs. 15 through 24). Zones of progressive amalgamation, which include free-floating mud clasts, have been interpreted as debris flows. As a consequence of extensive slumping, some sediments in these deformed and partly detached intervals have been overturned, e.g., between 145.5 and 151.2 mbsf (Sections 128-799A-17H-1 through 128-799A-17H-3; judging from trends in bioturbation and apparent magnetic declination: "Olduvai slump"; "Paleomagnetism" section, this chapter).

Coarse-grained and normally graded beds consisting of foraminiferal oozes (concentrations of *Globigerina*), immature

sands, and volcaniclasts in the upper 47 m have been attributed to sediment transport and redeposition by turbidity flows (Figs. 25 through 28). Some of these beds are intimately associated with vitric ash beds, and a cause-and-effect relationship is highly probable (such as volcanic seismic activity that triggers gravity flows; Fig. 29). The unusual concentration of the diatom species *Rhizosolenia curvirostris* in dark silty clays in the interval 116.5 to 116.8 mbsf (Section 128-799A-14H-1 at 0-30 cm) may be result from sediment-sorting processes, such as winnowing or sorting within a turbidity flow.

Distinct bioturbation is not common in this unit, and burrowed intervals are restricted to sediments between 62.2 and 62.3, 80.3 and 80.9, 88.0 and 88.3, 104.2 and 105.0, 142.0 and 152.2, 156.2 and 156.4, and between 162.5 and 162.9 mbsf (Fig. 30). Vague mottling is evident throughout the lower part of Unit I (117-170 mbsf) and may be indicative of burrowing in water-saturated sediments, which lack sufficient cohesion to preserve clear burrow morphology.

According to paleomagnetic and biostratigraphic correlations (see "Sediment Accumulation Rates" section, this chapter), the sediments of Unit I include the Quaternary and extend well into the upper Pliocene (0-2.4 Ma). The average sediment accumulation rate is 71 m/my. (5.7 g/cm²/k.y., based on a mean dry-bulk density of 0.80 g/cm³; "Physical Properties" and "Sediment Accumulation Rates" sections, this chapter).

Unit II

Cores 128-799A-20H through 128-799-49X; depth, 170-457 mbsf. Age: late Pliocene to late Miocene.

The transition from Unit I to subjacent Unit II is gradual, located between approximately 155 and 170 mbsf. The

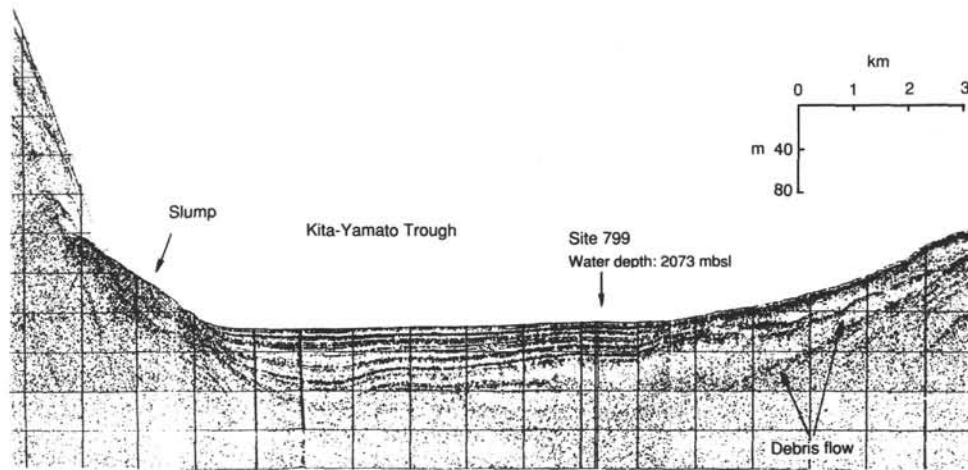


Figure 14. Profile of the 3.5-kHz seismic record crossing Site 799, showing seismic signature of a slump block and debris flows. The profile from left to right is from NW to SE (149°).

boundary at 170 mbsf represents the deepest occurrence of interbedded dark/light sediments (see "apparent rhythmic sedimentation in Unit I" below). Sediments in Unit II consist of diatomaceous ooze, clayey diatomaceous ooze, clayey diatomaceous mixed sediment, and diatomaceous clay. Nanofossil- and carbonate-rich sediments, as well as sediments rich in sponge spicules, occur as minor lithologies throughout this unit. Sediments in Unit II appear fairly homogeneous (although this may be partly an artifact induced by XCB recovery) and differ from those of Unit I by having more abundant biosilica, less abundant terrigenous components, far less abundant foraminifers, markedly fewer vitric ash layers, distinctly more common bioturbation, and by the almost complete absence of interbedded dark/light sequences, and of substantial soft-sediment deformation.

Biosiliceous debris is the most abundant component in Unit II, and its distribution is fairly uniform throughout this unit (Figs. 12, backpocket, and 13). The biogenic silica fraction is dominated by diatoms, and the ratio of sponge spicules to diatoms varies widely, without significant temporal trends. Abundance of silicoflagellates is below 1%, but these persist throughout the unit.

Carbonate-rich zones are present as well-lithified, pale gray dolomite beds and concretions (prominent at 247.0, 260.5, 261.9, 341.6, and 394.6 mbsf), which commonly preserve the pre-compaction primary sedimentary structures. Carbonates also occur as poorly lithified, yellowish brown to olive, thin chalky layers (which are present as diffuse patches that have disseminated carbonate particles), and concretions. These chalky intervals may be dolomite-cemented zones, originally rich in calcareous fossils (dolomite was confirmed by XRD analysis in several cases; see "Authigenic Carbonates," this section). In smear slides, the carbonates appear as 1- to 5- μm -sized, single crystals of high birefringence, clustered in polycrystalline aggregates of up to 20 μm in diameter. These frequently occurring carbonate crystals may be replaced by calcareous nanofossils.

A 2-cm-thick zone rich in sand-sized glauconite (as much as 10% by visual estimate) is present at 374.2 mbsf (Section 128-799A-41X-6 at 147–150 cm).

A peculiar exotic component was found in this unit: a well-rounded rhyolitic pebble (4 × 1.5 cm), embedded in

diatomaceous ooze, present at 260.5 mbsf (Section 128-799A-30X-1 at 1–3 cm).

The sediments of Unit II range in age from late Pliocene to late Miocene; the exact age of the lower part, however, is not well-constrained (see both "Biostratigraphy" and "Paleomagnetism" sections, this chapter). The time span during which this unit accumulated has been estimated as 3.9 m.y. (2.4–6.3 Ma). Accordingly, the estimated accumulation rate for this unit is 73 m/m.y., which corresponds to 4.55 g/cm²/k.y. (based on a mean dry-bulk density of 0.62 g/cm³; "Physical Properties" and "Sediment Accumulation Rates" sections, this chapter).

Unit III

Cores 128-799A-50X through 128-799A-52X and 128-799B-1R through 128-799B-37R; depth, 457–800 mbsf.
Age: late to middle Miocene.

Sediments of Unit III consist of siliceous claystone and porcellanite, intercalated with beds, laminae, and concretions of authigenic carbonate. The transition from Unit II to Unit III is characterized by the diagenetic transformation of opal-A to opal-CT and a corresponding increase in wet-bulk density (see "Physical Properties" section, this chapter). This mineralogic recrystallization occurs in a transitional zone in the interval of 414 mbsf (shallowest occurrence of opal-CT as detected by XRD analysis) to approximately 457 mbsf. Within this zone, intervals of opal-A coexist with intervals of opal-CT. The transformation from opal-CT to authigenic quartz occurs in a transitional zone between 528 and 585 mbsf, with the deepest occurrence at 585 mbsf (see "Silica Diagenesis and Rock Characterization," below). Unusual examples of authigenic quartz are documented by the presence of quartz-replaced centric diatoms (*Coscinodiscus*?) in small discrete laminae at 582.4 and 635.7 mbsf (Figs. 31 and 32).

Authigenic carbonate is present in Unit III as beds (maximum thickness approximately 50 cm), laminae, lenses, and concretions. Siderite (shallowest occurrence at 433 mbsf) and dolomite are the principal authigenic carbonate phases (see "Authigenic Carbonates" below). Carbonate concretions having pyritic cores are common throughout this unit (shallowest occurrence at 498.5 mbsf; Figs. 33 and 34). Recrystallized foraminifers and nanofossils were recognized as pre-

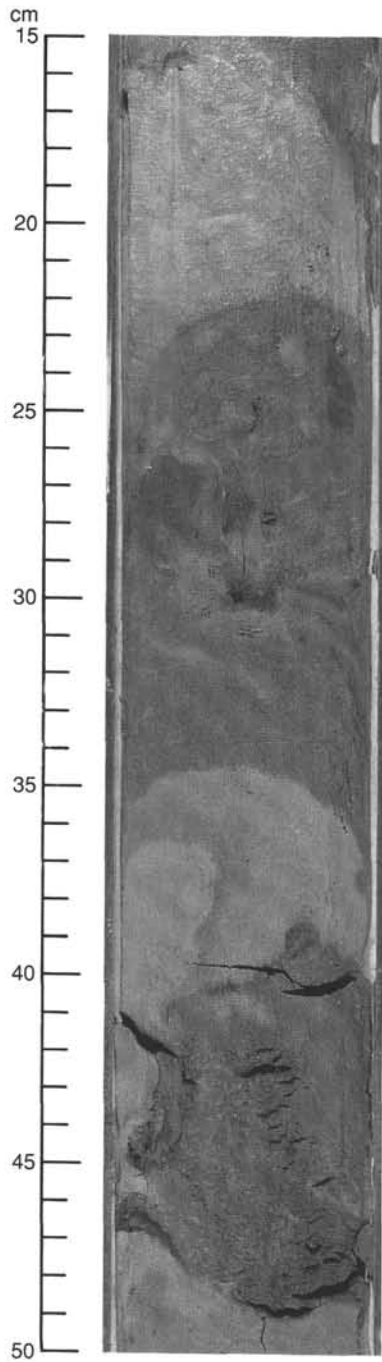


Figure 15. Section 128-799A-3H-1 at 15–50 cm: Slumped diatomaceous (dark-colored) and clay-rich (light-colored) sediments with slump-induced repetition of ash layers.

cursors of the authigenic carbonate phases in some samples (e.g., at approximately 550 mbsf; Cores 128-799B-11R and 128-799B-12R).

Decimeter-scaled, dark-colored, laminated intervals alternating with light-colored, bioturbated intervals are present at approximately 490 mbsf (Section 128-799B-5R-1), 572 mbsf (Section 128-799B-14R-4), and 581 mbsf (Section 128-799B-15R-3). The dark-colored laminated intervals are generally silica-rich, whereas the light-colored intervals tend to be enriched in clay (Fig. 35). In general, sediments in the

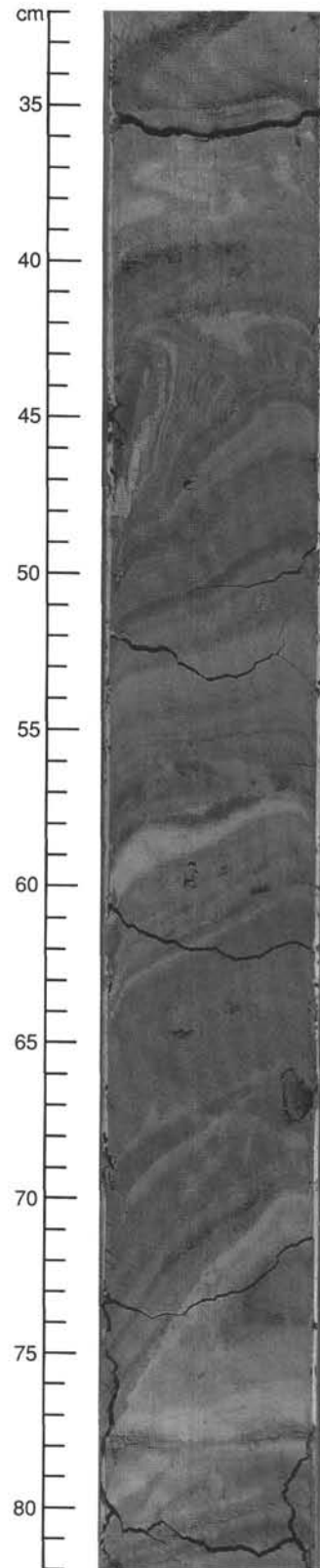


Figure 16. Section 128-799A-6H-2 at 32–82 cm: Disharmonic slump folds; included are thinly laminated sediments that range from diatomaceous oozes to silty clays. These different lithologies (with contrasting physical properties) have probably influenced the rheology of this slump.

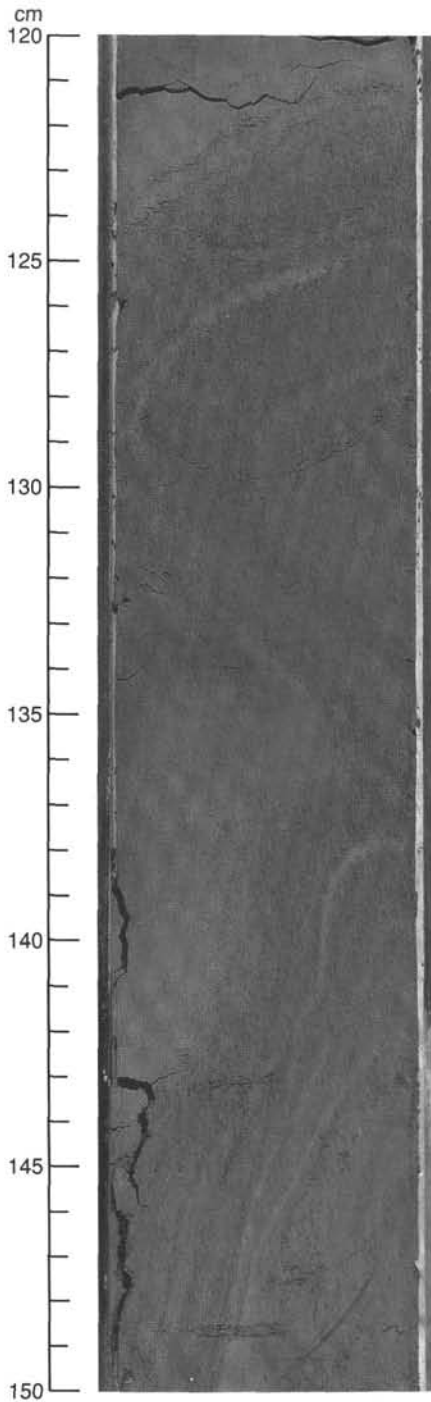


Figure 17. Section 128-799A-6H-2 at 120–150 cm: Slump fold.

upper part of Unit III (457–606 mbsf) are predominantly finely laminated, with only small intervals showing bioturbation, whereas the sediments in the lower part of Unit III (606–800 mbsf) are predominantly bioturbated. Bioturbation consists almost exclusively of subhorizontal burrows of the ichnogenus *Planolites*; some display “*spreiten*” and resemble *Teichichnus* or *Zoophycos* (Figs. 36 through 42). In rare cases, these burrows are cross-cut by prominent vertical burrows or vice versa (Figs. 40 and 41). In the lower part of Unit III, horizontal burrows were flattened during burial

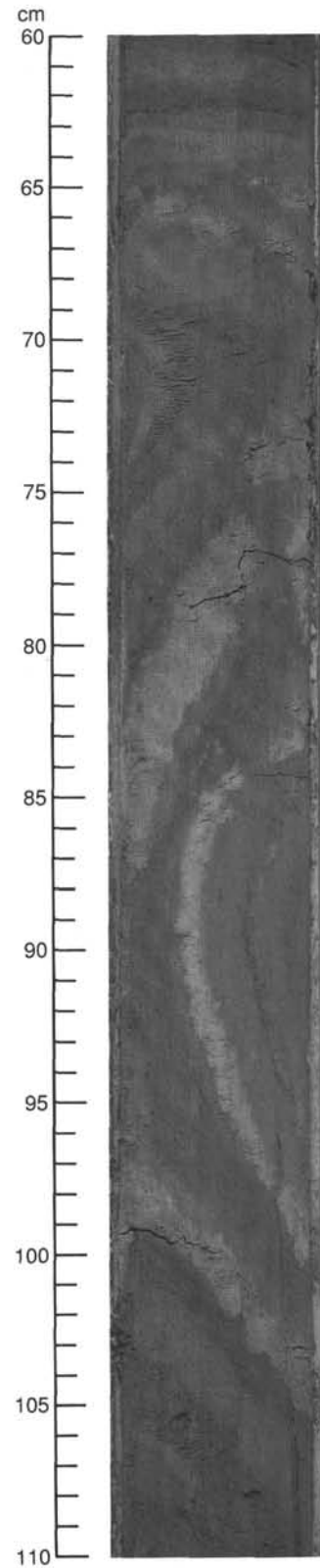


Figure 18. Section 128-799A-7H-2 at 60–110 cm: Slump fold, indicated by three vitric ash layers at 66 to 105 cm.

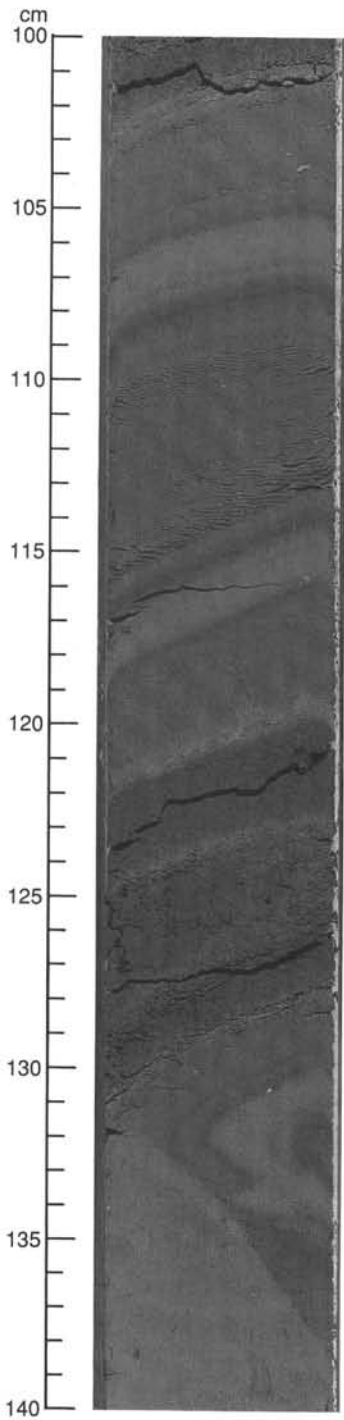


Figure 19. Section 128-799A-8H-2 at 100–140 cm: Slump-folded, thinly bedded sequence (top) in fault contact with a homogeneous clay (bottom).

compaction, yielding a crudely laminated fabric that resembles depositional laminae (Figs. 36, 37, 40, and 42).

Normal faults occur throughout Unit III and are especially common between 580 to 700 mbsf. These are accompanied by rare conjugate normal faults and apparent reverse faults. Below approximately 560 mbsf, fine networks of veins appear

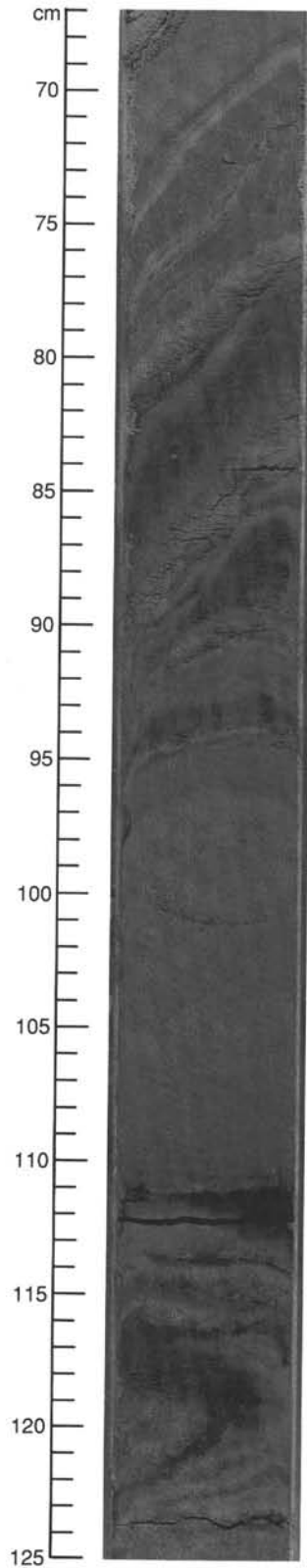


Figure 20. Section 128-799A-9H-2 at 67–125 cm: Slump-related structures.

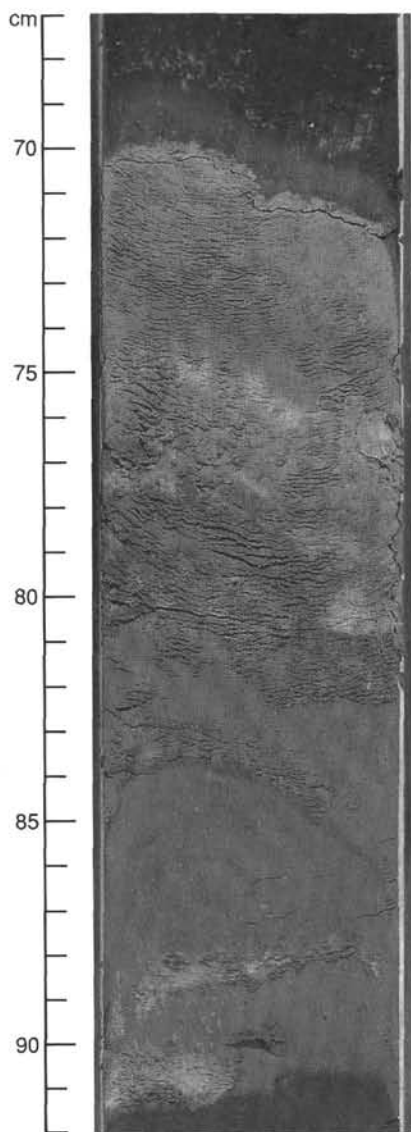


Figure 21. Section 128-799A-8H-6 at 70–90 cm: Overturned slump packet with a normally graded ash layer (90). The stratigraphic base of the ash layer is overturned and its top is disrupted (compare with Fig. 27).

in great abundance. These have been interpreted as water-escape structures (see “Sedimentary Structures,” below).

Volcaniclastic layers are rare in Unit III, with the exception of the uppermost part. They are generally semilithified and are described as tuffs (see “Ash Layers and Tephrochronology,” below).

Unit III ranges in age from middle to late Miocene (see “Biostratigraphy” and “Paleomagnetism” sections, this chapter). Because of the poor biostratigraphic data collected in Unit III and in lower units, we cannot reconstruct exact sedimentation rates.

Unit IV

Cores 128-799B-38R through 128-799B-60R; depth, 800–1020 mbsf. Age: middle to early Miocene.

Unit IV is distinguished by the presence of finely laminated to thinly bedded siliceous claystone and porcellanite, both of which are closely interbedded with carbonate-rich laminae, lenses, and nodules (Figs. 43 through 50). Thin, sharply based

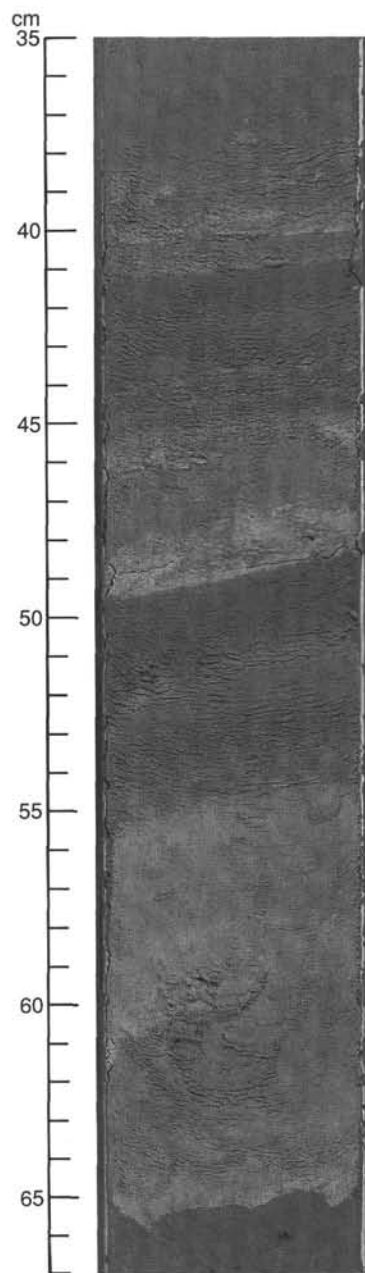


Figure 22. Section 128-799A-8H-5 at 34–67 cm: Graded ash layers in normal position at interval 40 to 66 cm. Note load cast at the base of lower layer. Type G, graded acidic ash layers 89 and 90 (compare with Fig. 26).

and normally graded layers of quartz silt and fine- to coarse-grained sand and glauconite are common throughout Unit IV (Figs. 49 through 52). These siliciclastic layers, which range from 1 mm to approximately 30 cm thick, have been interpreted as distal turbidite deposits. A single, much thicker (about 1.5 m thick) and very uniform bed of siliceous claystone, underlain by a thin layer of pyrite-rich sand at 879 mbsf (Section 128-799B-46R-3), may also represent a turbidite sequence. The laminated fabric in the siliceous sediments of Unit IV is most conspicuously defined by the occurrence of diagenetic carbonate. Fine laminations within dark-colored siliceous claystones that lack diagenetic carbonate are commonly sharply bounded, well-defined, and in some cases, marked by low-angle truncations.

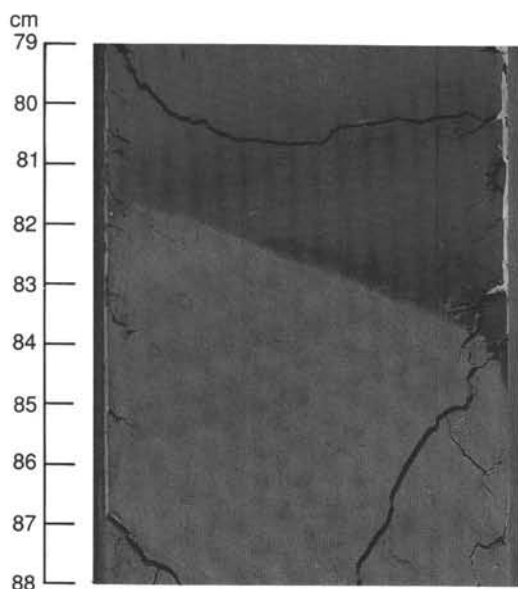


Figure 23. Section 128-799A-6H-4 at 79–88 cm: Oblique section of a fault contact between a slumped thinly bedded packet (top) and a more homogeneous ooze (bottom) at 82–84 cm.

Pyrite is common in the interval from 875 to 980 mbsf (Cores 128-799B-46R through 128-779B-56R). This mineral occurs (1) as fine-grained concentrations at the center of authigenic carbonate concretions, (2) as disseminated microcrystals (maximum 1-mm diameter) throughout the sediments, and (3) in the silt-sized fraction of turbidite sands.

In the interval from 981.3 to 1002.5 mbsf (Sections 128-799B-57R-1 at 19 cm to 128-799B-59R-2 at 41 cm), a distinct sequence of gray, altered, volcanic rhyolitic tuff is present. This sequence consists of a zeolitic tuff, with silt-sized quartz, feldspar, and biotite. Between 990.8 and 991.3 mbsf (Section 128-799B-58R-1 from 0 to 52 cm), an internally faulted tuff breccia is included. Basal parts in this bed are calcitized, probably resulting from diagenetic replacement. The same may hold true for a calcitized interval within the zeolitic tuff at 992.6 mbsf (Section 128-799B-58R-2 at 30–40 cm; Figs. 53 and 54; see "Volcanic ash and Tephrochronology," below).

In the interval from 886.8 to 887.1 mbsf (Section 128-799B-46R-2 at 30–50 cm), a clastic dike is present (Fig. 55).

In general, sediments in Unit IV display close resemblance to the middle to lowermost upper Miocene Onnagawa Formation of the Japan Sea and eastern Honshu (Tsuchi, 1981).

Preliminary micropaleontological shipboard analyses indicate a middle to early Miocene age for Unit IV.

Unit V

Cores 128-799B-61R through 128-799B-67R; depth, 1020–1084 mbsf. Age: early Miocene.

Sediments in Unit V consist of siliceous claystone and claystone with silt and include abundant intercalations of coarse-grained sands and sandstones. Relative to Unit IV, diagenetic carbonates are rare, the abundance of diagenetic quartz decreases, and siliciclastic turbidites become more frequent, thicker, and include coarser fractions. Sediments in Unit V are remarkably enriched in detrital components, in comparison to the sediments of Unit IV. The sand beds reach a maximum thickness of 5 m (interval from 1021 to 1026 mbsf, Core 128-799B-61R); the average thickness, however, is approximately 1 cm (Figs. 56 through 58). Internal structures such as normal grading, cross laminations, sharp bases with

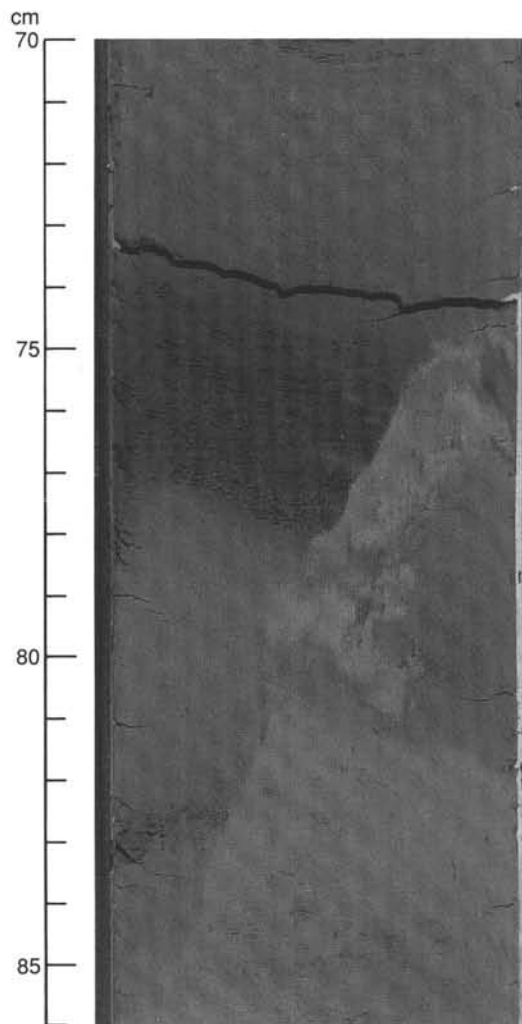


Figure 24. Section 128-799A-7H-4 at 70–86 cm: Oblique fault.

load casts, and internal planar laminations suggest turbulent deposition from gravity-driven flows. Redeposition from shallow areas may be indicated by the inclusion of shallow-water benthic foraminifers, wood fragments, plant debris, and calcareous shell material in the sands, which are interbedded in claystones containing deep-water benthic foraminifers (1500–2000 m water depth; see "Biostratigraphy" section, this chapter). These sands are generally poorly sorted and immature. They consist of angular quartz grains that range from granule to silt-size and include feldspar, biotite, glauconite, pyrite, dark lithic fragments, and fossil debris (fish remains, plant debris, and biogenic calcareous fragments). Very coarse sands include rock fragments of granule- and small pebble-size (e.g., 1033.2–1034.3 mbsf; Sections 128-799B-62R-3 and 128-799B-62R-4). From 1019.8 to 1022.8 mbsf (Sections 128-799B-61R-1 and 128-799B-61R-2), several occurrences of intimately interstratified, crudely laminated silt, clay, and sand with silicified(?) plant fragments and diffuse sand-filled pots (burrows[?]) closely resemble flaser bedding, which is commonly found on tidal flats. The origin of these unusual deposits is enigmatic.

The fine-grained "background" sediments in Unit V display scattered bioturbation. The precise age of Unit V is uncertain; shipboard micropaleontological results indicate an early Miocene age without further constraint.

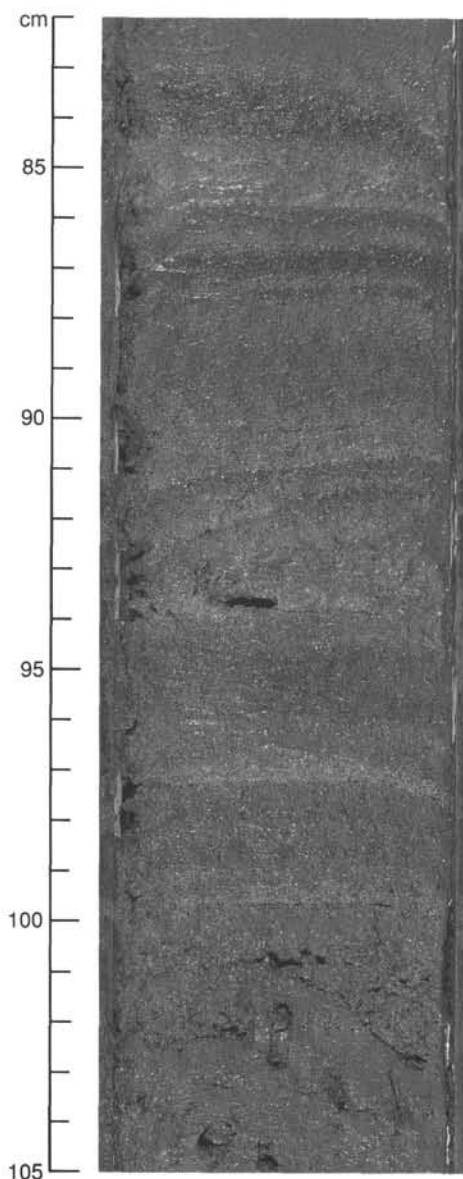


Figure 25. Section 128-799A-2H-3: Laminated foraminifer- and sand-rich turbidite at 83–101 cm. Note scoured, oblique base, and internal low-angle truncations.

Sedimentary Structures

Soft-Sediment Features

The most common soft-sediment deformation structures found in Hole 799A are related to syndepositional, gravity-induced processes. In particular, distinct slump folds were encountered in Unit I, from 10.0 to 11.2 and from 40 to 79 mbsf, and these are associated in places with debris flows.

The shallowest occurrence of slump folds and discordant bedding is in the interval from 10.0 to 11.2 mbsf, from Section 128-799A-2H-7 to the top part of Core 128-799A-3H. Slump folding is particularly well exposed in Section 128-799A-3H-1 at 15–50 cm (Fig. 15), although the bulk geometry has been overprinted by drilling disturbance.

Good examples of slump folds that are associated with detachment faults and bedding truncation occur between 40 and 78 mbsf; on the 3.5-kHz records, this part of the sedimen-

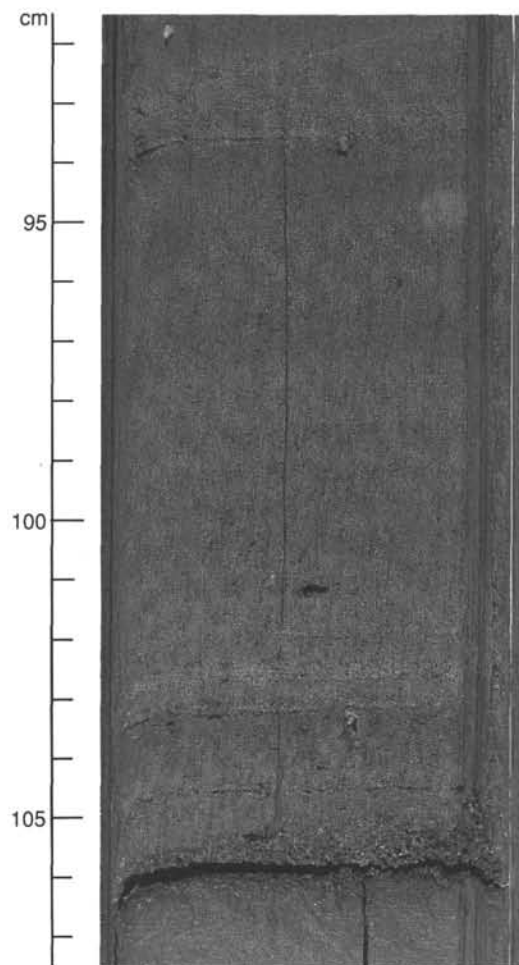


Figure 26. Section 128-799A-2H-4 at 92–107 cm: Laminated, normally graded event bed with sharp, probably erosive, lower boundary; vitric ash at the base.

tary column clearly corresponds to a slumped unit (Fig. 14). A sequence of dysharmonic folds is well-exposed in Section 128-799A-6H-2 at 32 to 82 cm (40 mbsf; Fig. 16) and at 120 to 150 cm in the same section (42.2 mbsf; Fig. 17). Similar features are present in Sections 128-799A-7H-2 at 60 cm (Fig. 18) to 128-799A-7H-3 at 145 cm (51.2–53.6 mbsf); 128-799A-7H-6 at 0–10 cm (56.6 mbsf); 128-799A-8H-2 at 50–140 cm (approximately 61.5 mbsf; Fig. 19); 128-799A-8H-6 at 40–90 cm (66.5 mbsf); and 128-799A-9H-1 at 45 cm to 128-799A-9H-CC at 25 cm (68.7–78.0 mbsf; Fig. 20).

At 66.9 mbsf (Section 128-799A-8H-6 at 70 cm), inverted sediments are documented by an overturned, normally graded ash layer and bioturbation-linked criteria (Fig. 21), whereas the ash layer found 1.55 m above this layer exhibits a normal upward-facing orientation (Fig. 22). The thickness of slumped packets ranges from a few tens of centimeters to more than 2 m. The tightly folded intervals in Cores 128-799A-6H to 128-799A-9H have a distinctly banded appearance. Many thinly bedded to thickly laminated and coarse-grained event strata are present in this banded part of the section. There may be a genetic relationship between the presence of coarse-grained (e.g., porous and permeable) deposits having interbedded clay-rich (e.g., impermeable and thixotropic) sediments, and the soft-sediment deformation structures. These compositional differences and high sedimentation rates most likely resulted in elevated pore pressures and consequent

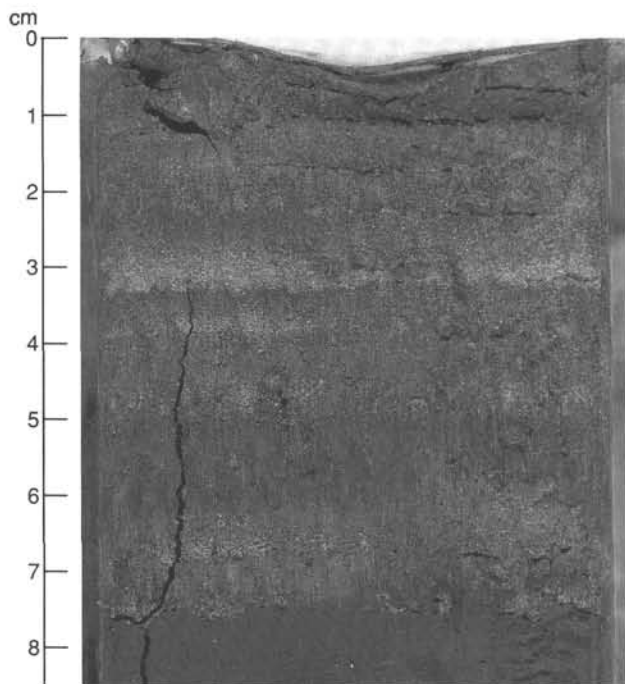


Figure 27. Section 128-799A-2H-6 at 0–8 cm: Normally graded, internally laminated foraminifer and sand-rich turbidite with erosive base.

sediment failure (slumping, faulting, etc.), for instance in response to an earthquake or sediment loading. The observed thin layering also is favorable for the onset of fold geometry. Estimating the true strike of fold hinges and the true sense of gliding motion was difficult because of the two-dimensional geometry seen in the core sections, which in some cases are oblique to the structures. However, by combining our visual observations, the orientation of the APC cores, and the paleomagnetic results, we can infer an axis of rotation of beds that trends approximately east-northeast and west-southwest to east-west with a southward sense of transport, which is consistent with the general morphology of the site (see “Background and Scientific Objectives” section, this chapter).

Instability and slope-related phenomena also are documented by debris-flows and isolated mud clasts, which are exemplified between 56 and 68 mbsf in Sections 128-799A-7H-5 at 60–65 cm and 100 cm, and 128-799A-8H-3 at 50–70 cm. Ultimately, another aspect of this unstable environment can be documented by sharp fault contacts. The apparent dip of faults in the core-splitting section varies from 20° to 65°. The visible offset component, when determined, is always a down-dip, extensional, normal slip. Examples of these contacts can be seen in Sections 128-799A-6H-4 at 82 cm (44.8 mbsf; Fig. 23), 128-799A-7H-1 at 65 cm (49.7 mbsf), 128-799A-7H-4 at 80 cm (54.3 mbsf; Fig. 24), 128-799A-7H-6 at 60 cm (58.2 mbsf), and 128-799A-8H-2 at 131 cm (61.5 mbsf; Fig. 19).

Another interval in which scattered sediments have been affected by gravity gliding and/or normal faulting is present between 116.5 and 165.0 mbsf, from Cores 128-799-14H to 128-799A-18H. Normal faults, as seen in Section 128-799A-14H-1 at 25–40 cm (116.8 mbsf; Fig. 59) or 128-799A-15H-1 at 140–145 cm (127.6 mbsf), exhibit a maximum apparent dip of 50° to 60°. The most abundant features are nonhorizontal lithologic boundaries. At a section scale, bedding dips (from 30° to 60°) are clearly visible in Core 128-799A-18H (155.7–164.0 mbsf) at different levels. However, slump-fold hinges were not identified in this depth interval. At a larger scale, a

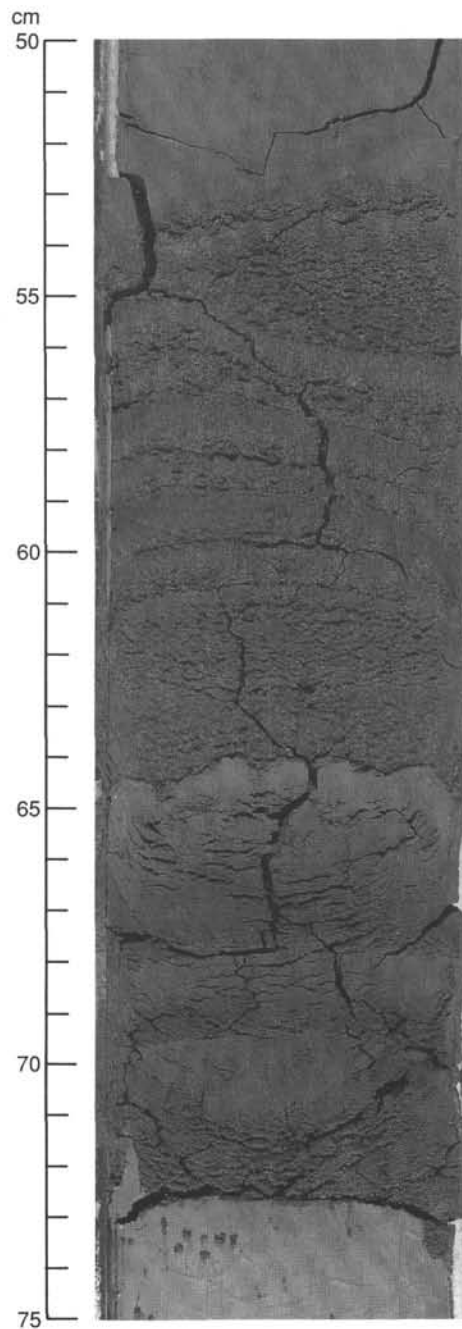


Figure 28. Section 128-799A-4H-6 at 50–75 cm: Two normally graded, turbiditic ash beds. Note laminations and low-angle truncations in upper ash bed.

large slumped packet may be present in the interval from 145.5 to 150.0 mbsf; burrowing features and paleomagnetic measurements suggest that the first three sections of Core 128-799A-17H have been overturned.

In Hole 799B, limited additional evidence for slumping and soft-sediment deformation and for fluid-escape structures occurs from Cores 128-799B-7R (499.7 mbsf) to 128-799B-56R (977 mbsf). The structure seen in Section 128-799B-7R-1 at 70–77 cm (approximately 500.4 mbsf; Fig. 60) has been interpreted as the product of sediment gliding: a small slump fold, involving the upper light carbonate level, bounded at the base by a shallow shear zone, may be associated with reverse and normal faults that developed in the underlying layer.

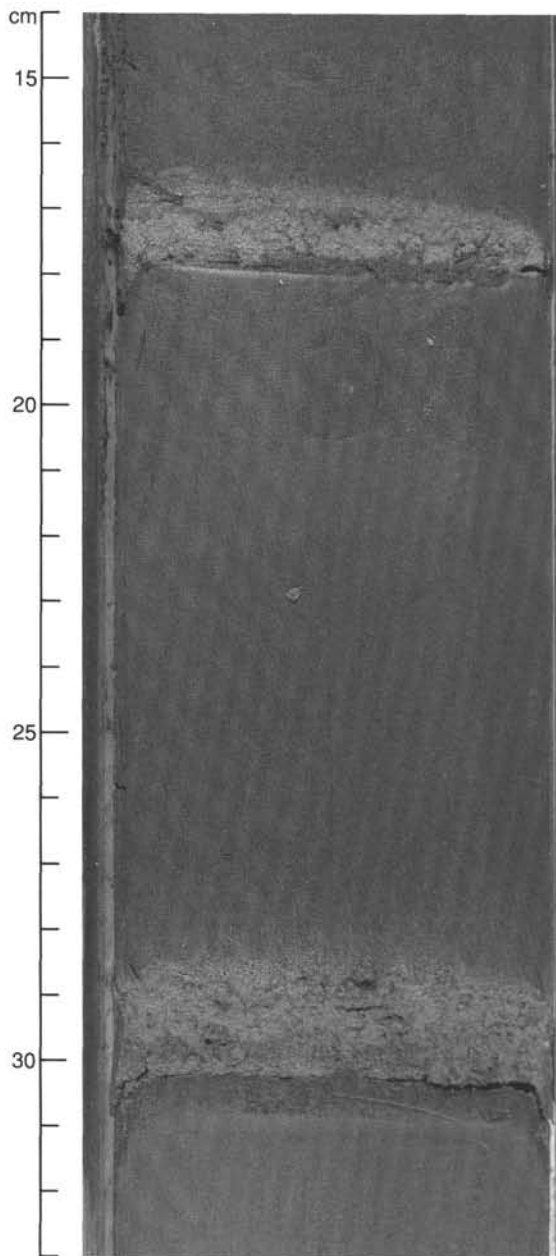


Figure 29. Section 128-799A-3H-4 at 14–33 cm: Two examples of foraminiferal turbidites (*Globigerina* ooze) overlying crystal-rich vitric layers. Ash layers 19 and 20.

Early interstratal folding is present in Core 128-799B-21R (approximately 635.0 to 637.5 mbsf) and again in Core 128-799B-47R (approximately 887.7 mbsf). In this last example (Fig. 45), the light laminations inclined at 30° to 60° exhibit reverse faults in the upper part, in the folded area, and normal faults in the lower part. At a larger scale, from Cores 128-799B-17R to 128-799B-67R (596.3–1084.0 mbsf), bedding dip varies from 0° to 25° . Except for a few cores that already are oriented from paleomagnetic measurements, the dip azimuth is not generally available; therefore, comparison of bedding orientations was difficult, although the bedding dips determined here are oriented consistently toward the northwest. However, a general folding that may have resulted from a compressive phase is unlikely; this does not appear in the seismic profiles, and the absence of unconformities and abrupt

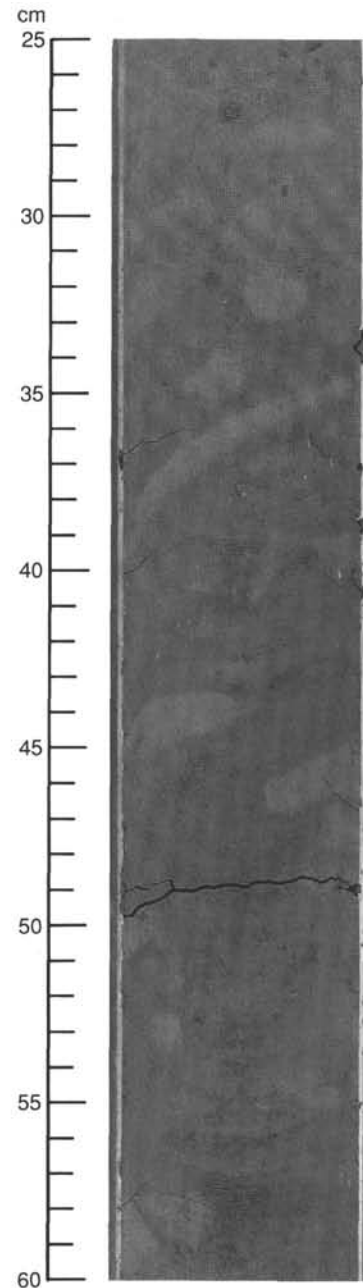


Figure 30. Section 128-799A-18H-6 at 25–60 cm: Large subhorizontal burrows (*Planolites*?) in silty clay with diatoms, infilled with silty clay, similar to and probably derived from the overlying bed.

changes in sedimentation exclude such a compressive tectonic event. Block-tilting phenomena (see below) and differential subsidence of the center of the trough are assumed to be the main factors; however, sediment slumping may account for the bedding dip of particular inclined intervals bounded by horizontal or very shallow-dipping parts.

The last category of early sedimentary deformation structures seen at Site 799 is water-escape features. In Hole 799A, these were observed in the clayey layers that underlie more coarse-grained ash beds in Sections 128-799A-51X-1 at 97–107 cm (462.9 mbsf; Fig. 61) and 128-799A-51X-2 at 45–48 cm (463.8 mbsf; Fig. 62). These have been interpreted as small-scale mud plumes or flame structures with intervening sandy load casts; they are associated with small faults that exhibit

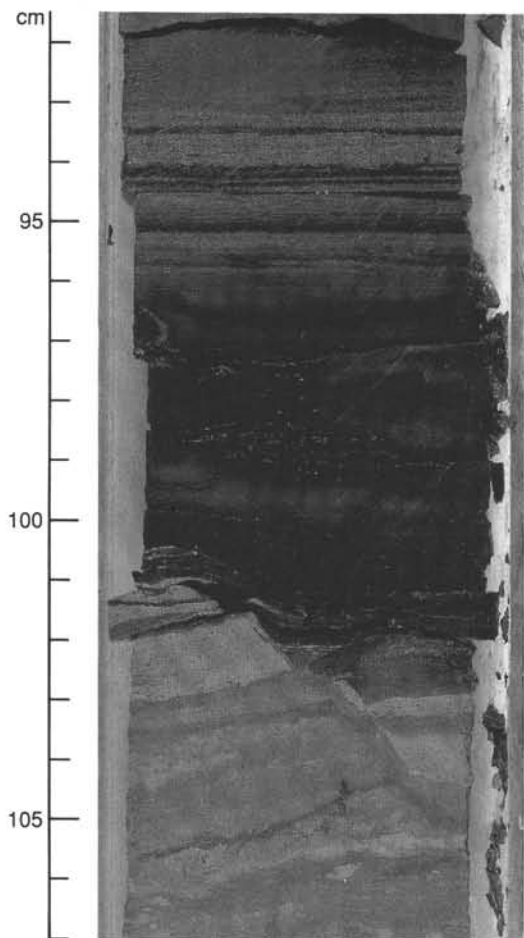


Figure 31. Section 128-799B-15R-4 at 92–107 cm: Laminated sediments at 92–96 cm contain abundant quartz-replaced centric diatoms (confirmed by XRD). The light-colored interval from 101 to 107 cm is carbonate-rich and possesses irregular laminations. A prominent normal fault having two visible surfaces of fault slip indicates tilting of miniblocks and an accommodation of offset by differential compaction of the overlying claystone. Numerous gray concretions that contain carbonate and pyrite are present.

mainly a normal, in some cases a rotational (curviplanar and concave upward), offset and interfere with bioturbation-induced structures. Some of these faults seem to have been important during the fluid drainage. In Hole 799B, a similar flame structure occurs in Section 128-799B-16R-1 at 35 cm (586.9 mbsf) in a thinly laminated sequence. In Section 128-799B-47R-2 (approximately 887.1 mbsf), a 20-cm-long, vertical structure has been interpreted as a sand dyke (Fig. 55) that is responsible for the early vertical contact between an ashy claystone and a laminated siliceous claystone.

Brittle Features

There is no natural boundary between the aforementioned water-escape features and some of the structures described next; flame structures and early fractures are often associated.

In Hole 799A, tectonic structures are rarely observed. With the exception of the effect of gradual compaction, no conspicuous deformation features were recognized until 452 mbsf, in Core 128-799A-50X. Only a few dark veins, rarely branching, are present; for example in Section 128-799A-50X-1 at 59–68 cm (452.9 mbsf), where they are cut obliquely by the core splitting section and exhibit a small normal offset along the longest vein (Fig. 63).

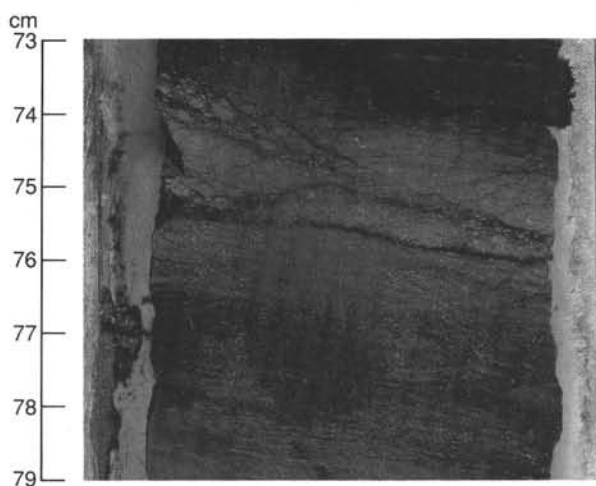


Figure 32. Section 128-799B-22R-1 at 73–79 cm: Probably cataclastic fractures of light-colored silicified bed within dark porcellanite. This unusual structure may be attributed to highly brittle deformation and grain breakage along a shear zone. The shattered appearance of this light-colored sediment may be attributable to the presence of quartz-replaced centric diatoms, a distinctive but uncommon feature of sediments in Unit III.

One microfault (steeply dipping) apparently exhibits a reverse offset in Section 128-799A-50X-5 at 33 cm (459.1 mbsf; Fig. 64). It may represent an oblique section of a small early strike-slip or rotational slip plane. One younger fault surface, with slickensides, was observed dipping about 60° in Section 128-799A-51X at 86–92 cm (464.3 mbsf); This has been interpreted as a normal fault.

In contrast, many fractures were observed in Hole 779B. These include fairly abundant dewatering veins of various geometries, healed faults, and faults with slickensides.

Vein structures are present from Core 128-799B-12R (approximately 547.9 mbsf) to Core 128-799B-30R (723.7 mbsf) and appear again in Core 128-799B-56R (971.5–972.5 mbsf). These are especially well-developed in Cores 128-799B-24R to 128-799B-27R (663.8–702.1 mbsf). There, they occur within siliceous claystones and are generally strata-bound, where they occur within zones that range from 3 mm to 4 cm thick. They are commonly characterized by nested sets of subparallel intrastratal microfractures that display complex dendritic branching at their upper and lower extremities (Figs. 65 through 67). Up to four orders of dendritic branching can be recognized with the naked eye (Fig. 42); finer-scale bifurcations are evident under magnification. In some cases, fractures appear to anastomose, whereas in others they remain dendritic and may even cross-cut older microfractures.

Crosscutting relationships between vein structures and associated fabrics indicate that vein formation post-dates bioturbation, authigenic precipitation of some carbonate concretions, and significant burial compaction, whereas these relationships pre-date some prominent episodes of normal faulting (Fig. 68). In addition, several of the normal faults that we observed are arranged parallel to and intersecting with vein networks, which suggests a genetic relationship between the formation of veins and fault movement (Fig. 69).

Dewatering veins encountered in Core 128-799B-56R (971.5–972.5 mbsf) exhibit a simpler geometry; they are basically branching veins, subperpendicular to bedding and strata-bound.

The intrastratal vein networks may reflect episodic dewatering of partially consolidated sediments, a product of abrupt

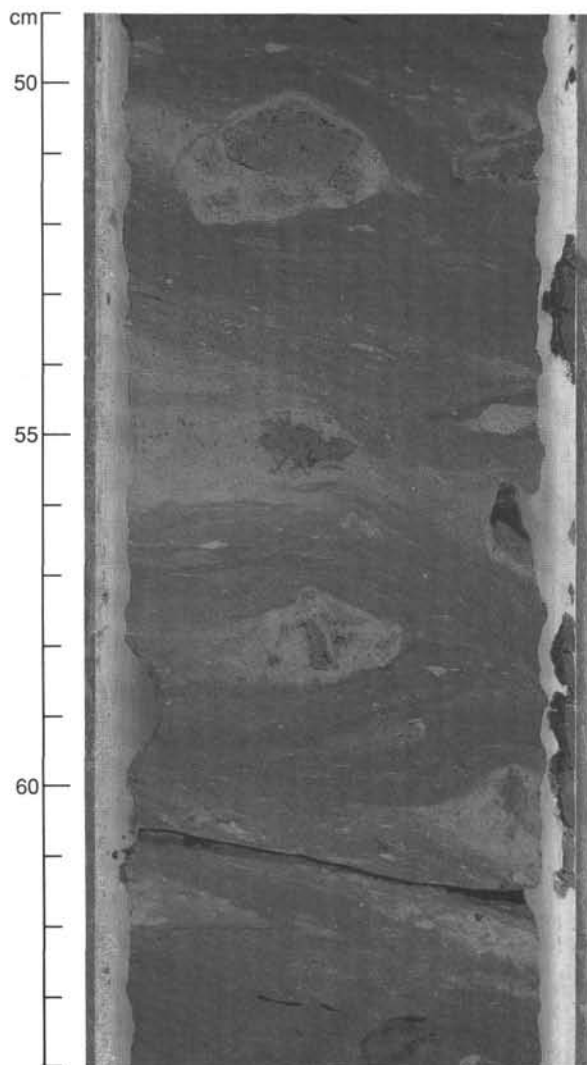


Figure 33. Section 128-799B-18R-5 at 49–64 cm: Mixed carbonate/pyrite concretions are well preserved in this core. The color of oxidized pyrite within concretions is intermediate between the dark gray of the siliceous claystone host sediment and the light gray of the carbonate concretion. Note differential compaction of sedimentary laminae around concretions, which attests to their early diagenetic origin. On the right side of the core at 50.5 cm, note large benthic foraminifers, which have been replaced by diagenetic carbonate.

compactional adjustment to rapid accumulation of sedimentary overburden. Where sedimentation rates are high or where early cementation of sediments has enhanced sedimentary yield strength, substantial sedimentary loading may commonly occur without compactional readjustment; as a consequence, pore fluid pressure increases. When the compactional yield strength of the sediments is finally exceeded, sediment failure and episodic compaction occurs (Bryant et al., 1981).

The abrupt compaction of water-saturated sediments and consequent decrease in porosity results in the expulsion of pore fluids under high pressure. In this preliminary interpretation, the formation of intrastatal vein networks has been attributed to expulsive fluid escape under the aforementioned conditions. Many vein structures at Site 799, particularly in Hole 799B, reflect the nearly instantaneous transition from matrix pore fluid under high pressure to conduit-controlled fluid escape during episodes of abrupt burial compaction. Intrastatal vein networks generally display dendritic branching; however, the genetic reason for bifurcations is unknown.

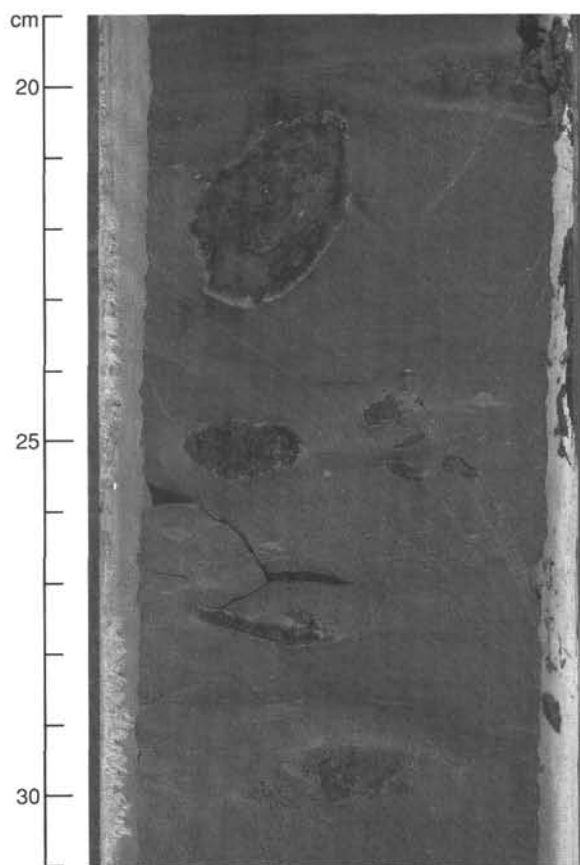


Figure 34. Section 128-799B-25R-3 at 19–31 cm: Dark, pyrite-rich carbonate concretions displaying differential compaction within a siliceous claystone that possesses a laminated texture. Large veins are present from 26 to 31 cm; bifurcating, crosscutting, and anastomosing structures are well-illustrated in this interval.

Vein branching probably occurred during the transition from conduit-controlled flow to intergranular fluid flow, during the re-attainment of equilibrium pore-fluid pressure.

In addition to the veins (and locally associated with them), numerous early healed normal faults are present in Hole 799B from Cores 128-799B-9R (519.0 mbsf) to 128-799B-47R (890 mbsf). These faults exhibit an offset of barely 1 mm up to 2 cm and have a shallow dip of 30° or less. They reflect a bedding-parallel extension, affect the more competent layers (silt, carbonate), and quickly die out in the clayey beds (Fig. 70). Some display the geometry of curvilinear listric faults. The faults are locally grouped in an *en-echelon* set, cutting the affected layer in a series of tilted blocks (Fig. 71) and leading, at the end, to boudinage and stratal disruption (Fig. 65). Their links with the dewatering veins suggest that they formed very early, while water content was still high.

A peculiar and unusual structure is the apparently cataclastic shallow-dipping shear zone that developed in Section 128-799B-22R-1 at 73–75 cm (645.4 mbsf; Fig. 32). This zone has been tentatively attributed to brittle deformation of the light-colored silicified bed. Further study will be needed to evaluate the distribution of grain breakage along this shear zone. The apparent motion includes a flat normal fault.

Other healed normal faults, of greater size, exhibit a larger dip angle (50°–60° on average) and an offset that ranges from 1 to 5 cm (Figs. 39, 72, and 73). Some conjugate sets are present (Fig. 74) and may delimitate small grabens, as in Section 128-799B-47R-1 at 150 cm (894.6 mbsf; Fig. 49).

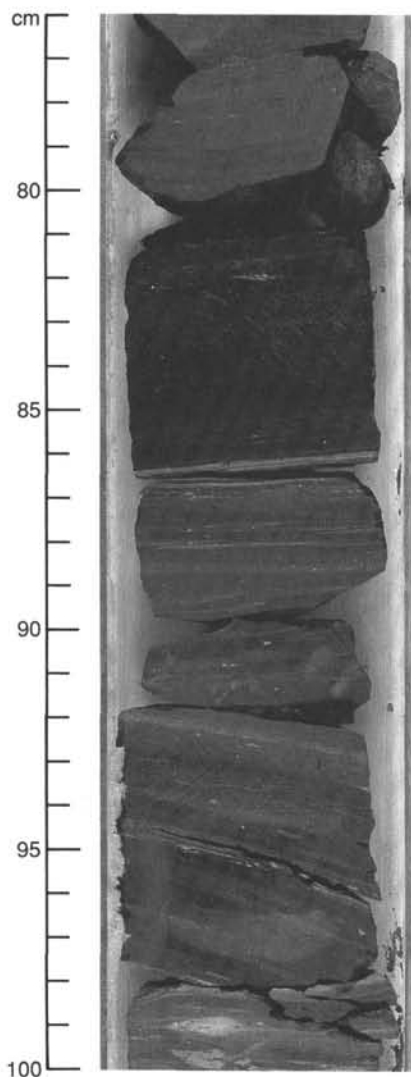


Figure 35. Section 128-799B-26R-1 at 76–100 cm: Dark interval (86.5–81.5 cm) of siliceous claystone with faint laminations contrasts sharply with lighter-colored siliceous claystones that contain an abundance of diagenetic carbonate laminae. Note the irregular and subhorizontal arrangement of light-gray flattened spots within larger burrows; These may represent colonization of large-burrow interiors by smaller burrowing organisms.

These grabens also are arranged in *en-echelon* sets of listric faults in places (Fig. 44), and the faulted blocks may exhibit a 10° to 15° tilt (Fig. 31), the offset being accommodated by differential compaction and/or supple bending of less competent overlying layers. When opened or broken by drilling disturbance (Fig. 44), these faults show slickensided surfaces. This block-tilting model may be a small-scale analog of the structures seen in the Miocene part of the sedimentary column in the seismic records.

The last category of normal faults seen in Hole 799B consists of open, sharp slickensided faults, usually steeply dipping (60° – 80°), with slickenlines having a high pitch angle (Fig. 75). These occur principally in Cores 128-799B-10R to 128-799B-12R (529.0–553.6 mbsf), 128-799B-17R (602.3–602.8 mbsf), from Section 128-799B-23R-2 (656.7 mbsf) to 128-799B-29R-2 (714.9 mbsf), and in Section 128-799B-46R-2 (877.9 mbsf). In some cases, similar surfaces bear slickensides that have a moderate to low pitch angle (50° – 30°), which

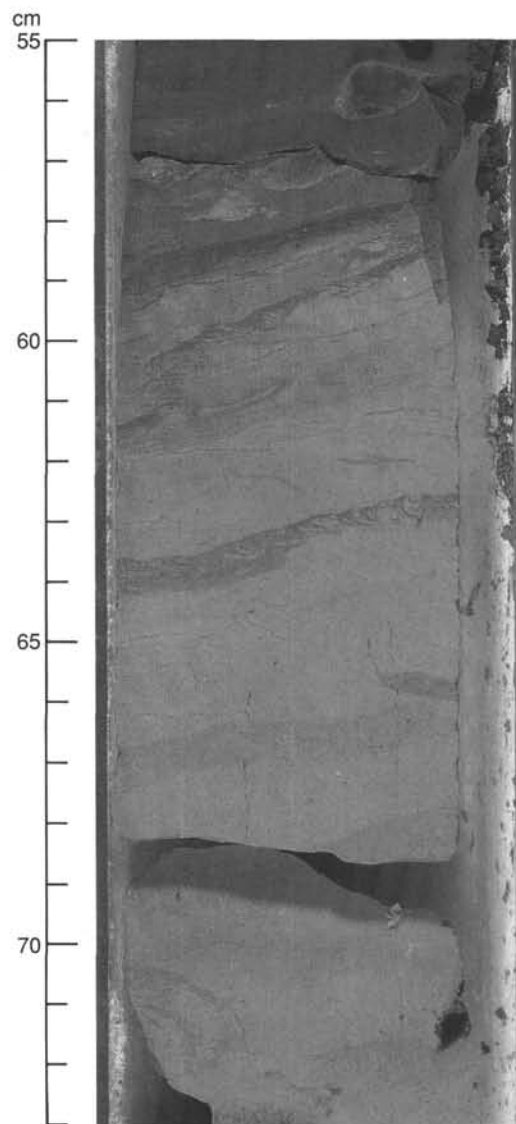


Figure 36. Section 128-799B-27R-1 at 55–73 cm: Subhorizontal deposit feeding traces with well-developed *spreiten* (e.g., meniscate backfills) are well-preserved in this light-colored carbonate bed (59.5–73.0 cm). A vertical succession from large open burrows upward to highly flattened burrows is evident in this sample. Siliceous claystone in the upper part of the photograph contains irregular carbonate concretions; a pyrite-rich concretion centered on a flattened horizontal burrow is present at 56.5 cm.

indicates a significant strike-slip component. We have not determined whether all these faults represent a single set.

The chronologic relationships between these three morphologic groups, although not clear for each individual case, seem to correspond to a succession in time. However, the first two may partially overlap. The last obviously post-dates the early structures, concomitant with the dewatering history, while it affected a more cohesive material having a high angle of internal friction. Deciphering the presence of possibly more than one faulting phase to account for these steep slickensided faults will require more and better orientation measurements. Stratigraphic levels up to the upper Miocene were affected by such structures.

Last, five healed faults having an apparent reverse offset were observed in Hole 799B. Some of these are clearly related to slump structures and early normal faults (Figs. 45 and 61).

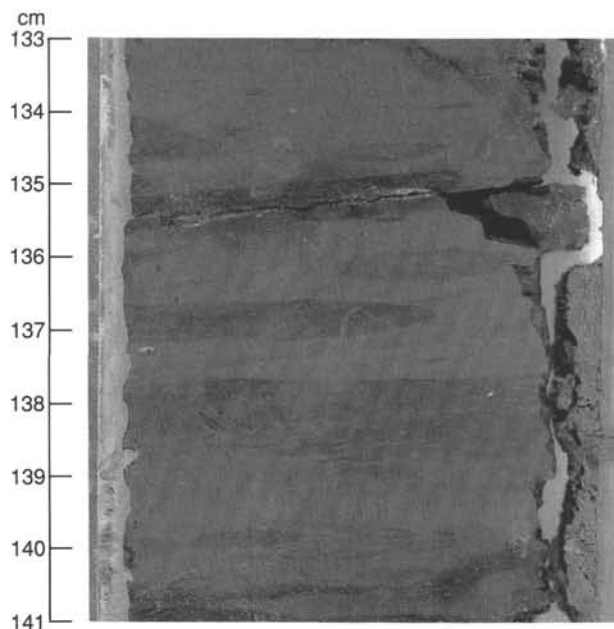


Figure 37. Section 128-799B-11R-4 at 133–141 cm: Dark-colored horizontal deposit-feeding burrows (*Planolites*) in lighter-colored siliceous claystone; compactional flattening of burrows is clearly evident.

Others do not exhibit this relationship in the core-cut section (Fig. 76). However, their shapes and sizes, the very small offsets, and their scarcity do not allow us to conclude that any regional compression phase occurred. Reverse offsetting from local contraction related to early bedding-parallel shearing on a slope is more likely; i.e., a mechanism similar to the one inferred for the early deformation of the sediments of the Japan Trench inner wall (Knipe, 1986); no reverse, slickenside-bearing fault was determined.

For our preliminary conclusion, we emphasize the general extensional tectonic regime that prevailed from the early Miocene to Holocene. Such a regime already is fairly well expressed by early structures developed in the middle Miocene (and upper lower Miocene[?]) sediments. At least one phase of late Miocene or post-Miocene faulting was responsible for the steep faults with slickensides, which in most cases exhibit a normal offset, but in a few cases also exhibit a strike-slip motion. These faults were developed from 464 mbsf in Hole 799A to 877 mbsf in Hole 799B; i.e., their occurrence is restricted to middle to upper Miocene sediments. From 165 mbsf (uppermost Pliocene) to 463 mbsf, no conspicuous fault-induced structure was observed. Thus, taking into account the evidence for deepening of the Kita-Yamato Trough provided by the benthic foraminiferal assemblage (see "Biostratigraphy" section, this chapter) and the resumption of volcanism, both at the beginning of the Pliocene, we may speculate that one important faulting phase took place during the latest Miocene or earliest Pliocene that resulted in the aforementioned faults. At a general scale, this phase corresponds to the "second tectonic stage" of Honza (1979). The phase is consistent with the onlap of the "stratified layer" onto the "transparent layer" that was reported from the seismic profiles around the Yamato Ridge (Tamaki, 1988) and the age (early Pliocene) proposed for this disconformity after the results of Leg 31 (Karig, Ingle, et al., 1975). This phase is also in agreement with the clear onlap seen in seismic lines crossing the Yamato Trough. The last period of instability,

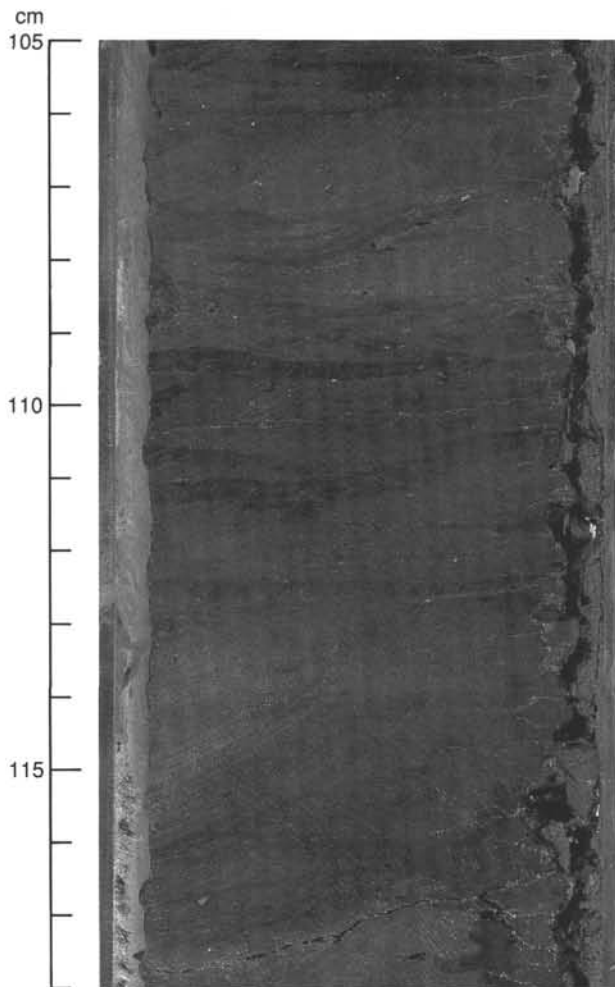


Figure 38. Section 128-799B-17R-3 at 105–118 cm: Numerous horizontal burrows are evident; conspicuous *spreiten* are evident in burrows centered at 111.5 and 116 cm.

documented by the association of normal faults and slumps observed in the Hole 799A cores, began in the latest Pliocene.

Gravitational Compaction

Incipient fissility appears in Core 128-799A-30X at approximately 263 mbsf. This first occurrence is much shallower than that at Site 798. Fissility becomes fairly well developed in the clayey layers at approximately 460 mbsf. In the cores of Hole 799B, fissility remains clearly apparent in the claystone, but is obscure to the naked eye in the silica-rich rocks, such as porcellanite. Differential compaction is noticeable around early diagenetic pyrite and carbonate nodules (Fig. 34) and above tilted blocks (Fig. 31).

Authigenic Carbonates

Site 799 sediments are characterized by the abundant and variable occurrence of authigenic carbonates; more than 200 nodular intervals, layers, and beds of authigenic carbonate were recovered from Site 799, whereas only two dolomite beds were encountered at Site 798. Authigenic carbonates encountered at Site 799 include calcite, dolomite, and siderite, as revealed by XRD analysis (Fig. 77). Dolomite is the predominant authigenic carbonate phase. The d_{104} spacing of Site 799 dolomites ranges between 2.91 to 2.97 Å, which is larger than the value of stoichiometric dolomite; hence, Site



Figure 39. Section 128-799B-17R-5 at 47–102 cm: Subhorizontal deposit-feeding burrows are prominent between 65 and 87 cm. A prominent, healed normal fault is evident from 79 to 92 cm. An open fault at 55 cm has slickensides, which are not evident in the photograph.

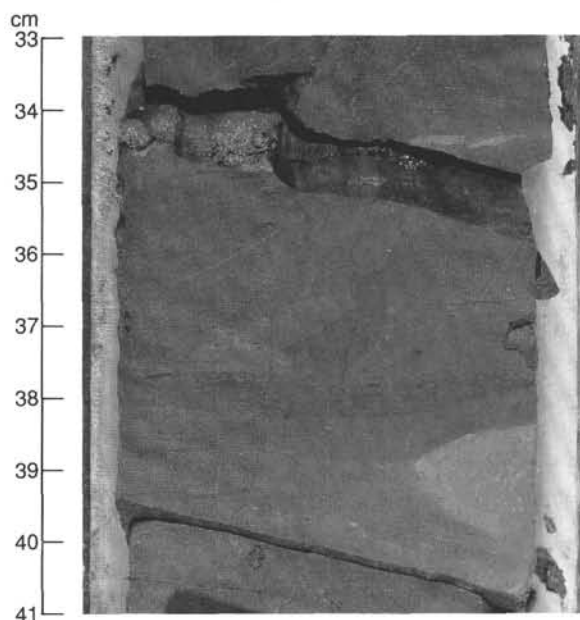


Figure 40. Section 128-799B-24R-1 at 33–41 cm: Compressed vertical burrow, crosscut by a horizontal burrow at 38 cm. Slickensides are present along a normal fault at 34.5 cm.

799 dolomites may represent calcian dolomite or, more likely, ferroan dolomite or ankerite.

The shallowest occurrence of dolomite is at 12.7 mbsf (Section 128-799A-3H-2 at 50 cm, confirmed by XRD analysis). Dolomite occurs throughout lithologic Units I through V, whereas occurrences of siderite are restricted to sediments below 433.7 mbsf in Unit II (Section 128-799A-48X-1 at 77–79 cm; Fig. 77).

The depth of the shallowest occurrence of authigenic calcite is uncertain because of the difficult visual discrimination between authigenic and biogenic calcite using smear slides, especially when calcareous microfossils are partly dissolved or recrystallized. Foraminifers and nanofossils diminish downward, and the deepest, XRD-detectable amount of biogenic calcite was encountered at 200.4 mbsf (Section 128-799A-22X-5 at 60–61 cm). The surprising occurrence of nanofossils and foraminifers in Core 128-799A-39X (345.9–355.6 mbsf) in a mixture with dolomite crystals is peculiar. Artificial contamination can be excluded because this assemblage was observed in different sections of this core. Natural “contamination” by sediment reworking is possible, and this process is the subject of current investigations.

Authigenic calcite occurs as a subhedral overgrowth of nanofossils and foraminifers and as recrystallized nanofossils. Clay- to silt-sized, anhedral grains in semilithified dolomite layers in lithologic Units I and II and well-lithified, dolomite-siderite layers in Unit III may be authigenic.

Authigenic dolomite at Site 799 occurs as (1) disseminated rhombs, (2) pasty “patches,” (3) “chalky” layers, (4) thin hard layers, (5) hard nodules, (6) thick hard beds, and (7) dolomite-cemented sandstone, whereas authigenic siderite occurs as (1) disseminated rhombs, (2) thin hard layers, and (3) hard nodules.

1. The shallowest occurrence of disseminated dolomite rhombs, approximately 4 to 15 μm in diameter, was detected at 12.7 mbsf (Section 128-799A-3H-2 at 50 cm). The shallowest occurrence of disseminated siderite is at 457.3 mbsf (Section 128-799A-50X-4 at 58–59 cm). Dolomite and siderite

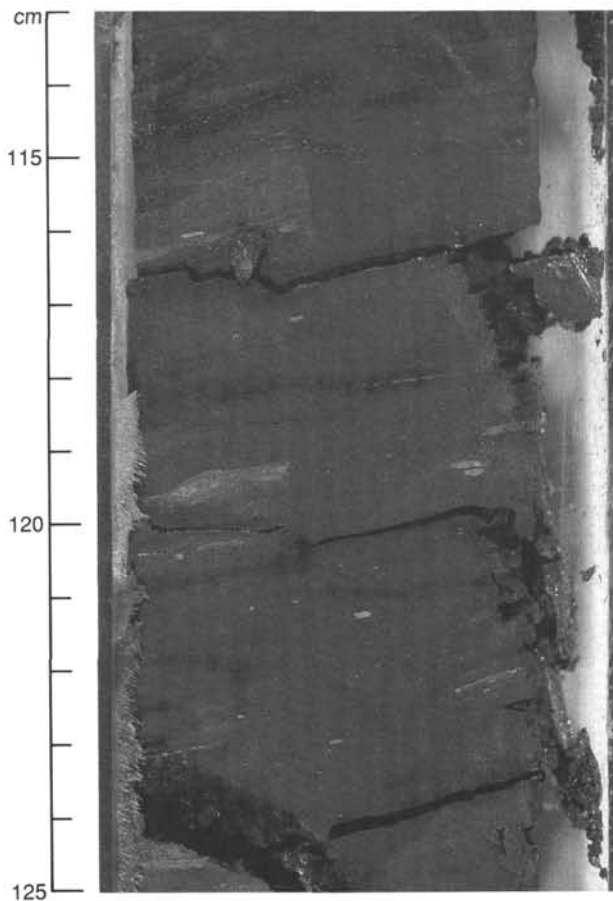


Figure 41. Section 128-799B-28R-1 at 113–125: Large vertical burrows are uncommon but conspicuous in siliceous claystones of Unit III. This burrow may truncate a lamination of diagenetic carbonate at 119.5 cm.

rhombs occur in all five lithologic units; dolomite content of the sediments range up to 10%.

2. Pale olive (5Y6/4), olive yellow (5Y6/6), or less commonly, yellow (5Y7/6), unlithified to semilithified, irregularly shaped, and podlike pasty nodules or “patches” (0.3–7 cm in diameter) are identified as carbonate concentrations and carbonate-rich areas (Fig. 78). They frequently occur in mottled and bioturbated sediments, and some “patches” may have formed in and around burrows. The shallowest occurrence was encountered at 99.7 mbsf (Section 128-799A-12H-2 at 95–96 cm). These patches occur in the lower part of Unit I and throughout Unit II; however, they are absent in Units III, IV, and V. The dolomite content in these patches ranges from 10% to 47%.

3. Olive (5Y5/4) to pale olive (5Y6/4) and less frequently, yellow (5Y7/6) to pale yellow (5Y7/4-7/3), semilithified, or partly lithified, thin “chalky” layers (0.5–12 cm thick; Figs. 79 and 80), are composed of 4% to 35% dolomite and may include minor amounts of calcite. Upper and lower boundaries of these layers are generally gradational. Nannofossil- and foraminifer-rich sediments may have been a possible precursor to this group of authigenic carbonates. The shallowest occurrence of such layers was observed at 12.7 mbsf (Section 128-799A-3H-2 at 50–51 cm); they are scattered throughout Unit I and are more abundant in Unit II. These patches are absent in Units III, IV, and V. The degree of lithification and dolomite content of “chalky” layers tends to increase with increasing depth of burial, and the top and bottom boundaries of these layers also become sharper. How-

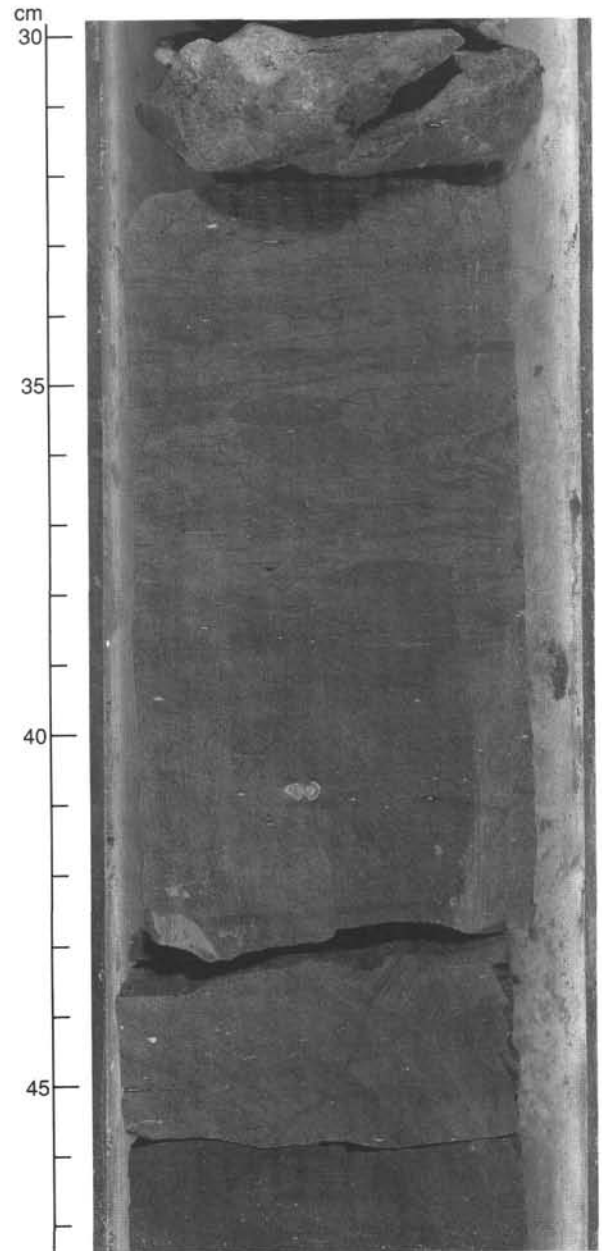


Figure 42. Section 128-799B-21R-1 at 30–47 cm: Horizontal, deposit feeding burrows that have been flattened by burial compaction are a common feature of many crudely laminated porcellanites in Unit III. Finely branching and anastomosing microfracture/vein networks post-dating bioturbation are also well-developed. Note how these fracture networks are weakly confined to specific horizontal intervals. This observation suggests that subhorizontal anisotropies in sediment strength and/or permeability existed during expulsive dewatering episodes of vein formation. Vein bifurcations and anastomosing fabric at the upper extremities of vein networks may be observed at 36 and 42 cm. Veins from 44.5 to 47.0 cm exhibit a sigmoidal geometry and well-ordered bifurcations at their distal extremities. A “NE-SW”-trending fracture displaying several millimeters of apparent normal offset is present at 40–47 cm.



Figure 43. Section 128-799B-45R-2 at 2–12 cm illustrates well-developed laminations and elongated nodules of diagenetic carbonate in dark porcellanite; scattered sand-sized glauconite grains are evident in the upper several centimeters of the photograph.

ever, semilithified, pasty dolomite layers still were found in the lower part of Unit II.

4. Pale olive (5Y6/4) to yellow (5Y7/6), entirely lithified, thin, hard layers occur below 434 mbsf, in the lowermost part of Unit II, in Unit III, and in Unit IV; however, these layers do not occur in Unit V. The thickness and color of these hard layers are similar to those of the chalky layers and may represent a well-lithified variety of these chalky layers. The majority of these hard layers contain significant amounts of siderite (8 of 10 layers examined). For instance, a 4-cm-thick, pale olive (5Y6/4), hard layer in Section 128-799A-48X-1 at 73–77 cm, 433.6 mbsf, contains approximately 40% siderite and 30% dolomite. Hard layers of siderite are abundant in Unit III, and less abundant in Unit IV. A 14-cm-thick, pale olive (5Y6/4), hard layer at 553.1 mbsf (Section 128-799B-12R-4 at 72–86 cm) is composed entirely of siderite (Fig. 81).

5. Gray (5Y6/1) to light gray (5Y7/1, 5Y7/2), or less frequently, pale yellow (5Y7/3, 5Y7/4), fully lithified, relatively small (0.5–4 cm in diameter) dolomite nodules first appear at 106.8 mbsf (Section 128-799A-12H-CC at 25–26 cm); these occur throughout Units I, II, III, and IV (Fig. 82). Some nodules in the lower part of Unit I and the upper part of Unit II are subangular to subrounded and may be broken fragments, especially in sediments that have been severely disturbed by drilling. Those nodules in Units II, III, and IV become more round and spheroidal to ellipsoidal. In some cases, the nodules display a zoned structure that consists of a gray (5Y5/1) to light gray (5Y7/1) pyritic core and yellow (5Y7/6) to olive yellow (5Y6/6) rim (Figs. 33 and 83). Figure 83 presents fully lithified and zoned nodules that were found at 459.9 mbsf (Section 128-799A-50X-6 at 8–12 cm). These

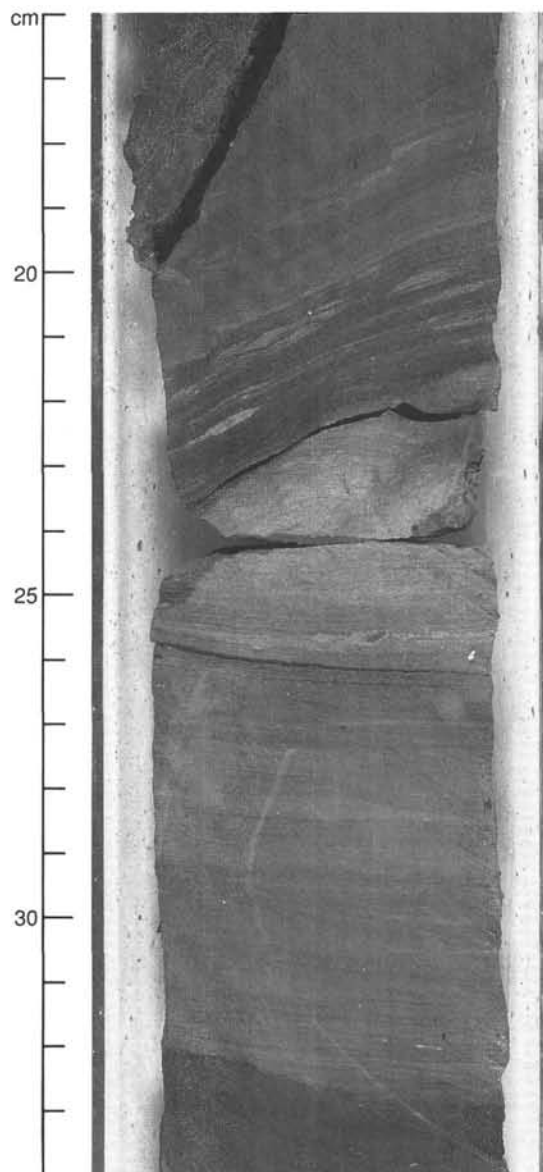


Figure 44. Section 128-799B-46R-4 at 16–34 cm: Very finely laminated siliceous claystone with dolomitic intervals; note sharply based and finely laminated bed at 32.5 cm, with load casts (?) and a small normal fault having approximately 3 mm of offset at 21.5 cm.

nodules occur in a 5-cm-thick, yellow (5Y7/6), hard dolomite-siderite layer. Laminations and flattened burrows in the hard layer are deformed and bent around the zoned nodules. This suggests that these zoned nodules formed early within relatively soft sediments, before major compaction. The hard dolomite-siderite layer formed later, after significant compaction.

6. Light gray (5Y7/1) to light greenish gray (5GY7/1), fully lithified, thick dolomite beds were encountered at five horizons: 247.1 mbsf (Section 128-799A-28X-1 at 0–12 cm) in Unit II; 465.8 mbsf (Section 128-799A-51X-CC at 5–35 cm) in Unit III; 730.8 mbsf (Section 128-799B-31R-1 at 0–54 cm); 762.6 mbsf (Sections 128-799B-34R-2 at 130–150 cm, and 128-799B-34R-3 at 0–19 cm) in Unit III; and 934.4 mbsf (Section 128-799B-52R-2 at 0–50 cm) in Unit IV. These five horizons were clearly detected by logging (see “Logging” section, this chapter). The shallower bed occurs as broken fragments in

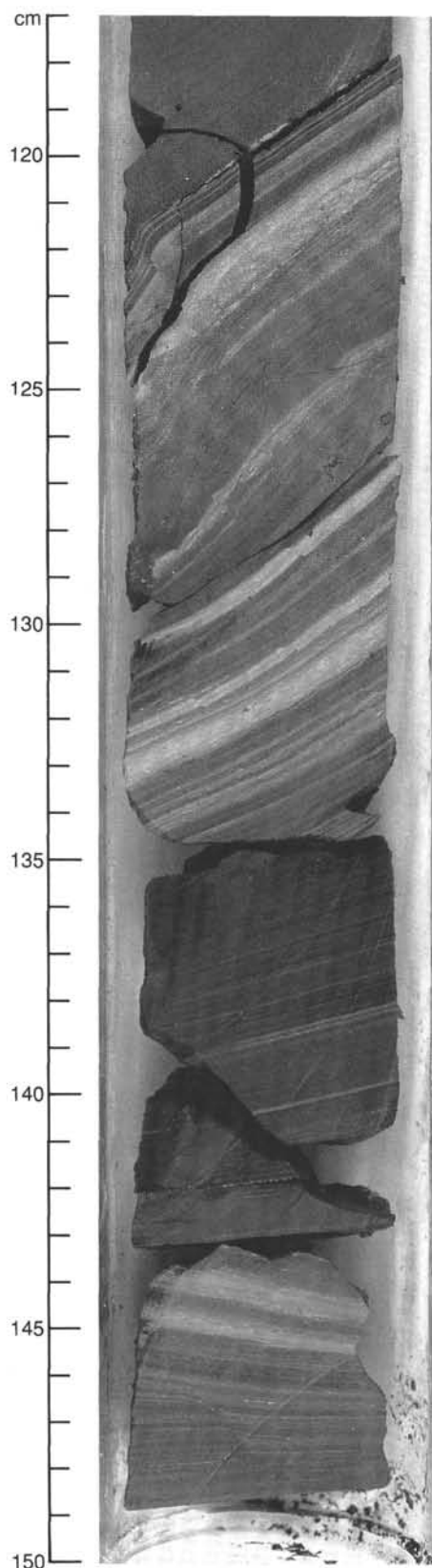


Figure 45. Section 128-799B-47R-2 at 117–150 cm: Laminae of white diagenetic carbonate in dark siliceous claystone. Ductile deformation and numerous *en echelon* and normal faults from 121 to 132.5 and from 146 to 150 cm may record slumping of partly consolidated sediments that contained early diagenetic carbonate laminae.

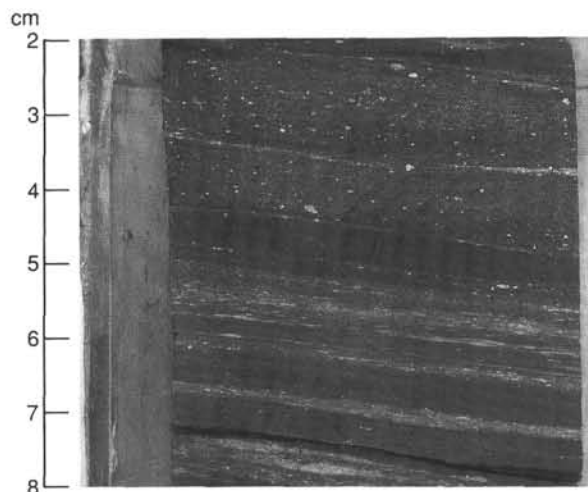


Figure 46. Section 128-799B-47R-4 at 2–8 cm: Crudely laminated white fragments of diagenetic carbonate in dark porcellanite.

sediments that were severely disturbed by drilling; the apparent thickness is 12 cm. Logging data suggest that the dolomite bed is considerably thicker, perhaps 1 to 2 m (see “Downhole Measurements” section, this chapter). The dolomite bed at 465.8 mbsf is 28 cm thick and exhibits a sharp boundary with the overlying porcellanite bed. The bottom part of the dolomite horizon was fractured during drilling. The dolomite content within the lower portion was estimated at 70% to 80% from XRD peak intensities. Neither calcite nor siderite were detected from these thick authigenic dolomite beds. The dolomite beds generally contain well-preserved diatoms, whereas most diatoms in the host sediments are dissolved. This suggests that these dolomite beds formed at relatively shallow burial depths, prior to significant silica diagenesis.

7. Light gray (5Y7/1) and light greenish gray (5GY8/1), dolomite-cemented, fine to medium sandstone occurs exclusively in Unit V. Thicknesses range from 1.5 to 3 cm and are primarily controlled by the thickness of the host sandstone layers. Sand-filled burrows in Unit V are often cemented by dolomite.

The frequency and degree of lithification of dolomitic chalky layers, hard layers, and patches in Site 799 sediments imply that the degree of carbonate diagenesis increases with depth of burial. Because siderite was encountered below 434 mbsf, authigenic carbonates in the lowermost part of Unit II through Unit V may represent advanced stages of carbonate diagenesis. Authigenic siderite has been considered to characterize a late stage of carbonate diagenesis in marine strata (e.g., Curtis, 1977; Matsumoto and Matsuhisa, 1986; Matsumoto, 1989). This has been explained as the result of decreasing concentrations of magnesium and increasing concentrations of ferrous iron during the late diagenetic stage. Note, however, that the occurrence and distribution of authigenic carbonates at Site 799 do not simply correspond to the depth of burial. Unlithified, pasty carbonate patches coexist with fully lithified, hard dolomite-siderite layers, and hard, thick dolomite beds occur at both shallow and deep levels.

The pore water chemistry at Site 799 (see “Inorganic Geochemistry” section, this chapter) is not entirely consistent with the distribution of authigenic carbonates. In a rough sense, downhole variations in calcium, magnesium, and the calcium/magnesium ratio are consistent with biogenic calcite recrystallization above 100 mbsf. However, we noted that authigenic calcite and dolomite commonly co-occur through-

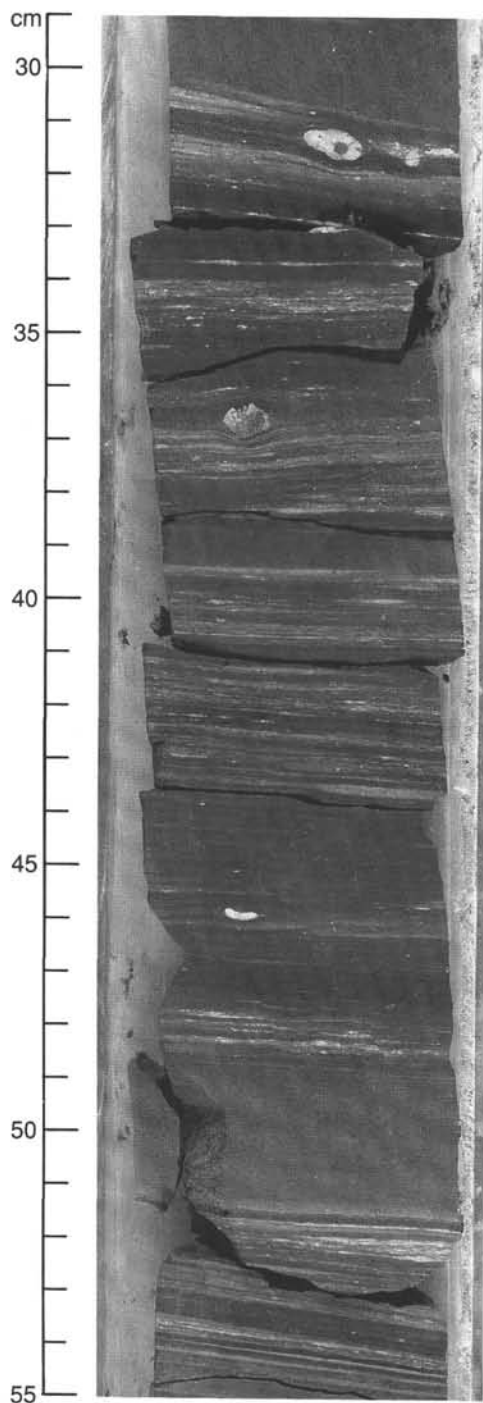


Figure 47. Section 128-799B-47R-4 at 29–55 cm: Irregular, white, carbonate-rich laminae and flattened lenticular concretion of diagenetic carbonate; the large pyrite and carbonate concretions centered at 31.5 to 36.5 cm are associated with differential compaction, thus testifying to their early diagenetic origin. A silty, normally graded bed is present above 55 cm.

out the upper 325 m at Site 799A, even within intervals of relatively low pH and alkalinity (275–450 mbsf; see “Inorganic Geochemistry” section, this chapter). These observations imply that the abundance of authigenic carbonate does not necessarily reflect the present pore water chemistry and that

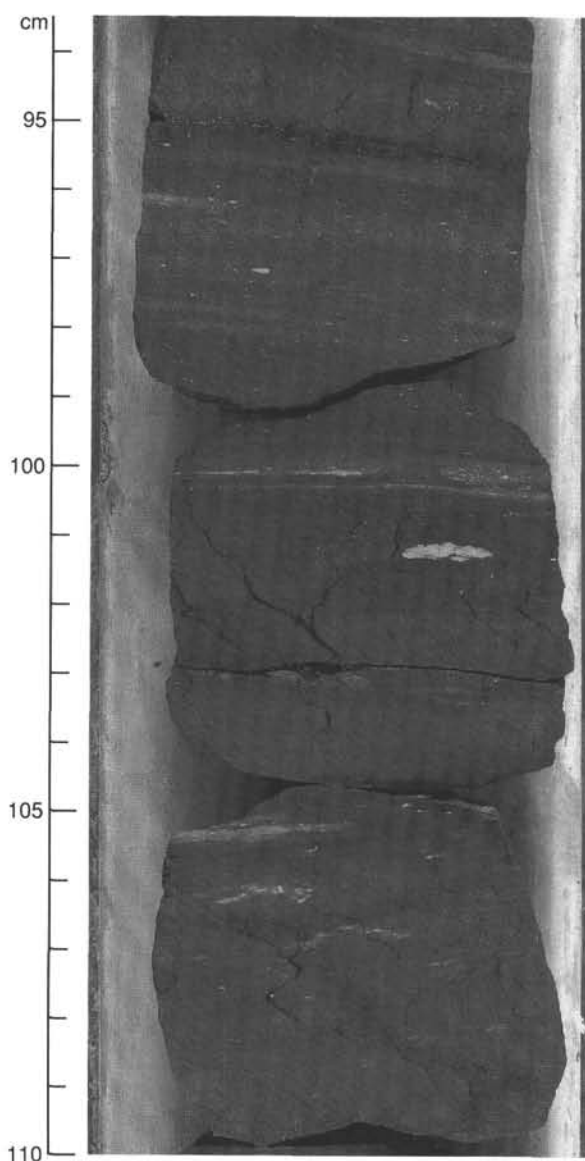


Figure 48. Section 128-799B-38R-1 at 94–110 cm: Laminations defined by sand- to silt-sized grains and minor concretions of diagenetic carbonate in porcellanite. Prominent vein structures are centered at 95, 102.5, and 108 cm; note intricate bifurcations of individual veins and anastomosis of some vein arrays. Crude, sigmoidal geometry is evident at 108 cm.

contents of authigenic carbonates in Site 799 sediments are not always in chemical equilibrium with ambient pore waters.

The occurrence of abundant authigenic carbonates at Site 799 may be related to the frequent intercalation of foraminifer- and nannofossil-rich intervals as a precursor bed, and to slower sedimentation rates (see “Sediment Accumulation Rates” section, this chapter). Calcareous microfossils often are overgrown or replaced by authigenic carbonates, while the decrease downhole in abundance of biogenic calcite is inversely related to an increase downhole in authigenic dolomite, as detected by XRD analysis (Fig. 77). Decreased accumulation rates may have been responsible for the formation of the exceptionally thick and fully lithified dolomite beds at Site 799.

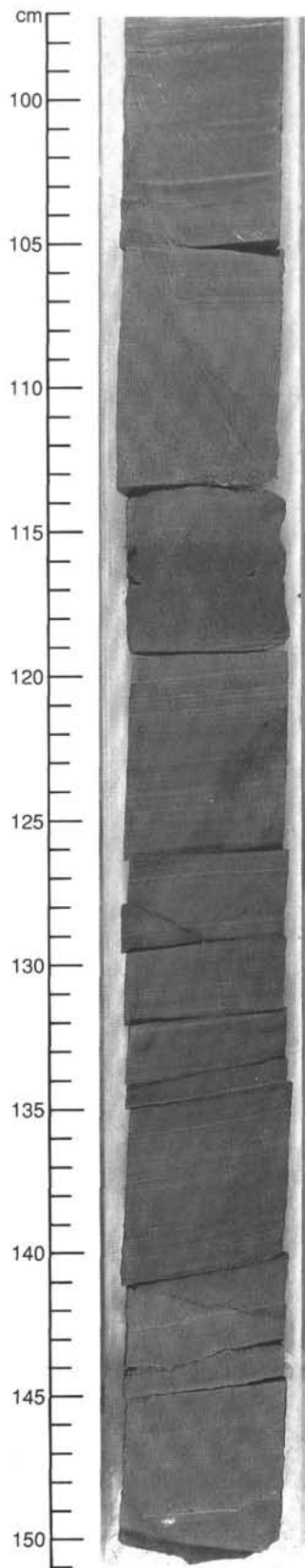


Figure 49. Section 128-799B-47R-1 at 97–150 cm: Finely laminated siliceous claystone interbedded with normally graded siliceous siltstone. Note normally graded bed from 119 to 114 cm; 1.5 cm of apparent offset on a normal fault is evident at the top of this bed, where it contrasts with the overlying laminated siliceous claystone.

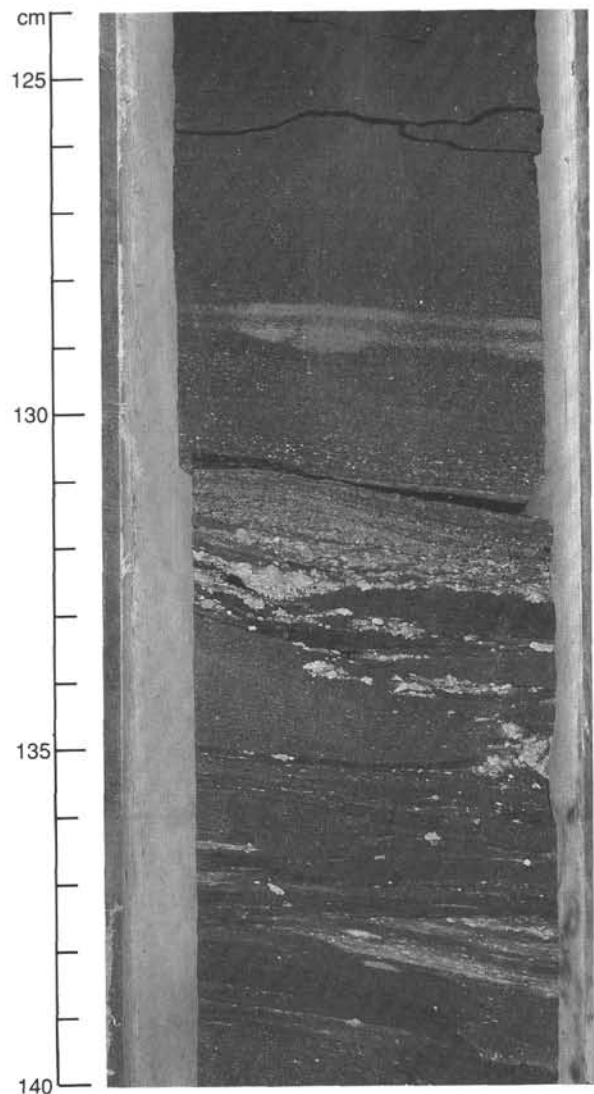


Figure 50. Section 128-799B-47R-3 at 124–140 cm: Laminated siliceous clay interbedded with siliceous silt. A normally graded unit with sand and white particles of diagenetic carbonate possesses a sharp irregular base at 132 cm and extends upward beyond the top of the photo. Disturbed wavy laminae and chaotically distributed angular sand-sized particles of diagenetic carbonate may testify to the erosion and fragmentation of early diagenetic carbonate by turbulent currents associated with gravity-driven event deposits. From 133.0 to 134.5 cm, chambered benthic foraminifers are recognizable at the cores of some carbonate grains.

Silica Diagenesis and Characterization of Siliceous Rocks

The transformation from opal-A to opal-CT occurs in Site 799 sediments mainly in the interval from 414 to 457 mbsf (Fig. 84). Distinct dissolution of diatom frustules was observed in smear slides at depths as shallow as 390 mbsf (Core 128-799A-43X). The shallowest occurrence of opal-CT (distinctly noted during visual description) was at 414 mbsf (Section 128-799A-46X-1 at 80–88 cm), where an interval of hackly sediment containing abundant opal-CT (confirmed by XRD analysis) occurred. Opal-CT also was determined at various intervals in Cores 128-799A-48X and 128-799A-49X, and cherty nodules occur at 434 mbsf (Section 128-799A-48X-1). However, between 414 and 457 mbsf, most sediments contain well-pre-

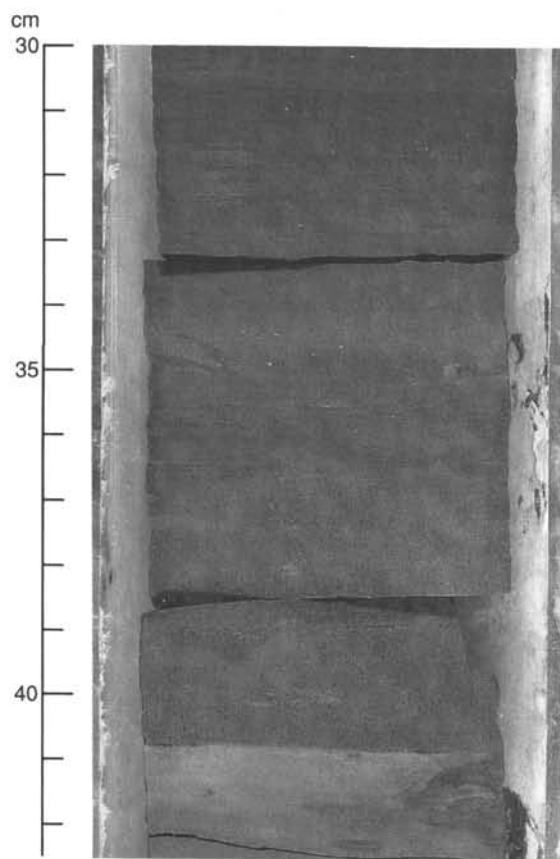


Figure 51. Section 128-799B-40R-1 at 30–42 cm: In this photo, a sharply based and normally graded bed composed of glauconite-bearing porcellanite with silt and sand (33–41 cm) is overlain by weakly laminated to bioturbated porcellanite.

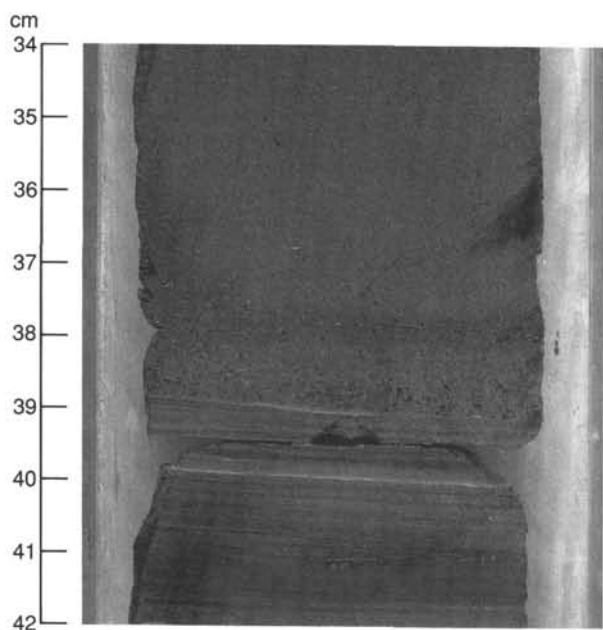


Figure 52. Section 128-799B-45R-2 at 34–42 cm: Very finely laminated dark porcellanite (39–42 cm) sharply overlain by a normally graded siliceous siltstone bed with detrital sand and glauconite.

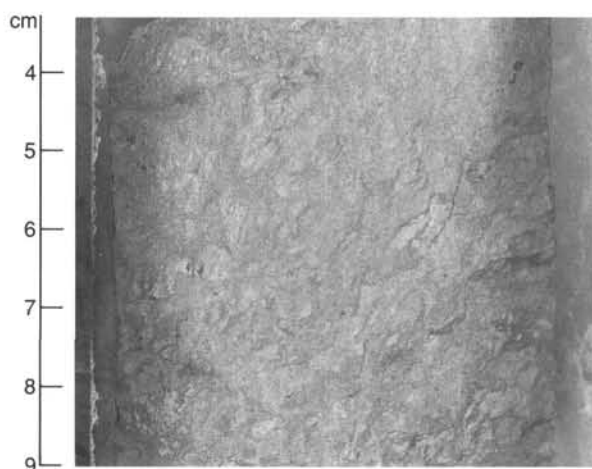


Figure 53. Section 128-799B-58R-1 at 3–9 cm: Brecciated and calcitized upper portion of a prominent altered rhyolitic tuff near the base of Unit IV.

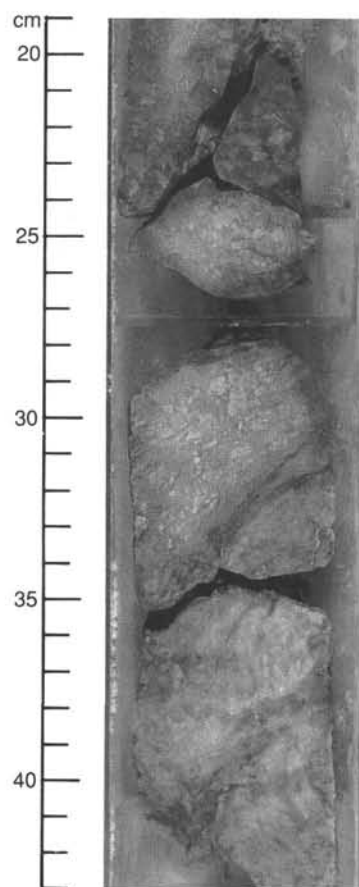


Figure 54. Section 128-799B-58R-1 at 19–43 cm: Calcitized portion of the lower part of the prominent altered rhyolitic tuff near the base of Unit IV.

served diatomaceous and spicular debris that exhibits little evidence of marked dissolution or fragmentation. At about 457 mbsf (Section 128-799A-50X-4 at 18 cm), an abrupt change in nearly all sediments is apparent, with markedly higher cohesion and density down the section. With few exceptions, only traces and small fragments of siliceous debris are present in smear slides below this depth, and opal-CT is ubiquitous (Fig. 84).

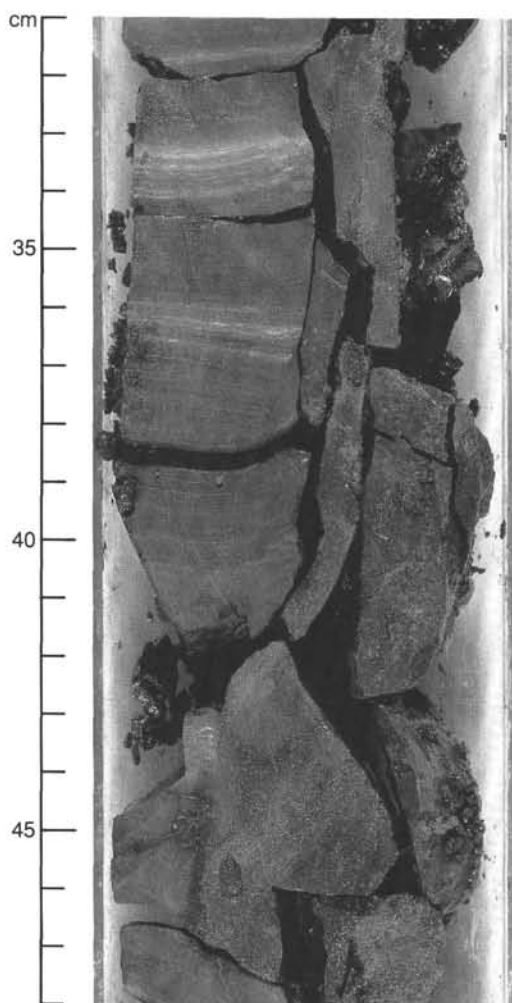


Figure 55. Section 128-799B-47R-2 at 31–48 cm: Clastic dike on the right side of core section. Note the brittle deformation within the siliceous claystones along the boundary of the dike at 39 to 41 cm. Normal faults at 33 to 34 cm are cut off by the clastic dike, and obviously are not related to its emplacement.

Other indications of an abrupt change related to silica diagenesis at this depth are (1) decrease in dissolved silica in interstitial water—from values exceeding $1450 \mu\text{M}$ at 436 mbsf (Section 128-799A-48X-2 at 140–150 cm) to about $860 \mu\text{M}$ at 465 mbsf (Section 128-799A-51X-2 at 140–145 cm; see “Inorganic Chemistry” section, this chapter); (2) an abrupt increase in average saturated bulk density (measured by well logs) from about 1.4 to about 1.7 g/cm^3 at about 459 mbsf (see “Downhole Measurements” section, this chapter); and (3) an abrupt increase in measured dry-bulk density from values of generally $<0.8 \text{ g/cm}^3$ to values ranging from 1.1 to 1.8 g/cm^3 at 457 to 458 mbsf (see “Physical Properties” section, this chapter).

The transformation from opal-CT to quartz occurs in Site 799 sediments mainly in the interval from 545 to 585 mbsf. All samples in Hole 799B contain opal-CT at depths shallower than 546 mbsf, and the deepest occurrence of opal-CT (determined by XRD analysis) was at 582 mbsf (Section 128-799B-15X-4 at 95 cm). Between 546 and 577 mbsf, only one sample contained detectable opal-CT (Core 128-799B-12X at 71 cm). However, because of the broad principal diffraction peak of opal-CT, amounts of less than 20% are not reliably detected, especially in detrital-rich samples. In any case, the opal-CT to quartz transformation was not associated with a markedly

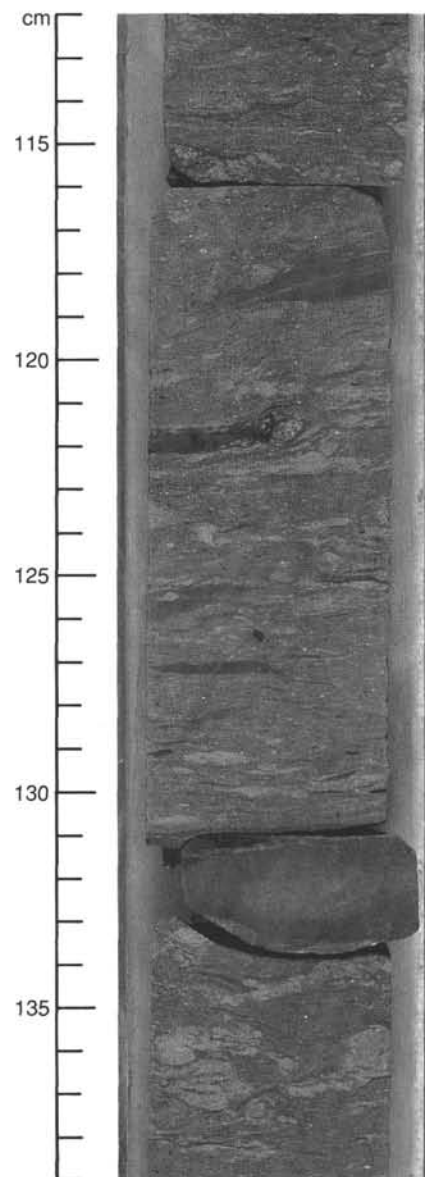


Figure 56. Section 128-799B-61R-1 at 112–139 cm: Distinctive coarse interval, regarded as an intimate interstratification of silt, clay, and sand. Light gray, irregular pods of light gray, fine sand at 134 to 137 cm may be burrows or root traces; dark, horizontally lying fragment at 122 cm may be a silicified(?) plant fragment. Stratification superficially resembles flaser bedding.

abrupt change in physical properties similar to the change associated with the opal-A/opal-CT boundary.

Our preliminary estimates of the temperature of the silica-phase transformations are 40° to 45°C for opal-A to opal-CT, and 53° to 57°C for opal-CT to quartz, based on a geothermal gradient of 98°C/km , measured in Hole 799A (see “Downhole Measurements” section, this chapter). These temperatures are in the expected range for the opal-A to opal-CT transition, but are low compared with published values for the opal-CT to quartz transformation (Murata et al., 1977; Pisciotto, 1981; Keller and Isaacs, 1985). However, measured temperature values often are lower than true equilibrium values and are preliminary values only.

Partly to evaluate the abundance of biosilica and diagenetic silica in terms of silica diagenetic processes and partly to check our lithologic descriptions, two sets of siliceous sedi-

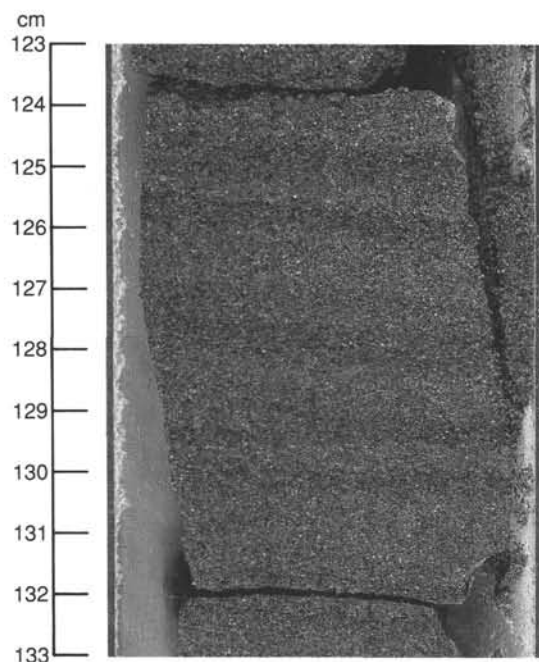


Figure 57. Section 128-799B-61R-4 at 123–133 cm: Planar laminations in medium- to coarse-grained sand. Lighter-colored subunit is sharply based and grades upward into the overlying darker layer. Textural contrasts between these two layers are unclear. Salt-and-pepper appearance of these sands may be attributable to enrichment with lithic grains.

ment samples were analyzed chemically from Site 799. The first set comprises seven samples within the opal-A zone at Hole 799A, where biogenic opal was measured by dissolution. Total opal was determined by time-series analyses of samples dissolved in NaOH (DeMaster, 1979). The second set comprises 12 samples that were analyzed for major oxides by X-ray fluorescence (XRF) analyses (see Tables 3 and 4). Both sample sets include some samples having minor carbonate contents.

Estimates of the abundance of biosilica and diagenetic silica (based on chemical analyses) are presented in Table 3. Silica estimates from XRF results were obtained by assuming a constant ratio of $\text{Al}_2\text{O}_3/\text{SiO}_2$ in the detrital fraction, as determined for Site 798 (ratio of 0.334 to 0.308; see "Site 798" chapter, this volume). The rock name and visual estimates of silica abundance also are shown.

The main result of the chemical analyses was that these allowed us to confirm the abundance of diagenetic silica in samples below the opal-A/opal-CT boundary, particularly among the quartzose siliceous claystones that form the predominant lithology in Hole 799B. In addition, these chemical analyses showed that the textural terms used for describing the siliceous rocks have value for distinguishing broad abundance ranges of diagenetic silica. Although the ranges overlap somewhat, silica values decrease from chert to porcellanite to siliceous claystone: three samples identified as cherts have 65% to 83% diagenetic silica, the two samples identified as porcellanites have 62% to 72% diagenetic silica, and the five samples identified as siliceous claystones have less abundant silica, in the range of 13% to 55%. The results also show that biosilica has been generally overestimated from smear slides and that many sediments that are identified as diatom ooze (biosilica >60%) have much less biosilica; in one case, as little as 13%. By contrast, diagenetic silica was estimated more accurately, except in the two samples where silica ranges from 10% to 15%.

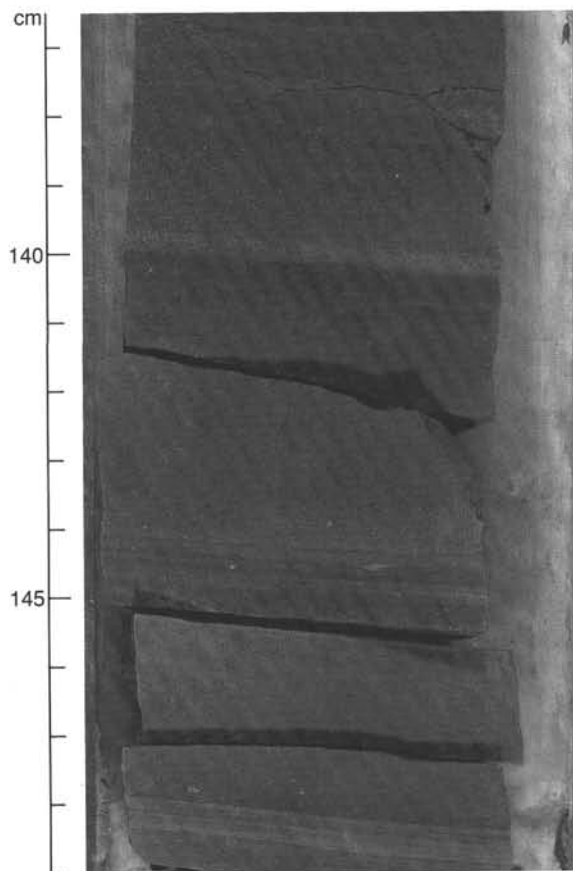


Figure 58. Section 128-799B-62R-1 at 136–149 cm: Sharply based and normally graded silty beds at 136 to 140 and 140 to 144 cm may reflect distal turbidites within Unit V.

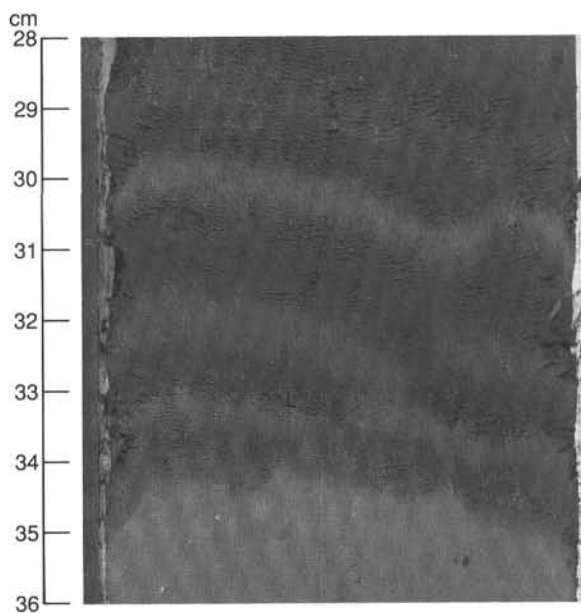


Figure 59. Section 128-799A-14H-1 at 28–36 cm: Normal fault.

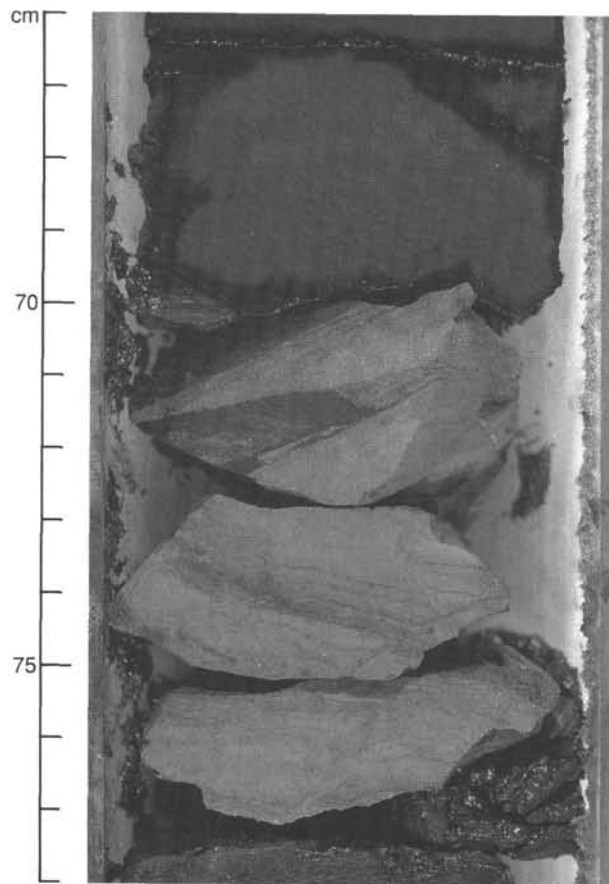


Figure 60. Section 128-799B-7R-1 at 66–78 cm: Dark gray massive porcellanite associated with light olive gray massive carbonate layer at 70 to 77 cm. A shallow, dipping fault of unknown primary orientation is evident in the rock fragment centered at 71.5 cm; complexly intersected orthogonal faults are visible from 72 to 75 cm. Reverse faults appear at 73–75 cm; a normal fault is present at 76 cm.

Rhythmic Sedimentation in Unit I

Sediments at Site 799 are rhythmically bedded in major intervals between 0 and 170 mbsf and exhibit light/dark alternations on a centimeter-to-meter scale. These visually apparent rhythms juxtapose variegated sediments of diverse composition. The dark/light color alternations may be similar to the Quaternary sediments at Site 798 (Figs. 85 through 88). However, the record at Site 799 has been commonly punctuated by event deposits of reworked allochthonous sediments that include volcanic sands, ash, foraminiferal oozes, nannofossil oozes, and mixed sediments. These allochthonous beds complicate our perceptions of what may be oceanographic rhythms at Site 799 and their correlation with dark/light alternations from Site 798.

These dark/light rhythms at Site 799 can be distinguished by (1) complex internal variability in bedding thickness and composition, (2) the difficult nature of distinguishing autochthonous hemipelagic sediment from tractive-deposited event strata, and (3) the distinctive punctuation of the sequence by dark-colored sediment gravity-flow deposits. At Site 799, sedimentary rhythms are highly variable in composition and thickness; consequently, two major types of apparently rhythmic bedding have been described, although we recognize that these types are artificial end-members and are an inadequate representation of the observed complexity (Figs. 86 and 87).

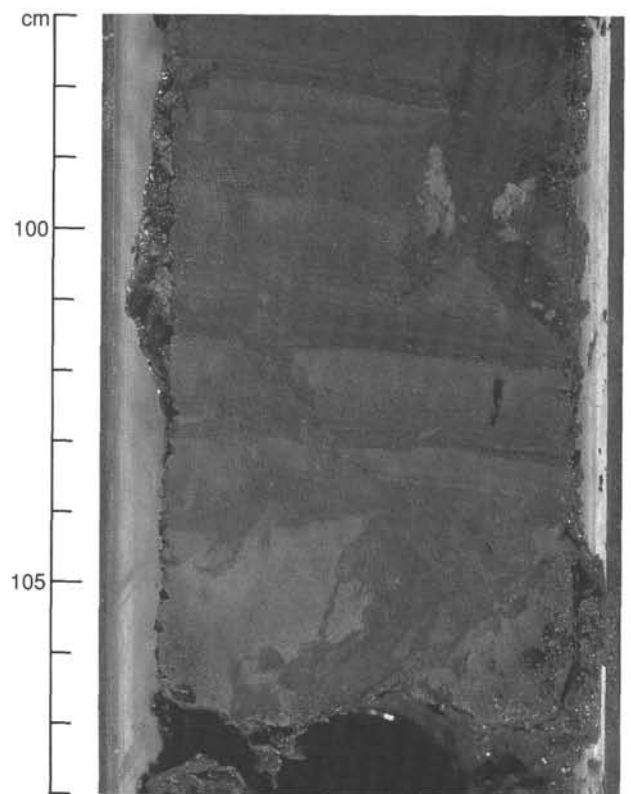


Figure 61. Section 128-799A-51X-1 at 97–108 cm: Soft-sediment water-escape flame structures and faults in an ash-rich laminated turbiditic level. Type TT, ash layer 195.

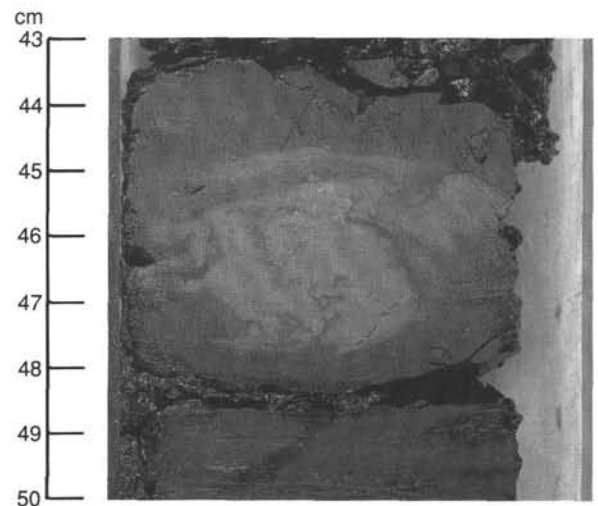


Figure 62. Section 128-799A-51X-2 at 43–50 cm: Small-scale water-escape flame structure and load cast at the ash/claystone interface at 45–48 cm.

The first type of rhythmic bedding is reflected by the 3- to 60-cm-scale rhythmic interbeds of gray and olive gray silty clay and silty clay with diatoms that alternate with darker (dark olive gray to olive) sediments of similar composition. This type of rhythmic alternation is well developed in the interval from Cores 128-799A-2H through 128-799A-5H (1.2–39.5 mbsf). The gradational nature of many contacts between dark/light sedimentary units may suggest that these rhythms

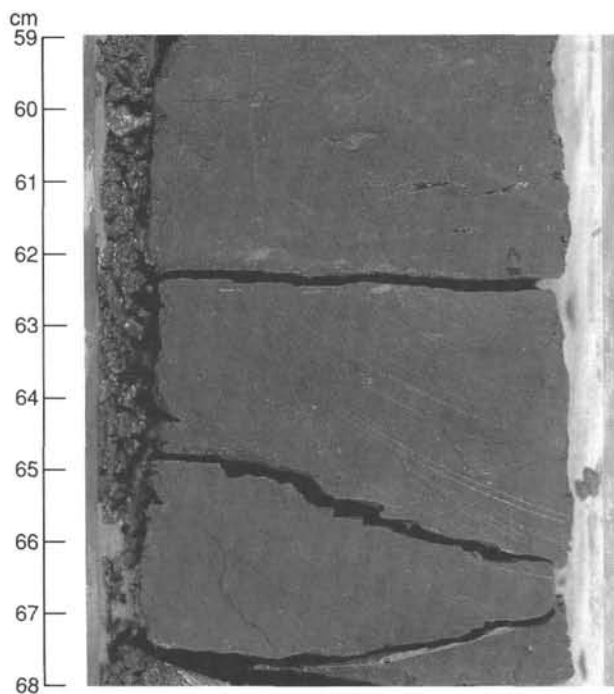


Figure 63. Section 128-799A-50X-1 at 59–68 cm: Dark veins in claystone, small normal offset visible along the longest one.

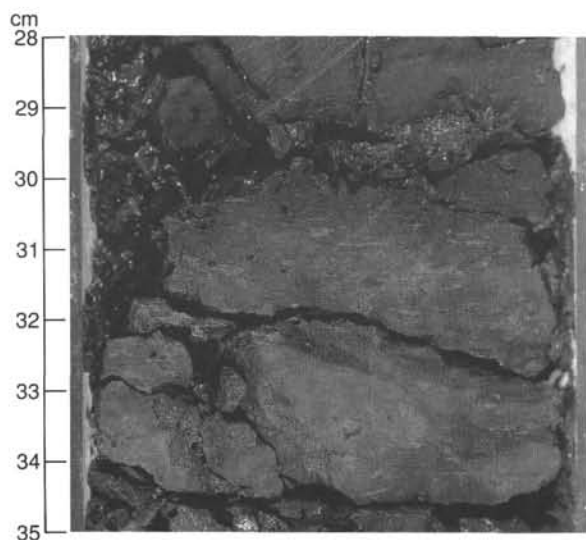


Figure 64. Section 128-799A-50X-5 at 28–35 cm: Small fault, with apparent reverse offset, at 33 cm and normal offset of underlying dark and light layers at 33–34 cm.

reflect paleoenvironmental oscillations in the Yamato Trough region of the Sea of Japan during the late Quaternary.

The second major type of apparent rhythmic bedding is reflected in the dark interbeds in the interval from Cores 128-779A-2H to 128-799A-19H (1.2–174.5 mbsf). Very dark gray to dark olive gray sediments that range from 1 to 14 cm thick are sharply interbedded with lighter-colored host sediments. Compositions of these very dark sediments include silty clay; diatomaceous clay; diatomaceous-clayey mixed sediment; and diatomaceous ooze with volcanic glass, silt, diatoms, foraminifers, and nannofossils as commonly observed minor components. In addition, many dark sediments

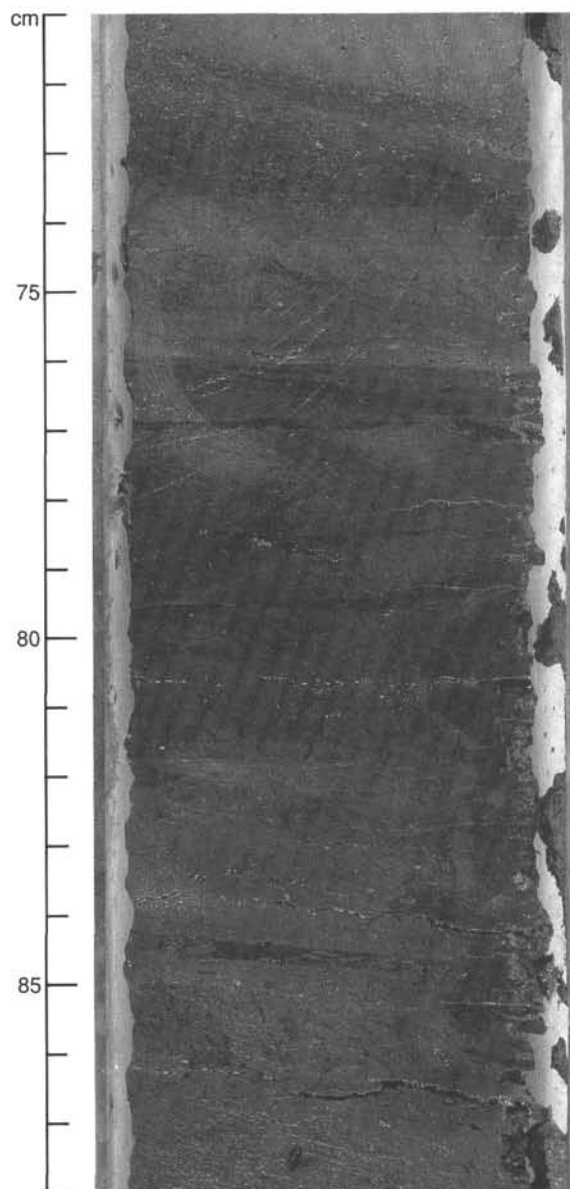


Figure 65. Section 128-799B-17R-1 at 71–88 cm: Erratic vein structures centered at 75, 81, and 86 cm are prominent in this photograph. At 84.5 cm, a flattened horizontal burrow with *spreiten* (e.g., meniscate backfill) is present. The puzzling structure on the right side of the core from 79.0 to 86.5 cm may be a vertical burrow with a complex oxidation halo.

possess sharp or scoured bases (Fig. 87) and are internally plane laminated (in some cases with low-angle truncations; Fig. 25). All of these features are consistent with an interpretation that most dark and/or sharply based sedimentary units are event beds, whose allochthonous sediments were transported by turbulent, gravity-driven flows.

Our initial shipboard analysis suggests that sedimentary rhythms are present in APC-collected sediments at Site 799; however, it is difficult to characterize these complex patterns of sedimentation. A persistent problem that should be addressed when evaluating apparent sedimentary rhythms in any shore-based analyses will be to distinguish autochthonous pelagic sediments (which may record oceanographic changes in the overlying water column) from event beds (which record sedimentary reworking from adjacent source areas). Visual

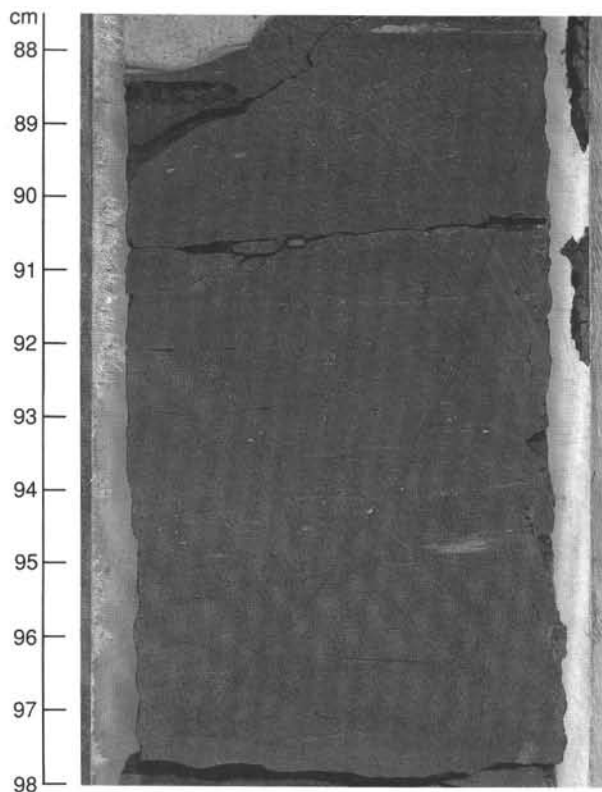


Figure 66. Section 128-799B-19R-6 at 88–98 cm: Carbonate concretion and microfractures. Dendritic and anastomosing microfracture networks are present in this siliceous claystone; many of these veins possess a sigmoidal geometry, which may be attributed to the presence of a bedding[008c]-parallel shear couple during intervals of episodic sediment dewatering. A normal fault having several millimeters of normal offset trends “NE-SW” from 88.5 to 97 cm. Close inspection reveals the presence of numerous small, anastomosing veins and minor conjugate offsets along this prominent fault.

inspection and preliminary shipboard analyses were inadequate for making this fundamental distinction.

Volcanic Ash and Tephrochronology

More than 230 ash layers and three thick rhyolite tuffs were observed in the recovered material from Holes 799A and 799B. However, several ashes in the upper part of Hole 799A have been repeated by slumping. Removing the obvious repetitions leaves 223 discrete ash and three tuffaceous layers, which represent 226 successive volcanic events preserved in the sedimentary record that dates from early Miocene to Holocene. In addition, there are pockets or pods of ash, although fewer than at Site 798. Significant features of these discrete ash layers and tuffs are presented in Table 5. The number and thickness of volcanic layers has been used to estimate the chronologic evolution of nearby explosive volcanic activity, as was done for Site 798.

Petrographic and Sedimentary Aspects

The definition of ash layers and dispersal of volcanic glass in the background sediments, the minerals and types of glass recognized in the ash layers; their grain-size distributions; the distinction of “acid” and “basic” petrochemical groups; the separation of different layers into homogeneous (Type H), graded (Type G), heterogeneous (Type T), and turbiditic (Type TT) lithologies; and the recognition of symsedimentary and post-sedimentary processes of bioturbation, erosion, and slumping are all similar to those described in “Site 798” (this

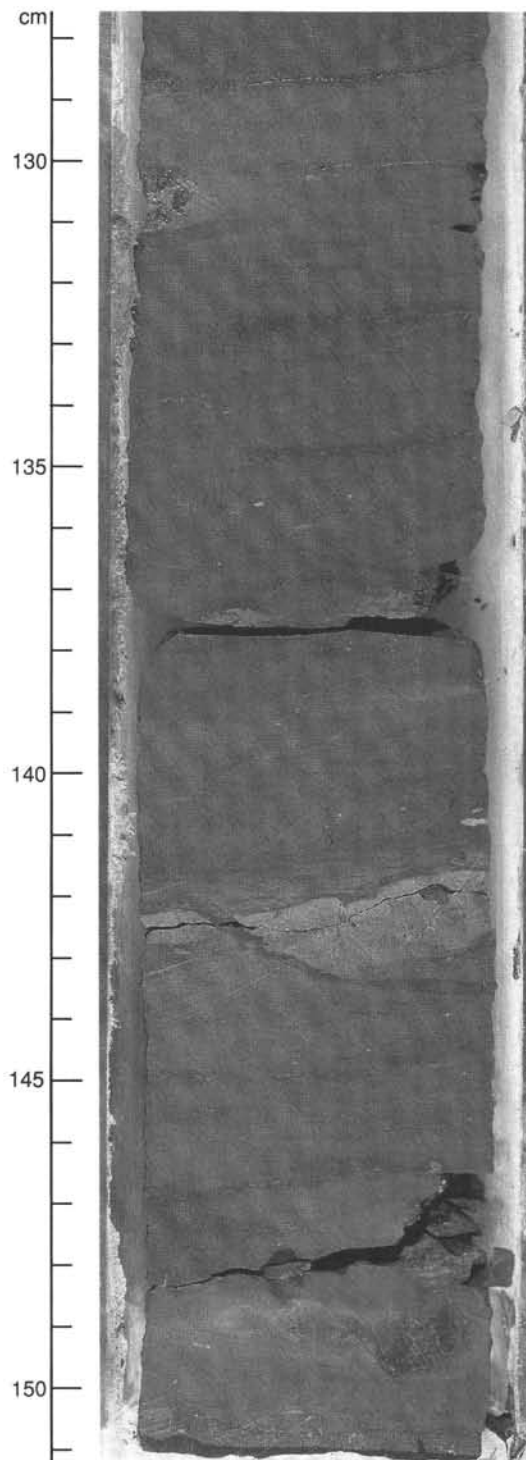


Figure 67. Section 128-799B-25R-1 at 128–151 cm: Sigmoidal vein arrays (130–142 cm) are clearly contrasted with low-angle, anastomosing vein structures (143–151 cm); a diagenetic carbonate concretion lies at the boundary between these two structural domains. We are unclear whether the light gray structure that crosscuts the concretion is a low-angle fault or whether it is a burrow.

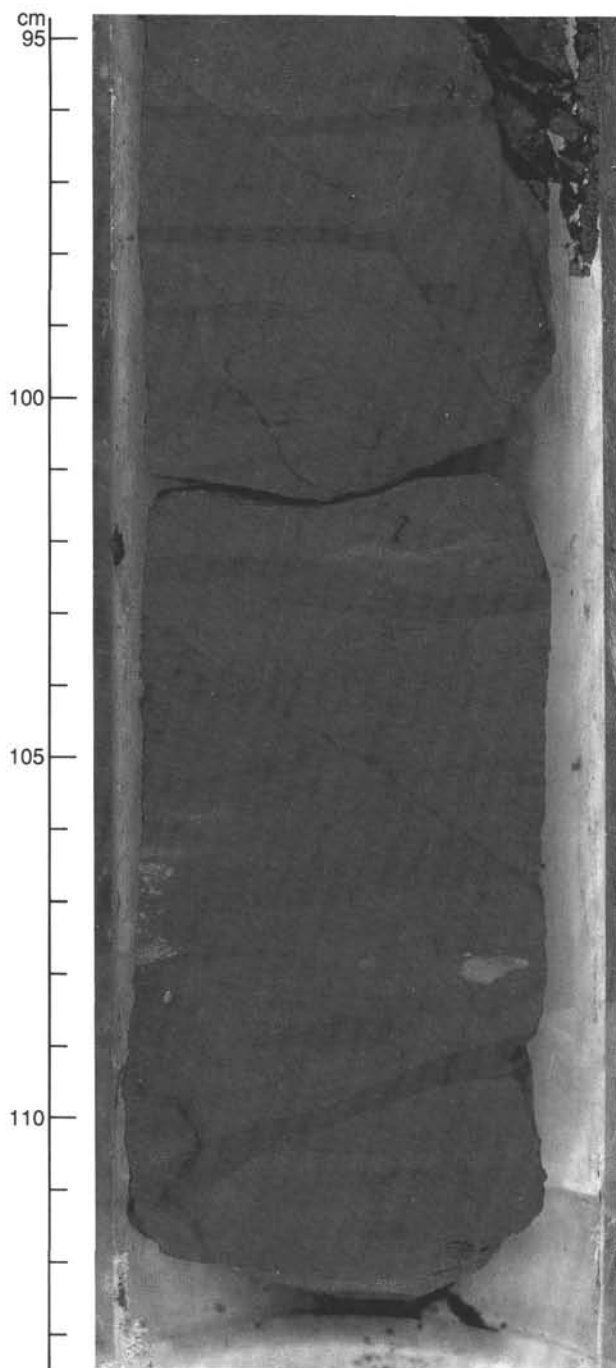


Figure 68. Section 128-799B-21R-1 at 95–113 cm: The genetic sequence of sedimentation, bioturbation, precipitation of a carbonate concretion, measureable burial compaction, sediment dewatering along doubly bifurcating vein arrays and normal apparent offset along “NW-SE” trending faults is evident within this example of porcellanite. Differential compaction of sediment around the white carbonate concretion at 108 cm is clear. Well-developed intrastratal microfracture networks are present at 102 and 107 cm; note how the two-dimensional orientation of veins is subparallel within individual sets, yet approximate a conjugate relationship when the two sets are compared. The two prominent normal faults at 95–100 and 103–107 cm clearly post-date bifurcated microfracture networks.

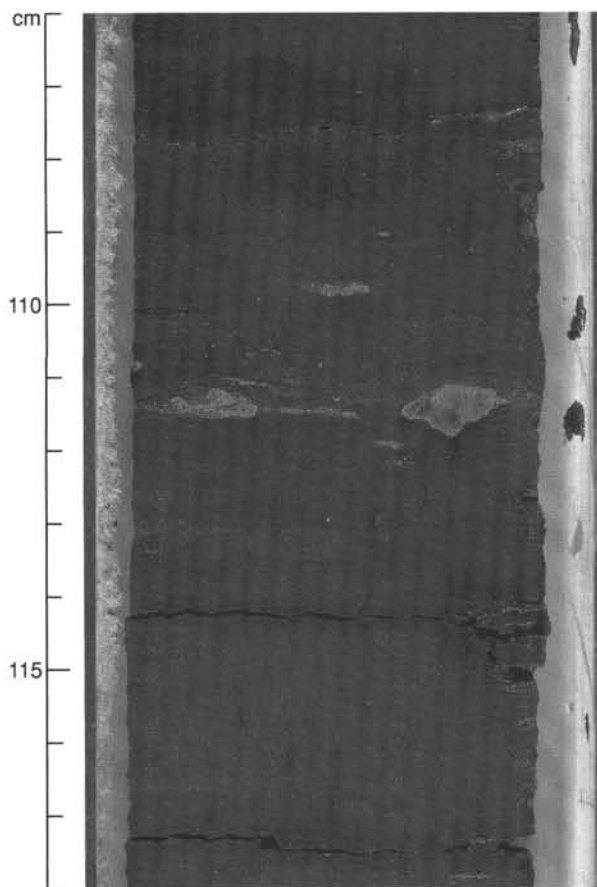


Figure 69. Section 128-799B-27R-2 at 106–118 cm: Sigmoidal vein networks are well-preserved in this siliceous claystone from Unit IV. The bulk fabric of the vein arrays seems to record a crude foliation that trends “NW-SE”; a fault from 110 to 114 cm is parallel to this over structural trend and possesses approximately 4 mm of normal apparent offset.

volume). All the ash layers are air-fall pyroclasts. Homogeneous ash layers (199 and 203) are illustrated in Figures 89 and 90. Good examples of graded layers (89 and 90) and slightly graded layers (205) are shown in Figures 22 and 91. A heterogeneous turbiditic deposit (layer 195), disrupted by dewatering structures, is shown in Figure 61. Some additional features of ashes at Site 799 are worth pointing out.

Several occurrences of thin, crystal-rich layers were encountered in Cores 128-799A-5H, 128-799A-7H, 128-799A-10H, and 128-799A-11H, which are devoid of any apparent bioturbation. These range from 0.01 to 0.5 cm thick, with a few to 1 cm thick. These crystal-rich layers commonly are overlain by beds of similarly sized foraminifers (Fig. 29). This and the absence of the finest glass shards and clay suggest size- and particle-sorting in turbulent currents. This observation has an important consequence for quantifying ash layers because each crystal-rich bed does not necessarily correspond to a single volcanic event. In such cases, we counted a volcanic event if more than 30% of its volcanic material had accumulated in a sediment having many crystal-rich beds.

Slumping, which may perturb the ash record, is an important post-sedimentary process in the upper sedimentary column in Cores 128-799A-6H to 128-799A-9H (40–79 mbsf). Examples are shown in Figures 15 and 21. However, in general, bioturbation is less important at Site 799 than at Site 798.

The proportion of “intermediate” to “basic” ash layers is low (<5%). Basic ash layers are scarce in the upper sedimentary

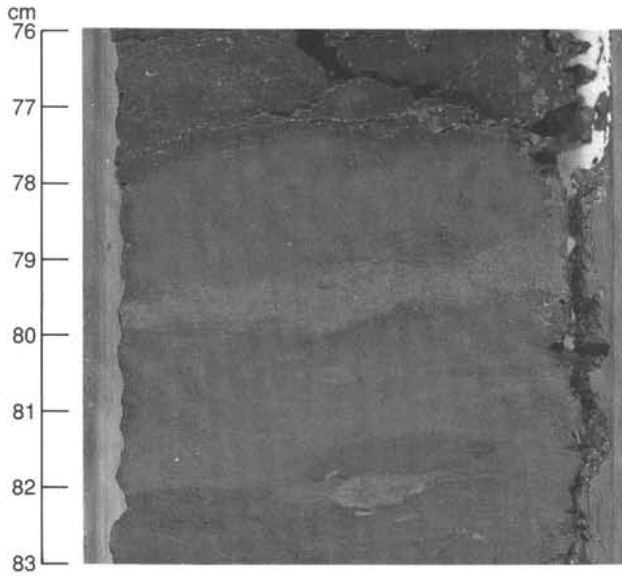


Figure 70. Section 128-799B-13R-2 at 76–83 cm: Early normal fault in coarse-grained layer at 81–83 cm; note also burrows and small concretion at 82.5 cm.

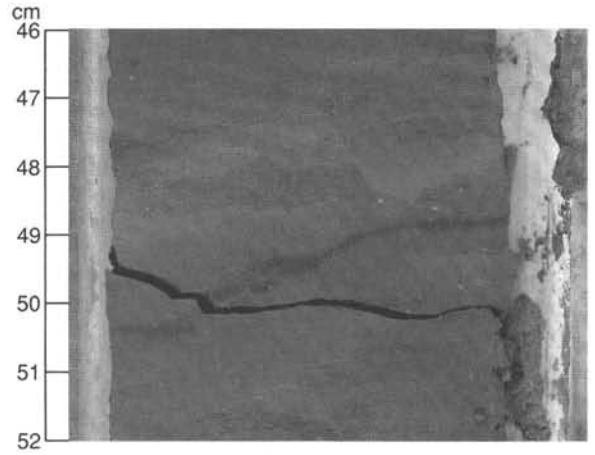


Figure 72. Section 128-799B-12R-1 at 46–52 cm: Normal fault in siliceous claystone; note prominent offset from 48 to 49 cm. This fault and many similar structures die out at their distal extremities.

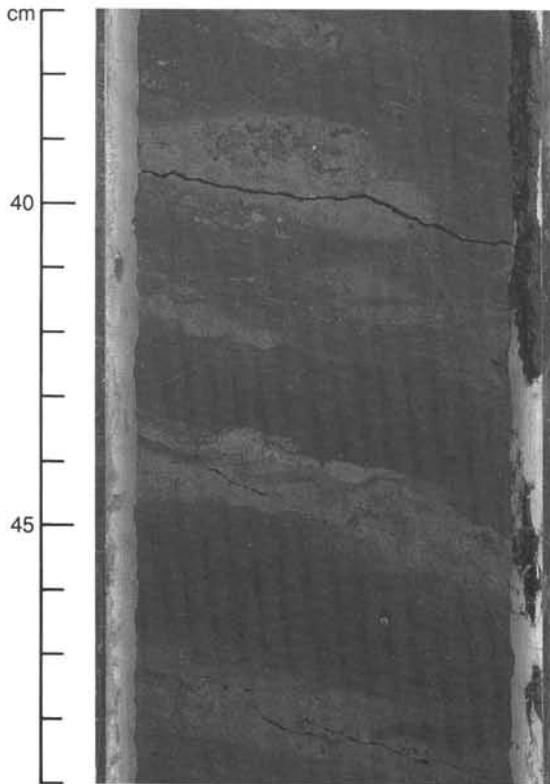


Figure 71. Section 128-799B-18R-6 at 37–49 cm: Carbonate concretions and diffuse laminae of diagenetic carbonate impart a crudely laminated fabric to this siliceous claystone. Disseminated pyrite is evident in the large concretion at 39 cm. Finely dendritic and anastomosing vein structures are present in the lower half of the photograph. Crosscutting relationships at 47.5, 44.0, and 41.5 cm indicate that veining postdated authigenic precipitation of these carbonate concretions. At 41.5 cm, *en-echelon* normal faults having approximately 2 mm of offset may be observed.

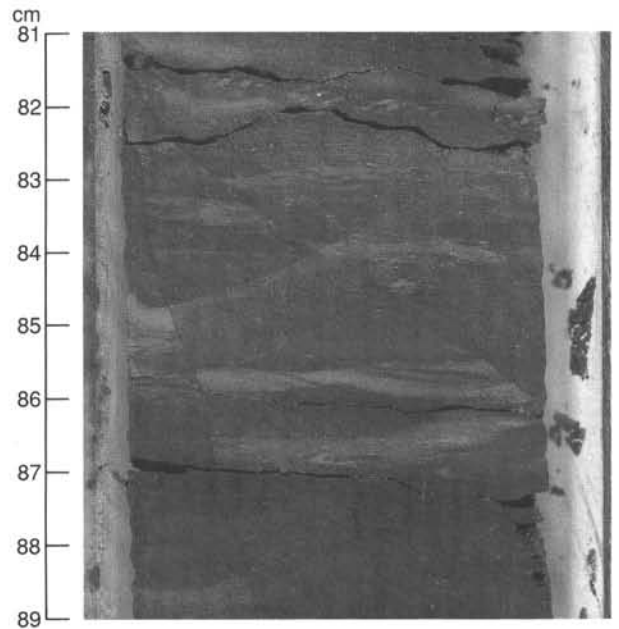


Figure 73. Section 128-799B-27R-4 at 81–89 cm: The unusual structure from 82 to 92 cm is difficult to interpret. Two prominent fault surfaces are present in this interval; note how the fault on the left side “dies out” at its lower distal extremity into underformed siliceous claystone. Unsharply bounded laminations (which are useful for interpreting apparent fault offset) are composed of diagenetic carbonate.

column, but increase in abundance from 610 to 950 mbsf (Hole 799B). A 20-cm-thick basic tuff (layer 217) was recovered at 880 mbsf in Section 128-799B-46R-4. This layer contains more than 50% light brown glass fragments, which are totally altered to celadonite, iron hydroxides, and zeolites, and include quartz, feldspar, amphibole, and biotite. Turbidite sequences from 800 mbsf to the bottom of Hole 799B commonly include coarse-grained quartz, feldspar, and subordinate altered volcanic glass, as well as glauconite in a sparse clayey cement where fibrous zeolite may have crystallized. Below 1020 mbsf, the sand occurrences are abundant and thick. This and their composition indicate the proximity of an igneous terrain that consists of both volcanic and plutonic rocks.

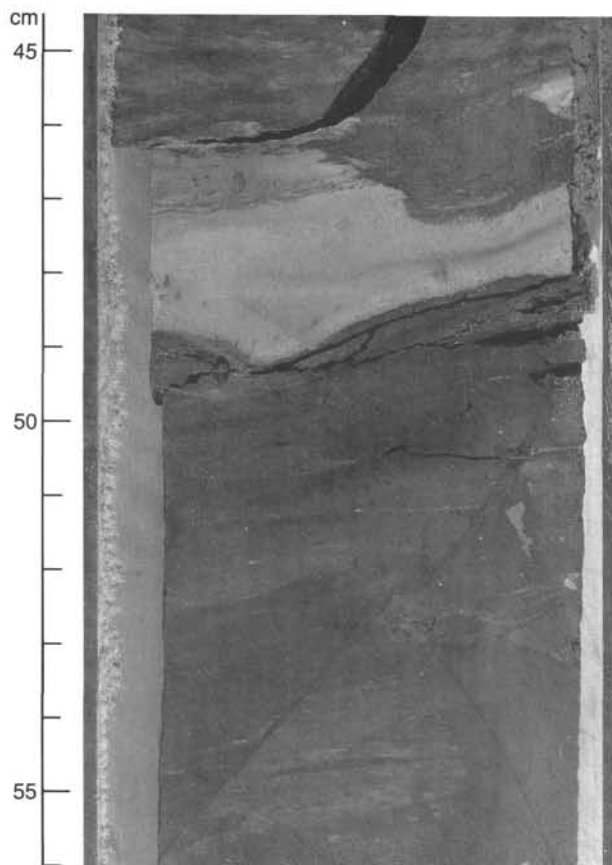


Figure 74. Section 128-799B-27R-5 at 45–56 cm: The prominent, light-colored bed at 46–49 cm is an ash bed, hosted by dark, crudely laminated siliceous claystone with burrows. The ash layer has altered to quartz and stilbite. A region of brittle deformation from 49 to 56 cm consists of two conjugate fault structures.

Most of the “acidic” layers are homogeneous. Only 6% normally graded and 2% heterogeneous lithologies were encountered. The proportions of lithologic types are consistent with the more distant location of Site 799 from the main explosive volcanoes of the Japan Arc during the Quaternary and Pliocene, compared with that of Site 798. The increased distance to the source areas had a selective effect in terms of concentrating the more acidic products that originated in explosive eruptions, as well as of well-sorted fragments. The frequency of thick ash layers (Fig. 92) indicates a greater proportion of thin layers, compared with those at Site 798. However, somewhat enigmatic is the total number of ash layers and the total thickness of volcanic material, both of which are significantly increased in Site 799. This might be explained by the better preservation of the tephra deposits (less bioturbation) or by the conditions of the tephra supply. These conditions changed drastically in the Miocene sequence (Hole 799B), where, except for the prominent rhyolite tuff, ash beds are fewer and less acidic, and biotite is abundant.

During the early Miocene, a huge rhyolitic eruption originated from a nearby explosive volcano. This eruption probably was submarine, as evidenced by the presence of tuff breccia in Section 128-799B-58R-1 at 0–53 cm, and the admixture with sediment originating from moderate to deep water. A total of 6.71 m of this tuff was recovered in Section 128-799B-57R-1 at 19 cm, to 128-799B-59R-2 at 41 cm. Results of the XRF analysis of this tuff are given in Table 6. A sharp increase in the natural gamma ray (NGR) log record, obtained from downhole measurements, accurately estimated

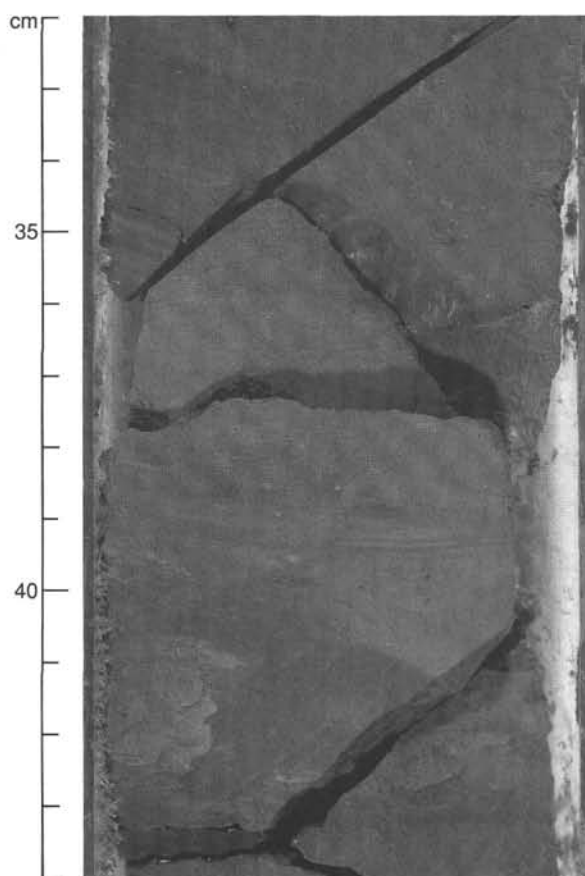


Figure 75. Section 128-799B-24R-2 at 32–44 cm: Note well-developed slickensides at 34.5–38.5 cm with sigmoidal and inclined veins from 32 to 44 cm. Veins show an apparent subparallel arrangement in two dimensions, which is also parallel to prominent breakage surfaces in the core. Mineralization of vein interiors may create small-scale weaknesses in the rock fabric that influence breakage during core recovery. The weakly mineralized surface of such a fracture is visible from 40.5 to 43.5 cm. Millimeter-scale, *en-echelon* normal offsets along vein surfaces are evident at 37.5 cm.

the thickness of this tuff as 24 m (see “Downhole Measurements” section, this chapter). Three beds were distinguished using natural gamma-ray spectrometry; these are separated by two thin sedimentary layers. The upper, 6-m-thick bed (982–988 mbsf) is a fine silt- to clay-sized homogeneous siliceous and clayey tuff. The middle, 15-m-thick bed (990–1005 mbsf) is heterogeneous. The upper 53 cm is a tuff breccia that includes clayey sediment fragments and that has been locally replaced by calcite in large rhombic and radiating crystals (Fig. 53). Below this bed, a 20-cm-thick layer of coarse-to-medium, silt-sized volcanic material mixed with some clayey sediment is present. The remainder of the bed consists of homogeneous, fine silt-sized tuff. The lower bed, which is approximately 3 m thick (1006–1009 mbsf), is a homogeneous and fine silt-sized tuff and includes, in its uppermost part, a 13-cm-thick, totally calcitized zone (Fig. 54). The volcanic material has been entirely altered (see below), but glass fragments can still be recognized.

The chemical composition of the finer, homogeneous section of this tuff bed (Table 6) is clearly related to a calc-alkaline rhyolitic magma, which is characterized by a low niobium content. The rock has suffered little post-sedimentary chemical modification, except for hydration (loss on ignition of 5.65%), and the leaching of calcium, and probably potas-

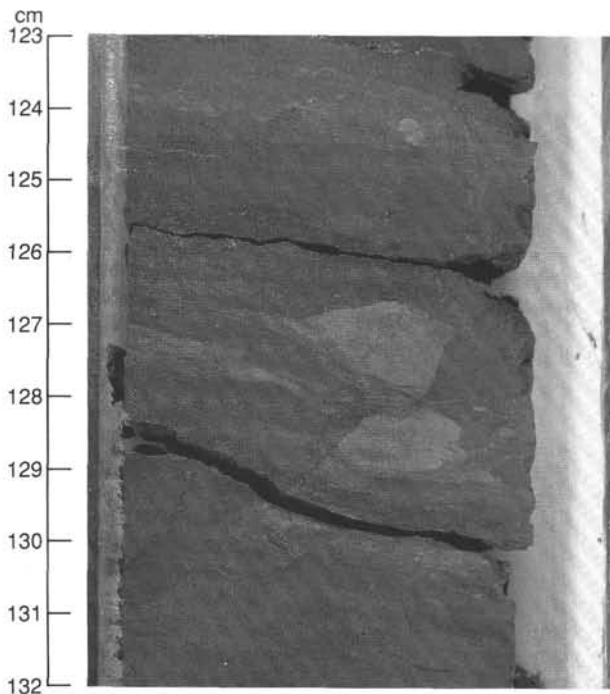


Figure 76. Section 128-799B-27R-3 at 123–132 cm: An apparent reverse fault from 126.5 to 131.0 cm bisects a carbonate concretion and reflects approximately 1 cm of apparent vertical offset along a parallel fracture to the left.

sium and sodium. Removal of calcium from the main part of the tuff is the probable explanation for the calcite concentration in the upper part of the middle and lower beds.

Alteration

Most of the glass is fresh in the upper part of Hole 799A, but alteration was recognized in the deeper part and in Hole 799B. Beginning with layer 182 at 286 mbsf, glass in Hole 799A has been incipiently altered to smectite. Two layers, 186 and 194 at 323 and 450 mbsf, respectively, have been totally altered to smectites (186) and smectites with opal-CT (194). In layers 197 and 198 at 464 mbsf in Hole 799A, colorless volcanic shards have been partly cemented by opal-CT. Basic glasses in Hole 799B have been commonly altered to iron oxides, sideromelane, smectites (celadonite), and rare zeolite. Acidic glasses in Hole 799B have been totally altered to quartz and smectites, i.e., halloysite and zeolite. Zeolite was determined optically as stilbite (platy habit or sheaflike aggregates on former glass shards, e.g., layer 209 in Fig. 74; low extinction angle and negative elongation). Two successive kinds of alteration of acidic glasses were found downhole in Site 799. Alteration increases from 280 to 450 mbsf, with smectites and minor opal, opal-CT, and zeolite as main products. From 450 mbsf to the bottom of Hole 799B at 1084 mbsf, alteration produced mainly silica. This silica is either opal-CT, e.g., at 464 mbsf where glass has been totally altered, or quartz, e.g., in layer 199 at 569 mbsf. The amount of smectite in these silica-rich alteration zones is low. The relative proportions of halloysite and stilbite are variable; e.g., layer 202 is particularly rich in platy crystals of stilbite.

Tephrochronology and Accuracy of the Record

We assigned a Holocene age to the top of the sedimentary column. Hole 799A ends in upper Miocene strata at 468.7 mbsf, while Hole 799B ends in lower Miocene beds at 1084.0 mbsf. With the exception of the last cores, recovery in Hole

799A was excellent, with only minor hiatuses. In spite of soft-sediment reworking in the first 200 m, the overall record of the ash layers is satisfactory for tephrochronology. Extensive slumping between 40 to 75 mbsf in Hole 799A caused repetition of beds, which rendered our interpretation of depth vs. age relationships somewhat difficult to decipher. Layers may have been removed by debris flows or may have eroded from the subjacent beds. From 220 mbsf to the bottom of Hole 799A at 468.7 mbsf, we recovered few ash layers. These were difficult to recognize because their color and macroscopic texture were similar to the host sediment, which results from incipient alteration to smectite and overprinting by oxidized pyrite. Moreover, with a progressive increase in lithification at 350 mbsf, the ash beds have been partially dispersed and thinned by dewatering and bioturbation. Recovery in Hole 799B was adequate for tephrochronologic purposes, but hiatuses still have not been recognized because of the scarcity of biostratigraphic and reliable paleomagnetic data (see "Biostratigraphy" and "Paleomagnetism" sections, this chapter).

Logging data helped to provide a more complete record. The FMS registered resistive ash layers in Hole 799A from 105 mbsf (below the casing bottom) to near the bottom of the hole (see "Downhole Measurements" section, this chapter). All significant ash beds observed by FMS were effectively recovered in cores down to 180 mbsf. From 180 mbsf to the bottom of Hole 799A, the FMS registered the recovered layers and recorded an additional 32 ash-bedlike signals, of which a few may be nonlithified carbonate beds (in the interval from 220 to 350 mbsf). These additional layers are listed as "Logged" in Table 5. Ash layers could not be distinguished with confidence in Hole 799B, where the rocks are more lithified and dolomite is abundant. Furthermore, the quality of the shipboard FMS images is unsatisfactory for obtaining layer thicknesses. The additional layers recorded by the FMS in Hole 799A have been combined with those counted from the core record for tephrochronologic purposes.

Tephrochronology and Estimated Ages

Ages for each of the recovered 198 ash layers from Hole 799A presented in Table 5 were estimated from their depths below the seafloor by means of a best-fit model that was constructed from shipboard paleomagnetic dates and the fossil record (see "Biostratigraphy" and "Paleomagnetism" sections, this chapter). Depths were corrected for core expansion where necessary (from high gas pressure) in the same manner as for Site 798 by multiplying the interval in the core by 100 times the reciprocal of the percentage of recovery. Gas pressures high enough to cause significant extrusion of the sediment from the core barrel were encountered only in the upper parts of Hole 799A. Ages were estimated from Figure 93, which was obtained by fitting straight-line interpolations of age vs. depth below the seafloor to each successive pair of paleomagnetic and fossil data points (see "Biostratigraphy" and "Paleomagnetism" sections, this chapter). The paleomagnetic data for the Sidufjall (4.41–4.49 Ma) and Thvera (4.59–4.79 Ma) events have a high degree of uncertainty and were not used. Instead, a linear interpolation was used between the Nunivak/Gilbert (4.26 Ma) and Gilbert/Chron 5 (5.41 Ma) events. Ages in Hole 799B could not be determined from shipboard micropaleontologic and paleomagnetic data.

Record of Volcanic Activity

Figure 94 presents variations in the number of ash layers (to which the layers from the FMS record have been added) and their thicknesses at Site 799 as a function of depth. The estimated ages for Hole 799A permit the presentation of the number of ash layers and their thicknesses as a function of

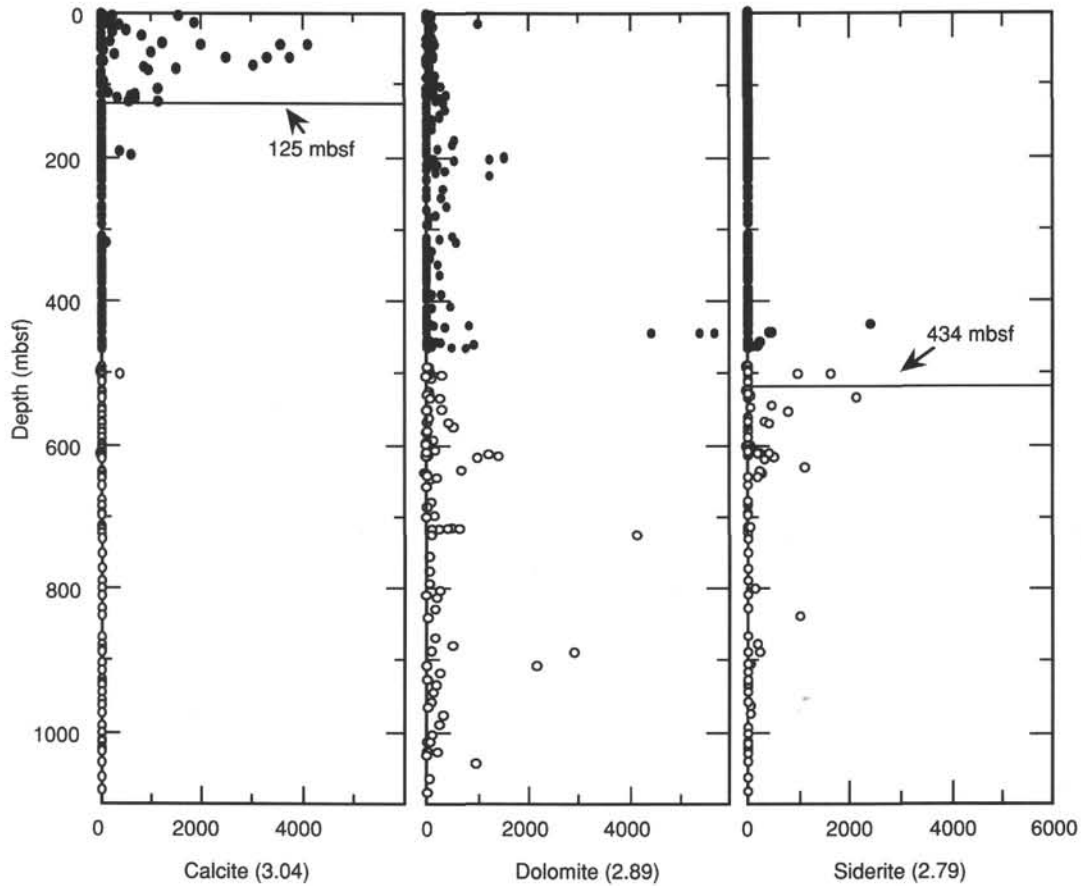


Figure 77. XRD peak intensities of calcite, dolomite, and siderite at Site 799. Closed circles represent samples from Hole 799A; open circles are data from Hole 799B.

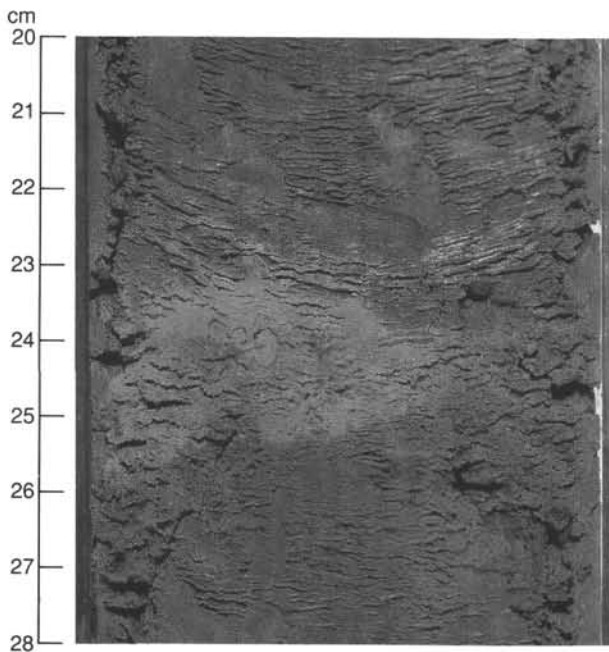


Figure 78. Section 128-799A-36X-5 at 20–28 cm: Pale yellow, semilithified carbonate concretion (“patch” at 23–26 cm) in slightly burrowed diatomaceous ooze in Unit II. The carbonate in this patch consists of silt-sized crystals of authigenic dolomite.

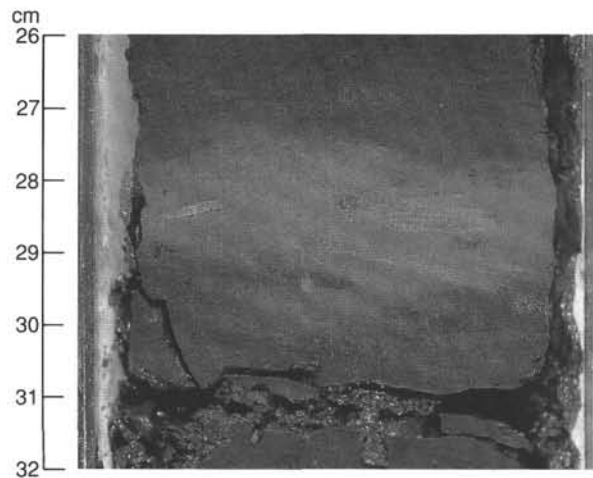


Figure 79. Section 128-799A-47X-6 at 26–32 cm: Semilithified chalky carbonate layer in moderately burrowed, laminated siliceous claystone of Unit II.

time (Fig. 95). These are related to the volume and importance of explosive activity.

Major changes in volcanic activity led us to recognize 10 different phases. These are numbered from youngest to oldest as V1 to V10, but have been described in chronological order, starting with the oldest.

V10: The oldest recorded activity corresponds mainly to the 24-m-thick rhyolite tuff that appears to be the

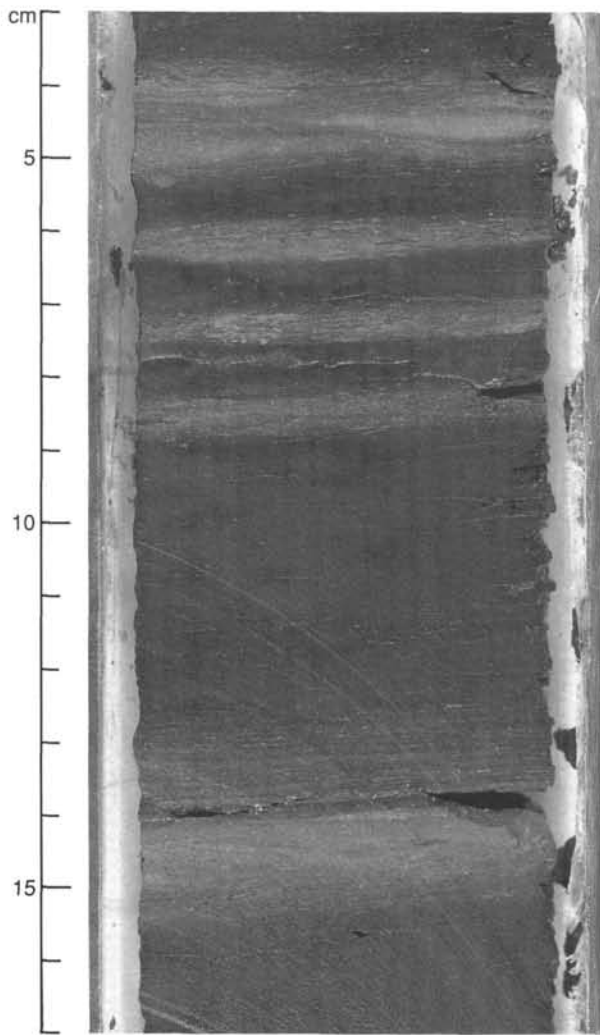


Figure 80. Section 128-799B-8R-4 at 3–17 cm: Unsharply bounded (wispy) laminations (3–9 cm) and planar laminations (12.5–14.0 cm) of diagenetic carbonate in dark olive gray siliceous claystone. Some of these layers may be the product of recrystallization of primary sedimentary laminae that were enriched in calcareous microfossils.

product of a large, nearby explosive eruption. The underlying thick deposition of sand indicates the proximity of the source terrane. This activity, dated as probable early Miocene, is located between 950 and 1010 mbsf.

- V9: This volcanic activity, recorded from 950 to 750 mbsf, was more or less intermediate in composition, with the exception of a thick basic tuff and frequent basic volcanic material dispersed. This indicates the proximity of an immature volcanic chain. An early to middle Miocene age is assumed.
- V8: Moderate activity recorded in the interval from 470 to 560 mbsf produced more evolved magmatic products that were emitted during some plinian eruptions.

No volcanic products were recovered from 470 to 560 mbsf. This hiatus may result from either quiescence or the submergence of nearby volcanoes. The following phases, V7 to V1 (for which estimated were obtained), were recovered in Hole 799A and are described below:

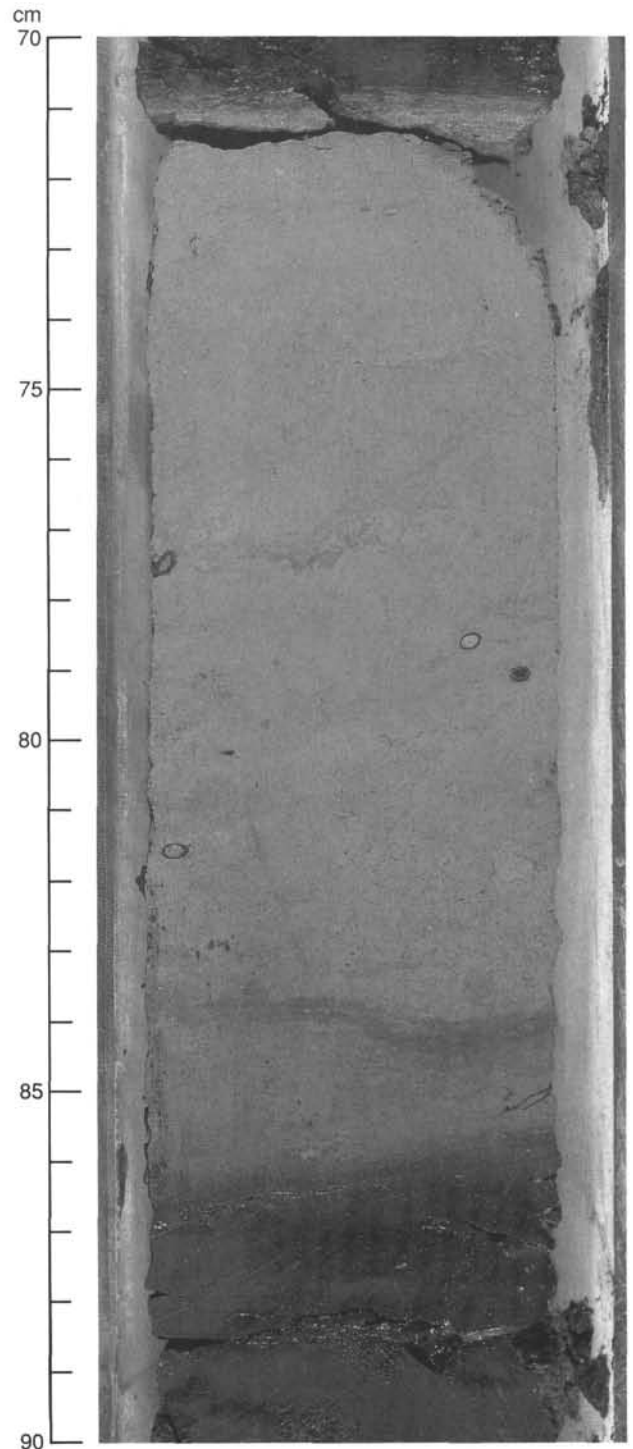


Figure 81. Section 128-799B-12R-4 at 70–90 cm: Light-colored carbonate bed with veins and dark, silt-sized grains. Note fine-scale anastomosis of veins and minor fault offsets in the interval centered at 77 cm. Prominent dark tubules in the central section of the carbonate bed are of uncertain identity. XRD analysis revealed that this light-colored carbonate bed is composed of 100% siderite.

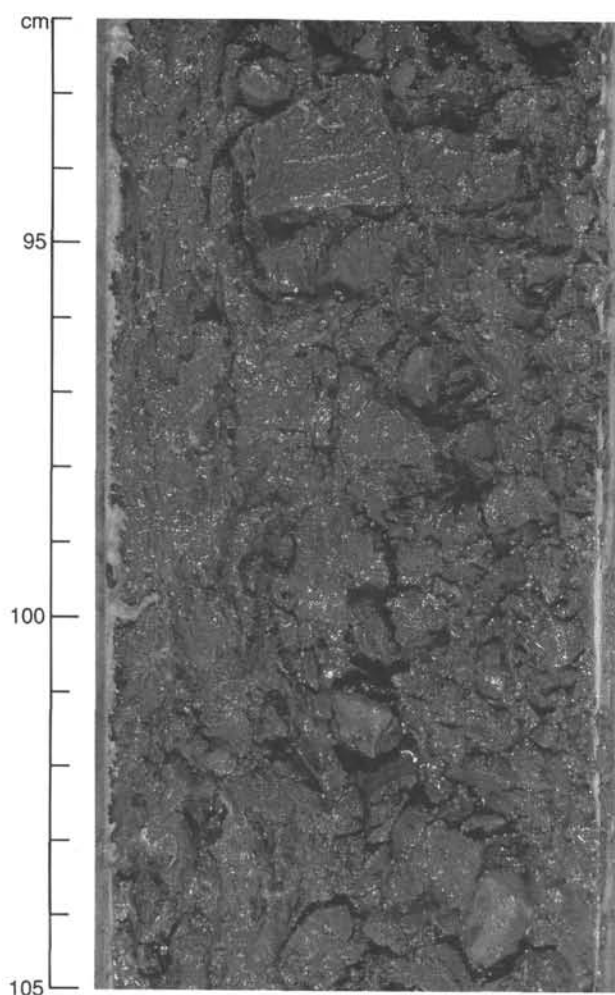


Figure 82. Section 128-799A-23X-4 at 92–105 cm: Well-lithified carbonate nodules at 93, 97, 101, and 104 cm in drilling-disturbed diatomaceous ooze of Unit II. These nodules are dolomitic, as determined by XRD.

- V7: A new active phase was recorded near the bottom of Hole 799A, in upper Miocene strata, that ranges in age from 5.5 to 6.6 Ma. The sampled layers and the FMS information indicate a fairly important volcanic phase of plinian to ultra plinian-type. Magmatic products are acidic to intermediate.
- V6: The lower Pliocene sediments document slightly weaker volcanic activity of the same type as V7 and range in age from 4.2 to 5.5 Ma.
- V5: Moderate activity from 1.9 to 3.4 Ma that resulted in mainly thin acidic deposits was recorded.
- V4: A clear increase in activity from 1.3 to 1.9 Ma was registered. A thick, heterogeneous layer indicates the close proximity of an important volcano.
- V3: The most important explosive volcanism recorded in Hole 799A occurred between 0.6 to 1.3 Ma.
- V2: A period of relative volcanic quiescence between 0.4 and 0.6 Ma was distinguished.
- V1: The tephra record clearly indicates a renewal of important volcanism since 0.4 Ma.

The volcanic history in the Site 799 area may be summarized into three main periods:

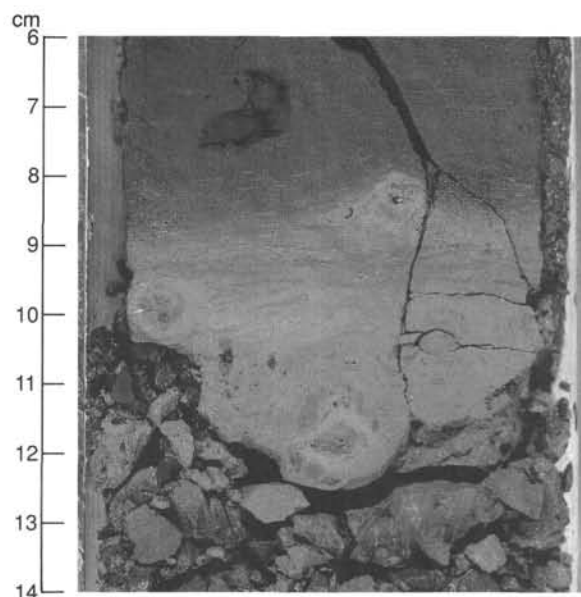


Figure 83. Section 128-799A-50X-6 at 6–14 cm: Zoned nodules having dark gray pyritic cores, surrounded by a gray to light gray dolomitic rim, included in a well-lithified dolomite-siderite layer of Unit III. Note differential compaction of sedimentary laminae and subhorizontal burrows around the nodules, which suggests that the pyritic dolomite nodules formed prior to compaction, whereas the dolomite-siderite bed formed after compaction.

1. Early Miocene to middle Miocene: proximal volcanic chain with submarine rhyolite tuff and basic detritus from land.
2. Middle Miocene to late Miocene: moderate activity of an immature, and then a more mature, arc.
3. Early Pliocene to Holocene: acidic supply from a distant mature arc registering variations of activity.

Comparison with Site 798 and Possible Origin of the Volcanic Material

Comparison of Site 798 with Site 799 (Hole 799A) over the depth interval that they overlap provides interesting insights (Fig. 96), keeping in mind that Site 799 is more distant from the volcanic arcs and so is almost devoid of basic magmatic product. Site 798 phase V5 (4–3.5 Ma) does not appear at Site 799. If the former were supplied, at that time, by nonevolved volcanoes (see “Lithostratigraphy” section, “Site 798” chapter, this volume), the more distant Site 799 was unlikely to have been reached by a significant amount of air-fall deposit. Site 799 phase V5 (3.4–1.9 Ma) has been only poorly recorded at Site 798, up to the beginning of Site 798 phase V4 (2.4 Ma). This may indicate at least partly different origins of their respective volcanic materials. Site 799 should have been more easily supplied from the volcanic islands of the Korean plateau, from the volcanoes of northeastern China, and even from the northern and northeastern volcanoes of Japan. The volcanic arc appears to have become emergent during phase V4 of both sites, beginning at 1.9 Ma. This emergence of the arc also explains the most important volcanic event phase recorded at Site 799, in the middle Pleistocene (phase V3). The same relative decrease in volcanic activity at about 0.4 to 0.5 Ma was observed in the two sites. A final significant pulse at Site 799 was not registered nearly as strongly at Site 798, suggesting again that volcanic sources feeding Site 799 were remote from Site 798.

The tephra markers of the Sea of Japan (see “Lithostratigraphy” section, “Site 798” chapter, this volume) were not

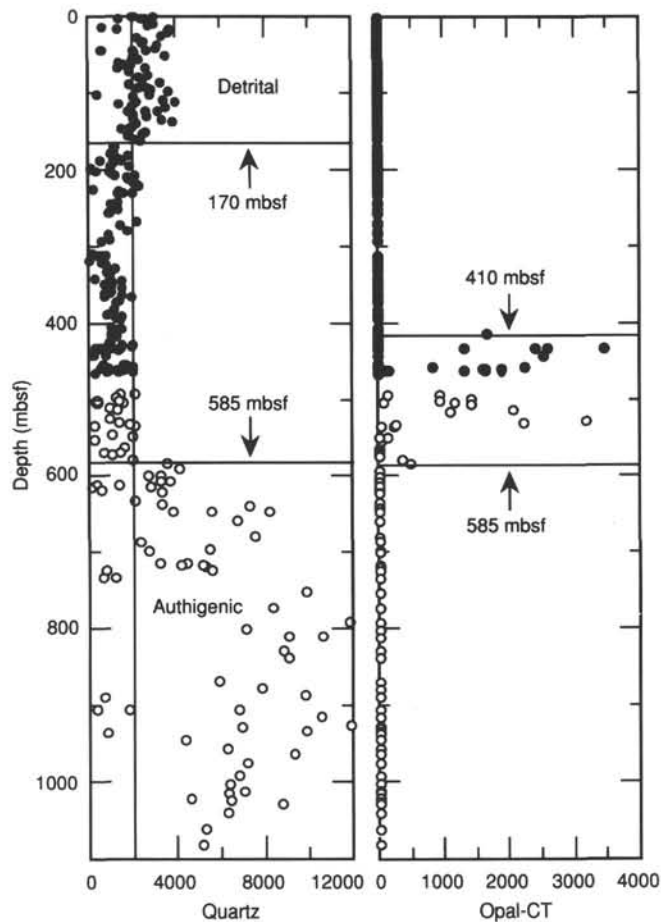


Figure 84. XRD peak intensities of the silica in selected samples from Site 799. Closed circles represent samples from Hole 799A; open circles are data from Hole 799B.

identified in Site 799, although the first four ash layers, more or less reworked in the water-saturated upper part of the hole, may be candidates for the Aira-Tn (AT) event.

Depositional History

Site 799 is located near the axis of the northeast-southwest trending Kita-Yamato Trough (water depth, 2073 mbsl), which is flanked to the northwest by the Kita-Yamato Bank (with a minimum water depth of 458 m within 25 km of Site 799) and to the southeast by the Yamato Bank (with a minimum water depth of 236 m within 28 km of Site 799; Fig. 97). These distinctive isolated banks are composed of a complex of internally fault-bounded blocks of volcanic and granitic rocks. Seismic reflection records and dredge recoveries of Miocene sediments, as well as of Miocene volcanic and Mesozoic granitic rocks, suggest that major areas on top and along the slope of these areas are sediment-starved or barren (Tamaki, 1988; Barash, 1986; Kobayashi, 1985; Honza, 1979; Iwabuchi, 1968). Drilling at Site 799 penetrated a prominent sediment-filled graben structure having a sediment thickness of approximately 1300 m above acoustic basement (K. Suyehiro, pers. comm., 1989). The 1084-m-thick sequence of sediments recovered at Site 799 provides a detailed record of the geologic history of this particularly mountainous area over the past 20 Ma.

Time-Specific Observations

The lower Miocene lithologic Unit V contains abundant coarse-grained sandstones, which include minor amounts of granules and small pebbles. The dominance of angular quartz and the presence of feldspar, biotite, shale intraclasts, glauconite, and mafic rock fragments indicate textural immaturity, which suggests close proximity to source areas. The composition of the sandstones probably reflects a mixed provenance from granitic and volcanic rocks. Sedimentary structures, such as load casts, normal grading, internal planar lamination, and rare cross-lamination, suggest sediment transport in gravity-driven, turbulent currents. The inclusion of miliolid benthic foraminifers and abundant calcareous shell fragments suggests that some coarse-grained detritus was derived from nearby shallow-water source areas (see "Biostratigraphy" section, this chapter). The presence of plant debris and wood fragments indicates emergence of these areas during the early Miocene. The host sediments, in which these shallow-water sediments have been redeposited, consist of siliceous claystones and claystones that contain a benthic fauna of deep-water affinities (1500–2000 m water depth, according to "Biostratigraphy" section, this chapter). The rare occurrence of diagenetic carbonates relative to the superjacent units may reflect deposition near the CCD.

The late early to middle Miocene interval, as documented in Unit IV, was a period of deposition of finely laminated to thinly bedded siliceous sediments, which are intimately interlaminated with intervals rich in authigenic carbonate. The local presence of recognizable foraminifers within the carbonate-rich intervals suggests that accumulations of calcareous fossil debris served as a precursor of these beds. Some fine laminations within the siliceous claystones and porcellanites are sharply bounded and are rarely separated by low-angle truncations. These probably reflect turbulent deposition in the upper-plane bed flow regime (Harms et al., 1975). The presence of a hydrodynamically active sedimentary environment is also indicated by the abundance of thin siliciclastic turbidites that typically include glauconite. The redeposited silt- to fine sand-sized turbiditic sediment contains shallow-water foraminifers, which were probably derived from the adjacent highs.

A substantial contribution of proximal volcanism is recorded by the recovery of approximately 6.2 m of altered rhyolitic tuff near the base of Unit IV. Logging results indicate that this distinctive interval is more than 20 m thick (See "Downhole Measurements," section this chapter).

The sediments in Unit III consist of middle to upper Miocene siliceous claystones and porcellanites, intercalated with abundant authigenic carbonates and minor vitric tuffaceous beds. The upper 149 m (457–606 mbsf) are predominantly laminated, whereas the lower 194 meters (606–800 mbsf) are mainly burrowed. The lower part of Unit III documents a first major phase of bioturbation in the sedimentary record of Site 799. The dominance of laminations in the upper part of Unit III records a return to inhospitable conditions at the seafloor in the late middle or early late Miocene. This general trend was punctuated by scattered short-term oscillations in bottom-water conditions, as suggested by the local presence of dark-colored, laminated or moderately burrowed, silica-rich intervals, interbedded with light-colored, bioturbated, and generally more detritus-rich intervals.

The presence of small numbers of freshwater diatoms in the uppermost part of Unit III at 461.8 mbsf (see "Biostratigraphy" section, this chapter) point to the partly reworked character of preserved biota, as well as to the presence of nearby emergent areas.

Table 4. Compilation of XRF measurements of major elements for selected samples of Site 799.

Sample	Depth (mbsf)	SiO ₂	TiO ₂	Al ₂ O	Fe ₂ O ₃	MnO	MgO	CaO	Na ₂ O	K ₂ O	P ₂ O ₅	Total
Hole 799A												
35X-4, 55	312.35	83.17	0.24	6.28	2.41	0.56	1.96	0.56	3.27	1.38	0.06	100.0
48X-1, 46	433.36	85.96	0.28	6.73	2.36	0.35	1.61	0.36	0.97	1.51	0.06	100.2
48X-1, 109	433.99	93.38	0.13	3.33	1.08	0.41	0.86	0.27	0.24	0.71	0.04	100.4
48X-1, 121	434.11	78.71	0.35	9.08	3.75	0.37	2.94	0.39	2.79	1.87	0.06	100.3
50X-5, 125	459.55	94.30	0.15	3.91	1.20	0.41	0.63	0.28	0.41	0.79	0.05	102.1
51X-1, 50	462.40	85.74	0.31	7.60	2.75	0.12	1.59	0.24	0.98	1.53	0.05	100.9
51X-1, 66	462.56	63.76	0.68	16.37	6.33	0.34	4.59	0.57	2.30	3.31	0.09	98.3
Hole 799B												
17R-3, 62	599.92	64.58	0.63	16.44	6.37	0.93	4.20	0.88	1.97	3.55	0.11	99.7
27R-2, 93	694.93	72.36	0.51	13.19	4.70	0.30	3.08	0.50	1.72	2.76	0.17	99.3
39R-1, 86	809.56	88.36	0.22	5.26	2.01	0.69	1.26	0.42	0.63	1.08	0.09	100.0
51R-3, 59	926.59	78.64	0.45	10.79	3.64	0.34	2.22	0.58	1.51	2.26	0.15	100.6
61R-6, 4	1027.34	82.31	0.36	8.68	3.27	0.20	1.48	0.49	1.38	1.64	0.12	99.9

The abundance of normal faults and related water-escape structures in the interval from 580 to 700 mbsf may indicate a phase of active extensional tectonism during the middle and probably early late Miocene.

The upper Miocene to upper Pliocene sediments in Unit II are highly biosiliceous. According to biostratigraphy (see "Biostratigraphy" section, this chapter), the preserved flora is dominated by *Coscinodiscus marginatus*. The abnormal concentration of this robust diatom may either reflect original low-diversity populations of *C. marginatus*, or may be an artifact of selective dissolution of less robust species in the water column and the underlying sediments.

Bioturbation is common in Unit II sediments and includes both mottling (probably reflecting bioturbation within unconsolidated sediments) and distinct, deposit-feeding burrows. These types of endobenthic activity indicate the presence of well-oxygenated bottom waters during most of the Pliocene.

Judging from the low frequency of ash layers in Unit II, volcanic activity remained at a low level throughout most of the Pliocene.

Unit I consists of a heterogeneous suite of biosiliceous, calcareous, and terrigenous sediments that accumulated during the late Pliocene and the Quaternary. High levels of terrigenous detritus in the intervals between 105 and 150 mbsf and from 0 to 50 mbsf indicate that terrigenous sedimentation prevailed during the last 0.45 Ma, as well as between 2.1 and 1.1 Ma. In the intervening period between 1.1 and 0.45 Ma, a mixed sedimentation regime dominated. Pelagic sediments from this time interval were dominated by calcareous nannofossils and diatom floras; the great variability in dominance of these differing biogenic components may reflect important and repetitive changes in the nutrient content of the surface waters at that time.

Substantial portions of Unit I were deposited by gravity-driven flows. Soft-sediment deformation structures, such as slump folding, sliding along detachment surfaces, and the development of an amalgamated fabric suggestive of liquefaction within debris flows, are prominent. Normally graded, sharply based sequences point to the influence of turbidity currents, especially during the last 0.4 Ma. In this time interval, turbiditic sequences include *Globigerina* oozes and immature sands, the latter probably derived from the sediment-barren, granitic exposures of the Kita-Yamato Bank. The frequency of volcanic ashes in Unit I is much greater than in Unit II; the observed close relationship between volcanic ash layers and turbidite beds in many cases indicates that phases of volcanic activity and simultaneous seismic activity may have functioned as the triggering mechanisms for events

of sediment disturbance and transport in some occurrences (Fig. 29).

Carbonate-rich intervals are common throughout Unit I; however, they are mostly restricted to small intervals within the largely biosiliceous sediments. Prominent pristine, i.e., unaltered, nannofossil-rich sediments are limited to the period between 1.1 and 0.4 Ma. Carbonate-rich intervals younger than 0.4 Ma consist predominantly of rapidly deposited foraminiferal sediments. The presence of nannofossil-rich vs. diatomaceous sediments may reflect changes in nutrient content of the surface waters within the Sea of Japan, as previously mentioned; another possibility is subsidence below the CCD after 0.4 Ma, or a shallowing of the CCD at that time. The modern depth of Site 799 is at the deeper end of the present level of the CCD in the Sea of Japan (1500–2100 m; Ichikura and Ujiie, 1976), and CCD fluctuations in concert with vertical movements of the basement may have affected CaCO₃ preservation at Site 799 during the late Pleistocene.

Sediment reworking and/or current-induced concentration (by winnowing) may have played a role in the genesis of the interbedded, Quaternary dark/light sediments, as suggested by the sharply based, dark-colored intervals that exhibit internal grading. On the other hand, a primary geochemical oceanographic signal must be taken into account, given the high abundance of total organic carbon in the dark intervals (up to almost 6%; see "Organic Geochemistry" section, this chapter). Differentiation between these alternative interpretations is problematic because of difficulty in distinguishing allochthonous sediments from those that record steady hemipelagic sedimentation. Intriguing as well is the observed presence of terrigenous organic matter in some of the dark-colored intervals, whereas the analyzed organic matter in the light-colored intervals is of marine origin. Nevertheless, we assume that a combination of oceanographic as well as tectonic changes within the Sea of Japan were responsible for the accumulation of the dark-colored, laminated, and organic-rich sequences.

The cause of the almost complete absence of bioturbation within the upper 105 m (last 1.1 Ma) is enigmatic, for the bottom water in the modern Sea of Japan is well-oxygenated. Sediments within Unit I below this depth are generally mottled and indicate thorough biogenic soft-sediment reworking.

Structural Observations

The strain ellipsoid, as measured during logging in Hole 799A (see "Downhole Measurements" section, this chapter), indicates the presence of a relative compressional stress field in the northeast-southwest direction, parallel to the Kita-Yamato Trough. Although the vertical component within this

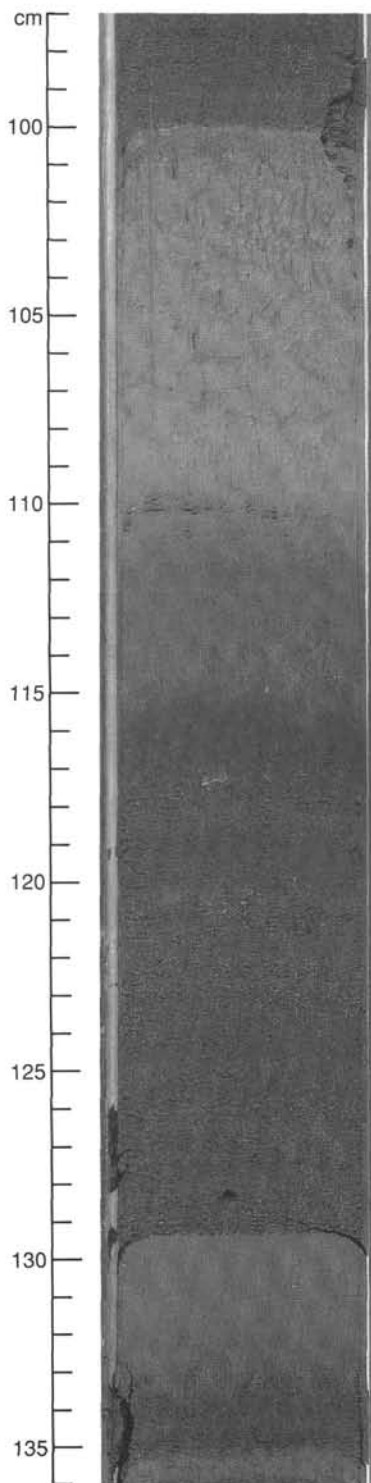


Figure 85. Section 128-799A-3H-1 at 97–136 cm: Dark, organic-rich, normally graded and laminated interval of diatomaceous ooze with foraminifers, overlain by a light-colored, homogeneous, massive silty clay with diatoms at 100–130 cm. Note sharp base of the dark interval.

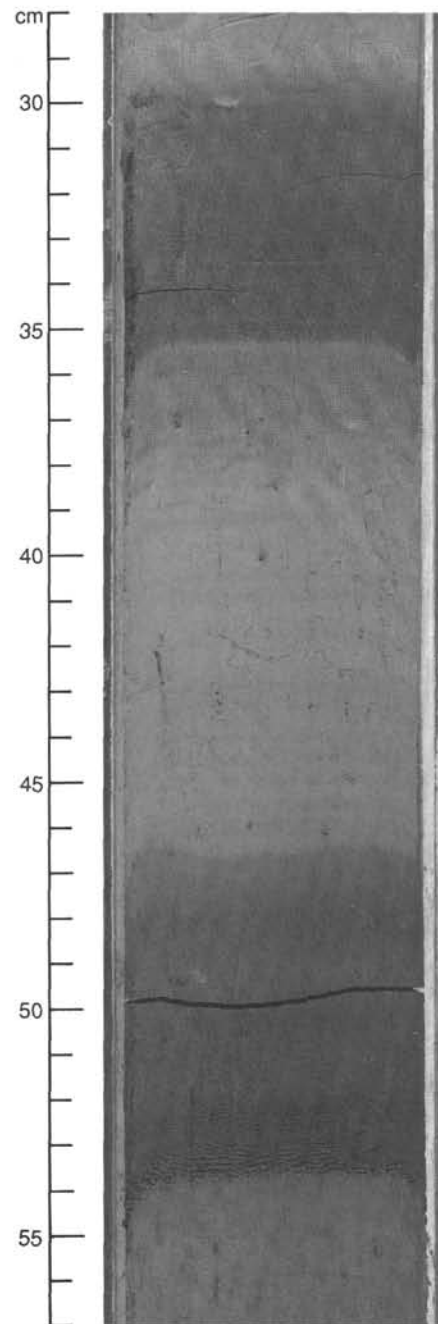


Figure 86. Section 128-799A-4H-2 at 28–57 cm: Fine-grained dark intervals of diatomaceous ooze, intercalated in light-colored clays at 30–54 cm. Note the sharp bases of the dark intervals.

stress field is unknown, and the extrapolation from this single measurement to the entire vicinity of Site 799 is highly tentative, this measurement may indicate the present-day absence of compression along the northwest-southeast axis, perpendicular to the structural axes of the Kita-Yamato and the Yamato banks.

Deformational structures in Units III, IV, and V in the recovered sequence at Site 799 essentially consist of normal faults. They suggest the prevalence of extensional tectonism throughout the Miocene. The abundance of normal faults and complex vein networks in Unit III may reflect a phase of tectonic activity during the middle and probably early late Miocene. The occurrence of slickensided faults, presumably

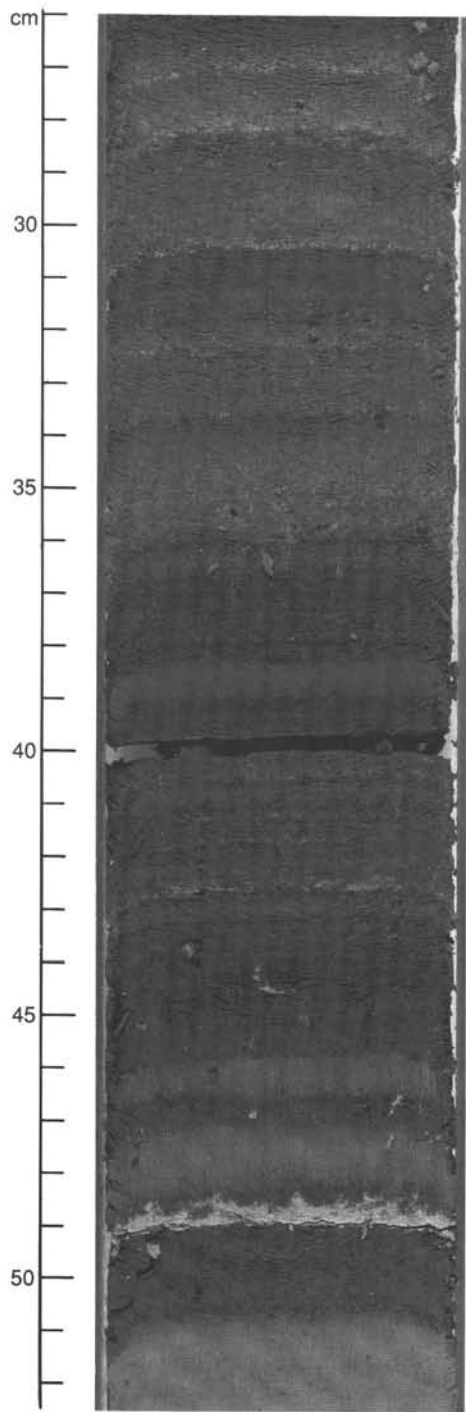


Figure 87. Section 128-799A-12H-5 at 26–52 cm: Dark, laminated interval of clayey diatomaceous ooze, overlying silty clays with diatoms at 25–51 cm. Note the distinct, normally graded laminae.

of late Miocene/early Pliocene age, indicates a further phase near the Miocene/Pliocene boundary. These faults include both normal and possible strike-slip components.

Given the substantial relative elevations during the early and late Miocene, as documented by the allochthonous shallow-water faunas and freshwater floras, as well as by the influx of proximal portions of turbidites in the early Miocene, and given the reconstructed early Miocene water depths, Miocene topography and bathymetry probably resembled the

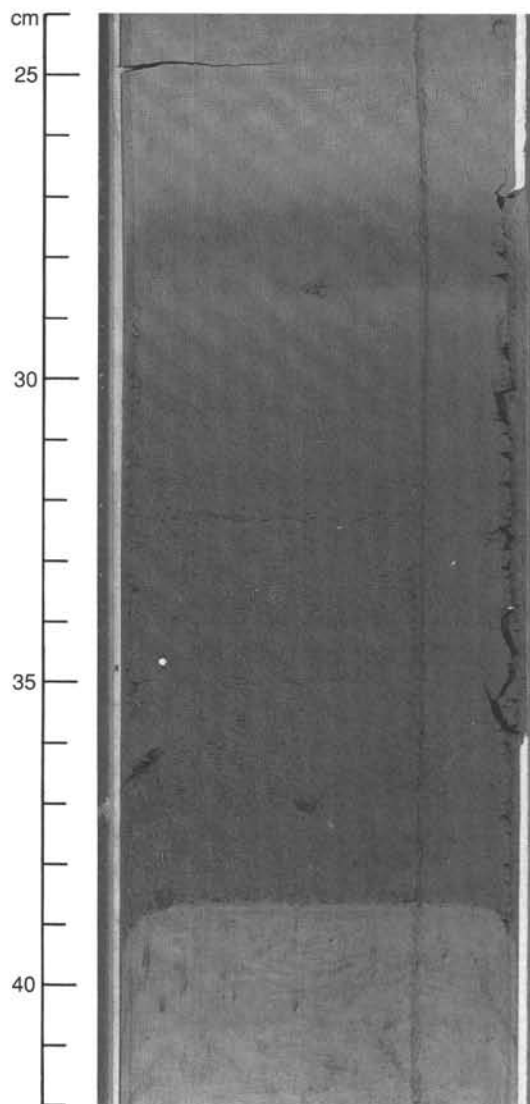


Figure 88. Section 128-799A-3H-7 at 24–42 cm: Dark, laminated interval of diatomaceous ooze, overlain by light-colored diatomaceous clayey mixed sediment.

present-day configuration, with the exception of the presence of emergent rises.

Assuming emergence of the Kita-Yamato and Yamato banks during the early and late Miocene and considering the present elevation of these bank tops (minimal water depths are 397 and 236 mbsl, respectively), we suggest a bulk subsidence rate of about 500 m during the last 20 m.y. The subordinate occurrence of coarse turbidites within the stratigraphic section at Site 799 (exception is the lower Miocene Unit V) suggests that both banks were not subjected to major vertical movements during the Neogene. The Kita-Yamato Trough probably experienced stronger subsidence, if the assumption of approximately equal seafloor depths throughout the Neogene and Quaternary holds true. The subsidence rate for the last 20 m.y. would in this case approximate the present thickness of the sedimentary column, which corresponds to at least 1300 m. This indicates differential subsidence within the Kita-Yamato area, which is also well-expressed by the horst-graben configuration evident from seismic reflection profiles (Fig. 97). A first-hand calibration of the major reflectors in the seismic profiles with our sedimentary column and a general

Table 5. Ash layers at Site 799.

Layer number	Depth (mbsf)	Thickness (cm)	Petrogr. group	Lith. type	Glass (%)	Age (k.y.)
1	1.30	0.5	A	H	50	18.2
2	2.11	0.2	A	H	40	29.5
3	2.23	0.5	A	H	50	31.2
4	2.34	1.5	A	H	50	32.7
5	3.32	18.0	A	TT	80	46.4
6	3.65	15.0	A	TT		51.1
7	3.89	6.0	A	TT		54.4
8	4.54	0.3	A	H		63.5
9	4.72	0.5	A	H		66.0
10	6.76	0.5	A	H		94.6
11	7.25	0.3	A	H		101.4
12	7.27	0.3	A	H		101.7
13	11.18	6.0	A	TT		156.4
14	11.83	1.0	A	H		165.5
15	14.39	5.0	A	TT		201.3
16	14.71	0.8	A	H		205.8
17	15.04	10.0	A	TT		210.4
18	15.05	0.8	A	H		210.5
19	15.38	0.2	A	H		215.2
20	15.51	0.2	A	H		217.0
21	15.73	0.4	A	H		220.1
22	15.97	0.2	A	H		223.4
23	15.99	0.3	A	H		223.7
24	17.03	0.2	A	H	55	238.2
25	17.52	0.1	A	H	55	246.5
26	17.62	0.1	A	H		246.5
27	17.66	0.4	A	H		247.1
28	18.10	0.1	A	H		253.2
29	18.70	0.3	A	H		261.6
30	18.79	0.1	AB	H		262.9
31	19.09	0.1	A	H	55	267.1
32	19.42	0.1	A	H	55	271.7
33	21.61	0.5	A	H		302.3
34	21.83	0.2	A	H		305.4
35	23.81	0.3	A	H		333.1
36	23.86	0.1	A	H		333.8
37	26.20	0.1	A	H		350.7
38	26.23	0.2	A	H		350.9
39	26.25	0.2	A	H		351.0
40	26.89	0.1	A	H		354.6
41	27.13	0.2	A	H		355.9
42	27.18	0.1	A	H		356.2
43	27.20	0.1	A	H		356.3
44	27.23	0.1	A	H		356.5
45	28.44	11.0	A	G	70	363.3
46	28.53	8.0	AB	G	70	363.8
47	29.07	0.4	A	H		366.9
48	30.09	0.2	A	H		372.6
49	30.15	0.2	A	H		373.0
50	30.65	0.1	A	H		375.8
51	31.05	0.2	B	H		378.0
52	31.10	0.1	A	H		378.3
53	31.38	0.1	A	H		379.9
54	31.74	2.0	A	H		381.9
55	32.77	0.3	A	H		387.7
56	33.88	0.1	A	H		394.0
57	35.56	1.0	A	H		403.4
58	36.20	0.5	B	H	72	407.0
59	38.68	0.3	A	H		421.0
60	38.90	0.8	A	H		422.3
61	39.35	0.3	A	H		424.8
62	39.55	0.2	B	H		425.9
63	41.47	0.5	A	H		436.7
64	41.91	0.2	A	H		439.2
65	42.15	0.1	A	H		440.6
66	42.23	0.1	A	H		441.0
67	44.90	1.0	A	H		456.1
68	47.30	2.5	A	T		470.4
69	49.95	0.4	A	H		486.7

Table 5 (continued).

Layer number	Depth (mbsf)	Thickness (cm)	Petrogr. group	Lith. type	Glass (%)	Age (k.y.)
70	50.11	0.8	A	H		487.7
71	50.75	0.4	A	H		491.7
72	50.94	0.3	AB	H	40	492.8
73	51.39	1.6	A	G	75	495.6
74	51.47	0.8	A	H	80	496.1
75	51.51	0.3	A	H	75	496.3
76	51.78	1.2	A	H		498.0
77	52.93	0.2	A	H	30	505.1
78	53.51	1.0	A	G	75	508.6
79	53.53	0.3	A	H	80	508.8
80	56.45	0.3	A	H		526.7
81	56.65	1.5	A	H		528.0
82	56.89	0.3	A	H		529.4
83	57.37	1.0	A	G		532.4
84	57.46	0.2	A	H		532.9
85	59.50	0.6	A	H		545.5
86	61.02	0.2	A	H		554.8
87	63.01	0.2	A	H	40	567.1
88	64.30	1.0	A	H		575.0
89	65.19	4.0	A	G	90	580.5
90	65.35	11.0	A	G		581.5
91	65.84	0.1	A	H		584.5
92	67.45	0.4	AB	H		594.4
93	69.00	0.4	A	H		603.9
94	69.51	0.5	A	H		607.0
95	70.53	0.1	A	H		613.3
96	70.56	1.2	A	G		613.5
97	70.64	1.3	A	G		614.0
98	70.68	0.4	A	H		614.2
99	70.72	0.3	A	H		614.5
100	70.92	0.2	A	H		615.7
101	70.93	0.3	A	H		615.8
102	70.95	0.4	A	H		615.9
103	70.98	0.4	A	H		616.1
104	72.34	0.4	A	H		624.5
105	73.19	0.3	A	H		629.7
106	74.00	1.0	A	H		634.7
107	74.78	0.2	A	H		639.5
108	74.79	0.2	A	H		639.5
109	74.80	0.1	A	H		639.6
110	74.88	0.2	A	H		640.1
111	75.06	0.1	A	H		641.2
112	75.12	1.2	A	H		641.6
113	75.14	0.4	A	H		641.7
114	75.15	0.3	A	H		641.7
115	78.45	0.1	A	H		662.0
116	79.71	0.1	A	H		669.8
117	80.29	1.0	A	H		673.3
118	80.66	0.1	A	H		675.6
119	82.05	0.2	B	H	30	684.2
120	83.86	9.0	A	T	90	695.3
121	83.99	12.0	A	T	90	696.1
122	84.37	0.1	A	H		698.4
123	84.47	0.1	A	H		699.1
124	85.33	0.2	A	H		704.3
125	85.37	0.1	A	H		704.6
126	85.65	0.1	A	H		706.3
127	85.72	3.5	A	H		706.7
128	85.92	1.0	A	H	95	708.0
129	86.36	0.1	A	H		710.7
130	86.51	0.1	A	H		711.6
131	87.29	3.5	A	H		716.4
132	87.31	2.0	A	H		716.5
133	87.40	2.0	A	H		717.1
134	87.52	1.0	A	H		717.8
135	89.69	0.3	A	H		739.1
136	89.85	0.8	A	H		746.8
137	89.99	0.2	A	H	90	753.5
138	90.49	0.8	A	H		777.5

Table 5 (continued).

Layer number	Depth (mbsf)	Thickness (cm)	Petrogr. group	Lith. type	Glass (%)	Age (k.y.)
139	90.65	0.2	A	H		785.2
140	91.46	0.7	A	H		824.1
141	91.49	0.2	A	H		825.5
142	91.97	0.8	A	H		848.6
143	92.84	0.1	A	H		890.3
144	93.36	0.4	A	H		912.6
145	93.40	0.8	A	H		913.6
146	93.58	0.8	A	H		917.9
147	93.92	0.5	A	H		926.1
148	94.28	0.3	A	H		934.8
149	94.86	5.5	A	G	99	948.8
150	95.33	0.1	A	H		960.2
151	95.35	0.2	A	H		960.7
152	95.36	0.1	A	H		960.9
153	95.72	0.8	A	H		969.6
154	97.45	0.2	A	H		1006.8
155	97.46	0.2	A	H		1007.0
156	97.49	0.2	A	H		1007.7
157	100.75	0.6	A	H	98	1075.0
158	101.05	0.2	A	H		1081.2
159	101.38	0.5	A	H		1088.0
160	101.76	0.1	A	H		1095.9
161	101.91	0.2	A	H		1099.0
162	103.69	0.2	A	H		1135.7
163	106.34	1.0	A	H		1190.5
164	109.92	4.0	A	H		1286.3
165	117.96	0.5	A	H		1508.4
166	119.01	18.0	A	T	90	1537.4
167	120.35	0.2	A	H		1574.4
168	126.30	1.5	A	G		1725.3
169	143.31	0.3	A	H		2027.9
170	145.07	0.2	A	H		2053.2
171	146.40	1.0	A	H		2072.4
172	152.99	0.5	A	H	62	2167.3
173	157.50	0.5	A	H	60	2232.3
174	160.06	0.2	A	H		2269.2
Logged	163.20					2314.4
175	171.32	1.0	A	H	85	2431.4
176	171.85	0.1	A	H		2439.1
177	173.74	0.1	A	H		2466.3
178	174.68	0.8	A	H		2499.2
179	179.86	1.5	A	H		2721.2
Logged	195.60					3050.7
180	199.12	1.5	A	H		3092.1
Logged	199.30					3094.2
Logged	205.00					3161.3
Logged	207.70					3193.1
Logged	213.20	3.0				3257.8
Logged	216.40					3259.4
Logged	218.00					3314.3
181	219.60	0.3	A	H		3333.1
182	286.76	5.5	A	H	55	4207.7
Logged	292.90					4259.3
Logged	296.90					4293.0
Logged	299.20					4329.7
Logged	308.70					4463.2
183	310.68	0.5	A	H	90	4458.5
184	311.16	0.5	A	H	90	4463.9
185	315.19	0.5	A	H	90	4509.1
186	323.16	2.5	A	H		4498.5
Logged	342.30					4813.2
187	344.53	5.5	A	G	95	4838.2
Logged	346.30					4858.0
Logged	351.00					4910.8
Logged	352.90					4932.1
Logged	380.90					5246.2
Logged	393.60					5388.6
188	395.31	1.5	A	H	90	5407.8

Table 5 (continued).

Layer number	Depth (mbsf)	Thickness (cm)	Petrogr. group	Lith. type	Glass (%)	Age (k.y.)
Logged	397.30					5440.4
Logged	397.90					5449.5
Logged	398.80					5463.0
Logged	403.20					5529.4
Logged	409.90					5630.4
Logged	411.30					5651.5
Logged	413.90					5695.0
Logged	416.10					5712.9
Logged	418.50					5732.4
Logged	419.40					5739.7
Logged	421.00					5752.7
Logged	423.90					5960.8
189	426.12	0.3	A	H		5855.6
190	429.18	0.3	A	H		5986.3
191	430.30	1.0	A	H		6034.1
Logged	441.00					6218.1
Logged	442.20					6236.1
Logged	447.80					6320.4
192	453.44	0.3	A	H		6405.3
192	454.03	0.5	A	H		6414.1
194	455.17	5.0	A	H		6432.4
195	463.01	13.0	A	TT	50	6559.8
196	463.12	0.6	A	H		6561.5
197	463.47	1.0	A	H		6567.2
198	463.86	2.0	A	H		6573.6
199	569.14	0.8	A	H	60	
200	579.31	0.1	A	H		
201	582.01	0.5	A	H		
202	582.45	0.1	A	H		
203	610.61	2.0	AB	H		
204	615.92	2.0	AB	H		
205	645.07	5.0	A	G		
206	645.60	1.0	A	H		
207	674.19	0.1	A	H		
208	674.65	0.8	A	H		
209	698.99	2.0	A	G	90	
210	700.11	0.4	A	H		
211	740.85	0.1	A	H		
212	751.10	0.2	B	H		
213	800.21	1.0	AB	H		
214	808.58	6.0	A	G	60	
215	827.32	2.0	A	H		
216	837.51	1.0	A	H		
217	879.96	20.0	B	?		
218	885.50	0.3	AB	H		
219	885.60	0.1	AB	H		
220	885.68	0.2	AB	H		
221	886.52	0.2	AB	H		
222	963.25	0.2	A	H		
223	964.01	2.0	A	H		
224	982.60	111.0	A	H		
224	982.93	33.0	A	H		
224	983.12	19.0	A	H		
224	992.30	150.0	A	H		
224	993.34	104.0	A	H		
224	993.77	43.0	A	H		
224	1002.00	150.0	A	H		
224	1002.41	41.0	A	H		

Lithologic types: H = homogeneous; G = graded; T = heterogeneous; TT = Turbidite. Petrographic groups: A = acidic; B = basic; AB = mixed acidic and basic or intermediate. Layers indicated by "Logged" were recorded by the FMS, but were not recovered in core. Layers 1 through 198 are from Hole 799A, and layers 199 through 224 from Hole 799B. The thick rhyolite tuff near the base of Unit IV is listed collectively as layer 224. Ages could not be determined for ashes in Hole 799B (compare "Ash Layers" section with "Tephrochronology" section, this chapter).

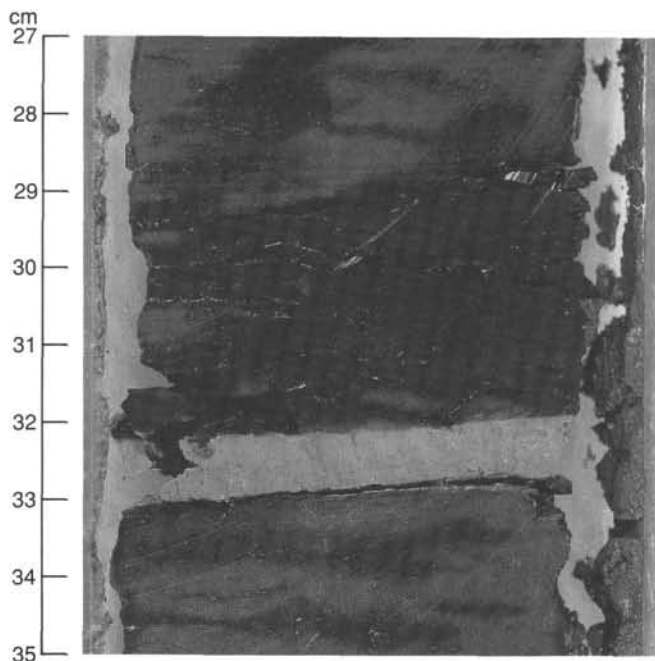


Figure 89. Section 128-799B-14R-2 at 27–35 cm: Light gray vitric ash in dark siliceous claystone at 32–33 cm (layer 199). This layer has been altered to quartz, opal-CT, smectite, and stilbite. Note also laminations in siliceous claystone from 27 to 29 cm.

and broad interpretation of the sediment configuration within the Kita-Yamato Trough indicate phases of accelerated subsidence during the early to latest Miocene and periods of stagnation during the Pliocene.

BIOSTRATIGRAPHY

Introduction

Microfossils occur with variable abundances and preservation states throughout Site 799. In general, calcareous microfossils are most abundant and best preserved in Quaternary sediments, although they are scattered in Miocene and Pliocene samples. Biosiliceous sediments are few to abundant in Hole 799A down to Section 128-799A-52X-CC, below which they are absent. Several cores above 128-799A-50X exhibit increased dissolution of even the more robust siliceous microfossils, while the interval below about 160 m (Section 128-799A-18H-CC) shows increased dissolution of the more fragile diatoms, leaving behind an assemblage enriched in the diatom species *Coscinodiscus marginatus*. Benthic foraminifers indicate a mid-to-upper bathyal depth above Sample 128-799A-33X-CC and a lower bathyal depth below this level. However, distinct lithologic intervals occur in this unit that may reflect paleoceanographic events, rather than simple redeposition events (see “Lithostratigraphy” section, this chapter). The Quaternary sequence of Hole 799A is also marked by abrupt changes in sediment type and rates of sedimentation, probably as a result of slumping off nearby ridges. We found evidence of reworking of older (Miocene-Pliocene) microfossils in Quaternary sediments commensurate with sedimentologic evidence of downslope redeposition (see “Lithostratigraphy” section, this chapter). Miocene and Pliocene sediments are dominantly pelagic and show increased dissolution of both the biocalcareous and biosiliceous components with depth. A summary of established zonations for all microfossil groups studied at Site 799 is shown in Figures 98 and 99.

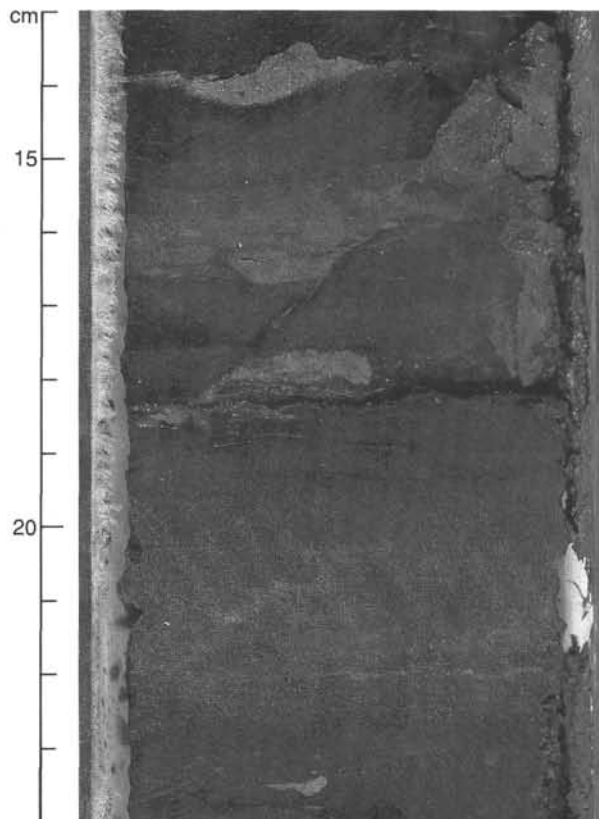


Figure 90. Section 128-799-18R-4 at 13–24 cm: A silty ash layer (19–22.5 cm) and a normal fault with a strike-slip component (?) (13–18.5 cm) are prominent features in this dark siliceous claystone. The ash layer (203) is of intermediate composition and has been altered to quartz, halloysite, sideromelane, and stilbite.

Diatoms, calcareous nannofossils, and silicoflagellates and ebridians were best used to zone Hole 799A. Because of their poor preservation and low diversity, it was difficult to use calcareous nannofossils or planktonic foraminifers for zonations below the Quaternary. It seems likely that with more closely spaced samples, it will be possible to use changes in coiling directions of *Neogloboquadrina pachyderma* to zone the late Quaternary into glacial/interglacial intervals. Diatom and silicoflagellate datum levels are not always consistent with those identified at Site 798 and in the North Pacific (Koizumi and Tanimura, 1985). For example, the *N. kamtschatica* (diatom) and *D. jimlingii* (silicoflagellate) datums, which are found at the same level in Site 798, occur at widely differing levels at Site 799. Similarly, we had a problem identifying the Miocene/Pliocene boundary. Because of the increased dissolution of diatoms in the lower part of the section at Hole 799A, zonal markers were not always present. This is also true of the radiolarians and silicoflagellates. Therefore, we relied primarily on an interpretation of the magnetostratigraphy to identify the approximate position of the Miocene/Pliocene boundary. Additional biostratigraphic work will be needed to determine if the selection of this level is valid.

Hole 799B is simply a downsection continuation of Hole 799A. Because Hole 799A bottomed just below the opal-A/opal-CT boundary, Hole 799B is almost entirely devoid of microfossils, particularly diatoms and silicoflagellates. Scattered occurrences of radiolarians, calcareous nannofossils, and diatoms permitted us to identify the middle Miocene in this hole, as well as the early Miocene. On the basis of our microfossil data, Hole 799B probably bottomed in lower

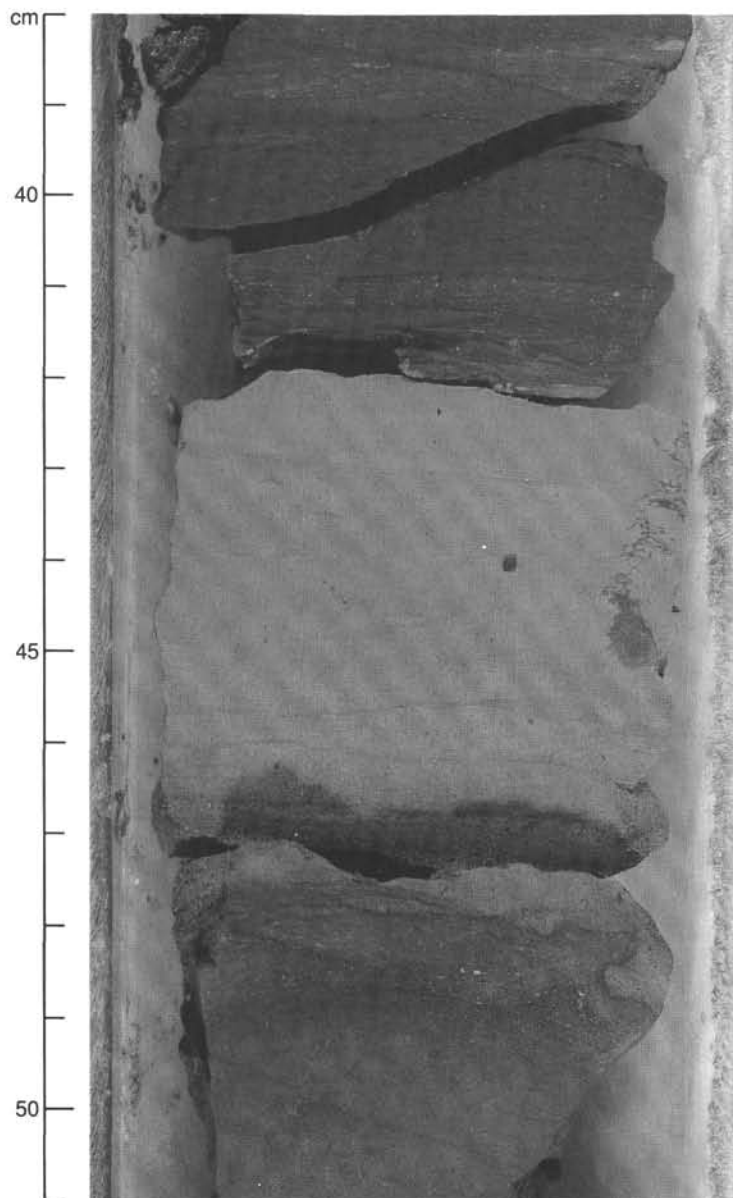


Figure 91. Section 128-799B-22R-1 at 38–51 cm: Light-colored tuffaceous bed within darker porcellanite. Small faults are present from 38 to 39 cm, 45 to 46 cm, and 49 to 50 cm. An unusual structure of unknown origin is present at the right margin of the tuff bed. The tuff bed also exhibits an upward decrease in size and abundance of dark grains, an observation that may suggest normal-grading.

Miocene sediments. The middle Miocene/lower Miocene boundary was placed in Sample 128-799B-57R-CC on the basis of the following information:

1. An earlier form of the radiolarian *Didymocyrtilis mamifera* was observed in Sample 128-799B-48R-CC. The FAD of this species occurs in the upper part of the lower Miocene, and the LAD occurs slightly above the base of the middle Miocene *D. alata* Zone.

2. The calcareous nannofossil assemblage in Sample 128-799B-56R-CC is restricted to early Miocene nannofossil Zones CN3, CN4, or middle Miocene Subzone CN5a. If this assemblage is restricted to Subzone CN5a, then the early Miocene/middle Miocene boundary must lie below this core.

Upper Miocene sediments probably were encountered, but because of the absence of diagnostic age indicators, we cannot be sure of the level. Placement of the early Miocene/middle Miocene and middle Miocene/late Miocene boundaries in Figure 99 thus are based on limited data and should be viewed as best estimates that are subject to change. Because of poor preservation, we draw no definitive paleoenvironmental information for the lower part of this hole. All microfossil data are summarized in Table 7, which also includes paleomagnetic reversal boundaries (see "Paleomagnetism" section, this chapter).

Diatoms

Diatoms are generally present throughout much of Hole 799A, sometimes in considerable abundance; only near the

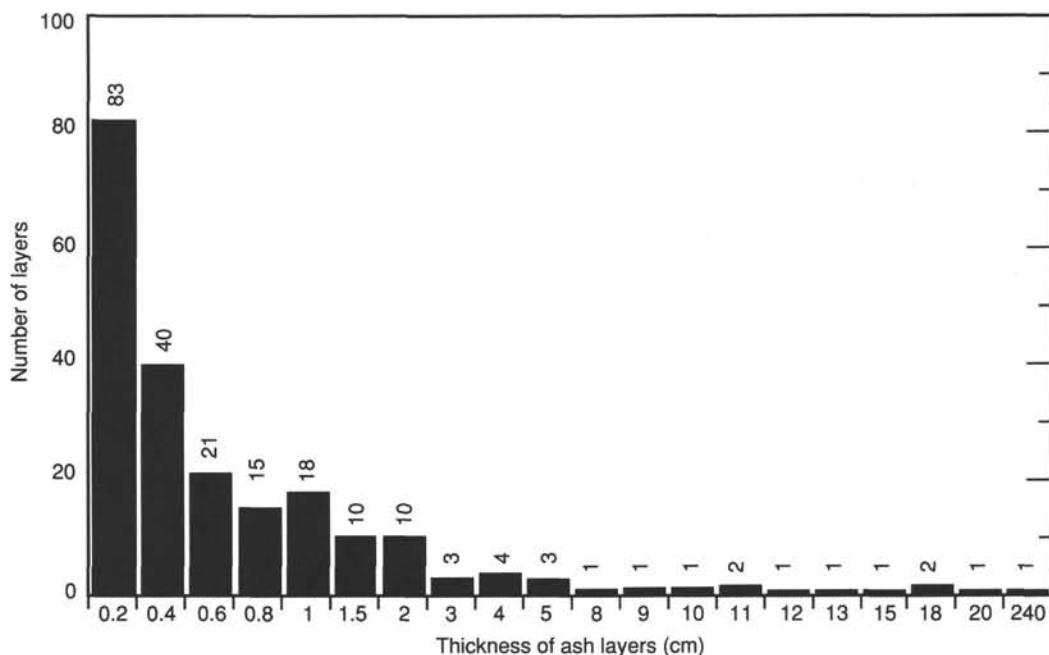


Figure 92. Frequency of occurrence of ash layers of different thicknesses at Site 799. Data are from Table 5.

Table 6. Chemical analysis of major and trace elements of the rhyolitic tuff in Sample 128-799B-58R-2, 74-77 cm.

Major elements (in wt%)		Minor elements (in ppm)	
SiO ₂	76.95	Nb	12.1
TiO ₂	0.22	Zr	125.5
Al ₂ O ₃	14.22	Y	58.6
Fe ₂ O ₃	2.05	Sr	181.7
MnO	0.05	Rb	86.1
MgO	2.60	Zn	9.9
CaO	0.57	Cu	3.6
Na ₂ O	1.38	Ni	8.4
K ₂ O	2.05	Cr	3.8
P ₂ O ₅	0.04	V	11.5
		Ce	89.9
Total:	100.11	Ba	504.9
LOI:	5.65		

bottom of the hole do they disappear completely from the sediment. Based upon diatom biostratigraphy, drilling at Hole 799A probably penetrated the upper Miocene sequence. We had some difficulty, however, when using diatoms in the lower part of the section represented in Hole 799B. Dissolution was so extensive that although we were dealing largely with a diatom ooze, only the more robust species were preserved. In most cases, this proved to be *Coscinodiscus marginatus*, a species that is most abundant in present-day transitional waters and ranges from the middle Cretaceous to the present.

Samples 128-799A-1H-CC through 128-799A-5H-3, 146 cm, contain few-to-common, poor-to-moderately well-preserved diatoms (Table 8) and were assigned to the *Neodenticula seminae* Zone. Assemblages within this zone represent both warm-water and temperate origins and may reflect the alternating glacial and interglacial conditions characteristic of this part of the Quaternary. Besides the nominate taxon, diatom species include *Thalassiothrix nitzschioides*, *T. nitzs-*

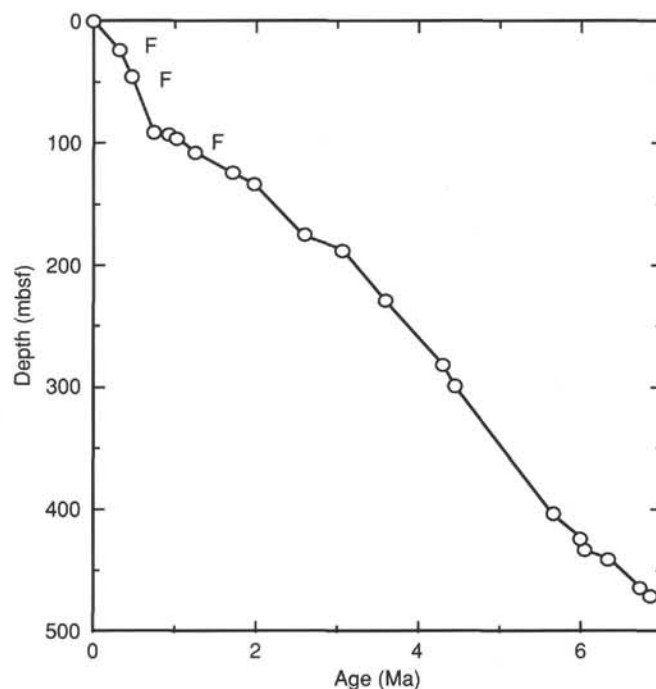


Figure 93. Model used to estimate the ages of ashes at Hole 799A. F = fossil datum; other points are paleomagnetic boundaries. See text for detail.

chioides var. *parva*, *Coscinodiscus marginatus*, *Pseudoeunotia doliolus*, and *Rhizosolenia hebetata*. Samples 128-799A-5H-6, 30 cm, through 128-799A-13H-CC contain common-to-abundant, moderately to well-preserved diatoms belonging to the *Rhizosolenia curvirostris* Zone. The top of this zone is defined by the last occurrence of the nominate taxon and its base by the last occurrence of *Actinocyclus oculatus*. Within the lower part of this zone (Sample 128-799A-12H-6, 51 cm), the LAD of the silicoflagellate *Mesocena elliptica* was ob-

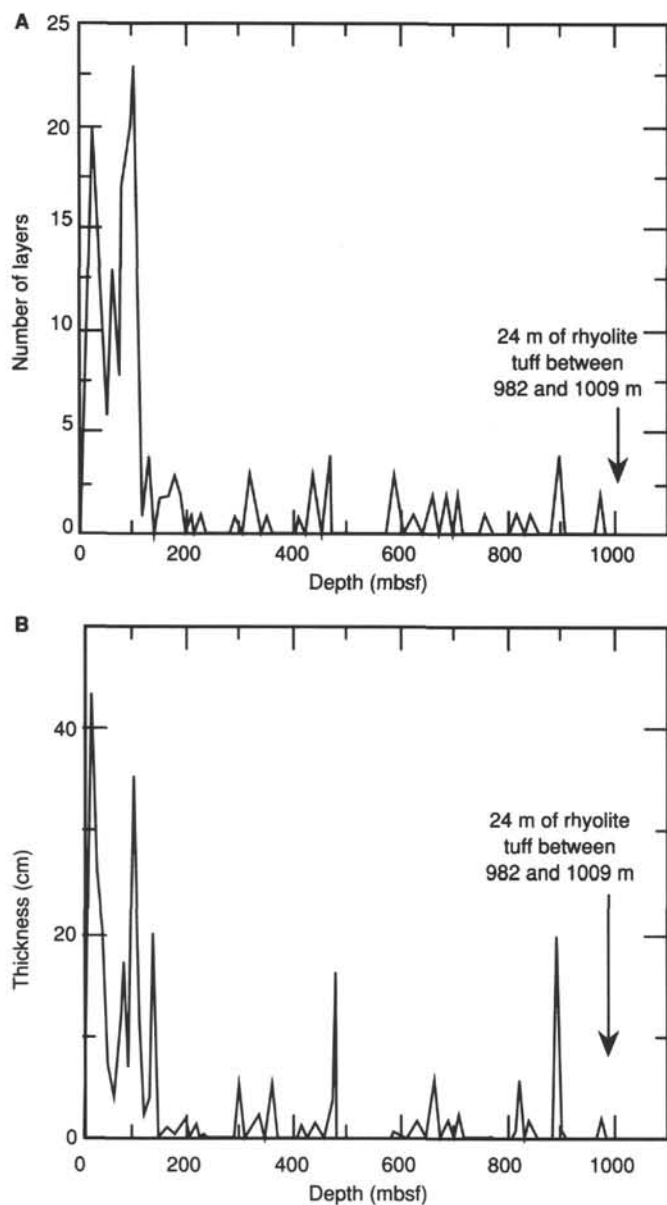


Figure 94. Number (by visual inspection and FMS data) and thickness of ash layers at Site 799 as a function of depth from Figure 93. Data are from Table 5. The more than 20-m-thick rhyolite tuff near the base of Unit IV was omitted.

served. This species has been useful for helping to identify the interval between the base of the Brunhes Chron and the top of the Jaramillo Subchron (Hays et al., 1969). Diatom species found in this zone include *P. doliolus*, *N. seminae*, *Thalassiosira lineata*, *Rhizosolenia hebetata*, *C. excentricus*, and *T. nitzschioides*.

The top of the *A. oculus* Zone is defined by the LAD of the nominate taxon. In Hole 799A, this species is scattered and usually rare. In some instances, we did not find it at all, but the samples were still assigned to that zone on the strength of stratigraphic position. In contrast to Site 798, the *A. oculus* Zone in this site is short and extends from Samples 128-799A-13H-CC to 128-799A-14H-CC. This zone contained few-to-common, poor-to-moderately well-preserved diatoms.

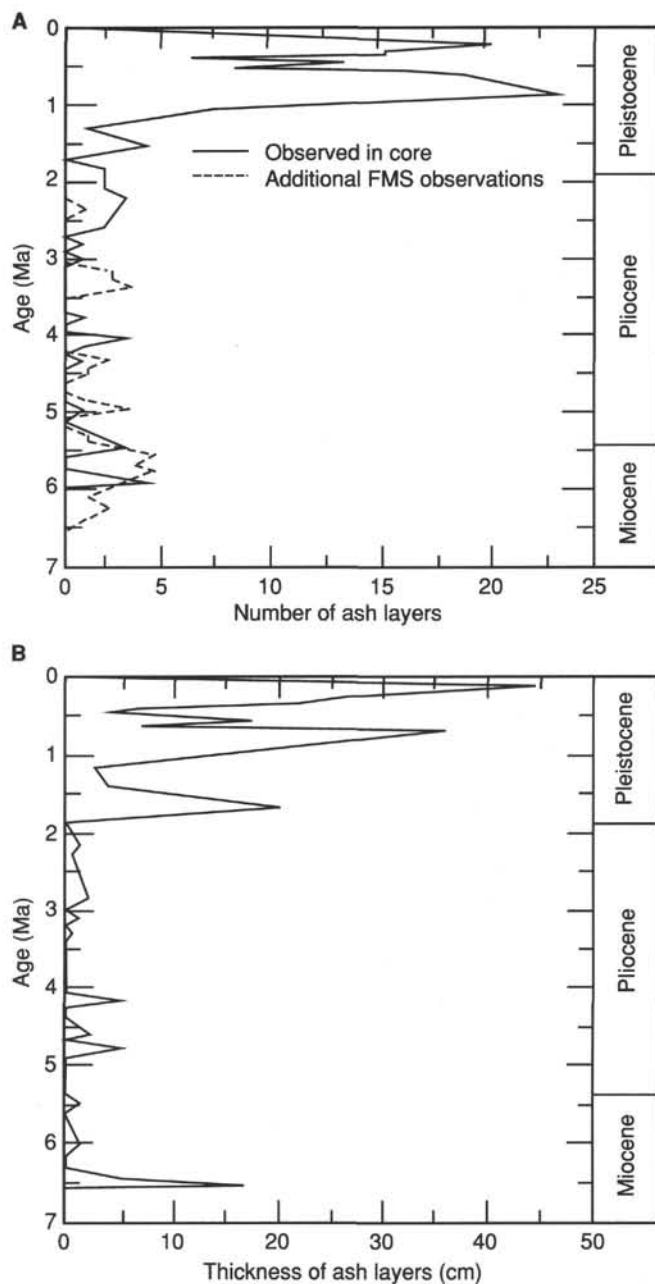


Figure 95. Number (by visual inspection and FMS data) and thickness of ash layers in Hole 799A as a function of estimated age from Figure 93. Data are from Table 5. The Pleistocene/Pliocene boundary is at 1.88 Ma and the Pliocene/Miocene boundary at 5.41 Ma.

Besides the nominate taxon, the assemblage in this interval includes *N. seminae*, *R. curvirostris*, *C. radiatus*, *C. excentricus*, and *T. nitzschioides*.

Samples 128-799A-16H-CC through 128-799A-21X-CC are in the *N. koizumii* Zone (late Pliocene). Diatoms are few to common in this zone, and these are generally moderately well preserved. Besides the nominate taxon, species include *T. nitzschioides* and varieties, *C. marginatus*, *C. excentricus*, and *T. oestrupii*. This zone often contained abundant *C. marginatus* and *T. nitzschioides*. The former species becomes numerically dominant in the next zone below and increases in dominance toward the bottom of the hole.

The underlying *Neodenticula kamschatica*-*N. koizumii* Zone extends below Sample 128-799A-22X-CC. The base of

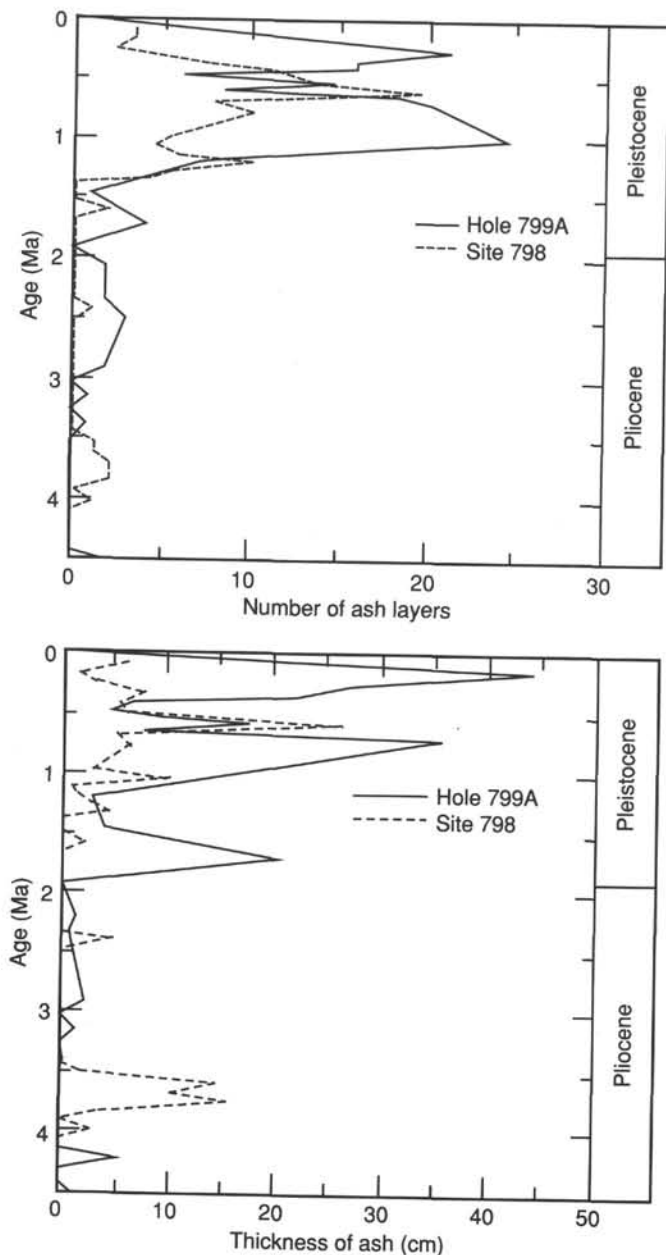


Figure 96. Comparison of Site 798 with Site 799 in the number and thickness of ash layers observed in core.

this zone is defined by the first occurrence up the section of *N. koizumi*. However, preservation becomes poor in the lower part of this zone. By that, we mean that the less robust diatoms have been removed (dissolved) from the assemblage, leaving *C. marginatus* and fragments of *T. nitzschioides*. The base of this zone could not be defined with any certainty, and we tentatively placed it in Sample 128-799A-23X-CC. Diatoms are generally abundant through this interval, but preservation is poor. The assemblage tends toward a monospecific community with *C. marginatus* dominating. Also observed within this zone was *N. kamtschatica*, *T. nitzschioides*, and *N. rolandii*.

The top of the *Neodenticula koizumii*-*N. kamtschatica* Zone, defined by the last occurrence of *N. kamtschatica*, occurs in Sample 128-799A-22X-CC. The last appearance of this species is a well-known datum, which in the North Pacific, occurs near the top of the Gauss magnetic chron (Koizumi and Tanimura, 1985). This datum may be used to identify those paleoenvironmental and paleoclimatic events

that are known to occur in the late Gauss and early Matuyama chrons (see, for example, Shackleton and Opdyke, 1977; Prell, 1985; Shackleton et al., 1984).

Sample 128-799A-24X-CC is the top of the *Thalassiosira oestrupii* Zone. This zone is defined by the first appearance of the nominate taxon at its base (128-799A-37X-CC) and the first appearance of *N. koizumii* at its top. Unfortunately, we found few specimens of *T. oestrupii* in this zone, nor did White and Koizumi during Leg 127 (Tamaki, Pisciotto, Allan, et al., in press). However, we can identify this interval on the basis of stratigraphic position. *N. kamtschatica* disappears below Sample 128-799A-37X-CC, whereas in the North Pacific, it ranges down into the late Miocene (Koizumi and Tanimura, 1985). Because this species is also robust, it is probable that this is a true first appearance in this region. Burckle and Opdyke (1985) noted that the first appearance of this species in the low-latitude North Pacific is diachronous with the earliest occurrences in the late Miocene in the higher-latitude North Pacific and later occurrences near the Miocene/Pliocene boundary in middle latitudes. It seems likely that in the restricted Sea of Japan, this species might make an even later appearance.

Samples 128-799A-37X-CC to 128-799A-50X-2, 300 cm, cannot be ascribed to any specific zone because of the absence of zonal markers. Apparently, silica dissolution has removed the more weakly silicified forms from this part of the section, so that only the more robust forms have been preserved. For this reason, *C. marginatus* is the predominant form in this interval, with some *T. nitzschioides* also present. However, it is apparent from stratigraphic and magnetostratigraphic considerations that the Miocene/Pliocene boundary has been crossed and that drilling at Hole 799A reached the late Miocene. An acme of *C. marginatus* in the late Miocene/early Pliocene of the North Pacific has been described by a number of scientists (Burckle and Opdyke, 1977; Akiba, 1982). Burckle and Opdyke (1977), working with paleomagnetically dated samples from the North Pacific, noted that this acme persisted into the upper part of magnetic Chron 7, below which dissolution destroyed all evidence of diatoms. Results from Hole 799A, both stratigraphic and paleomagnetic, are not inconsistent with those results.

Samples 128-799A-50X-CC to 128-799A-52X-CC are completely barren of diatoms. However, the upper two sections of Core 128-799A-50X contain abundant diatoms, with *C. marginatus* being the most abundant. This interval is interesting, however, in that a few specimens of freshwater diatoms (most notably *Melosira* sp.) were observed. Equally interesting is that near the shore, brackish-water forms (most notably *Actinopterychus senarius*) were present. Although marine diatoms remain numerically dominant (*A. senarius* represents about 1% of the total assemblage), the presence of freshwater and brackish-water (benthic) forms suggests either a temporal or a spatial proximity to a terrestrial environment.

Hole 799B was a continuation of Hole 799A and was entirely below the opal-A/opal-CT boundary. For that reason, diatoms were rare and usually were in a poor state of preservation. Sample 128-799B-33R-CC contained few diatoms in varying states of preservation. Nearshore forms, such as *Terpsinoe* sp. and *Arachnoidiscus* sp., were relatively well preserved. However, except for *C. marginatus*, the more open-ocean forms were in a poor state of preservation. We observed *Annellus* cf. *A. californicus* as well as *Thalassiosira tappanae* in this sample. However, preservational conditions make these identifications tentative. Their occurrence in this sample indicates an early middle Miocene age (the *Coscinodiscus lewisianus* Zone). Of special interest was the presence in Sample 128-799B-33R-CC of common pine pollen. These occurrences suggest either a predominately pine source on

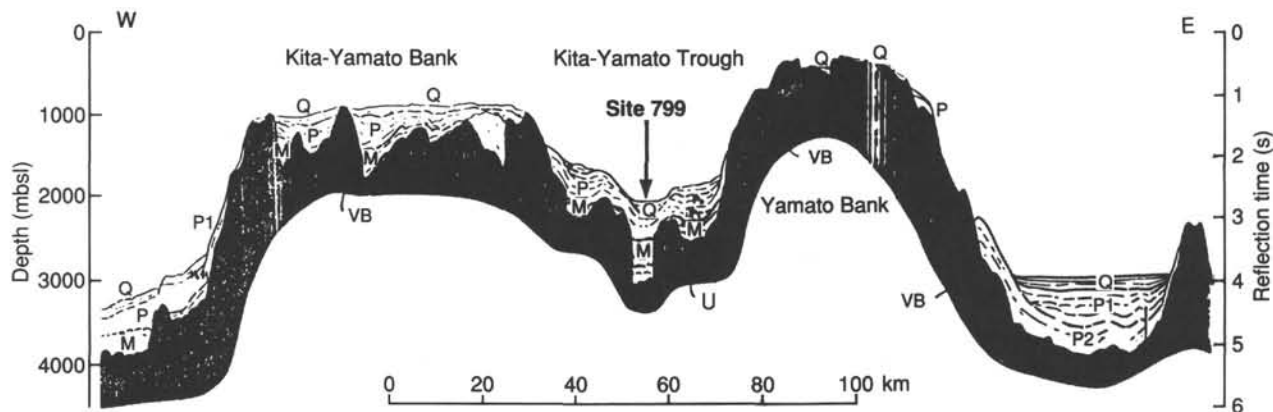


Figure 97. East-west cross section through the Kita-Yamato Trough, flanked by the Kita-Yamato and the Yamato Banks. Note the distinct graben structure at Site 799. Symbols are the same as in Figure 10.

Japan or Southeast Asia or that the Sea of Japan was broad at this time, perhaps as large as, or larger than, it is today.

Sample 128-799B-44-CC also contains diatoms, but no nearshore forms. Because of this, preservation is poor. *C. marginatus* is present as well as some poorly preserved specimens of *Cestodiscus*. The aspect of the assemblage, although partially dissolved, suggests an early Miocene age. The nearshore diatoms in Sample 128-799B-33R-CC probably came from the Kita-Yamato Bank, suggesting that this feature was emergent during at least part of the middle Miocene. Other than that, no paleoenvironmental inferences can be drawn from diatom occurrences in Hole 799B, except that these assemblages represent marine conditions.

Radiolarians

As in Hole 798A on the Oki Ridge, low species abundance and absence of index forms in Hole 799A make any attempt at zonation difficult. The occurrence of *Cycladophora davisiana* continues intermittently from the uppermost sample examined (128-799A-1H-CC) downward to Sample 128-799A-18H-CC (164.8 mbsf). In Sample 128-799A-13H-CC (116.5 mbsf), scattered occurrences of *Sphaeropyle langii* were observed; these probably signal the top of the *S. langii* Zone. If this datum is substantiated by later analysis, then the section above this level may be considered the *Cycladophora davisiana* Zone. In Sample 128-799A-46X-CC, well-preserved specimens of *Lychnocano manipponica*, *Stichocorys delmontensis*, *S. peregrina*, and *Anthocorys (?) akitaensis* were observed, and the occurrence of *Lychnocano nipponica* continues down to Sample 128-799A-49X-CC, whereas *Anthocorys (?) akitaensis* and *Stichocorys delmontensis* were recovered again in Sample 128-799A-51X-CC.

Finding these species below Core 128-799A-46X is significant for the following reasons:

1. Although geological occurrences of these taxa in the Sea of Japan coastal region of Honshu extend upward to the *Thecosphaera japonica* Zone (late late Miocene to early early Pliocene), they are generally observed in the *Lychnocano nipponica* Zone (late middle to early late Miocene) (Nakaseko and Sugano, 1973). Their occurrence in Hole 799A is thus compatible with the interpretation of shipboard paleomagnetic analyses.

2. A similar assemblage was reported from DSDP Site 302 (Ling, 1975), the only known such occurrence from submarine sediments of the Sea of Japan, and its age is considered within the "*Denticula* (= *Neodenticula*) *kamshatica*" (diatom) Zone of Koizumi (1975). The top of this diatom zone is defined by

the initial appearance of *Neodenticula koizumii*, which has been placed near the bottom of the Gauss Chron at 3.36 to 3.7 Ma (Koizumi, 1975; Koizumi and Tanimura, 1985), or between the "b" and "c" subchrons of Gilbert Chron, which has been estimated at 4.2 Ma in the northwestern Pacific (Barron, 1980). Therefore, these two occurrences can be considered as time-correlative.

3. Their occurrence suggests that some of the radiolarian species can survive the critical silica diagenetic transformation from the opal-A to opal-CT phases, based on the observation that the opal-A/opal-CT boundary for Hole 799A sediments is between Cores 128-799A-46X and 128-799A-48X (see "Lithostratigraphy" section, this chapter).

In general, poorly preserved and rare radiolarians were observed in 10 out of 65 core-catcher samples that were examined from Hole 799B, except Sample 128-799B-48R-CC (904.2 mbsf), which contained "Few" (see "Explanatory Notes" chapter, this volume) specimens (see Table 8). All specimens had been totally recrystallized, so that, in most cases, even their identification to a generic level was difficult. Nevertheless, some age-diagnostic species were observed in a few samples, and the oldest radiolarian assemblage of late early Miocene-early middle Miocene age was identified from the Sea of Japan sediments.

Cyrtocapsella tetrapera and other *Spongodiscus* sp. in Sample 128-799B-31R-CC (740.5 mbsf) were the oldest radiolarians that we were able to positively identify from this hole, indicating that this sample is most likely in the middle Miocene *Cyrtocapsella tetrapera* Zone, according to published data from the coastal regions of the western Honshu (Nakaseko and Sugano, 1973). Although a few specimens occur in samples of higher horizons (Samples 128-799B-5R-CC; 128-799B-7R-CC; 128-799B-9R-CC; 128-799-10R-CC; and 128-799B-27R-CC), they had been completely recrystallized so that identification was not possible. In Samples 128-799B-32R-CC and 128-799B-38R-CC, in addition to several specimens of *Cyrtocapsella tetrapera*, and *Spongodiscus* sp., spherical forms probably belonging to the genus *Thecosphaera* were observed. In Sample 128-799B-48R-C, although all radiolarians had been completely recrystallized, the occurrence of moderately well-preserved specimens of *Cyrtocapsella cornuta*, *C. tetrapera*, *Didymocyrtis mammifera*, *Lithopera renzae*, and *Spongodiscus* sp. were recognized. The recovery of *Didymocyrtis mammifera* and *Lithopera renzae* from this hole is significant because their occurrence suggests a late early Miocene to early middle Miocene age (Berggren et al., 1985; Sanfilippo et al., 1985). Furthermore, these radiolarians have

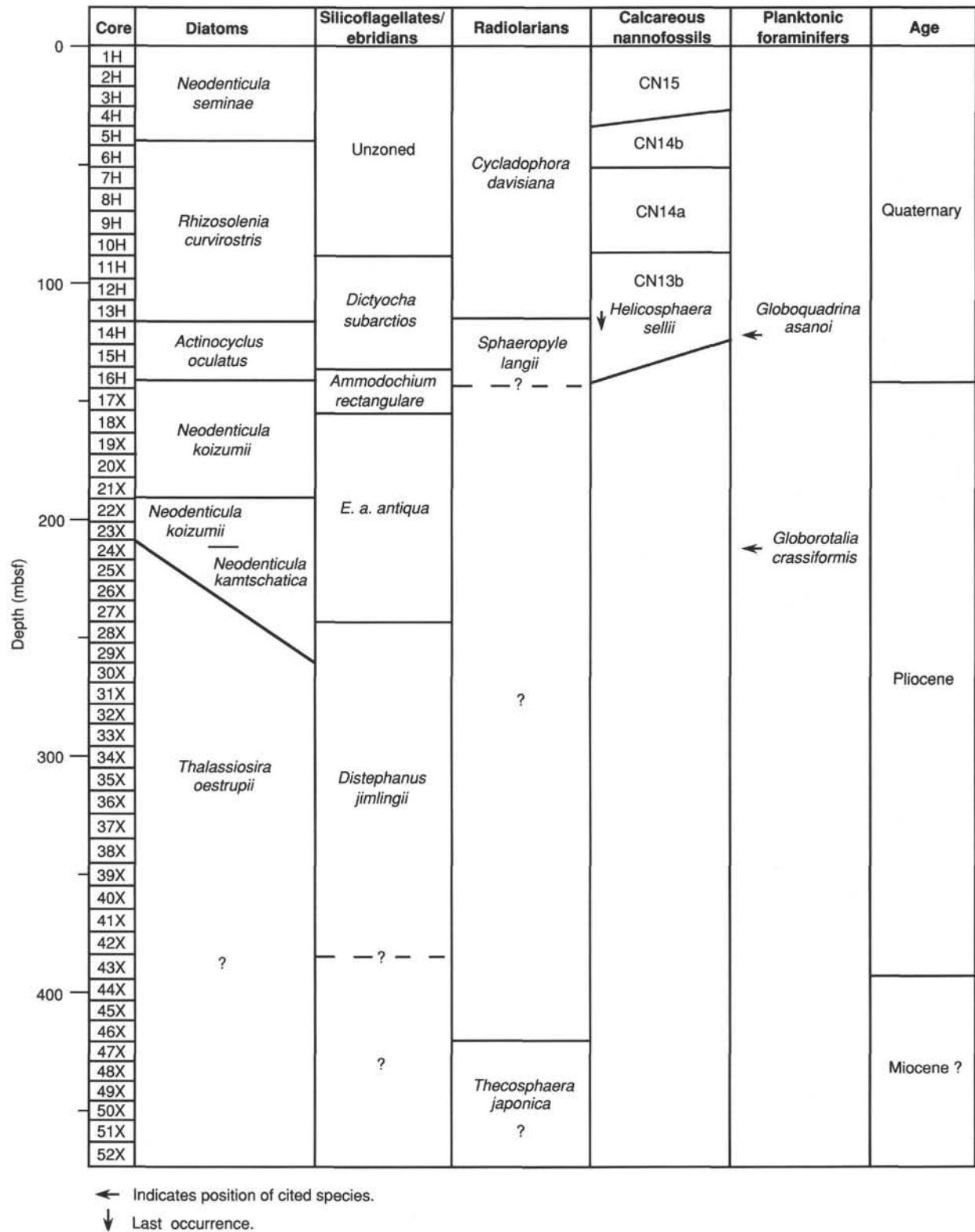


Figure 98. Summary of established zonations for all microfossil groups studied at Hole 799A. All samples represent core-catcher samples.

been reported thus far only from the middle- to low-latitude regions, thus suggesting warm-water conditions during this time.

Except for Sample 128-799B-50R-CC (923.3 mbsf), which contains specimens of *Spongodiscus*, radiolarians were completely absent below Sample 128-799B 49R-CC (913.6 mbsf) to the bottom of the hole (1084.0 mbsf; Section 128-799B-67R-CC).

Silicoflagellates and Ebridians

Silicoflagellates and ebridians were observed in most core-catcher samples examined from Hole 799A, but their abundance was generally less than at Site 798. Only rare specimens of *Dictyocha mandrai* were observed in Samples 128-799A-1H-CC and 128-799A-2H-CC, except for scattered *Distephanus slavnicci* in Sample 128-799A-8H-CC. For all practical purposes, the uppermost section down to Sample 128-798A-11H-CC (97.2 mbsf) may be considered barren of these microfossils. Surprisingly, *Distephanus octangulatus* was absent from this hole; thus, the uppermost section (97 m) has not been zoned. In Sample 128-799A-11H-2, 29 cm (89.29 mbsf), the joint occurrence of *Dictyocha subarctios* and *Mesocena elliptica* was recognized, suggesting that the top of the *Dictyocha subarctios* Zone is located between this sample and the next younger sample, 128-799A-11H-1, 115 cm (88.65 mbsf), which in turn indicates the proximity of the Brunhes/Matuyama chron boundary. The *Dictyocha subarctios* Zone extends downward to Sample 128-799A-15H-5, 121 cm (133.3 mbsf), and the Pliocene *Ammodoichium rectangulare* Zone was recognized by the appearance of the nominate taxon in Sample 128-799A-15H-CC (135.8 mbsf). We consider Sample 128-799A-17H-CC (155.2 mbsf) as the top of the *Ebriopsis antiqua antiqua* Zone because of the LAD of the nominate taxon. Based on biomarkers at Site 798, this zone occurs slightly above the Matuyama/Gauss chron boundary (ca. 2.48 Ma).

The next datum level recognized from Hole 799A was the highest occurrence of *Distephanus jimlingii*, which was observed in Sample 128-799A-28X-CC (250.9 mbsf). According to data from Site 798, this datum level was placed near the top of the Gauss Chron at ca. 2.6 Ma, which suggests an unusually high sedimentation rate toward the end of the Gauss Chron.

The *Distephanus jimlingii* Zone extends downward to at least Sample 128-799A-35X-CC (316.9 mbsf) and is characterized by the continuous presence of the nominate taxon. Rare occurrences of this species was noted in Samples 128-799A-40X-CC and 128-799A-42X-CC. According to a detailed investigation by Kobayashi (1988), the lower limit of this zone is defined by the initial appearance of *D. jimlingii*, which corresponds to the Miocene/Pliocene boundary in this region.

Although *Ammodoichium rectangulare* and *Ebriopsis antiqua* occur continuously down to Sample 128-799A-48X-CC (442.6 mbsf), no other age-diagnostic forms were observed in these samples, and this group of siliceous microfossils was absent down to the bottom of Hole 799A, Section 128-799A-52X-CC (468.7 mbsf).

Neither silicoflagellates nor ebridians were observed in core-catcher samples examined for Hole 799B.

Calcareous Nannofossils

Calcareous nannofossils are rare to abundant within the first 23 cores drilled from Hole 799A in the Kita-Yamato Trough. Quaternary nannofossil Zone CN15 through Subzone CN13b are defined within the first 15 cores. The remaining core-catcher samples, from Cores 128-799A-24X through 128-799A-52X at 468.7 mbsf, are barren of nannofossils. With few exceptions, descriptions of nannofossils from each core are from core-catcher samples only. In general, the calcareous

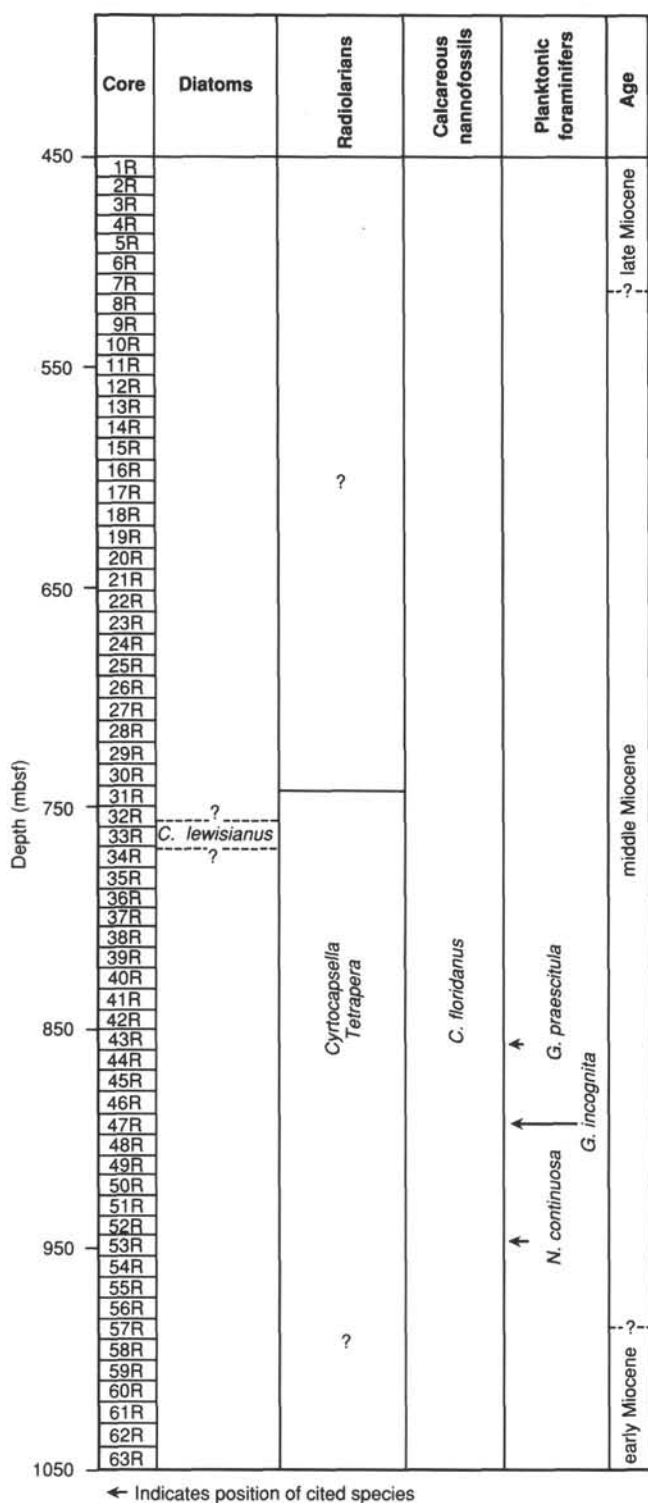


Figure 99. Summary of established zonations for all microfossil groups studied at Hole 799B. All samples represent core-catcher samples.

Table 7. Summary of all paleomagnetic and fossil datum levels for Site 799.

Core no.	Section, interval (cm)	Depth range (mbsf)	Diatoms	Silicoflagellates and ebridians	Radiolarians	Calcareous nannofossils	Planktonic foraminifers	Dextral <i>N. pachy.</i>	Sinistral <i>N. pachy.</i>	Paleomagnetics	Age (Ma)
1H		0–1.2						6	68		
2H		1.2–10.7						4	67		
3H		10.7–20.3						11	55		
4H		20.3–29.9						8	65		
5H-2	100	33.3–33.3	LAD <i>R. curvi.</i>								0.34
5H		29.9–39.5						7	68		
6H-4	10	45.6–45.6				LAD <i>P. lacunosa</i>					0.46
6H		39.5–49.1						5	82		
7H		49.1–58.7						12	65		
8H		59.7–68.3						4	43		
9H		68.3–77.9						20	71		
10H		77.9–87.5						5	69		
11H		89.5–89.5						2	16	B/M boundary	0.73
11H-2	29	90.7–90.7		LAD <i>D. subarcticus</i>							
11H		93.25–93.25								M/J boundary	0.91
11H		96.15–96.15								J/M boundary	0.98
12H		97.2–106.8						1	1		
13H		106.8–116.5			LAD <i>S. langlii</i>	LAD <i>H. sellii</i>		5	1		1.2
14H		123.45–123.45								M/O boundary	1.66
14H		116.5–126.1					CD10/11	32	4		
15H		133.05–133.05								O/M boundary	1.88
15H		126.1–135.8		LAD <i>A. rect.</i>				10	4		
17H		145.5–155.2		LAD <i>E. a. antiqua</i>							
19H	7	174–174								M/G boundary	2.47
21X		184.5–184.5								G/K boundary	2.92
22X		193.8–203.5	LAD <i>D. kamts.</i>								
25X		225.29–225.29								G/Gil. boundary	3.4
28X		247.1–250.9		LAD <i>D. jimlingii</i>							
31X		276.34–276.34								Gil/N boundary	4.12
33X		292.98–292.98								N/Gil. boundary	4.26
40X		362.29–362.29								Gil./S boundary	4.41
41X		367.17–367.17								S/Gil. boundary	4.49
41X		370–370								T/Gil. boundary	4.59
41X		365.3–375		FAD <i>D. jimlingii</i>							
42X		383.7–383.7									4.79
44X		394.61–394.61								Gil./S boundary	5.4
46X		414.51–414.51			LAD <i>A. akitaensis</i>						5.7
47X		424.36–424.36									5.78
47X		431.15–431.15									6.07
50X		454.21–454.41									6.42
51X		462.41–462.41									6.55

All samples represent core-catcher samples unless otherwise indicated. Age based on combined paleomagnetic and fossil data.

nannofossils recovered at this site have been poorly preserved and exhibit a high degree of etching and dissolution (Table 8).

Nannofossils in Samples 128-799A-1H-CC and 128-799A-2H-CC can be assigned tentatively to the latest Quaternary Zone CN15. Preservation within these samples is moderate, and abundances of species range from rare to abundant. Some of the dominant species in these samples include *Emiliana huxleyi*, *Gephyrocapsa oceanica*, *Helicosphaera carteri*, *Calcidiscus leptoporus*, and *Coccolithus streckerii*. Shore-based SEM analysis will be necessary to confirm the presence of *E. huxleyi*.

Because of the poor degree of preservation, calcareous nannofossils in Sample 128-799A-3H-CC can be assigned only to late Quaternary nannofossil Zones CN15 or CN14b. Within these first three cores, nannofossils exhibit moderate to intense dissolution. We had difficulty in consistently distinguishing *Emiliana huxleyi* from poorly preserved species of *Gephyrocapsa* and *Reticulofenestra*, which also are present within the first three cores.

Samples 128-799A-4H-CC and 128-799A-5H-CC have been tentatively assigned to Zone CN14b on the basis of the apparent absence of *E. huxleyi* and *Pseudoemiliana lacunosa*

and on stratigraphic position. Species that range in abundance from few to most abundant in these samples are *Gephyrocapsa sinuosa*, *G. aperta*, *G. oceanica*, *G. caribbeanica*, and *B. bigelowii*. Abundant small reticulofenestrids and gephyrocapsids, particularly, characterize the core-catcher sample from Core 128-799A-5H. Further analysis of these samples will be necessary to confirm the absence of *E. huxleyi*.

The LAD of *Pseudoemiliania lacunosa* defines the top of middle to early Quaternary Subzone CN14a and was found in Sample 128-799A-6H-4, 10 cm. Samples 128-798A-6H-4, 10 cm, through 128-799A-9H-CC may be placed within Subzone CN14a. Because the core-catcher samples from Cores 128-799A-6H and 128-799A-8H were barren of calcareous nannofossils, smear-slide Samples 128-799A-7H-1, 1 cm, and 128-799A-8H-7, 75 cm, were taken directly from the cut surfaces of the cores. These cores contain common-to-most abundant nannofossils, which generally reflects the same species diversity and types found up the section. Common-to-abundant species in this interval include *G. oceanica*, *G. sinuosa*, *G. aperta*, *C. streckerii*, and *C. pelagicus*. Species that are few to common within this interval are *P. lacunosa*, *G. caribbeanica*, *B. bigelowii*, *C. leptoporus*, and *Pontosphaera* sp.

The first occurrence of *G. oceanica* in Sample 128-799A-10H-CC may define the top of early Quaternary Subzone CN13b in this section. The base of this zone is impossible to distinguish because of the extremely poor preservation and sporadic occurrences of the carbonate fossils down the section. However, paleomagnetic data from this site may limit the depth to which this zone can extend; the lower Matuyama/Olduvai boundary was identified in Core 128-799A-15H. The last occurrence of *Helicosphaera sellii* at this site was observed in Sample 128-799A-13H-CC. The LAD of *H. sellii* defines the top of Gartner's (1977) early Quaternary *H. sellii* Zone and occurs within Subzone CN13b. Abundances of calcareous nannofossil in the core-catcher samples from Cores 128-799A-10H and 128-799A-12H are rare to common. In core-catcher samples from Cores 128-799-13H and 128-799A-15H, preservation is poor to moderate. In Sample 128-799A-11H-3, 38 cm, nannofossils are abundant and *B. bigelowii* is common. Core-catcher samples from Cores 128-799A-11H and 128-799A-14H are barren of nannofossils.

It is interesting to note that nannofossils from Samples 128-799A-13H-5, 96 cm, and 128-799A-14H-5, 66 cm, are almost monospecific assemblages of highly recrystallized *C. pelagicus*. Furthermore, these samples also contain a high percentage of carbonate debris that ranges in diameter from less than 1 to 15 μm . XRD results of a sample selected for carbonate analysis 4 cm up the section from Sample 128-799A-14H-5, 66 cm, show that the calcite-to-dolomite peak area ratio is approximately 1.5 (see "Lithostratigraphy" section, this chapter). We suspect that the calcium needed to produce the carbonate grains that dominate the nonbiogenous component of the samples came from *in-situ* dissolution of calcareous nannofossils at these horizons and subsequent recrystallization. *C. pelagicus*, one of the most dissolution-resistant calcareous nannofossils, is all that remains of an assemblage that most probably was as diverse as those found up the section within this hole.

Core-catcher samples from Cores 128-799A-15H through 128-799A-52X (bottom of Hole 799A) are barren of nannofossils, with the exception of rare, small, reticulofenestrid species in Core 128-799A-23X. However, within this bottom interval, smear slides were made from the split core surface, where carbonate preservation looked promising. Two samples were taken from Core 128-799A-15H, four samples from Core 128-799A-16H, seven samples from Core 128-799A-17H, two

samples from Core 128-799A-18H, one additional sample from Core 128-799A-22X-3, two samples from Core 128-799A-23X, and two samples from Core 128-799A-24X. All these samples were barren of calcareous nannofossils.

As part of their core description, the shipboard sedimentologists were alert for any visual indications of carbonate intervals within the core. If an interval seemed carbonate-bearing, a smear slide was made from the interval, and the percentages of nannofossils, foraminifers, and inorganic carbonate were tabulated by the sedimentologists. Using these descriptions, those samples containing nannofossils were described for biostratigraphic purposes from intervals having little biostratigraphic control. A short summary of these descriptions follows.

Sample 128-799A-39X, 5 cm: Rare-to-few poorly preserved *C. pelagicus* and unidentifiable nannofossils; age unknown.

Sample 128-799A-36X-4, 50 cm: Rare, poorly preserved, unidentifiable calcareous nannofossils of unknown age.

Sample 128-799A-21X-5, 134 cm: Common (in abundance), poorly preserved, four to five *Reticulofenestra* cf. *pseudoumbilica*, *C. pelagicus*, and small reticulofenestrids of unknown age.

Sample 128-799A-15H, 42 cm: Common (in abundance), poorly preserved, highly recrystallized *C. pelagicus* reminiscent of those in Sample 128-799A-14H-5, 96 cm (see description for this interval above); age unknown.

Samples 128-799A-13H-3, 21 cm, and 128-799A-13H-1, 52 cm: These samples were described in an effort to locate the last occurrence of *H. sellii* at this site. Although nannofossils are most abundant in Section 128-799A-13H-1, 52 cm, *H. sellii* is absent. Unfortunately, Section 128-799A-13H-3 at 21 cm is barren of nannofossils.

A drastic reduction with depth in nannofossil preservation down to the Pliocene/Pleistocene boundary was located within Core 128-799A-15H at this site.

Hole 799B was drilled to 450.0 mbsf and then was rotary-cored to a depth of 1084 mbsf. Only 0.22 m of sediment was recovered from the first four cores. Sample 128-799B-2R-1, 10 cm, contains abundant highly dissolved coccoliths that were impossible to identify. Two to three euhedral carbonate grains also are abundant in this sample. No sediment was recovered in Cores 128-799B-1R, 128-799B-3R, or 128-799B-4R.

Sample 128-799B-5R-1, 30 cm, contains common, moderately preserved *Reticulofenestra pseudoumbilica*, *Pontosphaera* sp., and large (10–14 μm) *Dictyococcites* sp. *R. pseudoumbilica* has a LAD at approximately 3.5 Ma (Haq and Takayama, 1984). Thus, Sample 128-799B-5R-1, 130 cm, is probably no younger than 3.5 Ma. Samples 128-799B-5R-CC and 128-799B-66R-CC are barren.

Samples 128-799B-7R-3, 113 cm, and 128-799B-7R-CC contain few-to-common *Reticulofenestra* sp. smaller than 6 μm in diameter, *Pontosphaera* sp. with only distal rims preserved, *C. pelagicus*, *Calcidiscus* sp., and *Dictyococcites* sp. The assemblages in both samples are highly dissolved and recrystallized.

Core-catcher samples from Cores 128-799B-8R through 128-799B-12R are barren of calcareous nannofossils. These samples also contain less than 5% carbonates. As discussed above, the clay-sized, anhedral, carbonate debris found throughout the entire cored sequence may be the remnants of calcareous nannofossils.

Core-catcher samples from Cores 128-799B-13R and 128-799B-14R contain scattered, highly dissolved, unidentifiable coccoliths. The intense degree of dissolution of these specimens makes them difficult to distinguish from sphenoliths. Observations of highly dissolved placoliths up the section and the "unidentifiable nannofossils" in these cores, as well as

Table 8. Summary of preservation and abundance of all microfossil groups for Site 799.

Core	Diatoms		Radiolarians		Silicoflagellates		Calcareous nannofossils		Planktonic foraminifers		Benthic foraminifers	
	Abundance	Preservation	Abundance	Preservation	Abundance	Preservation	Abundance	Preservation	Abundance	Preservation	Abundance	Preservation
128-798A-												
1H	C	M	R	M	F	M	R	M	C	G	R	M
2H	C	M	F	M	R	M	A	P	A	M-G	A	G
3H	C	M	R	M	B	M	R	P	C-A	G	R	P
4H	F	P	F	M	B	M	F	M	A	G	R	P
5H	F	P	F	M	R	P	A	M	A	G	A	M
6H	F	P	B	M	B	M	B	B	A	G	R	P
7H	F	P	R	M	B	M	C	P	A	G	R	P
8H	C	M-G	R	M	R	M	B	M	R	M	R	M
9H	C	M	R	M	R	M	A	P	A	M-G	R	P
10H	C	M	R	P	B	M	F	P	C-A	G	R	P
11H	F	M	B	M	B	M	B	M	R	M	R	P
12H	C	P	R	P	R	M	R	P	R	M	F	P
13H	C	P	R	M	R	M	F-C	P	R	M	R	P
14H	F	P	B	M	B	M	F	M	F	M	R	P
15H	F-C	P	R	M	R	M	F	P	F	M	R	P
16X	C	P	R	M	B	M	B	M	B	R	R	P
17X	C-A	P	R	M	R	M	B	M	R	M	R	M
18X	A	P	R	M	R	M	B	M	B	R	R	M
19X	A	P-M	F	M	R	M	B	M	R	R	R	M
20X	C-A	P	R	M	R	M	B	M	R	P-M	R	P
21X	A	P	R	M	R	M	B	M	B	R	R	P
22X	A	P-M	R	M	R	M	B	M	R	P	R	P
23X	C-A	P	R	M	R	M	R-F	P	R	P	R	P
24X	C	P	R	M	R	M	B	M	R	P	R	P
25X	C-A	P	R	M	R	M	B	M	B	R	R	P
26X												
27X	A	P-M	R	M	R	M	B	M	B	R	R	P
28X	A	M	R	M	R	M	B	M	R	P	R	P
29X	C-A	P-M	R	M	R	M	B	M	B	R	R	P
30X	F-C	P	R	M	F	M	B	M	B	R	R	P
31X	C	P	R	M	F	M	B	M	R	P	R	M
32X	C	P	R	M	F	M	B	M	B	R	R	P
33X	C	P	R	M	F	M	B	M	B	R	R	P
34X	C	P	R	M	F	M	B	M	B	R	R	P
35X	C	P-M	R	M	F	M	B	M	B	R	R	P
36X	C	P	B	M	R	M	B	M	B	R	R	P
37X	C-A	P	R	M	R	M	B	M	R-F	P	B	R
38X	C	P	R	M	R	M	B	M	B	R	R	M
39X	C	P	R	M	R	M	B	M	B	R	R	P
40X	C	P	R	M	F	M	B	M	R	P	R	P
41X	C	P	B	M	R	M	B	M	R	P	R	P
42X	F-C	P	R	M	R	M	B	M	R	P	R	P
43X	C	P	R	M	R	M	B	M	B	R	R	P
44X	F	P	B	M	R	M	B	M	R	P	R	P
45X	C	P	R	M	R	M	B	M	B	R	R	P
46X	C	P	R-F	M	R	M	B	M	R	P	R	P
47X	C	P	R	M	R	M	B	M	B	R	B	R
48X	C	P	R	M	R	M	B	M	B	R	B	R
49X	C	P	R	M	R	P	B	M	B	R	B	R
50X	B		B		B		B		B		R	P
51X	B		B		B		B		B		R	P
52X	B		B		B		B		B		R	B
128-799B-												
1R	N S		N S		N S		N S		N S		N S	
2R	R	P	N S		N S		A	P	N S		N S	
3R	N S		N S		N S		N S		N S		N S	
4R	N S		N S		N S		N S		N S		N S	
5R	B		R	M	B		C	M	B		B	
6R	B		B		B		B		B		B	
7R	B		R	M	B		C	P	R	P-M	C	P
8R	B		B		B		F	P	R	P	F	M
9R	B		R	P	B		B		R	P	F	P
10R	B		R	P	B		B		B		F	P
11R	B		B		B		B		R	P	R	P
12R	B		B		B		B		B		R	P
13R	B		B		B		R	P	B		R	P
14R	B		B		B		R	P	B		R	P
15R	B		B		B		B		R	P	R	P
16R	B		B		B		B		B		R	P
17R	B		B		B		B		B		R	P
18R	R	P	B		B		B		B		R	P
19R	B		B		B		B		B		R	B

Table 8 (continued).

Core	Diatoms		Radiolarians		Silicoflagellates		Calcareous nannofossils		Planktonic foraminifers		Benthic foraminifers	
	Abundance	Preservation	Abundance	Preservation	Abundance	Preservation	Abundance	Preservation	Abundance	Preservation	Abundance	Preservation
20R	B		B		B		B		B		R	P
21R	B		B		B		F	P	B		B	
22R	B		B		B		B		B		B	
23R	R	M	B		B		B		B		B	
24R	B		B		B		R-F	P	B		B	
25R	B		B		B		R	P	B		B	
26R	B		B		B		B		B		B	
27R	B		R	P	B		B		B		R	P
28R	B		B		B		R	P	B		B	
29R	B		B		B		B		B		R	P
30R	B		B		B		B		B		R	P
31R	B		R	P	B		B		R	P	B	
32R	B		R	P-M	B		B		R	P	B	
33R	R	P	B		B		B		B		B	
34R	B		B		B		B		B		B	
35R	B		B		B		B		B		B	
36R	B		B		B		B		B		B	
37R	B		B		B		B		B		B	
38R	B		R	P	B		B		B		B	
39R	B		B		B		B		B		R	P
40R	B		B		B		B		B		B	
41R	B		B		B		B		B		B	
42R	B		B		B		B		B		B	
43R	B		B		B		B		R	P-M	R	P
44R	R	P	B		B		B		R	P	R	P
45R	B		B		B		B		R	P	R	P
46R	B		B		B		B		B		B	
47R	B		B		B		B		B		B	
48R	B		F	M	B		B		B		R	P
49R	B		B		B		B		B		B	
50R	B		R	P	B		B		B		B	
51R	B		B		B		B		B		B	
52R	B		B		B		B		B		B	
53R	B		B		B		B		R	P	R	P
54R	B		B		B		B		B		B	
55R	B		B		B		B		R	P	R	P
56R	B		B		B		R	P	R	P	R	P
57R	B		B		B		B		R	P	B	
58R	B		B		B		B		B		B	
59R	B		B		B		B		B		B	
60R	B		B		B		B		B		B	
61R	R	P	B		B		B		R	P	R	P
62R	B		B		B		B		R	P	R	P
63R	B		B		B		B		R	P	B	
64R	B		B		B		R	P	B		R	P
65R	B		B		B		B		R	P	B	
66R	B		B		B		B		B		B	
67R	B		B		B		B		B		B	

All samples represent core-catcher samples. B = barren, R = rare, C = common, A = abundant; P = poor, M = moderate, G = good, N S = no sample.

those farther down the section, indicate that some placoliths may have crossed-polar interference figures characteristic of the sphenoliths when observed at 0°. However, upon rotation of this stage the characteristic interference figures at 45° were not observed. If these "unidentifiable nannofossils" are indeed sphenoliths, then the high degree of dissolution/recrystallization has altered them to the extent that they do not exhibit the characteristic crossed-polar figures at 45°. For this report, however, we think that these "unidentifiable nannofossils" are most probably highly dissolved placoliths, although the unlikely possibility that some of them might be sphenoliths has not been entirely ruled out. *Coccolithus pelagicus* is common in Sample 128-799B-14R-CC.

Core-catcher samples of Cores 128-799B-15R through 128-799B-20R are barren of calcareous nannofossils. However, Sample 128-799B-17R-3, 92 cm, contains scattered abundances of unidentifiable nannofossils. Furthermore, core-catcher samples from Cores 128-799B-16R and 128-799B-17R,

although barren of nannofossils, are composed of approximately 60% nannofossil-sized carbonate. This carbonate may be all that is left of a nannofossil- or foraminiferal-rich deposit that has been diagenetically altered.

Sample 128-799B-21R-CC contains few unidentifiable coccoliths. The core-catcher samples from Cores 128-799B-22R and 128-799B-23R are barren of nannofossils. Core 128-799B-24R-CC contains rare-to-few unidentifiable nannofossils. Unidentifiable nannofossils also are present in core-catcher samples from Core 128-799B-25R.

Core-catcher samples from Cores 128-799B-26R through 128-799B-28R and Core 128-799B-30R are barren of nannofossils. Rare abundances of poorly preserved unidentifiable coccoliths are present in core-catcher samples from Cores 128-799B-29R, 128-799B-31R, and 128-799B-32R.

All core-catcher samples from Cores 128-799B-33R through 128-799B-55R are barren of nannofossils. All the samples within this interval contain less than 10% nannofossil-

sized anhedral carbonate, with the exception of samples from the core-catcher samples of Cores 128-799B-39R and 128-799B-45R, which contain approximately 80% nanofossil-sized anhedral carbonate, and Cores 128-799B-51R and 128-799B-54R, which contain approximately 60% clay-sized anhedral carbonate.

The core-catcher sample from Core 128-799B-56R contains rare occurrences of poorly preserved *Cyclicargolithus* sp., *B. bigelowii*, *C. pelagicus*, and six-rayed discoasters reminiscent of *Discoaster deflandrea* and *Discoaster variabilis*. The presence of *Cyclicargolithus* within this core may restrict this sample to an age no younger than middle Miocene Subzone CN5a. However, additional shore-based study has shown evidence of reworked Mesozoic nanofossils in this core. Because no marker species have yet been identified in this sample and because stratigraphic control is nonexistent for this interval, even a broad estimate of the age of this sample would be unreliable at this time. This is unfortunate because the nanofossil assemblage within this core represents the lowest stratigraphic level that fossil genera have been identified in Leg 128 cores. We hope that additional shore-based study of this and other cores will yield additional information that will enhance the biostratigraphic resolution within this crucial lower interval.

Core-catcher samples from Cores 128-799B-57R through 128-799B-63R are barren of nanofossils. The carbonate content in these cores generally is less than 5%. Core-catcher samples from Core 128-799B-64R contain rare unidentifiable nanofossils. Core-catcher samples from Cores 128-799B-65R through 128-799B-67R are barren of nanofossils and contain less than 1% carbonate.

Throughout most of the cored sequence at Site 799, the sediments are composed of laminated sequences of lighter-colored carbonate laminae and darker siliceous claystone and porcellanite laminae (see "Lithostratigraphy" section, this chapter). We suspect that during the entire time represented in the cored sequence, marine conditions prevailed, coccolithophores flourished at this site within the Sea of Japan, and coccolithophores were deposited as a component of the sediment. However, in the layer of sediment where the most nanofossils accumulated, these were dissolved to provide a source of calcium for the dolomitic, lighter-colored laminae observed throughout most of the section.

Planktonic Foraminifers

The planktonic foraminiferal assemblages found in core-catcher samples from Hole 799A exhibit variable levels of preservation and abundance (Tables 7 and 8). Samples 128-799A-1H-CC through 128-799A-15H-CC contain rare-to-abundant planktonic foraminifers. Core-catcher Samples 128-799A-16H-CC through 128-799A-46X-CC contain rare, recrystallized specimens. Below this level, no planktonic foraminifers were observed. In general, preservation of planktonic foraminifers from this site ranges from poor to good. The scattered delicate forms (such as *Globigerinita uvula* and *Globigerina quinqueloba*) that occur commonly in the cool-temperate fauna of this region suggest dissolution. Further evidence for dissolution exists in the top four cores of this site, where sutures of some specimens have been deepened, creating impressions of sutural apertures similar to the genus *Globigerinoides*.

Foraminifer-rich sequences deposited by sediment gravity flows dominated Cores 128-799A-1H through 128-799A-15H. The mixing of fauna in these turbidite sequences was easily detected in some samples, especially in Sample 128-799A-4H-CC, where the planktonic foraminiferal assemblage includes two distinct groups of specimens that could be separated on

the basis of color; one group has a distinct yellow color, whereas the other *in-situ* group is white. Few age-diagnostic species occur at this site. Therefore, detection of reworking within the turbidites, based on the mixing of foraminifers of different ages, was impossible.

The ages of the core-catcher samples from Site 799 range from late Miocene through Pleistocene, based on diatom, nanofossil, silicoflagellate, and magnetostratigraphic data (Table 7). Few age-diagnostic planktonic foraminifers occur in those assemblages recovered. *Globoquadrina asanoi* (Sample 128-799A-14X-CC) and *Globorotalia crassaformis* (Sample 128-799A-24X-CC), which are important Quaternary markers according to Kennett and Srinivasan (1983), Lagoe and Thompson (1988), and Maiya, et al. (1976), were observed. However, these species did not occur in enough samples to allow us to recognize first or last appearance datums. The dominant species in these assemblages include *G. bulloides* (s.l.), *Globigerina quinqueloba*, *Globigerinita uvula*, and *Neogloboquadrina pachyderma*. This assemblage is typical of Pliocene and Pleistocene subarctic-to-cool temperate assemblages in the North Pacific. Some accessory species (other than the age-diagnostic forms mentioned above) are scattered in the core-catcher samples from Hole 799A. These include *Globigerinita glutinata*, *Globigerinoides ruber*, and *Neogloboquadrina dutertrei*. A number of rarer taxa were identified tentatively. These include *G. cf. asanoi*, *Globorotalia cf. puncticulata*, *N. cf. dutertrei*, *Neogloboquadrina cf. continua*, and *Neogloboquadrina cf. kagaensis*.

Previous analyses of changes in the coiling direction of *N. pachyderma* revealed Pliocene and Pleistocene trends, which permit correlation with well-calibrated datums in the North Pacific (Ingle, 1977; Ujiie and Ichikura, 1973; Lagoe and Thompson, 1988). Lagoe and Thompson (1988) established standard coiling direction (CD) intervals for *N. pachyderma*. Here, preliminary quantitative analysis (Fig. 100) allowed us to approximate the boundaries between the standard CD intervals, CD10 and CD11 at the base of Core 128-799A-14H, permitting the separation of early Pleistocene Zone N22 (Table 7). Unlike the Site 798 sequence, the CD8/CD9 boundary, which correlates with the Brunhes/Matuyama boundary, was not detected in Site 799. This probably results from mixing of faunas during downslope transport.

Changes in coiling directions of *Neogloboquadrina pachyderma* record fluctuations in surface temperature at Hole 799A (Fig. 100). The mixed dextral/sinistral and predominantly dextral intervals represent times when the Tsushima Current, a branch of the Kuroshio Current, had a stronger influence in the Sea of Japan. Based on our preliminary counts, the surface temperatures in the early Pleistocene were warmer than those in the later Pleistocene, suggesting connection of the Sea of Japan to the Pacific Ocean via the Tsushima Current. The presence of *Globigerinoides ruber* (Sample 128-799A-13H-CC), which is a tropical-to-warm subtropical taxon, serves as additional support for the increased influence of the Tsushima Current in the Sea of Japan in the early Pleistocene. Further recognition of the CD intervals of Lagoe and Thompson (1988) at this site will be possible after quantitative study of additional samples.

Rare, poorly preserved planktonic foraminifers occur in some of the core-catcher samples from Hole 799B. For the most part, samples from this hole are barren (Table 8). In general, the specimens found have been badly recrystallized and often flattened, making identification of specimens very difficult. In some samples, only fragments of specimens were found (Samples 128-799B-62R-CC and 128-799B-63R-CC). Although no specific signs of dissolution are evident in the specimens found, it is clear from observations of the unproc-

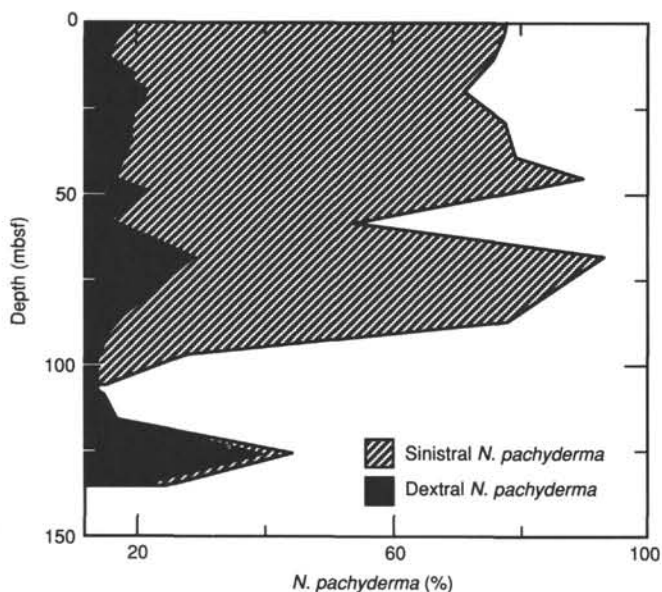


Figure 100. Data from Table 7 for dextral and sinistral *N. pachyderma* plotted on an area graph and showing the number of sinistral and dextral specimens in the analyzed core-catcher samples from Hole 799A.

essed core-catcher samples and cores that rocks from this hole included abundant assemblages of foraminifers before diagenesis. This is evident from the presence of abundant molds and casts of foraminifers and from the high amounts of diagenetic carbonate throughout the section in Hole 799B. Study of thin sections of these rocks perhaps may reveal more about the nature of the foraminiferal assemblages of this hole.

The age of samples from Hole 799B ranges from early to middle Miocene, based mainly on radiolarian assemblages. On the basis of species ranges in Kennett and Srinivasan (1983), the few age-diagnostic planktonic foraminifers observed in Hole 799B agree well with ages derived from radiolarians (Fig. 98). *Globorotalia incognita*, an early Miocene form, occurs in Sample 128-799B-47R-CC. *Globorotalia praescitula*, a late-early to early-middle Miocene species, was found in Samples 128-799B-43R-CC and 128-799B-44R-CC. *Neogloboquadrina continua*, which occurs throughout the Miocene, was found in Sample 128-799B-53R-CC. However, these species did not occur in enough samples to allow for recognition of first and last appearance datums. The species most often encountered in this hole are *Globigerina bulloides* s.l. and *Globigerina praebulloides*. Other species observed in Hole 799B include *Globigerina angustiumbilocata* (Sample 128-799B-56R-CC), *Globorotalia* cf. *archoemenardii* (Sample 128-799B-44R-CC), and *Neogloboquadrina* cf. *continua* (Sample 128-799B-61R-CC).

We find it difficult to remark on surface paleotemperature fluctuations in the Sea of Japan during the early to late Miocene on the basis of the rare, poorly preserved foraminiferal assemblages recovered at Hole 799B. However, the occurrences of *G. praescitula* and *G. cf. archoemenardii* (Samples 128-799B-43R-CC and 129-799B-44R-CC), which are temperate-to-warm subtropical species, provide evidence that during the middle Miocene, the Sea of Japan was connected to the Pacific Ocean via the Tsushima Strait or by other channels that allowed entrance of Kuroshio surface waters. We are not able to comment on the surface temperatures

during the early Miocene on the basis of the foraminiferal species identified here.

Benthic Foraminifers

In general, rare, poorly preserved benthic foraminifers are present throughout the section in Hole 799A (except for Samples 128-799A-37X-CC, 128-799A-47X-CC, 128-799A-48X-CC, 128-799A-49X-CC, and 128-799A-53X-CC). The faunal assemblages indicate upper-to-lower bathyal water depths, based on the interpretations of van Morkhoven et al. (1986). A few specimens of the neritic species *Quinqueloculina* sp. and *Triloculina* sp. are present in most samples from Sample 128-799A-2H-CC through Sample 128-799A-44X-CC. We assume that the occurrences of these taxa are the result of downslope contamination from shallower depths.

Sediments of Hole 799A may be subdivided into the following four intervals on the basis of the distribution of benthic foraminifers:

1. Interval 1 (Samples 128-799A-1H-CC through 128-799A-14H-CC, except Sample 128-799A-8H-CC): the main constituents in this interval are *Bolivina pacifica*, *Cassidulina norcrossi*, *C. norvangi*, *Stainforthia fusiformis*, and *Epistominella pulchella*. This fauna is similar to that found at Site 798 and represents upper-to-middle bathyal depths.

In three samples (128-799A-1H-CC, 128-799A-5H-CC, and 128-799A-9H-CC), an increase in relative abundance of *B. pacifica* (more than 40% of the population) was observed. Last occurrences of important elements of the "Tertiary-type" population (Matoba, 1984), *Epistominella pulchella*, *Valvulineria sadonica*, and *Oridorsalis umbonatus*, were observed in Samples 128-799A-4H-CC, 128-799A-8H-CC, and 128-799A-12H-CC, respectively.

2. Interval 2 (Sample 128-799A-8H-CC and the interval from Sample 128-799A-15H-CC through Sample 128-799A-21X-CC): the fauna in this interval is characterized by the dominance of *Miliammina echigoensis*, associated with fragments of *Martinottiella communis*. These species indicate deep (lower bathyal), stagnant bottom-water conditions. The stratigraphic range of *Miliammina echigoensis* is known to be limited to the Neogene of the Sea of Japan coast of northern Honshu, Japan (Matsunaga, 1963; Ikebe and Maiya, 1981; Matoba, 1984); therefore, its occurrence in Sample 128-799A-8H-CC (Quaternary) a result of reworking from older sediments.

3. Interval 3 (Samples 128-799A-22X-CC through 128-799A-32X-CC): although foraminiferal specimens are rare, this interval is characterized by the occurrence of calcareous forms, such as *Melonis pompilioides*, *Gyroidina* sp. A, and *Uvigerina* sp.; however, no agglutinated forms were observed. This fauna represents deposition in middle bathyal depths.

4. Interval 4 (Samples 128-799A-33X-CC through 128-799A-51X-CC): *Martinottiella communis* is predominant in this interval and is associated with a few specimens of *Globobulimina affinis*. In Sample 128-799A-50X-CC, two specimens of *Cyclammina cancellata* were observed. This fauna may represent lower bathyal water depths, based on the presence of both *M. communis* and *C. cancellata*.

In general, benthic foraminifer assemblages in Hole 799B are low in abundance. Rare, poorly preserved benthic foraminifers were observed in Samples 128-799B-7R-CC through 128-799B-20R-CC (except Sample 129-799B-19R-CC, which is barren), but these were absent or extremely rare in the rest of the samples. Even in these foraminifer-bearing samples, fragmentation and recrystallization of the foraminiferal tests are common throughout the core.

Cassidulina sp. is predominant in Samples 128-799B-7R-CC through 128-799B-9R-CC. The fauna from Samples 128-799B-10R-CC to 128-799B-20R-CC are characterized by the predominance of agglutinated forms, such as *Cribrostomoides* cf. *crassimargo*, *Cyclammina cancellata*, and *Martinottiella communis*. A few specimens of *C.* cf. *crassimargo*, *M. communis*, (?)*Uvigerina* sp., and (?)*Epistominella* sp. were observed in several samples between Samples 128-799B-21R-CC and 128-799B-64R-CC. These species indicate middle-to-lower bathyal depths.

A neritic-to-uppermost bathyal species, *Cassidulinoides* sp., was observed in Samples 128-799B-45R-CC and 128-799B-53R-CC, and one specimen of a neritic species, *Quinqueloculina* sp., was recognized in Sample 128-799B-61R-CC. The presence of these species suggests deposition in shallower depths in the basal part of the hole or redeposition of these species into deeper water.

Paleoenvironment

Microfossil data from the Kita-Yamato Trough are summarized in Figures 98 and 99. The chronology of the events depicted in these illustrations is constrained by microfossil and paleomagnetic datums and by ages extrapolated from a diagram of the sedimentation rates for this site (see "Sedimentation Rates" section, this chapter).

Poorly preserved, early to middle Miocene microfossil assemblages in Hole 799B indicate warm surface-water temperatures for the Sea of Japan during that time (Fig. 98). Radiolarian assemblages found in Samples 128-799B-31R-CC, 128-799B-32R-CC, and 128-799B-48R-CC were presently found only in lower latitude regions and, therefore, suggest connection of the Sea of Japan to the Pacific Ocean via the Tsushima Strait or other openings that allowed warmer northward-flowing water to enter that sea. Planktonic foraminifers in Samples 128-799B-43R-CC and 128-799B-44R-CC include temperate-to-warm subtropical globorotalids that support the flow of Kuroshio waters into the Sea of Japan during the middle Miocene. The connection of the Sea of Japan with the Pacific Ocean during middle Miocene time via deeper sills may be related to both local tectonic and global eustatic changes.

Early to middle Miocene, neritic and upper bathyal benthic foraminifers and diatoms in Hole 799B reflect downslope transport in the Kita-Yamato Trough. In general, the *in-situ* benthic foraminifers suggest a lower-to-middle bathyal depth (1500–2000 m) for the trough at this time. The presence of specimens of *Cassidulinoides* sp. (128-799B-45R-CC and 128-799B-53R-CC) and *Quinqueloculina* sp. (128-799B-61R-CC) reflects redeposition from the adjacent shallow bank tops of the Yamato Rise. Occurrence of nearshore diatoms in Sample 128-799B-33R-CC serves as additional support for sediment reworking in Hole 799B.

Upper Miocene sediments in Hole 799A contain a lower bathyal benthic foraminiferal assemblage indicative of water depths of 2000 m or possibly deeper. These same sediments contain low abundances of freshwater diatoms (Sample 128-799A-50R-CC) in a predominantly marine flora that includes both benthic and pelagic forms. The presence of the clearly redeposited freshwater and common benthic diatom taxa suggest temporal or spatial proximity to a terrestrial environment. Significantly, geochemical data from Core 128-799A-51X indicate water of lower chlorinity just below this horizon (see "Inorganic Geochemistry" section, this chapter). These data, together with earlier reports of questionable upper Miocene freshwater diatomaceous sediment on the flank of Kita-Yamato Bank (Burckle and Akiba, 1978; Barash, 1986), point to the possibility that portions of the Yamato Rise were

emergent during the late Miocene and a lake and/or river existed on one of the islands.

Late Miocene to early Pliocene paleoceanographic conditions in the Yamato Rise area are indicated by radiolarians in Sample 128-799A-46X-CC. These sediments contain a warm-to-temperate radiolarian assemblage within the *Thecosphaera japonica* Zone, which suggests the influence of the relatively warm-water Tsushima Current at Site 799. These conditions, in turn, call for a late Miocene gateway between the open Pacific and the Sea of Japan, permitting the entrance of warm Kuroshio water into the back-arc sea during this time.

In contrast to latest Miocene/earliest Pliocene radiolarians, diatom assemblages in Hole 799A indicate cooler surface-water temperatures and little or no influence of warm Tsushima water. Of special interest are the Miocene/Pliocene sediments in Samples 128-799A-50X-CC through 128-799A-22X-CC, which contain nearly monospecific diatom assemblages dominated by *Coscinodiscus marginatus*. Pliocene indications of cooler surface-water temperatures at Site 799 suggest closure of the proto-Tsushima Strait or other southern gateways in the Sea of Japan, beginning in latest Miocene to early Pliocene time. Severance of the connection probably involved tectonic uplift in the southern area of the sea. Later, global paleoclimatic events involving the onset of intense Northern Hemisphere glaciation at 2.47 Ma initiated a period of increasingly frequent and higher-amplitude eustatic events that periodically isolated the Sea of Japan, with most, if not all, surface water entering from the north and an Oyashio Current source.

Warmer Pleistocene climatic events, including the interval of the Pliocene/Pleistocene boundary, apparently saw increased introduction of warm Tsushima water, as marked by more diverse (and warm) diatom assemblages and dextral-coiling populations of the planktonic foraminifer *Neogloboquadrina pachyderma* in Samples 128-799A-15H-CC through 128-799A-13H-CC. In contrast, late Pleistocene planktonic foraminiferal assemblages are dominated by sinistral *N. pachyderma* specimens indicative of arctic and/or subarctic surface-water temperatures and an exclusively Oyashio Current or local origin for surface water in the Sea of Japan.

Benthic foraminifers in Hole 799A provide information about water depths and redeposition of sediments in the Kita-Yamato Trough from late Miocene through Holocene time. Displaced shallow-water species, including neritic forms of *Triloculina* and *Quinqueloculina*, are scattered in Samples 128-799A-2H-CC through 128-799A-44X-CC, which clearly indicates shallow water depths on the adjacent bank tops of the Yamato Rise during Pliocene and Pleistocene time. Lower bathyal benthic biofacies dominate *in-situ* late Miocene through early Pliocene samples (128-799A-50X-CC to 128-799A-33X-CC), whereas uppermost Pliocene through Quaternary sediments contain exclusively middle and upper bathyal assemblages. These trends suggest that the Kita-Yamato Trough may have been uplifted in middle or late Pliocene time.

PALEOMAGNETISM

Introduction

All polarity transitions at magnetochron boundaries within the Pleistocene, Pliocene, and perhaps the uppermost Miocene were recognized at Site 799. Determining polarity transitions was difficult in the Pleistocene section because of major slump features that vary in thickness from 30 cm to 20 m. These features are particularly characteristic of Cores 128-799A-2H through 128-799A-15H. Further difficulty in determining polarity transitions was encountered in the XCB

cores as a result of drilling disturbances and weak magnetization. The difficulties encountered were unfortunate in light of the fact that high sedimentation rates at this site were promising for high-resolution magnetic stratigraphy. Correlating distinct magnetic signals with different sedimentary structures, such as slump and turbidite deposits, must be resolved. Post-cruise demagnetization experiments initiated on board the *JOIDES Resolution* will permit further definition of the geomagnetic polarity pattern in Hole 799A.

In Hole 799B, the direction of the paleomagnetic field has been recorded in the sparse layers of porcellanite, dolomites, and coarse-grained sandstones only, but is overprinted by one or two components within the siliceous clays. Shipboard investigations conducted on these sediments were limited by insufficient equipment and time. Shore-based investigations must resolve the problems that involved the multicomponent magnetization of Hole 799B sediments.

Experimental Procedures

Natural remanent magnetizations (NRM) and remanence after demagnetization were measured with the 2-G Enterprises passthrough cryogenic magnetometer (see "Explanatory Notes" chapter, this volume). The archive halves of APC cores were measured at intervals of 10 cm and were demagnetized with peak fields of 10 and 15 mT. One discrete cube (7 cm³ in volume) was taken from each undisturbed section of every XCB core and then demagnetized with peak fields of 2, 5, 10, 15, and 20 mT, respectively. Cores 128-799B-5H to 128-799B-20H were oriented with the multishot camera, but results cannot be considered absolute because correction of the declination data yielded both reliable and unreliable directions. Furthermore, abnormal values caused by field disturbances around void spaces, highly disturbed intervals, and section edges were noticed on a measuring log and then deleted from the data file, following the criteria used in Site 798 (see "Paleomagnetism" section, "Site 798" chapter, this volume). After this processing, declination, inclination, and intensity values were plotted vs. depth (Figs. 101 and 102) to compare the paleomagnetic record of Hole 799A with the geomagnetic time scale (Berggren et al., 1985).

Cores 128-799B-5R to 128-799B-67R were only slightly disturbed during drilling and splitting. Consequently, the measurements and demagnetization experiments with peak fields at 5, 10, and 15 mT were conducted with the passthrough cryogenic magnetometer. In addition, discrete cube samples (7 cm³ in volume) and minicores (12 cm³ in volume) were taken from each section of every core and from each separate lithology. Pilot discrete samples were measured with the Minispin and then demagnetized at sometimes up to 90 mT with the Schoenstedt AF demagnetizer. Thermal demagnetization up to 620°C was performed for a group of seven samples using the Schoenstedt thermal demagnetizer and the discrete sample device of the cryogenic magnetometer. The declination, inclination, and intensity values of NRM and remanence after demagnetization with 10 mT were plotted vs. depth, but declination values reflect only the rotation of the core during rotary drilling (Fig. 103).

Results

The highest NRM intensity value (25 mA/m) was measured in Core 128-799A-3H (14 mbsf). In general, the intensities decrease with depth and range on the order of 0.1 mA/m down to 75 mbsf and on the order of 10⁻¹ mA/m down to the bottom of the hole (Figs. 101 and 102). NRM intensities lower than 0.1 mA/m were rarely observed in Cores 128-799A-15H to 128-799A-20H. However, low intensities were easily recorded after the 10 and 15 mT demagnetization steps, but the related

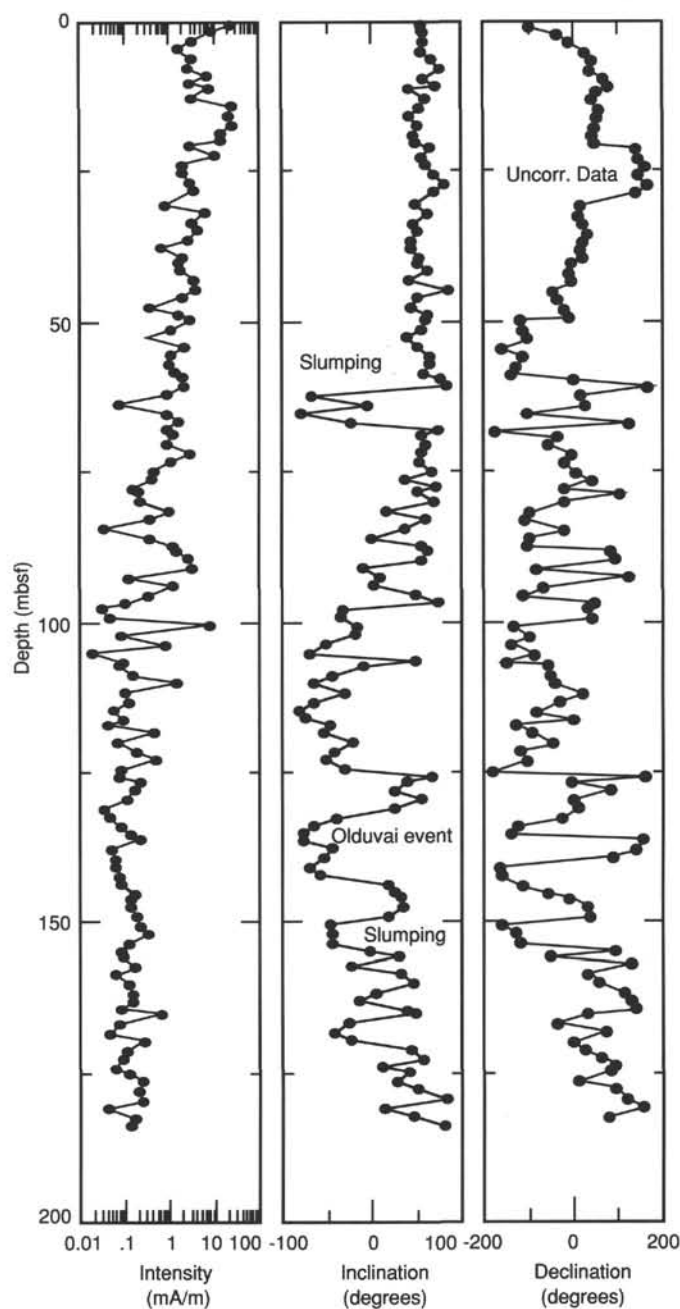


Figure 101. Intensity, inclination, and declination vs. depth of Cores 128-799A-1H to 128-799A-20H after 15 mT demagnetization. The intensity decreases with depth. Some of the polarity changes correlate with slump structures.

dispersion of the remanence directions reflects insufficient sensitivity of the magnetometer, rather than instability of the carriers of remanence. Consequently, demagnetization leads to less scattering of remanences if NRM intensities are high (Fig. 104) and to unreliable directions if the NRM intensity is near the resolution of the instrument (Fig. 105). Therefore, directions after 15-mT-peak field demagnetization between 0 and 160 mbsf are reliable, but the stability of remanences below 160 mbsf should be discussed by means of Zijdeveld diagrams.

The most remarkable features in the paleomagnetic record in the sediment column of Hole 799A are deviations of declination and inclination, which cannot be explained as

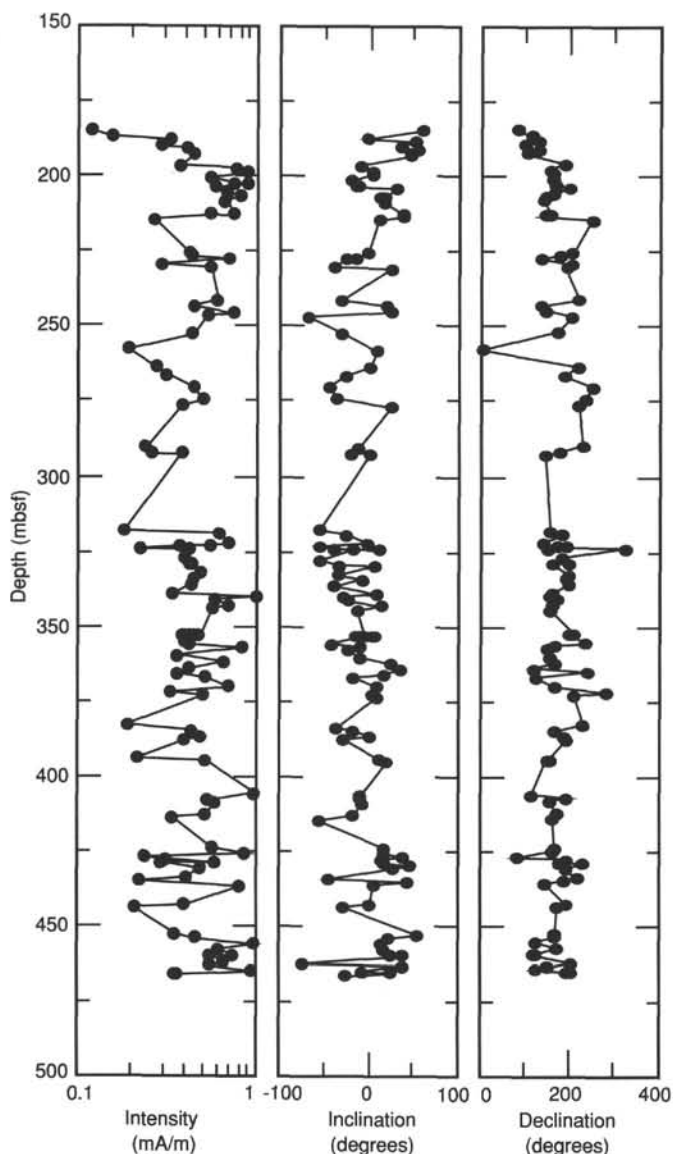


Figure 102. Intensity, inclination, and declination vs. depth of Cores 128-799A-21X to 128-799A-51X. The plot shows NRM.

abnormal behavior of the magnetic minerals or by polarity changes of Earth's magnetic field, because the polarity pattern is well established. Limited deviation of the declination of Cores 128-799A-4H and 128-799A-7H can be explained easily by an inaccurate multishot camera correction. In addition, Core 128-799A-8H shows two intervals with reversed polarity between 62 and 63 mbsf and between 65 and 68 mbsf, respectively (Fig. 101). These intervals do not correspond to the geomagnetic time scale (Berggren et al., 1985), but may be a result of the slump structures that were observed by the sedimentologists between 40 and 70 mbsf (see "Lithostratigraphy" section, this chapter).

A major deviation from the well-known polarity pattern was observed in Cores 128-799A-16H and 128-799A-17H between 142.2 and 151.2 mbsf (Fig. 101). Because of the position of this interval within the sediment column, this deviation might easily be interpreted as the Olduvai event. However, the shipboard sedimentologists reported slumping structures in this same interval (see "Lithostratigraphy, this chapter"); hence, this interval has been excluded from further

magnetostratigraphical considerations. Similar slump features of smaller scale also mask the polarity pattern between 80 and 180 mbsf. Future investigations may determine whether these are also correlated with sediment structures or sediment types.

Despite the presence of slumping disturbance, the polarity transitions at the magnetochron boundaries were recognizable in Hole 799A (Fig. 106). The Brunhes/Matuyama boundary is present at 89.85 mbsf, and the upper and lower boundary of the Jaramillo event occur at 93.25 and 96.15 mbsf, respectively. The Olduvai event occurs between 123.45 and 133.05 mbsf and the Matuyama/Gauss boundary is represented by the polarity transition at 173.55 mbsf.

The stability of the normal polarities is well supported by demagnetization experiments (Fig. 107). The reversed polarities within the Gauss epoch are stable only at 196.42 mbsf (Fig. 108), and can be referred to the Kaena event. The polarity transition at 225.29 mbsf indicates the Gauss/Gilbert boundary.

As a result of the sparse number of samples and the weak magnetizations below the Gauss/Gilbert boundary, all paleomagnetic data concerning this part of Hole 799A should be considered with skepticism. Nevertheless, reversed polarity, as indicated by the Zijderveld diagrams (Fig. 109; 229.78, 254.43, 340.18, 367.17, and 388.19 mbsf) prevails down to Core 128-799A-44H (394.61 mbsf). This interval was interrupted by normal polarities of moderate stability at 276.34 mbsf, which may represent the Nunivak event and at 362.2 mbsf, which might be correlated to one of the remaining three normal events of the Gilbert Chron (Fig. 110). Farther down the hole, stable normal polarity predominates (Fig. 111; 409.12, 431.15, and 460.20 mbsf).

Sedimentation rates may be calculated from depth and age of the polarity transitions. Paleomagnetic data yield values of 125 m/m.y. for the Brunhes Chron and 65 m/m.y. for the Matuyama, Gauss, and Gilbert chrons (Fig. 112).

In Hole 799B (Fig. 103), intensities range on the order of 10^{-1} mA/m. Intensities on the order of 1 and 10^{-1} mA/m are sparse; the highest value (4.2 mA/m) was measured in Core 128-799B-35R (770.05 mbsf) and can be related to a higher content of volcanic material in the sediments of this interval (see "Lithostratigraphy" section, this chapter). The lowest value occurs in Core 128-799B-33R (750.75 mbsf). Positive inclination values dominate down the hole. Some of the sparse negative inclination values disappear after the 10-mT-peak field demagnetization. For example, demagnetization converts the interval between 610 and 665 mbsf to positive inclination values (Figs. 103A and 103B). Despite the considerably stable inclination angles, an interpretation based on normal polarity of Earth's magnetic field during or shortly after deposition does not agree with the polarity time scale, which shows mixed polarity for the lower and middle Miocene. Furthermore, this positive inclination is restricted to the siliceous clays. The thin layers of porcellanite, dolomite, and sandstones in the clay yield stable positive and negative directions. These observations led us to infer that the siliceous clays have been remagnetized and that the thin porcellanite, dolomite, and sandstone layers might have conserved the original paleofield directions.

Intensive demagnetization experiments were initiated aboard the ship to examine the overprint and to determine the paleofield direction within the siliceous clays. Zijderveld diagrams and intensity plots show the typical behavior of these siliceous clays during AF-demagnetization (Fig. 113). The intensity decreases rapidly with mean destructive field (MDF) values that range between 7 and 11 mT, perhaps indicating magnetite in a multidomain configuration as the

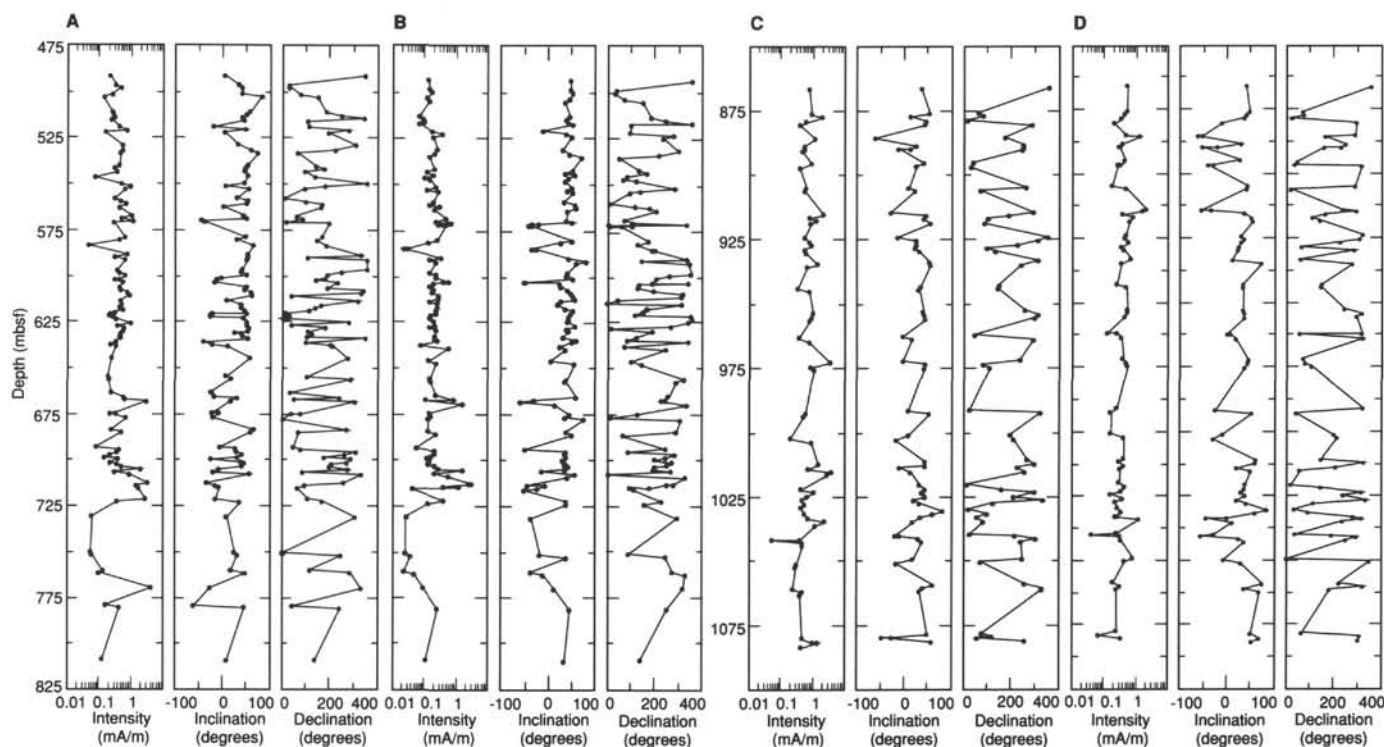


Figure 103. Inclination, declination, and intensity vs. depth of Cores 128-799B-5R to 128-799B-39R (A) before and (B) after 10 mT demagnetization and of Cores 128-799B-45R to 128-799B-67R (C) before and (D) after 10 mT demagnetization. The reversals between 610 and 665 mbsf were not observed after demagnetization.

carrier of the remanence. The direction of the remanence remains stable after the destruction of a weak component, which points down (Fig. 113A) or up the hole (Figs. 113B and 113C) and can easily be recognized as drilling remanence. In contrast, the declination and inclination do not point to the origin of the system (Fig. 113C), indicating that the demagnetization fields applied were not sufficient to determine a third, yet unknown, component that perhaps represents the paleo-field direction.

A stable negative inclination parallel to a reversed paleo-field direction was reported only from Samples 128-799B-35R-1, 155 cm (771.05 mbsf) and 128-799B-62R-4, 105 cm (1035.05 mbsf). This indicates that the remagnetization of the siliceous clays took place during a time of dominant normal polarity.

The porcellanite and dolomite samples remained stable during the AF demagnetization of the archive halves (Figs. 114A and 114B), but the intensity of a corresponding discrete sample decreased only slightly during thermal demagnetization up to 300°C (Fig. 114C). This might indicate the presence of hematite and additional hydrohematite or pyrrhotite. The intensity increase at 350°C may have been caused by the dehydration of hydrohematite and at higher temperatures, by the transformation of hematite to magnetite.

The resolution of the shipboard cryogenic magnetometer was excellent during long core measurements because of the high volume of the archive halves. Unfortunately, the demagnetization coils within this instrument cannot exceed peak fields of >20 mT, which were insufficient to demagnetize the siliceous clays of Hole 799B. On the other hand, sufficient peak fields can easily be produced with the Schoenstedt AF demagnetizer, but the resolution of the Minispin and the cryogenic magnetometer were insufficient for measuring the low intensities observed during the demagnetization of cubes or minicores of 7 or 12 cm³ in volume. Therefore, to isolate the original remanence by cleaning up the secondary magnetization of siliceous clay samples, further AF demagnetization at

higher peak fields and thermal demagnetization must be conducted in shore-based laboratories.

SEDIMENT ACCUMULATION RATES

Estimates of sedimentation rates for Site 799 are based upon magnetic reversal stratigraphy and selected biostratigraphic datum levels. These data include nine magnetic reversals and three microfossil datum levels (Table 9). Although no radiolarian or foraminiferal datum levels were used in this section, these groups still were useful for verifying the stratigraphy. Microfossil datum levels were used only minimally because of uncertainties in their application and because many of them have not been directly tied to an absolute age chronology. Sedimentation rates for 12 intervals were calculated from the age vs. depth relationship (Table 7; Fig. 115). In addition, we calculated the sediment accumulation rate (g/cm²/k.y.) using the averaged dry-bulk density for each interval (see "Physical Properties" section, this chapter). The accumulation rates tend to agree well with sedimentation rates, but differences between the two values increase with depth, probably from increased compaction.

Sedimentation rates for Hole 799A range from as low as 15 m/m.y. to much more than 175 m/m.y., with an average rate of approximately 70 m/m.y. Rates tend to be anomalously high when datum levels are far apart and anomalously low when they are close together. Several possible sources of error (or uncertainty) exist when constructing these curves. One is dictated by the fact that when defining microfossil datum levels, we generally examined only core-catcher samples. These were usually about 9 to 10 m apart. Another source of error deals with the age assignments given to microfossil datum levels. In general, these are based upon sedimentation rates from a known absolute age datum (usually a magnetic reversal). Such data assume a constant sedimentation rate, which is almost never the case. A third source of error involves uncertainty when identifying specific magnetic rever-

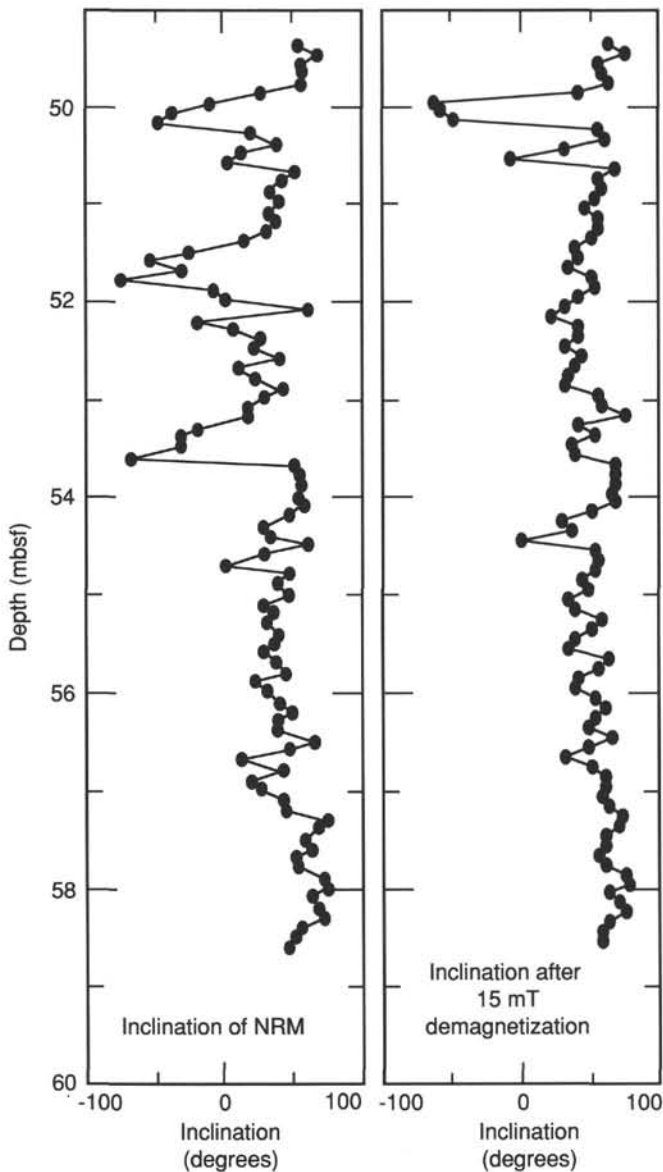


Figure 104. Plot of inclination vs. depth of Core 128-799A-7H before and after demagnetization. The dispersion is minimized after 15 mT demagnetization. The negative inclination at 50 mbsf is related to a slump structure.

sals. This was particularly true for the reversals in the Gilbert Chron. To obviate this uncertainty, we simply calculated a sedimentation rate for the entire Gilbert Chron.

Given the above reservations, we noted higher rates in Hole 799A in the Quaternary (particularly the late Quaternary) and rates nearer or below the overall average in the Pliocene. Sedimentation rates for the late Quaternary (which includes relatively high amounts of volcanic ash) are in excess of 100 m/m.y. These rates are partly a function of mass wasting off the surrounding high ridges of Yamato, Kita-Yamato, and Takuyo banks. Rates in the early Pleistocene and late Neogene are much lower, but more variable, possibly because of compaction, diagenesis, and differences in the relative influx of biogenic and nonbiogenic detritus. Sedimentation rates for Hole 799B were not calculated for obvious reasons. Because of overprinting, no magnetic reversal stratigraphy was avail-

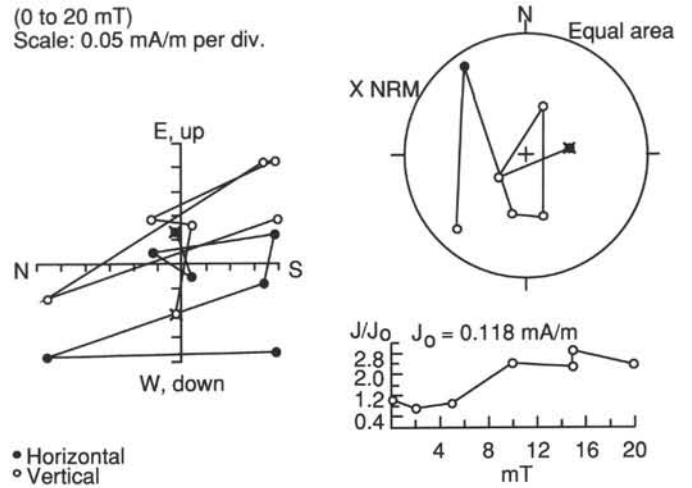


Figure 105. Zijderveld plot (left), equal area projection (top left), and intensity plot (right, down) of the demagnetization of Sample 128-799A-21X, 47 cm. The behavior of the remanence is unstable.

able for this hole and because of extreme dissolution, no continuous biostratigraphic record was available.

INORGANIC GEOCHEMISTRY

This section summarizes the results of shipboard analyses of dissolved constituents in the interstitial water of sediments recovered from Site 799 in the Kita-Yamato Trough, Sea of Japan. Based on the concentration gradients of these interstitial waters, this site can be divided into four intervals. Interval I (0–44 mbsf): interstitial-water chemical composition is influenced by early diagenetic processes that involve decrease in pH, increase in alkalinity, manganese, and removal of lithium, and phosphate mobilization within the zone of intense sulfate reduction. Interval II (44–220 mbsf) is dominated by organic matter decomposition and biogenic carbonate recrystallization reactions. Interval III (220–436 mbsf) is influenced by biogenic silica dissolution, dolomitization, and shows some evidence for crystallization of clay minerals. Interval IV (436–600 mbsf) is characterized by a sink for silica, hydrogen ion, and magnesium, a source for calcium, and variable concentrations of chlorinity, salinity, and strontium. The geochemical character of Interval IV suggests the influence of at least two different fluid sources.

Handling of Samples and Analytical Techniques

A total of 49 interstitial-water samples from 31 cores were collected at Site 799. Of the 31 cores sampled, 16 were sampled at adjacent intervals in Hole 799A. Interstitial waters from adjacent intervals were removed by standard ODP stainless-steel squeezing techniques (Manheim and Sayles, 1974) and by the newly developed Teflon-lined squeezer (Brumsack et al., unpubl. data, 1989), intended for extraction of interstitial waters for analyses of trace metals. All intervals sampled in Hole 799B were squeezed using the standard ODP stainless-steel squeezer. Shipboard analyses were performed using the procedures described by Gieskes and Peretsman (1986). Intervals squeezed by the stainless-steel and Teflon-lined squeezers and the results of shipboard analyses are presented in Table 10. The interstitial waters for adjacent intervals squeezed using both the stainless-steel and Teflon-lined tools generally exhibit good agreement for major dissolved ions. Dissolved manganese concentrations are lower in the Teflon tool squeezed water. Alkalinity and pH are repeat-

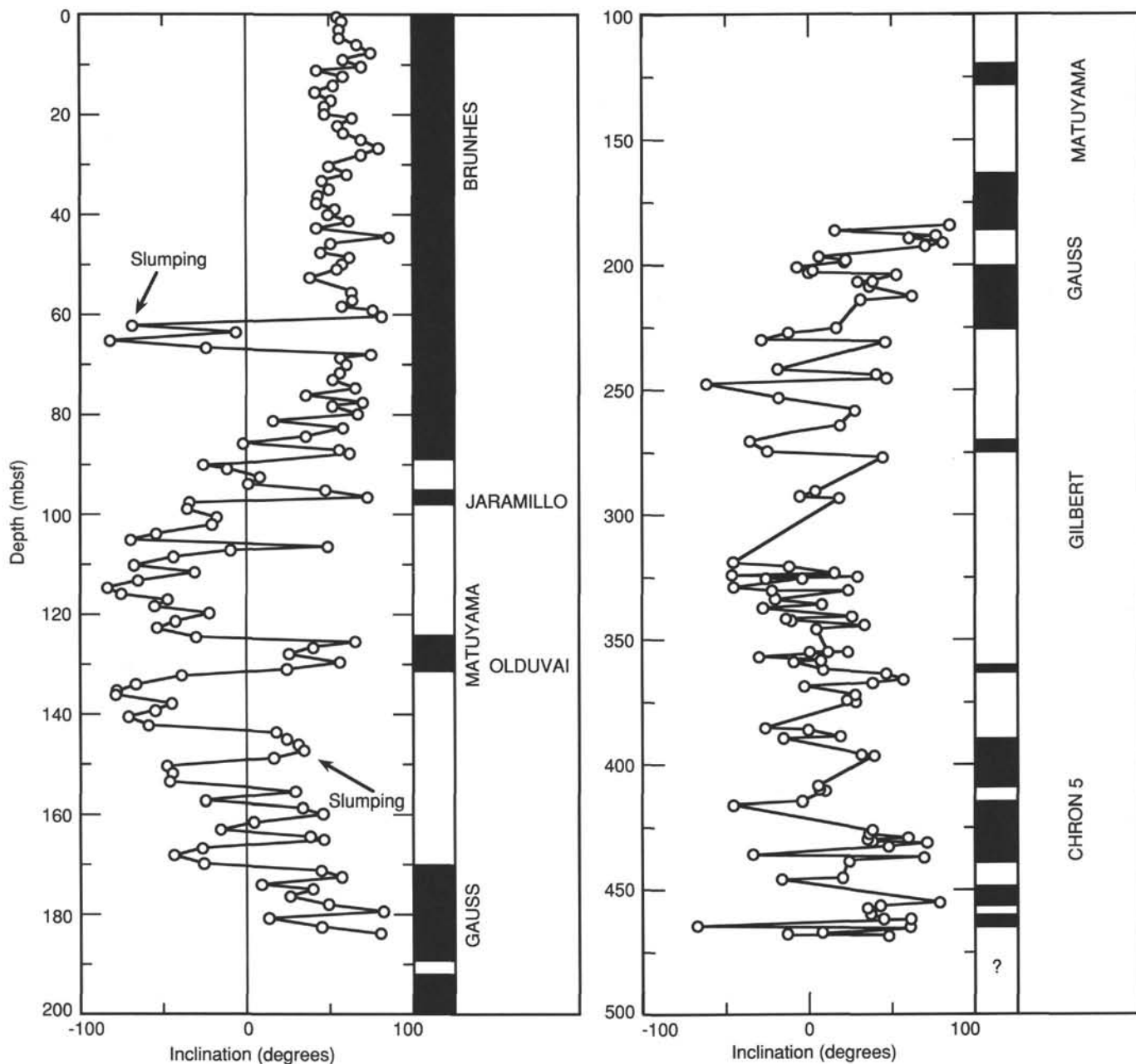


Figure 106. Hole 799A polarity pattern. Despite the disturbances, the polarity transitions are reliable down to the Gauss/Gilbert boundary. Patterns below this boundary will need to be confirmed.

edly lower in fluids squeezed in the Teflon-lined squeezer. This may be attributed to exposure to atmospheric CO_2 during the slower squeezing process into open vials inherent in the plastic squeezer procedure.

Salinity and Chlorinity

Distributions of salinity and chlorinity are shown in Figure 116. Salinity decreases from 34 to 32 g/kg between 0 and 36 mbsf, then increases to between 33 and 34 g/kg by 44 mbsf. The distribution of chlorinity is scattered in the upper 250 mbsf and below 460 mbsf. Both salinity and chlorinity decrease slightly between 220 and 435 mbsf, then exhibit variable concentrations below 435 mbsf, with values as low as 28 g/kg and 501 mM, respectively.

Manganese and Sulfate

Distributions of manganese and sulfate are presented in Figure 117. Sulfate decreases to 3 mM by 16 mbsf and is nearly depleted by 28 mbsf. Dissolved manganese goes through a small minimum at 44 mbsf, increases to near $30 \mu\text{M}$ between 100 and 435 mbsf, then increases again to as high as $63 \mu\text{M}$ between 435 mbsf and the deepest sample at 600 mbsf.

Alkalinity, pH, Phosphate, and Ammonium

Distributions of alkalinity, pH, phosphate, and ammonium are shown in Figure 118. Alkalinity concentration shows a maximum of 42.1 mM at 73 mbsf, then a steady decrease in concentration to near 7 mM at the bottom of Hole 799B. The

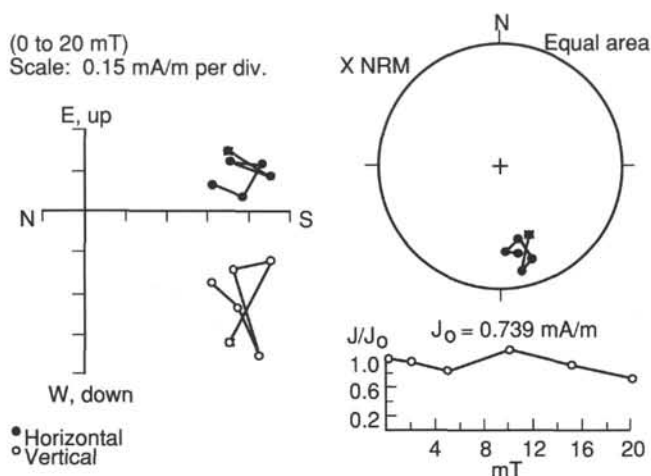


Figure 107. Demagnetization of Sample 128-799A-23X-6, 134 cm. The diagrams indicate stable normal polarity for the Gauss Chron.

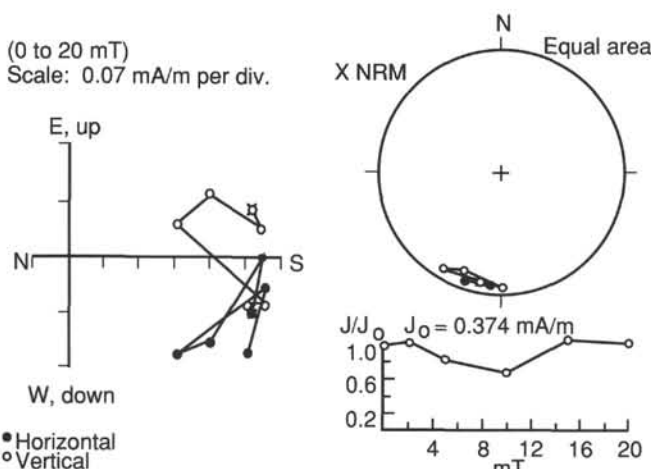


Figure 108. Demagnetization of Sample 128-799A-22X-2, 112 cm. The considerable stable reversed polarity possibly reflects the Kaena event.

pH of interstitial waters decreases from 8.0 at the topmost sampling interval to 7.4 at 44 mbsf, increases slightly to about 7.7, and remains nearly constant to 268 mbsf. Below 268 mbsf, pH decreases gradually to 5.3 at 435 mbsf. Below 435 mbsf, pH increases sharply to 6.5 at 464 mbsf, at the bottom of Hole 799A, and then continues to increase to a pH higher than 7 in interstitial waters recovered from Hole 799B. Dissolved phosphate exhibits a sharp increase from 75.8 to 197 μM within the first 28 mbsf, then decreases steadily to near zero by 320 mbsf. Ammonium concentration increases steadily from 362 μM at 2.6 mbsf to 5674 at 436 mbsf, then decreases slightly from below 436 mbsf in Hole 799A to the bottom of Hole 799B.

Calcium, Magnesium, and Strontium

Distributions of calcium, magnesium, and strontium and magnesium/calcium (Mg/Ca) molar ratios are given in Figure 119. The concentration of dissolved calcium decreases rapidly in the upper 50 m from 9.1 mM at 2.7 mbsf and then shows exhibits less rapid decrease to 2.8 mM at 220 mbsf in Hole 799A. We recorded an increase in concentration of calcium in interstitial waters at Hole 799B to between 8 and 9 mM at 531 to 600 mbsf. Concentrations of magnesium remain nearly constant between 43 and 45 mM from the uppermost sampling

interval to 220 mbsf, then decrease steadily to the bottom of Hole 799B. Strontium values increase from 111 μM at the top of Hole 799A to nearly 274 μM at the bottom of Hole 799A. Dissolved strontium decreases sharply to between 158 and 211 μM , then increases to between 225 and 257 μM by the deepest sampling interval of Hole 799B.

Silica, Lithium, and Potassium

Distributions of silica, lithium, and potassium are presented in Figure 120. The concentrations of silica and lithium exhibit similarly shaped profiles above 380 mbsf, with steadily increasing values. Below 380 mbsf, silica concentration decreases sharply from 1596 to 857 μM , and continues to decrease to 265 μM at 600 mbsf. Below 380 mbsf, lithium increases rapidly from between 80 and 90 μM to 227 μM of dissolved lithium at 498 mbsf, then decreases sharply to near 150 μM by 600 mbsf. Dissolved potassium decreases from between 11 and 13 mM at the top of Hole 799A to less than 4 mM at 600 mbsf.

Discussion

Based on gradients observed in interstitial-water profiles, Site 799 can be divided into four intervals:

1. Interval I (0–44 mbsf): In the upper 44 m, the chemical composition of the interstitial water is dominated by early diagenetic processes related to sulfate reduction and the early stages of decomposition of organic matter. Concentration of sulfate decreases to nearly zero by 28 mbsf. The decreased salinity in the upper 36 m of sediment reflects the decrease in dissolved sulfate within a zone of intense sulfate reduction. Below this zone of sulfate utilization, the total salinity increase can be attributed to increased concentrations of biogenic metabolites produced by bacterially mediated degradation of organic matter. Alkalinity increased in response to organic matter decomposition. Just below the zone of sulfate reduction, before methanogenesis began, the early stages of organic matter degradation may have released organic acids, which contribute to the pH minimum at 44 mbsf. Dissolved organic acid concentrations were not measured aboard the ship and must wait for shore-based analysis. The dissolved manganese minimum coincides with the pH minimum and is related to redox-controlled manganese mobilization in near-surface sediments below the zone of sulfate depletion. Release of phosphate during the early stages of diagenesis and organic matter decomposition is documented by a strong phosphate maximum at 36 mbsf, followed by phosphate removal to nearly zero by 300 mbsf. The dissolved lithium profile shows a minimum at 28 mbsf.

2. Interval II (44–220 mbsf): Interstitial-water ion concentrations in Interval II are influenced by organic matter degradation and biogenic carbonate recrystallization. Organic matter decomposition accounts for the increase in ammonium from 362 μM in the topmost sampling interval to 5746 μM at 380 mbsf. The decomposition of organic matter also accounts for the alkalinity rise from 11 mM at 2.6 mbsf to a maximum of 41 mM at 73 mbsf. Biogenic carbonate recrystallization and inorganic calcite precipitation accompanied the alkalinity increase, leading to a decrease in dissolved calcium from 9.1 mM in near-surface sediments to 2.7 mM at 220 mbsf. Biogenic carbonate recrystallization was accompanied by the release of strontium to the interstitial water, as indicated by the steady increase of dissolved strontium from 111 μM to between 230 and 240 μM by 220 mbsf. Progressive recrystallization of nannofossils was observed in smear slides throughout this interval (see "Lithostratigraphy" section, this chapter).

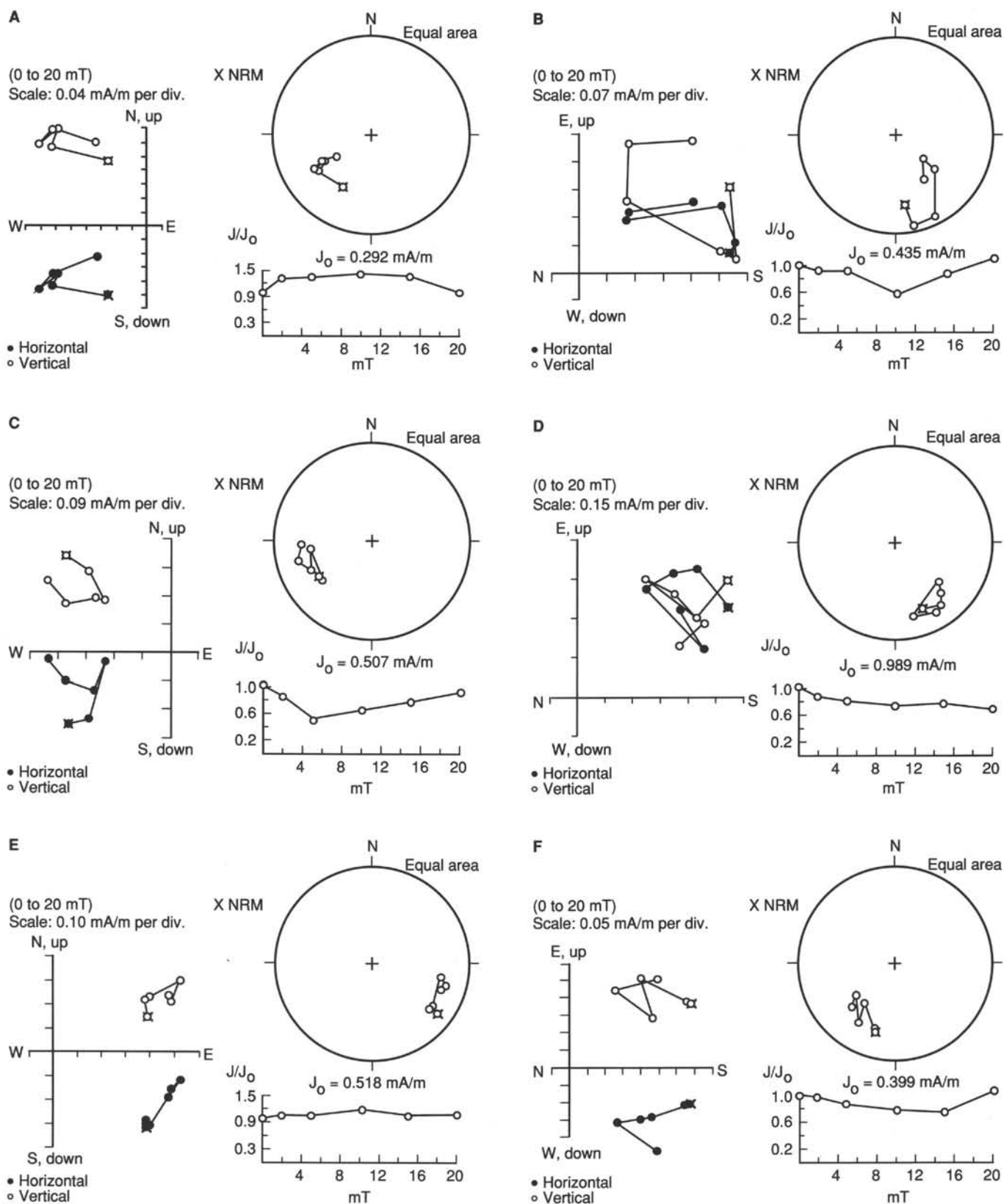


Figure 109. Demagnetization of A. Samples 128-799A-25X-5, 98 cm, B. 128-799A-29X-2, 3 cm, C. 128-799A-31X-3, 107 cm, D. 128-799A-38X-3, 98 cm, E. 128-799A-41X-2, 37 cm, and F. 128-799A-43X-3, 59 cm. The diagrams support the prevailed reversed polarity between 225.29 and 394.61 mbsf, typical for the Gilbert Chron.

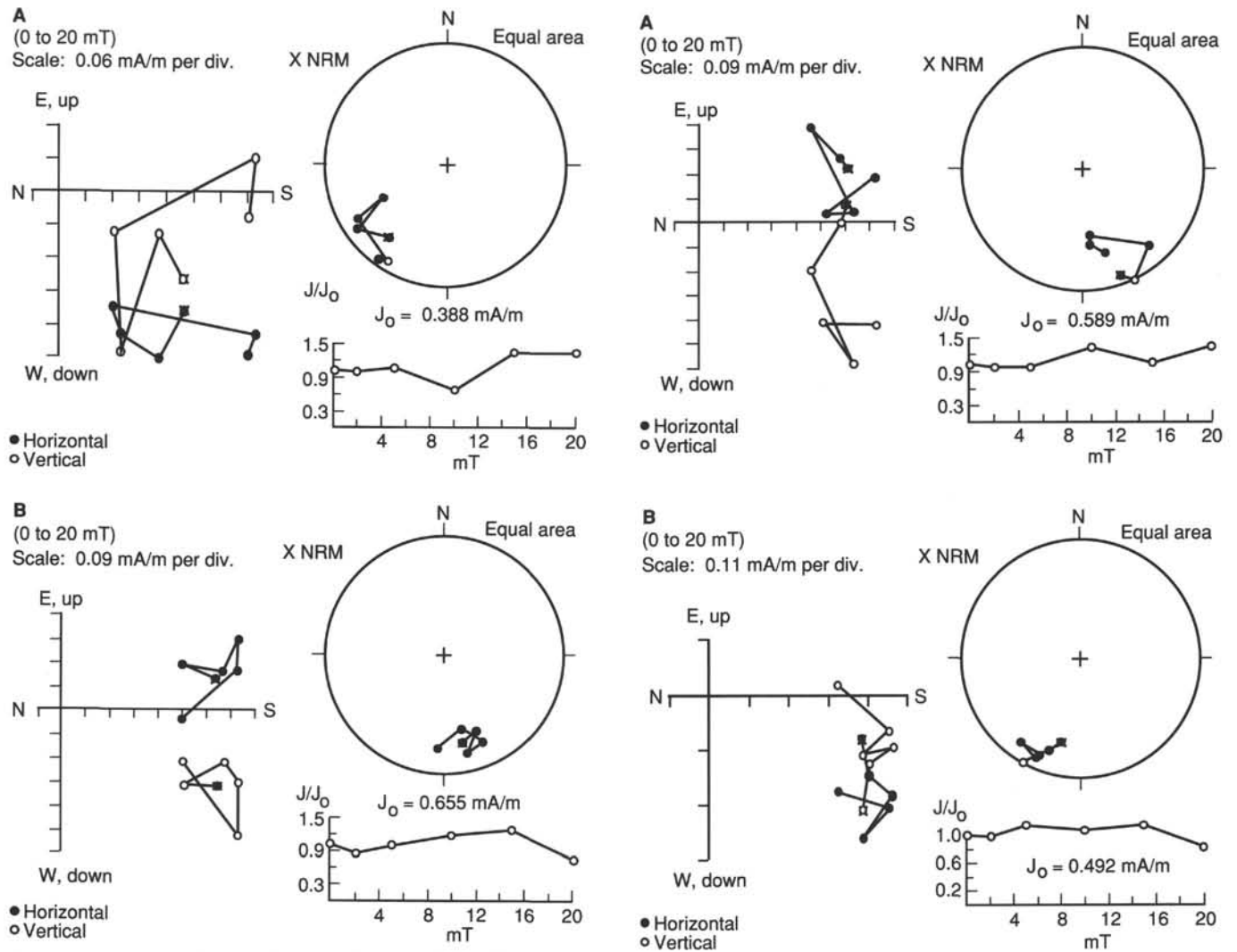


Figure 110. Demagnetization of A. Samples 128-799A-31X-5, 14 cm, B. 128-799A-40X-5, 69 cm. These stable normal polarities may be related with events of the Gilbert Chron.

Chlorinity concentrations remain nearly constant in interstitial waters of Interval II. Dissolved silica and potassium concentrations exhibit a slight increase and decrease, respectively, while lithium and pH remain nearly constant. The minor increase in silica concentration can be attributed to biogenic silica dissolution and/or diffusion along permeable sand layers present in this interval (see "Lithostratigraphy" section, this chapter). Nearly constant values for silica, potassium, lithium, and pH suggest that the crystallization of clay minerals has not actively altered the chemical composition of the interstitial waters in Interval II. The concentration of dissolved magnesium remains nearly constant between 43 and 45 mM to 130 mbsf. Below 130 mbsf, dissolved magnesium has been removed by dolomitization, which is discussed below.

3. Interval III (220–436 mbsf): Within Interval III, dolomitization, biogenic silica (opal-A) dissolution, and crystallization of clay minerals influenced the chemical composition of interstitial waters. Dolomitization was indicated by magnesium removal and calcium release, which resulted in a sharp turn-around in the Mg/Ca profile at 220 mbsf. Further indication that dolomitization dominated carbonate recrystallization within Interval III is seen in the strontium profile. The

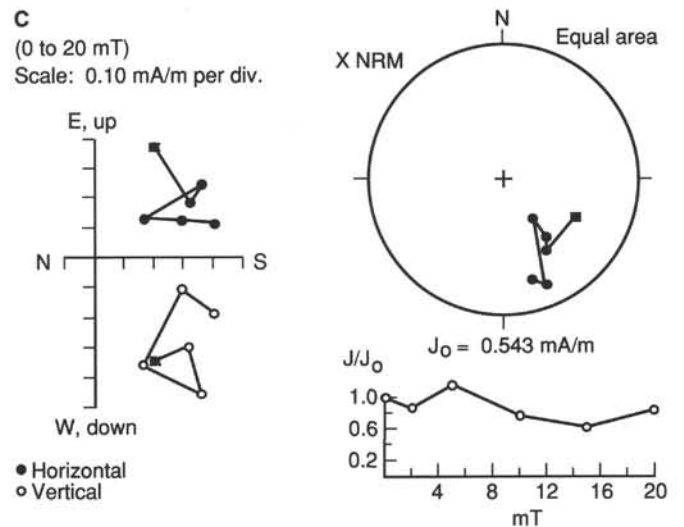


Figure 111. Demagnetization of A. Samples 128-799A-45X-4, 72 cm, B. 128-799A-47X-6, 35 cm, C. 128-799A-50X-6, 42 cm, supporting the normal polarity below 394.61 mbsf, which may have been generated in the uppermost Miocene (Chron 5).

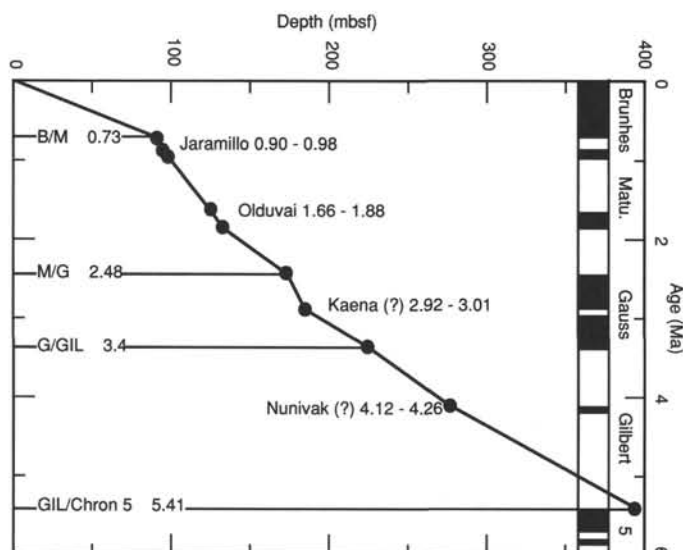


Figure 112. Sedimentation rates of Hole 799A. These rates are 127 m/m.y down to the Brunhes/Matuyama boundary and 65 m/m.y down to Chron 5.

concentration of dissolved strontium in interstitial waters increases more slowly between 220 and 436 mbsf than in the biogenic calcite recrystallization zone of Interval II. Between 220 and 380 mbsf, concentrations of dissolved silica and lithium increase from 1057 to 1596 μM and from 50 to 141 μM , respectively, reflecting the dissolution of biogenic silica. The concentration of dissolved silica begins to decrease below 380 mbsf, while the concentration of lithium continues to increase. This reflects the opal-A/opal-CT transition, where the formation of opal-CT removed silica from solution, but excluded lithium from the solid phase. Opal-CT first appears in the sediments below 400 mbsf (see "Lithostratigraphy" section, this chapter). The crystallization of clay minerals is suggested by the removal of dissolved potassium, decreasing alkalinity, and the decrease in pH between 220 and 436 mbsf. Ultrafiltration of interstitial waters by clay minerals may account for the decrease in chlorinity and salinity we observed below 220 mbsf (Henshaw and Coplen, 1973).

4. Interval IV (436–600 mbsf): This interval is marked by decreases in concentrations of dissolved alkalinity, silica (1480 to 857 μM), magnesium (27 to 16 mM), and ammonium (5674 to 3671 μM), increases in dissolved calcium (4.9 to 9.1 mM), and variable concentrations of chlorinity (524 to 506 mM), salinity (31.2 to 29.8 g/kg), strontium (158 to 257 μM), and potassium (2.9 to 5.1 mM). Concentrations of dissolved lithium goes through a sharp maximum within this interval, at 498 mbsf. The pH of interstitial waters increases from 4.9 at 408 mbsf to 7.6 at 600 mbsf. The abrupt change in the compositional character of interstitial waters coincides with low-porosity and high bulk-density layers (see "Physical Properties" section, this chapter) composed of dolomite and opal-CT (see "Lithostratigraphy" section, this chapter).

A low-permeability layer separates the fluids in Interval IV from communication with the overlying interstitial waters. This is clearly evident from the sharp changes in concentrations of several components (e.g., pH, alkalinity, silica, and strontium). The recovery of altered rhyolites in the bottom of Hole 799B (see "Lithostratigraphy" section, this chapter) provides evidence that basement alteration did influence the composition of interstitial waters. We would expect basement alteration reactions to result in consumption of magnesium

and addition of calcium and strontium to interstitial fluids. Basement alteration as a sink for chlorinity is more difficult to justify, although a wide range of concentrations in chlorinity of fluids associated with hydrothermal reactions have been reported that range from twice to one-half that of normal seawater (Seyfried et al., 1986; Han et al., 1989). The presence of thick sand intervals in the bottom sections of Hole 799B provided excellent conduits for fluid migration. These sand layers can be correlated across the basin (see "Lithostratigraphy, this chapter), giving us a wide range of possibilities for water sources and mechanisms that should be reflected in the chemical composition of the interstitial waters. For example, Neogene freshwater sediments in the northeast flank of the Yamato Bank have been inferred from micropaleontological evidence (Burckle and Akiba, 1978; Tsoy et al., 1985; Barash, 1986). Migration of brackish fluids through these sand layers might be a source of the low chlorinity values observed between 552 and 600 mbsf. Similarly, horizontal advection of fluids that are less diagenetically altered and nearer the normal chemical composition of seawater may explain the chemical composition of fluids observed between 464 and 531 mbsf. Mechanisms that are not exclusive but may act together to affect the chemical composition of interstitial waters will be needed to explain the compositional changes observed below the lithologic barrier that isolates Interval IV fluids from overlying interstitial waters.

ORGANIC GEOCHEMISTRY

Shipboard organic geochemical analyses of samples from Site 799 consisted of determinations of inorganic carbon, total carbon, nitrogen, and sulfur of 309 samples, 138 analyses of volatile hydrocarbons in sediments, 36 analyses of volatile hydrocarbons in gas voids, and three determinations of high-molecular-weight hydrocarbons in sediments. Samples analyzed for carbon, nitrogen, and sulfur included those collected for physical properties, sedimentology, X-ray diffraction, and volatile hydrocarbon analysis. The Rock-Eval instrument on board the *JOIDES Resolution* was inoperable during drilling at Site 799. Consequently, no shipboard Rock-Eval data are available for this site. The analytical methods used are outlined in the "Explanatory Notes" (this volume). More detailed descriptions of methods are given in Emeis and Kvenvolden (1986).

Volatile Hydrocarbons

Hydrocarbon gases in sediments and gas voids were analyzed routinely as part of the ODP pollution prevention and safety program. Hydrocarbon gases in sediments were monitored using the headspace technique, while those in gas voids were collected in vacutainers. The results of headspace and vacutainer analyses for C_1 - C_4 hydrocarbons using the Carle gas chromatograph are presented in Tables 11 and 12. Duplicate samples were analyzed using the HP 5890 natural gas analyzer to provide additional information about the presence and abundance of C_1 - C_7 hydrocarbons.

The sediments at Site 799 contained large amounts of hydrocarbon gas. Methane concentrations in headspace samples ranged from 14 to 155,000 ppm, while ethane and propane concentrations ranged from below detection limits to 2693 and 1476 ppm, respectively (Fig. 121, Table 11). Heavier C_4 - C_7 hydrocarbons, identified using the HP 5890 analyzer, included isopentanes, *n*-pentane, neopentane (2,2-dimethylpropane), *n*-hexane, *n*-heptane, cyclopentane, methylcyclopentane, and methylcyclohexane. Concentrations of many of these heavier hydrocarbons were as high as 600 ppm in headspace samples. The abundance of C_2 - C_7 hydrocarbons observed indicates that a significant portion of the gas encountered at Site 799 had a

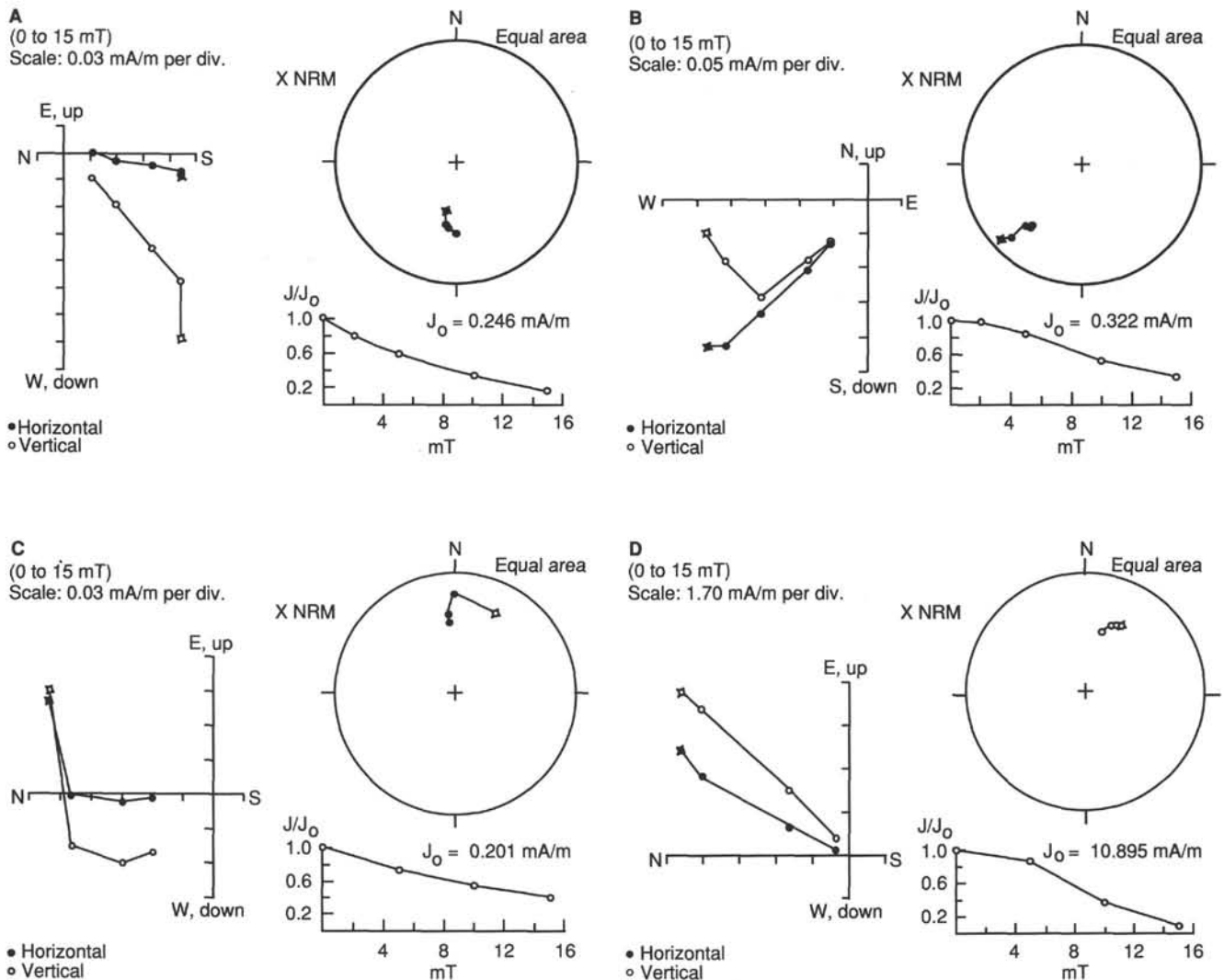


Figure 113. Demagnetization of archive halves at A. 128-799B-8R-2, 135 cm, B. 128-799B-9R-3, 5 cm, C. 128-799B-19R-5, 15 cm, and D. 128-799B-62R-4, 105 cm. The diagrams show the typical behavior of siliceous clay during demagnetization. See text for further explanation.

thermogenic origin. The ratios of methane to higher hydrocarbons decreased gradually with depth to 420 mbsf, where C_1/C_2 decreased rapidly from 900 to 300. The ratios then again decreased slowly to 1059 mbsf, where the abundance of propane, isobutane, and *n*-butane increased rapidly (Table 11, Fig. 121). Although the absolute concentrations of gas were high, calculations following von Rad and Haq et al. (1990) and Claypool and Kvenvolden (1983) indicated that the pore waters were not saturated with gas.

Vacutainer samples were collected from 25 of the 51 cores obtained at Site 799. Methane was the predominant gas in the vacutainer samples, with concentrations ranging from 490,000 to 932,000 ppm. Ethane concentrations ranged from 230 to 1200 ppm, and propane concentrations from 9 to 409 ppm (Fig. 122, Table 12). Methylcyclopentane and cyclohexane were noted in vacutainer samples collected below 288 mbsf.

Safety Considerations

The decision to continue coring at Site 799 in the presence of large amounts of apparently thermogenic gas was predicated on four factors.

1. The ratios of methane to other higher hydrocarbons decreased smoothly with depth. As a zone of petroleum generation or accumulation is approached, the amounts of higher hydrocarbons will increase rapidly, causing the C_1 /higher hydrocarbon ratios to decrease dramatically (e.g., Hunt, 1979). No sustained, rapid declines in the C_1 to higher hydrocarbon ratios were observed prior to the termination of coring. Even though the absolute values of the ratios were low, the gradual changes in these ratios with depth indicated that drilling could proceed safely.

2. The C_5 - C_7 hydrocarbons observed in headspace and vacutainer samples had been reported from shore-based headspace studies performed for samples from other DSDP and ODP sites (e.g., Sites 467 and 471; Whelan and Hunt, 1981, and Site 603; Schaefer and Leythaeuser, 1987). Drilling at these sites was continued without incident, thus the mere presence of these compounds did not indicate a significant drilling hazard.

3. Neopentane was an abundant component of the hydrocarbon gases. The occurrence of significant amounts of neopentane indicates that petroleum generation is at a very

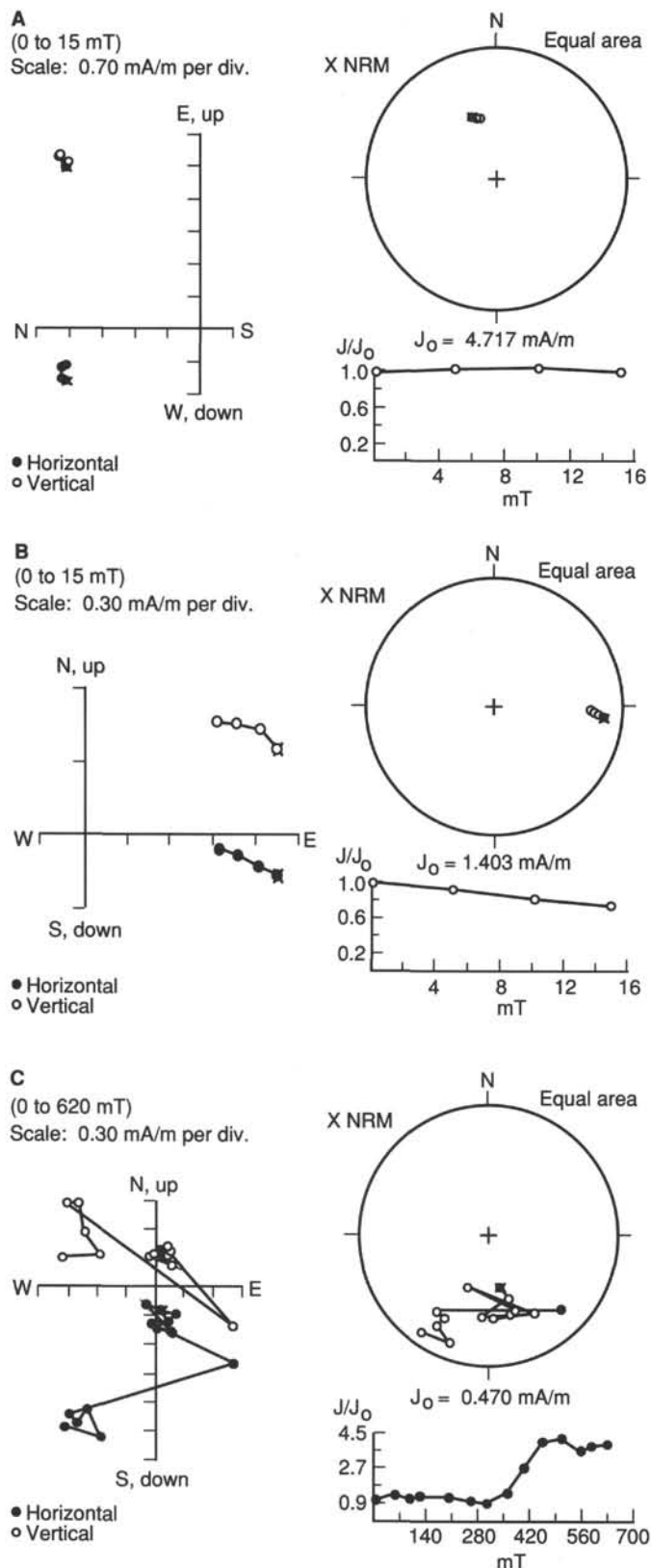


Figure 114. Demagnetization of archive halves at A. Sample 128-799B-10R-4, 135 cm (porcellanite), B. Sample 128-799B-29R-2, 105 cm (dolomite), and C. Thermodemagnetization of the corresponding Sample 128-799B-29R-2, 106 cm (dolomite). See text for further explanation.

early stage and that the hazards to drilling are low (Emeis and Kvenvolden, 1986).

4. Samples from each core below 460 mbsf were examined for evidence of liquid hydrocarbons. Samples for headspace gas analysis were taken from at least two locations in each core, and splits of these samples were examined for ultraviolet fluorescence, using 1,1,1-trichloroethane as a solvent.

Two samples were collected from Core 128-799B-65R for headspace gas analysis. One of these samples (128-799B-65R-2, 0–3 cm) exhibited a slow, pale yellowish-white “cut” fluorescence and left an amber colored residual cut. This sample yielded large amounts of ethane, propane, and butane during headspace gas analysis (Table 12). Three samples were selected from Core 128-799B-66R for headspace gas analysis (128-799B-66R-1, 0–3 cm; 128-799B-66R-1, 56–59 cm; and 128-799B-66R-2, 88–91 cm), and each of these samples exhibited similar “cut” fluorescence. Prompted by these observations, drilling was terminated at 1084 mbsf.

A rapid decrease in the ratios of C_1 /higher hydrocarbons was observed from 420 to 464 mbsf. This pattern is similar to the decline in C_1/C_2 and C_1/C_3 that caused us to stop drilling at Site 798 (see “Site 798” chapter, this volume). In both cases, the decrease of C_1/C_2 coincides with the opal-A/opal-CT transition (see “Lithostratigraphy” section, this chapter). These observations suggest that abundances of heavier hydrocarbon gases might be expected to increase at the opal-A/opal-CT transition and that this phenomenon does not necessarily indicate that hazards to drilling exist.

Carbon, Nitrogen, and Sulfur

Inorganic carbon, total carbon, total nitrogen, and total sulfur were determined routinely on samples collected for measuring physical properties. Carbon-nitrogen-sulfur (C-N-S) data also were obtained from samples collected for volatile hydrocarbon, X-ray diffraction, sedimentology, and interstitial water analysis. These data are presented in Table 13. Records for the organic carbon and equivalent percentage of calcium carbonate are presented graphically in Figure 123. When interpreting the calcium carbonate record, note that dolomite and siderite are abundant at Site 799 (see “Lithostratigraphy” section, this chapter) and therefore Figure 123 indicates the maximum calcium carbonate content. In addition, because the dolomite and siderite occur in thin laminae and as small concretions, they are often not sampled by the 24-mm (internal diameter) cylinder used for collecting samples for physical properties analysis. The calcium carbonate record in Table 13 and Figure 123 is representative of the major lithology, and the local high carbonate contents reflect sampling of the carbonate laminae or concretions.

The sediments encountered at Site 799 contain abundant organic matter, with total organic carbon (TOC) ranging from 0.24% to 5.66%. Calcium carbonate contents are variable and range from 0.25% to 79.8%. In lithologic Unit I (0–170 mbsf), both organic and inorganic carbon values vary by as much as a factor of 10 over short (10 cm) intervals, which reflects the light and dark sediment cycles present in this unit (Fig. 123; “Lithostratigraphy” section, this chapter).

In Unit II (170–457 mbsf), the carbonate content is lower than in Unit I and exhibits less variability (Fig. 123). Carbonate content increases below 400 mbsf in intervals where abundant dolomite and siderite concretions have been described. Organic carbon contents also are less variable in Unit II than in Unit I (Fig. 123).

Unit III (457–800 mbsf) contains relatively little carbonate and abundant organic carbon. The organic carbon record reflects the presence of laminated sediments from 457 to 606

Table 9. Sedimentation and accumulation rates calculated on Hole 799A based on selected microfossil and paleomagnetic data.

Datum levels	Age (Ma)	Depth (mbsf)	Sedimentation rate (m/m.y.)	MDBD* (g/cm ³)	Accumulation rate (g/cm ² /k.y.)
LAD <i>R. curvirostris</i>	0.34	24.00	71.00	0.68	4.80
LAD <i>P. lacunosa</i>	0.46	45.00	175.00	0.75	13.10
B/M boundary	0.73	89.00	163.00	0.86	14.00
Top Jaramillo	0.91	93.00	22.00	0.82	1.80
Bottom Jaramillo	0.98	96.00	43.00	0.94	4.04
LAD <i>H. sellii</i>	1.20	116.00	91.00	0.71	6.46
Top Olduvai	1.66	123.00	15.00	1.09	1.63
Bottom Olduvai	1.88	133.00	45.00	0.83	3.73
Top Gauss	2.47	174.00	69.00	0.76	5.24
Gauss/Gilbert	3.40	225.00	55.00	0.60	3.30
Top Gilbert/Chron 5	5.41	394.00	84.00	0.59	4.90
Chron 5/Chron 6	6.07	431.00	56.00	0.64	3.58

*Mean dry-bulk density.

mbsf, with elevated organic carbon contents and the predominance of burrowed sediments from 606 to 800 mbsf and with organic carbon contents that are low relative to the laminated section (Fig. 123; "Lithostratigraphy" section, this chapter). Unit III is also distinctive for the extreme variability exhibited by the records of total nitrogen and total sulfur (Figs. 124 and 125).

The carbon, nitrogen, and sulfur records for Unit IV (800–1020) are grossly similar to those for the burrowed portion of Unit III. Sediments in Unit V (1020–1084 mbsf) are richer in organic carbon than those in Unit IV and exhibit some of the highest carbon to nitrogen (C/N) ratios observed at Site 799 (Fig. 124).

High-Molecular-Weight Hydrocarbons

Three samples of sediment were extracted and analyzed for high-molecular-weight hydrocarbons. The purpose of these analyses was to gain more information regarding the thermal maturity and source of the lipid fraction of the organic matter. Interstitial-water squeeze cakes from Samples 128-799A-9H, 140–145 cm; 128-799A-21X-4, 145–150 cm; and 128-799A-51X-2, 140–145 cm, were freeze-dried and extracted as described in the "Explanatory Notes" (this volume). Chromatograms for all three samples are similar; the chromatogram obtained from Sample 128-799A-51X-2, 140–145 cm is shown in Figure 126. Extracts from all three samples comprise largely *n*-alkanes from *n*-C₁₅ to *n*-C₁₉, indicating that much of the lipid fraction was derived from algal material. A strong odd/even *n*-alkane predominance indicates a low level of thermal maturity.

Discussion

The sediments at Site 799 have been enriched in organic carbon relative to open-marine sediments, which indicates enhanced deposition or preservation of organic matter. Conditions favorable for deposition and preservation of organic carbon-rich sediments include high surface-water productivity, oxygen-deficient or anoxic bottom waters, rapid burial, or high influxes of terrigenous organic matter (Demaison and Moore, 1980). The C-N-S data obtained on board the ship and the sedimentological observations may provide information regarding the relative importance of each of these variables.

Plots of total nitrogen vs. organic carbon and total sulfur vs. organic carbon provide information about the source and preservation of organic matter in the units described at Site 799. The relative importance of marine and terrigenous sources of organic matter can be assessed by considering the C/N ratios of the sediments. A plot of total nitrogen vs. carbon

for all samples analyzed at Site 799 is shown in Figure 127. This plot suggests that the organic matter is predominantly marine (C/N is approximately equal to 10). The figure also indicates that the samples that have the highest organic carbon contents also have the highest C/N ratios, suggesting greater relative abundances of terrigenous organic matter (Bordowsky, 1965). When plotted on a total sulfur vs. carbon diagram, the sediments at Site 799 exhibit extreme variations in C/S ratios (Fig. 127). This scatter results from variations in the availability of sulfate during diagenesis (sedimentation rate or water chemistry) and from variations in the "quality" of organic matter as food for sulfate-reducing bacteria. The carbon and sulfur data obtained for Units IV and V do exhibit systematic variations in C-S space. These data plot subparallel to the normal marine trend defined by Berner and Raiswell (1984), but are displaced to lower C/S ratios (Fig. 128) and may indicate anoxic conditions during deposition of Units IV and V (see Leventhal, 1983). The C/N ratios for these sediments are high (Table 13, Fig. 128) and reflect preservation of refractory terrigenous organic matter deposited in turbidites (see "Lithostratigraphy" section, this chapter).

The combination of rapid sedimentation rates, abundant biosiliceous debris, and high organic carbon contents suggests high surface-water productivity over the Kita-Yamato Trough. The preservation of organic carbon-rich sediments at Site 799 results from three factors:

1. High surface-water productivity and possible anoxic bottom waters resulted in preservation of organic carbon-rich sediments.
2. Influxes of more refractory, terrigenous organic matter that increased the organic carbon content to nearly 6.5% locally.
3. Periodic rapid burial of organic matter by turbidites that enhanced preservation of organic carbon.

PHYSICAL PROPERTIES

Introduction

Coring during Leg 128 on the Yamato Trough sampled a 1084-m-thick sedimentary sequence that ranged from Holocene to Miocene in age. Physical properties measured routinely for cores recovered at Site 799 include GRAPE-density, compressional-wave velocity, and thermal conductivity from whole-round core sections. On split cores, index properties like wet-bulk density, dry-bulk density, water content (expressed as weight of water relative to total dry weight), grain density, porosity, and vane-shear strength were

determined. The methods used are described in detail in the "Explanatory Notes" (this volume). Results of the determined physical properties at Site 799 are summarized in Tables 14 to 18.

Index Properties

The distribution of index properties, such as wet-bulk density, water content, porosity, and grain-density, are plotted relative to depth below the seafloor in Figures 129 through 132.

Here, we refer to downhole variations of physical property units. Physical property units are defined as depth intervals where similar trends of physical properties were recorded.

Wet-bulk density (Fig. 129) generally varies from 1.26 to 2.72 g/cm³, values above and below these limits are subject to determination errors. The wet-bulk density profile can be divided into four different units with increasing depth below the seafloor. Unit 1 corresponds to the upper 123 m of sediments, where wet-bulk density varies between 1.26 and 1.84 g/cm³ and generally increases with increasing depth. The upper boundary of Unit 2 is marked by a decrease of wet-bulk density to values that range between about 1.50 and 1.70 g/cm³. Below this boundary, wet-bulk density generally decreases with increasing depth to minimum values in the range of 1.27 to 1.28 g/cm³ at a depth of 322 mbsf. This zone also marks the boundary between Units 2 and 3. The wet-bulk densities of Unit 3 increase with increasing depth. The upper boundary of Unit 4 is characterized by a rapid increase of wet-bulk density to the maximum value of 2.72 g/cm³ at a depth of about 444 mbsf. Below this depth, wet-bulk densities ranging from 1.47 to 2.52 g/cm³ were recorded.

Water content, expressed relative to dry weight (Fig. 130 and Table 14), exhibits variations between 264% and 5%. Like the profile for wet-bulk density, the profile for water content can be divided into four different units corresponding to the depth intervals defined above. Unit 1 is characterized by high contents of water and by a generally decreasing trend with increasing depth. Unit 2 shows an increase in water content to a depth of 322 mbsf. At this depth interval, a water content of 178% was determined. The water content of Unit 3 decreases with increasing depth. The upper boundary of Unit 4 is marked by an abrupt decrease in water content to a minimum value of about 5%. Below this boundary, water contents ranging from 124% to 4.8% were recorded.

Porosity (Fig. 131) ranges roughly between 88% and 11%. The profile for porosity can also be divided into four different units with increasing depth below the seafloor. In Unit 1, porosity values vary from 88% to 57% and exhibit a decrease with increasing depth. Unit 2 is characterized by an increase in porosity with increasing depth, whereas Unit 3 shows a slight decrease in porosity values. An abrupt decrease can be observed for the porosity values of Unit 4.

Grain density (Fig. 132) varies in the range of 2.10 and 2.86 g/cm³, values above and below these limits are subject to determination errors. The profile for grain density can be divided into three major units with increasing depth below seafloor. The boundaries of these units correspond to those defined earlier, except that the boundary at a depth of about 444 mbsf does not show up for grain density. Grain densities of Unit 1 vary from 2.15 to 2.85 g/cm³, but most values are in the range of 2.60 to 2.80 g/cm³. Unit 2 is characterized by a decrease of grain density with increasing depth below seafloor, whereas grain densities are increasing again in Unit 3.

GRAPE-Measured Density

Figure 133 presents the GRAPE-measured density of Hole 799A. This figure illustrates the original data points (as recorded by GRAPE and a smoothed curve) and shows the running

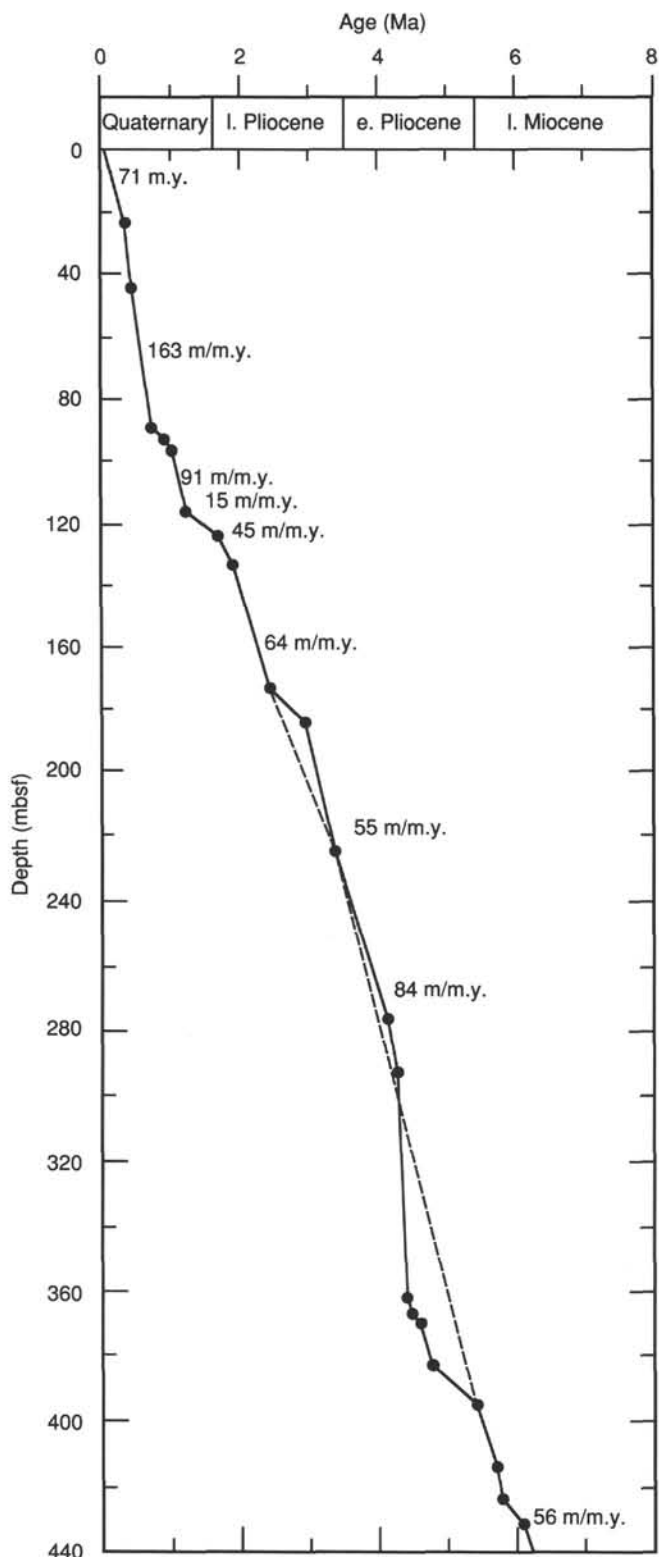


Figure 115. Sedimentation rates for upper Miocene through Quaternary sediments for Hole 799A.

Table 10. Chemical composition of interstitial waters from Site 799.

Core, section, interval (cm)	Depth (mbsf)	Volume (mL)	pH	Alkalinity (mM)	Salinity (g/kg)	Chlorinity (mM)	PO ₄ ³⁻ (μM)	NH ₄ ⁺ (μM)
128-799A-2H-1, 145-150	2.65	32	7.97	11.77	34.0	539	75.8	362
3H-4, 130-135	16.50	28	7.78	32.51	33.5	534	196.3	1665
3H-4, 135-140	16.55	45	7.74	33.22	33.5	531	161.2	1565
4H-5, 145-150	27.75	29	7.72	37.70	32.5	535	197.9	2038
5H-4, 145-150	35.85	23	7.60	38.05	32.0	531	193.1	2467
6H-3, 140-145	43.90	35	7.39	37.85	33.0	532	134.0	2396
6H-3, 145-150	43.95	40	7.40	38.81	32.5	530	127.7	2439
7H-3, 145-150	53.55	33	7.60	40.30	33.5	539	169.1	2610
8H-3, 145-150	63.15	30	7.74	39.90	33.5	537	167.6	3026
9H-3, 140-145	72.70	33	7.69	41.23	33.5	533	173.9	3126
9H-3, 145-150	72.75	50	7.48	42.13	33.8	545	156.4	2811
10H-3, 145-150	82.35	35	7.88	40.61	33.1	530	146.8	3426
12H-4, 140-145	103.10	55	7.67	38.89	33.3	536	109.8	3441
12H-4, 145-150	103.15	68	7.55	40.37	33.2	530	104.8	3412
15H-4, 140-145	132.00	44	7.92	36.79	32.7	531	88.4	3942
15H-4, 145-150	132.05	47	7.62	38.40	32.7	533	96.0	3684
18H-4, 140-145	161.10	9						
18H-4, 145-150	161.15	62	7.68	36.96	32.8	529	83.4	3885
21X-4, 140-145	190.00	30	7.50	33.72	33.0	538	71.4	4071
21X-4, 145-150	190.05	45	7.61	34.63	33.8	540	81.5	4056
24X-5, 140-145	220.50	34	7.71	30.13	32.5	535	52.6	4400
24X-5, 145-150	220.55	50	7.68	31.25	33.5	536	48.8	3942
27X-2, 140-145	244.30	30	7.50	28.32	32.5	541	48.8	4357
27X-2, 145-150	244.35	40	7.57	31.14	33.0	540	65.8	4185
30X-5, 140-145	267.90	36	7.71	25.87	32.4	536	34.3	4472
30X-5, 145-150	267.95	50	7.61	26.80	32.5	536	40.6	4758
33X-5, 140-145	295.30	41	6.53	25.68	32.3	534	29.9	4844
33X-5, 145-150	295.35	33	7.19	26.09	32.5	535	35.0	4758
36X-3, 140-145	321.30	48	6.10	22.76	6.10	533	3.5	5216
36X-3, 145-150	321.35	46	6.70	25.03	32.3	534	41.9	5059
39X-3, 140-145	350.30	39	5.83	21.65	32.0	529	10.4	5302
39X-3, 145-150	350.35	35	6.42	23.55	32.1	532	19.2	5130
42X-4, 140-145	380.90	40	5.01	20.59	31.6	530	4.2	5746
42X-4, 145-150	380.95	47	5.97	21.38	31.7	529	8.6	5288
45X-3, 140-145	408.30	27	4.95	19.26	31.6	525	2.9	5374
45X-3, 145-150	408.35	34	5.68	21.67	31.7	522	3.5	5202
48X-2, 140-150	435.80	44	5.25	18.52	31.6	524	0.4	5674
51X-2, 140-145	464.80	18			29.8			4715
51X-2, 145-150	464.85	10	6.54	19.97		506	1.6	
799B-5R-3, 130-140	493.9	30	7.53	9.67	32.2	531		5429
6R-2, 140-150	497.5	9	7.10		31.0	525		4203
7R-2, 140-150	502.6	25	7.19	11.45	30.4	528		5045
10R-2, 140-150	531.5	22	7.37	11.38	30.0	525		5045
12R-3, 140-150	552.3	12	7.42		28.2	501		3641
15R-4, 140-150	582.9	11	7.51	8.23	29.5	508		4306
16R-3, 140-150	591.0	21	7.31	6.83	29.5	514		4927
17R-3, 140-150	600.7	17	7.58	7.09	29.8	512		4794
18R-5, 140-150	613.3	0						
21R-1, 140-150	636.3	0						

Squeezer type: SS = standard ODP stainless-steel squeezer, BH = Brumsack-Murray, Teflon-lined squeezer.

average of five data points. GRAPE-measurements were restricted to a total depth of about 350 mbsf because of drilling disturbances and biscuiting. In the upper section of Hole 799A (0-160 mbsf), densities in the range of 1.31 to 2.20 g/cm³ were determined, but most densities varied between about 1.51 and 1.90 g/cm³. Below 160 mbsf, density abruptly decreases to values in the range of 1.30 to 1.70 g/cm³. In general, a decrease of GRAPE-measured density with increasing depth below seafloor was observed. Although the GRAPE-measured densities exhibit a greater scatter of data because of degassing cracks and core disturbance, a general correlation with the wet-bulk densities determined by the pycnometer method exists.

Compressional-Wave Velocity

Sonic velocities were measured by the continuous *P*-wave logger and the Hamilton Frame device (Tables 15 and 16). Because of the high amount of gas in the sediments, sonic velocities determined at Hole 799A were restricted to the upper 50 mbsf. All sonic velocities measured range from 1390 to 1610 m/s. In the upper 20 mbsf, sonic velocity is scattered

around a mean value of about 1500 m/s (Fig. 134). Two zones of higher velocities exist in the upper 20 mbsf. The first zone is located between roughly 3.0 and 3.7 mbsf, the second zone at a depth of about 15 mbsf. Below the depth of 20 mbsf, velocity data generally exhibit a greater scatter and a decreasing trend with increasing depth below seafloor.

The sonic velocities of Hole 799B are listed in Table 16. These measured velocities range from 1383 m/s (Sample 128-799B-6R-3, 10-15 cm) to 4880 m/s (Sample 128-799B-31R-1, 9-11 cm). These high velocity values correspond to a hard dolomite layer. With increasing depth of burial, sonic velocity generally increases (Fig. 135).

Thermal Conductivity

Thermal conductivity was routinely determined for four sections from each core from the mud line to a total depth of about 675 mbsf. Results are shown in Table 17 and Figure 136. These thermal conductivities vary between 0.68 and 2.28 W/(m · K), values above and below these limits are subject to determination errors. With increasing depth below seafloor,

Table 10 (continued).

SiO ₂ (μM)	Mg ⁺² (mM)	Ca ⁺² (mM)	K ⁺ (mM)	Sr ⁺² (μM)	Mg/Ca ratio	SO ₄ ⁻² (mM)	Li ⁺ (μM)	Mn ⁺² (μM)	Squeezer
537	48.9	9.1	11.0	111	5.4	19.6	42	60	BS
734	44.4	6.3	13.4	118	7.0	2.9	32	10	BS
743	44.8	6.4	12.9		7.0	2.9	32	11	SS
1055	43.9	5.6	13.1	125	7.8	0.1	27		BS
1007	44.0	4.9	12.2	135	9.1	0.0	35	9	BS
775	44.3	4.3	11.5	138	10.4	0.0	39	5	BS
771	44.9	4.4	11.2	145	10.3	0.1	44	4	SS
911	43.4	4.3	12.2	147	10.1	0.0	49	6	BS
928	44.3	4.2	11.6	154	10.6	0.3	39	12	BS
930	43.9	4.1	10.8	159	10.8	0.0	53	16	BS
921	45.3	4.2	10.8	162	10.7	0.0	52	14	SS
1040	44.2	3.9	12.9	172	11.5	0.0	45	28	BS
990	45.0	3.7	11.8	176	12.0	0.1	50	20	BS
1070	44.1	3.6	11.2	172	12.3		63	24	SS
838	41.7	3.6	12.3	174	11.6		43	17	BS
896	43.8	3.7	12.0	193	11.9	0.0	50	28	SS
				213					BS
1132	43.9	3.4	9.6	213	13.0		54	32	SS
1123	42.8	3.1	9.7	215	14.0		45	26	BS
1106	43.1	3.2	8.2	223	13.5	0.2	50	33	SS
1057	41.6	2.8	9.7	232	15.1		56	32	BS
1080	41.6	3.0	11.1	232	14.0	0.2	60	30	SS
1199	39.8	3.3	7.9	240	12.0		56	34	BS
1209	40.6	3.2	8.4	249	12.6	0.1	55	32	SS
1222	37.8	3.4	8.3	230	11.1		58	25	BS
1272	38.6	3.5	9.6	245	11.0	0.4	48	30	SS
1242	36.1	3.2	7.3	254	11.2		64	28	BS
1257	36.0	3.6	7.0	261	10.1	0.2	71	27	SS
1478	33.2	4.1	7.7	242	8.1		80	21	BS
1506	34.2	4.0	7.9	271	8.5	0.3	66	33	SS
1467	31.9	4.3	7.6	242	7.4		77	21	BS
1484	32.5	4.5	6.8	262	7.2	0.2	96	33	SS
1570	29.5	4.5	6.9	242	6.6		82	24	BS
1596	30.6	4.5	7.0	249	6.8	0.4	98	24	SS
1506	26.6	4.8	6.0	281	5.5		111	20	BS
1527	27.7	5.0	6.0	259	5.5	0.3	103	36	SS
1480	24.5	4.9	5.1	257	5.0	0.2	141	21	SS
857	22.8	5.4	3.7	266	4.2		177	45	BS
				274		0.0		68	SS
779	22.1	6.6	4.6	158	3.4		196	22	SS
802	22.4	8.1	4.5	211	2.8		227	34	SS
791	20.7	7.5	5.1	193	2.8		207	29	SS
733	18.6	8.8	4.6	163	2.1		227	30	SS
690	20.4	9.1	3.2	225	2.2		234	42	SS
600	17.9	8.7	2.9	257	2.1		195	39	SS
378	16.6	9.4	3.2	254	1.8		149	32	SS
265	16.9	8.5	3.1	247	2.0		166	63	SS

the profile for thermal conductivity profile can be divided into four different units that correspond to the same depth intervals as the profiles for water content and wet-bulk density. Unit 1 is characterized by values of thermal conductivity scattered around 1.0 W/(m · K). Thermal conductivities of Unit 2 decrease with increasing depth below seafloor, whereas an increase in thermal conductivity with increasing depth below seafloor was recorded for Unit 3. The boundary between Units 3 and 4 is marked by a slight increase of thermal conductivity.

Undrained Shear Strength

Values of measured Torvane shear strength are listed in Table 18 and plotted vs. depth in Figure 137. Determined shear strengths were restricted to Cores 128-799A-1H to 128-799A-20H because of coring disturbance in XCB and RCB cores.

Shear strength values vary between 1.60 and 96.1 kPa. With increasing depth, shear strength generally increases. Shear strength values exhibit a linear increase from a depth of 0.44 to 37.60 mbsf. At a depth of about 41 mbsf, shear strength increases abruptly to a value of 35 kPa. A second zone of high shear strength values was determined at the depth interval between 96 and 182 mbsf.

Relationships of Physical Properties to Lithology

Based on visual core descriptions and smear slides, evaluation of the sedimentary record of Hole 799A can be divided into three major lithologic units (see "Lithostratigraphy" section, this chapter). The upper 170 mbsf of the sedimentary column are generally characterized by a greater influence of terrigenous material, turbidites, and debris flow deposits. The depth range from about 170 to about 460 mbsf is marked by a high amount of siliceous material. A maximum of siliceous material was recorded at a depth of about 330 mbsf. The depth interval around 460 mbsf shows the transition of opal-A to opal-CT.

A comparison of physical properties with lithology reveals that the upper 120 mbsf is characterized by generally higher wet-bulk densities and grain densities, but lower values for the water content and porosity were recorded in the same interval. The silica-rich depth interval shows generally lower values for wet-bulk and grain densities, whereas higher porosities and water content values were determined. The lowest wet-bulk and grain densities in lithologic Unit II were recorded at a depth of about 330 mbsf, where a maximum of siliceous material was observed. This zone is also characterized by high values for water content and porosity. The above

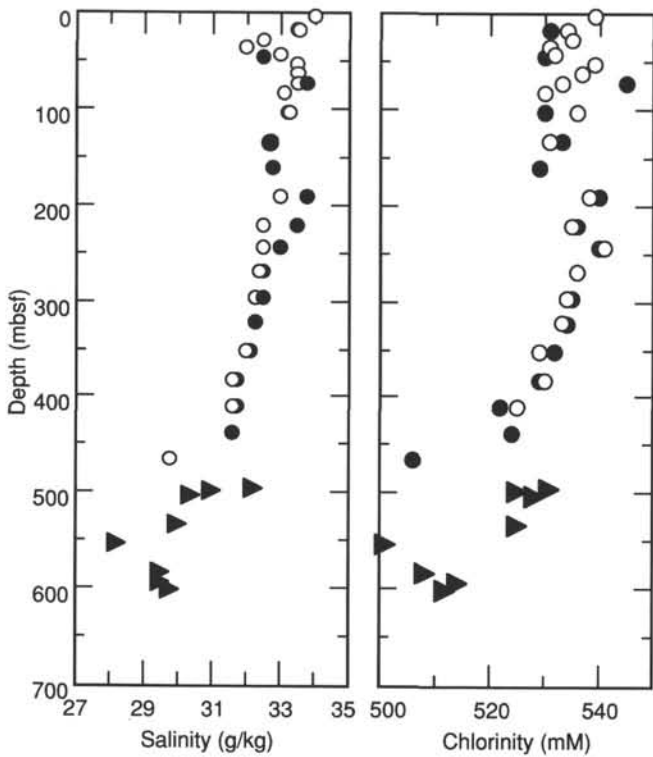


Figure 116. Interstitial-water salinity and chlorinity concentrations vs. depth, Site 799. Closed circles = standard ODP stainless-steel squeezer in Hole 799A, open circles = Brumsack-Murray, Teflon-lined squeezer in Hole 799A, closed triangles = Hole 799B.

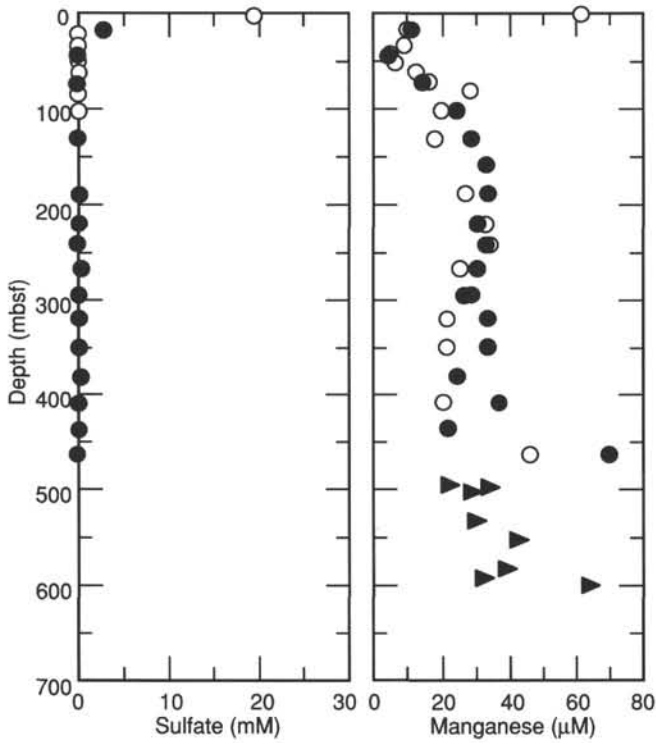


Figure 117. Interstitial-water manganese and sulfate concentrations vs. depth, Site 799. Closed circles = standard ODP stainless-steel squeezer, Hole 799A; open circles = Brumsack-Murray, Teflon-lined squeezer, Hole 799A; closed triangles = Hole 799B.

observations generally confirm the findings of Einsele (1982) and Holler (1985, 1989) for sediments rich in biogenic silica.

The boundary between opal-A and opal-CT is marked by high wet-bulk densities and generally low water-content and porosity values at a depth of about 458 mbsf. This change in physical properties corresponds to a dramatic change in logging data (see "Downhole Measurements" section, this

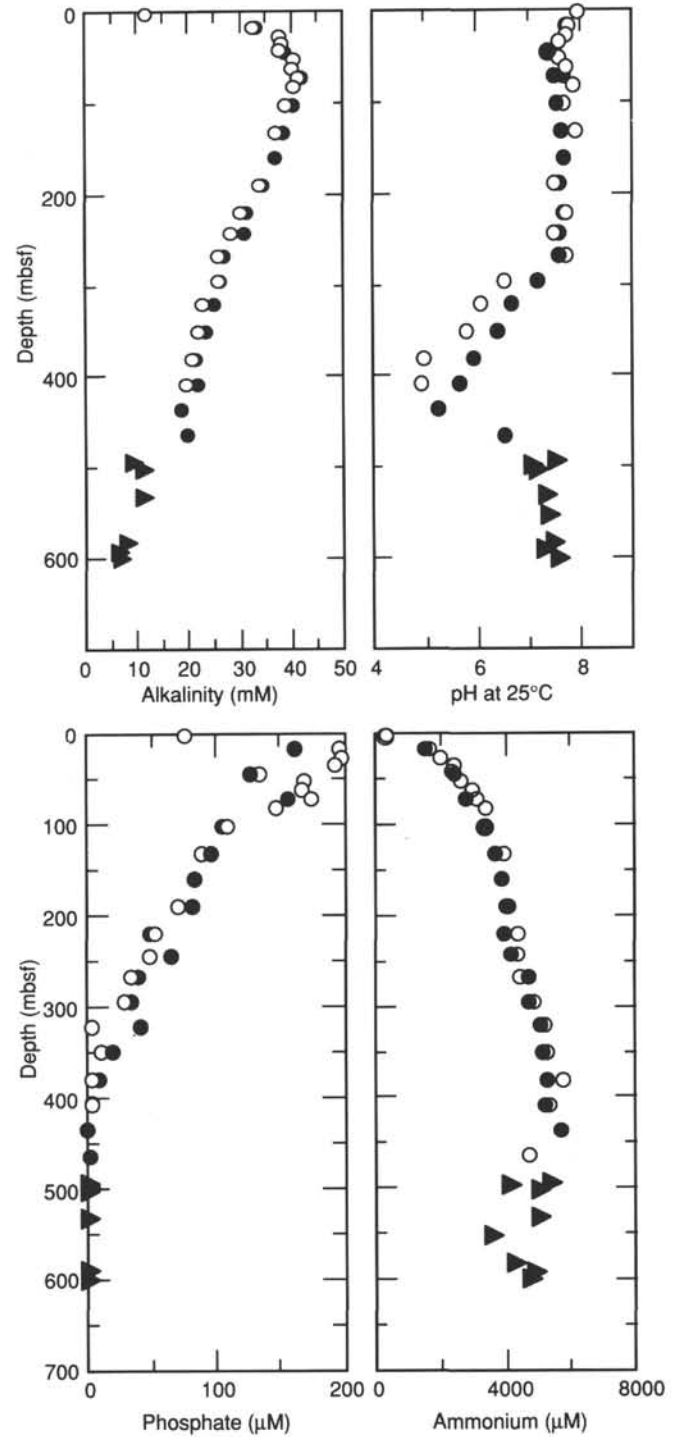


Figure 118. Interstitial-water alkalinity, pH, phosphate, and ammonium concentrations vs. depth, Site 799. Closed circles = standard ODP stainless-steel squeezer, Hole 799A; open circles = Brumsack-Murray, Teflon-lined squeezer, Hole 799A; closed triangles = Hole 799B.

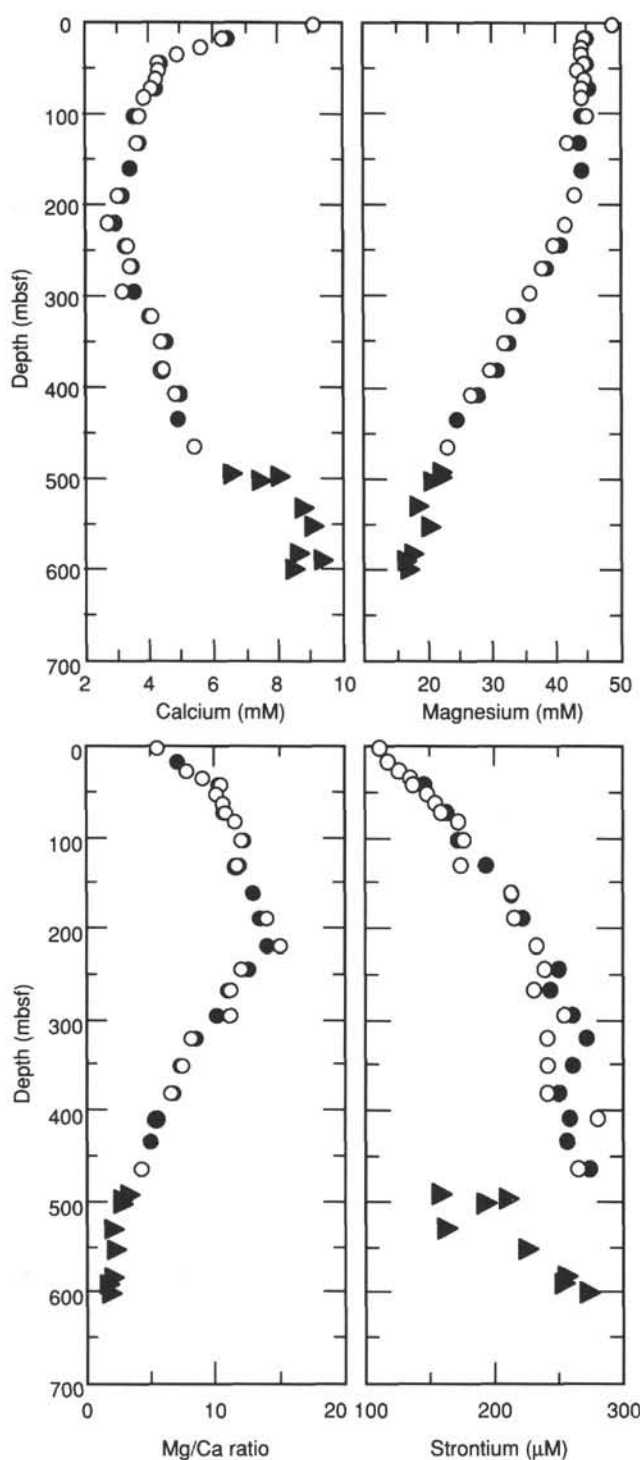


Figure 119. Interstitial-water calcium, magnesium, Mg/Ca molar ratio, and strontium concentrations vs. depth, Site 799. Closed circles = standard ODP stainless-steel squeezer, Hole 799A; open circles = Brumsack-Murray, Teflon-lined squeezer, Hole 799A; closed triangles = Hole 799B.

chapter) and pore-water geochemistry (see "Inorganic Geochemistry" section, this chapter).

DOWNHOLE MEASUREMENTS

Two complete suites of four Schlumberger logs each were run at Holes 799A and 799B. The four tool strings used were the seismic stratigraphy, FMS, lithoporosity, and geochemical

tool combinations; the Lamont-Doherty temperature logging tool (TLT) was added to the base of each of these tool strings. In addition, the Barnes/Uyeda temperature probe was deployed eight times during APC coring at Hole 799A. A vertical seismic profiling (VSP) experiment was conducted at the end of standard logging at Hole 799B. These tool strings and their applications are described in the "Explanatory Notes" (this volume). A summary of the logging programs at Holes 799A and 799B is shown in Tables 19 and 20.

Logging Operations

Drilling at Hole 799A stopped at 468.7 mbsf; hole conditioning consisted of a wiper trip and pumping of a minimal amount of polymer mud to help stabilize the clays. Capillary suction tests had been conducted for four core-catcher samples taken at 160, 190, 326, and 365 mbsf, all of which gave low freshwater suction times, which indicated that these clays should be stable in the presence of the brackish fluid in the hole. This stability was reflected during the 25 hr of downhole logging, because hole conditions were excellent, with no indication of any bridge formation. Pipe was set at the relatively deep value of 104.6 mbsf as a result of the soft nature of the uppermost sediments in the hole.

Hole 799B was rotary cored from the base of the cement casing shoe at 450 mbsf to total depth (TD) at 1084 mbsf. Casing was set at Hole 799B so that there would be ~20 m of overlap with the bottom of Hole 799A. Logging data are particularly significant at this hole, partly because of excellent quality and partly because of the poor overall core recovery (44%). For certain depth intervals where lithology varied rapidly, recovery was exceedingly poor (~10%) and, as demonstrated by the logs, the recovered sediment was often unrepresentative of the drilled lithologic succession. Drilling diagnostics during the wiper trip after coring demonstrated that the hole was virtually free of bridges or other obstructions. Four standard logging combination tools were run at Hole 799B, and the excellent quality of these data results, in part, to the favorable hole conditions. During logging, the bottom of the hole became progressively shallower (1046–1026 mbsf) than the original drilling to total depth (1084 mbsf), which suggests that the hole was gradually accumulating fill. The VSP was run after the four combination runs had been completed.

Quality of Logs

The quality of the logs at Site 799 was generally excellent. Tool sticking and borehole washout problems, which often compromise log quality, were not evident. In Hole 799A, orthogonal FMS calipers indicated that the borehole diameter was mostly in the range of 12 to 14 in. and that it was slightly elliptical throughout the hole. However, two sections of the borehole, at 150 to 225 mbsf and at 385 to 440 mbsf exhibit a more marked ellipticity, with the long and short axes being about 15 and 11 in., respectively. The lower of these two sections was probably enlarged as a result of increased fluid circulation, which was applied during drilling to facilitate the penetration of a much harder zone of rock immediately below. The sonic velocity log, which is susceptible to poor hole conditions, exhibited only a minimum of cycle skipping, which has been removed by processing. This log is shown in Figure 138.

Tools were calibrated before and after each of the logging runs to ensure quality control. The wireline heave compensator was used during all logging runs to neutralize the effect of the ship's heave on tool position relative to the borehole wall. Depth correlation among logging runs was good, with no major depth shifting necessary; depth measurements were

Table 11. Volatile hydrocarbon data from headspace analysis, Site 799.

Core, section, interval (cm)	Depth (mbsf)	C ₁ (ppm)	C ₂ (ppm)	C ₃ (ppm)	<i>i</i> -C ₄	<i>n</i> -C ₄	C ₁ /C ₂	C ₁ /C ₂₊
128-799A-2H-1, 130-135	2.50	14	0	0	n.d.	n.d.		
3H-5, 0-5	16.70	123	2	0	n.d.	n.d.	62	62
4H-6, 0-5	27.80	31,212	12	0	n.d.	n.d.	2,601	2,601
5H-5, 0-5	35.90	51,199	11	0	n.d.	n.d.	2,654	4,654
6H-4, 0-5	44.00	64,749	15	0	n.d.	n.d.	4,047	4,047
7H-4, 0-5	53.60	26,528	10	0	n.d.	n.d.	2,653	2,653
8H-3, 148-150	63.18	49,152	17	2	n.d.	n.d.	2,891	2,587
9H-3, 148-150	72.78	48,140	21	4	n.d.	n.d.	2,245	1,886
10H-4, 148-150	83.88	63,024	31	5	n.d.	n.d.	2,033	1,751
11H-4, 145-150	93.45	9,315	13	2	n.d.	n.d.	717	621
12H-4, 145-150	103.15	8,563	16	5	n.d.	n.d.	535	408
13H-4, 145-150	112.75	4,579	5	0	n.d.	n.d.	916	916
14H-2, 0-5	118.00	66,351	27	3	n.d.	n.d.	2,457	2,212
15H-5, 0-5	132.10	8,966	9	1	n.d.	n.d.	996	897
16H-3, 0-5	138.80	23,112	19	3	n.d.	n.d.	1,216	1,051
17H-2, 0-5	147.00	47,846	35	8	n.d.	n.d.	1,367	1,113
18H-5, 0-5	161.20	62,578	29	4	n.d.	n.d.	2,158	1,896
19H-5, 0-5	170.80	42,090	28	4	n.d.	n.d.	1,503	1,315
19H-5, 0-4	170.80	11,668	0	0	n.d.	n.d.		
20H-3, 145-150	178.95	55,704	30	4	n.d.	n.d.	1,859	1,640
21X-4, 125-130	189.85	50,781	32	4	n.d.	n.d.	1,587	1,411
22X-4, 145-150	199.75	49,925	33	6	n.d.	n.d.	1,513	1,280
23X-4, 145-150	209.45	54,137	45	9	n.d.	n.d.	1,203	1,003
24X-6, 0-5	220.60	17,439	21	4	n.d.	n.d.	830	698
25X-5, 145-150	230.25	51,148	36	6	n.d.	n.d.	1,421	1,218
27X-3, 0-5	244.40	31,856	24	4	n.d.	n.d.	1,327	1,138
29X-4, 0-5	255.40	9,654	17	2	n.d.	n.d.	568	508
30X-6, 0-5	268.00	37,270	32	5	n.d.	n.d.	1,165	1,007
31X-2, 0-4	271.70	13,280	10	0	n.d.	n.d.	1,328	1,328
31X-2, 0-5	271.70	61,287	44	4	n.d.	n.d.	1,393	1,277
32X-2, 0-5	279.70	13,151	23	3	n.d.	n.d.	572	506
33X-4, 0-5	292.40	47,346	31	0	n.d.	n.d.	1,527	1,527
33X-4, 0-4	292.40	12,792	9	0	n.d.	n.d.	1,421	1,421
34X-4, 0-5	302.10	7,528	11	0	n.d.	n.d.	684	684
34X-4, 0-4	302.10	6,755	0	0	n.d.	n.d.		
36X-4, 0-5	321.40	48,511	32	0	n.d.	n.d.	1,516	1,516
37X-4, 0-5	331.10	43,293	28	0	n.d.	n.d.	1,546	1,546
37X-4, 0-4	331.10	6,733	0	0	0	0		
38X-3, 145-150	340.65	28,756	28	2	0	0	1,027	959
39X-4, 0-5	350.40	39,599	34	2	0	0	1,165	1,100
40X-4, 0-5	360.10	33,155	33	2	0	0	1,005	947
41X-1, 0-5	365.30	9,834	26	2	0	0	378	351
42X-5, 0-5	381.00	42,451	53	3	0	0	801	758
43X-4, 0-5	389.10	35,529	37	2	0	0	960	911
44X-1, 0-5	394.30	80,064	67	32	0	0	1,195	809
45X-4, 0-5	408.40	68,719	68	3	0	0	1,011	968
46X-4, 0-5	418.10	61,464	57	1	0	0	1,078	1,060
47X-5, 0-5	429.30	60,757	67	2	0	0	907	881
48X-1, 0-5	432.90	55,106	57	3	0	0	967	918
50X-3, 148-150	456.78	75,678	103	5	0	0	735	701
51X-2, 110-115	464.50	87,430	125	3	0	0	699	683
128-799B-2R-CC, 0-5	459.50	8	0	0	0	0		
5R-3, 125-130	493.85	65,733	241	15	0	0	273	257
5R-3, 126-130	493.86	19,030	140	16	0	0	136	122
6R-2, 140-145	497.50	90,283	270	12	0	0	334	320
7R-2, 140-145	502.60	110,691	397	17	5	0	279	264
7R-3, 0-2	502.70	52,699	242	16	7	0	218	199
8R-3, 0-3	512.30	77,121	303	21	15	0	255	227
10R-2, 0-2	530.10	138,812	510	36	33	2	272	239
11R-6, 0-2	545.80	96,347	587	69	102	8	164	126
12R-4, 0-2	522.40	72,509	295	33	60	6	246	184
13R-4, 148-150	563.58	65,238	273	24	61	3	239	181
14R-2, 148-150	570.28	125,935	600	32	82	0	210	1??
15R-2, 148-150	579.98	83,409	560	31	132	0	149	1??
16R-3, 138-140	590.98	143,143	606	23	89	0	236	199
17R-4, 0-5	600.80	120,867	529	25	78	0	228	191
18R-6, 0-3	613.40	72,322	312	18	54	0	232	188
19R-4, 0-3	620.10	119,471	427	18	50	0	280	241
20R-4, 0-5	629.70	111,739	505	31	89	5	221	177
21R-2, 0-5	636.40	130,164	419	16	43	0	311	272

Table 11 (continued).

Core, section, interval (cm)	Depth (mbsf)	C ₁ (ppm)	C ₂ (ppm)	C ₃ (ppm)	i-C ₄	n-C ₄	C ₁ /C ₂	C ₁ /C ₂₊
22R-1, 0-5	644.60	39,765	422	30	91	6	94	72
23R-1, 145-150	655.65	99,838	381	20	55	0	262	219
24R-1, 145-150	665.25	83,280	436	37	52	4	191	157
25R-2, 0-5	675.00	96,134	301	18	55	0	319	257
26R-2, 0-5	684.70	132,074	353	13	28	0	374	335
27R-2, 0-3	694.00	91,645	317	21	49	0	289	237
28R-4, 0-2	706.60	95,448	537	48	95	7	178	139
29R-6, 0-3	719.30	111,067	646	58	107	7	172	136
30R-2, 0-2	722.90	116,340	406	26	47	0	287	243
31R-1, 148-150	732.28	93,729	1,338	118	202	17	70	56
32R-1, 60-62	741.10	116,207	1,318	128	232	22	88	68
33R-3, 0-2	753.20	134,401	705	59	88	7	191	156
34R-2, 0-3	761.30	100,712	558	57	86	6	180	142
35R-1, 0-4	769.50	62,016	143	12	19	0	434	356
36R-1, 0-3	779.20	68,309	168	18	32	0	407	313
36R-2, 0-3	780.70	68,970	405	51	71	4	170	130
37R-1, 0-5	788.90	98,651	939	157	272	19	105	71
38R-1, 0-5	798.50	114,993	840	105	140	11	137	105
38R-1, 145-150	799.95	77,951	538	81	110	8	145	106
39R-1, 0-5	808.10	115,164	619	76	93	8	186	145
39R-1, 102-107	809.12	130,670	744	106	144	12	176	130
40R-1, 0-5	817.80	142,045	2,308	222	330	32	52	49
41R-1, 0-5	827.10	102,922	502	87	98	17	205	146
41R-1, 50-55	827.60	58,632	274	59	67	13	214	142
42R-1, 0-2	836.80	57,401	309	83	90	21	186	114
42R-1, 73-75	837.53	65,417	252	49	44	10	260	184
42R-CC, 0-2	837.55	117,043	823	180	156	42	142	97
43R-1, 36-38	846.76	95,337	362	83	51	17	263	186
45R-2, 0-2	867.30	114,857	670	223	114	43	171	109
46R-3, 0-2	878.30	142,743	890	290	141	51	160	104
47R-2, 0-5	886.50	143,120	916	310	155	56	156	100
47R-3, 145-150	889.45	91,743	679	324	193	71	135	72
48R-2, 0-5	896.10	119,078	721	272	146	53	165	100
48R-2, 140-145	897.50	78,895	593	278	161	63	133	72
49R-1, 0-5	904.20	113,498	1,765	657	435	164	64	38
49R-2, 85-90	906.55	85,608	404	185	108	41	212	116
50R-2, 0-5	915.10	79,155	307	120	55	21	258	157
50R-4, 54-57	918.64	85,263	475	232	136	55	180	95
51R-1, 0-5	923.30	103,895	711	327	191	75	146	80
51R-2, 147-150	926.27	111,453	627	289	125	70	178	100
51R-5, 0-5	939.30	108,077	480	195	98	35	225	134
52R-1, 0-5	932.90	118,813	624	235	118	47	190	116
52R-2, 140-143	935.80	116,510	716	3,333	201	82	163	87
53R-1, 148-150	944.08	107,706	528	222	116	49	204	118
54R-1, 148-150	953.68	158,240	1,329	413	201	37	119	80
55R-1, 148-150	963.28	133,523	697	266	62	28	192	127
56R-1, 148-150	972.98	144,565	833	326	153	71	174	105
57R-1, 148-150	982.58	84,414	184	68	25	13	459	291
58R-1, 148-150	992.28	99,750	173	51	16	9	577	401
59R-1, 148-150	1001.98	75,963	107	36	13	8	710	463
60R-3, 0-3	1013.20	104,394	538	280	133	85	194	101
60R-4, 57-59	1015.27	117,014	655	367	197	128	179	87
61R-3, 0-3	1022.80	54,274	220	176	105	71	247	95
61R-6, 0-3	1027.30	107,439	764	536	343	233	141	57
62R-2, 145-150	1032.45	115,174	694	497	309	114	166	71
62R-3, 145-150	1033.95	8,141	97	127	89	65	84	22
62R-4, 103-108	1035.03	101,787	647	476	239	178	157	66
63R-2, 0-5	1040.60	92,299	722	614	191	279	128	51
63R-3, 54-56	1042.64	105,393	718	552	344	235	147	57
64R-1, 0-5	1048.80	101,674	503	340	181	129	202	88
64R-2, 23-25	1050.53	75,563	533	580	437	332	142	40
65R-1, 0-3	1058.40	98,729	595	453	247	188	166	67
65R-2, 0-3	1059.90	154,766	2,693	1,476	934	724	57	27
66R-1, 0-3	1068.10	127,944	1,061	825	452	373	121	47
66R-1, 56-59	1068.66	90,314	702	782	534	449	127	37
66R-2, 88-91	1069.57	128,448	1,559	1,183	823	598	82	31
67R-2, 0-2	1079.20	116,175	767	657	348	279	151	57
67R-3, 0-2	1080.70	140,481	1,166	828	395	328	120	52

n.d. = not determined.

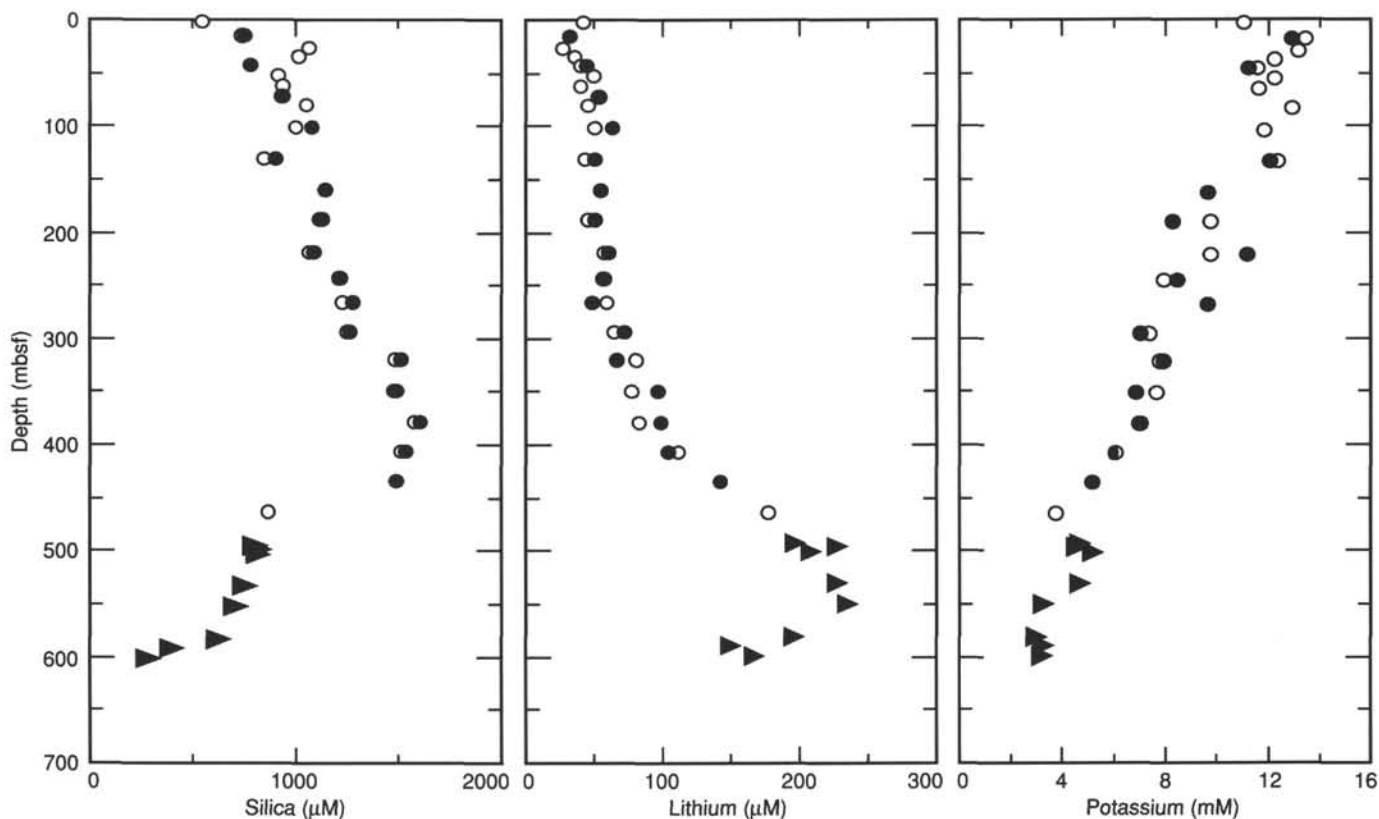


Figure 120. Interstitial-water silica, lithium, and potassium concentrations vs. depth, Site 799. Closed circles = standard ODP stainless-steel squeezer, Hole 799A; open circles = Brumsack-Murray, Teflon-lined squeezer, Hole 799A; closed triangles = Hole 799B.

originally recorded in feet below rig floor, but have been converted to meters below seafloor for comparison with other shipboard data.

All of the logs will be subject to post-cruise processing to correct borehole effects, such as washouts and mud composition, but with the good hole conditions encountered at Hole 799A, these should be fairly minor. The exception being the data recorded from the geochemical spectroscopy tool (GST), which will require considerable post-cruise processing at Lamont-Doherty Geological Observatory. These spectral data require deconvolution to account for the disproportionate absorption effect of large atoms, such as chlorine. References made to silicon, iron, calcium, sulfur, chlorine, and hydrogen at this stage thus are only qualitative, and the log plots are not shown. However, the natural gamma-ray spectroscopy tool (NGT) produces reliable values for the concentration of potassium, thorium, and uranium, but the aluminum log produced by the aluminum clay tool (ACT) is generally not significantly affected by post-cruise processing. The FMS also requires considerable computer processing at Lamont-Doherty to produce the final images, although preliminary images are produced on board the ship within 2 days after logging. Full processing on board the ship of the images should be possible during future cruises.

During logging at Hole 799B, the seas were calm and while this should have been favorable for logging, several problems arose from this condition. The wireline heave compensator had difficulty coping with the low-amplitude waves; thus, it overheated and was temporarily inoperable during the first and fourth logging runs. This caused depth offsets within the seismic stratigraphic and geochemical logging runs that will need to be corrected during post-cruise processing. We decided not to use the heave compensator during FMS logging,

but shipboard processing of these data shows that the FMS log contains numerous regularly spaced, stretched intervals of ~30 cm, each indicating that the tool was being jerked up the borehole by the ship's heave.

Log Characteristics

Site 799 can be divided into six units based on the wireline logs. In Hole 799A logs, Unit I can be recognized from the base of the pipe (105 mbsf) to 154 mbsf; Unit II, from 154 to 435 mbsf; Unit III, from 435 to 458 mbsf; and Unit IV, from 458 to TD at 468 mbsf.

The boundary between Units I and II was selected where a slight decrease in the baseline of the total gamma ray curve occurs (Fig. 138). Associated with this decrease is a slight decrease in bulk density from 1.5 to 1.4 g/cm³. The change in gamma-ray and density readings may reflect a decrease in clay content in the underlying unit.

Unit II shows little variation in log patterns, except for several isolated shaley layers of 1 to 1.5 m thick at depths of 308, 324, and 344 mbsf (Fig. 138). These are recognized by sharp peaks or increases in the gamma-ray (SGR) curve, higher resistivity readings, higher aluminum content, and an increase in bulk density. Several of these layers were observed in the cores as more lithified, clay-rich layers.

A dolomite layer was identified from the logs at 247 to 248.2 mbsf (Fig. 138) by much lower gamma-ray readings, high resistivity, an increase in sonic velocity (decreasing sonic traveltime), as well as by a sharp increase in abundance of calcium from the GST. The velocity contrast of the dolomitic layer produced cycle-skipping in the sonic log at this depth. In addition, the layer had a density of 2.2 g/cm³ and a low porosity (thermal neutron porosity TNPH of 0.33). The caliper log indicated a constriction in hole diameter at this depth,

Table 12. Volatile hydrocarbon data from vacutainer analysis, Site 799.

Core, section, interval (cm)	Depth (mbsf)	C ₁	C ₂	C ₃	<i>i</i> -C ₄	<i>n</i> -C ₄	C ₁ /C ₂	C ₁ /C ₂₊
128-799A-14H-2, 130-134	119.3	913,227	447	38	n.d.	n.d.	2,043	1,883
18H-2, 143-146	158.13	793,891	493	52	n.d.	n.d.	1,610	1,457
19H-1, 83-87	165.63	884,340	584	61	n.d.	n.d.	1,514	1,371
20H-1, 43-55	174.93	898,586	638	72	n.d.	n.d.	1,408	1,266
21X-5, 10-13	190.2	932,916	715	73	n.d.	n.d.	1,305	1,184
22X-5, 20-23	200	679,200	516	50	n.d.	n.d.	1,316	1,200
23X-4, 123-130	209.23	646,811	529	52	n.d.	n.d.	1,223	1,113
24X-4, 120-126	218.8	790,020	686	64	n.d.	n.d.	1,152	1,053
25X-5, 48-56	229.28	560,603	535	50	n.d.	n.d.	1,048	958
27X-4, 12-20	246.02	594,713	560	43	n.d.	n.d.	1,062	986
30X-4, 139-141	266.39	886,231	925	59	n.d.	n.d.	958	901
31X-4, 84-105	275.54	745,362	722	34	n.d.	n.d.	1,032	986
32X-3, 122-126	282.42	581,290	16	0	n.d.	n.d.	36,331	36,331
33X-5, 55-57	294.45	491,892	472	19	n.d.	n.d.	1,042	1,002
37X-6, 5-8	334.15	590,596	644	15	n.d.	n.d.	917	896
37X-6, 148-149	335.58	686,193	263	13	11	0	2,609	2,391
38X-3, 118-120	340.38	950,012	956	21	0	0	994	972
38X-7, 12-15	345.32	484,789	918	409	58	16	528	346
39X-6, 138-148	354.78	865,601	951	26	0	0	910	886
40X-5, 36-40	361.96	887,722	957	24	0	0	928	905
40X-5, 37-40	361.97	708,508	260	13	6	0	2,725	2,539
42X-1, 77-103	375.77	892,682	1,147	22	0	0	778	764
42X-1, 78-103	375.78	773,726	338	12	7	0	2,289	2,167
44X-1, 114-116	395.44	578,290	878	12	0	0	659	650
45X-4, 106-110	409.46	571,367	762	10	0	0	750	740
46X-5, 3-5	419.63	855,137	382	9	8	0	2,239	2,143
46X-5, 122-125	420.82	833,535	1,200	11	0	0	695	688
47X-5, 72-77	430.02	611,129	808	9	0	0	756	748
50X-3, 20-24	455.5	1,592	4	0	0	0	398	398
50X-4, 59-62	457.39	634,935	860	9	0	0	738	720
51X-2, 50-57	463.9	578,225	827	9	0	0	699	666
128-799B-11R-3	541.3	723,593	1,286	31	18	51	563	522
12R-3	550.9	322,451	553	17	13	0	583	553
13R-3	560.6	757,561	1,680	30	32	0	451	435
14R-3	570.3	790,785	1,852	27	37	52	427	402
17R-3	599.3	648,145	1,590	22	40	0	408	392

n.d. = not detected.

suggesting that the layer is more competent than the sediments above or below it; the hole diameter above this layer has been enlarged to more than 15 in. because of washouts of softer lithology and narrows to 13 in. in this layer (bit size is 9 7/8 in.).

Unit III is defined by pronounced peaks in the resistivity log. These peaks result from cemented or silicified layers (see "Lithostratigraphy" section, this chapter). Associated with the higher resistivities are increases in bulk density to 1.5 g/cm³ or more. The layers having higher density and resistivity in the interval from 437 to 458 mbsf (Fig. 138) probably represent layers where opal-A has been converted to opal-CT (see "Lithostratigraphy" section, this chapter).

Unit IV has a well-defined increase in bulk density of 1.7 to 1.8 g/cm³ at 458 mbsf. Associated with this increase in density is an increase in resistivity (lower porosity). The SGR did not record this interval because it was at the bottom of the hole. However, the increased density and higher resistivity suggest that these beds are more lithified or better cemented. The layers having the highest resistivity and bulk density correspond to chert and dolomite layers that were observed in Cores 128-799A-51X and 128-799A-52X (see "Lithostratigraphy" section, this chapter).

Hole 799B can be subdivided into four units based on changes in the character of the logs: Unit III from 440-455 mbsf, Unit IV from 455-800 mbsf, Unit V from 800-1010 mbsf and Unit VI from 1010 mbsf to TD (Fig. 139). The uppermost two units, Units III and IV, correspond to the same units that were recovered in the bottom of Hole 799A. The siliceous claystones of Unit III from the top of the logged interval (440

to 455 mbsf) are characterized by relatively low gamma-ray, bulk-density, resistivity, and sonic-velocity values. These responses reflect the low clay content and relatively high porosities of these sediments.

As at Hole 799A, Unit IV is indicated by sharp increases in gamma-ray, bulk-density, and resistivity values and intermittently high sonic velocities (Fig. 139). Core recovery in the uppermost portion of Unit IV was poor at Hole 799B, but Hole 799A sediments indicated numerous thin, dolomite and/or siderite layers, and diagenetic opal-CT was abundant. The FMS images clearly resolve these as discrete high-resistivity (low porosity) layers. These layers become more abundant and generally thicker in the lower portion of Unit IV, particularly between 710 and 790 mbsf (Fig. 140). For example, the high calcium, low iron abundances from the GST suggest that the resistivity and velocity peak centered at 732 mbsf is probably a dolomite layer, which the FMS images indicate is more than 2 m thick. The neutron-density values of these sediments average 2.7 g/cm³, which is consistent with standard physical-property estimates. Note that core recovery was poor throughout the 455 to 800 mbsf interval of Unit IV because of drilling contrasts of the interbedded lithologies.

Below ~575 mbsf in Unit IV, the shipboard XRD data indicate that opal-CT is being replaced by authigenetic quartz (see "Lithostratigraphy" section, this chapter). As shown in Figure 139, all the physical-property logs demonstrate an appropriate response to this change: all bulk densities, resistivities, and sonic velocities increase significantly.

The transition to Unit V at 800 mbsf is characterized by a gradual shift to increasingly higher bulk densities, resistivities,

Table 13 . Concentrations of inorganic carbon, total carbon, total nitrogen, and total sulfur in samples from Site 799.

Core, section, interval (cm)	Depth (mbsf)	Total carbon (%)	Inorganic carbon (%)	Organic carbon (%)	CaCO ₃ (%)	Nitrogen (%)	Sulfur (%)	C _{org} /N	C _{org} /S
128-799A-1H-1, 5-6	0.05	1.20	0.11	1.09	0.9	0.10	0.12	10.90	0.08
1H-1, 19-20	0.19	1.23	0.17	1.06	1.4	0.16	0.18	6.62	5.89
1H-1, 44-48	0.44	1.36	0.08	1.28	0.7	0.18	0.18	7.11	7.11
1H-1, 65-66	0.65	1.55	0.11	1.44	0.9	0.14	0.18	10.30	8.00
1H-1, 100-101	1.00	1.78	0.55	1.23	4.6	0.16	0.51	7.69	2.41
2H-1, 30-32	1.50	1.50	0.48	1.02	4.0	0.11	0.74	9.27	1.38
2H-1, 107-109	2.27	3.27	1.76	1.51	14.7	0.14	0.94	10.80	1.60
2H-2, 76-80	3.46	1.13	0.13	1.00	1.1	0.08	0.82	12.50	1.22
2H-4, 74-78	6.44	1.54	0.33	1.21	2.7	0.15	0.57	8.06	2.12
2H-6, 44-48	9.14	1.18	0.16	1.02	1.3	0.14	0.86	7.28	1.18
3H-2, 10-15	12.30	2.48	1.77	0.71	14.7	0.11	0.25	6.40	2.80
3H-4, 6-11	15.26	1.58	0.42	1.16	3.5	0.11	1.94	10.50	0.60
3H-5, 25-30	16.95	1.71	0.39	1.32	3.3	0.13	0.87	10.10	1.52
3H-6, 10-15	18.30	1.40	0.17	1.23	1.4	0.13	0.79	9.46	1.55
4H-2, 20-25	22.00	0.97	0.65	0.32	5.4	0.04	0.29	8.00	1.10
4H-4, 20-25	25.00	1.60	0.46	1.14	3.8	0.13	0.56	8.77	2.03
4H-6, 0-5	27.80	2.86	0.13	2.73	1.1	0.25	3.05	10.90	0.90
4H-6, 20-23	28.00	3.16	0.11	3.05	0.9	0.29	1.17	10.50	2.60
5H-2, 20-25	31.60	1.57	1.19	0.38	9.9	0.07	0.79	5.40	0.48
5H-4, 20-25	34.60	1.96	0.79	1.17	6.6	0.15	1.13	7.80	1.03
5H-6, 20-25	37.60	1.33	0.41	0.92	3.4	0.09	2.45	10.00	0.38
5H-6, 20-25	37.60	1.33	0.41	0.92	3.4	0.09	2.45	10.00	0.38
5H-7, 41-42	39.31	6.50	5.69	0.81	47.4	0.09	0.02	9.00	40.00
5H-7, 51-52	39.41	7.44	6.06	1.38	50.5	0.09	0.13	15.30	10.60
6H-2, 20-25	41.20	2.50	1.32	1.18	11.0	0.11	0.88	10.70	1.34
6H-3, 145-146	43.95	3.48	2.42	1.06	20.2	0.09	1.19	11.80	0.89
6H-3, 147-148	43.97	8.79	6.21	2.58	51.7	0.20	0.18	12.90	14.30
6H-3, 149-150	43.99	8.82	6.10	2.72	50.8	0.19	0.38	14.30	7.16
6H-4, 20-25	44.20	1.54	0.14	1.40	1.2	0.15	0.78	9.33	1.79
6H-6, 20-25	47.20	1.09	0.31	0.78	2.6	0.09	3.14	8.60	0.25
7H-2, 40-44	51.00	0.97	0.40	0.57	3.3	0.08	1.28	7.10	0.45
7H-4, 40-44	54.00	3.15	1.65	1.50	13.7	0.13	0.56	11.50	2.68
7H-6, 38-42	56.98	1.30	0.65	0.65	5.4	0.07	0.75	9.30	0.86
8H-2, 19-31	60.39	2.80	2.06	0.74	17.2	0.09	0.23	8.20	3.20
8H-2, 70-74	60.90	3.78	3.42	0.36	28.5	0.07	0.23	5.10	1.50
8H-2, 96-98	61.16	4.54	3.44	1.10	28.7	0.10	0.19	11.00	5.79
8H-3, 62-64	62.32	4.72	4.20	0.52	35.0	0.08	0.05	6.50	10.00
8H-4, 60-64	63.80	1.07	0.56	0.51	4.7	0.07	0.85	7.30	0.60
8H-6, 50-54	66.70	6.03	0.39	5.64	3.2	0.12	0.17	47.00	33.20
8H-6, 148-149	67.68	4.34	0.10	4.24	0.8	0.34	0.80	12.50	5.30
9H-2, 30-35	70.10	5.38	4.29	1.09	35.7	0.08	0.11	13.60	9.91
9H-4, 5-10	72.85	2.07	1.23	0.84	10.2	0.10	0.53	8.40	1.60
9H-6, 30-35	76.10	2.32	1.78	0.54	14.8	0.05	0.15	11.00	3.60
10H-1, 25-30	78.15	2.16	1.32	0.84	11.0	0.10	0.16	8.40	5.20
10H-4, 25-30	82.65	1.22	0.39	0.83	3.2	0.10	1.30	8.30	0.64
10H-6, 120-125	86.60	0.62	0.17	0.45	1.4	0.05	0.92	9.00	0.49
11H-2, 20-25	89.20	0.59	0.18	0.41	1.5	0.11	1.34	3.70	0.31
11H-4, 60-65	92.60	0.96	0.07	0.89	0.6	0.13	0.59	6.80	1.50
11H-4, 145-150	93.45	1.91	0.29	1.62	2.4	0.12	1.20	13.50	1.35
11H-6, 100-105	96.00	0.67	0.27	0.40	2.2	0.05	0.54	8.00	0.74
12H-2, 20-25	98.90	0.62	0.34	0.28	2.8	0.05	0.63	5.60	0.44
12H-4, 30-35	102.00	1.75	1.05	0.70	8.7	0.06	0.64	11.00	1.10
12H-5, 16-18	103.36	4.80	1.92	2.88	16.0	0.23	0.36	12.50	8.00
12H-6, 20-25	104.90	2.38	1.69	0.69	14.1	0.11	0.76	6.30	0.91
13H-2, 26-31	108.56	1.07	0.40	0.67	3.3	0.10	0.66	6.70	1.00
13H-4, 20-25	111.50	1.73	0.88	0.85	7.3	0.12	0.96	7.10	0.88
13H-4, 145-150	112.75	1.00	0.30	0.70	2.5	0.10	1.13	7.00	0.62
13H-6, 20-25	114.50	3.43	2.89	0.54	24.1	0.09	0.83	6.00	0.65
14H-1, 2-3	116.52	5.30	0.29	5.01	2.4	0.33	2.49	15.20	2.01
14H-2, 45-45	118.40	1.12	0.90	0.22	7.5	0.06	0.49	3.60	0.45
14H-5, 2-3	122.52	4.61	4.16	0.45	34.7	0.03	0.00	15.00	—
14H-5, 40-45	122.90	1.69	1.45	0.24	12.1	0.05	0.30	4.80	0.80
14H-6, 30-35	124.30	0.43	0.09	0.34	0.7	0.10	0.65	3.40	0.52
15H-2, 55-59	128.15	0.35	0.11	0.24	0.9	0.06	0.92	4.00	0.26
15H-4, 54-58	131.14	0.56	0.13	0.43	1.1	0.09	0.97	4.80	0.44
15H-5, 0-5	132.10	0.44	0.03	0.41	0.2	0.09	0.78	4.50	0.52
15H-6, 54-58	134.14	2.55	0.93	1.62	7.7	0.16	1.15	10.10	1.41
16H-2, 60-65	137.90	0.40	0.24	0.16	2.0	0.03	1.08	5.30	0.15
16H-4, 60-65	140.90	2.58	1.02	1.56	8.5	0.16	1.53	9.75	1.02
16H-6, 60-65	143.90	2.42	0.93	1.49	7.7	0.15	1.12	9.93	1.33
17H-2, 0-5	147.00	1.46	0.10	1.36	0.8	0.14	0.83	9.71	1.64
17H-2, 55-60	147.55	1.91	0.37	1.54	3.1	0.11	1.00	14.00	1.54

Table 13 (continued).

Core, section, interval (cm)	Depth (mbsf)	Total carbon (%)	Inorganic carbon (%)	Organic carbon (%)	CaCO ₃ (%)	Nitrogen (%)	Sulfur (%)	C _{org} /N	C _{org} /S
17H-4, 40-45	150.40	1.85	0.18	1.67	1.5	0.18	1.39	9.28	1.20
17H-6, 40-45	153.40	2.81	0.33	2.48	2.7	0.22	0.95	11.30	2.61
18H-2, 25-30	156.95	0.91	0.19	0.72	1.6	0.07	0.87	10.00	0.83
18H-4, 40-45	160.10	2.55	0.28	2.27	2.3	0.21	1.33	10.80	1.70
18H-6, 40-45	163.10	3.14	1.15	1.99	9.6	0.18	1.44	11.00	1.38
19H-4, 15-20	169.45	0.57	0.04	0.53	0.3	0.09	0.56	5.90	0.94
19H-5, 0-5	170.80	0.84	0.06	0.78	0.5	0.10	0.55	7.80	1.40
20H-2, 20-25	176.20	3.42	2.15	1.27	17.9	0.13	0.92	9.77	1.38
20H-4, 20-25	179.20	1.13	0.17	0.96	1.4	0.12	0.66	8.00	1.40
20H-6, 20-25	182.20	2.76	2.02	0.74	16.8	0.11	1.32	6.70	0.56
21X-2, 20-25	185.80	0.52	0.04	0.48	0.3	0.09	0.57	5.30	0.84
21X-4, 20-25	188.80	1.34	0.09	1.25	0.7	0.08	0.48	15.60	2.60
21X-4, 125-130	189.85	0.61	0.07	0.54	0.6	0.09	0.79	6.00	0.68
21X-6, 20-25	191.80	0.98	0.54	0.44	4.5	0.08	0.57	5.50	0.77
22X-2, 77-81	196.07	1.38	0.23	1.15	1.9	0.14	1.35	8.21	0.85
22X-3, 5-7	196.85	5.84	5.28	0.56	44.0	0.10	0.11	5.60	5.10
22X-4, 34-38	198.64	0.91	0.07	0.84	0.6	0.11	0.97	7.60	0.86
22X-6, 34-38	201.64	0.87	0.39	0.48	3.2	0.05	0.93	9.60	0.51
22X-6, 67-69	201.97	6.99	6.16	0.83	51.3	0.07	0.02	12.00	41.00
22X-6, 130-132	202.60	1.77	0.74	1.03	6.2	0.15	0.19	6.86	5.42
23X-2, 29-33	205.29	3.95	2.08	1.87	17.3	0.14	0.61	13.30	3.06
23X-4, 20-24	208.20	1.39	0.16	1.23	1.3	0.13	0.88	9.46	1.40
23X-4, 21-25	208.21	0.76	0.11	0.65	0.9	0.09	0.56	7.20	1.10
23X-4, 148-150	209.48	2.59	0.63	1.96	5.2	0.16	1.30	12.20	1.51
23X-6, 16-20	211.16	2.34	0.80	1.54	6.7	0.12	1.16	12.80	1.33
24X-2, 132-136	215.92	1.23	0.12	1.11	1.0	0.12	0.74	9.25	1.50
24X-4, 98-102	218.58	2.25	1.02	1.23	8.5	0.11	0.91	11.20	1.35
24X-6, 20-24	220.80	2.07	0.54	1.53	4.5	0.15	1.13	10.20	1.35
25X-2, 112-116	225.42	1.04	0.08	0.96	0.7	0.12	1.51	8.00	0.64
25X-4, 113-117	228.43	1.34	0.22	1.12	1.8	0.12	0.79	9.33	1.42
25X-5, 148-150	230.28	1.40	0.07	1.33	0.6	0.13	1.02	10.20	1.30
25X-6, 112-116	231.42	0.59	0.04	0.55	0.3	0.10	0.70	5.50	0.78
27X-2, 25-29	243.15	1.32	0.15	1.17	1.2	0.13	0.73	9.00	1.60
27X-3, 0-5	244.40	2.20	1.07	1.13	8.9	0.09	0.64	12.50	1.76
29X-2, 25-30	252.65	3.00	0.13	2.87	1.1	0.09	0.07	31.90	41.00
29X-4, 0-5	255.40	2.24	1.38	0.86	11.5	0.08	0.52	11.00	1.60
29X-4, 22-27	255.62	1.19	0.18	1.01	1.5	0.12	0.90	8.41	1.12
30X-6, 55-60	268.55	3.08	1.32	1.76	11.0	0.05	0.27	35.20	6.52
31X-2, 0-5	271.70	1.62	0.11	1.51	0.9	0.14	1.06	10.80	1.42
32X-2, 50-55	280.20	1.37	0.47	0.90	3.9	0.11	0.82	8.20	1.10
32X-4, 50-55	283.20	1.86	0.25	1.61	2.1	0.15	0.63	10.70	2.55
33X-4, 0-5	292.40	0.98	0.13	0.85	1.1	0.08	0.85	10.00	1.00
33X-4, 66-71	293.06	0.56	0.03	0.53	0.2	0.09	0.51	5.90	1.00
35X-2, 66-70	309.46	0.71	0.09	0.62	0.7	0.16	0.65	3.90	0.95
35X-4, 21-22	312.01	0.46	0.04	0.42	0.3	0.07	0.67	6.00	0.62
35X-4, 55-57	312.35	0.63	0.18	0.45	1.5	0.06	0.40	7.50	1.10
35X-4, 66-70	312.46	0.58	0.10	0.48	0.8	0.07	0.49	6.80	0.98
35X-4, 98-99	312.78	0.60	0.07	0.53	0.6	0.07	0.61	7.60	0.87
35X-4, 137-138	313.17	0.56	0.05	0.51	0.04	0.06	0.55	8.50	0.93
35X-4, 141-142	313.21	1.32	0.77	0.55	6.4	0.07	0.56	7.80	0.98
35X-6, 66-70	315.46	0.54	0.08	0.46	0.7	0.09	0.70	5.10	0.66
36X-2, 30-34	318.70	1.06	0.40	0.66	3.3	0.09	0.47	7.30	1.40
36X-4, 30-34	321.70	0.71	0.13	0.58	1.1	0.10	0.60	5.80	0.96
36X-6, 30-34	324.70	0.56	0.04	0.52	0.3	0.09	0.69	5.80	0.75
37X-2, 68-72	328.78	0.59	0.06	0.53	0.5	0.10	0.94	5.30	0.56
37X-4, 0-5	331.10	1.05	0.24	0.81	2.0	0.09	0.84	9.00	0.96
37X-6, 24-28	334.34	0.95	0.08	0.87	0.7	0.11	0.64	7.90	1.30
38X-4, 29-33	340.9	1.14	0.19	0.95	1.6	0.12	0.73	7.90	1.30
38X-6, 29-33	343.99	0.63	0.02	0.61	0.2	0.13	0.84	4.70	0.72
39X-2, 40-44	347.80	1.41	0.73	0.68	6.1	0.12	0.84	5.60	0.81
39X-4, 0-5	350.40	0.70	0.16	0.54	1.3	0.23	0.73	2.30	0.74
39X-4, 40-44	350.80	1.33	0.17	1.16	1.4	0.14	0.89	8.28	1.30
39X-6, 40-44	353.80	1.58	0.37	1.21	3.1	0.15	1.03	8.06	1.17
40X-2, 94-98	358.04	0.98	0.06	0.92	0.5	0.11	0.74	8.30	1.20
40X-4, 0-5	360.10	1.29	0.33	0.96	2.7	0.12	1.07	8.00	0.90
40X-4, 103-107	361.13	0.84	0.04	0.80	0.3	0.10	0.61	8.00	1.30
40X-6, 107-111	364.17	2.24	1.33	0.91	11.1	0.12	1.03	7.60	0.88
41X-1, 0-5	365.30	1.48	0.34	1.14	2.8	0.12	1.23	9.50	0.93
41X-2, 23-28	367.03	0.75	0.04	0.71	0.3	0.09	0.33	7.90	2.10
41X-4, 52-57	370.32	1.57	0.06	1.51	0.5	0.16	0.81	9.44	1.86
41X-6, 30-35	373.10	0.93	0.06	0.87	0.5	0.11	0.66	7.90	1.30
42X-6, 80-85	383.30	2.77	0.98	1.79	8.2	0.16	1.04	11.20	1.72
43X-2, 40-45	386.50	1.05	0.14	0.91	1.2	0.12	0.88	7.60	1.00

Table 13 (continued).

Core, section, interval (cm)	Depth (mbsf)	Total carbon (%)	Inorganic carbon (%)	Organic carbon (%)	CaCO ₃ (%)	Nitrogen (%)	Sulfur (%)	C _{org} /N	C _{org} /S
43X-4, 0-5	389.10	1.86	0.59	1.27	4.9	0.12	0.58	10.60	2.19
43X-4, 40-45	389.50	1.92	0.42	1.50	3.5	0.15	0.79	10.00	1.90
43X-6, 40-45	392.50	2.54	0.31	2.23	2.6	0.20	1.22	11.10	1.83
44X-1, 0-5	394.30	2.04	0.39	1.65	3.3	0.13	0.47	12.70	3.51
44X-2, 10-15	395.90	1.54	0.31	1.23	2.6	0.15	1.14	8.20	1.08
45X-2, 44-49	405.84	2.30	1.63	0.67	13.6	0.11	0.92	6.10	0.73
45X-4, 0-5	408.40	0.48	1.23	4.0	0.15	1.09	8.20	1.13	
45X-4, 47-52	408.87	1.33	0.10	1.23	0.8	0.14	1.07	8.87	1.15
46X-1, 83-84	414.43	0.88	0.04	0.84	0.3	0.04	0.53	21.00	1.60
46X-2, 20-25	415.30	0.85	0.04	0.81	0.3	0.14	0.94	5.80	0.86
46X-4, 0-5	418.10	1.19	0.05	1.14	0.4	0.16	1.06	7.12	1.07
46X-4, 20-25	418.30	1.15	0.05	1.10	0.4	0.14	0.79	7.86	1.39
46X-6, 20-25	421.30	1.42	0.06	1.36	0.5	0.15	0.55	9.06	2.47
47X-2, 101-103	425.81	2.22	0.33	1.89	2.7	0.18	1.33	10.50	1.42
47X-4, 126-130	429.06	2.89	1.16	1.73	9.7	0.19	1.03	9.10	1.68
47X-5, 0-5	429.30	1.63	0.37	1.26	3.1	0.18	1.03	7.00	1.22
47X-6, 144-148	432.24	2.60	0.45	2.15	3.7	0.20	1.45	10.70	1.48
48X-1, 0-5	432.90	1.16	0.06	1.10	0.5	0.12	0.80	9.16	1.37
48X-1, 30-31	433.20	1.58	0.17	1.41	1.4	0.15	0.84	9.40	1.68
48X-1, 43-43	433.33	0.94	0.09	0.85	0.7	0.13	1.24	6.50	0.69
48X-1, 44-46	433.34	1.02	0.13	0.89	1.1	0.08	0.64	11.00	1.40
48X-1, 61-62	433.51	1.78	0.44	1.34	3.7	0.13	0.57	10.30	2.35
48X-1, 77-78	433.67	9.57	8.73	0.84	72.7	0.05	0.02	17.00	42.00
48X-1, 95-96	433.85	2.04	0.84	1.20	7.0	0.11	0.74	10.90	1.62
48X-1, 109-111	433.99	0.55	0.10	0.45	0.8	0.05	0.31	9.00	1.40
48X-1, 121-122	434.11	1.08	0.10	0.98	0.8	0.11	0.79	8.90	1.20
48X-2, 46-50	434.86	0.94	0.03	0.91	0.2	0.13	0.75	7.00	1.20
48X-3, 31-31	436.21	5.66	4.57	1.09	38.1	0.12	0.18	9.08	6.05
49X-CC, 38-39	443.95	4.61	0.38	4.23	3.2	0.32	1.68	13.20	2.52
50X-2, 88-92	454.68	3.26	0.21	3.05	1.7	0.26	1.39	11.70	2.19
50X-3, 148-150	456.78	2.62	0.91	0.71	7.6	0.28	1.03	6.11	1.66
50X-4, 22-23	457.02	0.20	0.07	0.13	0.6	0.12	0.90	1.10	0.14
50X-4, 58-59	457.38	4.41	1.44	2.97	12.0	0.25	1.25	11.90	2.37
50X-4, 93-97	457.73	2.89	0.36	2.53	3.0	0.21	1.06	12.00	2.38
50X-5, 62-63	458.92	3.72	0.35	3.37	2.9	0.26	1.40	12.90	2.41
50X-5, 69-70	458.99	3.26	0.01	3.25	0.1	0.23	0.96	14.10	3.38
50X-5, 125-127	459.55	0.98	0.09	0.89	0.7	0.10	0.61	8.90	1.40
50X-5, 140-141	459.70	1.60	0.05	1.55	0.4	0.13	0.77	11.90	2.01
50X-6, 38-40	460.18	1.63	0.15	1.48	1.2	0.13	0.41	11.40	3.61
50X-6, 40-41	460.20	1.86	0.06	1.80	0.5	0.16	0.90	11.20	2.00
50X-6, 76-77	460.56	4.51	3.52	0.99	29.3	0.11	0.80	9.00	1.20
51X-1, 3-5	461.93	1.47	0.31	1.16	2.6	0.12	0.73	9.66	1.59
51X-1, 20-21	462.10	2.97	1.62	1.35	13.5	0.16	0.70	8.44	1.93
51X-1, 50-51	462.40	1.31	—	—	—	0.11	0.81	—	—
51X-1, 66-67	462.56	2.21	0.18	2.03	1.5	0.20	0.97	10.10	2.09
51X-1, 126-127	463.16	1.64	0.31	1.33	2.6	0.16	1.31	8.31	1.01
51X-2, 80-84	464.20	4.70	3.77	0.93	31.4	0.14	1.13	6.60	0.82
51X-2, 110-115	464.50	1.77	0.37	1.40	3.1	0.14	1.34	10.00	1.04
128-799B-5R-1, 14-18									
5R-1, 90-94	490.50	4.40	0.08	4.32	0.7	0.31	1.77	13.90	2.44
5R-2, 40-44	491.50	4.47	0.26	4.21	2.2	0.32	1.87	13.10	2.25
6R-1, 33-38	494.93	5.80	0.14	5.66	1.2	0.41	2.87	13.80	1.97
6R-3, 10-15	497.70	3.12	0.18	2.94	1.5	0.24	1.13	12.20	2.60
7R-1, 20-25	499.90	3.60	0.07	3.53	0.6	0.28	1.02	13.10	3.46
7R-3, 30-35	503.00	4.58	0.05	4.53	0.4	0.35	1.24	12.90	3.65
8R-1, 95-99	510.25	2.97	0.09	2.88	0.7	0.22	1.11	13.10	2.59
8R-3, 53-57	512.83	3.36	0.16	3.20	1.3	0.26	1.27	12.30	2.52
8R-6, 16-20	516.96	3.17	0.07	3.10	0.6	0.21	1.10	14.70	2.82
9R-2, 91-95	521.41	2.90	0.16	2.74	1.3	0.20	1.14	13.70	2.40
9R-4, 123-125	524.73	2.68	0.12	2.56	1.0	0.18	0.57	14.20	4.49
10R-2, 0-2	530.10	3.59	0.35	3.24	2.9	0.28	1.25	11.60	2.59
10R-2, 127-131	531.37	2.83	0.20	2.63	1.7	0.22	1.18	11.90	2.23
10R-4, 64-67	533.74	3.18	0.27	2.91	2.2	0.26	1.38	11.20	2.11
11R-2, 23-26	540.03	3.41	0.74	2.67	6.2	0.21	0.49	12.70	5.45
11R-5, 29-31	544.59	3.76	0.24	3.52	3.0	—	0.18	—	19.50
11R-6, 0-2	545.80	4.61	0.46	4.15	3.8	0.31	1.23	13.40	3.37
11R-7, 32-35	547.62	4.05	0.29	3.76	2.4	0.30	0.86	12.50	4.37
12R-3, 34-37	551.24	4.64	—	—	—	0.33	1.40	—	—
12R-4, 0-2	552.40	3.88	1.82	2.06	15.2	0.18	1.12	11.40	1.84
12R-4, 71-74	553.11	10.91	9.57	1.34	79.7	0.09	0.05	14.90	26.80
13R-1, 56-61	558.16	4.33	2.33	2.00	19.4	0.21	1.41	9.52	1.42
13R-3, 60-65	561.20	2.64	0.25	2.39	2.1	0.23	1.10	10.40	2.17

Table 13 (continued).

Core, section, interval (cm)	Depth (mbsf)	Total carbon (%)	Inorganic carbon (%)	Organic carbon (%)	CaCO ₃ (%)	Nitrogen (%)	Sulfur (%)	C _{org} /N	C _{org} /S
13R-4, 148-150	563.58	3.21	0.23	2.98	1.9	0.25	2.34	11.90	1.27
14R-1, 85-90	568.15	4.57	1.76	2.81	14.7	0.25	1.54	11.20	1.82
14R-2, 148-150	570.28	4.32	0.14	4.18	1.2	0.2	1.10	19.00	3.80
14R-3, 55-60	570.85	3.67	1.00	2.67	8.3	0.18	1.13	14.80	2.36
15R-1, 25-30	577.25	6.55	0.19	6.36	1.6	0.38	1.35	16.70	4.71
15R-2, 148-150	579.98	6.49	1.52	4.97	12.7	0.31	2.19	16.00	2.27
15R-4, 5-10	581.55	5.14	0.11	5.03	0.9	0.36	3.20	14.00	1.57
16R-1, 80-85	587.40	3.91	0.11	3.80	0.9	0.18	0.24	21.10	15.80
16R-3, 110-115	590.70	3.45	0.46	2.99	3.8	0.24	0.77	12.40	3.88
16R-3, 138-140	590.98	4.65	0.14	4.51	1.2	0.29	1.21	15.50	3.73
17R-1, 25-30	596.55	2.19	0.36	1.83	3.0	0.19	1.29	9.63	1.42
17R-3, 35-40	599.65	2.43	0.31	2.12	2.6	0.18	0.55	11.80	3.85
17R-4, 0-5	600.80	3.96	0.88	3.08	7.3	0.26	1.39	11.80	2.21
17R-5, 30-35	602.60	2.26	0.63	1.63	5.2	0.11	0.03	14.80	54.30
18R-1, 143-147	607.33	2.90	0.99	1.91	8.3	0.19	0.99	10.00	—
18R-3, 89-91	609.79	4.33	0.35	3.98	2.9	0.23	0.51	17.30	7.80
18R-4, 139-141	611.79	2.70	0.93	1.77	7.7	0.18	0.62	9.83	2.85
18R-6, 0-3	613.40	5.19	3.10	2.09	25.8	0.16	0.58	13.00	3.60
19R-1, 77-81	616.37	3.43	0.74	2.69	6.2	0.24	1.35	11.20	1.99
19R-3, 80-84	619.40	4.47	1.76	2.71	14.7	0.22	0.56	12.30	4.84
19R-4, 0-3	620.10	2.87	0.54	2.33	4.5	0.15	0.75	15.50	3.10
19R-5, 55-59	622.15	3.18	0.35	2.83	2.9	0.22	1.28	12.80	2.21
20R-1, 83-86	626.03	3.11	0.08	3.03	0.7	0.28	1.24	10.80	2.44
20R-3, 34-37	628.54	5.94	0.22	5.72	1.8	—	0.26	—	22.00
20R-3, 96-100	629.16	—	0.78	—	6.5	—	—	—	—
20R-5, 62-63	631.82	9.45	4.69	4.76	39.1	—	0.24	—	19.80
20R-5, 108-112	632.28	3.32	0.24	3.08	2.0	0.30	1.52	10.20	2.02
21R-2, 61-65	637.01	2.54	—	—	—	0.14	0.70	—	—
21R-3, 80-84	638.70	1.93	0.52	1.41	4.3	0.10	0.05	14.10	28.20
22R-1, 6-9	644.66	3.73	0.42	3.31	3.5	0.32	1.45	10.30	2.28
22R-1, 87-88	645.47	3.79	0.66	3.13	5.5	—	0.06	—	52.10
23R-2, 50-55	656.20	1.57	0.39	1.18	3.2	0.10	0.26	11.80	4.54
24R-1, 10-15	663.90	—	0.15	—	1.2	—	—	—	—
24R-3, 10-15	666.90	1.21	0.08	1.13	0.7	0.23	1.45	4.91	0.78
25R-1, 60-65	674.10	1.98	0.16	1.82	1.3	0.21	1.22	8.66	1.49
25R-3, 90-95	677.40	1.63	0.21	1.42	1.7	0.12	0.16	11.80	8.87
26R-1, 120-125	684.40	4.32	1.38	2.94	11.5	0.32	1.56	9.19	1.88
27R-1, 108-112	693.58	1.19	0.11	1.08	0.9	0.16	1.49	6.75	0.73
27R-3, 112-117	696.62	1.47	0.35	1.12	2.9	0.12	0.77	9.33	1.45
28R-1, 40-45	702.50	1.47	0.11	1.36	0.9	0.17	1.26	8.00	1.08
28R-3, 40-45	705.50	2.50	0.54	1.96	4.5	0.18	1.62	10.90	1.21
28R-5, 40-45	708.50	2.11	0.19	1.92	1.6	0.19	2.10	10.10	0.91
29R-2, 100-105	714.30	2.13	0.46	1.67	3.8	0.18	1.56	9.28	1.07
29R-4, 75-80	717.05	2.93	0.56	2.37	4.7	0.13	0.19	18.20	12.50
29R-6, 70-75	720.00	—	0.08	—	0.7	—	—	—	—
30R-1, 85-87	722.25	1.96	0.18	1.78	1.5	0.16	2.05	11.10	0.87
31R-1, 9-11	730.89	11.19	10.53	0.66	87.7	0.05	0.03	13.00	22.00
32R-1, 59-61	741.09	2.74	0.56	2.18	4.7	0.14	1.19	15.60	1.83
33R-1, 69-72	750.89	2.35	0.16	2.19	1.3	0.14	1.46	15.60	1.50
34R-1, 14-18	759.94	2.16	0.09	2.07	0.7	0.13	1.52	15.90	1.36
35R-2, 42-44	771.42	3.96	0.18	3.78	1.5	0.21	2.05	18.00	1.84
36R-1, 137-141	780.57	2.28	0.21	2.07	1.7	0.14	1.20	14.80	1.72
37R-1, 55-57	789.45	2.41	0.24	2.17	2.0	0.13	1.02	16.70	2.13
38R-1, 65-67	799.15	1.99	0.39	1.60	3.2	0.11	1.17	14.50	1.37
38R-1, 143-144	799.93	4.31	0.71	3.61	5.9	—	—	—	—
39R-1, 103-105	809.13	2.60	0.72	1.88	6.0	0.12	1.26	15.60	1.49
40R-1, 4-6	817.84	2.94	0.20	2.74	1.7	0.21	1.08	13.00	2.54
41R-1, 4-6	827.14	0.97	0.07	0.90	0.6	0.08	0.80	11.00	1.10
42R-1, 21-23	837.01	3.68	1.94	1.74	16.2	0.11	1.97	15.80	0.88
45R-1, 123-125	867.03	1.52	0.10	1.42	0.8	0.12	1.35	11.80	1.05
46R-1, 34-36	875.64	2.17	0.32	1.85	2.7	0.16	1.32	11.50	1.40
46R-3, 93-95	879.23	1.72	0.04	1.68	0.3	0.13	1.15	12.90	1.46
47R-1, 136-138	886.36	2.17	0.09	2.08	0.7	1.55	12.20	1.34	—
47R-2, 102-103	887.52	10.19	9.36	0.83	78.0	—	0.28	—	2.90
47R-3, 111-113	889.11	2.42	0.16	2.26	1.3	0.20	0.16	11.30	14.10
48R-2, 96-100	897.06	3.07	0.12	2.95	1.0	0.23	1.76	12.80	1.67
49R-1, 48-50	904.68	—	0.07	—	0.06	—	—	—	—
50R-1, 54-58	914.4	1.92	0.43	1.49	3.6	0.12	0.96	12.40	1.55
51R-2, 78-82	925.58	1.95	0.19	1.76	1.6	0.17	1.40	10.30	1.26
51R-5, 20-24	929.50	—	0.12	—	1.0	—	—	—	—
52R-1, 13-16	933.03	—	0.52	—	4.3	—	—	—	—
53R-2, 0-4	944.10	2.12	0.68	1.44	5.7	0.17	1.38	8.47	1.04
54R-1, 19-23	952.39	2.89	0.24	2.65	2.0	0.23	1.32	11.50	2.01
54R-3, 43-45	955.63	1.95	0.13	1.82	1.1	0.20	1.55	9.10	1.17

Table 13 (continued).

Core, section, interval (cm)	Depth (mbsf)	Total carbon (%)	Inorganic carbon (%)	Organic carbon (%)	CaCO ₃ (%)	Nitrogen (%)	Sulfur (%)	C _{org} /N	C _{org} /S
55R-1, 63-65	962.43	2.47	0.78	1.69	6.5	0.16	1.06	10.50	1.59
56R-2, 4-6	973.04	2.51	0.98	1.53	8.2	0.23	1.66	6.65	0.92
58R-1, 74-76	991.54	0.20	0.08	0.12	0.7	0.38	0.26	0.31	0.46
59R-1, 54-56	1001.04	0.14	0.07	0.07	0.6	0.22	0.29	0.32	0.24
60R-1, 21-23	1010.41	2.08	0.04	2.04	0.3	0.19	1.70	10.70	1.20
60R-3, 65-67	1013.85	2.58	0.04	2.54	0.3	0.18	2.33	14.10	1.09
61R-1, 105-109	1020.85	2.28	0.15	2.13	1.2	0.17	1.48	12.50	1.44
61R-3, 103-105	1023.83	0.48	0.26	0.22	2.2	0.05	0.88	4.40	0.25
61R-5, 43-45	1026.23	3.34	0.52	2.82	4.3	0.20	1.75	14.10	1.61
62R-2, 13-17	1031.13	2.88	0.74	2.14	6.2	0.13	1.33	16.40	1.61
62R-4, 44-48	1034.44	3.22	0.67	2.55	5.6	0.18	1.52	14.10	1.68
63R-1, 119-123	1040.29	3.40	1.75	1.65	14.6	0.12	0.86	13.70	1.92
63R-3, 43-45	1042.53	2.97	0.32	2.65	2.7	0.18	1.50	14.70	1.76
64R-1, 0-4	1048.80	8.28	7.24	1.04	60.3	0.08	0.14	13.00	7.43
65R-1, 83-85	1059.23	3.92	0.04	3.88	0.3	0.23	2.28	16.80	1.70
65R-3, 14-16	1061.54	3.20	0.04	3.16	0.3	0.18	1.99	17.50	1.59
66R-2, 48-50	1069.17	3.29	0.04	3.25	0.3	0.19	2.31	17.10	1.40
67R-1, 145-147	1079.15	2.42	0.05	2.37	0.4	0.11	1.54	21.50	1.54
67R-3, 9-11	1080.79	3.41	0.03	3.38	0.2	0.21	3.06	16.10	1.10

Note: Calcium carbonate and organic carbon contents have been calculated as noted in "Explanatory Notes" (this volume).

and sonic velocities, suggesting a more rigid lithology. However, a pronounced decrease in these properties occurs at ~850 mbsf, and the increase in gamma-ray values below this depth suggests that there is an increase in clay content in this unit. The core description data indicate that small turbidites are common in the sediments recovered in this unit; thus, the lower velocities and increased gamma-ray values may be reflecting this change. From 980 to 1010 mbsf, a dramatic increase in the gamma-ray values with a corresponding decrease in resistivity reflect the thick, massive ash layer that was recovered in Cores 128-799B-57R, 128-799B-58R, and 128-799B-59R (Fig. 139). In fact, logs indicate that this ash is composed of several discrete layers that are separated by sediments having similar characteristics of the overlying lithology.

Logging to total drilled depth (1084 mbsf) was not possible because of hole fill, which by the end of the final logging run (the GST combination), had reduced the measurable depth to 1026 mbsf. Core 128-799B-61R (1020-1029 mbsf) contained a massive, graded, silty sand unit that is probably the basal portion of a turbidite (see "Lithostratigraphy" section, this chapter). This dramatic change in lithology marks the beginning of Unit VI at 1020 mbsf, and unfortunately, this is almost the end of the loggable section. However, the resistivity and velocity data (Fig. 139) show a marked increase at this depth, which reflects the resistivity and low porosity of the sandstone unit.

Correspondence with Physical Properties Measurements

The magnitudes and trends of the wireline bulk density logs agree well with the gravimetric wet-bulk densities of core samples (Fig. 129; see "Physical Properties" section, this chapter). The high bulk-density values measured at 247 mbsf and at the bottom of Hole 799A correspond with high laboratory measurements of density at the same depths. There is also agreement with the GRAPE density measurements. However, the GRAPE values are slightly higher than either the wet-bulk density or the dry-bulk density measurements of the wireline logs. At the base of Hole 799A logs and at the top of Hole 799B logs at ~450 mbsf, there is a pronounced increase in wet-bulk density that is also apparent from the laboratory physical-properties data (see "Physical Properties" section, this chapter). This interval corresponds to an increase in

opal-CT content and may be reflecting increased sediment cementation and rigidity. Below ~600 mbsf in Hole 799B logs, a marked increase is seen in dolomite abundance. These dolomite layers range from disseminated grains, to wispy layers, to massive units up to ~2 m thick. The bulk densities from the thickest dolomite units (e.g., ~933 mbsf) reach peak wet-bulk-density values of ~2.7 g/cm³, which is consistent with laboratory values for this lithology.

Temperature Gradients from the Barnes/Uyeda Temperature Tool

The Barnes/Uyeda temperature tool was run every second core during APC drilling, starting at 39.5 mbsf and ending at 174.5 mbsf in Hole 799A. The temperature probe was thrust ~1 m into the sediment ahead of the drill bit and then left to equilibrate for 20 min. The seven readings define a straight line when temperature is plotted vs. depth, which is equivalent to a temperature gradient of 98°C/km (Fig. 141). Based on this gradient, the virgin bottom-hole temperature at 468 mbsf should be 46°C (Fig. 141).

The steady-state conducted heat flow can be estimated by plotting the cumulative thermal resistivity vs. temperature (Fig. 142), following the method used by Horai and Von Herzen (1985). Thermal conductivities were obtained from measurements of the core (see "Physical Properties" section, this chapter). Cumulative thermal resistivity (R) equals the sum of $1/\text{thermal conductivity } (k)$ times interval of depth (z) (cm^2/W^2) [$R = \sum 1/k \Delta z \text{ cm}^2/\text{W}^2$]. The cumulative thermal resistivity was calculated for the Barnes/Uyeda temperature measurements and a graph of temperature vs. cumulative resistivity was constructed (Fig. 142). The slope $\Delta t/\Delta R$ of this graph gives a constant heat flow of $Q = 96 \text{ mass W/m}^2$.

Temperatures below the depths actually measured by the Barnes/Uyeda temperature tool can be estimated from the thermal conductivity core measurements (see "Physical Properties" section, this chapter) and the heat-flow value. Temperature estimates at 395 mbsf (44.8°C) and 468.7 mbsf (TD; 53°C) are shown in Figure 142.

The TLT was used during all four logging runs in Hole 799A. Temperature for three of the runs was used to estimate virgin bottom-hole temperatures using the approximation of Desbrandes (1985). The temperature vs. $\log(t + dt)/dt$ gives the low virgin formation temperature estimate of 35°C for the

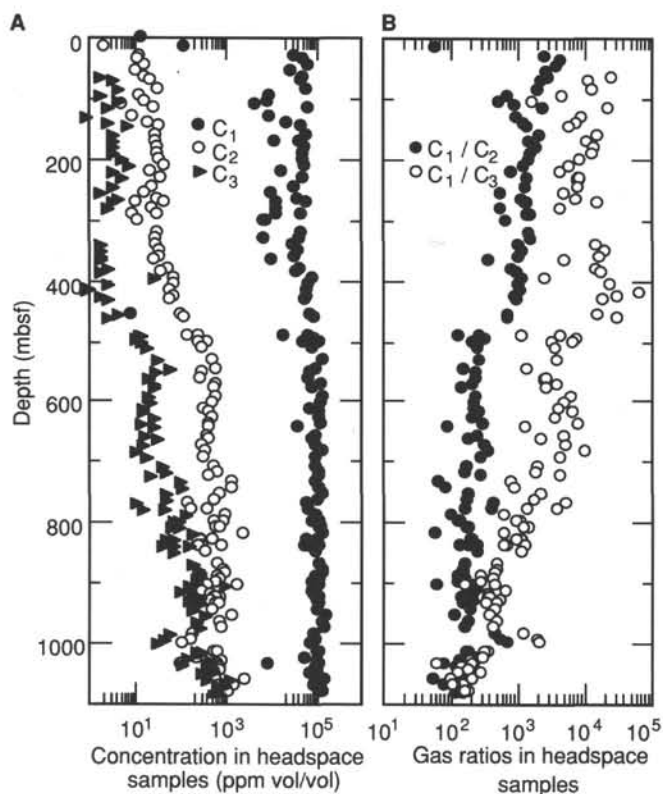


Figure 121. A. Concentration of methane (C_1), ethane (C_2), and propane (C_3) in sediments from Site 799. Concentrations are volume/volume in headspace. B. Methane/ethane (C_1/C_2) and methane/propane (C_1/C_3) ratios in headspace.

bottom of the hole (Fig. 143). This unrealistically low temperature is most likely the result of circulating cold seawater through the hole prior to measuring temperatures. The Desbrandes method assumes recirculation of the drilling fluid prior to logging, and thus it is probably invalid for holes drilled without a riser or circulating mud system.

The TLT was run on the first and fourth logging strings in Hole 799B, and the temperatures were recorded as a function of depth. The borehole temperature had about 12 hr to equilibrate prior to the first logging run and approximately 24 hr prior to the final logging run. The bottom-hole temperatures obtained from the first (1046 mbsf) and final logging runs (1026 mbsf) were 55° and 62°C, respectively. These data demonstrate that the borehole temperature had not attained equilibrium and that, as noted for Hole 799A, the TLT-measured temperature gradient was significantly less than expected, based on the Barnes/Udeya temperature probe data (98°C/km).

Geochemical Signature of Ash Deposits

Thin, highly resistive layers can be identified on the Hole 799A FMS field log; many of these are volcanic ash layers that have been identified at roughly correlative depths in the recovered cores (see "Lithostratigraphy" section, this chapter). Peirce, Weissel, et al. (1989) observed that basaltic ash sources at ODP Sites 747 and 752 were significantly enriched in thorium relative to uranium. They stated "The Th/U ratio of basalt andesites, andesites, and even high silica rhyolites averages 4:1, whereas that of pelagic sediments is <1:1." (Figs. 3–18 from Borehold Research Group, 1988). We have attempted to use this ratio to resolve the numerous ash layers at Site 799.

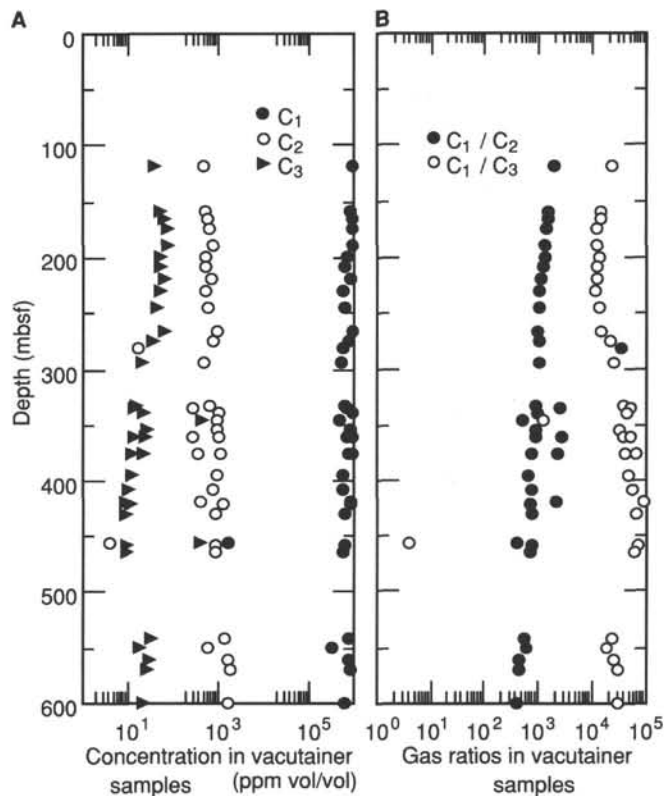


Figure 122. A. Concentration of methane (C_1), ethane (C_2), and propane (C_3) in gas voids from Site 799. Concentrations are volume/volume in vacutainer samples. B. Methane/ethane (C_1/C_2) and methane/propane (C_1/C_3) ratios in gas voids.

A log of the thorium/uranium (Th/U) variation with depth (Fig. 144) has been calculated from the thorium and uranium readings of the NGT, obtained during the geochemical tool run in Hole 799A. While the log shows long-period Th/U variations that exceed the ratio value of 4, the thicker ash layers were identified by sharp increases in the Th/U ratio as well as by sharp increases in the shallow-focused resistivity log (not shown). These layers are shown by arrows in Figure 144. There are numerous thin (<2 cm) ash layers, which are apparent in these cores < that were not resolved by the Th/U ratio log.

The intrinsic vertical resolution of the NGT is ~0.5 m; thus, the accuracy of the thorium, uranium, and potassium measurements is directly (and nonlinearly) proportional to the thickness of the layer in question. The Hole 799B log responses demonstrate that the massive rhyolitic ash deposit recovered in Cores 128-799B-57R to 128-799B-59R (980–1010 mbsf; see "Lithostratigraphy" section, this chapter) is actually several discrete layers that attain a cumulative thickness of ~30 m; therefore, this unit may be used to investigate the natural radiochemical properties of ash deposits. Figure 145 presents the total natural gamma-ray activity and the separate thorium and uranium gamma-ray components for the depth interval from 950 to 1050 mbsf. This figure demonstrates the significant thorium enhancement of the ash layers.

Formation Microscanner

The FMS has two orthogonally oriented calipers that can be used to measure borehole ellipticity. The caliper data indicate that the lower portion of Hole 799A is elliptical, with an 11- to 12-in. minimum diameter and a 14- to 15-in. maximum diameter. Below ~450 mbsf, the borehole passed

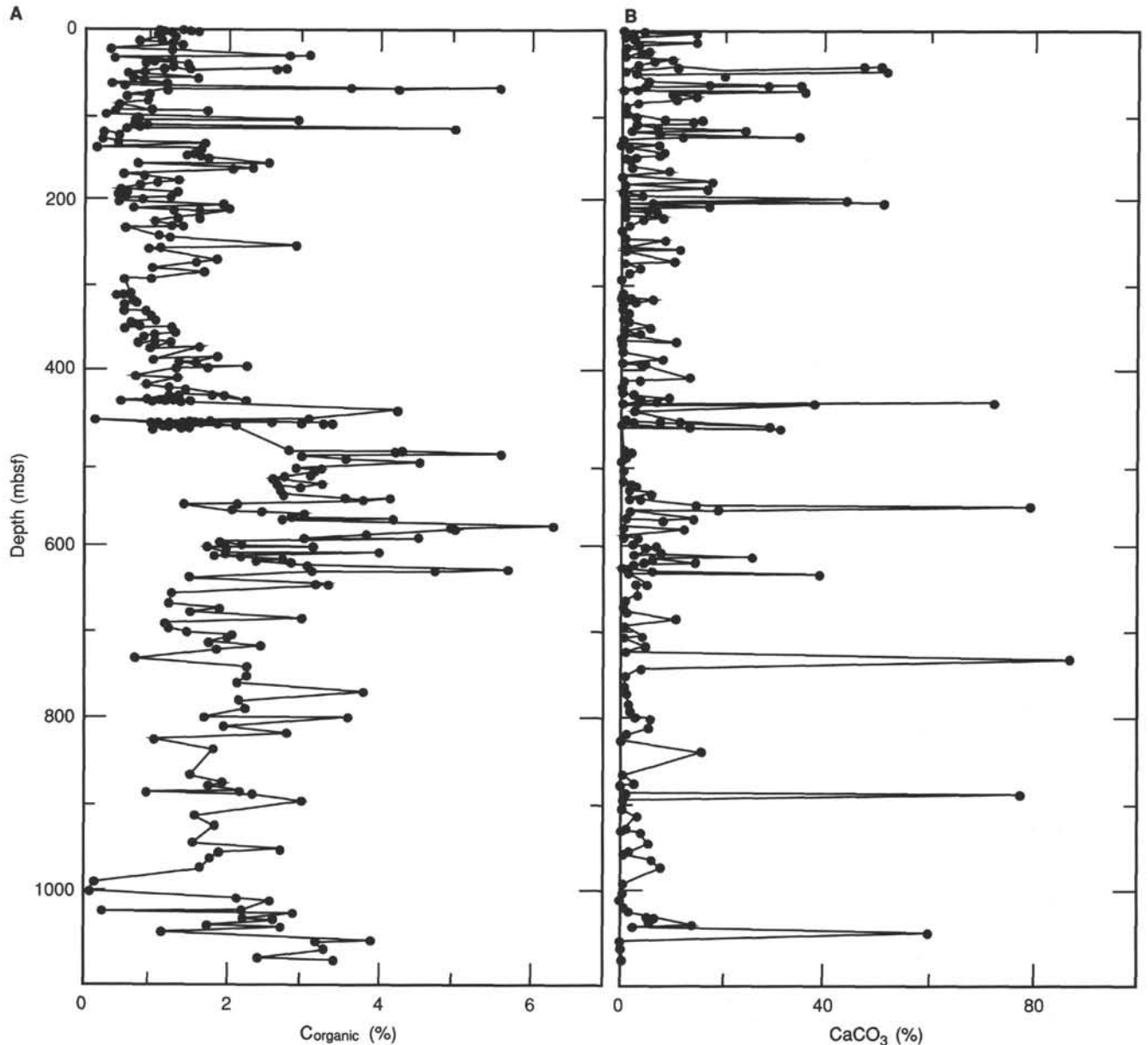


Figure 123. A. Total organic carbon contents of sediments at Site 799. B. Inorganic carbon contents of sediments at Site 799. Data are presented as equivalent percentages of calcium carbonate.

through several authigenic dolomite or chert layers, which did not demonstrate any significant borehole ellipticity. The orientation of the maximum ellipticity axis is consistently north-northwest to south-southeast from 385 to 440 mbsf (see Fig. 145).

This hole ellipticity may result from a preferred "break-out" orientation of the borehole caused by the regional stress field that was once active in the Yamato Trough region. When drilling through a competent formation subjected to a given stress field, the borehole will break out, or spall, in the direction of minimum compressive stress; hence, the maximum diameter of an elliptical borehole can indicate the minimum compressive stress orientation. It is apparent from Figure 146 that the breakout direction of the borehole is consistent with the north-northwest to south-southeast spreading direction of the Yamato Trough, which is thought to

have been active during the earliest Neogene (Oligocene-early Miocene rifting).

In addition, the microresistivity images from the FMS tool are useful for identifying the highly resistive ash layers and the numerous thin dolomite layers that were encountered in the core material recovered at Hole 799A. The "Lithostratigraphy" section (this chapter) describes the distribution of ash layers throughout the Hole 799A sediments. Here, FMS images were used to correlate between logs and core and to identify those ash layers that were not observed in the lowermost part of the hole because of poor core recovery. Ash layers observed using the FMS images were typically 1 to 5 cm thick, although several thicker layers were also observed. Comparison of the FMS ash layer depths with the Th/U log demonstrated that the Th/U log could only consistently resolve thick ash layers (>5 cm). Also, the several dolomite

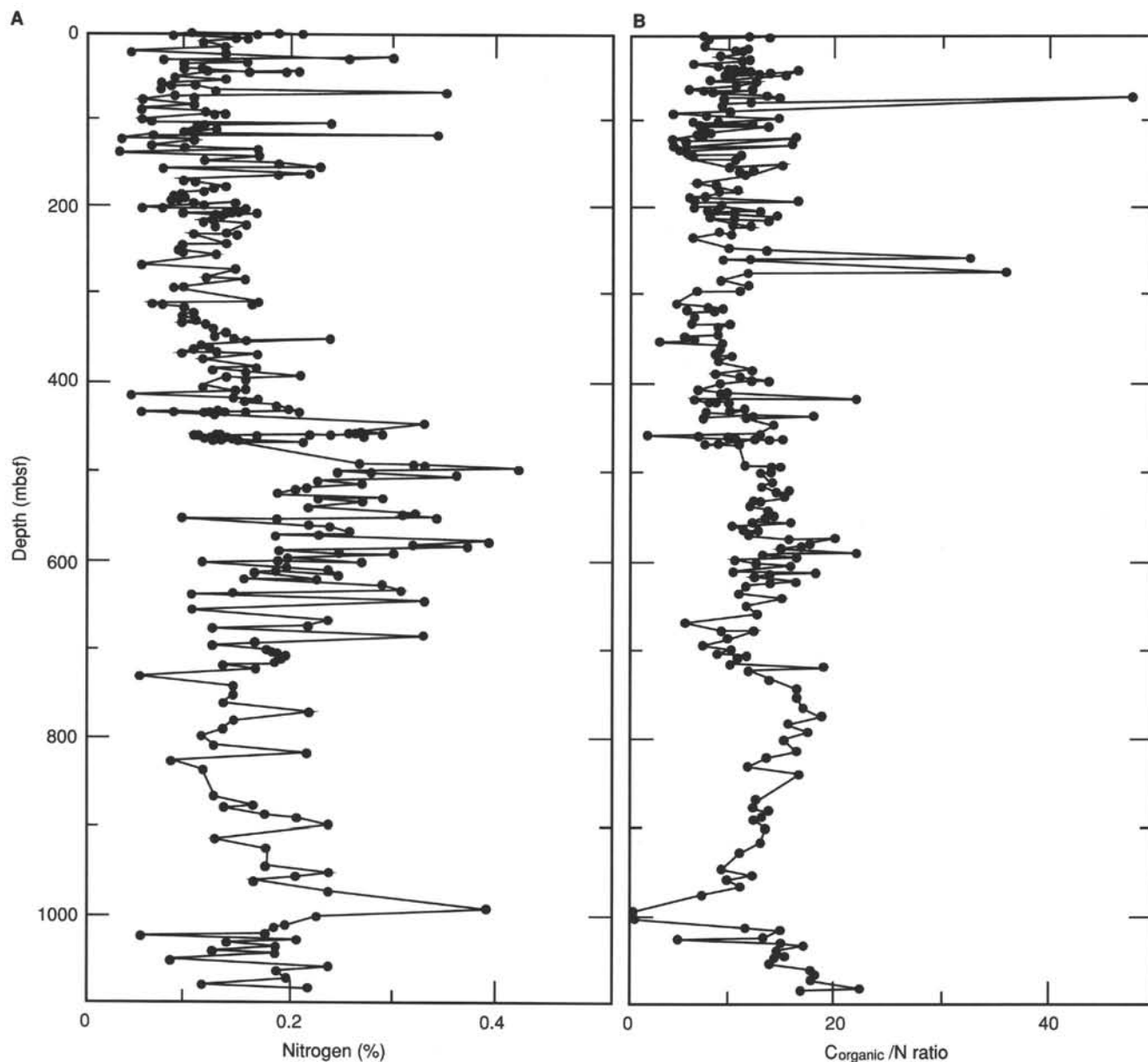


Figure 124. A. Total nitrogen content of sediments at Site 799. B. Ratio of organic carbon to total nitrogen (C/N) in sediments from Site 799.

layers (or nodules) that were observed at Hole 799A also are apparent in the FMS images as extremely high-resistivity, well-defined layers. In particular, the FMS images identify the three dolomite layers (between 0.5 to 1 m thick each) at approximately 459, 461, and 464 mbsf.

The FMS images from Hole 799B were of generally excellent quality. However, as noted earlier, the tool motion was irregular during logging because the heave compensator could not be used to counteract the ship's minor heave. The images from Hole 799B show considerably more fine-scale resistivity contrast than was apparent in the shallower sediments at Hole 799A. This may be a result of increased abundances of highly resistive dolomite that occur as discrete layers ranging from wispy to massive thicknesses (see "Lithostratigraphy" section, this chapter). Structure is also apparent from these FMS images. Figure 147 shows the microresistivity traces for the interval from 974 to 978 mbsf in Hole 799B, which is a sedimentary sequence directly

above the thick rhyolitic ash deposit at ~982 mbsf. The sinusoidal pattern defined by the four traces indicates dipping sedimentary structures: the magnetometer orientation and the amplitude of the sinusoid demonstrate that the layers are dipping 20° approximately due west.

Paleoclimatic Significance of the Logs

As a result of the low sedimentation rates encountered at Site 799 (~40 m/m.y.), the logs have a poorer time resolution than at Site 798 (~120 m/m.y.). The 15-cm log sampling interval is equivalent to ~4 k.y. at Site 799, whereas the same interval is roughly equivalent to 1 k.y. at Site 798. This difference is significant when trying to resolve orbital-scale (20–100 k.y.) variations in the logs. Furthermore, Site 799 is positioned in the Yamato Trough; thus, downslope turbidite and slump deposits may be expected to obscure sedimentary climate signals. Despite these problems, the logging data at

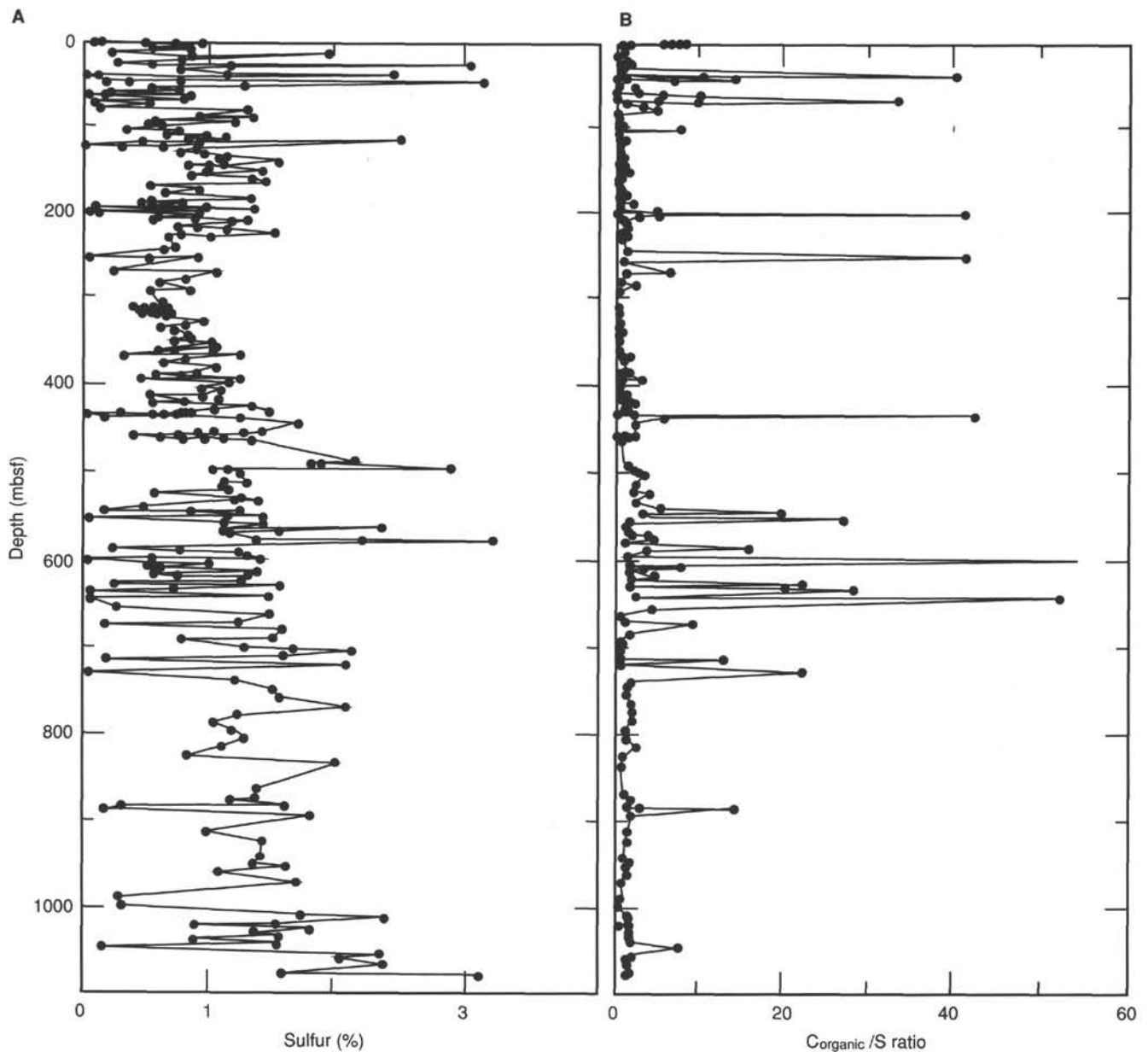


Figure 125. A. Total sulfur content of sediments at Site 799. B. Ratio of organic carbon to total sulfur (C/S) in sediments from Site 799.

Hole 799A do show some basic similarities with the excellent record obtained at Hole 798B.

Figure 148 shows a comparison between the gamma-ray logs obtained at Holes 799A and 798B for the 2.5- to 1.2-Ma interval. The Hole 799A age model is based upon the Olduvai Subchron (1.66 and 1.88 Ma) and Matuyama/Gauss Chron (2.47 Ma) paleomagnetic boundaries (see "Paleomagnetism" section, this chapter). The two gamma-ray records are roughly similar in their long-period variation, and several smaller-scale features also are common in both records, such as the increase in gamma-ray values at ~2.4 Ma. The somewhat earlier occurrence of the ~2.4 Ma maximum at Hole 799A may be indicative of the poorer quality of the paleomagnetic data at this hole. The gamma-ray logs at the two sites also are similar in their power spectra. As discussed in "Site 798" chapter (this volume), the Hole 798B gamma-ray log varies predominately at the 41 k.y. periodicity that corresponds to orbital obliquity (see Fig. 149). Power

spectra calculated for the Hole 799A gamma-ray log from 2.5 to 1.2 Ma indicate that the log also varies at a periodicity near 41 k.y. (~50 k.y.); the slightly longer periodicity here, again, may be a consequence of the poorer paleomagnetic stratigraphy at this site (Fig. 149). These data suggest that despite evidence for slumping and turbidite deposition at Hole 799A, the upper Pliocene-Pleistocene terrigenous (clay) sedimentation at this location is similar in character to the pelagic record recovered at Hole 799A. As at Hole 798B, the origin of this cyclic terrigenous signal may be connected to variations in the supply of eolian dust from Asia.

Vertical Seismic Profiler

The vertical seismic profiler (VSP) tool was run to determine the velocity distribution of the sediments, basement, and lower crust in the Yamato Trough. Processing of the VSP data will result in a vertical profile that can be compared to the

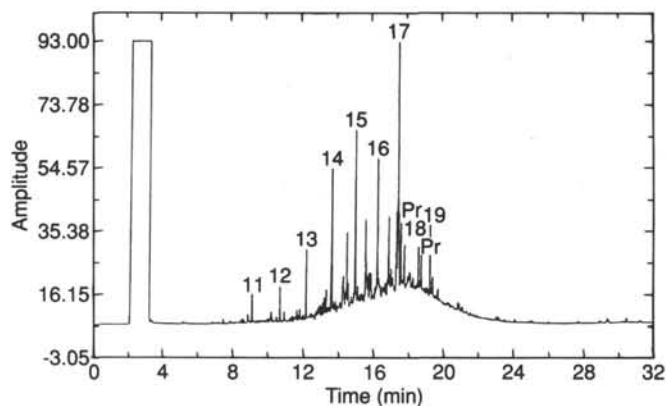


Figure 126. Chromatogram of aliphatic hydrocarbon extract obtained from interstitial-water squeeze cake Sample 128-799A-51X-2, 140-145 cm. The *n*-alkanes have been labeled with numbers indicating the number of carbon atoms in the compound. The isoprenoid hydrocarbons pristane and phytane have been labeled, Pr and Ph, respectively.

log-derived synthetic seismogram and the air-gun seismic line recorded during the Site 799 seismic surveys.

The energy source for the VSP experiment was a 400-in.³ water gun that was deployed 5 mbsf off the ship's fantail (Fig. 150). The horizontal offset of the water gun from the vertical centerline of the hole was 48 m. The zero-time, frequency, and wave shape of the sound signal of the water gun was measured using a hydrophone suspended 4.75 m below the water gun.

Downgoing and reflected seismic waves produced by the water gun were measured by the Schlumberger well seismic tool (WST) within the borehole; the WST consists of four vertically oriented 10-Hz geophones. The WST is pressed against the borehole wall by an extendable arm, and waveforms are digitally recorded and transmitted up the seven-conductor logging cable to the Schlumberger logging unit on board the ship. The VSP logging experiment required a total of 13 hr to complete.

Data were recorded at 15.25-m stations up the hole, starting at 1003 mbsf and ending at 384 mbsf. Two 15-shot sequences of different delay times (typically 1.6 and 2.8 s) were recorded for 3.0 s each, were stacked, and then normalized at each station from 1003 to 811 mbsf. The number of shots was subsequently reduced to nine between 796 and 384 mbsf on the basis of the observed quality of each shot record. Some of the data below ~900 mbsf were noisy because of ship operations that induced ringing in the drill string, and data collected within the pipe above 440 mbsf were adversely affected by poor cement-pipe contact at the casing shoe.

A field copy of the stacked traces at each station and the Schlumberger "Quick Look" processing were available after logging. The seismic profile has been derived from the stacked shot traces after the data were bandpass- and velocity-filtered and deconvolved to remove multiples (Fig. 151). The VSP results shown in Figure 151 indicate that acoustic basement is located ~120 m below the bottom of Hole 799B. The final processing step consisted of stacking all the upgoing waves after the first break; this gives the appearance of a synthetic seismogram, but is in fact composed of real seismic data (Fig. 152). The two main results of the VSP experiment will be (1) information about the depth and acoustic properties of deep structure (basement) below the borehole and (2) information regarding the vertical seismic properties of the drilled sequence, such as sonic velocity, acoustic impedance, and vertical acoustic structure.

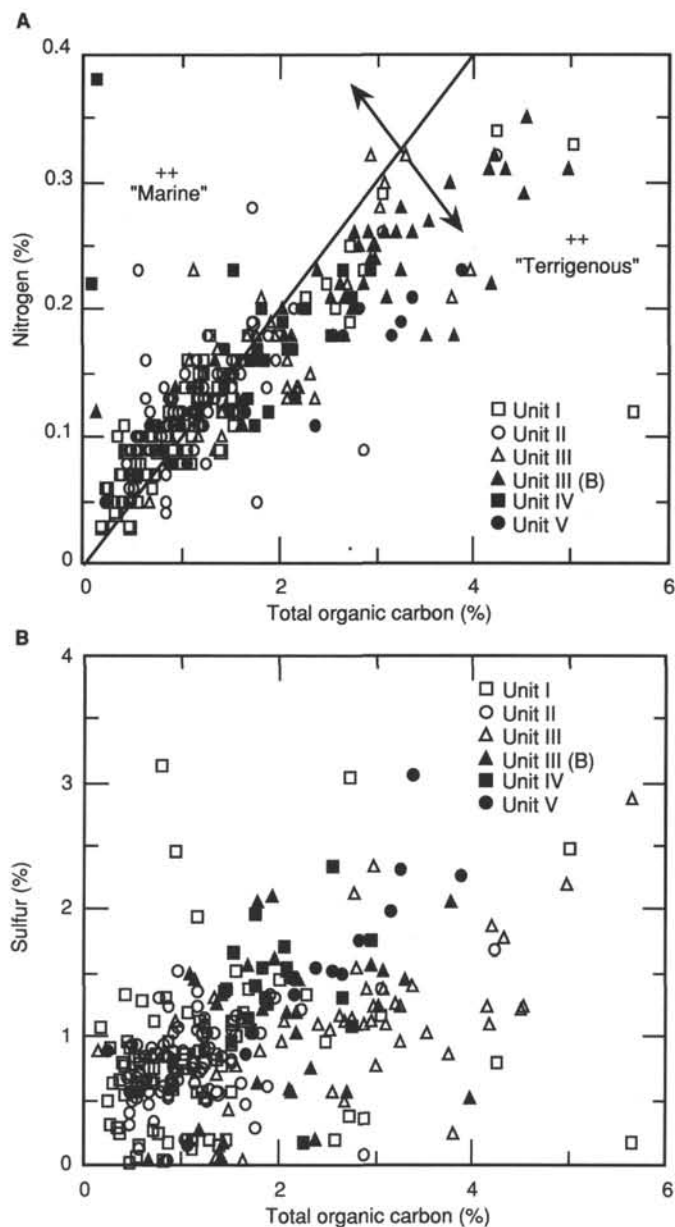


Figure 127. A. Plot of total nitrogen vs. total organic carbon for all samples from Site 799. The solid line designates a constant C/N ratio of 10. Samples with high C/N ratios contain larger fractions of terrigenous organic matter than samples with low C/N ratios. B. Plot of total sulfur vs. total organic carbon for samples from all lithologic units at Site 799. Unit III (B) refers to the burrowed section in Unit III from 606 to 800 mbsf.

SEISMIC STRATIGRAPHY

Available Data

The original location selected for proposed Site J2a-1 (Site 799) in the Kita-Yamato Trough was at shot 7120, Line 13-4 of a 48-channel seismic-reflection profile obtained by the Japan Petroleum Exploration Company in 1976 under the direction of the Japan National Oil Company (JNOC) (Figs. 153 through 155). Other seismic-reflection records in the vicinity of the Kita-Yamato Trough include Line J-1 of the multichannel data set collected by JNOC and a six-channel record (*DELP* Line 6) obtained by the Ocean Research Institute of the University of Tokyo; both of these lines parallel the strike of the trough

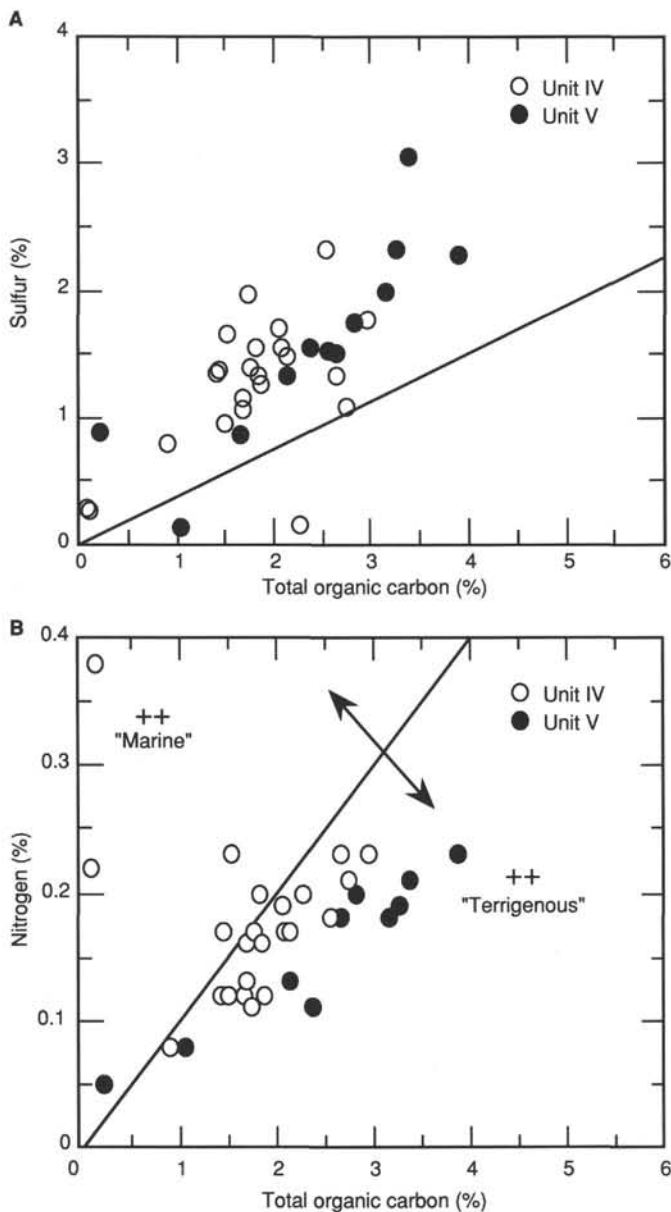


Figure 128. A. Plot of total sulfur vs. total organic carbon for samples from lithologic Units IV (800–1020 mbsf) and V (1020–1064 mbsf). The solid line designates the C-S values displayed by sediments deposited in normal marine settings (Bernier and Raiswell, 1984). B. Plot of total nitrogen vs. total organic carbon for samples from lithologic Units IV (800–1020 mbsf) and V (1020–1064 mbsf). The solid line designates a constant C/N ratio of 10.

(Figs. 154 through 156). There is also a single-channel seismic-reflection record (Line 38) within close proximity to Site 799, among a series of profiles run at a spacing of 15 nmi during the Geological Survey of Japan Cruise GH78-02 in 1978 (Honza, 1979; Figs. 154 and 157). An older Lamont-Doherty Geological Observatory (*Vema*) single-channel record, Line V2815, runs parallel to the strike of the trough (Figs. 154 and 158).

Single-channel, digital, seismic-reflection profiling was conducted during the approach of *JOIDES Resolution* to Site 799, both for site location and to obtain a crossing line across this site. Figure 153 shows the track of this survey, and Figure 159 illustrates the record across Site 799. The final location selected for Site 799 corresponds to shot point 7120 on JNOC

Line 13-4, as originally planned. The 3.5-kHz reflection record (Fig. 160) was used to correlate recovered samples with physical properties of the uppermost sediments at Hole 799A. Logging data are absent in this portion of the hole because soft sediments near the surface required the drill pipe to be kept at 104 mbsf during logging.

After drilling Site 799, we conducted a seismic survey in the same manner as the site approach. The purpose of this survey was to tie the record obtained by drilling with seismic information on the trough and the ridges (Fig. 150), so as to assemble a three-dimensional view of this failed rift.

Seismic Stratigraphy

The Kita-Yamato Trough represents a major structural and topographic depression that divides the Yamato Rise along a northeast-southwest trend. Seismic-reflection records that cross the trough show it to be a graben, with the thickest sediment column confined to the narrow central portion of the structure (Figs. 154, 155, and 157). All records show that acoustic basement is offset by the apparent faults demarcating the sides of the trough. Uplifted acoustic basement is most apparent beneath the Yamato and Kita-Yamato banks, which flank the trough. Seismic records also demonstrate that acoustic basement deepens slightly northeastward toward the center of the trough and that it then becomes shallower again (Fig. 158). Sediments depicted by reflection records show evidence of disturbance along the sides of the trough, perhaps representing slumping.

Four distinct seismic layers are discernible on single-channel records that cross the Kita-Yamato Trough (Figs. 157 and 158). From top-to-bottom, these layers are successively reflective, transparent, reflective again, and then transparent above acoustic basement. Small changes in the thicknesses of the top two layers are apparent within the trough proper, wherein the topmost layer thickens at the expense of the underlying layer and vice versa. The bottom two layers thus are thicker where the basement is structurally low. These same patterns are also found in other seismic records in the trough area, as described below.

Four major reflective surfaces and groups of reflectors can be recognized on the high quality JNOC-13-4 profile across the Kita-Yamato Trough (Fig. 155). The shallowest reflector occurs at 0.28 s below the seafloor, the second at 0.50 and 0.55 s, the third (representing a band of reflectors) at about 0.80 s, with the fourth reflector representing acoustic basement at 1.3 s in two-way traveltime (all subsequent references to time in this section also refer to two-way traveltimes). The reflective pattern indicates that sediments in the trough are deformed at depth.

The seismic characteristics of the intervals between the four reflectors noted above are as follows: (1) the uppermost interval consists of two layers, including a well stratified layer that parallels the bathymetry of the trough and a less stratified layer beneath; (2) a second transparent interval (0.28–0.5 s), which also parallels the sediment surface, while the base of this interval represents the most obvious boundary within the trough (Fig. 155); (3) a more opaque interval between 0.55 to 0.8 s; and (4) a fourth interval marked by a band of strong reflectors within which individual reflectors are deformed but continuous (Fig. 155); and (5) a fifth interval similar to the third interval, but more transparent toward the southeast margin of the trough.

The 3.5-kHz record across Site 799 is illustrated in Figure 160. The 3.5-kHz record at Site 798 on Oki Ridge exhibits good correlation with Quaternary volcanic ash layers (see "Site 798" chapter, this volume). However, the depth of signal penetration at Site 799 is only about 35 mbsf, compared

Table 14. Index properties data for Site 799.

Core, section, interval (cm)	Depth (mbsf)	Wet-bulk density (g/cm ³)	Dry-bulk density (g/cm ³)	Grain density (g/cm ³)	Porosity (%)	Wet water content (%)	Dry water content (%)	Void ratio
128-799A-1H-1, 44-48	0.44	1.26	0.35	2.77	88.0	72.5	263.8	7.13
2H-1, 76-78	1.96	1.47	0.69	2.70	75.3	53.2	113.6	2.99
2H-2, 20-25	2.90	1.71	1.05	2.82	63.7	38.7	63.1	1.73
2H-2, 76-80	3.46	1.52	0.80	2.54	69.5	47.6	90.8	2.25
2H-3, 72-74	4.92	1.43	0.64	2.77	77.3	55.4	124.0	3.36
2H-4, 74-78	6.44	1.44	0.65	2.74	77.0	55.2	123.2	3.29
2H-5, 74-76	7.94	1.55	0.80	2.75	71.5	47.9	92.1	2.47
2H-6, 44-48	9.14	1.38	0.57	2.66	79.3	49.2	144.9	3.76
2H-7, 24-26	10.44	1.38	0.55	2.76	80.6	60.2	151.3	4.08
3H-1, 11-13	10.81	1.33	0.49	2.71	82.5	63.5	174.3	4.61
3H-2, 10-15	12.30	1.42	0.63	2.76	77.2	55.4	124.0	3.34
3H-3, 10-12	13.80	1.53	0.79	2.78	72.2	48.5	94.3	2.55
3H-4, 6-11	15.26	1.57	0.88	2.77	68.0	43.6	77.4	2.09
3H-5, 12-14	16.82	1.39	0.94	2.72	56.4	32.6	48.3	1.28
3H-6, 10-15	18.30	1.57	0.83	2.81	71.2	47.1	88.9	2.44
3H-7, 10-12	19.80	1.58	0.88	2.74	68.7	44.7	80.9	2.17
4H-1, 20-22	20.50	1.42	0.59	2.73	79.2	58.3	140.1	3.73
4H-2, 20-25	22.00	1.62	0.92	2.75	67.4	43.1	75.9	2.04
4H-3, 20-22	23.50	1.44	0.65	2.67	76.3	54.9	121.7	3.17
4H-4, 20-25	25.00	1.51	0.76	2.71	72.5	49.5	98.0	2.60
4H-5, 20-22	26.50	1.53	0.79	2.76	71.9	48.3	93.6	2.53
4H-6, 20-25	28.00	1.38	0.56	2.56	79.0	49.6	147.5	3.68
5H-1, 3-5	29.93	1.45	0.67	2.60	74.9	53.7	115.9	2.94
5H-1, 31-33	30.21	1.71	1.05	2.84	63.4	38.2	61.8	1.72
5H-2, 20-25	31.60	1.57	0.82	2.79	71.6	47.7	91.1	2.48
5H-4, 202-25	34.60	1.47	0.68	2.74	75.7	53.4	114.7	3.07
5H-5, 20-22	36.10	1.58	0.85	2.72	69.6	46.0	85.2	2.26
5H-6, 20-25	37.60	1.65	1.06	2.75	60.5	36.1	56.5	1.51
5H-7, 10-12	39.00	0.78	0.41	2.71	71.1	47.9	91.8	2.43
6H-1, 115-117	40.65	1.53	0.70	2.69	75.9	54.2	118.3	3.10
6H-2, 20-25	41.20	1.49	0.74	2.73	73.0	50.0	100.2	2.67
6H-3, 37-39	42.87	1.58	0.85	2.69	69.8	46.5	86.8	2.28
6H-4, 20-25	44.20	1.47	0.69	2.67	75.1	53.2	113.6	2.97
6H-5, 20-22	45.70	1.35	0.63	2.67	84.9	53.0	112.7	2.93
6H-6, 20-25	47.20	1.63	0.92	2.81	68.0	43.3	76.4	2.10
7H-1, 34-36	49.44	1.66	1.00	2.71	64.0	40.0	66.6	1.76
7H-2, 40-44	51.00	1.71	1.06	2.79	62.9	38.1	61.4	1.67
7H-3, 40-42	52.50	1.62	0.94	2.75	66.3	42.0	72.5	1.95
7H-4, 40-44	54.00	1.63	0.95	2.74	66.0	41.8	71.9	1.92
7H-5, 42-44	55.52	1.54	0.80	2.75	71.5	48.0	92.3	2.47
7H-6, 38-42	56.98	1.68	1.00	2.62	63.9	40.6	68.2	1.75
7H-7, 38-40	58.48	1.58	0.86	2.81	70.1	45.8	84.5	2.31
8H-1, 70-72	59.40	1.53	0.76	2.69	72.8	50.1	100.2	2.64
8H-2, 70-74	60.90	1.56	0.81	2.75	71.7	48.2	93.0	2.49
8H-3, 80-82	62.50	1.56	0.84	2.59	68.4	45.7	84.3	2.13
8H-4, 60-64	63.80	1.59	0.86	2.72	69.4	45.7	84.3	2.24
8H-5, 70-72	65.40	1.50	0.74	2.70	73.2	50.5	101.8	2.68
8H-6, 50-54	66.70	1.48	0.52	2.73	83.4	65.0	185.3	4.93
8H-7, 70-72	68.40	1.70	1.03	2.82	64.3	39.2	64.5	1.78
9H-1, 25-27	68.55	1.50	0.74	2.73	73.7	50.8	103.4	2.76
9H-2, 30-35	70.10	1.64	0.97	2.71	65.0	40.9	69.2	1.83
9H-3, 11-13	71.41	1.57	0.87	2.71	68.2	44.5	80.3	2.12
9H-4, 5-10	72.85	1.54	0.82	2.68	69.9	46.7	87.4	2.29
9H-5, 117-119	75.47	1.66	1.00	2.71	63.9	39.9	66.3	1.75
9H-6, 30-35	76.10	1.67	1.01	2.75	63.8	39.4	65.1	1.74
10H-1, 25-27	78.15	1.59	0.89	2.76	68.3	44.1	79.0	2.13
10H-2, 25-30	79.65	1.55	0.84	2.72	69.4	45.7	84.1	2.23
10H-3, 25-27	81.15	1.60	0.72	2.22	72.9	55.0	122.1	2.64
10H-4, 25-30	82.65	1.62	0.93	2.78	67.4	42.9	75.0	2.04
10H-5, 135-137	85.25	1.46	0.70	2.57	73.6	52.3	109.4	2.74
10H-6, 120-125	86.60	1.63	0.94	2.76	66.8	42.5	73.8	1.99
11H-1, 95-97	88.45	1.56	0.75	2.57	73.4	51.9	108.0	2.71
11H-2, 20-25	89.20	1.47	0.70	2.86	75.9	52.6	110.8	3.10
11H-3, 78-80	91.28	1.54	0.80	2.76	71.7	48.1	92.7	2.50
11H-4, 60-65	92.60	1.43	0.64	2.68	76.5	55.1	122.5	3.21
11H-5, 20-22	93.70	1.53	1.04	2.83	56.9	32.2	47.5	1.31
11H-6, 100-105	96.00	1.67	0.99	2.79	65.1	40.3	67.6	1.84
12H-1, 30-32	97.50	1.57	0.87	2.70	68.2	44.6	80.4	2.12
12H-3, 45-47	100.65	1.36	0.58	2.38	76.3	57.7	136.5	3.17
12H-4, 30-35	102.00	1.74	1.02	2.64	65.0	41.6	71.1	1.83
12H-5, 20-22	103.40	1.28	0.46	2.15	79.4	64.2	179.0	3.76
12H-6, 20-25	104.90	1.51	0.74	2.84	74.3	50.8	103.22	2.86
13H-1, 20-22	107.00	1.47	0.68	2.74	75.8	53.5	115.1	3.08

Table 14 (continued).

Core, section, interval (cm)	Depth (mbsf)	Wet-bulk density (g/cm ³)	Dry-bulk density (g/cm ³)	Grain density (g/cm ³)	Porosity (%)	Wet water content (%)	Dry water content (%)	Void ratio
13H-2, 26-31	108.56	1.66	0.99	2.78	65.3	40.6	68.4	1.86
13H-3, 30-32	110.10	1.32	0.79	2.78	64.6	39.8	66.2	1.80
13H-4, 20-25	111.50	1.51	0.75	2.82	73.9	50.3	101.2	2.79
13H-5, 20-22	113.00	1.51	0.75	2.74	73.3	50.2	100.9	2.70
13H-6, 20-25	114.50	1.54	0.79	2.84	72.8	48.8	95.3	2.64
14H-1, 17-19	116.67	1.58	0.87	2.65	68.3	45.1	82.1	2.12
14H-2, 40-45	118.40	1.84	1.24	2.98	58.3	32.2	47.5	1.38
14H-3, 95-97	120.45	1.76	1.12	2.79	60.9	36.2	56.7	1.54
14H-4, 30-32	121.30	1.53	0.76	2.85	74.1	50.4	101.5	2.83
14H-5, 40-45	122.90	1.83	1.25	2.84	57.0	32.1	47.3	1.31
14H-6, 30-35	124.30	1.68	0.91	2.85	70.7	46.1	85.5	2.38
15H-1, 55-57	126.65	1.48	0.69	4.36	83.0	53.1	113.3	4.82
15H-2, 55-59	128.15	1.52	0.76	2.89	74.0	50.0	99.8	2.81
15H-3, 54-56	129.64	1.66	0.98	2.82	66.1	41.2	70.1	1.93
15H-4, 54-58	131.14	1.58	0.82	3.00	73.5	48.4	93.7	2.74
15H-5, 54-56	132.64	1.57	0.82	2.82	71.7	47.6	90.7	2.50
15H-6, 54-58	134.14	1.74	1.08	2.78	62.4	37.7	60.4	1.64
15H-7, 31-33	135.41	1.54	0.83	2.68	69.5	46.2	85.9	2.25
16H-1, 140-142	137.20	1.53	0.81	2.68	70.0	46.9	88.2	2.30
16H-2, 60-65	137.90	1.71	1.07	2.82	62.6	37.6	60.1	1.65
16H-3, 133-135	140.13	1.50	0.76	2.73	72.5	49.4	97.8	2.60
16H-4, 60-65	140.90	1.58	0.88	2.80	68.7	44.3	79.5	2.17
16H-5, 60-62	142.40	1.56	0.84	2.76	70.0	46.1	85.4	2.30
16H-6, 60-65	143.90	1.51	0.77	2.282	73.0	49.1	96.5	2.66
17H-1, 55-57	146.05	1.46	0.69	2.67	74.8	52.8	111.9	2.92
17H-2, 55-60	147.55	1.50	0.74	2.79	74.0	50.7	102.9	2.80
17H-3, 552-57	149.05	1.61	0.75	2.75	75.9	53.6	115.6	3.10
17H-4, 40-45	150.40	1.50	0.74	2.65	72.6	50.3	101.0	2.62
17H-5, 40-42	151.90	1.69	1.04	2.80	63.4	38.5	62.6	1.71
17H-6, 40-45	153.40	1.50	0.76	2.70	72.4	49.4	97.8	2.58
18H-1, 30-32	155.50	0.76	0.65	2.53	31.4	15.5	18.4	0.45
18H-1, 30-32	155.50	1.41	0.62	2.54	76.2	55.8	126.5	3.14
18H-2, 25-30	156.95	1.42	0.65	2.51	74.5	54.0	117.4	2.88
18H-3, 100-102	159.20	1.47	0.72	2.70	73.6	51.1	104.4	2.75
18H-4, 40-45	160.10	1.46	0.70	2.69	74.1	51.8	107.4	2.82
18H-5, 40-42	161.60	1.42	0.65	2.53	74.9	54.3	118.8	2.93
18H-6, 40-45	163.10	1.64	0.96	2.81	66.3	41.5	71.1	1.95
19H-1, 5-10	164.85	1.47	0.68	2.78	76.2	53.7	116.1	3.15
19H-2, 20-25	166.50	1.40	0.60	2.54	77.1	57.1	133.3	3.31
19H-3, 40-42	168.20	1.49	0.75	2.65	72.1	49.6	98.6	2.55
19H-4, 15-20	169.45	1.41	0.63	2.53	75.5	55.1	122.6	3.03
19H-5, 90-92	171.70	1.42	0.65	2.57	74.9	53.9	116.8	2.93
19H-6, 70-75	173.00	1.48	0.71	2.78	74.9	51.9	107.9	2.93
20H-1, 20-22	174.70	1.38	0.60	2.47	76.4	56.9	132.1	3.18
20H-2, 20-25	176.20	1.49	0.73	2.70	73.4	50.8	103.0	2.71
20H-3, 20-22	177.70	1.40	0.61	2.54	76.5	56.3	129.0	3.20
20H-4, 20-25	179.20	1.39	0.58	2.36	76.5	58.1	138.7	3.20
20H-5, 20-22	180.70	1.50	0.74	2.73	73.7	50.8	103.4	2.76
20H-6, 20-25	182.20	1.55	0.80	2.78	72.0	48.2	93.2	2.53
21X-1, 20-22	184.30	1.39	0.61	2.67	77.4	56.4	129.5	3.38
21X-2, 202-25	185.80	1.40	0.62	2.54	76.1	55.7	125.9	3.13
21X-3, 20-22	187.30	1.50	0.67	2.46	75.1	55.2	123.4	2.97
21X-4, 20-25	188.80	1.41	0.65	2.48	74.4	54.2	118.5	2.86
21X-5, 20-22	190.30	1.44	0.66	2.62	75.3	53.9	117.1	2.99
21X-6, 20-25	191.80	1.43	0.65	2.45	74.4	54.4	119.4	2.86
22X-1, 77-79	194.57	1.55	0.65	2.92	79.8	57.7	136.6	3.89
22X-2, 77-81	196.07	1.46	0.68	2.88	76.6	53.4	114.6	3.22
22X-3, 70-72	197.50	1.36	0.53	2.57	79.9	60.9	155.5	3.89
22X-4, 34-38	198.64	1.38	0.57	2.60	78.7	58.9	143.3	3.64
22X-5, 34-36	200.14	1.40	0.60	2.47	76.6	57.1	133.2	3.21
22X-6, 34-38	201.64	1.45	0.68	2.73	75.5	53.2	113.7	3.03
22X-7, 20-22	203.00	1.51	0.79	2.63	70.4	47.7	91.3	2.35
23X-1, 29-31	203.79	1.43	0.64	2.75	77.0	55.1	122.9	3.30
23X-2, 29-31	205.29	1.43	0.64	2.75	77.0	55.1	122.9	3.30
23X-3, 29-31	206.79	1.39	0.57	2.67	79.1	58.8	142.5	3.71
23X-4, 20-24	208.20	1.47	0.69	2.82	76.0	53.1	113.2	3.11
23X-5, 26-28	209.76	1.44	0.63	2.67	77.5	56.5	129.9	3.39
23X-6, 16-20	211.16	1.47	0.66	3.04	78.7	55.1	122.7	3.64
23X-7, 20-22	212.70	1.41	0.62	2.50	75.9	56.0	127.1	3.10
24X-1, 90-92	214.00	1.47	0.70	2.74	74.8	52.2	109.2	2.92
24X-2, 132-136	215.92	1.43	0.60	2.43	76.7	57.7	136.3	3.24
24X-3, 97-99	217.07	1.50	0.75	2.87	74.2	50.3	101.2	2.83
24X-4, 98-102	218.58	1.48	0.69	2.85	76.4	53.5	114.8	3.19

Table 14 (continued).

Core, section, interval (cm)	Depth (mbsf)	Wet-bulk density (g/cm ³)	Dry-bulk density (g/cm ³)	Grain density (g/cm ³)	Porosity (%)	Wet water content (%)	Dry water content (%)	Void ratio
24X-5, 99-101	220.09	1.44	0.64	2.74	77.5	55.8	126.3	3.38
24X-6, 20-24	220.80	1.49	0.70	3.15	77.8	53.0	122.6	3.46
25X-1, 104-106	223.84	1.83	1.23	2.83	57.4	32.6	48.3	1.34
25X-2, 112-116	225.42	1.38	0.55	2.70	80.1	60.0	150.3	3.96
25X-3, 110-112	226.90	1.43	0.66	2.54	74.6	53.9	116.7	2.89
25X-4, 113-117	228.43	1.40	0.59	2.59	77.6	57.5	135.2	3.41
25X-5, 113-115	229.93	1.45	0.72	2.72	73.1	50.3	101.2	2.68
25X-6, 112-116	231.42	1.41	0.56	2.28	77.4	60.2	151.0	3.35
25X-7, 43-45	232.23	1.40	0.59	2.92	79.9	57.9	137.3	3.92
27X-1, 29-31	241.69	1.39	0.59	2.40	76.5	57.8	136.7	3.20
27X-2, 25-29	243.15	1.39	0.58	2.57	78.3	58.5	141.1	3.54
27X-3, 108-110	245.48	1.35	0.60	2.42	75.2	55.8	126.0	2.98
27X-4, 21-25	246.11	1.36	0.56	2.28	76.4	58.8	142.6	3.17
29X-2, 25-30	252.65	1.36	0.58	2.35	75.9	57.4	134.9	3.09
29X-3, 21-23	254.11	1.33	0.55	2.23	76.0	58.7	142.3	3.10
29X-4, 22-27	255.62	1.33	0.51	2.40	79.6	61.9	162.8	3.82
29X-5, 90-92	257.80	1.41	0.61	2.71	78.1	56.9	132.0	3.50
30X-6, 55-60	268.55	1.39	0.58	2.66	78.5	58.0	138.3	3.59
31X-1, 15-17	270.35	1.41	0.63	2.50	75.3	55.2	123.2	3.00
31X-5, 25-30	276.45	1.37	0.59	2.62	77.6	57.1	133.1	3.40
32X-1, 50-52	278.70	1.37	0.58	2.55	77.6	57.8	136.7	3.40
32X-2, 50-55	280.20	1.36	0.54	2.61	79.8	60.4	152.4	3.88
32X-3, 50-52	281.70	1.34	0.53	2.45	79.0	60.6	154.0	3.68
32X-4, 50-55	283.20	1.34	0.53	2.46	79.0	60.5	153.0	3.68
32X-5, 40-42	284.60	1.36	0.55	2.54	79.0	59.8	148.7	3.69
33X-1, 100-102	288.90	1.36	0.55	1.77	72.0	59.2	145.0	2.51
33X-4, 66-71	293.06	1.33	0.45	2.25	81.2	65.8	192.6	4.22
35X-1, 66-68	307.96	1.38	0.59	2.40	75.8	56.8	131.4	3.08
35X-2, 66-70	309.46	1.35	0.55	2.22	76.0	58.8	143.0	3.10
35X-3, 66-68	310.96	1.32	0.51	2.27	78.2	61.3	158.7	3.52
35X-4, 66-70	312.46	1.32	0.51	2.32	78.8	61.7	160.9	3.64
35X-5, 66-68	313.96	1.31	0.50	2.33	79.2	62.1	163.7	3.72
35X-6, 66-70	315.46	1.33	0.50	2.28	78.9	62.2	164.6	3.66
36X-1, 30-32	317.20	1.34	0.47	2.29	80.8	64.7	183.4	4.10
36X-2, 30-34	318.70	1.30	0.45	2.16	80.5	65.7	191.2	4.04
36X-3, 30-32	320.20	1.28	0.45	2.23	80.6	65.1	186.2	4.05
36X-4, 30-34	321.70	1.27	0.46	2.29	80.3	64.0	177.8	3.98
36X-5, 30-32	323.20	1.33	0.52	2.28	78.1	61.1	157.1	3.50
36X-6, 30-34	324.70	1.31	0.46	2.37	81.1	64.5	181.5	4.20
37X-1, 68-70	327.28	1.37	0.55	2.49	78.7	59.8	148.9	3.63
37X-2, 68-72	328.78	1.38	0.57	2.48	77.7	58.5	140.9	3.42
37X-3, 24-26	329.84	1.39	0.56	2.49	78.5	59.5	147.0	3.58
37X-4, 24-28	331.34	1.32	0.47	2.36	80.7	63.9	177.1	4.08
37X-5, 24-26	332.84	1.31	0.48	2.34	80.3	63.5	174.2	3.98
37X-6, 24-28	334.34	1.36	0.52	2.40	79.6	62.0	163.1	3.82
37X-7, 24-26	335.84	1.32	0.47	2.24	80.1	64.3	179.9	3.94
38X-1, 29-31	336.49	1.36	0.55	2.46	78.1	59.2	145.1	3.49
38X-2, 29-33	337.99	1.37	0.59	2.45	76.6	57.3	134.1	3.21
38X-3, 29-31	339.49	1.39	0.56	2.57	78.9	59.3	145.8	3.66
38X-4, 29-33	340.99	1.35	0.53	2.10	76.7	61.1	157.1	3.22
38X-5, 29-31	342.49	1.37	0.53	2.66	80.7	61.3	158.5	4.11
38X-6, 29-33	343.99	1.44	0.62	2.65	77.5	56.8	131.3	3.39
38X-7, 10-14	345.30	1.45	0.67	2.61	75.2	54.0	117.3	2.99
39X-1, 40-42	346.30	1.39	0.60	2.48	76.4	56.7	131.1	3.17
39X-2, 40-44	347.80	1.37	0.55	2.63	79.8	60.1	150.9	3.87
39X-3, 40-42	349.30	1.39	0.59	2.63	78.2	57.8	137.0	3.52
39X-4, 40-44	350.80	1.36	0.53	2.57	80.3	61.4	158.9	3.99
39X-5, 40-42	352.30	1.42	0.63	2.46	75.6	55.8	126.4	3.04
39X-6, 40-44	353.80	1.43	0.64	2.59	76.3	55.5	124.8	3.16
39X-7, 40-42	355.30	1.35	0.56	2.24	75.7	58.2	139.1	3.05
40X-1, 94-96	356.54	1.55	0.81	2.73	71.5	48.1	92.9	2.47
40X-2, 94-98	358.04	1.34	0.52	2.32	78.8	61.6	160.2	3.64
40X-3, 94-96	359.54	1.39	0.59	2.34	75.7	57.3	134.0	3.06
40X-4, 103-107	361.13	1.39	0.61	2.33	74.6	55.9	126.7	2.88
40X-5, 96-98	362.56	1.39	0.59	2.55	77.1	57.1	133.1	3.32
40X-6, 107-111	364.17	1.48	0.67	2.62	75.7	54.5	120.0	3.07
40X-7, 50-52	365.10	1.39	0.60	2.66	77.7	56.9	132.2	3.43
41X-1, 50-52	365.80	1.40	0.58	2.51	77.9	58.5	141.1	3.46
41X-3, 61-63	368.91	0.97	0.44	2.47	74.8	54.8	121.2	2.93
41X-4, 52-57	370.32	1.36	0.61	2.47	75.4	55.5	124.9	3.01
41X-5, 50-52	371.80	1.38	0.58	2.31	75.7	57.5	135.6	3.06
41X-6, 30-35	373.10	1.37	0.60	2.35	75.2	56.5	129.9	2.98
42X-2, 23-28	376.73	1.33	0.54	2.25	76.5	59.3	145.8	3.20

Table 14 (continued).

Core, section, interval (cm)	Depth (mbsf)	Wet-bulk density (g/cm ³)	Dry-bulk density (g/cm ³)	Grain density (g/cm ³)	Porosity (%)	Wet water content (%)	Dry water content (%)	Void ratio
42X-2, 90-92	377.40	1.44	0.64	2.58	76.1	55.5	124.6	3.14
42X-6, 80-85	383.30	1.43	0.66	2.43	74.0	54.1	117.8	2.79
43X-1, 40-42	385.00	1.45	0.67	2.53	74.7	54.0	117.2	2.90
43X-2, 40-45	386.50	1.36	0.55	2.25	76.8	59.6	147.8	3.24
43X-3, 40-42	388.00	1.43	0.67	2.50	74.0	53.4	114.8	2.81
43X-4, 40-45	389.50	1.39	0.59	2.41	76.3	57.3	134.2	3.15
43X-5, 40-42	391.00	1.34	0.52	2.53	79.8	61.1	156.8	3.87
43X-6, 40-45	392.50	1.47	0.69	2.57	74.2	53.0	112.6	2.83
44X-1, 10-12	394.40	1.44	0.67	2.50	74.0	53.4	114.8	2.80
44X-2, 10-15	395.90	1.39	0.59	2.70	78.6	57.8	137.2	3.62
45X-1, 40-42	404.30	1.29	0.56	2.63	77.4	56.8	131.4	3.37
45X-2, 20-25	405.60	1.44	0.64	2.48	75.5	55.5	124.9	3.03
45X-2, 44-49	405.84	1.43	0.65	2.54	74.9	54.2	118.4	2.94
45X-3, 40-42	407.30	1.46	0.68	2.69	75.3	53.4	114.5	3.01
45X-4, 47-52	408.87	1.44	0.68	2.56	74.1	53.0	112.8	2.82
45X-5, 50-52	410.40	1.42	0.63	2.56	75.9	55.4	124.1	3.10
46X-1, 20-22	413.80	1.39	0.60	2.49	76.7	57.0	132.6	3.23
46X-3, 20-22	416.80	1.39	0.58	2.63	78.6	58.4	140.6	3.61
46X-4, 20-25	418.30	1.39	0.59	2.59	77.7	57.5	135.5	3.42
46X-5, 20-22	419.80	1.38	0.57	2.50	78.0	58.7	142.1	3.47
46X-6, 20-25	421.30	1.35	0.52	2.35	78.8	61.4	158.9	3.65
47X-1, 107-108	424.37	1.50	0.72	2.50	72.1	52.2	109.2	2.67
47X-2, 101-103	425.81	1.51	0.70	2.73	76.1	54.0	117.5	3.13
47X-3, 126-128	427.56	1.49	0.67	2.81	77.5	55.2	123.2	3.38
47X-4, 126-130	429.06	1.51	0.74	2.57	72.6	51.0	104.2	2.61
47X-5, 61-67	429.91	1.56	0.78	2.63	72.0	49.7	99.0	2.54
47X-6, 144-148	432.24	1.59	0.77	2.98	75.5	51.2	104.9	3.05
47X-7, 41-43	432.71	1.41	0.63	2.56	76.0	55.5	124.5	3.11
48X-1, 67-69	433.57	1.46	0.70	2.53	73.0	51.8	107.6	2.66
48X-2, 46-50	434.86	1.42	0.63	2.62	76.5	55.5	124.7	3.19
48X-3, 68-70	436.58	1.40	0.60	2.45	76.2	56.8	131.3	3.14
49X-1, 45-47	443.05	1.52	0.75	2.67	73.1	50.7	120.9	2.68
49X-CC, 14-18	443.71	2.72	2.60	2.83	11.3	4.4	4.6	0.13
50X-1, 88-90	453.18	1.47	0.70	2.44	72.5	52.1	108.9	2.59
50X-2, 88-92	454.68	1.48	0.74	2.65	72.3	49.9	99.4	2.57
50X-3, 88-90	456.18	1.47	0.66	2.37	74.5	55.3	123.8	2.87
50X-4, 93-97	457.73	1.78	1.15	2.67	59.2	35.5	54.9	1.43
50X-5, 68-70	458.98	1.80	1.29	2.44	48.6	28.1	39.2	0.93
50X-6, 38-40	460.18	1.93	1.61	2.21	30.3	16.6	19.9	0.43
51X-1, 80-82	462.70	2.04	1.68	2.29	32.6	17.6	21.4	0.48
51X-2, 80-84	464.20	1.78	1.14	2.87	61.3	35.9	55.9	1.57
51X-3, 80-82	465.70	1.82	1.21	2.70	57.1	33.3	49.9	1.32
128-799B-5R-1, 90-94	490.50	1.63	1.03	2.51	59.0	36.7	57.9	1.42
5R-2, 14-18	491.24	1.73	1.14	2.81	59.2	343.3	52.2	1.43
5R-3, 40-44	493.00	1.72	1.13	2.65	57.6	34.2	52.0	1.34
6R-1, 33-38	494.93	1.70	1.09	2.51	58.4	36.1	56.4	1.38
6R-3, 10-15	497.70	1.71	1.09	2.54	58.8	36.3	57.0	1.41
7R-1, 20-25	499.90	1.66	1.05	2.63	60.4	37.0	58.6	1.51
7R-3, 30-35	503.00	1.66	1.06	2.53	59.0	36.5	57.5	1.42
8R-1, 95-99	510.25	1.63	1.08	2.45	55.3	33.8	51.1	1.23
8R-3, 53-57	512.83	1.60	1.01	2.54	59.1	36.5	57.4	1.43
8R-6, 16-20	516.96	1.73	1.23	2.42	49.5	29.1	41.0	0.97
9R-2, 91-95	521.41	1.81	1.33	2.49	46.7	26.3	35.7	0.87
9R-4, 123-125	524.73	1.67	1.16	2.38	50.8	30.5	43.8	1.02
10R-2, 127-131	531.37	1.76	1.16	2.67	57.3	33.7	50.9	1.33
10R-4, 64-67	533.74	1.77	1.20	2.62	55.0	32.1	47.4	1.21
11R-2, 22-26	540.02	1.78	1.20	2.71	56.5	32.6	48.4	1.28
11R-5, 29-31	544.59	1.77	1.19	2.64	56.1	32.9	49.0	1.26
11R-7, 32-35	547.62	1.87	1.32	2.75	53.0	29.4	41.6	1.12
12R-3, 34-37	551.24	1.68	1.05	2.64	61.3	37.9	60.9	1.57
12R-4, 53-56	552.93	1.83	1.26	2.73	54.8	31.0	45.0	1.20
12R-4, 71-74	553.11	2.08	1.58	3.04	48.2	23.7	31.1	0.92
13R-1, 56-61	558.16	1.91	1.34	2.93	55.0	29.8	42.4	1.21
13R-3, 60-65	561.20	1.83	1.27	2.70	54.1	30.7	44.2	1.16
14R-1, 85-90	568.15	1.89	1.35	2.79	52.6	28.8	40.4	1.10
14R-3, 55-60	570.85	1.88	1.34	2.75	52.3	28.8	40.4	1.09
15R-1, 25-30	577.25	1.73	1.17	2.52	54.2	32.2	47.5	1.17
15R-4, 5-10	581.55	1.64	1.03	2.52	59.6	37.2	49.3	1.46
16R-1, 80-85	587.40	1.67	1.07	2.46	57.5	35.8	55.7	1.34
16R-3, 110-115	590.70	1.83	1.30	2.60	51.2	29.1	41.0	1.04
17R-1, 25-30	596.55	1.95	1.43	2.69	49.2	26.8	36.5	0.96
17R-3, 35-40	599.65	1.89	1.36	2.77	51.5	27.9	38.8	1.05

Table 14 (continued).

Core, section, interval (cm)	Depth (mbsf)	Wet-bulk density (g/cm ³)	Dry-bulk density (g/cm ³)	Grain density (g/cm ³)	Porosity (%)	Wet water content (%)	Dry water content (%)	Void ratio
17R-5, 30-35	602.60	1.91	1.39	2.79	50.9	27.4	37.7	1.03
18R-1, 143-147	607.33	1.96	1.45	2.76	48.8	25.9	35.0	0.94
18R-3, 89-91	609.79	1.88	1.36	2.70	50.9	28.0	38.9	1.03
18R-4, 139-141	611.79	1.90	1.34	2.80	53.5	29.4	41.7	1.14
19R-1, 77-81	616.37	1.98	1.48	2.72	47.4	25.2	33.7	0.89
19R-3, 80-84	619.40	1.87	1.32	2.61	51.7	29.4	41.6	1.06
19R-5, 55-59	622.15	1.95	1.44	2.69	48.6	26.3	35.6	0.94
20R-1, 83-86	626.03	1.89	1.37	2.69	50.2	27.5	38.0	1.00
20R-3, 96-100	629.16	1.94	1.44	2.78	48.5	25.6	34.4	0.93
20R-5, 108-112	632.28	1.94	1.42	2.72	49.4	26.7	36.4	0.97
21R-2, 61-65	637.01	1.80	1.23	2.69	55.5	32.0	47.0	1.23
21R-3, 80-84	638.70	1.93	1.45	2.85	48.5	25.1	33.6	0.93
22R-1, 6-9	644.66	1.84	1.27	2.67	53.8	30.7	44.2	1.15
23R-2, 50-55	656.20	1.86	1.31	2.74	53.0	29.4	41.7	1.12
24R-1, 10-15	663.90	1.97	1.45	2.76	49.5	26.5	36.0	0.97
24R-3, 10-15	666.90	1.91	1.39	2.75	50.8	27.6	38.1	1.02
25R-1, 60-65	674.10	1.88	1.38	2.62	48.8	27.0	36.9	0.94
25R-3, 90-95	677.40	1.91	1.43	2.69	46.9	25.0	33.4	0.88
26R-1, 120-125	684.40	1.78	1.19	2.72	57.3	33.3	50.0	1.33
27R-1, 108-112	693.58	2.01	1.55	2.73	43.9	22.5	29.0	0.77
27R-3, 112-117	696.62	1.98	1.49	2.84	48.2	25.0	33.3	0.92
27R-5, 21-25	698.71	1.89	1.38	2.72	49.6	26.8	36.7	0.97
28R-1, 40-45	702.50	1.99	1.53	2.76	45.2	23.2	30.3	0.82
28R-3, 40-45	705.50	1.99	1.53	2.71	44.5	23.1	30.0	0.79
28R-5, 40-45	708.50	2.02	1.56	2.74	44.2	22.7	29.3	0.79
29R-2, 100-105	714.30	2.03	1.54	2.71	45.6	23.9	31.4	0.83
29R-4, 75-80	717.05	1.95	1.46	2.69	46.9	25.0	33.3	0.87
29R-6, 70-75	720.00	1.97	1.49	2.63	45.1	24.1	31.7	0.81
30R-1, 85-87	722.25	2.04	1.59	2.62	42.2	22.0	28.3	0.72
31R-1, 9-11	730.89	2.65	2.53	2.84	12.3	4.8	5.0	0.14
32R-1, 59-61	741.09	2.17	1.88	2.60	28.0	13.2	15.2	0.39
33R-1, 69-72	750.89	2.07	1.70	2.63	36.7	18.3	22.4	0.57
34R-1, 14-18	759.94	1.94	1.48	2.63	44.7	23.8	31.2	0.80
35R-2, 42-44	771.42	1.99	1.55	2.61	42.2	22.1	28.3	0.72
36R-1, 137-141	780.57	2.19	1.90	2.63	28.8	13.5	15.6	0.40
37R-1, 55-57	789.45	2.21	1.93	2.58	26.4	12.4	14.1	0.36
38R-1, 65-67	799.15	1.99	1.57	2.61	40.3	20.7	26.2	0.67
39R-1, 103-105	809.13	2.15	1.78	2.66	34.9	17.0	20.5	0.53
40R-1, 4-6	817.84	2.03	1.64	2.58	38.0	19.4	24.1	0.61
41R-CC, 15-18	827.86	2.10	1.74	2.63	34.8	17.1	20.6	0.53
42R-1, 21-23	837.01	2.16	1.83	2.72	32.7	15.4	18.1	0.48
45R-1, 23-25	866.03	2.08	1.69	2.68	37.7	18.6	22.9	0.60
46R-1, 34-36	875.64	2.12	1.79	2.65	32.9	15.8	18.8	0.49
46R-3, 93-95	879.23	1.99	1.68	2.75	33.1	15.5	18.3	0.49
47R-1, 136-138	886.36	2.04	1.72	2.63	33.0	16.0	19.0	0.49
47R-3, 111-113	889.11	2.07	1.70	2.62	35.8	17.8	21.6	0.55
48R-2, 96-100	897.06	2.15	1.80	2.59	33.1	16.3	19.4	0.49
49R-1, 48-50	904.68	2.08	1.72	2.61	34.9	17.2	20.8	0.53
50R-1, 54-58	914.14	2.13	1.80	2.60	32.1	15.6	18.4	0.47
51R-2, 78-82	925.58	2.08	1.71	2.65	36.4	17.9	21.9	0.57
51R-5, 20-24	929.50	2.05	1.66	2.66	38.2	19.1	23.6	0.61
52R-1, 13-16	933.03	2.09	1.73	2.64	35.5	17.4	21.1	0.54
53R-2, 0-4	944.10	2.15	1.80	2.68	33.7	16.2	19.3	0.50
54R-1, 19-23	952.39	2.10	1.78	2.60	31.8	15.4	18.2	0.46
54R-3, 43-45	955.63	2.10	1.74	2.68	35.3	17.1	20.6	0.54
55R-1, 63-65	962.43	2.08	1.74	2.63	34.0	16.6	19.8	0.51
56R-2, 4-6	973.04	2.02	1.65	2.67	37.4	18.5	22.7	0.59
58R-1, 74-76	991.54	2.11	1.76	2.64	33.6	16.3	19.5	0.50
59R-1, 54-56	1001.04	2.11	1.75	2.68	35.5	17.3	20.9	0.54
60R-1, 21-23	1010.41	2.08	1.75	2.65	33.0	15.9	18.9	0.49
60R-3, 65-67	1013.85	2.16	1.86	2.61	29.7	14.1	16.4	0.42
61R-1, 105-107	1020.85	2.04	1.65	2.63	37.8	19.0	23.5	0.60
61R-3, 103-105	1023.83	2.18	1.83	2.66	32.7	15.6	18.5	0.48
61R-5, 43-45	1026.23	2.15	1.85	2.81	31.0	14.0	16.3	0.45
62R-2, 13-17	1031.13	2.13	1.82	2.64	31.0	14.7	17.2	0.44
62R-4, 44-48	1034.44	2.20	1.90	2.64	29.3	13.8	16.0	0.41
63R-1, 119-123	1040.29	2.25	1.94	2.66	29.2	13.6	15.7	0.41
63R-3, 43-45	1042.53	2.19	1.88	2.63	29.6	14.0	16.2	0.42
64R-1, 0-4	1048.80	2.52	2.32	2.86	19.5	7.9	8.6	0.24
65R-1, 83-85	1059.23	2.16	1.86	2.57	29.0	13.9	16.2	0.41
65R-3, 14-16	1061.54	2.22	1.94	2.59	26.6	12.5	14.2	0.36
66R-2, 48-50	1069.17	2.19	1.91	2.59	27.4	12.9	14.8	0.37
67R-1, 145-147	1079.15	2.13	1.82	2.59	30.4	14.6	17.2	0.43
67R-3, 9-11	1080.79	2.19	1.89	2.61	29.1	13.8	16.0	0.41

Table 15. Sonic velocities from Hole 799A (continuous P-wave logger).

Depth (mbsf)	Velocity (m/s)	Depth (mbsf)	Velocity (m/s)	Depth (mbsf)	Velocity (m/s)	Depth (mbsf)	Velocity (m/s)	Depth (mbsf)	Velocity (m/s)
0.1	1503.40								
0.2	1498.50								
0.3	1503.10	8.2	1496.38	15.6	1501.75	24.2	1477.40	34.2	1440.40
0.4	1500.83	8.3	1489.65	15.7	1497.73	24.3	1473.07	34.3	1481.20
0.5	1499.70	8.4	1494.88	15.8	1504.83	24.4	1440.94	34.7	1468.35
0.6	1502.00	8.5	1491.23	15.9	1497.28	24.5	1478.90	34.8	1431.40
0.7	1501.52	8.6	1491.65	16.0	1500.10	24.6	1456.98	34.9	1450.73
0.8	1499.67	8.7	1501.13	16.1	1497.95	24.7	1470.42	35.0	1449.23
0.9	1502.62	8.9	1504.43	16.2	1497.43	24.8	1535.00	35.1	1432.43
1.0	1505.13	9.0	1505.08	16.3	1495.10	24.9	1444.45	35.2	1454.98
1.4	1502.30	9.1	1489.67	16.9	1504.93	25.0	1448.90	35.3	1447.55
1.5	1500.85	9.2	1487.00	17.0	1503.33	25.1	1461.13	35.4	1455.33
1.6	1501.13	9.3	1490.20	17.1	1503.67	25.2	1445.48	35.5	1435.53
1.7	1502.03	9.4	1490.28	17.2	1503.53	25.3	1447.07	35.6	1483.00
1.8	1498.80	9.5	1492.50	17.3	1500.33	25.4	1451.00	35.7	1443.90
1.9	1497.90	9.6	1500.48	17.4	1501.97	25.5	1448.25	36.1	1442.00
2.0	1498.50	9.7	1506.20	17.5	1503.00	25.6	1446.28	36.2	1429.07
2.1	1510.05	9.8	1498.45	17.6	1498.38	25.7	1439.88	36.3	1485.10
2.2	1513.38	9.9	1496.34	17.7	1502.75	25.8	1446.40	36.4	1464.77
2.3	1516.78	10.0	1502.13	17.8	1493.03	25.9	1492.10	36.5	1460.68
2.4	1514.50	10.1	1498.06	17.9	1493.43	26.0	1451.15	36.6	1472.30
2.5	1499.95	10.2	1501.00	18.0	1492.80	26.1	1451.57	36.7	1473.07
2.6	1499.10	10.4	1506.13	18.1	1494.28	26.2	1478.53	36.8	1447.35
2.9	1499.47	10.5	1498.65	18.2	1498.13	26.4	1470.03	36.9	1450.00
3.0	1529.93	10.6	1495.84	18.3	1533.40	26.5	1446.70	37.0	1456.22
3.1	1544.53	10.7	1494.23	18.4	1499.07	26.6	1490.90	37.1	1436.23
3.2	1589.47	10.8	1496.86	18.5	1497.65	26.7	1470.65	37.2	1453.57
3.3	1570.75	10.9	1499.20	18.6	1496.27	26.8	1501.60	37.3	1449.63
3.4	1578.20	11.0	1496.88	18.7	1498.15	26.9	1489.16	37.4	1480.10
3.5	1551.87	11.1	1497.85	18.8	1499.10	27.0	1513.65	37.6	1398.40
3.6	1610.58	11.2	1569.60	18.9	1501.07	27.1	1507.07	37.7	1464.53
3.7	1563.60	11.3	1505.95	19.0	1495.57	27.2	1509.05	37.8	1471.00
3.8	1506.85	11.4	1492.83	19.1	1496.03	27.3	1500.40	37.9	1472.77
3.9	1542.60	11.5	1492.37	19.2	1493.20	27.4	1511.70	38.0	1476.73
4.0	1493.33	11.6	1493.28	19.3	1493.73	27.5	1468.87	38.1	1466.47
4.1	1494.22	11.7	1503.20	19.4	1498.13	27.6	1443.12	38.2	1467.03
4.2	1492.30	11.8	1489.95	19.5	1500.03	27.7	1416.03	38.3	1475.40
4.3	1502.80	11.9	1499.05	19.6	1496.68	27.9	1427.30	38.4	1455.47
4.4	1521.30	12.0	1515.32	19.7	1499.13	28.0	1435.17	38.5	1447.00
4.5	1499.22	12.1	1493.58	19.8	1504.10	28.1	1437.80	38.6	1426.40
4.6	1500.23	12.2	1488.90	19.9	1498.65	28.2	1500.03	38.7	1437.63
4.7	1513.73	12.3	1502.00	20.0	1495.93	28.3	1479.77	38.8	1414.27
4.8	1506.50	12.4	1495.20	20.1	1503.90	28.4	1477.33	38.9	1477.70
4.9	1497.93	12.5	1494.10	20.2	1493.38	28.5	1578.50	39.1	1479.90
5.0	1497.90	12.6	1496.13	20.3	1491.13	28.6	1448.05	39.2	1466.18
5.1	1514.23	12.7	1498.83	20.4	1510.70	28.7	1476.17	39.3	1412.90
5.2	1532.10	12.8	1498.95	20.5	1428.00	28.8	1539.90	39.4	1456.58
5.3	1508.53	12.9	1497.50	21.0	1445.20	29.0	1465.90	39.5	1472.53
5.4	1498.68	13.0	1494.20	21.1	1476.93	29.1	1475.65	39.6	1453.80
5.5	1498.47	13.1	1492.92	21.2	1461.27	29.2	1471.40	39.8	1543.75
5.6	1498.30	13.2	1494.47	21.3	1436.35	30.4	1474.60	44.5	1392.00
5.7	1499.83	13.3	1492.90	21.4	1469.70	30.5	1495.87	44.8	1456.10
5.9	1519.80	13.4	1498.54	21.5	1441.30	30.7	1459.80	44.9	1435.40
6.0	1515.35	13.5	1486.60	21.6	1467.03	30.8	1460.60	45.0	1468.10
6.3	1534.30	13.6	1484.56	21.7	1466.33	30.9	1451.20	45.1	1477.60
6.4	1517.70	13.7	1485.85	21.8	1477.45	31.0	1474.15	45.2	1469.50
6.5	1500.80	13.8	1499.00	21.9	1549.70	31.1	1469.20	45.4	1406.25
6.6	1505.78	13.9	1506.70	22.1	1445.40	31.2	1471.25	45.8	1402.70
6.7	1510.43	14.0	1498.98	22.2	1442.17	32.0	1476.85	45.9	1428.70
6.8	1509.03	14.1	1498.00	22.3	1476.80	32.1	1461.65	46.0	1390.60
6.9	1499.50	14.2	1504.73	22.4	1510.03	32.2	1436.73	46.1	1427.80
7.0	1493.15	14.3	1506.03	22.5	1491.20	32.3	1454.10	46.2	1448.65
7.1	1492.90	14.4	1526.20	22.6	1546.15	32.4	1436.47	46.3	1459.23
7.2	1495.33	14.5	1514.23	22.7	1493.02	32.5	1446.80	46.4	1415.00
7.3	1499.70	14.6	1529.30	22.8	1507.28	32.6	1429.47	46.5	1413.35
7.4	1498.20	14.7	1568.60	22.9	1467.07	32.7	1461.27	46.6	1431.45
7.5	1496.73	14.8	1505.80	23.0	1449.90	32.8	1460.90	46.7	1399.30
7.6	1494.27	14.9	1535.13	23.1	1525.28	32.9	1484.15	46.8	1381.90
7.7	1492.30	15.0	1582.95	23.2	1519.40	33.6	1450.60	47.7	1461.00
7.8	1491.95	15.1	1536.78	23.5	1511.55	33.7	1471.40	48.0	1530.30
7.9	1497.13	15.2	1566.50	23.8	1496.10	33.8	1426.93	50.2	1452.80
8.0	1491.90	15.3	1509.00	23.9	1489.85	33.9	1460.90		
8.1	1493.30	15.4	1503.50	24.0	1534.10	34.0	1433.00		
		15.5	1503.65	24.1	1467.83	34.1	1443.63		

Table 16. Sonic velocities from Hole 799B (discrete sample determinations).

Core, section, interval (cm)	Depth (mbsf)	Velocity (m/s)
128-799B-5R-2, 14-18	491.24	1598
6R-3, 10-15	497.70	1386
8R-1, 95-99	510.25	1834
8R-3, 53-57	512.83	1636
8R-6, 16-20	516.96	2185
9R-2, 91-95	521.41	2370
9R-4, 123-125	524.73	2149
10R-2, 127-131	531.37	1673
10R-4, 64-67	533.74	1809
11R-2, 22-26	540.02	1809
11R-5, 29-31	544.59	1899
12R-3, 34-37	551.24	1838
12R-4, 53-56	552.93	2316
12R-4, 71-74	553.11	2274
13R-1, 56-61	558.16	2214
14R-1, 85-90	568.15	1426
15R-1, 25-30	577.25	1640
17R-3, 35-40	599.65	1993
18R-1, 143-147	607.33	1762
18R-3, 88-91	609.78	1748
18R-4, 139-141	611.79	1708
19R-1, 77-81	616.37	1774
19R-3, 80-84	619.40	1711
19R-5, 55-59	622.15	1818
20R-1, 83-86	626.03	1803
20R-3, 96-100	629.16	1823
20R-5, 108-112	632.28	1772
21R-2, 61-65	637.01	1656
21R-3, 80-84	638.70	1764
22R-1, 6-9	644.66	1852
25R-3, 90-95	677.40	1863
27R-5, 21-25	698.71	1740
28R-1, 40-45	702.50	1931
30R-1, 85-87	722.25	1886
31R-1, 9-11	730.89	4880
32R-1, 59-61	741.09	2780
33R-1, 69-72	750.89	2064
34R-2, 14-18	761.44	1738
35R-2, 42-44	771.42	1855
36R-1, 37-41	779.57	2781
38R-1, 66-68	799.16	2291
41R-CC, 15-18	827.86	2238
42R-1, 21-23	837.01	2556
45R-1, 121-123	867.01	1837
46R-1, 34-36	875.64	2386
46R-3, 93-95	879.23	2107
47R-1, 136-138	886.36	2481
48R-2, 95-100	897.05	2185
49R-1, 48-52	904.68	1953
50R-1, 54-58	914.14	2313
51R-2, 78-82	925.58	2228
51R-5, 20-24	929.50	2191
52R-1, 13-16	933.03	2269
53R-2, 0-4	944.10	2177
54R-1, 19-23	952.39	2498
55R-1, 63-65	962.43	2409
56R-2, 4-6	973.04	2019
58R-1, 74-76	991.54	2464
59R-1, 54-56	1001.04	2412
60R-1, 21-23	1010.41	2271
62R-2, 13-17	1031.13	2502
62R-4, 44-48	1034.44	2554
63R-3, 43-45	1042.53	2219
64R-1, 0-4	1048.80	3488
65R-1, 83-85	1059.23	2465
65R-3, 14-16	1061.54	2279
66R-2, 48-50	1069.17	2219
67R-1, 145-147	1079.15	2439

with 100 mbsf at Site 798, which precludes equivalent correlation with the Site 799 ash record. The large slump structures apparent on the sides of Kita-Yamato Trough in the 3.5-kHz record are discussed in the "Lithostratigraphy" section (this chapter).

Correlation of Seismic Stratigraphy With Lithology at Site 799

A summary of the seismic-reflection record in the Kita-Yamato Trough and its correlation to the seismic record with lithology, logging, and other characteristics observed and measured at Site 799 are presented in Figure 161. VSP was run at this site; this allowed us to convert directly the seismic-wave traveltimes to depths. Further results from VSP data will require post-cruise data processing. The sonic-velocity log (see "Downhole Measurements" section, this chapter) shows that seismic velocity increases linearly from about 1.45 km/s at 110 mbsf to 1.6 km/s at 450 mbsf, with a number of spikes over the length of this trend. The largest spike in this record occurs at 440 mbsf and clearly corresponds to significant density, resistivity, and gamma-ray anomalies. Other notably abrupt changes can be observed at 250 and 400 mbsf. The opal-A/opal-CT boundary occurs at about 458 mbsf and is accompanied by other changes in lithology and physical properties (see "Lithostratigraphy" and "Physical Properties" sections, this chapter).

Seismic Interval 1 (0.0-0.3 s) represents sediments in which wet-bulk density increases and sonic velocity and porosity decrease with depth, as indicated by both laboratory measurements and logging data (see "Physical Properties" and "Downhole Measurements" sections, this chapter). The bottom of Interval 1 is marked by a sharp jump in bulk density. Seismic Interval 2 (0.3-0.55 s) begins within lithologic Unit II; the base of the seismic interval correlates with the base of the lithologic unit (Fig. 161). The reflector at 0.5 s correlates with spikes at 400 mbsf in logging data. The reflector at 0.55 s marks the bottom of Interval 2. Both bulk density and sonic velocity increase below this depth, which corresponds to the opal-A/opal-CT boundary. Interval 3 either includes or bottoms at the opal-CT/quartz transition boundary. Logging results show rather stable values above this level, concordant with the less-reflective acoustic nature. Many spikes in logging parameters were observed below, especially between 600 and 800 mbsf, which can be correlated to highly reflective beds in Interval 4. The top of Interval 5 coincides with the rhyolitic ash deposits recovered between 981 and 1002 mbsf, where the bulk density is not much affected, but the sonic velocity decreases.

Figure 162 represents a correlation of the 3.5-kHz record, sonic velocities, and recovered samples. Note that this section includes only the upper portion of the sedimentary sequence. Physical properties (other than sonic velocity) vary greatly within the depths represented by this record, which precludes meaningful correlations (see "Physical Properties" section, this chapter). Ash layers of significant thicknesses in the upper part of Hole 799A have been marked 3 to 7 in Figure 162; these layers may correlate with discrete increases in sonic velocity. However, assuming a velocity of 1.5 km/s within this part of the section, the correlation to 3.5-kHz reflectors is not obvious below 25 mbsf. Individual sand layers also seem to be correlative with discrete reflectors, probably because of associated density changes, as velocity changes are not significant. Although a thick volcanic ash bed occurs between 27 and 30 mbsf and is accompanied by a velocity change, this bed cannot be recognized in the 3.5-kHz record. More detailed study, including analysis of waveforms, may ultimately en-

Table 17. Thermal conductivities from Site 799.

Core, section, interval (cm)	Depth (mbsf)	Thermal conductivity (W/m · K)
128-799-1H-1, 40-41	0.4	1.775
2H-1, 60-61	1.8	0.983
2H-2, 60-61	3.3	0.965
2H-3, 60-61	4.8	1.026
2H-4, 60-61	6.3	1.000
3H-1, 50-51	11.2	0.893
3H-2, 50-51	12.7	0.752
3H-3, 50-51	14.2	1.065
3H-4, 42-43	15.6	1.092
4H-1, 30-31	20.6	0.955
4H-2, 30-31	22.1	1.117
4H-3, 30-31	23.6	1.070
4H-4, 35-36	25.2	1.046
5H-1, 25-26	30.2	1.082
5H-2, 25-26	31.7	0.951
5H-3, 25-26	33.2	0.953
5H-4, 25-26	34.7	0.837
6H-1, 40-41	39.9	0.938
6H-2, 40-41	41.4	0.990
6H-3, 40-41	42.9	1.004
6H-4, 40-41	44.4	0.866
7H-1, 45-46	49.6	0.851
7H-2, 45-46	51.1	1.083
7H-3, 45-46	52.6	1.068
7H-4, 45-46	54.1	1.006
8H-1, 45-46	59.2	0.817
8H-2, 45-46	60.7	1.012
8H-3, 45-46	62.2	0.930
8H-4, 45-46	63.7	0.970
9H-1, 50-51	68.8	1.110
9H-2, 50-51	70.3	1.073
9H-3, 50-51	71.8	0.888
9H-4, 50-51	73.3	0.960
10H-1, 60-61	78.5	0.824
10H-2, 60-61	80.0	0.914
10H-3, 60-61	81.5	1.029
10H-4, 60-61	83.0	1.024
11H-1, 50-51	88.0	1.076
11H-2, 50-51	89.5	0.891
11H-3, 50-51	91.0	1.221
11H-4, 50-51	92.5	0.949
12H-1, 60-61	97.8	0.988
12H-2, 60-61	99.3	1.068
12H-3, 60-61	100.8	0.723
12H-4, 60-61	102.3	1.019
13H-1, 60-61	107.4	0.942
13H-2, 60-61	108.9	1.015
13H-3, 60-61	110.4	1.173
13H-4, 60-61	111.9	0.890
14H-1, 50-51	117.0	0.985
14H-2, 50-51	118.5	1.119
14H-3, 50-51	120.0	1.062
14H-4, 50-51	121.5	1.064
15H-1, 30-31	126.4	0.988
15H-2, 30-31	127.9	1.075
15H-3, 30-31	129.4	1.123
15H-4, 30-31	130.9	1.016
16H-1, 40-41	136.2	1.084
16H-2, 40-41	137.7	1.130
16H-3, 40-41	139.2	1.068
16H-4, 40-41	140.7	1.007
17H-1, 40-41	145.9	1.040
17H-2, 40-41	147.4	0.969
17H-3, 40-41	148.9	0.959
17H-4, 40-41	150.4	1.007
18H-2, 40-41	157.1	0.836
18H-3, 40-41	158.6	0.834
18H-4, 40-41	160.1	0.949
19H-1, 50-51	165.3	1.496
19H-2, 50-51	166.8	1.261
19H-3, 50-51	168.3	1.360
19H-4, 50-51	169.8	1.339
20H-1, 30-31	174.8	0.736
20H-2, 30-31	176.3	0.903
20H-2, 30-31	177.8	0.850

Table 17 (continued).

Core, section, interval (cm)	Depth (mbsf)	Thermal conductivity (W/m · K)
20H-3, 30-31	177.8	0.850
20H-4, 30-31	179.3	0.861
21X-1, 40-41	184.5	0.887
21X-2, 42-43	186.0	0.856
21X-3, 40-41	187.5	0.875
21X-4, 36-37	189.0	0.900
23X-1, 40-41	203.9	0.753
23X-2, 40-41	205.4	0.858
23X-3, 40-41	206.9	0.784
23X-4, 40-41	208.4	0.822
24X-1, 40-41	213.5	0.811
24X-2, 40-41	215.0	0.810
24X-3, 40-41	216.5	0.811
24X-4, 40-41	218.0	0.809
25X-1, 40-41	223.2	0.902
25X-2, 40-41	224.7	0.807
25X-3, 40-41	226.2	0.759
25X-4, 27-28	227.6	0.780
27X-1, 40-41	241.8	0.848
27X-2, 40-41	243.3	0.815
27X-3, 40-41	244.8	0.779
27X-4, 40-41	246.3	0.800
29X-1, 50-51	251.4	0.718
29X-2, 50-51	252.9	0.753
29X-3, 50-51	254.4	0.761
29X-4, 50-51	255.9	0.868
30X-1, 45-46	261.0	0.844
30X-2, 45-46	262.5	0.822
30X-3, 45-46	264.0	0.885
30X-4, 45-46	265.5	0.912
31X-1, 50-51	270.7	0.818
31X-2, 50-51	272.2	0.833
31X-4, 50-51	275.2	0.846
32X-1, 50-51	278.7	0.867
32X-2, 50-51	280.2	0.815
32X-3, 50-51	281.7	0.866
32X-4, 45-46	283.2	0.774
33X-1, 40-41	288.3	0.802
33X-2, 40-41	289.8	0.863
33X-3, 40-41	291.3	0.658
33X-4, 40-41	292.8	0.817
34X-1, 40-41	298.0	0.466
34X-2, 40-41	299.5	0.712
34X-3, 40-41	301.0	0.842
34X-4, 40-41	302.5	0.683
35X-1, 40-41	307.7	0.767
35X-2, 40-41	309.2	0.794
35X-3, 40-41	310.7	0.807
35X-4, 40-41	312.2	0.805
36X-1, 40-41	317.3	0.770
36X-2, 40-41	318.8	0.759
36X-3, 40-41	320.3	0.704
36X-4, 40-41	321.8	0.755
37X-1, 50-51	327.1	0.732
37X-2, 50-51	328.6	0.848
37X-3, 50-51	330.1	0.825
37X-4, 50-51	331.6	0.804
38X-2, 50-51	338.2	0.687
38X-3, 50-51	339.7	0.789
38X-4, 50-51	341.2	0.805
39X-1, 60-61	346.5	0.761
39X-2, 60-61	348.0	0.836
39X-3, 60-61	349.5	0.846
39X-4, 60-61	351.0	0.821
40X-1, 40-41	356.0	0.733
40X-2, 40-41	357.5	0.843
40X-3, 40-41	359.0	0.806
40X-4, 60-61	360.7	0.811
41X-1, 50-51	365.8	0.813
41X-2, 50-51	367.3	0.886
41X-3, 50-51	368.8	0.770
41X-4, 50-51	370.3	0.834
42X-1, 40-41	375.4	0.715
42X-2, 40-41	376.9	0.793
42X-3, 40-41	378.4	0.777
42X-4, 40-41	379.9	0.888

Table 17 (continued).

Core, section, interval (cm)	Depth (mbsf)	Thermal conductivity (W/m · K)
43X-1, 30-31	384.9	0.765
43X-2, 30-31	386.4	0.838
43X-3, 30-31	387.9	0.900
43X-4, 30-31	389.4	0.726
44X-1, 43-44	394.7	0.915
44X-2, 75-76	396.6	0.911
45X-1, 40-41	404.3	0.769
45X-2, 40-41	405.8	0.937
45X-3, 40-41	407.3	0.879
45X-4, 40-41	408.8	0.862
46X-1, 40-41	414.0	0.879
46X-2, 40-41	415.5	0.806
46X-3, 40-41	417.0	0.864
46X-4, 40-41	418.5	0.807
47X-1, 25-26	423.6	0.899
47X-2, 25-26	425.1	0.960
47X-3, 25-26	426.6	0.815
47X-4, 25-26	428.1	0.863
48X-1, 60-61	433.5	0.798
48X-2, 60-61	435.0	0.766
48X-3, 60-61	436.5	0.874
49X-1, 50-51	443.1	0.705
50X-1, 43-44	452.7	0.910
50X-2, 100-101	454.8	1.075
50X-3, 43-44	455.7	0.806
50X-4, 90-91	457.7	0.994
51X-1, 40-41	462.3	0.951
51X-2, 40-41	463.8	1.050
51X-3, 20-21	465.1	0.793
128-799B-13R-2, 36-37	559.46	1.279
14R-3, 46-47	570.76	1.196
14R-3, 46-47	570.76	1.202
15R-2, 59-60	579.09	1.077
16R-2, 60-61	588.70	0.402
17R-2, 52-53	598.32	1.182
18R-2, 80-81	608.20	1.061
19R-2, 80-81	617.90	1.279
20R-2, 68-69	627.38	2.285
21R-2, 60-61	637.00	1.240
23R-2, 61-62	656.31	1.404
24R-3, 59-60	667.39	1.409
25R-2, 75-76	675.75	0.920

hance interpretations of the 3.5-kHz record and resolve apparent inconsistencies.

CONCLUSIONS

We essentially completed all of our objectives at Site 799: (1) to determine the depositional and tectonic history of the Kita-Yamato Trough, thought to be an ideal or typical environment for deposition of massive sulfide mineralization in a rifted continental arc setting; and (2) to obtain information about the paleoceanographic history in the Yamato Rise area and in the Sea of Japan in general. We were thwarted in fully completing objective 1 in that sharp increases in hydrocarbon gases and a fluorescent cut caused us to halt drilling at 1084 mbsf. VSP results indicate that acoustic basement rocks are located approximately 120 m below the base of Hole 799B; in short, we came within 12 cores of our stated objective. A detailed summary of the results and conclusions at Site 799 can be found at the beginning of this chapter. Hence, we simply highlight our key findings as these relate to our major objectives.

Depositional History of the Kita-Yamato Trough

The narrow Kita-Yamato Trough has been interpreted as a failed-rift within the larger Yamato Rise. The Yamato Rise is

Table 18. Torvane shear-strength measurements at Hole 799A.

Core, section, interval (cm)	Depth (mbsf)	Shear strength (kPa)
128-799A-1H-1, 44-48	0.44	1.6
2H-2, 73-75	3.43	2.4
2H-4, 75-77	6.45	6.7
2H-6, 45-47	9.15	7.8
3H-2, 10-12	12.30	6.3
3H-4, 10-12	15.30	10.4
3H-6, 10-12	18.30	12.4
4H-2, 20-22	22.00	17.1
4H-4, 20-22	25.00	18.4
4H-6, 20-22	28.00	18.6
5H-2, 20-22	31.60	22.1
5H-4, 20-22	34.60	18.6
5H-6, 20-22	37.60	22.6
6H-2, 20-22	41.20	35.3
6H-4, 20-22	44.20	40.2
6H-6, 20-22	47.20	32.4
7H-2, 40-42	51.00	41.7
7H-4, 40-42	54.00	41.7
7H-6, 40-42	57.00	42.7
8H-2, 70-72	60.90	18.6
8H-4, 60-62	63.80	23.5
8H-6, 50-52	66.70	33.3
9H-2, 30-32	70.10	47.1
9H-4, 5-7	72.85	39.2
9H-6, 30-32	76.10	41.2
10H-2, 25-27	79.65	47.1
10H-4, 25-27	82.65	37.3
10H-6, 120-122	86.60	55.9
11H-2, 20-22	89.20	51.0
11H-4, 60-62	92.60	52.0
11H-6, 100-102	96.00	80.4
12H-2, 20-22	98.90	68.6
12H-4, 30-32	102.00	73.5
12H-6, 20-22	104.90	83.4
13H-2, 26-28	108.56	85.3
13H-4, 20-22	111.50	72.6
13H-6, 20-22	114.50	83.4
14H-2, 40-42	118.40	80.4
14H-5, 40-42	122.90	85.3
14H-6, 30-32	124.30	86.3
15H-2, 62-64	128.22	44.1
15H-3, 101-103	130.11	69.6
15H-6, 130-132	134.90	83.4
16H-2, 60-62	137.90	90.2
16H-4, 60-62	140.90	93.2
16H-6, 60-62	143.90	91.2
17H-2, 55-60	147.55	87.3
17H-4, 40-45	150.40	93.2
17H-6, 40-45	153.40	96.1
18H-2, 25-30	156.95	80.4
18H-4, 40-45	160.10	86.3
18H-6, 40-45	163.10	93.2
19H-2, 20-25	166.50	76.5
19H-4, 15-20	169.45	72.6
19H-6, 70-75	173.00	66.7
20H-2, 20-25	176.20	83.4
20H-4, 20-25	179.20	91.9
20H-6, 20-25	182.20	78.5

a tectonically isolated continental fragment having a granitic basement and an overlying blanket of Miocene volcanic and volcanoclastic rocks. Seismic-reflection profiles clearly illustrate that the Kita-Yamato Trough is a graben having multiple normal faults that bound its central axis. Pre-cruise seismic estimates of total sediment thickness in the trough indicated that between 1200 and 1300 m of Miocene to Holocene sediments are present in the axis of this feature. This thickness is almost twice the average thickness of the sediment columns in the Japan and Yamato basins, the two largest basins in the Sea of Japan. The unusual thickness of sediments clearly implies that Kita-Yamato Trough has experienced

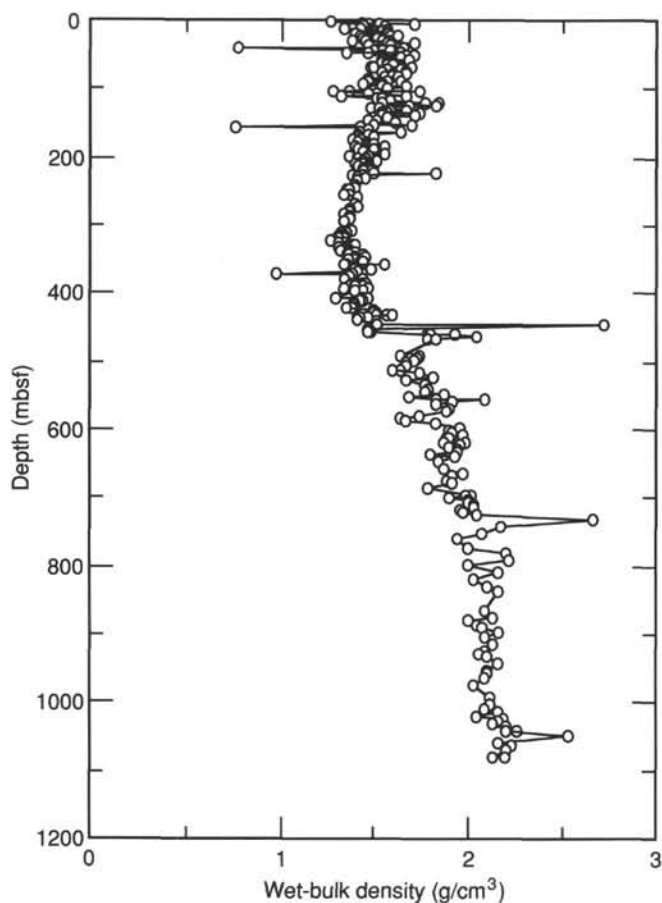


Figure 129. Wet-bulk density vs. depth for Site 799.

pronounced subsidence, probably accommodated by the continental crust beneath the Yamato Rise—as opposed to the surrounding oceanic and transitional crust presumably underlying adjacent basins.

Drilling penetrated 1084 m of marine sediment at Site 799. Reliable biostratigraphic and paleomagnetic ages are restricted to uppermost Miocene through Quaternary sediments at this site, with extensive and pervasive diagenetic alteration of both biosiliceous and biocalcareous sediments below 400 mbsf. Fortunately, rare and sporadic occurrences of both siliceous and calcareous microfossils provide tentative age control to the base of the Site 799 column. Calcareous nanofossils and radiolarians provide the oldest dates obtained in this sequence, with both groups indicating that lithologic Unit V at the base of Hole 799B is early Miocene in age.

Identifiable benthic foraminifers are scattered in lower and middle Miocene sediments and common in upper Miocene through Quaternary sediments. *In-situ* assemblages in all units indicate deposition of the entire Site 799 sequence occurred at middle and lower water depths, averaging near the modern water depth of 2084 m at Site 799. However, there is some faunal evidence that lower bathyal depths in excess of 2000 m may have occurred during the Pliocene.

The sedimentary history chronicled at Site 799 begins in the early Miocene, when coarse siliciclastic turbidite sands were deposited in a paleogeographic setting much different from that of the modern Sea of Japan. Terrestrial plant debris, shallow-water benthic foraminifers, and other evidence indicate that the sands were re-deposited from littoral and neritic environments and in close proximity to an insular or conti-

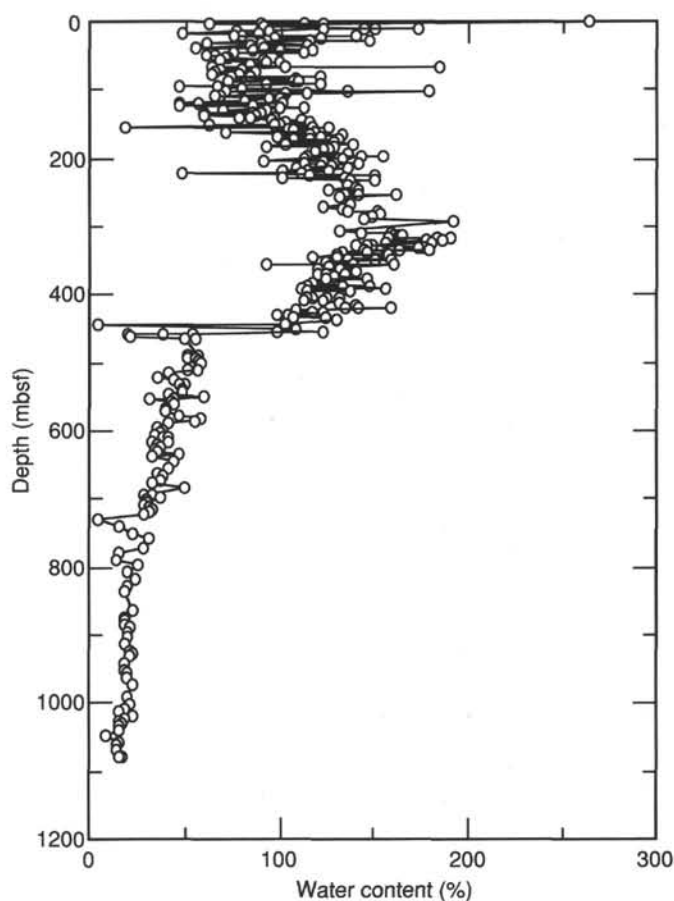


Figure 130. Water content (expressed relative to dry weight) vs. depth for Site 799.

ental shoreline. Composition of the sands reflects a mixed provenance from granitic and volcanic rocks. Intercalated claystones in these deposits contain lower bathyal foraminifers. A major and proximal volcanic event occurred in the Kita-Yamato Trough area in late early Miocene time, as marked by a 24-m-thick unit of altered rhyolitic tuff and tuff breccia. This rock is similar to rhyolitic rocks associated with the Miocene Kuroko massive sulfide deposits in northern Japan, and its occurrence at Site 799 was predicted prior to drilling on the basis of the analogy with the geologic setting of these latter deposits.

Upper lower Miocene through upper Miocene sediments are dominated by siliceous claystones and porcellanites, with abundant authigenic carbonate predominantly in the form of dolomite beds and nodules. These sediments are lithologically similar to portions of the Monterey Formation of California and can be correlated with the Onnagawa and lower Funakawa formations of northwestern Honshu. Both bioturbated and laminated intervals are present within these siliceous deposits and indicate sustained periods of oxygen-deficient bottom water occurred in the Kita-Yamato Trough area during early through late Miocene time. Suboxic to near-anoxic conditions are also indicated by high TOC values in laminated units. Evidence from other ODP sites in the Sea of Japan and well-known stratigraphies along the western coast of Honshu clearly illustrate that these distinctive siliceous lithologies are not restricted to the Kita-Yamato Trough sequence, but are a widespread Miocene facies within the Sea of Japan area as a whole. Although thin, distal turbidites occur in the lower portions of this facies at Site 799, these siliceous

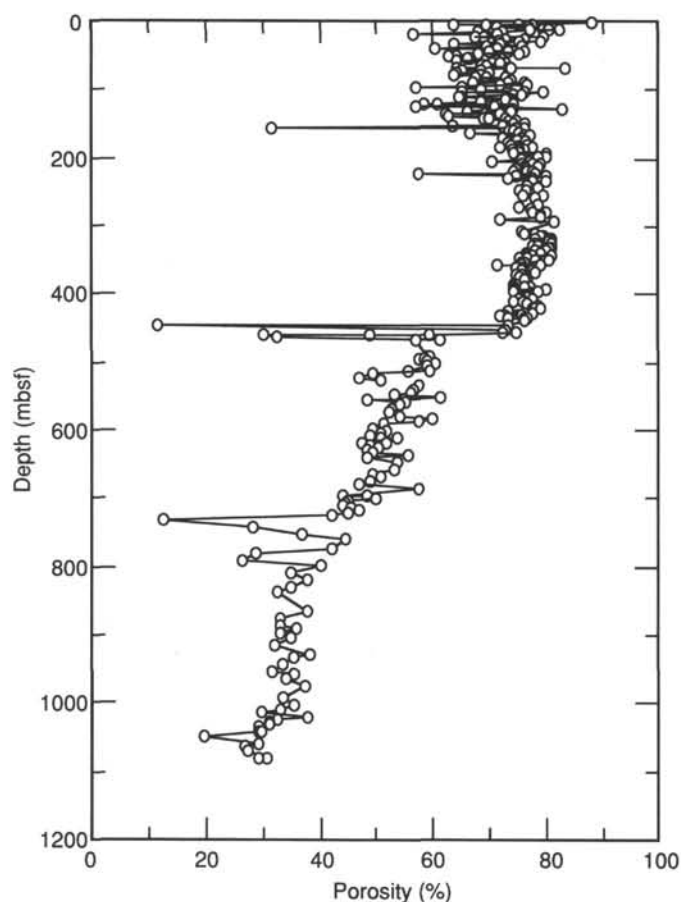


Figure 131. Porosity vs. depth for Site 799.

rocks are predominantly of hemipelagic and pelagic origin. The sediments exhibit distinct and systematic diagenetic changes with depth at Site 799, with the opal-A/opal-CT and opal-CT/authigenic quartz transitions observed in cores.

Upper Miocene through upper Pliocene sediments are also rich in biosiliceous sediments, indicating high productivity of siliceous plankton continued in the Yamato Rise area during this period. Again, these sediments constitute a local manifestation of a facies common to upper Miocene through upper Pliocene sediments elsewhere in the Sea of Japan. The sediments in this interval are commonly bioturbated, indicating normal oxic bottom water and circulation at Site 799 during most of latest Miocene and early Pliocene time.

Uppermost Pliocene through Quaternary sediments are also dominated by biosiliceous sediments, but also contain increasing amounts of terrigenous sediments. In addition, foraminiferal sands redeposited from adjacent bank tops appear in this portion of the column along with coincident evidence of soft-sediment deformation and slumping. In fact, 3.5-kHz seismic-reflection records clearly show large slump features on the flanks of the Kita-Yamato Trough, which can be directly correlated with sedimentary evidence of these events in Quaternary cores at Site 799. Volcanic ashes increase in abundance to a peak in late Pleistocene time.

A rough estimate of subsidence in the Kita-Yamato Trough over the past 20 m.y. suggests that differential subsidence can account for the approximately 1200 m of Lower Miocene through Quaternary sediments present in this feature. This same analysis indicates that the trough experienced accelerated periods of subsidence during early to late Miocene time

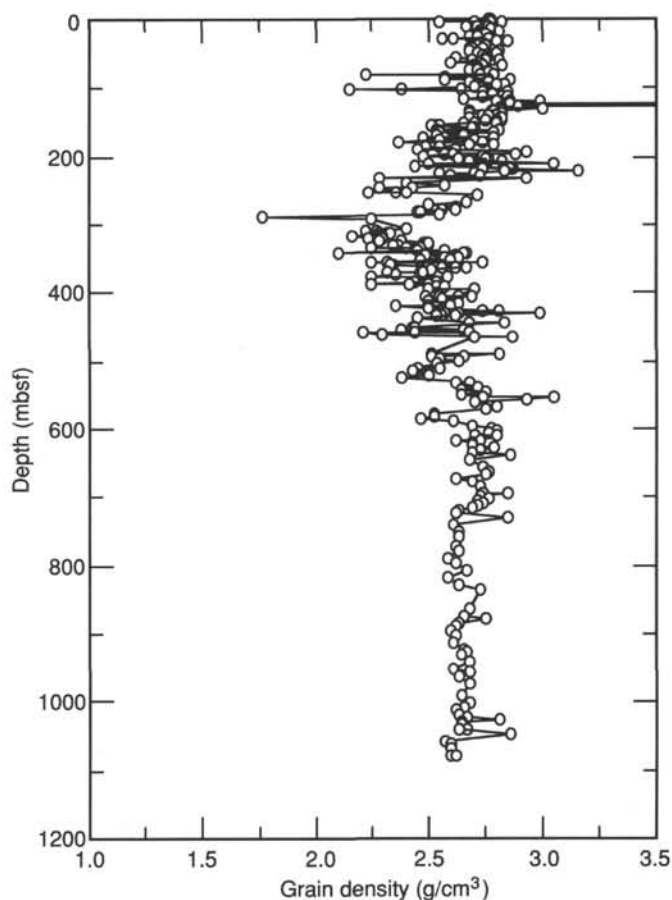


Figure 132. Grain density vs. depth for Site 799.

and a period of little or no subsidence during Pliocene time. Faults and dewatering structures in upper Miocene sediments at Site 799 suggest an episode of extensional tectonism may have occurred during this time. Significantly, the modern surface of the Kita-Yamato Trough is defined by a closed 2000-m contour, indicating that the trough is not brim full and that subsidence is continuing.

Paleoceanography

Scarcity of well-preserved siliceous and calcareous microfossils in the majority of Miocene sediments at Site 799 precludes a detailed paleoceanographic history for this period. However, the biosiliceous origin of the diagenetically altered siliceous claystones and porcellanites at this site and elsewhere in the Sea of Japan area indicates high primary productivity (e.g., diatoms) must have prevailed during Miocene time, as represented by these altered siliceous sediments, which in turn indicates vigorous vertical circulation. Most of the dolomitic laminae, beds, and nodules in these same sediments were probably derived from layers rich in calcareous nannofossils and planktonic foraminifers, suggesting alternating periods of dominance among these two groups of plankton and implied variations in surface temperatures and rates of vertical circulation. Analysis of rare identifiable radiolarian faunas and planktonic foraminifers in the middle Miocene portion of this section suggest warm surface-water temperatures and full circulation with the open Pacific Ocean. Alternatively, well-preserved calcareous and siliceous plankton in Quaternary sediments signal subarctic temperatures, with the exception of an apparent increase in surface temperatures about 2 Ma.

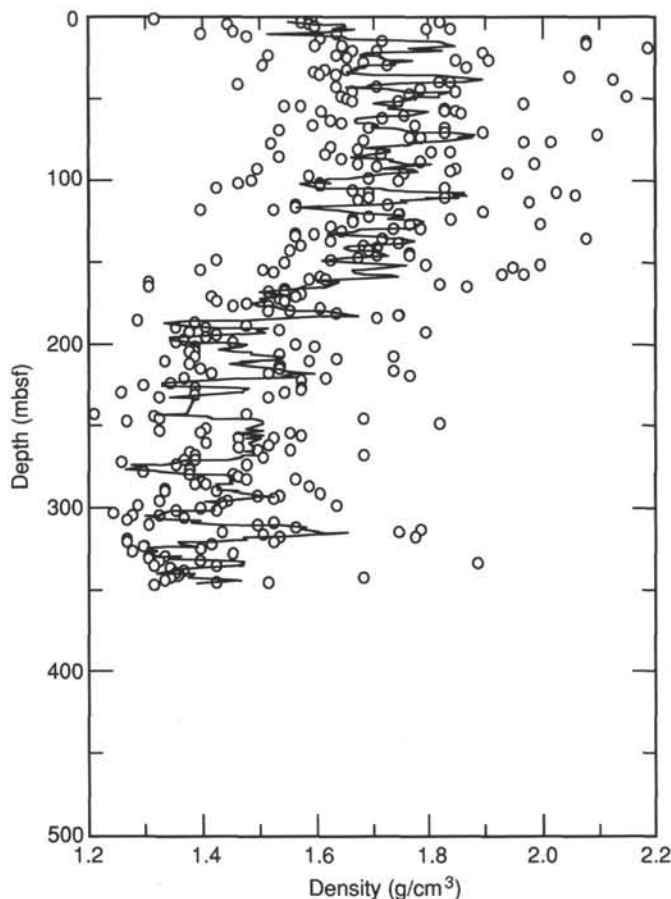


Figure 133. GRAPE-measured density for Hole 799A.

As noted earlier, intervals of laminated sediments and associated high TOC values mark pronounced periods of low-oxygen bottom water in early middle and late Miocene time, with some evidence of short periods of anoxic conditions present at Site 799 during the late Pliocene and Pleistocene. In contrast, the modern Sea of Japan is hyperventilated and fully oxic at all depths.

REFERENCES

Akiba, F., 1982. Reconsideration of the *Coscinodiscus marginatus* Zone—taxonomy and biostratigraphic significance of *Thalassionema schraderi*. *Bull. Tech. Lab. JAPEX*, 24:206–223.

Barash, M. S., 1986. The paleoceanographic conditions of formation of the late Miocene phosphorite horizon of the north Yamato Rise. *Oceanology*, 26:721–724 (in Russian).

Barron, J. A., 1980. Lower Miocene to Quaternary diatom biostratigraphy of Leg 57, off northeastern Japan, Deep Sea Drilling Project. In Scientific Party, *Init. Repts. DSDP*, 56, 57 (Pt. 2): Washington (U.S. Govt. Printing Office), 641–685.

Berggren, W. A., Kent, D. V., and Van Couvering, J. A., 1985. Cenozoic Geochronology. *Geol. Soc. Am. Bull.*, 96:1407–1418; 1499–1510.

Berner, R. A., and Raiswell, R. A., 1984. C/S method for distinguishing freshwater from marine sedimentary rocks. *Geology*, 12:365–368.

Bersenev, I. I., Lelikov, E. P., Bezverkhny, V. L., Yashchenkova, N. G., Sledin, V. G., Terezov, E. P., and Choi, I. V., 1987. *Geology of the Japan Sea. Pacific Oceanological Inst. (Vladivostok Monogr.)*, 23:139 (in Russian).

Borehole Research Group, 1988. *Ocean Drilling Program Wireline Logging Manual*, Vol. 3, *Perspectives on Scientific Logging from the Ocean Drilling Program*: New York (Columbia University).

Bordowsky, O. K., 1965. Sources of organic matter in marine basins. *Mar. Geol.*, 3:5–31.

Bryant, W. R., Bennett, R. H., and Katherman, C. E., 1981. Shear strength, consolidation, porosity, and permeability of oceanic sediments. In Emiliani, C. (Ed.), *The Oceanic Lithosphere, The Sea*, Vol. 7:1555–1616.

Burckle, L. H., and Opdyke, N. D., 1977. Late Neogene diatom correlations in the circum-Pacific. In Saito, T., and Ujiie, H. (Eds.), *Proc., First Int. Congr. on Pacific Neogene Stratigraphy*, Tokyo, 1976: Tokyo (Kaiyo Shuppan).

Burckle, L. H., and Akiba, F., 1978. Implications of late Neogene freshwater sediment in the Sea of Japan. *Geology*, 6:123–127.

Burckle, L. H., and Opdyke, N. D., 1985. Latest Miocene/earliest Pliocene diatom correlations in the North Pacific. In Kennett, J. P. (Ed.), *The Miocene Ocean: Paleooceanography and Biogeography*. *Geol. Soc. Am. Bull.*, 163:37–48.

Chough, S. K., 1984. Fine-grained turbidites and associated mass-flow deposits in the Ulleung (Tsushima) Back-arc Basin, East Sea (Sea of Japan). In Stow, D.A.W., and Piper, D.J.W. (Eds.), *Fine-Grained Sediments; Deep-Water Processes and Facies*. *Geol. Soc. Am. Spec. Publ.*, 15:185–196.

Claypool, G. E., Kvenvolden, K. A., 1983. Methane and other hydrocarbon gases in marine sediment. *Annu. Rev. Earth Planet Sci.*, 11:299–317.

Curtis, C. D., 1977. Sedimentary geochemistry: environments and process dominated by involvement of aqueous phases. *Phil. Trans. R. Soc. London*, A286:353–372.

Demaison, G. J., and Moore, G. T., 1980. Anoxic environments and oil source bed genesis. *AAPG Bull.*, 64:1179–1209.

DeMaster, D. J., 1979. The marine budgets of silica and ³²Si [Ph.D. dissert.]. Yale University.

Desbrandes, R., 1985. *Encyclopedia of Well Logging*: Paris (Institut Francais du Petrole Publications).

Einsele, G., 1982. Mass physical properties of Pliocene to Quaternary sediments in the Gulf of California, Deep Sea Drilling Project Leg 64. In Curran, J. R., Moore, D. G., et al., *Init. Repts. DSDP*, 64: Washington (U.S. Govt. Printing Office), 529–542.

Emeis, K. C., and Kvenvolden, K. A., 1986. Shipboard Organic Geochemistry on JOIDES Resolution. *ODP Technical Note 7*: College Station, TX (Ocean Drilling Program).

Gartner, S., 1977. Calcareous nannofossil biostratigraphy and revised zonation of the Pleistocene. *Mar. Micropaleontol.*, 2:1–25.

Geological Survey of Japan, 1982. *Geological Atlas of Japan*: Tokyo (Geol. Surv. of Japan).

Gieskes, J. M., and Peretsman, G., 1986. Water chemistry procedures aboard JOIDES Resolution—some comments. *ODP Technical Note 5*: College Station, TX (Ocean Drilling Program).

Gnibidenko, H., 1979. The tectonics of the Japan Sea. *Mar. Geol.*, 32:71–87.

Halbach, P., Nakamura, K., Wahsner, M., Lange, J., Sakai, H., Kaselitz, L., Hansen, R. D., Yamano, M., Post, J., Prause, B., Seifert, R., Michaelis, W., Teichmann, F., Kinoshita, M., Marten, A., Ishibashi, J., Czerwinski, S., and Blum, N., 1989. Probable modern analogue of Kuroko-type massive sulfide deposits in the Okinawa Trough back-arc basin. *Nature*, 338:496–499.

Han, M. W., Suess, E., and von Breyman, M., in press. Hydrothermal pore fluids from a sedimented back arc, King George Basin, Antarctica. In Bleil, U., and Thiede, J. (Eds.), *The Geologic History of the Polar Oceans: Arctic vs. Antarctic*: Dordrech, Holland (Kluwer Acad. Publ. Group).

Harms, J. C., Southard, J. B., Spearing, D. R., and Walker, R. G., 1975. Depositional environments as interpreted from primary sedimentary structures and stratification sequences. *Soc. Econ. Paleont. Mineral., Short Course Lect. Notes*, 2.

Haq, B., and Takayama, T., 1984. Neogene calcareous nannoplankton datum planes and their calibration to magnetostratigraphy. In Ikebe, N., and Tsuchi, R. (Eds.), *Pacific Neogene Datum Planes*: Tokyo (Univ. of Tokyo Press), 27–33.

Hays, J. D., Saito, T., Opdyke, N. D., and Burckle, L. H., 1969. Pliocene-Pleistocene sediment of the equatorial Pacific: their paleomagnetic, biostratigraphic and climatic record. *Geol. Soc. Am. Bull.*, 80:1481–1514.

Henshaw, R., and Coplan, T. B., 1973. Ultrafiltration by compacted clay membrane. II. Sodium ion exclusion at various ionic strengths. *Clay and Clay Minerals*, 12:397–421.

- Hilde, T. W. C., and Wagemen, J. M., 1973. Structure and origin of the Japan Sea. In Coleman, P. J. (Ed.), *The Western Pacific*: New York (Crane, Russak and Co., Inc.), 415-435.
- Hirata, H., Kinoshita, H., Suyehiro, K., and Suemasu, M., Matsuda, N., Ouchi, T., Katao, H., Koresawa, S., and Nagumo, S., 1987. Report on DELP cruises in the Japan Sea. Part II. Seismic refraction experiment conducted in the Yamato Basin, southwest Japan Sea. *Bull. Earthquake Res. Inst.*, 62:347-365.
- Holler, P., 1985. Geotechnical properties of Antarctic deep sea sediments. "Meteor" *Forsch.-Ergebnisse, Reihe C*, 39:23-36.
- _____, 1989. Mass physical properties of sediments from Bransfield Strait and northern Weddell Sea. *Mar. Geotechnol.*, 8:1-18.
- Honza, E., 1979. Geological investigation of the Japan Sea 1978 (GH-78 Cruise). *Geol. Surv. of Japan Cruise Rept.*, 13.
- Horai, K., and Von Herzen, R. P., 1985. Measurements of heat flow on Leg 86 of the Deep Sea Drilling Project, In Heath G. R., Burckle, L. H., et al., *Init. Repts. DSDP*, 86: Washington (U.S. Govt. Printing Office), 759-777.
- Hoshino, M., and Honma, H., 1966. Geology of submarine banks in the Japan Sea. *Chikyu Kagaku*, 82:10-16 (in Japanese with English abstract).
- Hotta, H., 1967. The structure of sedimentary layer in the Japan Sea. *Geophysics Bull., Hokkaido Univ.*, 18:111-131. (in Japanese).
- Hunt, J. M., 1979. *Petroleum Geochemistry and Geology*: San Francisco (W. H. Freeman and Co.).
- Ichikura, M., and Ujiie, H., 1976. Lithology and planktonic foraminifera of the Sea of Japan. *Bull. Natural Sci. Mus. (Tokyo), Ser. C (Geol.)*, 2:151-181.
- _____, 1976. Lithology and planktonic foraminifera of the Sea of Japan piston cores. *Bull. Nat. Sci. Mus., Ser. C (Geol.)*, 2:151-177.
- Ikebe, Y., and Maiya, S., 1981. Akita and Niigata areas. In Tsuchi, R. (Ed.), *Neogene of Japan*: Shizuoka (IGCP-114 Nat. Working Gr. Japan), 68-75.
- Ingle, J. C., 1977. Summary of late Neogene planktic foraminiferal biofacies, biostratigraphy, and paleoceanography of the marginal North Pacific Ocean. In Saito, T., and Ujiie, H. (Eds.), *Proc. First Int. Congr. on Pacific Neogene Stratigraphy*, Tokyo, 1976: Tokyo (Kaiyo Shuppan).
- Iwabuchi, Y., 1968. Submarine geology of the southeastern part of Japan Sea. *Tohoku Univ., Inst. Geol. Paleontol., Contr.*, 66:1-76 (in Japanese with English abstract).
- Isezaki, N., 1986. A geomagnetic anomaly map of the Japan Sea. *J. Geomag. Geoelec.*, 38:403-410.
- Iwabuchi, Y. and Moji, A., 1973. Summarization of submarine geology in each zone of the Japanese Upper Mantle Project. In Gorai, M., and Igi, S. (Eds.), *The Crust and Upper Mantle of the Japanese Area, 2. Geology and Geochemistry*: Kawasaki (Geol. Surv. of Japan), 138-162.
- Karig, D. E., Ingle, J. C., Jr., et al., 1975. *Init. Repts. DSDP*, 31: Washington (U.S. Govt. Printing Office).
- Kato, M., 1979. Age assigned to dredged siltstone samples and piston core samples. In Honza, E. (Ed.), *Geological Investigation of the Japan Sea (April-June 1978, GH 78-2 Cruise)*. Geol. Surv. of Japan, Cruise Rept., 13:67-69.
- Keller, M. A., and Isaacs, C. M., 1985. An evaluation of temperature scales for silica diagenesis in diatomaceous sequences including a new approach based on the Miocene Monterey Formation, California. *Geo-Mar. Lett.*, 5:31-35.
- Kennett, J. P., and Srinivasan, M. S., 1983. *Neogene Planktonic Foraminifera*: Strouberg, PA (Hutchinson Ross).
- Knipe, R. J., 1986. Microstructural evolution of vein arrays preserved in Deep Sea Drilling Project cores from the Japan Trench, Leg 57. In Moore, J. C. (Ed.), *Structural Fabrics in Deep Sea Drilling Project Cores from Forearcs*. Geol. Soc. Am. Mem., 166:75-87.
- Kobayashi, K., 1985. Sea of Japan and Okinawa Trough. In Nairn, A., Stehli, F., and Uyeda, S. (Eds.), *The Ocean Basins and Margins, Vol. 7a, The Pacific Ocean*: New York (Plenum Press), 419-458.
- _____, 1988. Neogene silicoflagellate biostratigraphy of the Japan Sea coastal region, with reference to DSDP Hole 438A. *Tohoku Univ., Sci. Repts., 2nd Ser. (Geol.)*, 59(1):1-98.
- Koizumi, I., 1975. Neogene diatoms from the western margin of the Pacific ocean. In Karig, D. E., Ingle, J. C., Jr., et al., *Init. Repts. DSDP*, 31: Washington (U.S. Govt. Printing Office), 779-819.
- _____, 1978. Neogene diatoms from the Sea of Japan. *Mar. Geol.*, 26:231-248.
- _____, 1979. Age assignments for sediment samples cored and dredged. In Honza, E. (Ed.), *Geological Investigation of the Japan Sea (April-June 1978, GH 78-2 Cruise)*. Geol. Surv. of Japan, Cruise Rept., 13:67-69.
- _____, 1988. Early Miocene proto-Japan Sea. *Paleontol. Soc. Korea*, 4:6-20.
- Koizumi, I., and Tanimura, Y., 1985. Neogene diatom biostratigraphy of the middle latitude western north Pacific, Deep Sea Drilling Project, Leg 86. In Heath, G. R., Burckle, L. H., et al., *Init. Repts. DSDP*, 86: Washington (U.S. Govt. Printing Office), 269-300.
- Lagoe, M. B., and Thompson, P. R., 1988. Chronostratigraphic significance of Late Cenozoic planktonic foraminifera from the Ventura Basin, California: potential for improving tectonic and depositional interpretation. *J. Foramin. Res.*, 18(3):250-266.
- Lelikov, E. P., and Bersenev, I. I., 1973. Early Proterozoic gneiss-migmatite complex in the southwestern part of the Sea of Japan. *Proc. Acad. Sci. U.S.S.R.*, 223:74-76 (in Russian).
- Leventhal, J. S., 1983. An interpretation of carbon and sulphur relationships in Black Sea sediments as indicators of environments of deposition. *Geochim. Cosmochim. Acta*, 47:133-137.
- Ling, H. Y., 1975. Radiolaria: Leg 31 of the Deep Sea Drilling Project. In Karig, D. E., Ingle, J. C., Jr., *Init. Repts. DSDP*, 31: Washington (U.S. Govt. Printing Office), 703-761.
- Ludwig, W. J., Murauchi, S., and Houtz, R. E., 1975. Sediments and structure of the Japan Sea. *Geol. Soc. Am. Bull.*, 86:651-664.
- Maiya, S., Saito, T., and Sato, T., 1976. Late Cenozoic planktonic foraminiferal biostratigraphy of northwest Pacific sedimentary sequences. In Takayanagi, Y., and Saito, T. (Eds.), *Progress in Micropaleontology*: New York (Micropaleontol. Press), 395-422.
- Manheim, F. T., and Sayles, F. L., 1974. Composition and origin of interstitial waters of marine sediments, based on deep sea drilling cores. In Goldberg, E. D. (Ed.), *The Sea*, Vol. 5: New York (Wiley Interscience), 527-568.
- Matoba, Y., 1984. Paleoenvironment of the Sea of Japan. In Oertl, H. J. (Ed.), *Benthos '83, 2nd Int. Symp. Benthic Foraminifers (Pau, April, 1983)*, 409-414.
- Matsumoto, R., 1989. Isotopically heavy oxygen-containing siderite derived from the decomposition of methane hydrate. *Geology*, 17:669-678.
- Matsumoto, R., and Matsuhisa, Y., 1986. Chemistry, carbon and oxygen isotopic ratio, and the origin of deep-sea carbonates at Sites 438, 439, and 584: Inner slope of the Japan Trench. In Kagami, H., Karig, D. E., Coulbour, W. C., et al., *Init. Repts. DSDP*, 87: Washington (U.S. Govt. Printing Office), 669-678.
- Matsunaga, T., 1963. Benthic smaller foraminifers from the oil fields of northern Japan. *Sci. Rept. Tohoku Univ., 2nd Ser. (Geol.)*, 35:67-122.
- Milashin, A. P., Snegovskoy, S. S., and Tuyezov, I. K., 1968. Structure of the sedimentary layer of the Japan Sea according to seismic reflection profiling data. *Proc. Acad. Sci. U.S.S.R.*, 183:1060-1063 (in Russian).
- Miyazaki, T., Tamaki, K., and Murakami, F., 1979. Geomagnetic survey. In Honza, E. (Ed.), *Geological Investigation of the Japan Sea (April-June 1978, GH78-2 Cruise)*. Geol. Surv. of Japan, Cruise Rept., 13:46-47.
- Murauchi, S., 1966. Explosion seismology. In Committee for Upper Mantle Project (Eds.), *Second Progress Report on the Upper Mantle Project of Japan (1965-1966)*: Tokyo (Science Council of Japan), 11-13.
- Murata, K. J., Friedman, I., and Madsen, J. D., 1977. Oxygen isotope relations between diagenetic silica minerals in Monterey Shale, Temblor Range, California. *Am. J. Sci.*, 277:259-272.
- Nakaseko, K., and Sugano, K., 1973. Neogene radiolarian. *Geol. Soc. Japan, Mem.*, 8:23.
- Niino, H., 1933. On bottom deposits of Yamato Bank in the Sea of Japan. *J. Geol. Soc. Japan*, 40:86-100 (in Japanese).
- _____, 1935. On the newly discovered bottom materials of the Kita-Yamato Bank. *J. Geol. Soc. Japan*, 42:676-684 (in Japanese). Ohmoto, H., and Skinner, B. J. (Eds.), 1983. *The Kuroko and Related Volcanogenic Massive Sulfide Deposits*: New Haven (Econ. Geol. Publ. Co.), Econ. Geol. Monogr., 5.

- Ohmoto, H., and Takahashi, T., 1983. Submarine calderas and Kuroko genesis. In Ohmoto, H., and Skinner, B. J. (Eds.), *The Kuroko and Related Volcanogenic Massive Sulfide Deposits*: New Haven (Econ. Geol. Publ. Co.), Econ. Geol. Monogr., 5:39–54.
- Peirce, J., Weissel, J., et al., 1989. *Proc. ODP, Init. Repts.*, 121: College Station, TX (Ocean Drilling Program).
- Pisciotta, K. A., 1981. Diagenetic trends in the siliceous facies of the Monterey Shale in the Santa Maria region, California. *Sedimentology*, 28:547–571.
- Prell, W., 1985. Pliocene stable isotope and carbonate stratigraphy (Holes 572C and 573A): Paleoceanographic data bearing on the question of Pliocene glaciation. In Mayer, L., Thayer, F., Thomas, E., et al., *Init. Repts. DSDP*, 85: Washington (U.S. Govt. Printing Office), 723–734.
- Sanfilippo, A., Westberg-Smith, M. J., and Riedel, W. R., 1985. Cenozoic radiolaria. In Bolli, H. M., Saunders, J. B., and Perch-Nielsen, K. (Eds.), *Planktonic Stratigraphy*: Cambridge (Cambridge Univ. Press), 631–712.
- Seyfried, W. E., Jr., Michael, E. B., and Janacky, D. R., 1986. Chloride depletion and enrichments in seafloor hydrothermal fluids: Constraints from experimental basalt alteration studies. *Geochem. Cosmochim. Acta*, 50:469–474.
- Shackleton, N. J., and Opdyke, N. D., 1977. Oxygen isotope and paleomagnetic evidence for early Northern Hemisphere glaciation. *Nature*, 270:216–219.
- Shackleton, N. J., Zimmerman, H., Kent, D. V., Hall, M. A., Roberts, D. G., Schnitker, D., Baldauf, J., Despraires, A., Homrighausen, R., Huddleston, P., Keene, J. B., Kaltenback, A. J., Krumsiek, K.A.O., Morton, A. C., Murray, J. W., and Westberg-Smith, J., 1984. Oxygen isotope calibration of the onset of ice rafting in DSDP Site 552: a history of glaciation in the north Atlantic region. *Nature*, 307:620–623.
- Schaefer, R. G., and Leythaeuser, D., 1987. Low-molecular weight hydrocarbons in sediments of Deep Sea Drilling Project Leg 93 Hole 603B, off the East coast of North America: In van Hinte, J. E., Wise, S. W., Jr., et al., *Init. Repts. DSDP*, 93: Washington (U.S. Govt. Printing Office), 1237–1244.
- Shimazu, M., 1968. Absolute age determination of granite in Yamato Bank. *Nihonkai (Japan Sea)*, Unpubl. manuscript, 55–56.
- Tamaki, K., 1988. Geological structure of the Japan Sea and its implications. *Bull. Geol. Surv. of Japan*, 39:269–365.
- Tamaki, K., Pisciotta, K. A., Allan, J., et al., in press. *Proc. ODP, Init. Repts.*, 127: College Station, TX (Ocean Drilling Program).
- Tamaki, K., Honza, E., Yuasa, M., Nishimura, K., and Murakami, F., 1981. Geological map of the central Japan Sea. *Geol. Surv. of Japan, Mar. Geol. Map Ser. 15*, Scale 1:1,000,000.
- Tsoy, I. B., Vashchenkova, N. G., Gorovaya, M. T., and Terekhov, Y. P., 1985. Discovery of continental deposits on the Yamato uplift (Sea of Japan). *Pacific Geol.*, 3:50–55 (in Russian).
- Tsuchi, R., 1981. *Neogene of Japan—Its Biostratigraphy and Chronology*: Shizuoka, Japan (Shizuoka Univ.).
- Tsuya, H., 1932. On some pebbles collected from the floor of the Japan Sea. *Bull. Earthquake Res. Inst., Tokyo Imperial Univ.*, 40:864–875.
- Ueno, N., Kaneoka, J., Ozuna, M., Zashu, S., Sato, T., and Iwabuchi, Y., 1971. K-Ar age, Sr isotopic ratio, and K/Rb ratio of volcanic rocks dredged from the Japan Sea. In Asano, S., and Udintsev, G. B. (Eds.), *Island Arc and Marginal Sea*: Tokai (Tokai Univ. Press), 305–309 (in Japanese).
- Ujiie, H., and Ichikura, M., 1973. Holocene to uppermost Pleistocene planktonic foraminifers in a piston core from off San'in District, Sea of Japan. *Trans. Proc. Paleontol. Soc. Japan*, N.S., 91:137–150.
- Uyeda, S., and Vaquier, V., 1968. Geothermal and geomagnetic data in and around the island of Japan. In Knopoff, L. (Ed.), *The Crust and Mantle of the Pacific Area*. Am. Geophys. Union, Monogr. Ser., 12:349–366.
- van Morkhoven, F.P.C.M., Berggren, W. A., and Edward, A. S., 1986. *Cenozoic Cosmopolitan Deep-Water Benthic Foraminifera*: Pau (Elf Aquitaine).
- Vasiliev, B. I., Karp, B. Y., Stroev, P. A., and Shevaldin, Y. V., 1975. *Structure of the Yamato Submarine Rise (Sea of Japan) From Geophysical Data* [M.S. thesis]. Moscow State Univ. (in Russian; discussed and referenced in Gnibidenko, 1979).
- von Rad, U., Haq, B. U., et al., 1990. *Proc. ODP, Init. Repts.*, 124: College Station, TX (Ocean Drilling Program).
- Whelan, J. K., and Hunt, J. M., 1981. C₁-C₈ hydrocarbons in Leg 63 sediments from Outer California and Baja California borderlands. In Yeats R. S., and Haq, B. U., et al., *Init. Repts. DSDP*, 63: Washington (U.S. Govt. Printing Office), 775–884.
- Yoshii, T., 1972. Terrestrial heat flow and features of the upper mantle beneath the Pacific and Sea of Japan. *J. Phys. Earth*, 20:271–285.
- Yuasa, M., Kanaya, H., and Terashima, S., 1979. Rocks and sediments. In Honza, E. (Ed.), *Geological Investigation of the Japan Sea (April–June 1978, GH78-2)*. Geol. Surv. of Japan, Cruise Rept. 13:54–60.

Ms 128A-106

NOTE: All core description forms (“barrel sheets”) and thin sections have been reproduced on specially coated paper and may be found in Section 3, at the end of the volume, beginning on page 405.

Formation microscanner images for this site are presented on microfiche in the back of this volume.

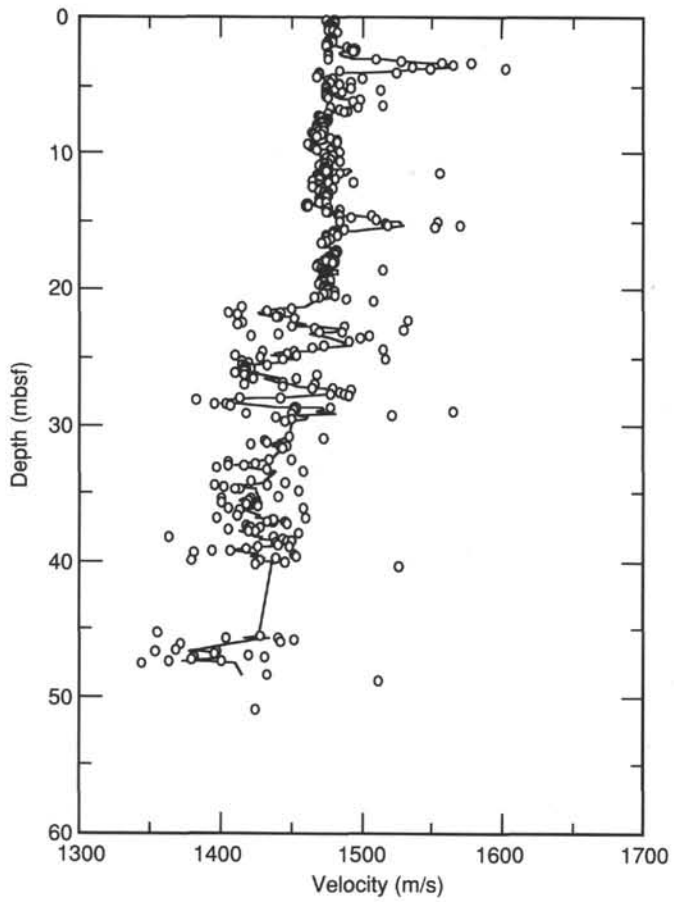


Figure 134. Sonic velocity for Hole 799A.

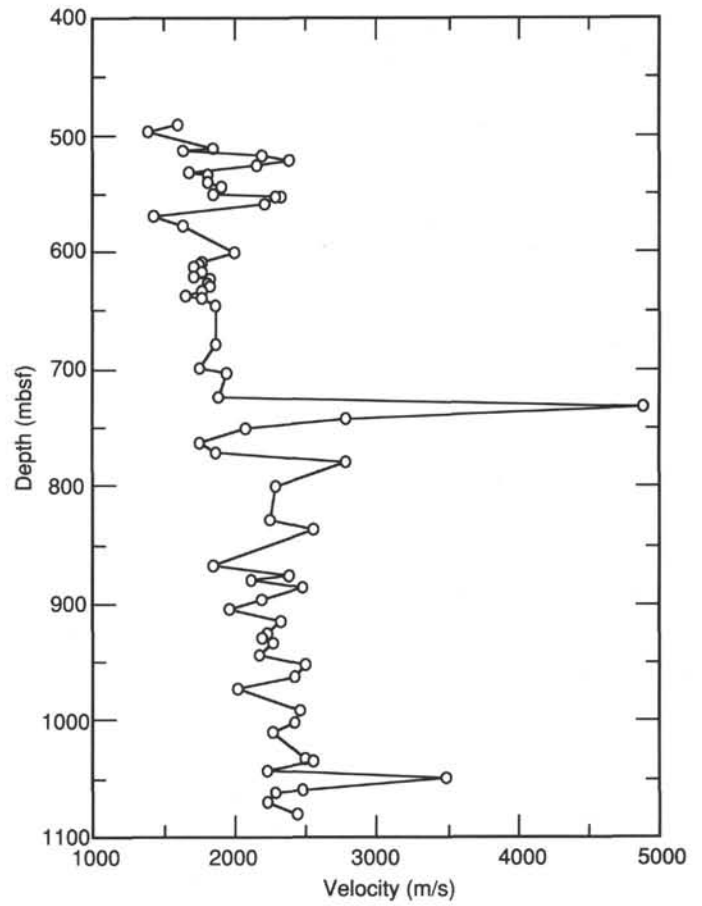


Figure 135. Sonic velocity for Hole 799B.

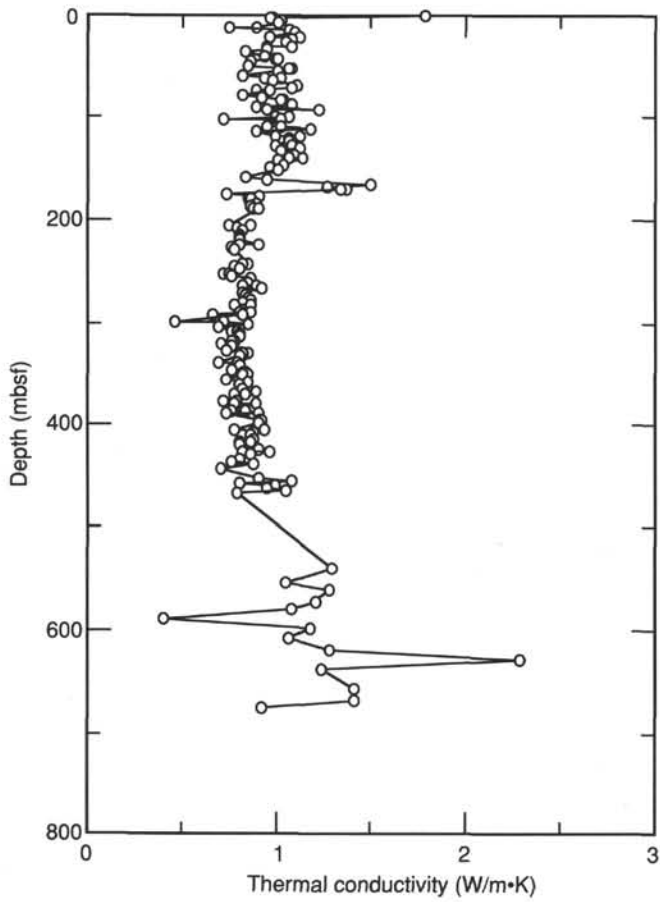


Figure 136. Thermal conductivity vs. depth for Site 799.

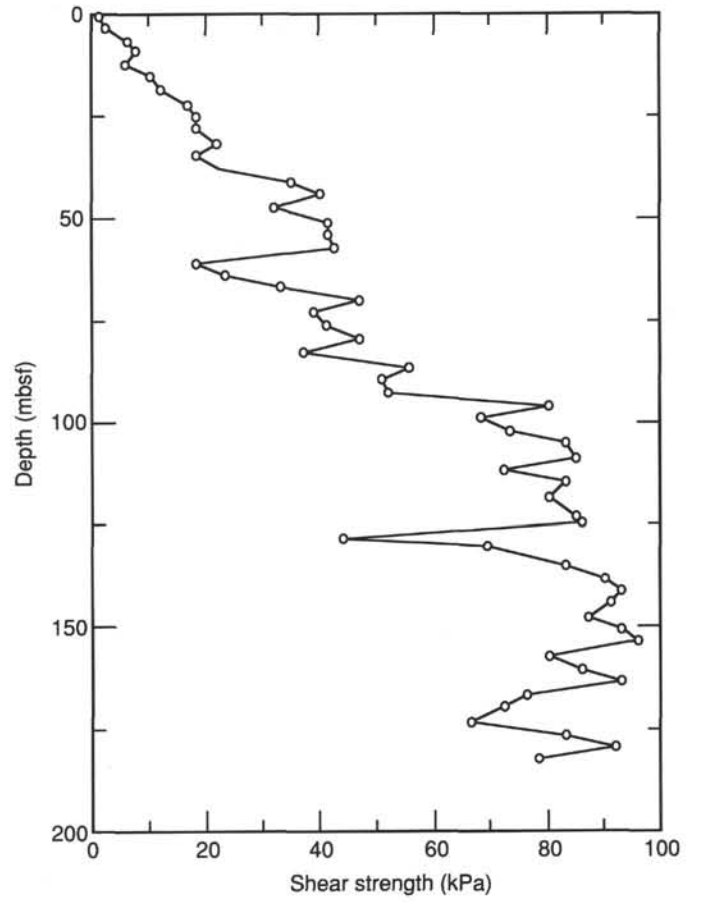


Figure 137. Undrained shear strength vs. depth for Hole 799A.

Table 19. Actual time schedule for logging operations at Hole 799A, listing individual tools run on each string.

Tool string	Time (UTC)	Procedure
Seismic stratigraphy (DITE-SDT-NGT)	RIH 0430 (9/17/89) POOH 0642	Log down to TD, log up to 277 mbsf. Run down to TD, log up to mud line.
Formation microscanner (FMS-NGT)	RIH 0835 POOH 1420	Run down to TD, log up to end of pipe. Run down to TD for repeat from TD to end of pipe.
Lithoporosity combination (LDT-CNT-NGT)	RIH 1659 POOH 1931	Run down to TD, log up to 384 mbsf. Run down to TD for main log up to end of pipe.
Geochemical combination (GST-ACT-NGT)	RIH 2110 POOH 0339 (9/18/89)	Run down to TD. Problem with GST. POOH to check wiring. Reenter hole 0035. Log up from TD. Pipe raised 30 m. GST fails at 75 mbsf, POOH.

DITE = phaser induction tool; SDT = digital sonic tool; NGT = natural spectrometry tool; LDT = lithodensity tool; CNT = compensated neutron tool; ACT = aluminium clay tool; GST = induced gamma-ray spectrometry tool; TD = total depth (468.7 mbsf); RIH = run in to hole; POOH = pull out of hole; end of pipe = 104.5 mbsf; times in UTC = Universal Time Coordinated. Total logging time = 25.25 hr., includes initial rig up and final rig down of tool strings.

Table 20. Actual time schedule for logging operations at Hole 799B, listing individual tools run on each string.

Tool string	Time (UTC)	Procedure
Seismic stratigraphy (DITE-SDT-NGT)	RIH 1415 (10/9/89) POOH 1810	Log down to TD (1049 mbsf) log up to 946 mbsf. Run down to TD, log up to 400 mbsf.
Formation microscanner (FMS-NGT)	RIH 1907 POOH 2325	Run down to TD (1045 mbsf) log up to 938 mbsf. Run down to TD for main run from TD to end of casing.
Lithoporosity combination (LDT-CNT-NGT)	RIH 2351 POOH 0235 (10/10/89)	Run down to TD (1033 mbsf) log up to 930 mbsf. Run down to TD, log up to 687 mbsf. Run down to 798 mbsf, log up to end of casing.
Geochemical combination (GST-ACT-NGT)	RIH 0425 POOH 1315	Run down to TD (1027 mbsf), log up to 781 mbsf. Run down to 890 mbsf, log up to 233 mbsf. (Logging through casing from 433 to 233 mbsf.)
Well seismic tool	RIH 1700 POOH 0400 (10/11/89)	Data recorded at 15.25 m stations from 1003 to 385 mbsf.

DITE = phaser induction tool; SDT = digital sonic tool; NGT = natural spectrometry tool; LDT = lithodensity tool; CNT = compensated neutron tool; ACT = aluminium clay tool; GST = induced gamma-ray spectrometry tool; RIH = run in to hole; POOH = pull out of hole; end of casing = 443 mbsf; drilled total depth (TD) = 1084 mbsf (decreases with logging due to hole fill). Total logging time = 40 hr., includes initial rig up and final rig down of tool strings.

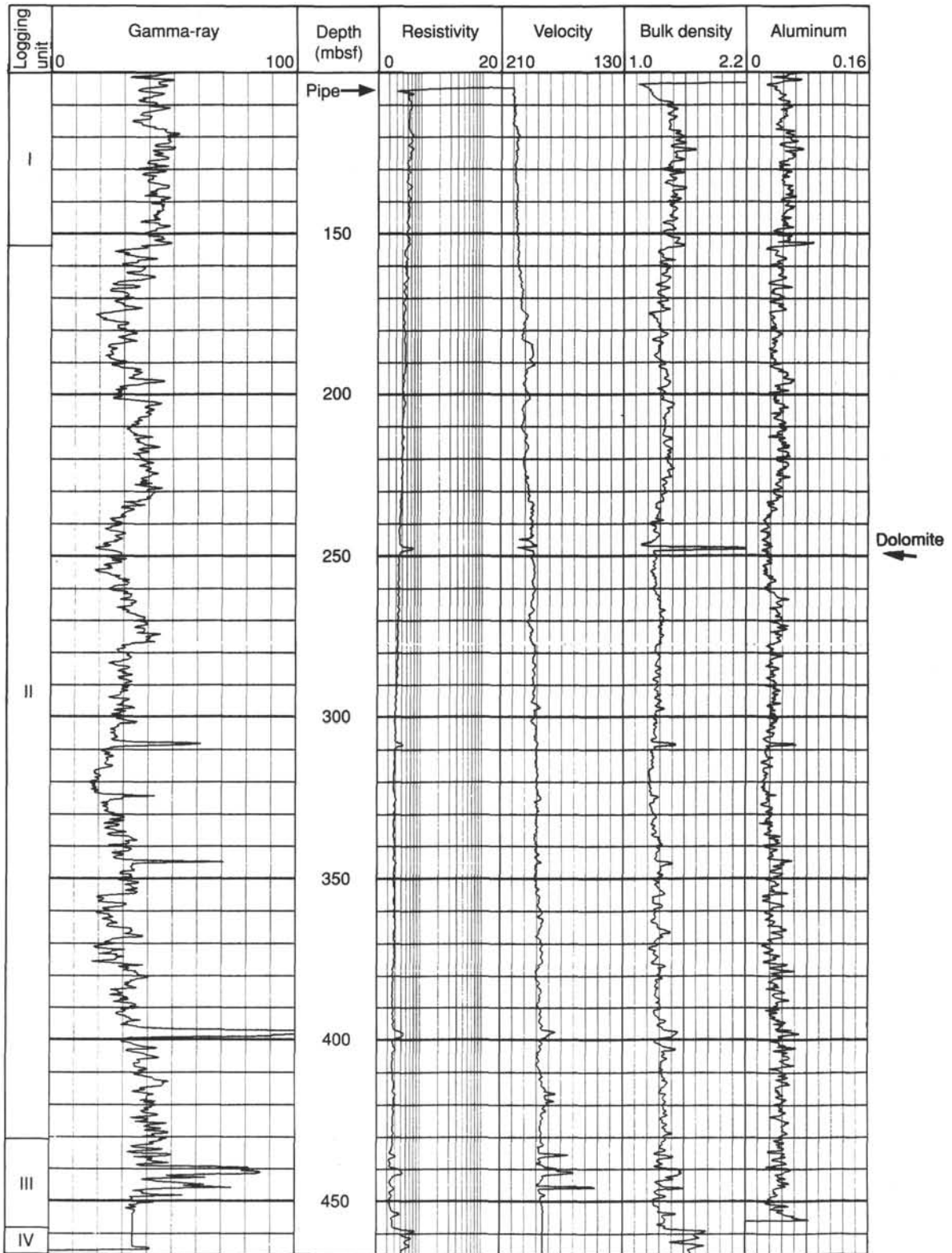


Figure 138. Log traces for Hole 799A: total gamma-ray (0–100 API unit scale), resistivity (0–20 ohm-m), sonic traveltime (210–130 μ s), bulk density (1.0–2.2 g/cm³), and aluminum (0–0.16 wt%). Stratigraphic units defined by the logging data are shown in the leftmost column.

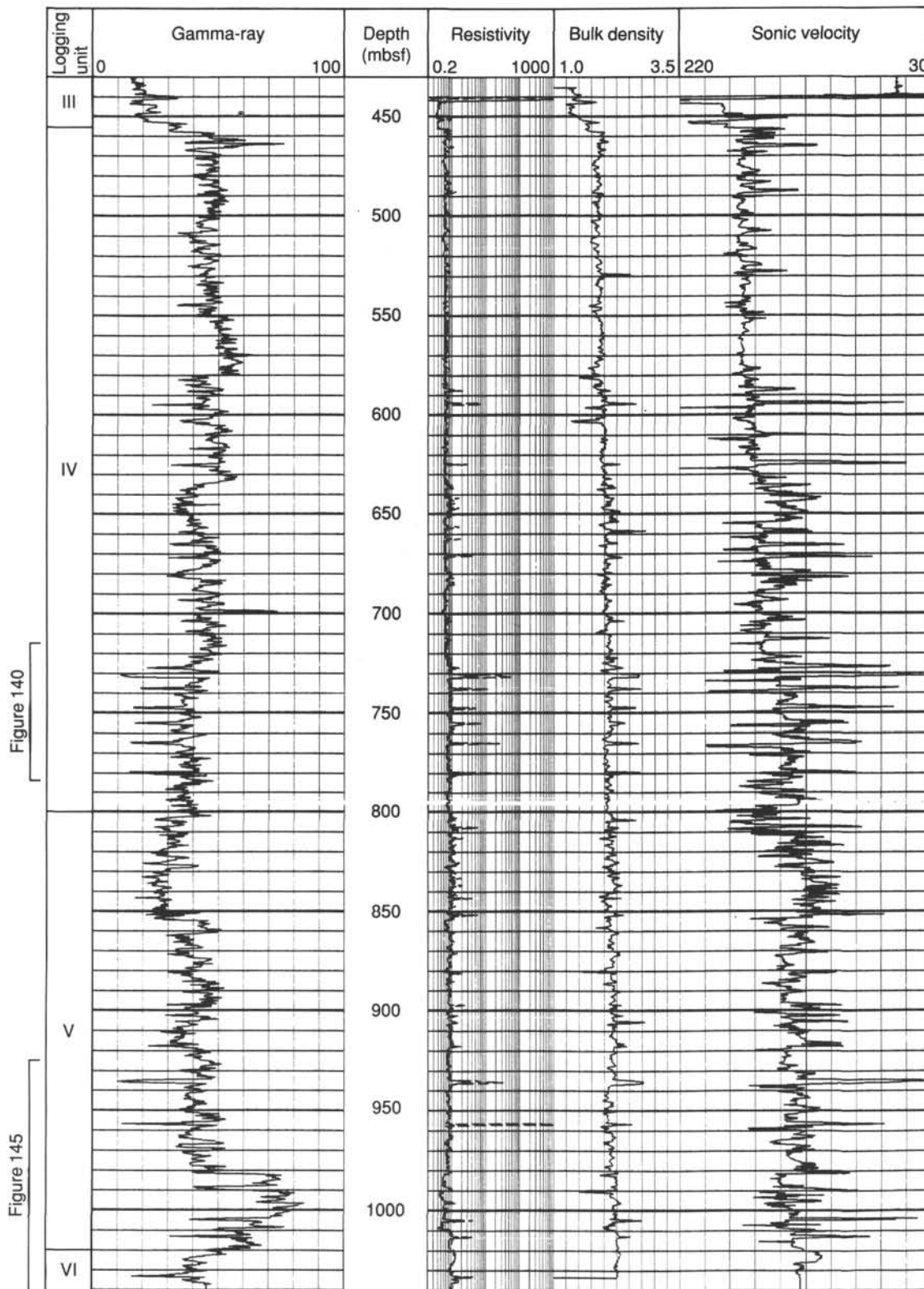


Figure 139. Plot of Hole 799B log data. From left to right: total natural gamma-ray (API units), resistivity (ohm-m), neutron bulk density (g/cm^3), and sonic travelltime (μs). Stratigraphic units defined by the logging data are shown in the leftmost column.

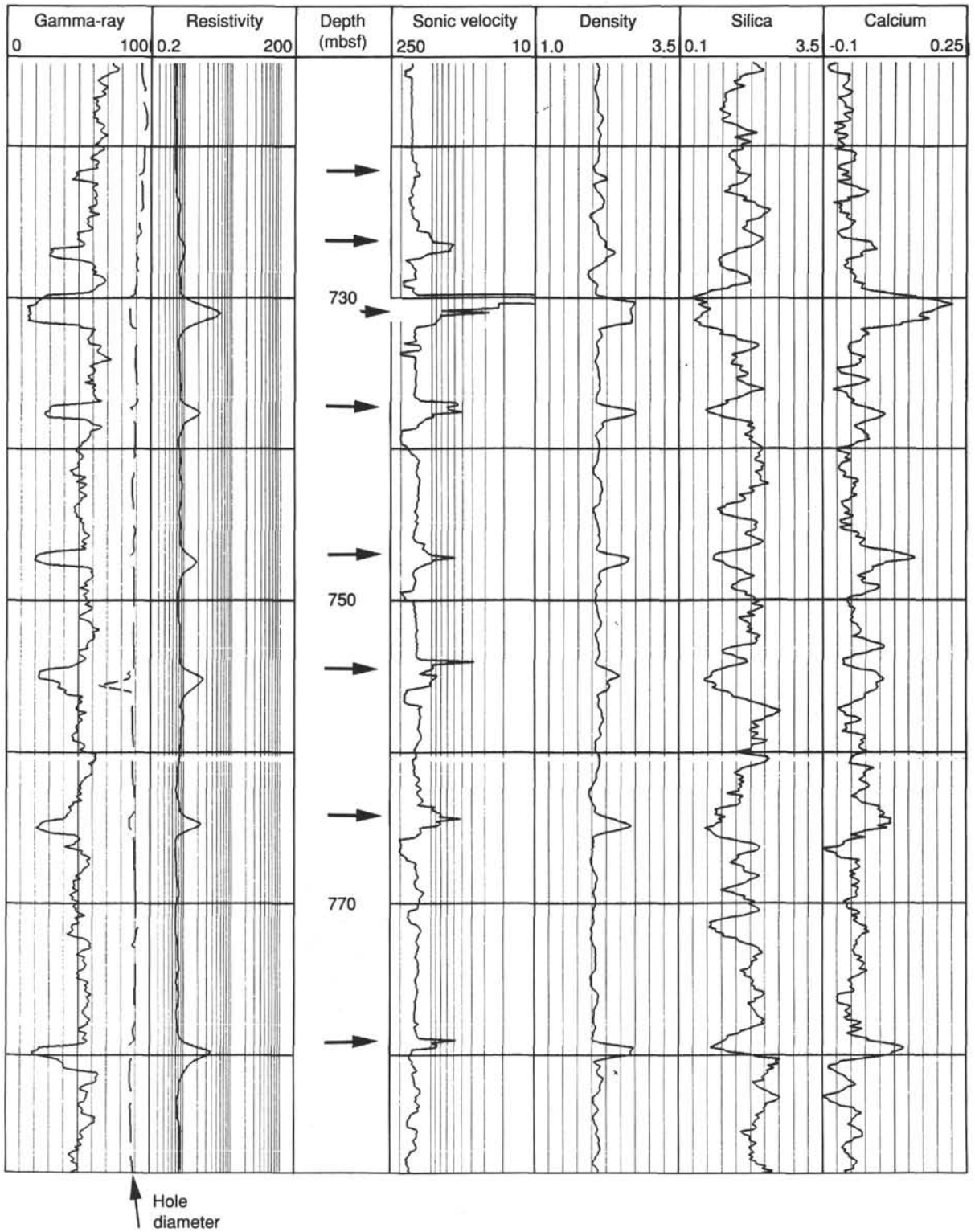


Figure 140. Expanded plot of selected logging data from 710 to 790 mbsf at Hole 799B. The dolomite layers (arrows) are defined by the sharp increases in resistivity, velocity, bulk density, and calcium, and sharp decreases in natural gamma-ray and silica.

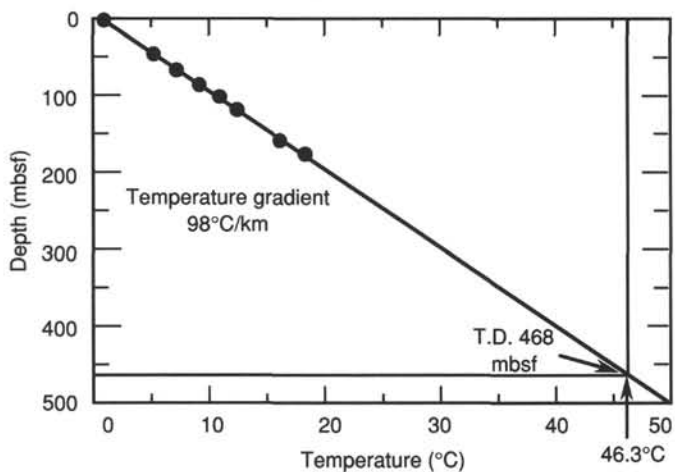


Figure 141. Barnes/Uyeda temperature probe results for Hole 799A. The extrapolated temperature at total depth (468.7 mbsf) is 46.3°C.

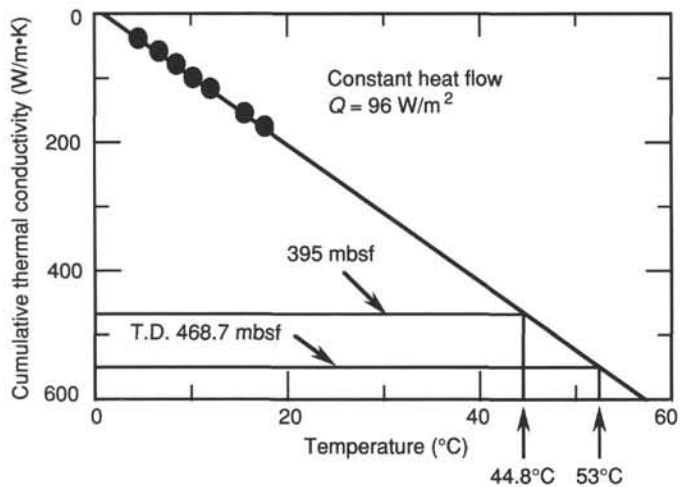


Figure 142. Borehole temperature measured with the Barnes/Uyeda probe vs. cumulative thermal conductivity measured for whole-round cores (from "Physical Properties" section, this chapter). The calculated heat flow at this site is 96 W/m².

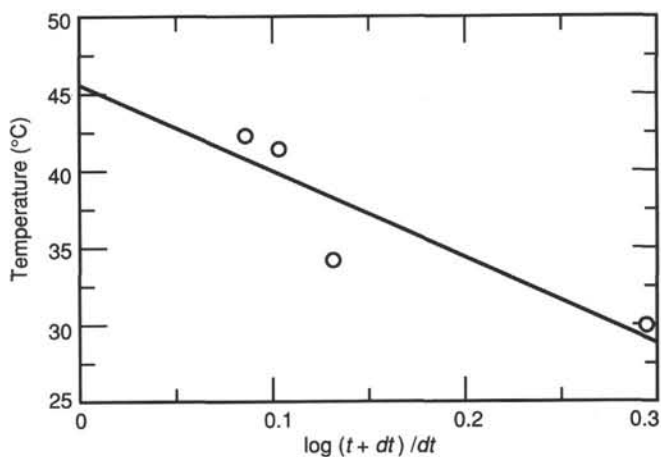


Figure 143. Desbrantes' (1985) method for determining borehole thermal gradients. The temperature at the bottom of the hole (as estimated from this method) is ~35°C, which is considerably less than the 46°C values obtained by extrapolation of the Barnes/Uyeda probe data. The lower temperature is probably a result of recirculation of cold seawater into the borehole during and after drilling.

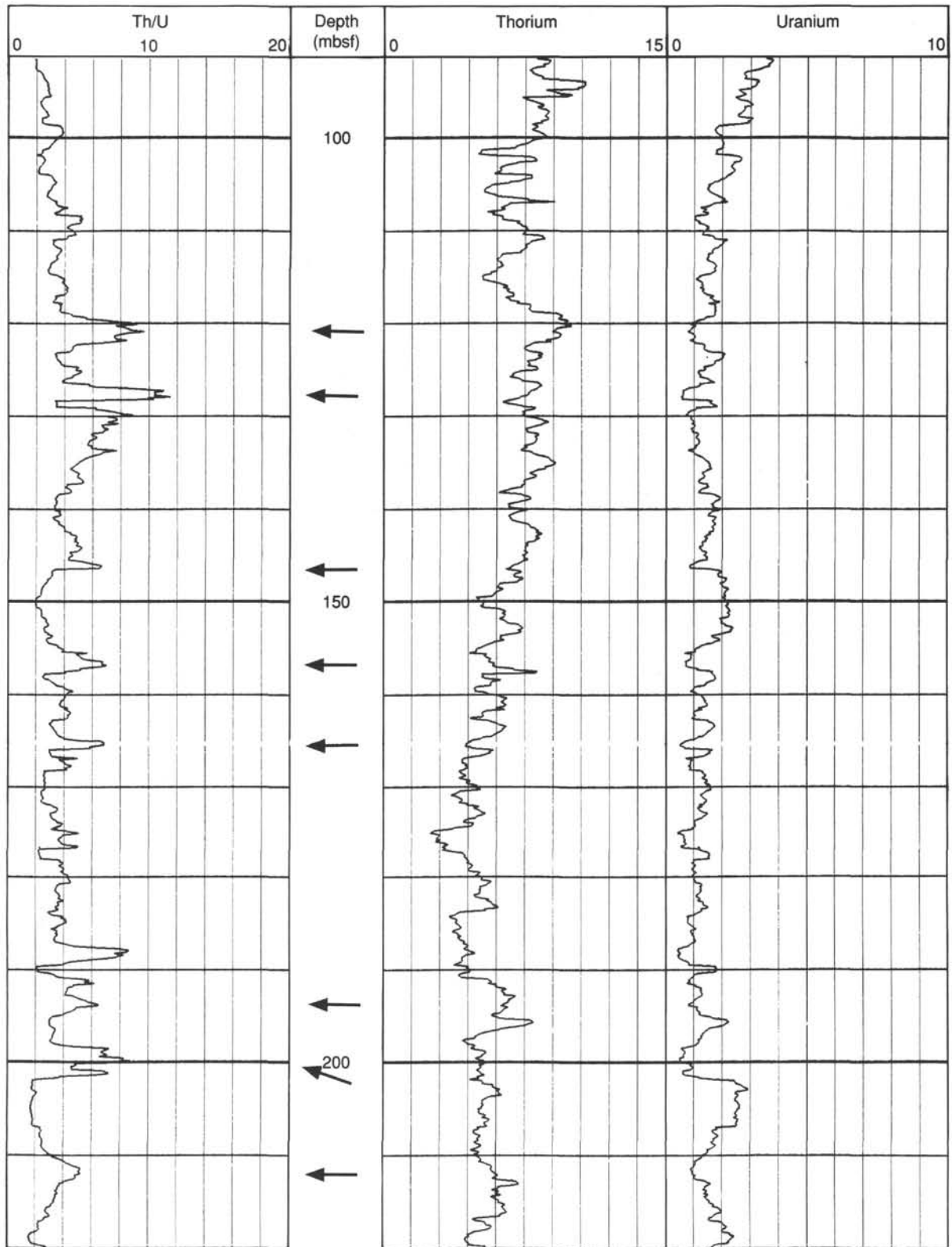


Figure 144. Thorium/uranium ratio, thorium and uranium logs from the NGT at Hole 799A.

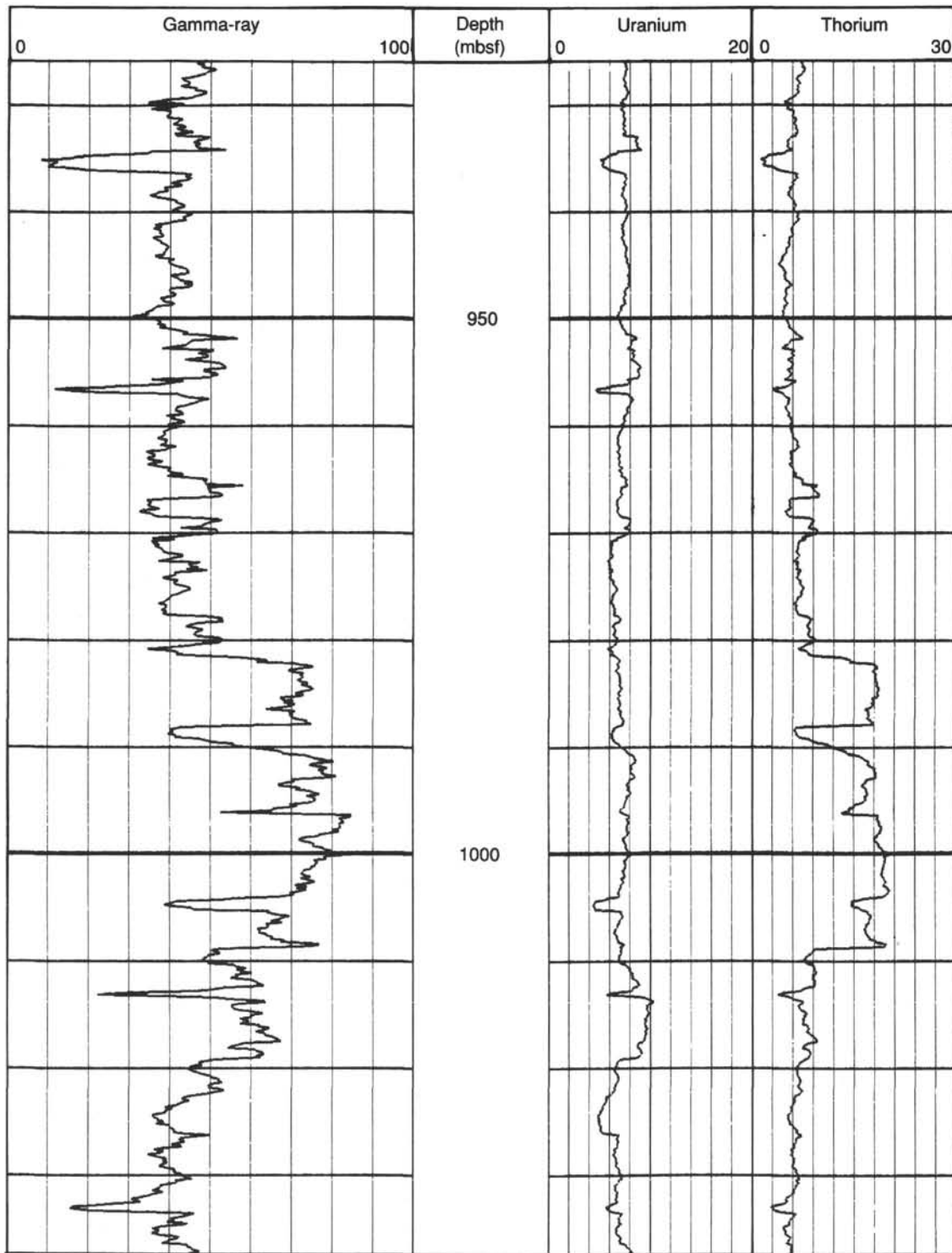


Figure 145. Plot of the NGT data for 960 to 1050 mbsf at Hole 799B. The high total SGR log values from 980 to 1010 mbsf reflect the high thorium content of the rhyolitic ash within this interval.

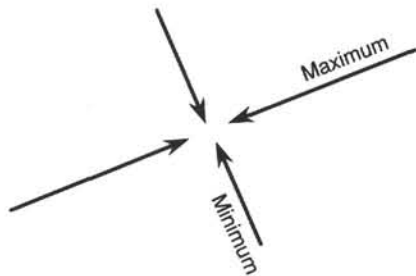
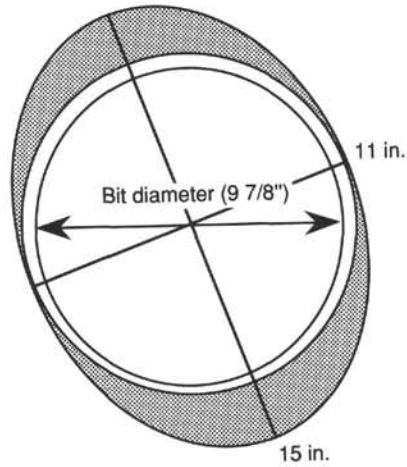


Figure 146. Measurements of borehole ellipticity using the orthogonal caliper data from the FMS. The lower half of Hole 799A exhibited the ellipticity (11 in. minimum axis and 15 in. maximum axis) and the orientation (NNW-SSE) shown above. Borehole ellipticity may be interpreted to reflect borehole breakout or spalling, which occurs along the axis of minimum compressive stress. The ellipticity orientation at Hole 799A is consistent with the paleospreading orientation of the Yamato Trough.

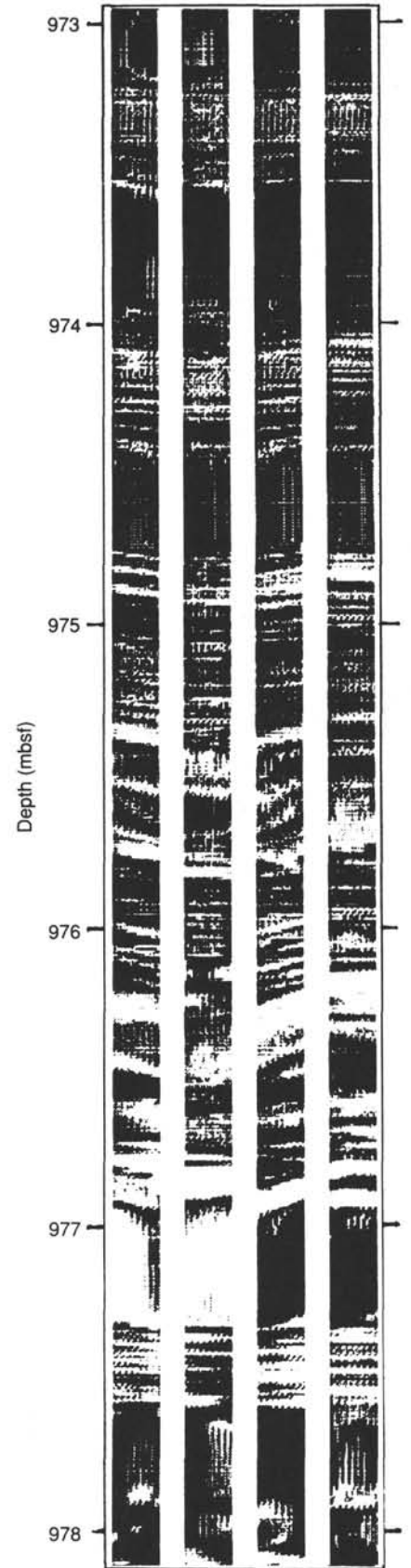


Figure 147. Plot of the FMS resistivity images from 974 to 978 mbsf in Hole 799B. The light intervals are most probably the highly resistive dolomite layers that were observed in cores from this depth (see "Lithostratigraphy" section, this chapter). The sinusoidal appearance of the layers and the tool magnetometer orientation indicate that these layers are dipping $\sim 20^\circ$ to the west.

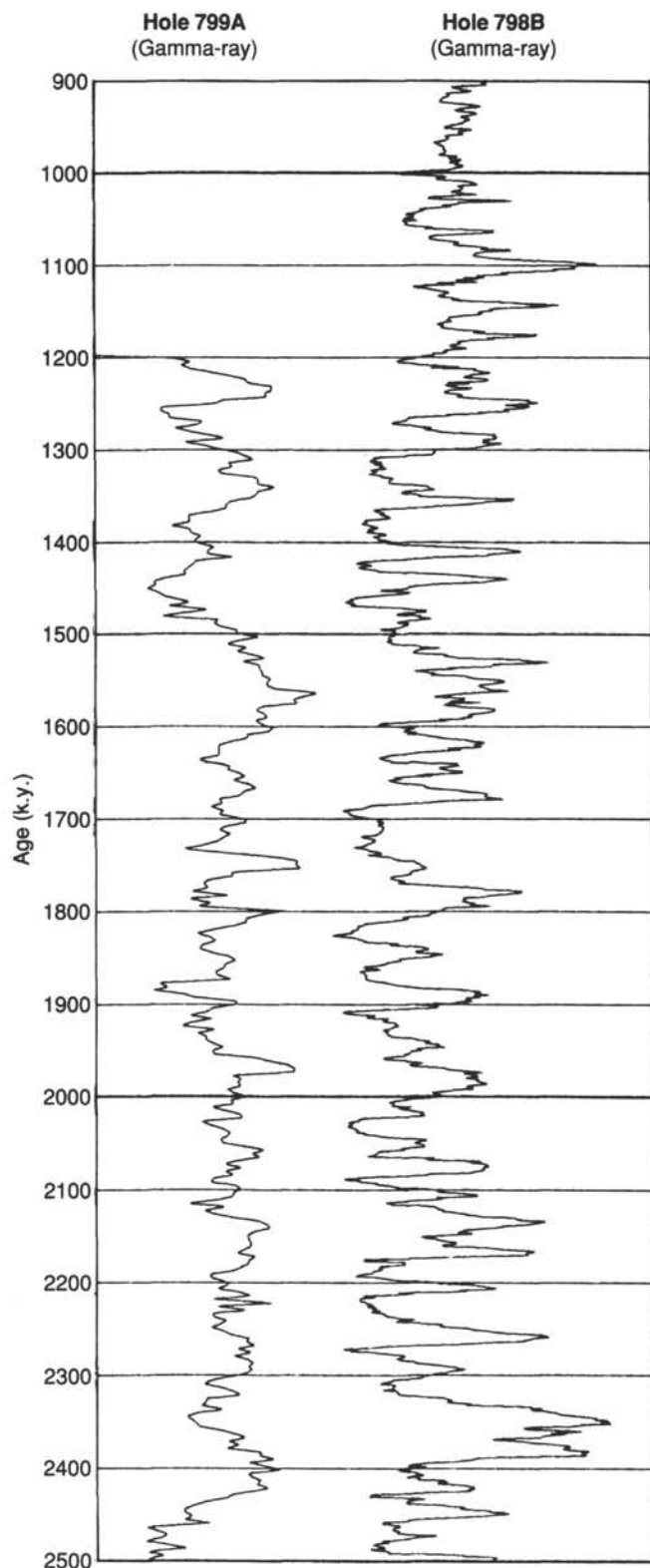


Figure 148. Plot of NGT data for Holes 799A and 798B; gamma-ray variations reflect clay mineral content. Age control for both sites was determined from their respective paleomagnetic stratigraphies. The sedimentation rate at Hole 798B was ~ 120 m/m.y., whereas the sedimentation rate at Hole 799A was ~ 40 m/m.y.. The two gamma-ray records are roughly comparable, despite significant differences in sedimentation rate and the existence of downslope deposits at Hole 799A (see text).

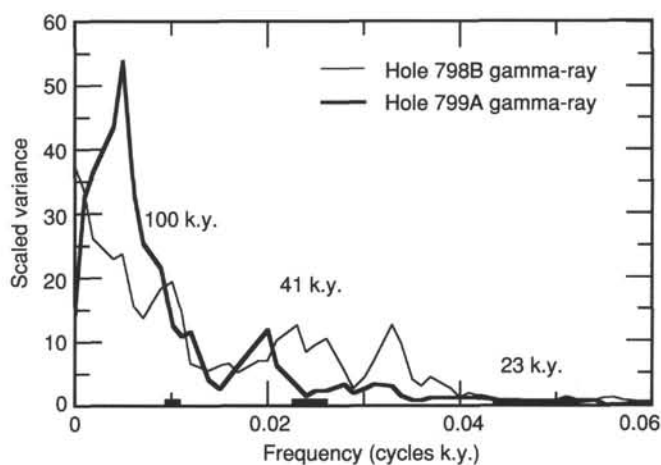


Figure 149. Comparison of gamma-ray power spectra at Hole 798B with those at Hole 799A. Note that both records have concentrations of variance at the frequency band roughly equivalent to the 41-k.y. periodicity (0.024 cycles/k.y.), corresponding to orbital obliquity. The Hole 799A peak is roughly equivalent to 50 k.y., and this may reflect the relatively poorer quality of the paleomagnetic age model at this site compared to Site 798B. The concentration of variance at orbital periodicities suggests that the two records (particularly Hole 798B) may be reflecting orbitally modulated variations in terrigenous sediment influx.

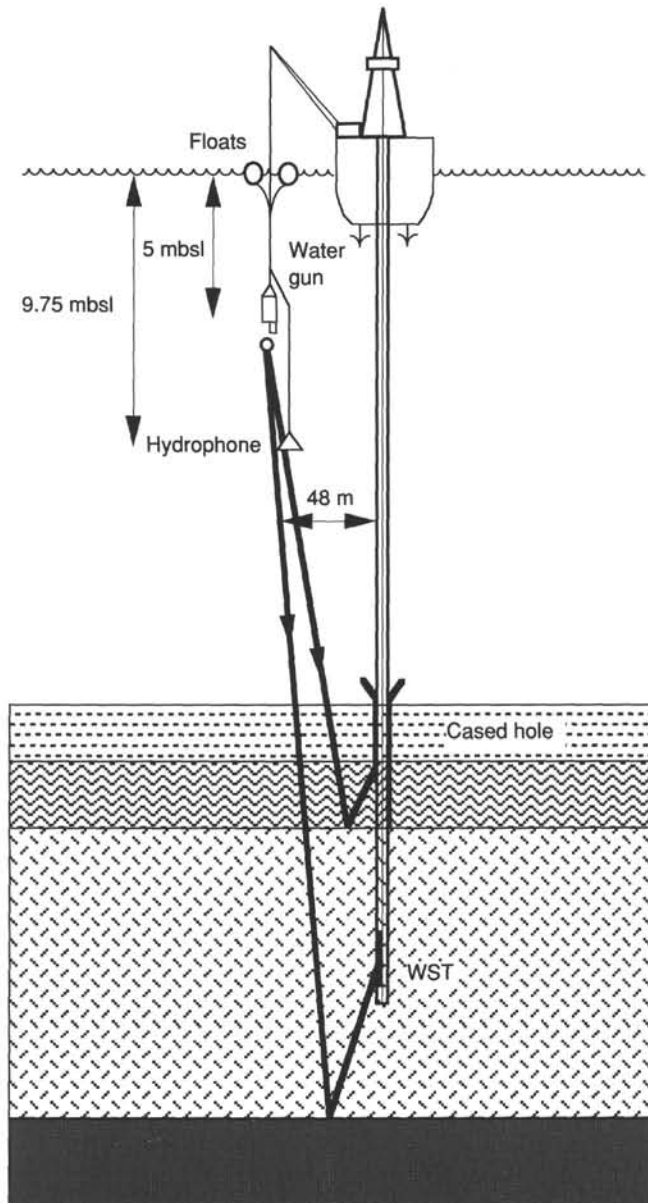


Figure 150. Configuration of VSP experiment at Hole 799B. Down-going and upgoing reflected waves are shown with dark lines. The location of the water gun and hydrophone in relation to ship and borehole is shown. WST = Schlumberger well seismic tool in the borehole.

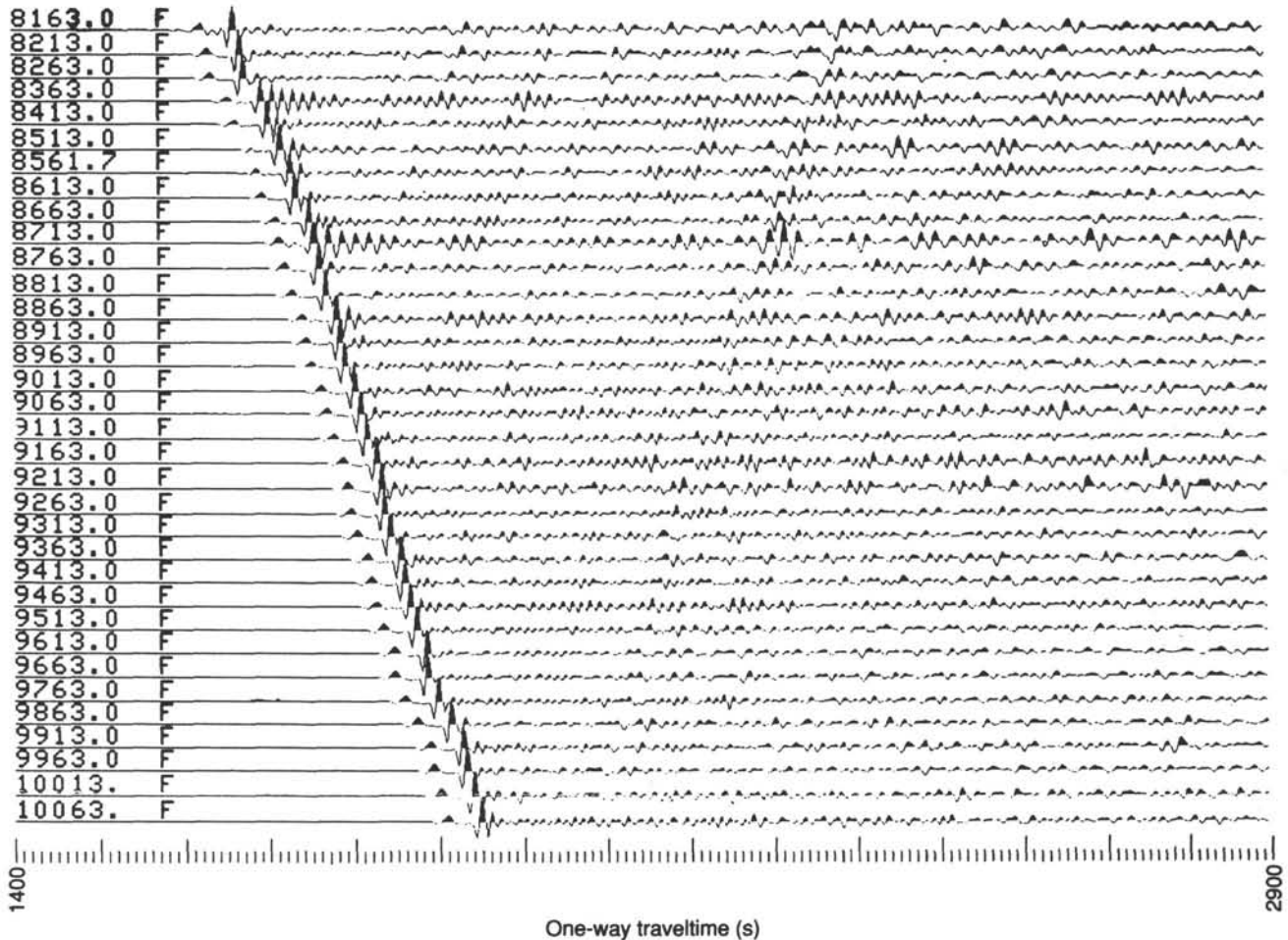


Figure 151. Depth trace ensemble of the VSP stacked shot data. The one-way traveltime of the direct wave is shown by the wave pattern downward to the right. Arrival times of reflected waves are shown by upward trending to the right.

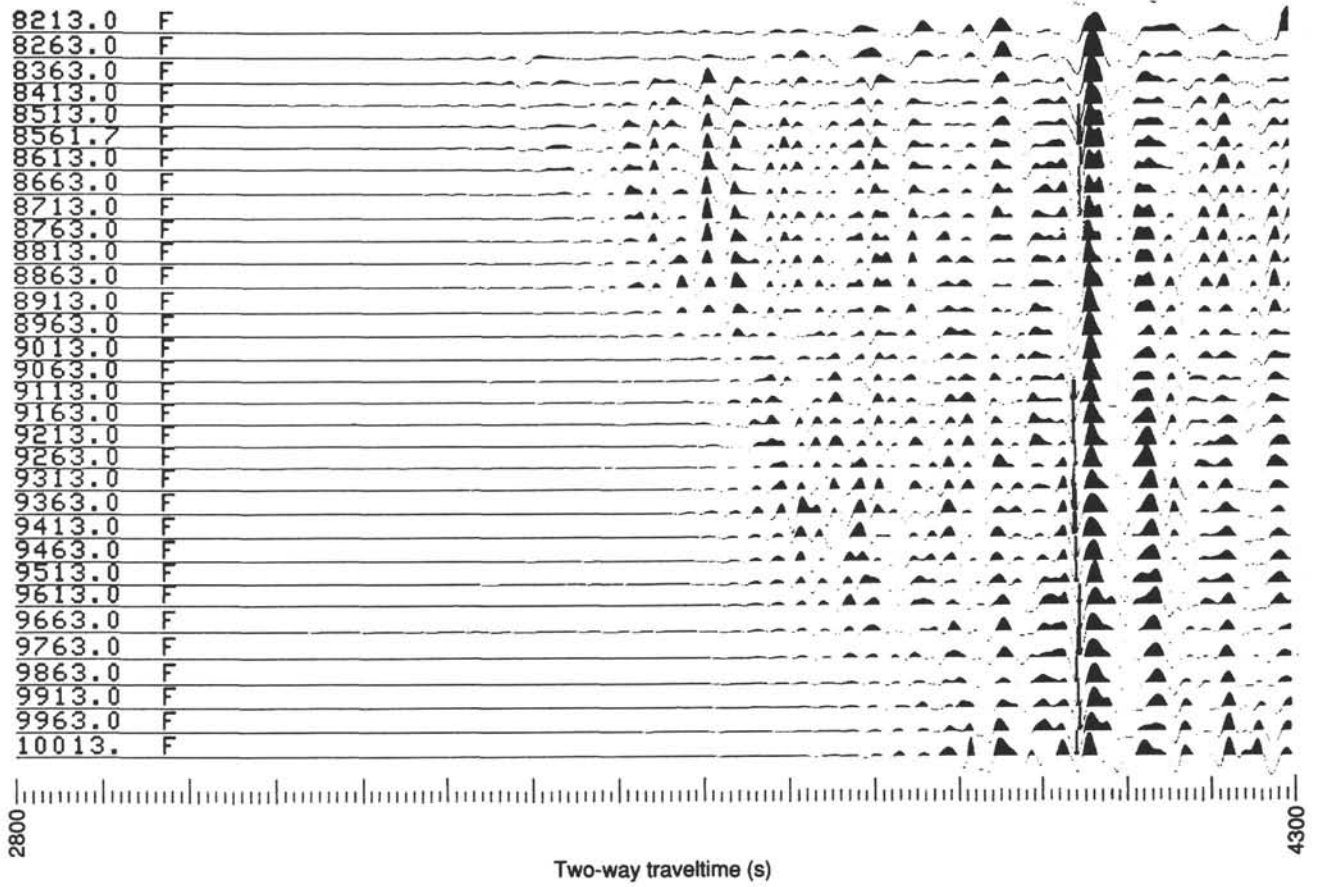


Figure 152. Upgoing reflected waves for 2800 to 4300 ms portion of the two-way travelttime, VSP depth trace ensemble filtered and stacked on the basis of the first break in the record.

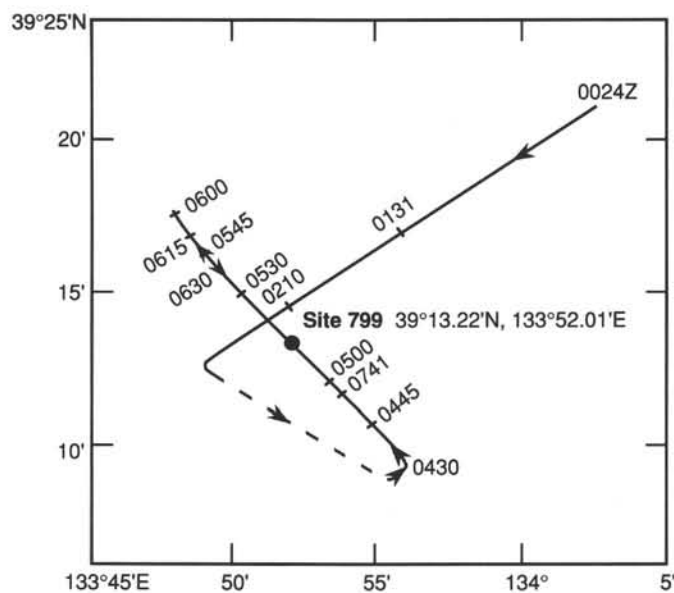


Figure 153. Location map of the immediate area surrounding Site 799. Seismic-reflection lines shot by *JOIDES Resolution* are marked by solid lines. Positions of *JOIDES Resolution* are plotted from GPS and NNSS signals.

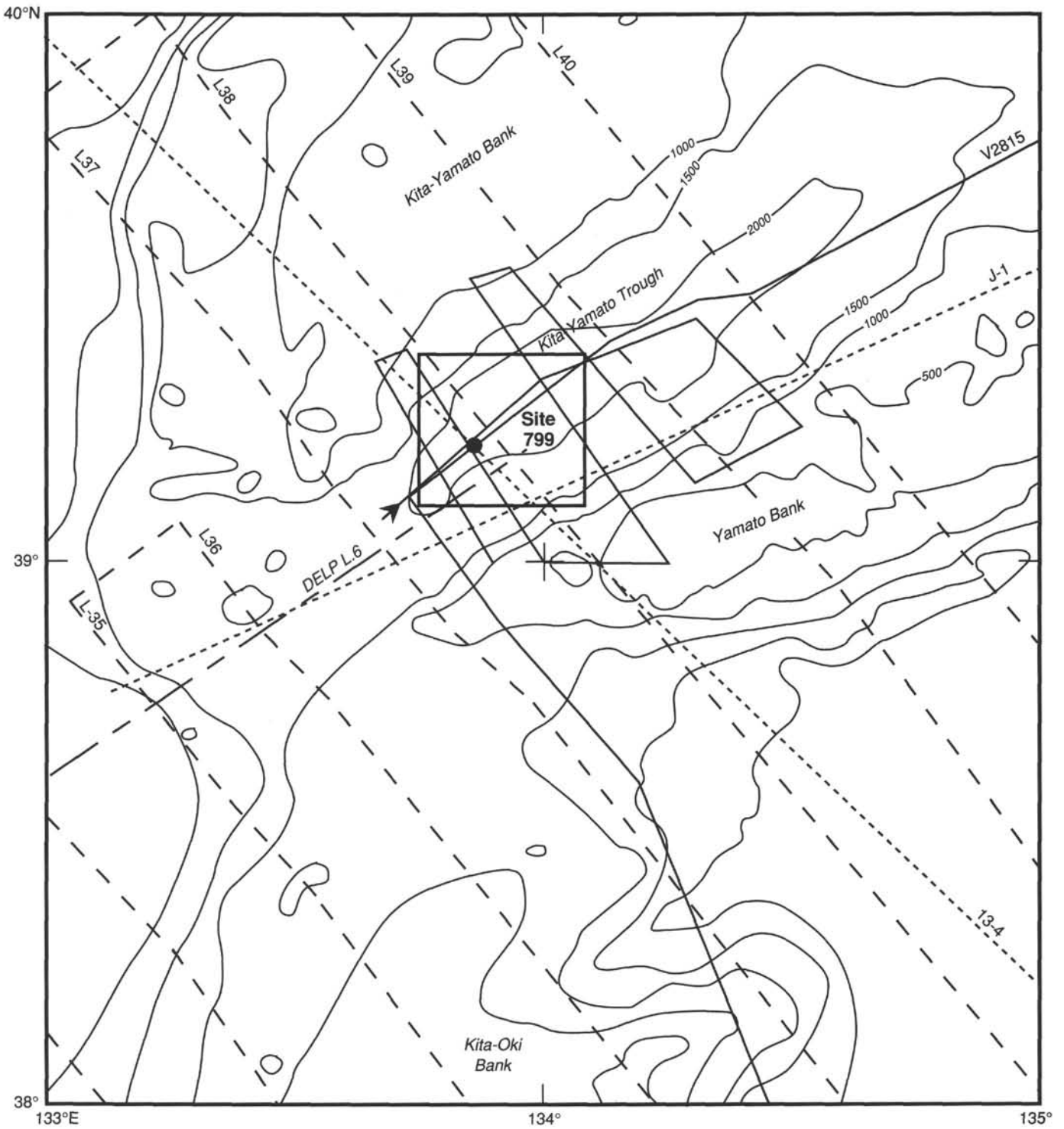


Figure 154. Bathymetric map of the Site 799 area; contour interval 500 m. Single-channel seismic-reflection lines of the Geological Survey of Japan are marked by dashed lines. Dotted lines represent multichannel seismic-reflection lines of the Japan National Oil Company. The thin solid line indicates the track of Lamont-Doherty Geological Observatory seismic-reflection line V2815. The subarea outlined by a rectangle is shown in Figure 153.

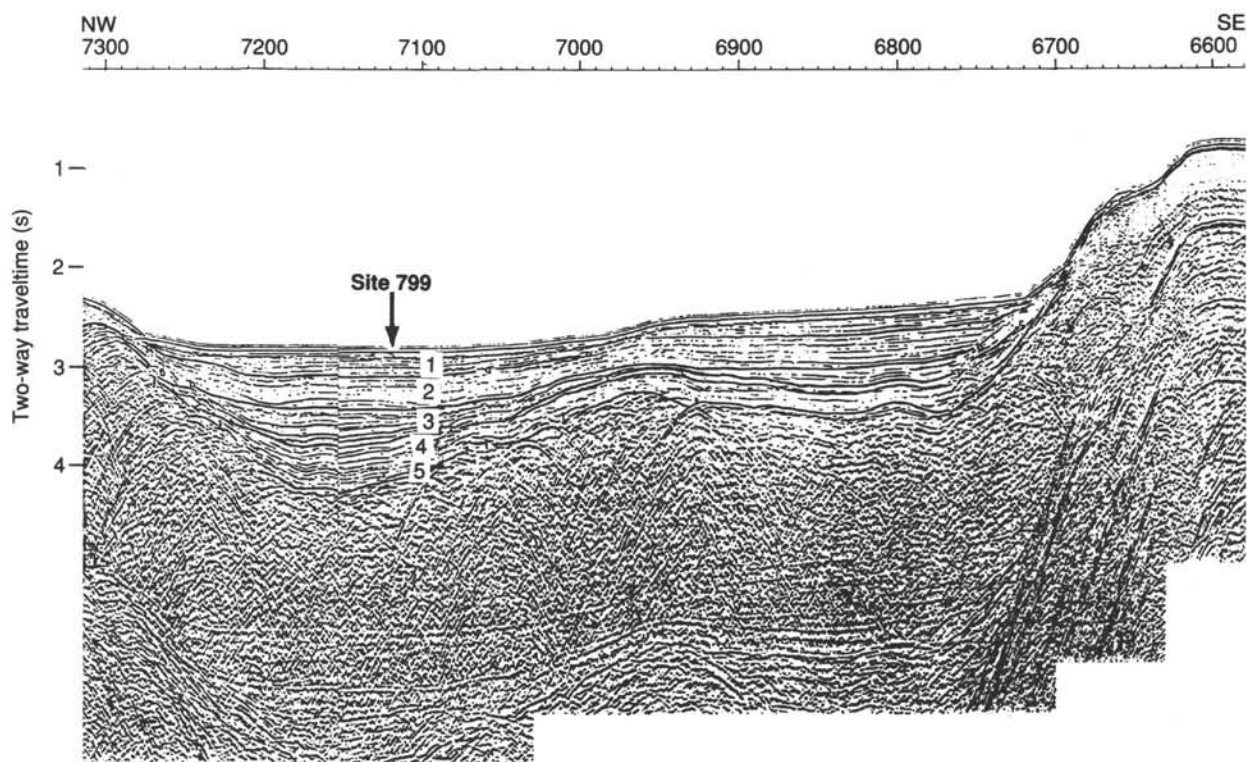


Figure 155. Seismic-reflection record from Line 13-4 of the Japan National Oil Company. The location for Site 799 (proposed Site J2a-1) is at shot point 7120 on this line. Two-way traveltime (s) in vertical axis. Seismic Intervals 1 through 5 at Site 799 are illustrated.

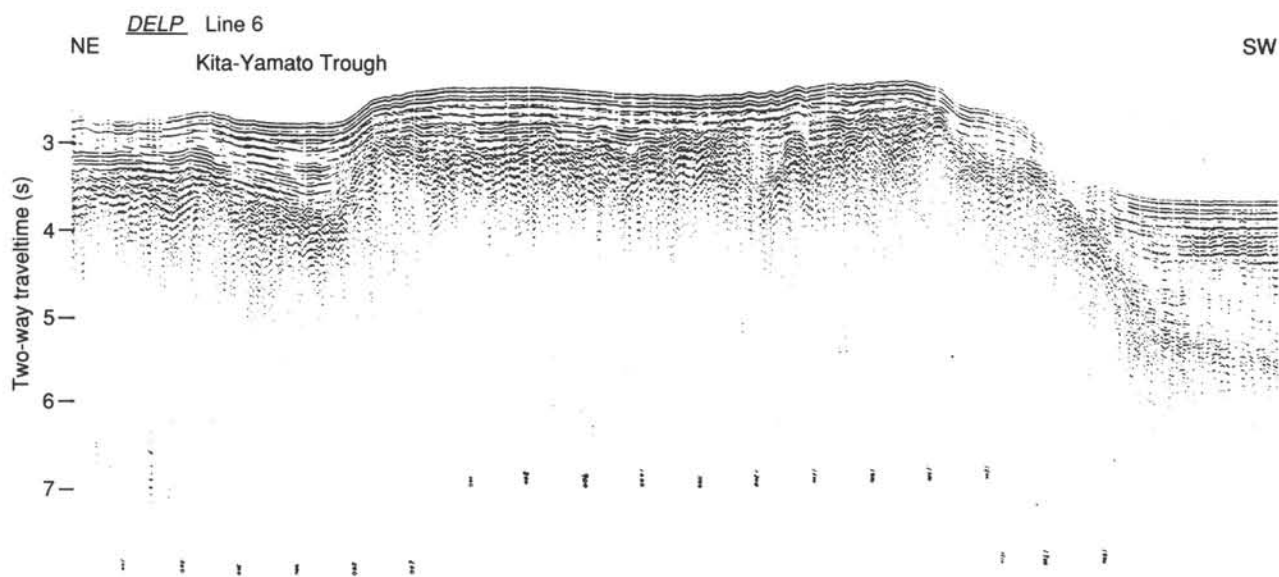


Figure 156. Shipboard monitor record of *DELP* Line 6 obtained by the Ocean Research Institute of the University of Tokyo. An additional track line that runs parallel to the trough axis is shown in Figure 154.

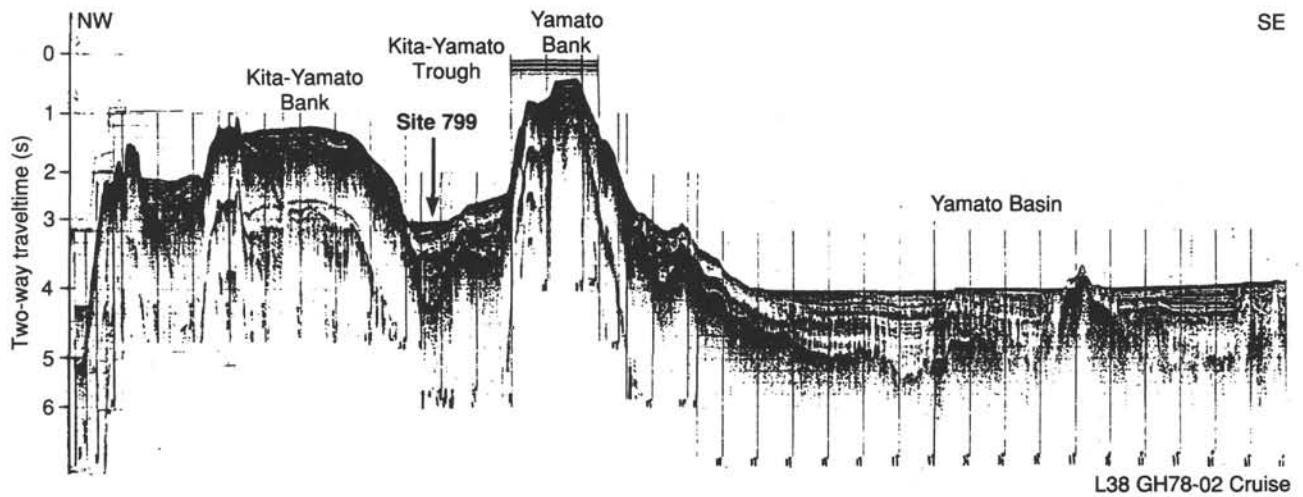


Figure 157. Single-channel seismic records in the Kita-Yamato Trough area obtained by the Geological Survey of Japan (Line L-38 obtained during Cruise GH78-02 in 1978). Track line is shown in Figure 154.

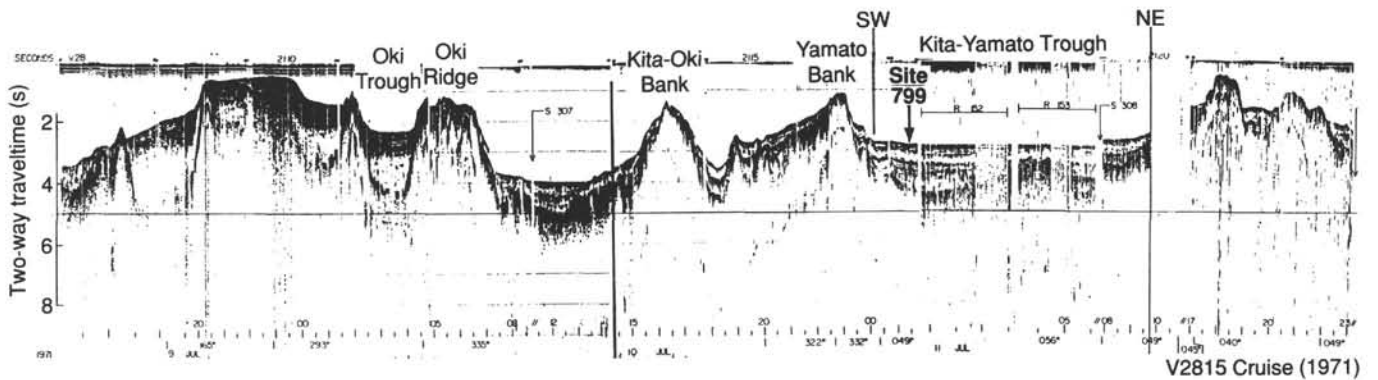


Figure 158. Single-channel seismic record obtained by Lamont-Doherty Geological Survey during *Vema* cruise V2815 in 1971. The track of this profile runs through the trough axis, as shown in Figure 154.

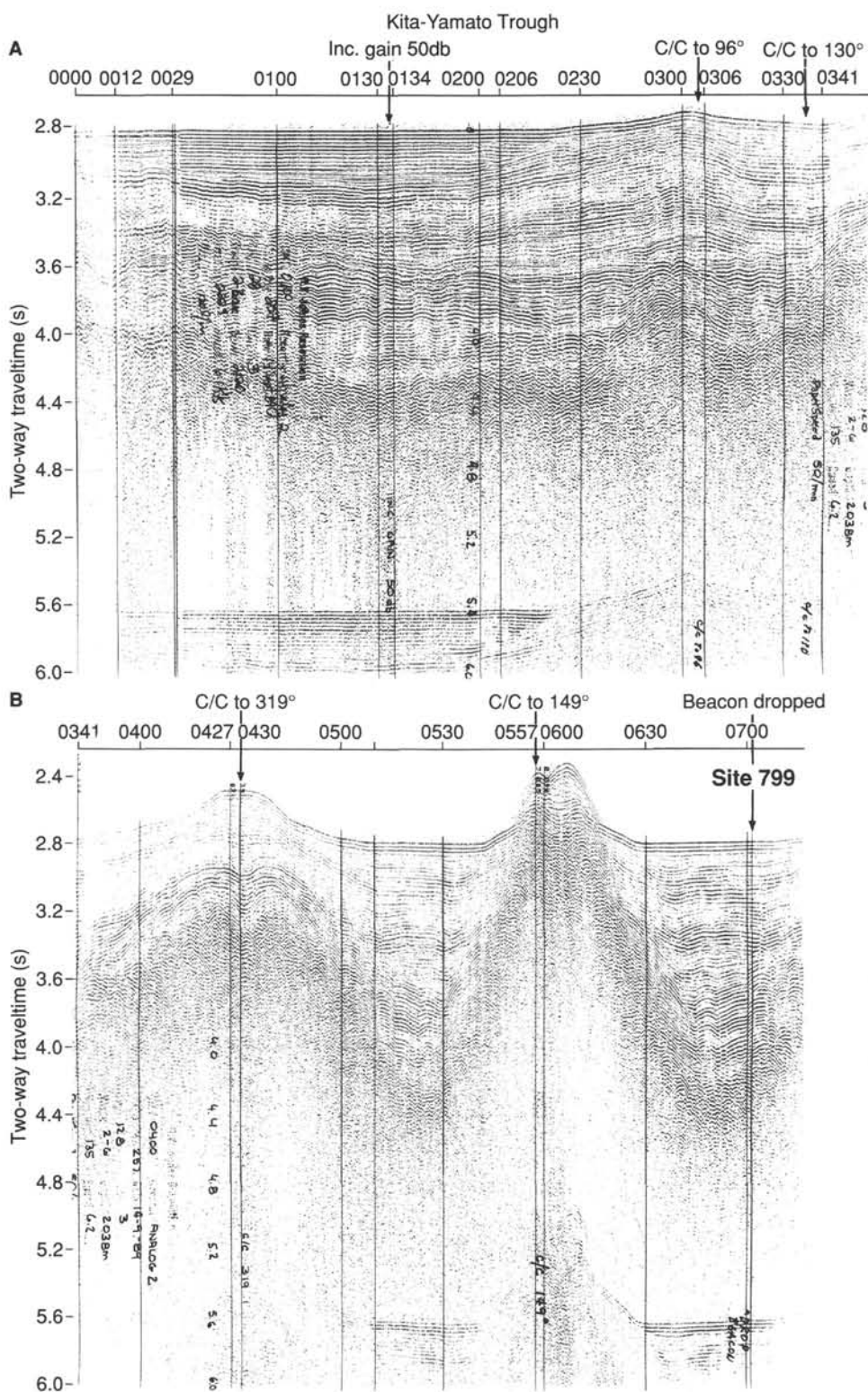


Figure 159. On board monitor record of the single-channel water-gun seismic survey conducted by *JOIDES Resolution* during approach to Site 799. Track line for this profile is shown in Figure 153.

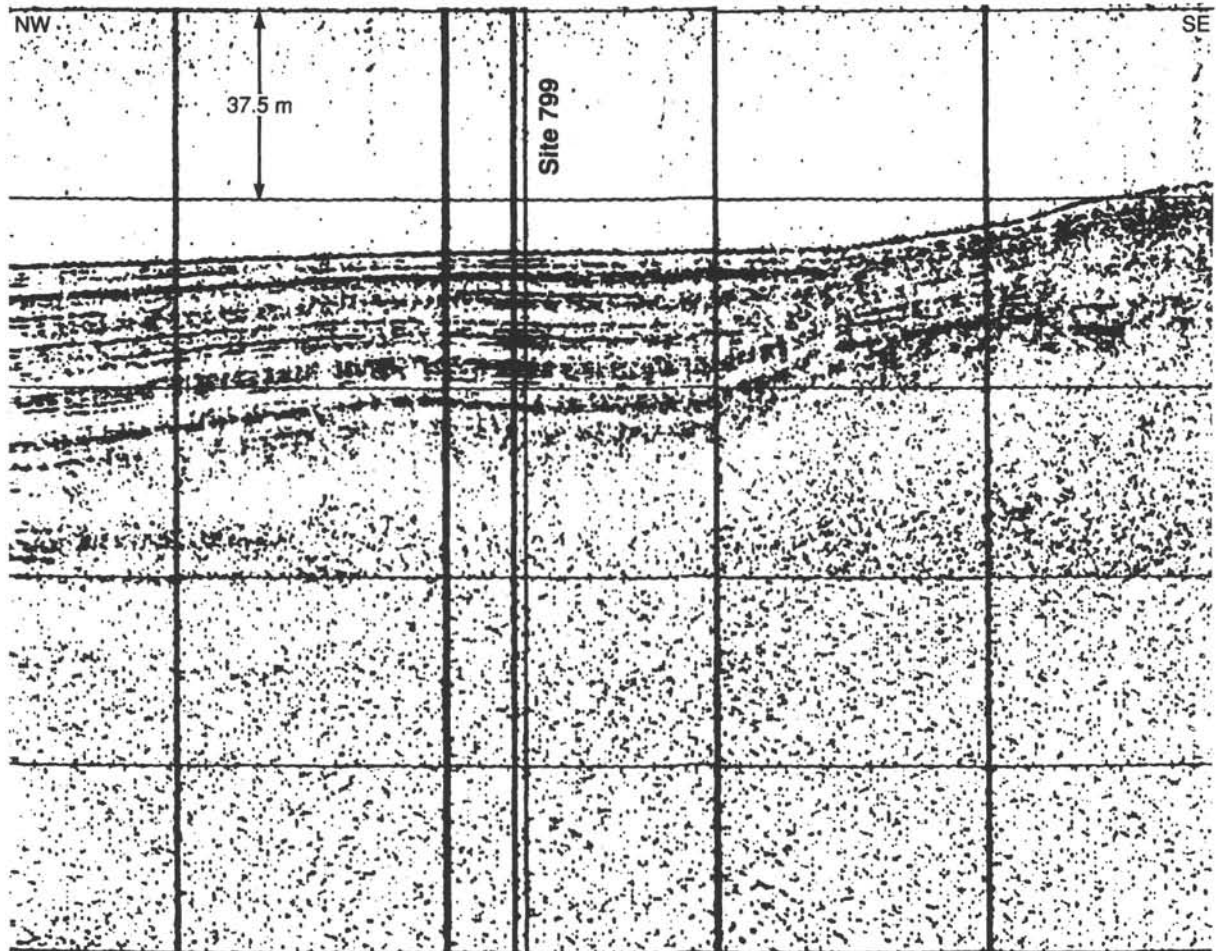


Figure 160. A portion of the 3.5-kHz acoustic-reflection profile record obtained by *JOIDES Resolution* during approach to Site 799 (see Fig. 153; 0650~715UTC).

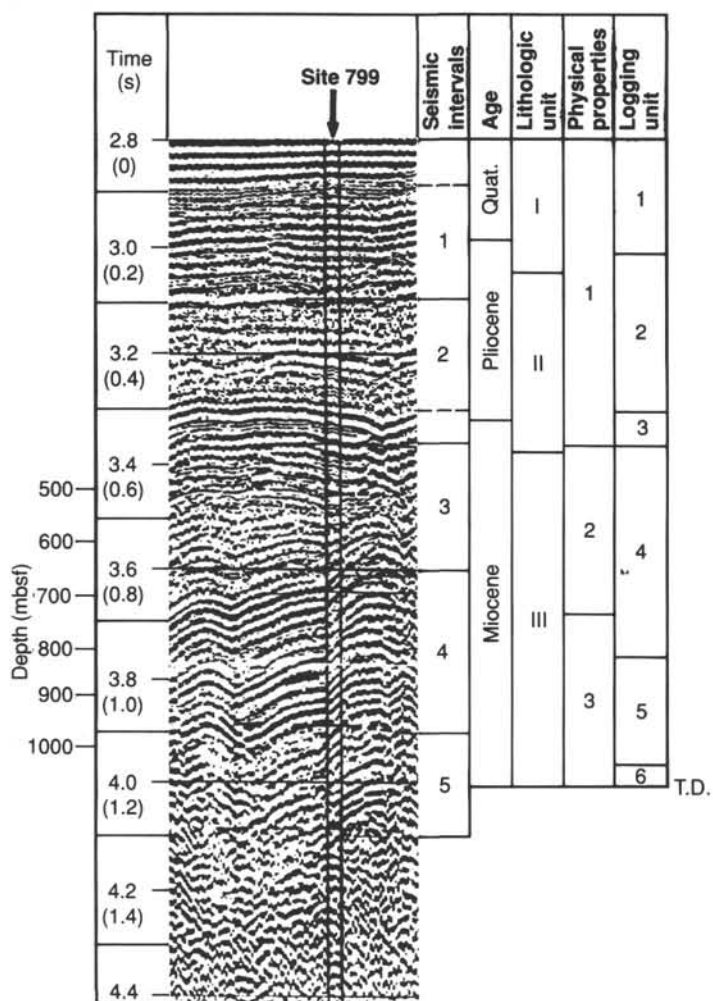


Figure 161. Summary of seismic stratigraphy in the Kita-Yamato Trough and correlations with lithostratigraphy, logging, and physical properties at Site 799. Unit divisions are from each section report. Depths from VSP data are indicated in the leftmost section. Seismic record was taken from Figure 159.

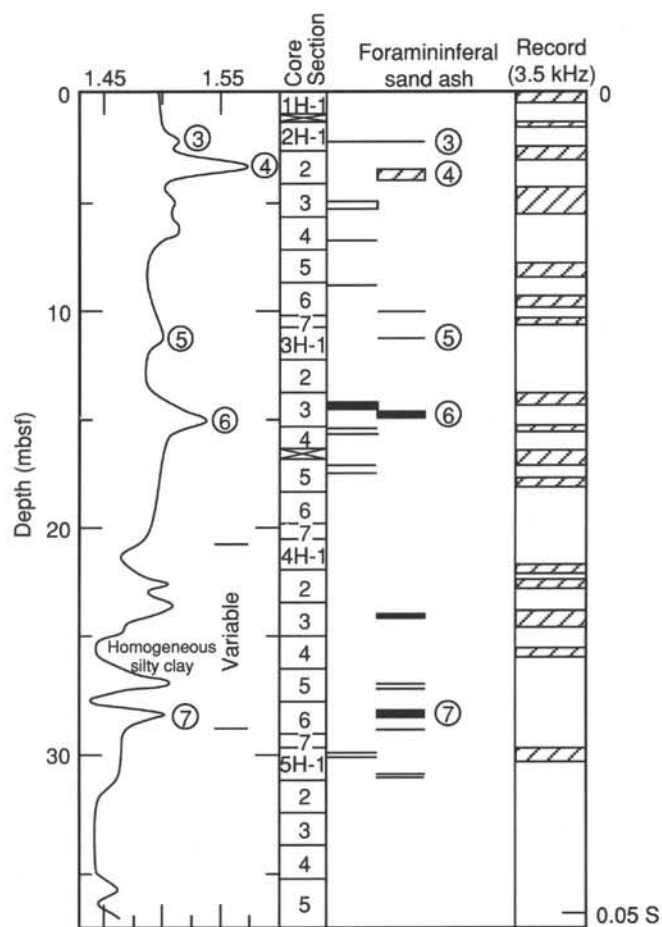
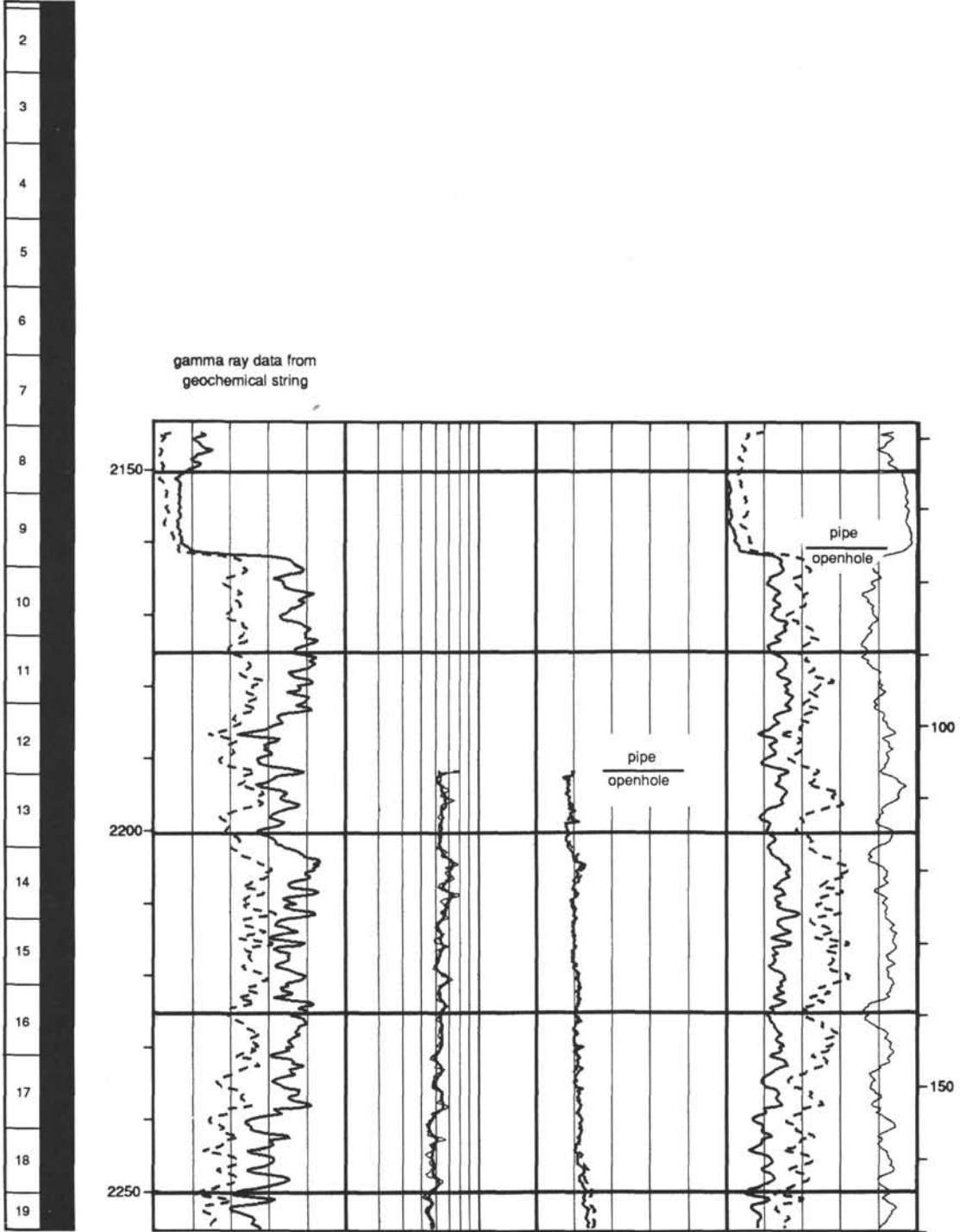


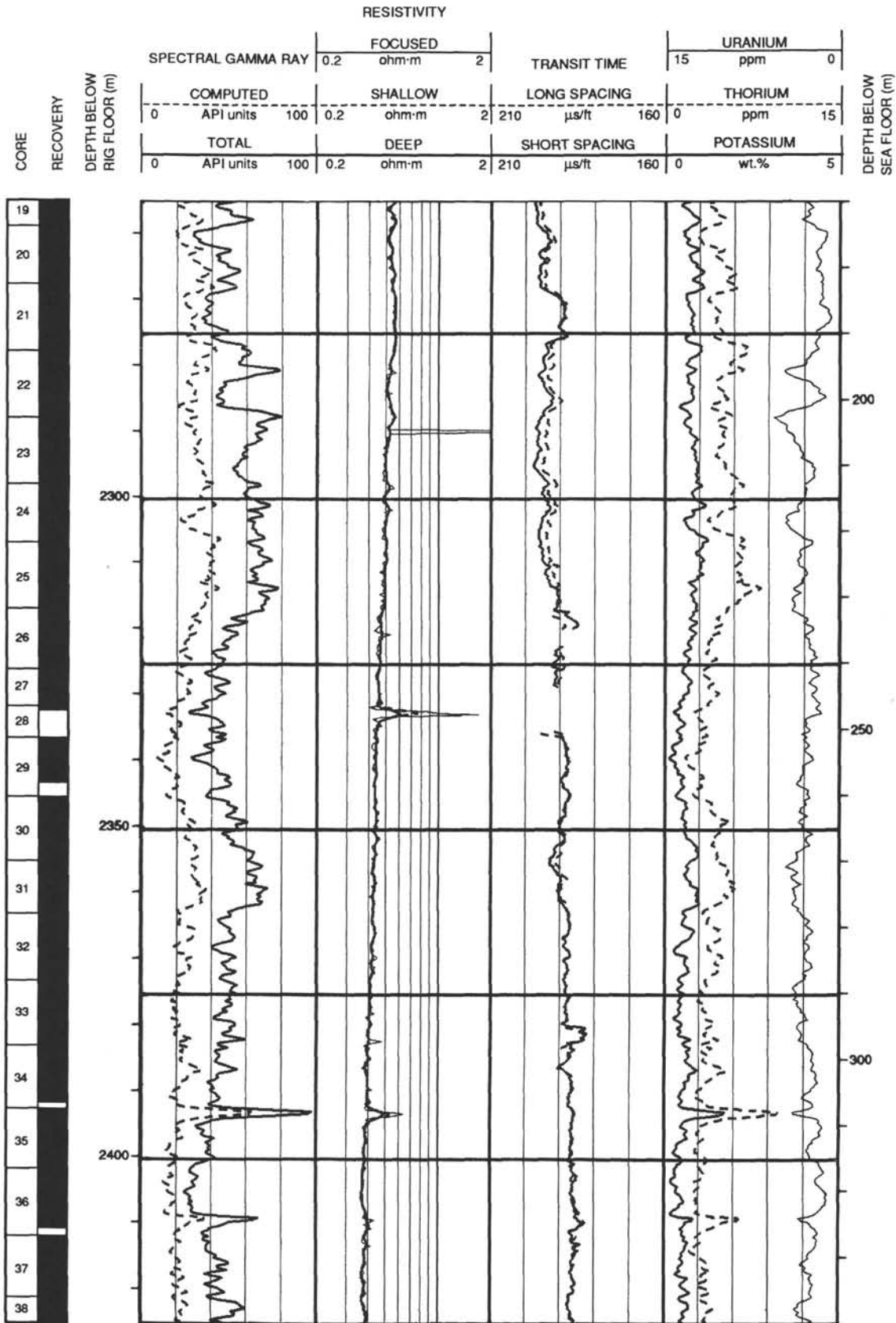
Figure 162. Correlation of 3.5-kHz acoustic-reflection record with sonic velocity measurements, recovered ash layers and sand layers at Site 799.

Hole 799A: Resistivity-Sonic-Gamma Ray Log Summary

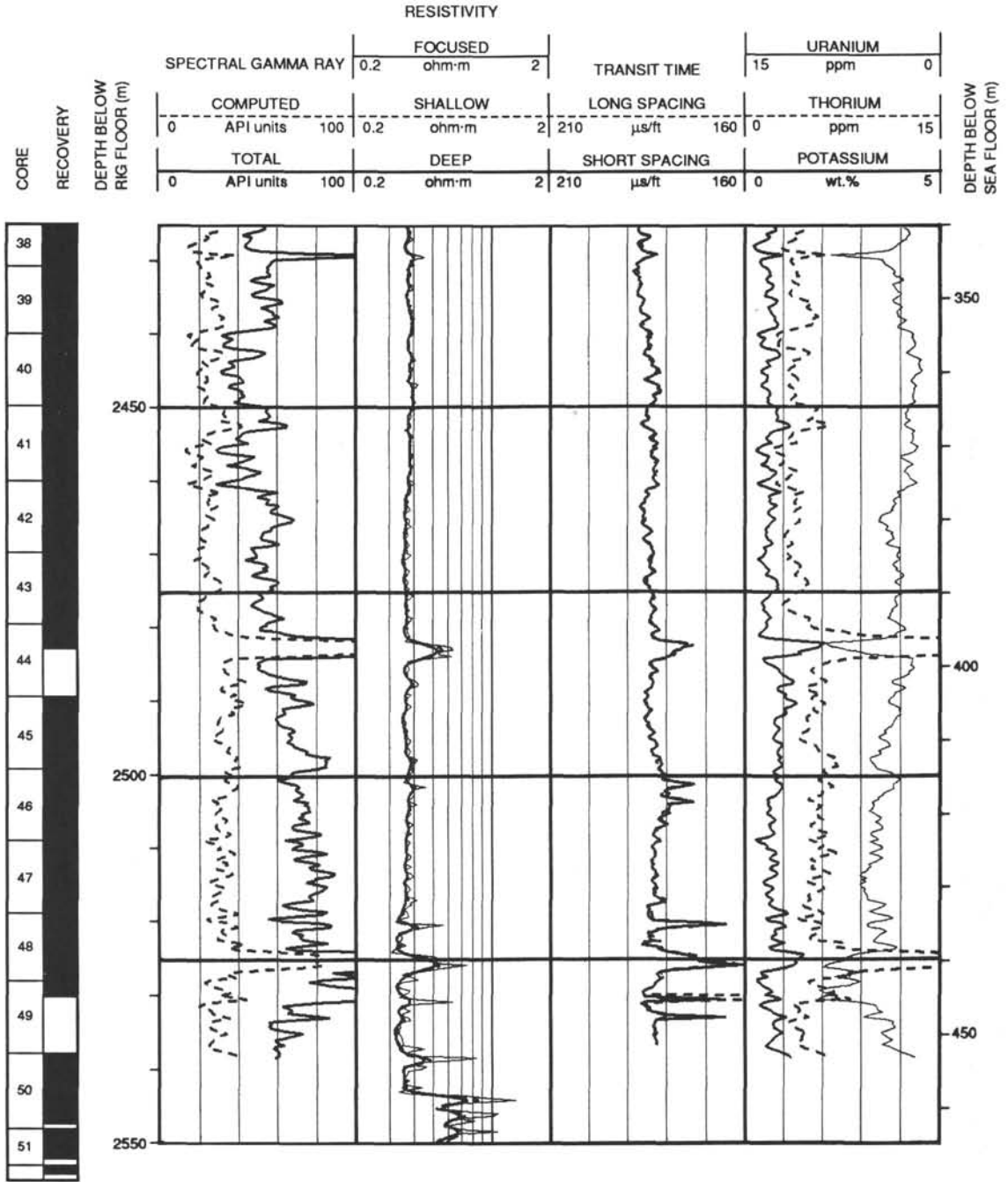
CORE RECOVERY	DEPTH BELOW RIG FLOOR (m)	RESISTIVITY								DEPTH BELOW SEA FLOOR (m)
		SPECTRAL GAMMA RAY		FOCUSED		TRANSIT TIME		URANIUM		
		0	100	0.2	2	210	160	0	15	
		API units		ohm-m		μ s/ft		ppm		
		COMPUTED		SHALLOW		LONG SPACING		THORIUM		
		0	100	0.2	2	210	160	0	15	
		TOTAL		DEEP		SHORT SPACING		POTASSIUM		
		0	100	0.2	2	210	160	0	5	
		API units		ohm-m		μ s/ft		wt.%		



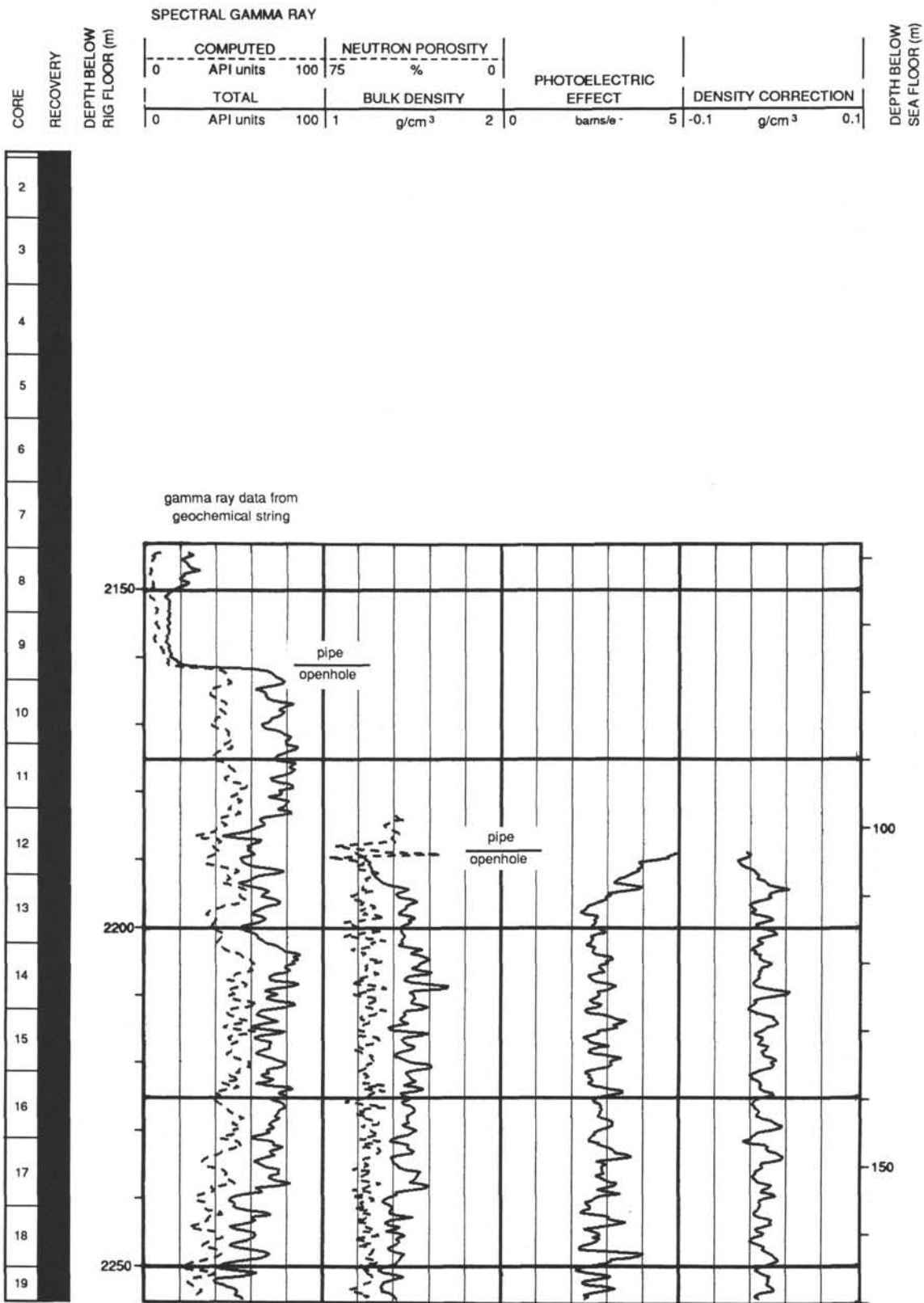
Hole 799A: Resistivity-Sonic-Gamma Ray Log Summary (continued)



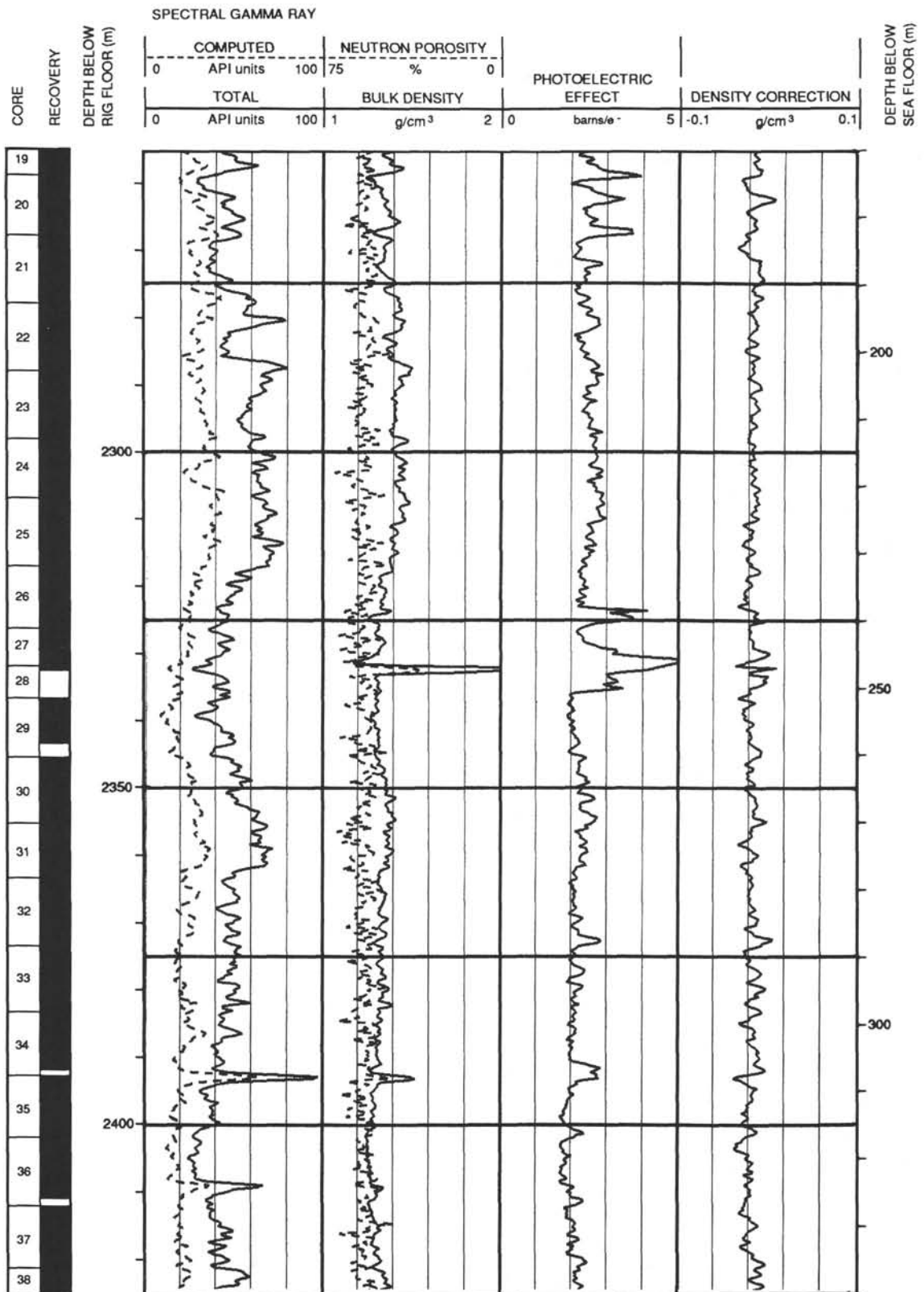
Hole 799A: Resistivity-Sonic-Gamma Ray Log Summary (continued)



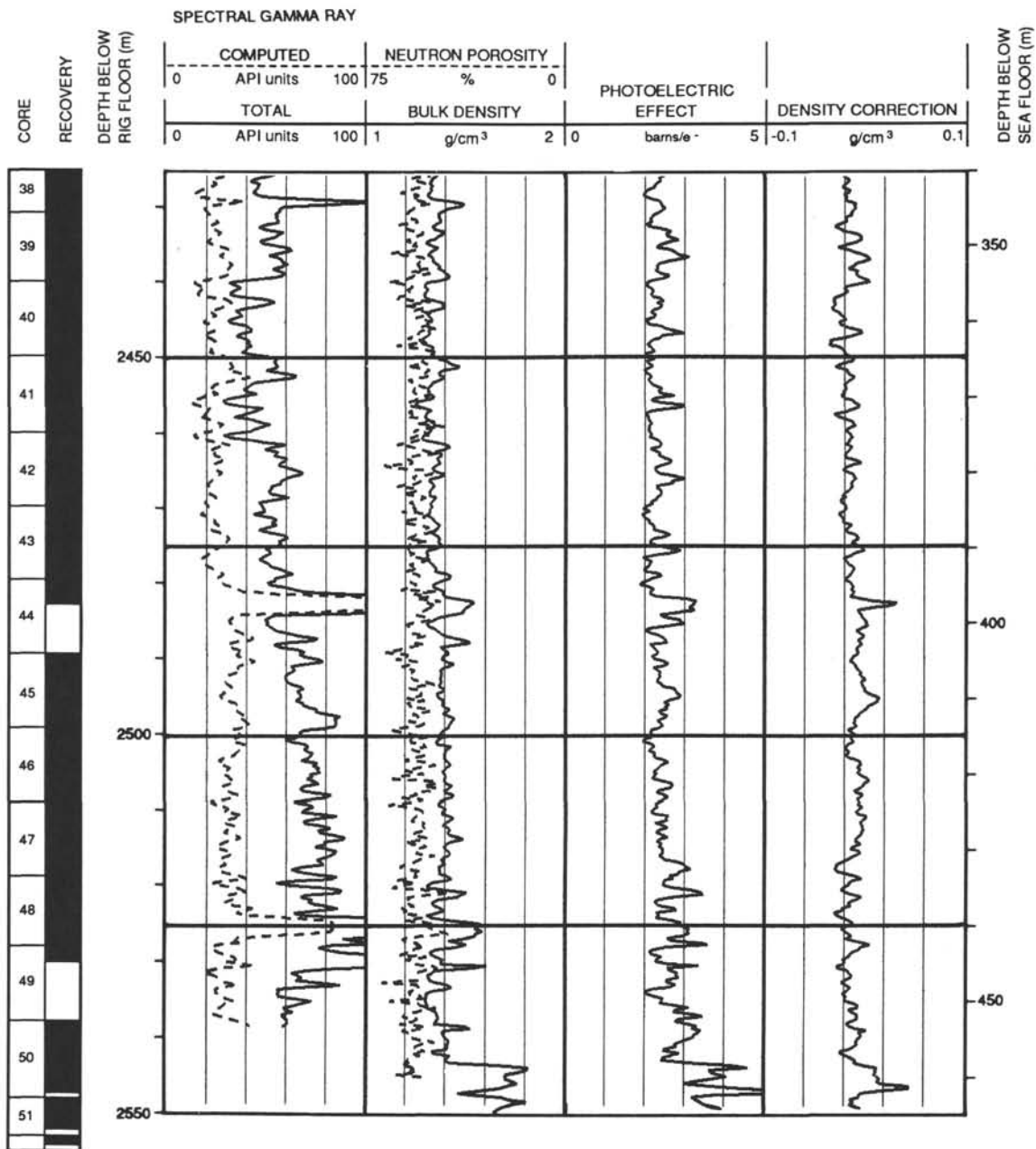
Hole 799A: Density-Porosity-Gamma Ray Log Summary



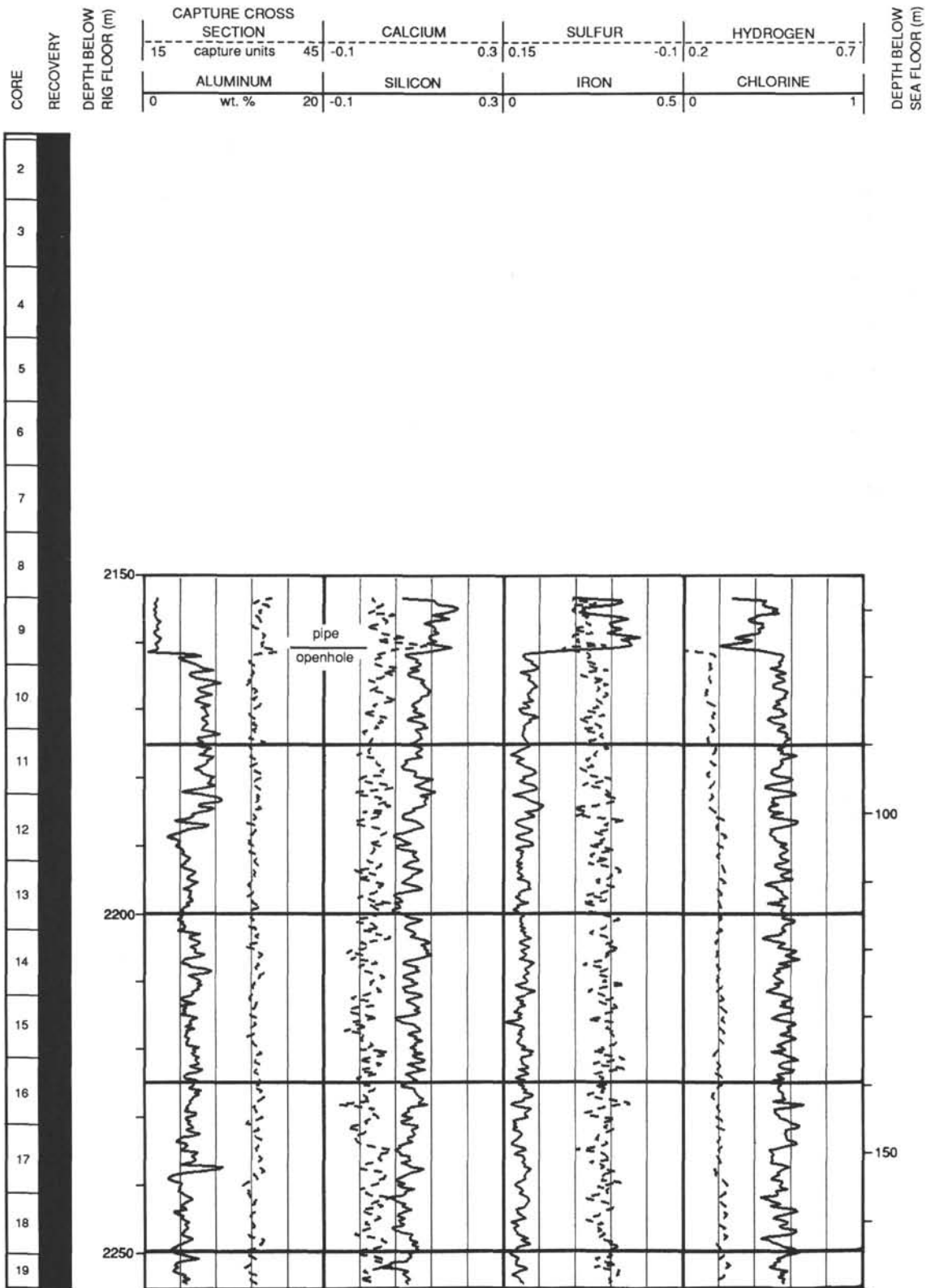
Hole 799A: Density-Porosity-Gamma Ray Log Summary (continued)



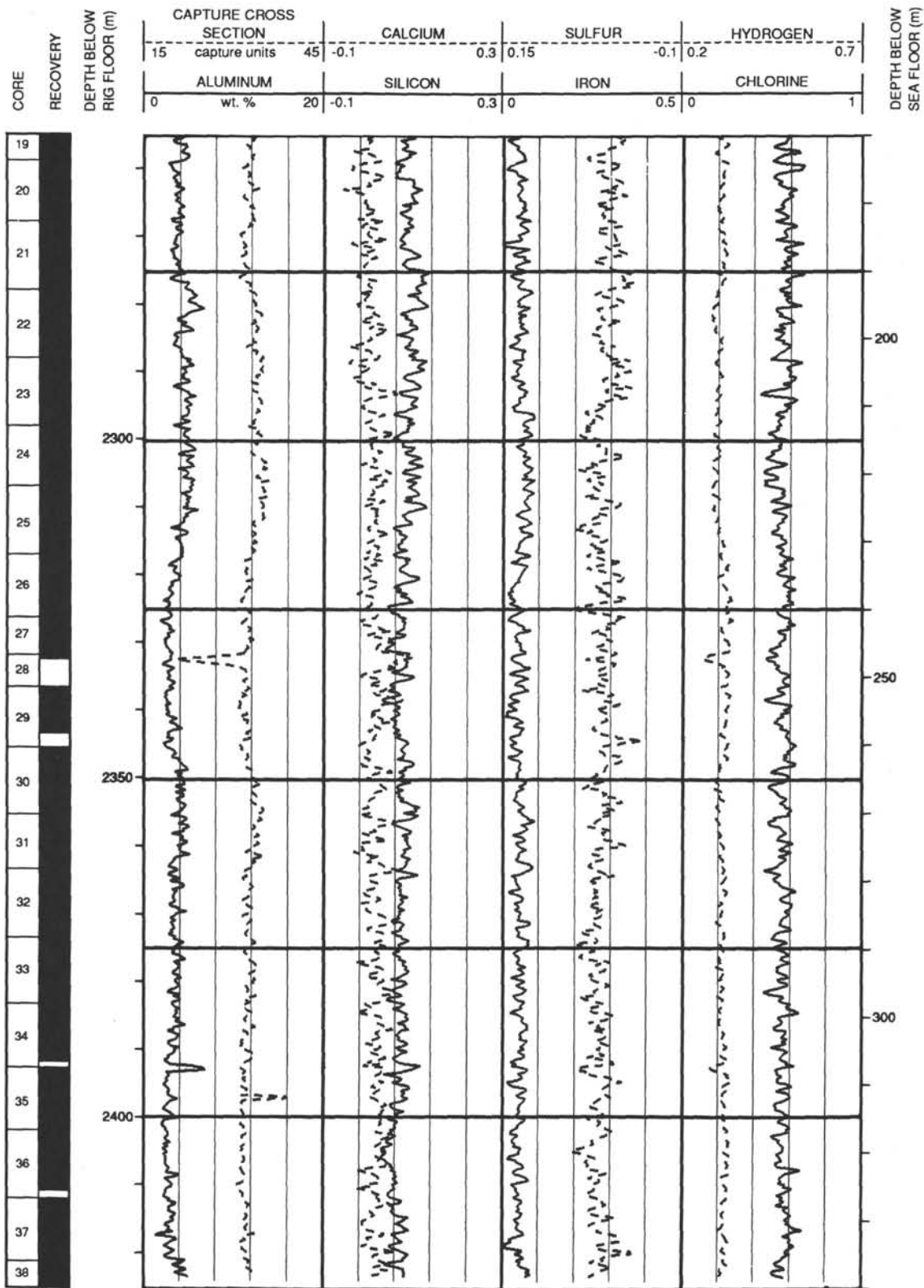
Hole 799A: Density-Porosity-Gamma Ray Log Summary (continued)



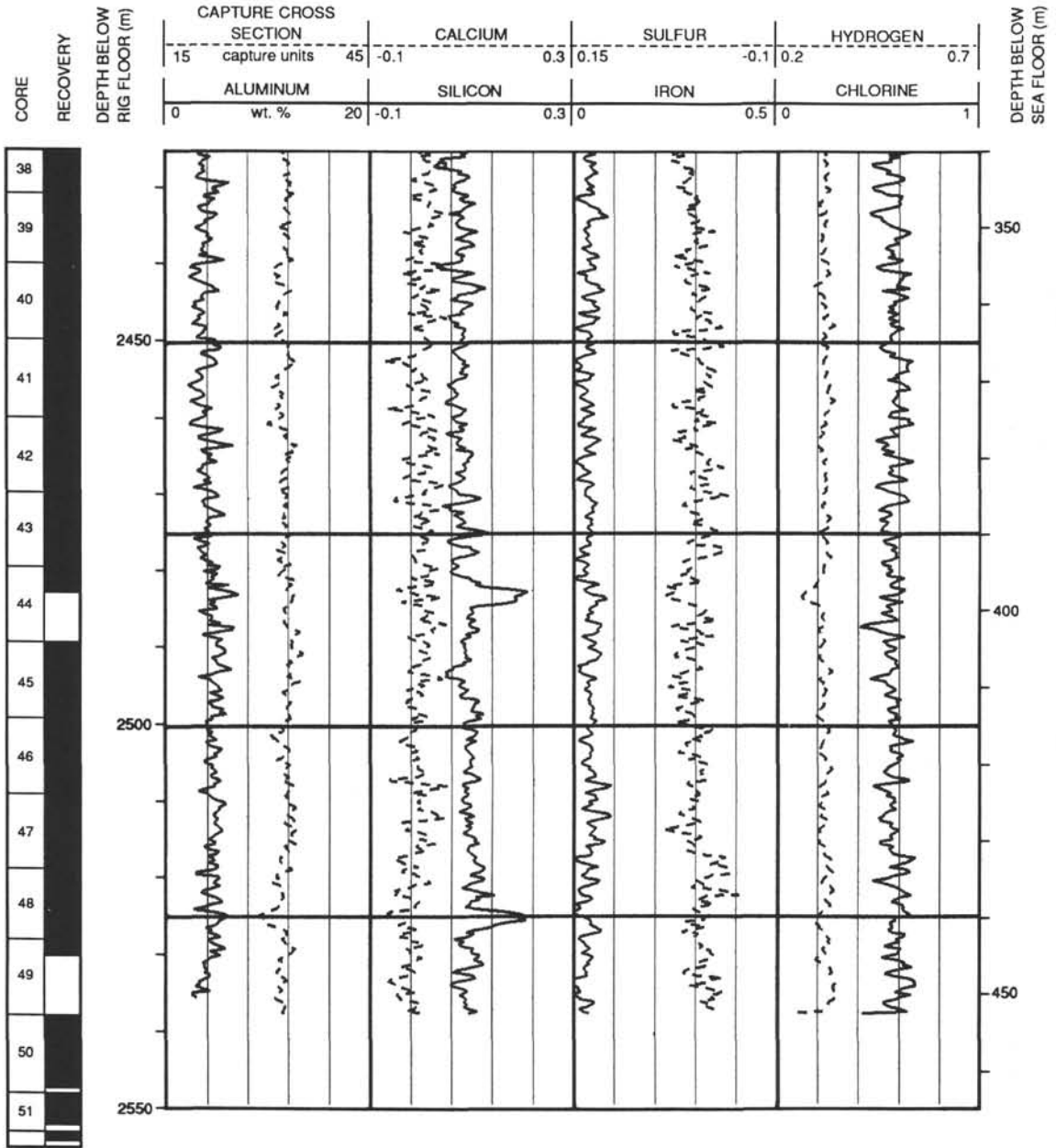
Hole 799A: Geochemical Log Summary



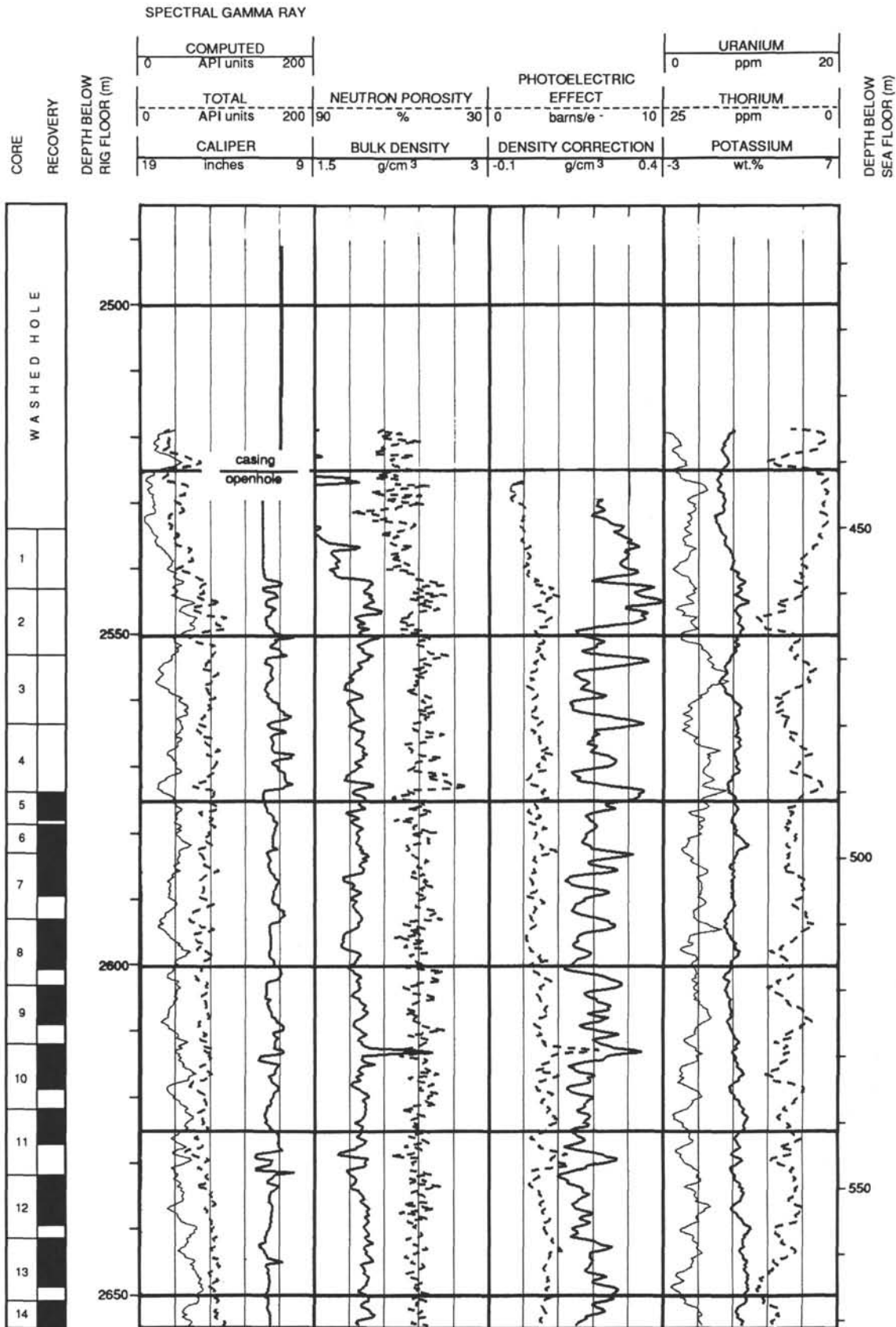
Hole 799A: Geochemical Log Summary (continued)



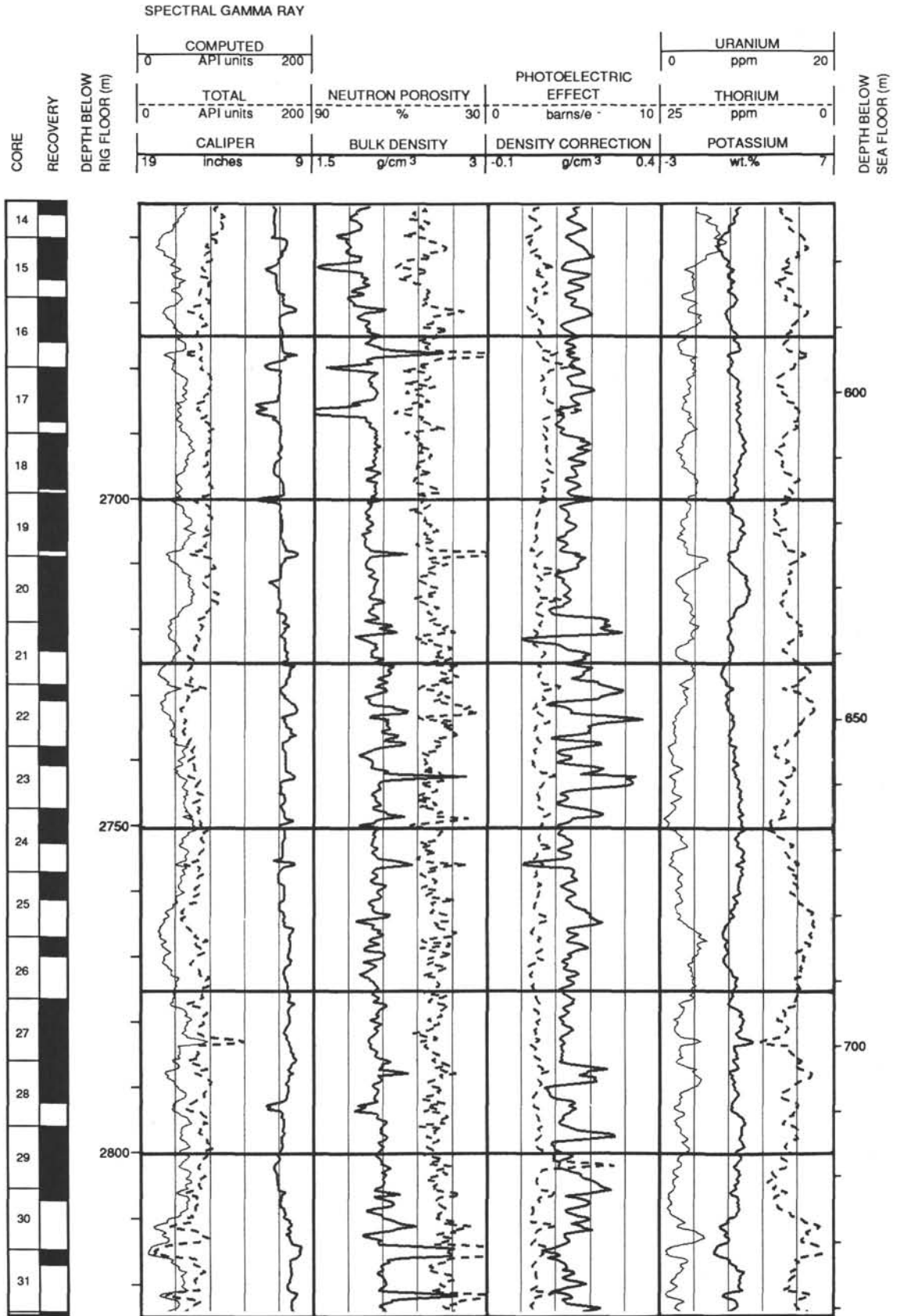
Hole 799A: Geochemical Log Summary (continued)



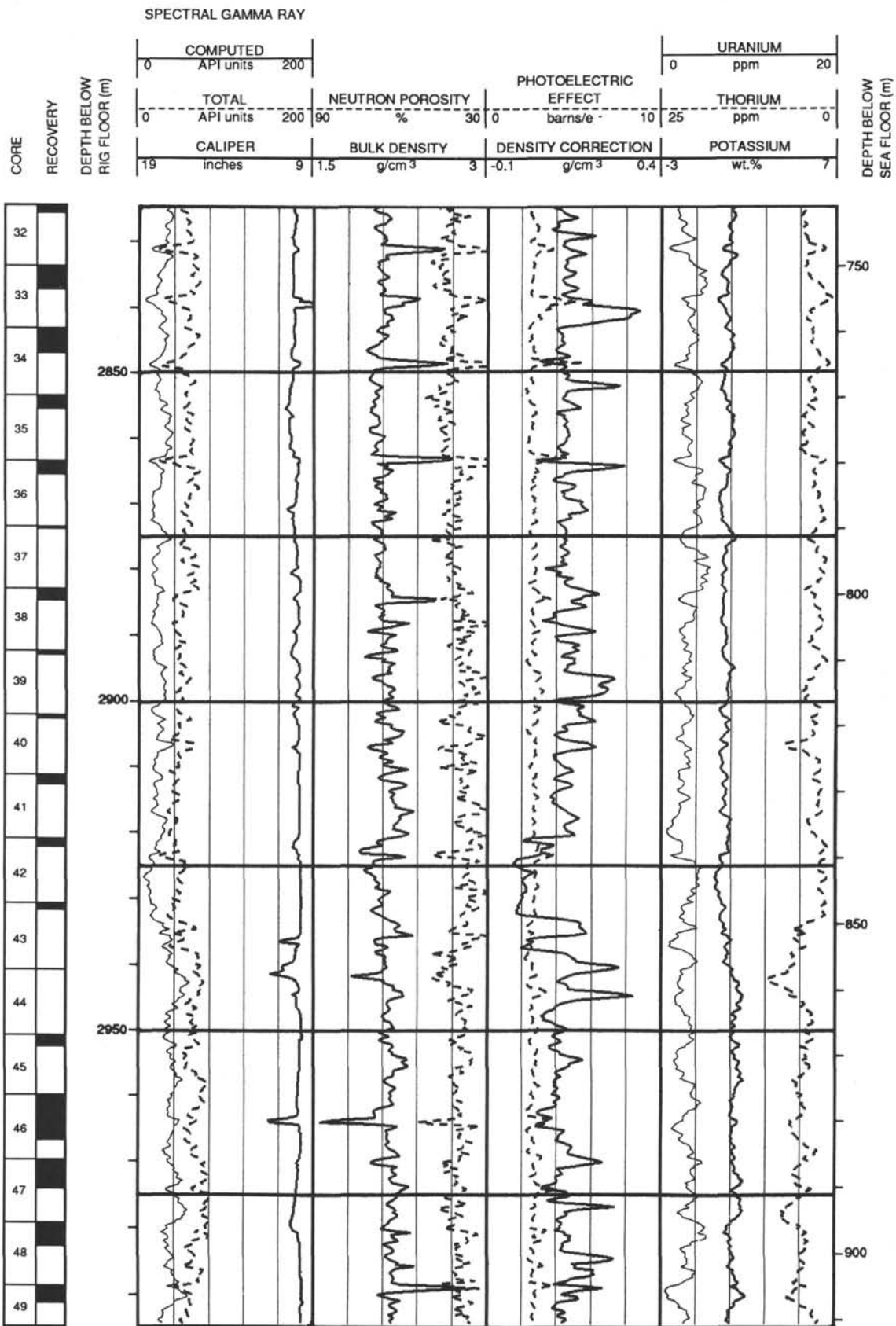
Hole 799B: Density-Porosity-Gamma Ray Log Summary



Hole 799B: Density-Porosity-Gamma Ray Log Summary (continued)

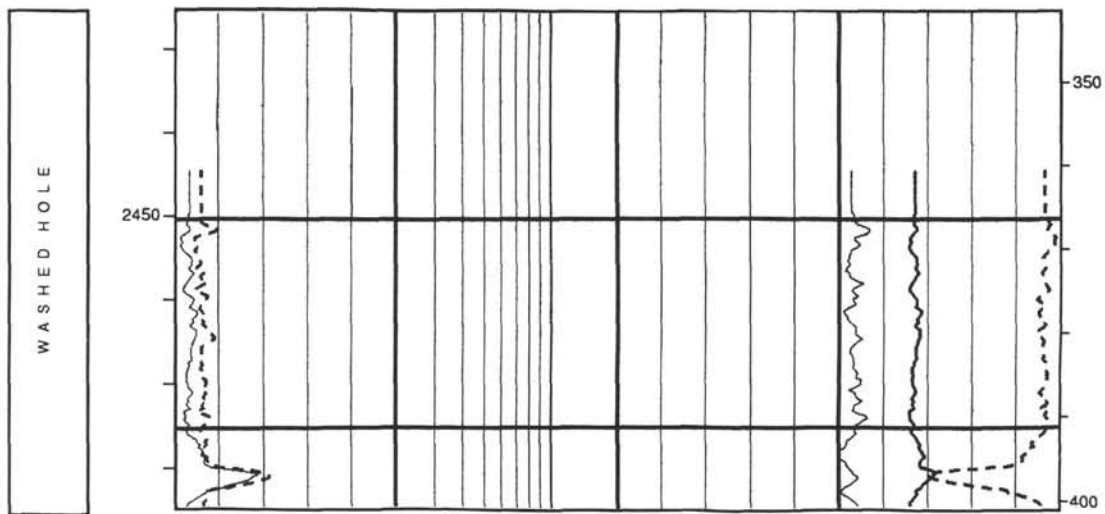


Hole 799B: Density-Porosity-Gamma Ray Log Summary (continued)

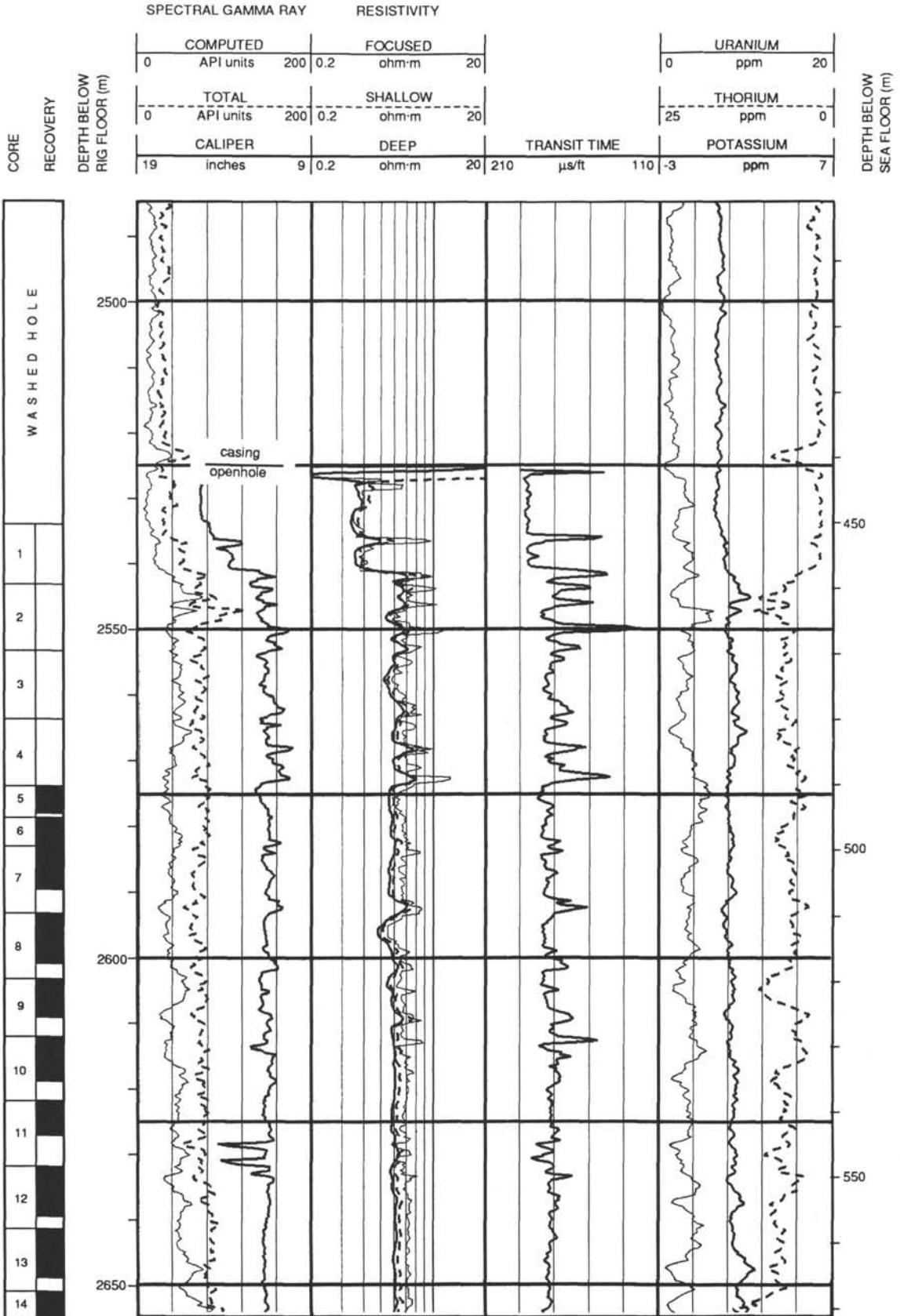


Hole 799B: Resistivity-Sonic-Gamma Ray Log Summary

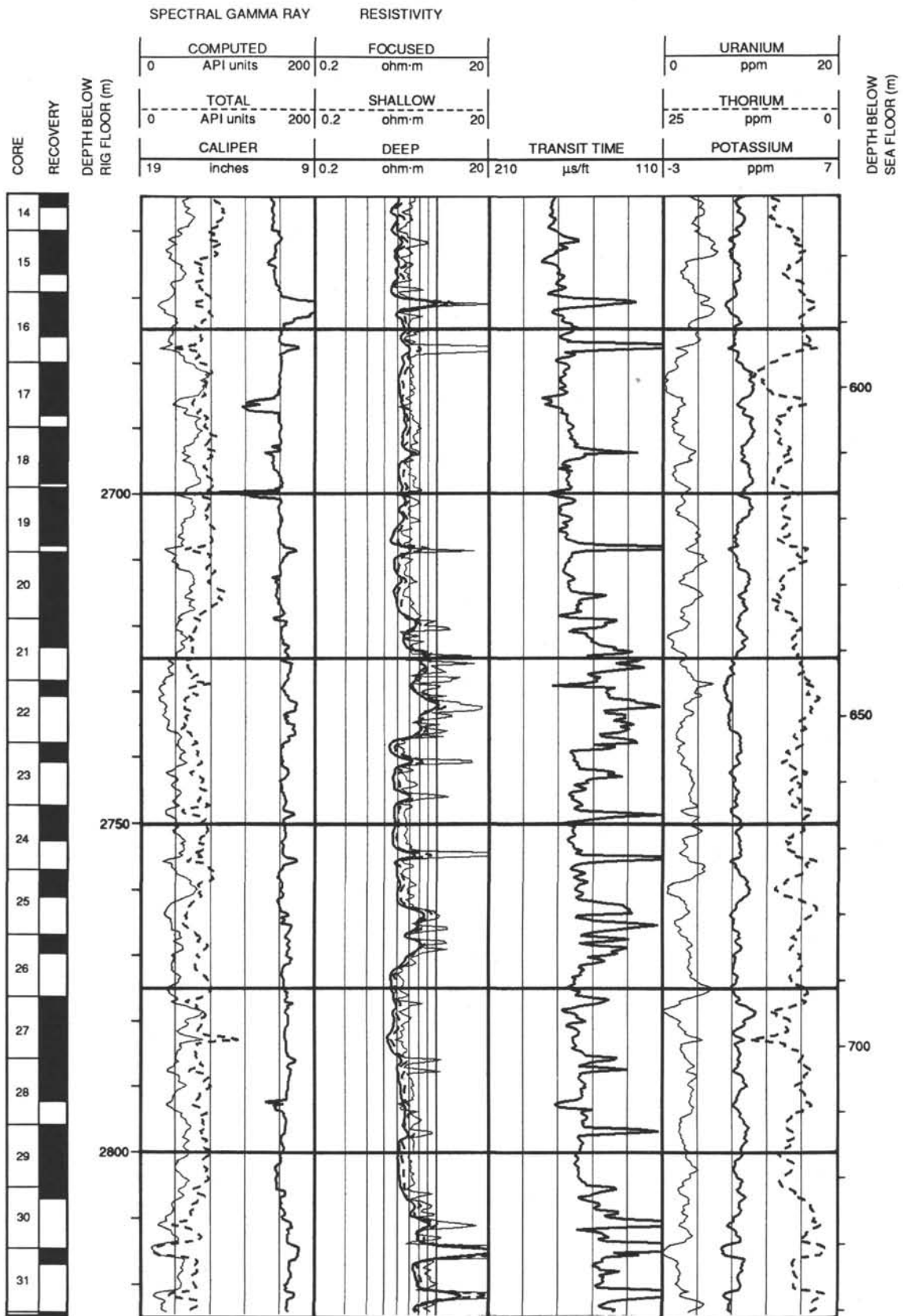
CORE RECOVERY	DEPTH BELOW RIG FLOOR (m)	SPECTRAL GAMMA RAY			RESISTIVITY			TRANSIT TIME			DEPTH BELOW SEA FLOOR (m)
		COMPUTED		0.2	FOCUSED		0.2	URANIUM			
		API units	200		ohm·m	20		0	ppm	20	
		TOTAL		0.2	SHALLOW		0.2	THORIUM			
API units	200	ohm·m	20		25	ppm		0			
		CALIPER		0.2	DEEP		POTASSIUM				
		inches	9		ohm·m	20	210	μs/ft	110	-3	ppm



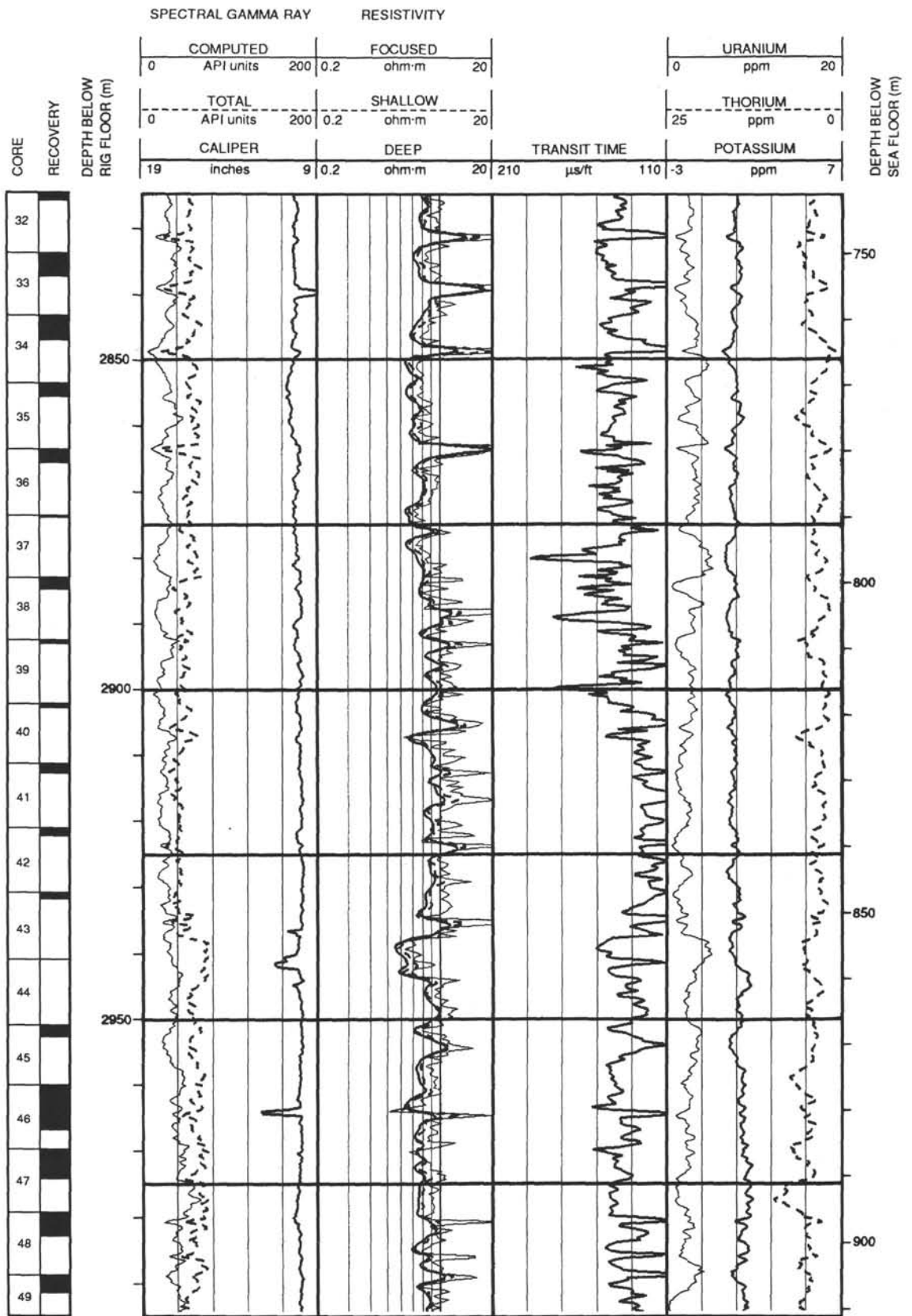
Hole 799B: Resistivity-Sonic-Gamma Ray Log Summary (continued)



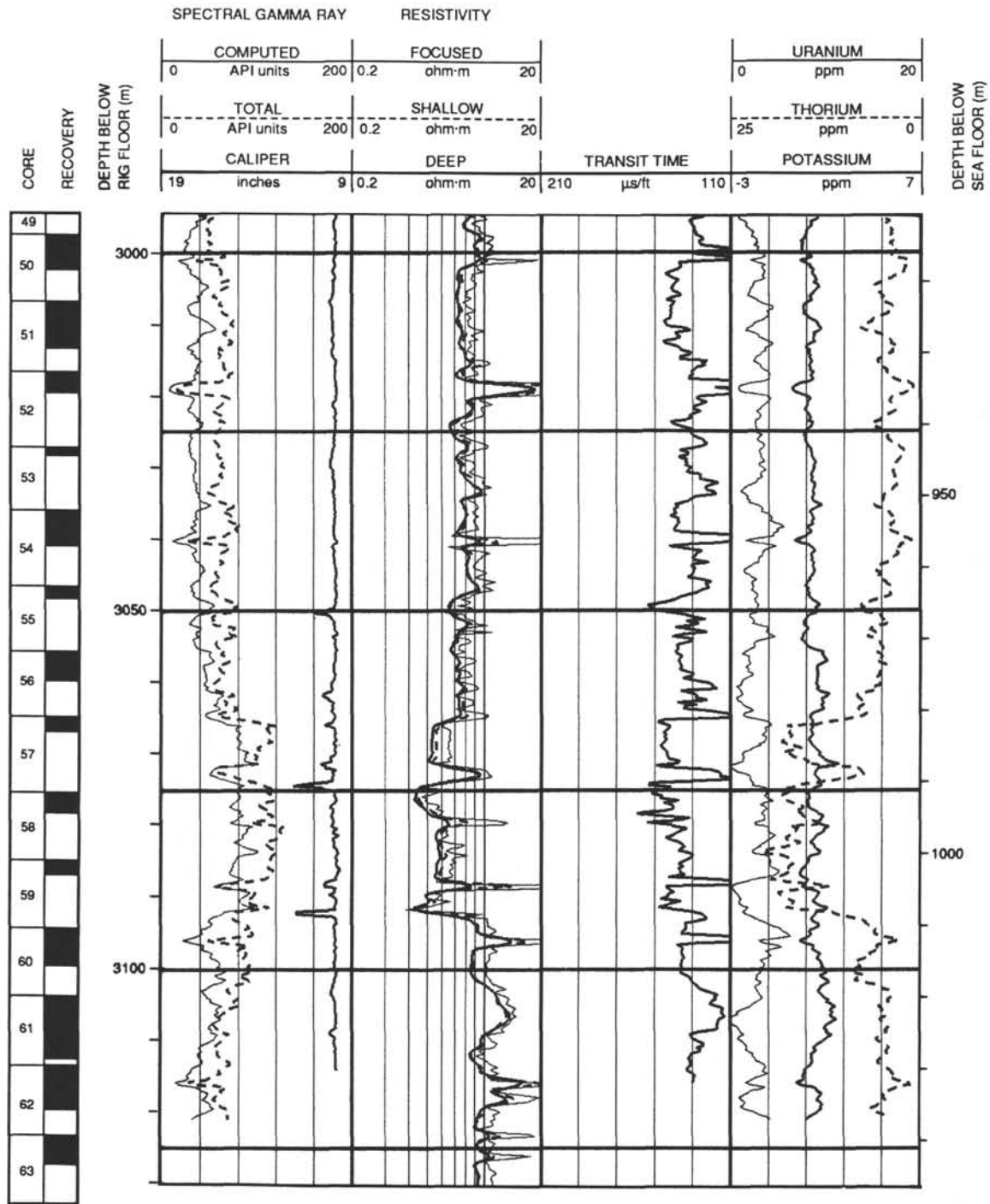
Hole 799B: Resistivity-Sonic-Gamma Ray Log Summary (continued)



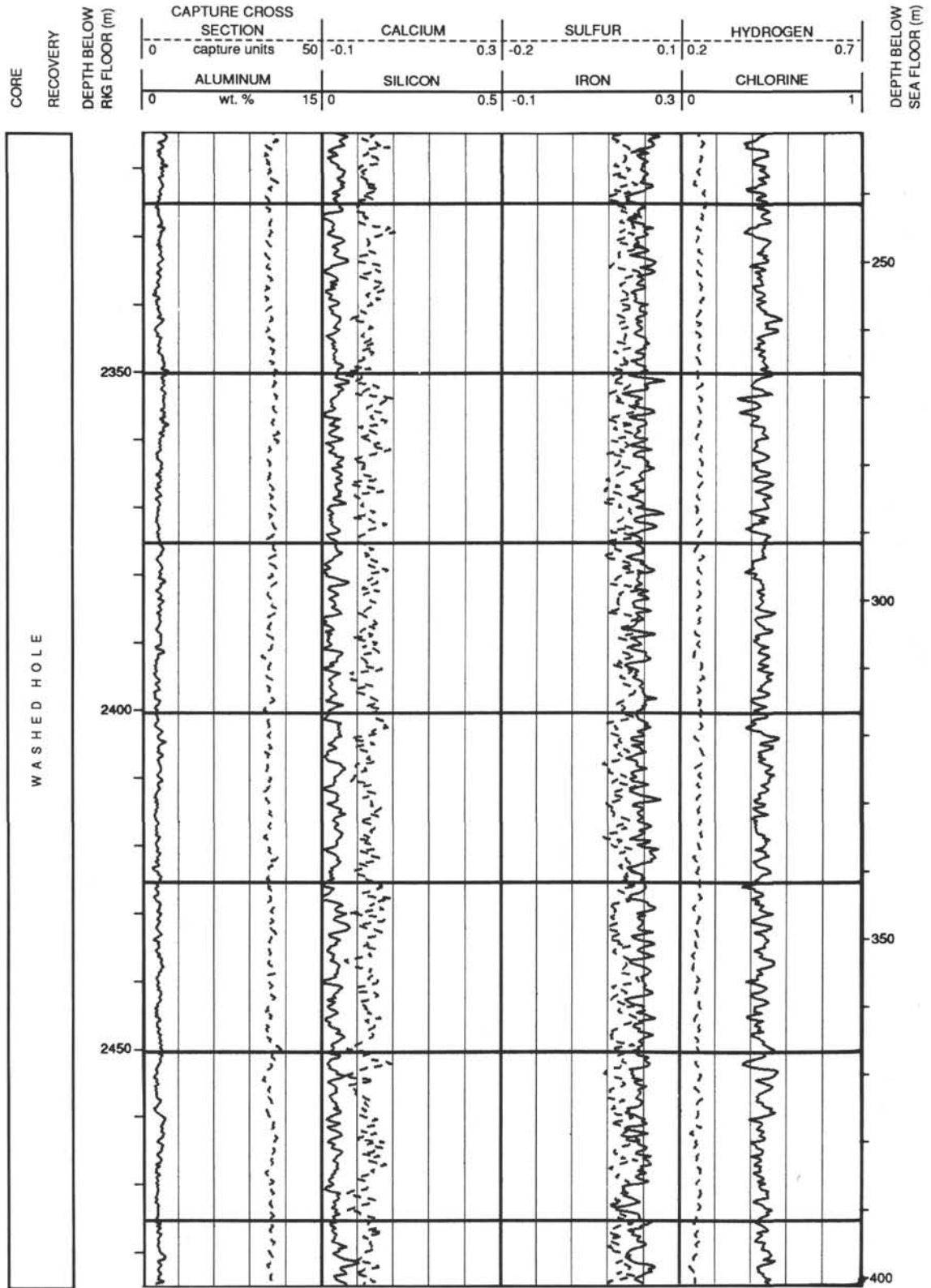
Hole 799B: Resistivity-Sonic-Gamma Ray Log Summary (continued)



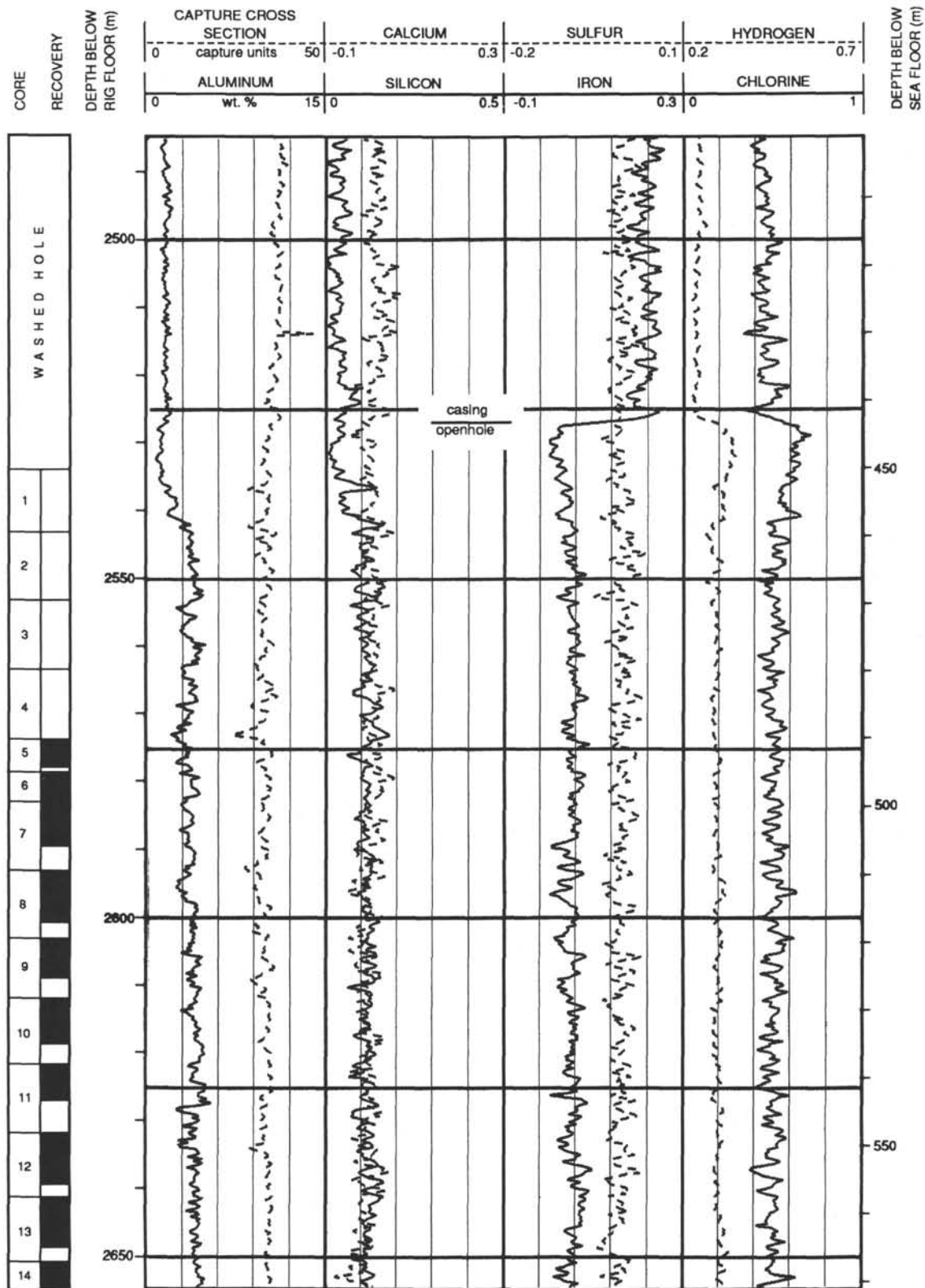
Hole 799B: Resistivity-Sonic-Gamma Ray Log Summary (continued)



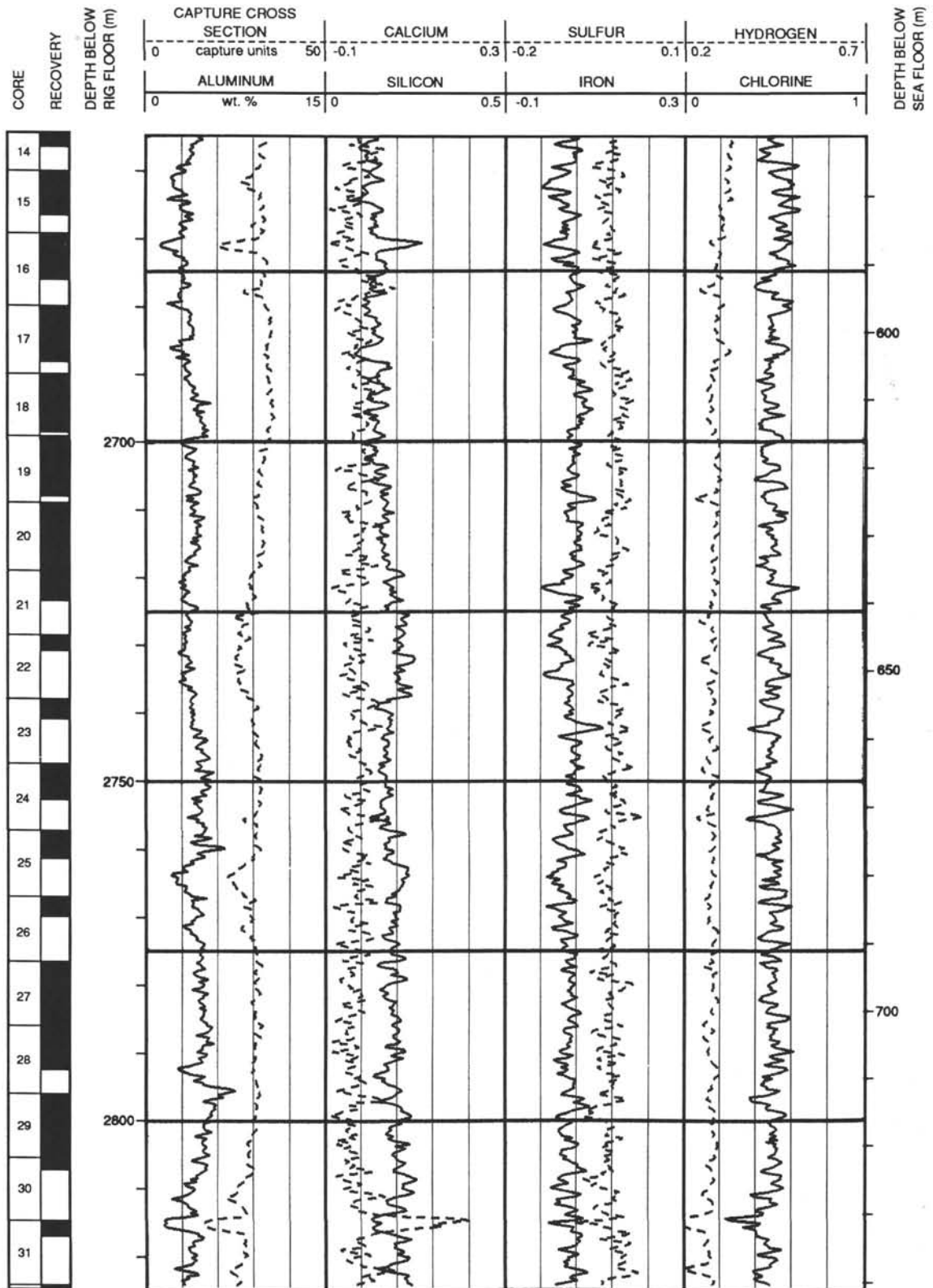
Hole 799B: Geochemical Log Summary



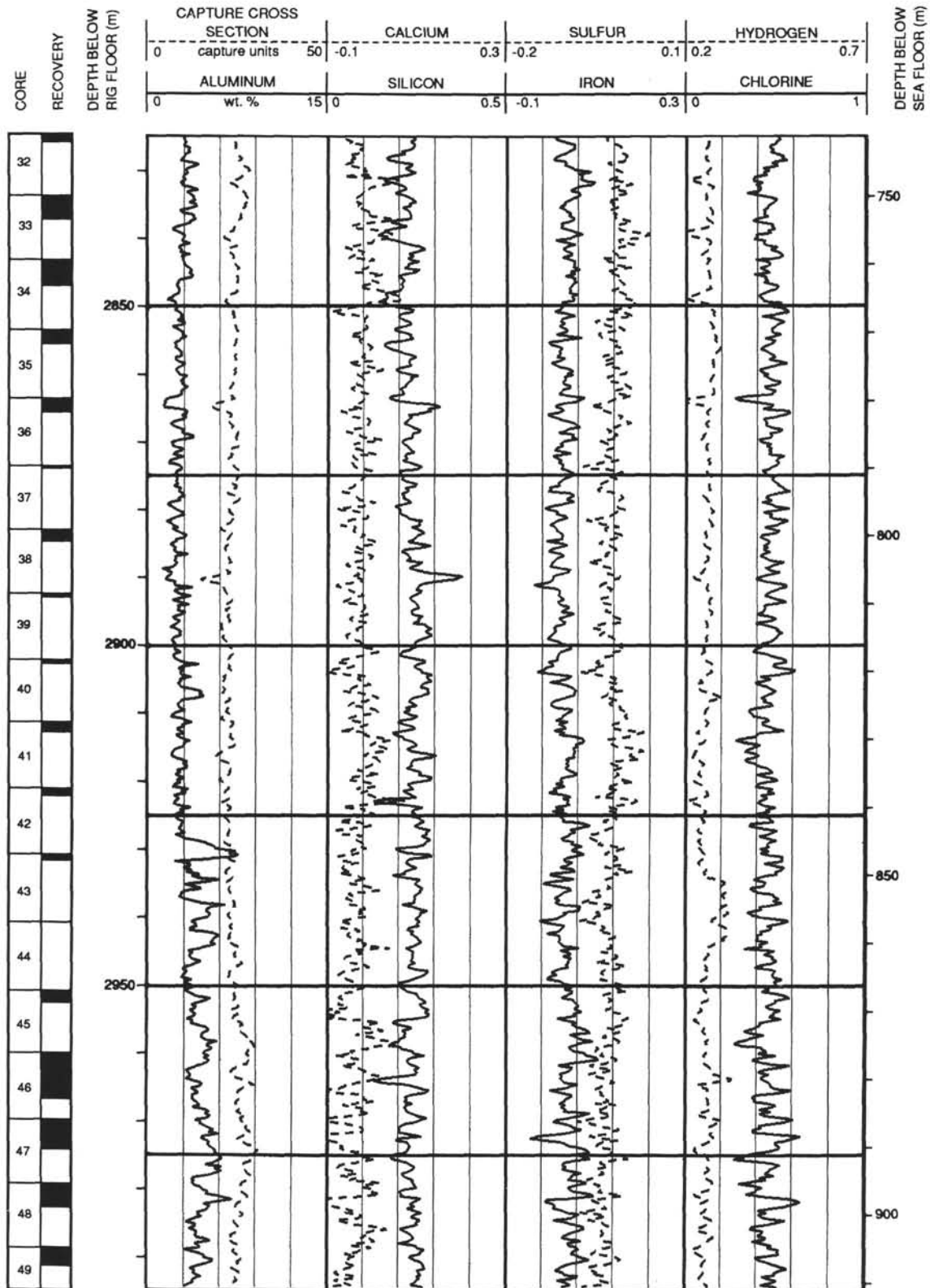
Hole 799B: Geochemical Log Summary (continued)



Hole 799B: Geochemical Log Summary (continued)



Hole 799B: Geochemical Log Summary (continued)



Hole 799B: Geochemical Log Summary (continued)

